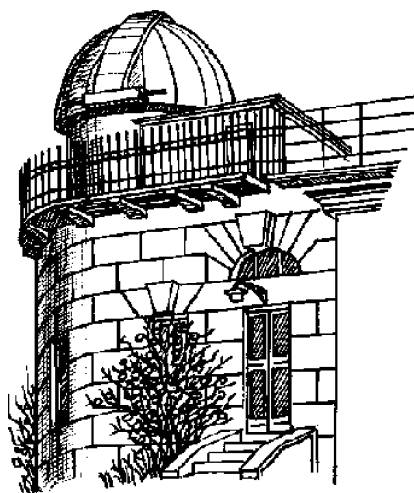


ODESSA ASTRONOMICAL PUBLICATIONS

**Volume 32
(2019)**



Astronomical Observatory
of I. I. Mechnikov Odessa National University

**ODESSA ASTRONOMICAL
PUBLICATIONS**

Volume 32
(2019)

Editorial Board:

- Editor-in-Chief* – Andrievsky S.M., Prof., RI "Astronomical Observatory"
Odessa I.I.Mechnikov National University
Executive Secretary – Kovtyukh V.V., ScD, RI "Astronomical Observatory"
Odessa I.I.Mechnikov National University
Technical editing – PhD Dragunova A.V., Strakhova S.L.

Advisory Editors:

Andronov I.L., ScD (Ukraine); Bagrov A.V., ScD (Russia); Bazey A.A., PhD (Ukraine); Eglitis I., PhD (Latvia); Ismailov N., PhD (Azerbaijan); Kim Y., ScD (Republic Korea); Koshkin N.I., PhD (Ukraine), Kucinskas A., PhD (Lithuania), Kudzej I., PhD (Slovakia); Lozitskiy V.G., ScD (Ukraine); Mishenina T.V., ScD (Ukraine); Novosyadlyj B.S., ScD (Ukraine); Panko E.A., ScD (Ukraine); Picazzio E., PhD (Brasil); Pilyugin L.S., ScD (Ukraine); Turner D., PhD (Canada); Udovichenko S.N., PhD (Ukraine); Ulyanov O.M., PhD (Ukraine); Vavilova I.B., PhD (Ukraine); Yushchenko A., PhD (Republic Korea); Zakhochay V., ScD (Ukraine); Zhuk A.I., ScD (Ukraine).

Address:

Astronomical Observatory, Odessa National University, E-mail: astronomical_observatory@onu.edu.ua
T. G. Shevchenko Park, Odessa, 65014, UKRAINE <http://www.astro-observ-odessa0.1gb.ua>
Tel.: + 38 048 722-84-42

The electronic version of the journal is on the web page: <http://oap.onu.edu.ua>

Одесские Астрономические Публикации
Издается с 1946 года (издание возобновлено в 1993 г., №6)

Свидетельство о государственной регистрации печатного средства массовой информации:
серия КВ № 14722-3693Р от 30.10.2008 г.

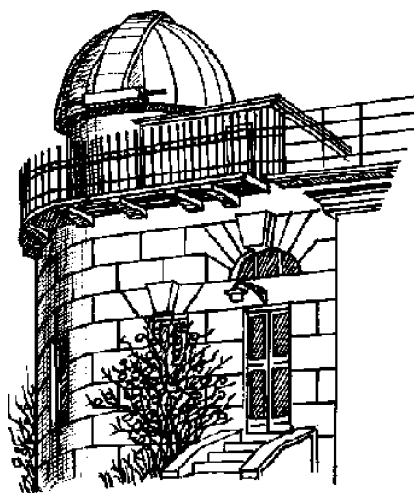
Журнал включен в список МОН Украины приказом МОНУ № 996 от 11.07.2017 г.

Печатается по решению Ученого совета НИИ "Астрономическая обсерватория" Одесского
национального университета имени И.И.Мечникова от 19 сентября 2019 г., протокол №6

Printed in UKRAINE
"PROMART" PUBLISHING COMPANY

ODESSA ASTRONOMICAL PUBLICATIONS

**Volume 32
(2019)**



CONTENTS

Cosmology, gravitation, astroparticle physics, high energy physics

Dmytriiev M.S., Gladush V.D. T-SOLUTIONS OF THE 5D KALUZA-KLEIN MODEL	6
Gladush V.D. CLASSICAL DESCRIPTIONS OF THE GEOMETRODYNAMICS OF CHARGED BLACK HOLES	10
Jenkovszky L., Shpenik A., Svintozelskyi V. GLUEBALLS	14
Khrantsov V.P., Dobrycheva D.V., Vasylenko M.Yu., Akhmetov V.S. DEEP LEARNING FOR MORPHOLOGICAL CLASSIFICATION OF GALAXIES FROM SDSS	21
Kotvytskiy A.T., Bronza E.S., Shablenko V.Yu. IMAGES DISTRIBUTION OF BINARY SYMMETRICAL GRAVITATIONAL LENS	24
Osmayev O.A., Shuvalova Yu.S., Bronza E.S., Matvienko K.I. SOME COROLLARY FACTS OF THE N-POINT GRAVITATIONAL LENS EQUATION IN A COMPLEX FORM	29
Panko E., Korshunov V., Yemelianov S., Zabolotnii V. LINEAR SUBSTRUCTURES IN GALAXY CLUSTERS	33
Serenkova I.A., Pankov A.A. INTERNATIONAL NUCLEAR DATA CENTERS NETWORK AND PROSPECTS OF ITS USE IN NUCLEAR POWER IN BELARUS	37
Tugay A.V., Shevchenko S.Yu. INFRARED COUNTERPARTS OF X-RAY GALAXIES	42
Vasylenko M.Yu., Dobrycheva D.V., Vavilova I.B., Melnyk O.V., Elyiv A.A. VERIFICATION OF MACHINE LEARNING METHODS FOR BINARY MORPHOLOGICAL CLASSIFICATION OF GALAXIES FROM SDSS	46

Astrophysics

Andrievsky S.M., Shereta A., Khrapaty S.V., Korotin S.A., Kovtyukh V.V., Kashuba V.I. DIFFUSE INTERSTELLAR BAND 6202 Å AS AN INDICATOR OF ORGANIC MATTER IN COSMOS: CEPHEID SPECTRA	52
Doikov D.N., Yushchenko A.V. OPTICAL LUMINOSITY OF ACTIVE GALACTIC NUCLEI AND THE INTENSITY OF ITS HARD RADIATION IN THE FORM OF PARTICLES AND QUANTA	55
Kuratova A.K., Miroshnichenko A.S., Zharikov S.V., Manset N., Khokhlov S.A., Raj A., Kusakin A.V., Reva I.V., Kokumbaeva R.I., Usenko I.A., Knyazev A.Y. SPECTROSCOPIC MONITORING OF THE B[E] OBJECTS FS CMa AND MO Cam	63
Mishenina T., Basak N., Kovtyukh V. CHEMICAL IMPRINTS IN ATMOSPHERIC ABUNDANCES IN PLANET- HOSTING STARS	66
Nazarenko V.V. THE ON- AND OFF-STATE GENERATIONS IN THE CASE OF THE THICK ACCRETION DISK AND UNDEFINED PRECESSION PERIOD. 3-D NUMERICAL HYDRODYNAMICAL SIMULATIONS IN ACCRETION DISK IN MICROQUASAR CYG X-1	70
Oknyansky V.L., Winkler H., Tsygankov S.S., Lipunov V.M., Gorbovsyoy E.S., F. van Wyk, Buckley D.A.H., Tyurina N.V. DISCOVERY OF MORE CHANGING LOOK EVENTS IN NGC 1566	75
Pyatnytskiy M.Yu. USING CONSUMER-GRADE DSLR CAMERA AND SMALL TELESCOPE TO FIND NEW VARIABLE STARS	79
Udovichenko S.N., Kovtyukh V.V., Keir L.E. LITHIUM-RICH CLASSICAL CEPHEID V1033 CYG: EVOLUTIONARY STATUS	83
Usenko I.A., Miroshnichenko A.S., Danford S., Kovtyukh V.V. PULSATIONAL ACTIVITY OF THE SMALL-AMPLITUDE CEPHEID POLARIS (α UMi) IN 2018-2019	87
Usenko I.A., Kniazev A.Yu., Katkov I.Yu., Kovtyukh V.V., Mishenina T.V., Miroshnichenko A.S., Turner D.G. SPECTROSCOPIC INVESTIGATIONS OF GALACTIC CLUSTERS WITH ASSOCIATED CEPHEID VARIABLES. III. COLLINDER 394 AND BB SGR	91

Radioastronomy

Isaeva E.A. FADING OF THE CONTINUUM OF NOISE STORMS IN THE DECAMETER RANGE RELATED TO CME	97
Orlov V.V., Lytvynenko O.A., Galanin V.V. MULTI-FREQUENCY RADIO INTERFEROMETRY ALGORITHM.....	100
Panishko S.K., Lytvynenko O.A. FREQUENCY DEPENDENCE OF THE IONOSPHERE SCINTILLATION PARAMETERS ON THE OBSERVATIONS OF COSMIC RADIO SOURCES AT THE DECAMETER WAVE RANGE	103
Tsvyk N.O. JOVIAN DECAMETER RADIO EMISSION: TO THE QUESTION ON THE SIZE OF SOURCES	105
Vasilenko N.M., Sidorchuk M.A. UTR-2 LOW FREQUENCY CONTINUUM SURVEY OF THE NORTHERN SKY. PART II.....	110

Sun, solar activity and astrobiology

Chornogor S.N., Kondrashova N.N. MULTI-WAVELENGTH OBSERVATIONS OF A LARGE SOLAR FLARE.....	114
Isaeva E.A. APPROXIMATION OF THE INTEGRAL ENERGY SPECTRUM OF PROTONS OF SCR IN THE RANGE OF > 1-850 MEV	119
Isaeva E.A. RELATIONSHIP OF THE PROTON FLUX INTENSITY WITH RELATIVE DISTANCE BETWEEN HARMONICS OF TYPE II RADIO BURSTS IN THE RANGE 25-180 MHZ	122
Lozitsky V.G., Baranovsky E.A., Lozitska N.I., Tarashchuk V.P. EVIDENCES FOR STRONG MIXED-POLARITY MAGNETIC FIELDS IN AREA OF A SEISMIC SOURCE ASSOCIATED WITH LARGE PROTON SOLAR FLARE	125
Pasechnik M.N. SOLAR PLASMA DYNAMICS DURING THE FORMATION AND DEVELOPMENT OF ELLERMAN BOMBS PAIR	130
Ryabov M.I., Sobitnyak L.I. STUDY OF EFFECTS OF LUNAR TIDAL WAVE PASSAGE IN UPPER ATMOSPHERE OF EARTH ACCORDING TO MONITORING DATA AT RADIO TELESCOPE «URAN-4» RI NANU	134
Sidorenkov N.S., Wilson Ian PEREGEE-SZYGY TIDES IN ATMOSPHERE	137

Solar system

Eglitis I. BALDONE OBSERVATORY IN THE CIRCLES OF TIME	142
Eglitis I. INVESTIGATION OF NEO ASTEROIDS 2006 VB14 AND 1986 DA.....	146
Kaliuzhnyi M., Zhang Z., Bushuev F., Shulga O., Bezrukovs V., Reznichenko O., Melnychuk S., Malynovskyi Y. ONGOING OPERATION AND PERSPECTIVES OF SIMPLE VLBI NETWORKS OF GEOSTATIONARY SATELLITES MONITORING	148
Konovalova N.A., Gorbanev Yu.M., Davruqov N.H. EVOLUTION OF COMET-LIKE ORBITS OF METEORITEPRODUCING GROUPS AND THEIR PARENT BODIES	151
Koshkin N., Melikyants S., Korobeinikova E., Shakun L., Strakhova S., Kashuba V., Romanyuk Ya., Terpan S. SIMULATION OF THE ORBITING SPACECRAFT TO ANALYSIS AND UNDERSTAND THEIR ROTATION BASED ON PHOTOMETRY	158
Kriuchkovskiy V., Bushuev F., Kaliuzhnyi M., Khalaley M., Kulichenko M., Shulga O. FIRST RESULTS OF CLARIFYING OF ORBITAL ELEMENTS OF LOW-ORBIT SPACECRAFT USING OBSERVATIONS OF THE RI "MAO" DOPPLER STATION	162
Kulichenko M.O., Shulga O.V., Gorbanev Yu.M. RESULTS OF POSITIONAL AND PHOTOMETRIC MEASUREMENTS OF METEOR TRAJECTORIES OBSERVED IN MYKOLAIV 2017-2018	165
Manchenko L.D. MODEL OF GRAVITATIONAL EFFECTS IN SATURN'S RINGS.....	168
Tevjashev A.D., Shostko I.S., Neofitnyi M.V., Kolomiyets S.V., Kyrychenko I.Yu., Pryimachov Yu.D. MATHEMATICAL MODEL AND METHOD OF OPTIMAL PLACEMENT OF OPTICAL-ELECTRONIC SYSTEMS FOR TRAJECTORY MEASUREMENTS OF AIR OBJECTS AT TEST.....	171
Vidmachenko A.P., Steklov A.F. MATERIAL OF COMETARY NUCLEI AND ASTEROIDS CAN BE STUDIED IN THE EARTH'S ORBIT ...	176

Astroinformatics

Akhmetov V.S., Andruk V.M., Protsyuk Yu.I., Relke H., Eglitis I. NEW ASTROMETRIC REDUCTION OF THE SUPERCOSMOS PLATE ARCHIVE: FIRST RESULTS	178
Andruk V., Eglitis I., Protsyuk Yu., Akhmetov V., Pakuliak L., Shatokhina S., Yizhakevych O. PHOTOMETRY OF STARS FOR ASTRONEGATIVES WITH A SINGLE EXPOSURE	181
Andruk V.M., Pakuliak L.K., Eglitis I., Yuldoshev Q., Mullo-Abdolv A., Shatokhina S.V., Yizhakevych O.M., Protsyuk Yu.I., Relke H., Akhmetov V.S., Muminov M.M., Ehgamberdiev Sh.A., Kokhirova G. ON THE FON ASTROPLATE PROJECT ACCOMPLISHMENT	185
Eglitis I., Yizhakevych O., Shatokhina S., Protsyuk Yu., Andruk V. ASTEROID SEARCH RESULTS FOR DIGITIZED ASTROPLATES OF 1.2m TELESCOPE IN BALDONE....	189
Maigurova N.V., Protsyuk Yu.I. PROBABILITIES OF PHYSICAL LINK BETWEEN THE COMPONENTS OF THE SELECTED MULTIPLE SYSTEMS FROM WDS CATALOG	192
Protsyuk Yu.I., Kovalchuk O.M., Andruk V.M. COMPARISON OF THE RESULTS OF PROCESSING OF CCD OBSERVATIONS OF SELECTED OPEN CLUSTERS	196
Shatokhina S.V., Kazantseva L.V., Andruk V.M. THE RE-PROCESSING RESULTS OF PHOTOGRAPHIC OBSERVATIONS OF ASTEROIDS WITH GAIA CATALOG AT THE MAO NAS OF UKRAINE	199
Shatokhina S.V., Yizhakevych O.M., Protsyuk Yu.I., Kazantseva L.V., Pakuliak L.K., Eglitis I., Relke H., Yuldoshev Q.X., Mullo-Abdolv A.Sh., Andruk V.M. ON THE "SOLAR SYSTEM BODIES" ASTROPLATE PROJECT OF THE UKRAINIAN VIRTUAL OBSERVATORY	203
Yuldoshev Q., Andruk V., Muminov M. THE ASTROMETRIC AND PHOTOMETRIC RESULTS OF DIGITIZED PLATES ON EPSON EXPRESSION 10000XL SCANNER WITH DIFFERENT RESOLUTIONS	208

Historical reviews

Ryazantsev G.B., Lavrenchenko G.K., Nedovesov S.S. THE PROBLEM OF "ZERO ELEMENTS" IN THE WORKS OF D. I. MENDELEEV. NEUTRON MATTER AS A PRIMARY COSMOLOGICAL AND MODERN DARK MATTER OF THE UNIVERSE ...	211
--	-----

COSMOLOGY, GRAVITATION, ASTROPARTICLE PHYSICS, HIGH ENERGY PHYSICS

DOI:<http://dx.doi.org/10.18524/1810-4215.2019.32.181750>

T-SOLUTIONS OF THE 5D KALUZA-KLEIN MODEL

M.S. Dmytriiev¹, V.D. Gladush²¹ Oles Honchar Dnipro National University,
Dnipro, Ukraine, oct.gaster@gmail.com² Oles Honchar Dnipro National University,
Dnipro, Ukraine, vgladush@gmail.com

ABSTRACT. We consider spherically-symmetric solution of the 5D Kaluza-Klein theory, which metric coefficients depend on time only. When we construct the appropriate 4+1 splitting of the five-dimensional space and then perform the conformal transformation we get the cosmological model with hypercylinder topology. There are scalar and electromagnetic fields with contact interaction. Besides this, these fields correspond to the inner region of the black hole in the appropriate choice of integration constants. Using 2+2+1 splitting technics and reduction we get the lagrangian of the model. After that we build the canonical formalism of the theory, which admits constraints. These are Hamilton, momentum and Gauss secondary constraints. Momentum constraint is satisfied trivially in the homogeneous case. From the Hamilton constraint we obtain the Einstein-Hamilton-Jacobi equation. 5D metric components arise from the solutions of this equation. Main puprpose of this work is to investigate properties of this metric. It turns out that the configurations with removable and unremovable electric field are possible to exist in this case [Gladush et al., 2015]. Removable electric field can be eliminated with 5D coordinate transformation. Time dependence of the spacetime metric conformal factor is researched. This conformal factor corresponds to the size of the Universe in cosmological model. It turns out that such model describes gravitational collapse of the Universe in the distant future. However, depending on the integration constants signs, there can present some relatively small initial inflation.

Keywords: five-dimensional space-time: Kaluza-Klein model; time-dependent solution: black hole model, cosmological model. **АНОТАЦІЯ.** Будується і досліджується сферично-симетричний розв'язок п'ятивимірної теорії Калуци-Клейна, метричні коефіцієнти якої залежать тільки від часу. При належному 4+1- розщепленні п'ятивимірного простору та конформному відображенні, вони відповідають космологічній моделі з гіперциліндричною топологією зі скалярним та електромагнітним полями, що взаємодіють між собою контактним чином. З

іншого боку, при відповідному виборі сталих інтегрування, вони відповідають внутрішній частині чорної діри п'ятивимірної теорії. За допомогою техніки 2+2+1-розщеплення простору і всіх супутніх величин та відповідної редукції отримується лагранжіан моделі. На основі одержаного лагранжіану будується канонічний формалізм теорії, що містить множники Лагранжа. Цим множникам відповідають вторинні гамільтонова, імпульсна та гаусова в'язі. У однорідному випадку імпульсна в'язь виконується тотожно, а з гамільтонової випливає рівняння Ейнштейна-Гамільтона-Якобі. Із розв'язків цього рівняння отримуємо компоненти метрики п'ятивимірного простору. Основний зміст цієї роботи полягає у вивченні цієї метрики. Виявляється, що у випадку, що розглядається, можливі розв'язки з усуним і не усуним електричним полем [Gladush et al., 2015]. У першому випадку, за допомогою відповідного п'ятивимірного координатного перетворення електричне поле може бути усунуто. Досліджується часова залежність конформного множника просторово-часової метрики, який описує розмір Всесвіту у космологічній моделі. Виявляється, що така модель описує гравітаційний колапс Всесвіту у віддаленому майбутньому. Втім, залежно від знаку сталих інтегрування, у цій космологічній моделі може бути присутнє початкове порівняно незначне розширення.

Ключові слова: п'ятивимірний простір-час: теорія Калуци-Клейна; Т-розв'язок: модель чорної діри, космологічна модель.

Used conventions: Greek indices μ, ν, ρ etc. run from 0 to 3, latin indices from the beginning of alphabet a, b, c etc. get values 0 and 1. Latin indices from the middle of alphabet i, j, k etc. get values 2 and 3.

1. Introduction

In the Kaluza-Klein theory, we start from the 5D space metrics and Einstein-Hilbert action for 5D gravitational field (ψ – 4D scalar field, A_μ – potential of the

electromagnetic field):

$$ds^{(5)2} = g_{\mu\nu} dx^\mu dx^\nu - e^{2\psi} (dz + A_\mu dx^\mu)^2 \quad (1)$$

$$\mathcal{S} = \int \sqrt{-g^{(5)}} \mathcal{R}^{(5)} dz d^4x \quad (2)$$

Here $\mathcal{R}^{(5)}$ and $\sqrt{-g^{(5)}}$ are the scalar curvature and metrics determinant for the 5D manifold, respectively. The last one consists of ordinary 4D space-time and the fifth dimension (which is parametrized by z coordinate). It is also assumed in the Kaluza-Klein theory that there is a Killing vector along this fifth dimension. Because of this assumption, geometrical quantities in our model do not depend on z as soon as such dependence does not have physical manifestation in the theory. From these facts after certain transformations (2) has the following form ($\mathcal{F}_{\mu\nu}$ is an electromagnetic strength tensor):

$$\mathcal{S} = \Delta l \int \left(\tilde{\mathcal{R}}^{(4)} + \frac{3}{2} (\tilde{\nabla}\psi)^2 + \frac{1}{4} e^\psi \mathcal{F}_{\rho\nu} \mathcal{F}^{\rho\nu} \right) \sqrt{-\tilde{g}} d^4x$$

$$\tilde{\mathcal{R}}^{(4)} = \tilde{\mathcal{R}}^{(4)}[\tilde{g}_{\mu\nu}] \quad g_{\mu\nu} = e^{-\psi} \tilde{g}_{\mu\nu} \quad (3)$$

In present article we research the spherically-symmetric solutions of the 5D Kaluza-Klein model, which depends on time only. Such solutions can represent the inner region of the black hole with scalar field or a cosmological model, if the event horizon of that field configuration does not exist.

We are going to work out the field model solutions using Hamilton-Jacobi method and to demonstrate usefulness of that methods for analysis of the homogeneous field configurations. Solution of the same problem can be found in [Hongya Liu et al., 1993], but, contrary to our treatment, that result was obtained through Einstein equations.

2. Initial treatment

In the spherically-symmetric case 4D spacetime metrics in ADM-parametrisation writes:

$$g_{\mu\nu} dx^\mu dx^\nu = e^{-\psi} \left[N^2 dt^2 - e^\lambda (dr + N^r dt)^2 - e^\rho d\sigma^2 \right]$$

$$d\sigma^2 = d\theta^2 + \sin^2 \theta d\phi^2 \quad (4)$$

Here λ , ψ and ρ are the dynamical variables of the model, N and N^r are the Lagrange multipliers. EM field potential has only 2 non-zero components, namely A_1 , which is a dynamical variable, and A_0 – Lagrange multiplier. Therefore, Hamilton function of the model depends on the variables λ , ρ , ψ , A_1 and their conjugate momentums P_λ , P_ρ , P_ψ , P_{EM} . Using (3) and (4), in the spherically-symmetric case we obtain from canonical approach this set of constraints:

$$\mathcal{H}_\perp \approx 0 \quad \mathcal{H}_r \approx 0 \quad \partial_r P_{EM} \approx 0 \quad (5)$$

These equalities manifest that action \mathcal{S} does not depend on time reparametrizations and diffeomorphisms of the r and z coordinates, respectively. Because of the field configuration homogeneity, second and third constraints are satisfied automatically. Particularly, from the third constraint we have that $P_{EM} = Q(t)$, where Q is an electric charge located in the spatial coordinate origin. Therefore, we have only one equation in our model, namely the Hamilton constraint $\mathcal{H}_\perp \approx 0$:

$$\mathcal{H}_\perp = P_\lambda^2 - 2P_\lambda P_\rho + \frac{1}{3} P_\psi^2 + Q^2 e^{\lambda-3\psi} - 4\kappa^2 e^{\lambda+\rho} = 0$$

$$\kappa = \int_0^{2\pi} d\phi \int_0^\pi \sin \theta d\theta \int_{r_1}^{r_2} dr \int_{z_1}^{z_2} dz = 4\pi \Delta z \Delta r \quad (6)$$

As we can see, \mathcal{H}_\perp does not contain A_1 , so the corresponding momentum is conserved – $Q = const.$

3. Einstein-Hamilton-Jacobi equation

3.1. Equation

Let us introduce a new set of generalized coordinates in our model:

$$\omega = \lambda - 3\psi \quad \xi = \lambda + \rho \quad \eta = \psi \quad (7)$$

New canonically conjugate momentums:

$$P_\lambda = P_\omega + P_\xi \quad P_\rho = P_\xi \quad P_\psi = -3P_\omega + P_\eta \quad (8)$$

Using (7) and (8) we simplify the expression for Hamilton constraint. Substituting momentums with derivatives of the action \mathcal{S} with respect to the appropriate conjugate coordinates, we get:

$$\left(\frac{\partial \mathcal{S}}{\partial \omega} \right)^2 - \left(\frac{\partial \mathcal{S}}{\partial \xi} \right)^2 + \frac{1}{3} \left(3 \frac{\partial \mathcal{S}}{\partial \omega} - \frac{\partial \mathcal{S}}{\partial \eta} \right)^2 + Q^2 e^\omega - 4\kappa^2 e^\xi = 0 \quad (9)$$

We have obtained the Einstein-Hamilton-Jacobi equation for our field configuration. Here is a solution of this equation:

$$\mathcal{S} = QA_1 + \frac{C_2}{4} \omega + C_2 \eta + s_\xi \int d\xi \sqrt{C_1^2 - 4\kappa^2 e^\xi} +$$

$$+ \frac{1}{2} s_\omega \int d\omega \sqrt{C_1^2 - \frac{1}{12} C_2^2 - Q^2 e^\omega}$$

C_1 and C_2 denote integration constants, s_ω and s_ξ are the sign constants – choosing them be equal to 1 or –1 we can get all 4 families of solutions for (9). As it mentioned in Hamilton-Jacobi method, now we differentiate \mathcal{S} with respect to C_1 , C_2 and Q :

$$\frac{\partial \mathcal{S}}{\partial C_1} = \beta_1 \quad \frac{\partial \mathcal{S}}{\partial C_2} = \beta_2 \quad \frac{\partial \mathcal{S}}{\partial Q} = \beta_Q$$

Here β_1 , β_2 and β_Q are some constants.

$$\begin{aligned}\beta_1 &= s_\xi C_1 \int \frac{d\xi}{\sqrt{C_1^2 - 4\kappa^2 e^\xi}} + \frac{C_1}{2} s_\omega \int F(\omega) d\omega \\ \beta_2 &= \frac{1}{4} \omega + \eta - \frac{1}{24} s_\omega C_2 \int F(\omega) d\omega \\ \beta_Q &= A_1 - \frac{1}{2} s_\omega \int Q F(\omega) e^\omega d\omega\end{aligned}\quad (10)$$

$F(\omega)$ function denotes:

$$F(\omega) = \left(\sqrt{C_1^2 - \frac{1}{12} C_2^2 - Q^2 e^\omega} \right)^{-1}$$

Constants β_1 , β_2 and β_Q describes the initial conditions, that are values of field variables at certain t_0 . As t_0 we can use the event horizon coordinate (see next section) of the field configuration, or just extremum point of the $R(t)$ function.

3.2. Time-dependent solution

Solving (10) with respect to ω , ξ , ρ and A_1 we obtain expressions for three field variables as functions of the fourth one and the integration constants. Particularly, ξ , ρ and A_1 can be expressed as functions of ω . However, it is convenient for further treatment to work out the field potentials as functions of time variable t . Due to the model reparametrization invariance, time coordinate can be chosen arbitrarily. We introduce t variable in the following way:

$$t = \int F(\omega) d\omega \quad (11)$$

We emphasize that time dependency could be chosen differently, that is using momentum definitions in the Lagrange and Hamilton-Jacobi approaches, e. g.:

$$P_\lambda = \frac{\partial \mathcal{L}}{\partial \dot{\lambda}} = \frac{\partial \mathcal{S}}{\partial \lambda}$$

The left part of this equation contains velocities and multiplier $N(t)$, but the right part consists only of coordinates. Choosing $N(t)$ and solving this differential equation we obtain time dependency.

Using (7), we write down components of the space-time metrics, EM field strength and scalar field as functions of time ($Q \neq 0$):

$$N = \frac{\kappa e^\rho e^{\frac{\lambda-\psi}{2}} \frac{d\rho}{dt}}{\frac{C_2}{4} + \frac{1}{2F(\lambda-3\psi)} s_\omega + s_\xi \sqrt{C_1^2 - 4\kappa^2 e^{\lambda+\rho}}} \quad (12)$$

$$e^{\lambda-\psi} = \frac{(C_1^2 - \frac{1}{12} C_2^2)}{Q^2} \cdot \frac{\exp[2\beta_2 + s_\omega \frac{1}{12} C_2 t]}{\cosh\left(\frac{t}{2} \sqrt{C_1^2 - \frac{1}{12} C_2^2}\right)} \quad (13)$$

$$e^{\rho-\psi} = R^2 = \frac{Q^2 C_1^2}{4\kappa^2 (C_1^2 - \frac{1}{12} C_2^2)} \cdot \frac{\exp[-4\beta_2 - s_\omega \frac{1}{6} C_2 t]}{\cosh^2\left(\beta_1 + s_\xi s_\omega \frac{1}{4} |C_1| t\right)} \quad (14)$$

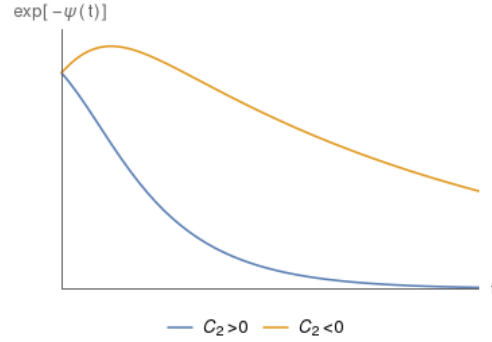


Fig. 1: Qualitative time dependency of the conformal factor $e^{-\psi}$ ($s_\omega = 1$)

$$\mathcal{F}_{01} = \frac{dA_1}{dt} = \frac{C_1^2 - \frac{1}{12} C_2^2}{-2s_\omega Q} \cosh^{-2} \left(\frac{t}{2} \sqrt{C_1^2 - \frac{1}{12} C_2^2} \right) \quad (15)$$

$$\psi = \beta_2 + s_\omega \frac{1}{24} C_2 t + \frac{1}{2} \ln \left[\cosh \left(\frac{t}{2} \sqrt{C_1^2 - \frac{1}{12} C_2^2} \right) \right] \quad (16)$$

Here we chose Lagrange multiplier N^r be equal to zero. As the field configuration is homogeneous such choice does not affect solutions listed above.

4. Solution properties

4.1. Event horizon

By definition, event horizon is an isotropic surface of the scale factor R :

$$(\nabla R)^2 \Big|_{t=t_g} = 0$$

Here $t = t_g$ denotes event horizon coordinate. Besides this, we require that scalar field ψ is equal to zero on the horizon (black hole does not have scalar "hairs"). From the following equalities, we obtain the event horizon coordinate t_g and integration constants condition under which field configuration has such horizon:

$$\frac{1}{N^2} \left(\frac{dR}{dt} \right)^2 \Big|_{t=t_g} = 0 \quad \psi(t = t_g) = 0 \quad (17)$$

From the first equality we have this complex of equations with respect to t_g :

$$\begin{cases} \frac{C_2}{4} + \frac{1}{2} s_\omega \sqrt{C_1^2 - \frac{1}{12} C_2^2 - Q^2 e^{\lambda-\psi} e^{-2\psi}} + \\ + s_\xi \sqrt{C_1^2 - 4\kappa^2 e^{\lambda+\rho}} \Big|_{t=t_g} = 0 \\ \tanh\left(\beta_1 + s_\xi s_\omega \frac{1}{4} |C_1| t_g\right) = -s_\xi \frac{1}{3} \frac{C_2}{|C_1|} \end{cases} \quad (18)$$

The first equation is transcendental, while the second immediately writes:

$$t_g = -\frac{4\beta_1 s_\xi s_\omega}{|C_1|} + s_\xi s_\omega \frac{4}{|C_1|} \operatorname{arcth} \left(-s_\xi \frac{1}{3} \frac{C_2}{|C_1|} \right) \quad (19)$$

Putting (19) to the second equation in (17) (using expression for ψ in (16)) we get the event horizon existence condition for integration constants.

Having (19) and initial data $\psi(t = t_g) = 0$ we get rid of β_1 and β_2 in the expressions for event horizon radius R_g and scalar field:

$$R_g = \frac{QC_1}{2\kappa\sqrt{C_1^2 - \frac{1}{12}C_2^2}} \frac{\cosh\left(\frac{t_g}{2}\sqrt{C_1^2 - \frac{1}{12}C_2^2}\right)}{\cosh\left[\operatorname{arcth}\left(-s_\xi\frac{1}{3}\frac{C_2}{|C_1|}\right)\right]} \quad (20)$$

$$\psi(t) = s_\omega\frac{1}{24}C_2(t - t_g) + \frac{1}{2}\ln\frac{\cosh\left(\frac{t}{2}\sqrt{C_1^2 - \frac{1}{12}C_2^2}\right)}{\cosh\left(\frac{t_g}{2}\sqrt{C_1^2 - \frac{1}{12}C_2^2}\right)} \quad (21)$$

4.2. Singularities of the spacetime geometry

In order to investigate geometrical singularities in present configuration we calculate the Kretchman invariant $K(t)$ for the obtained spacetime metrics (12)-(14). Singularities of this invariant as function of time (let us denote them as t_s) point to the geometrical singularities. By definition:

$$K(t) = \mathcal{R}_{\mu\nu\rho\sigma}^{(4)}\mathcal{R}^{(4)\mu\nu\rho\sigma}$$

It is quite complicated to get it in the direct calculation from spacetime metrics components. Because of this, we apply the 2+2 splitting technique to this issue. Firstly, let us represent spacetime manifold as a tensor product $\mathbb{R}^2 \otimes \mathbb{S}^2$, where the first multiplier (we denote it as $M^{(I)}$) is a two-dimensional manifold with time and radial coordinates, and the second one (which is denoted as $M^{(II)}$) is a two-dimensional sphere with radius $R(t)$. Secondly, we write tensor quantities in the vector basis adapted for splitting. According to this, Kretchman invariant can be written as follows:

$$K(t) = \mathcal{R}_{abde}^{(4)}\mathcal{R}^{(4)abde} + 2\mathcal{R}_{aibj}^{(4)}\mathcal{R}^{(4)aibj} + \mathcal{R}_{ikjl}^{(4)}\mathcal{R}^{(4)ikjl}$$

Using 2+2 splitting, we get:

$$\mathcal{R}_{abde}^{(4)} = \mathcal{R}_{bed}^{(I)f}g_{af} \quad \mathcal{R}_{aibj}^{(4)} = \frac{1}{R}(R_{,a})_{,b}\delta_{ij}$$

$$\mathcal{R}_{ikjl}^{(4)} = -\mathcal{R}_{jlk}^{(II)m}\delta_{im} - \frac{(\nabla R)^2}{R^2}(\delta_{kl}\delta_{ij} - \delta_{jl}\delta_{ik})$$

Here $\mathcal{R}_{bed}^{(I)f}$ and $\mathcal{R}_{jlk}^{(II)m}$ are components of the Riemann tensors of $M^{(I)}$ and $M^{(II)}$, respectively. Covariant derivatives $(R_{,a})_{,b}$ are calculated using metrics on $M^{(I)}$. Finally, we have:

$$K(t) = \frac{4}{R^4}\left[1 + (\nabla R)^2 + (\nabla R)^4\right] + \frac{4}{R^2}(R_{,a})_{,b}(R_{,d})_{,e}g^{ad}g^{be} + \mathcal{R}^{(I)2}(t) \quad (22)$$

Exact expression for the (22) as a function of time is quite long, so we do not show it here. As follows from our analysis, (22) diverges while two conditions are satisfied – when $R(t)$ or $N(t)$ become equal to zero. From (12)-(16) we have that the first condition is fulfilled when $t_s \rightarrow \infty$. It means that point $t \rightarrow \infty$ is a singularity of the black hole. Indeed, scale factor in that point is equal to zero – $R(t \rightarrow \infty) = 0$. So there is a gravitational collapse to the singularity in infinitely distant future for observer in the selected reference frame. In other words, it is geometrically impossible to build a two-dimensional sphere with non-zero radius and volume in such space.

The second condition is fulfilled if t_s satisfies the following equation:

$$-s_\omega\frac{1}{8}C_2 - s_\xi s_\omega\frac{1}{2}|C_1|\tanh\left(\beta_1 + s_\xi s_\omega\frac{1}{4}|C_1|t_s\right) + \frac{1}{4}\sqrt{C_1^2 - \frac{1}{12}C_2^2}\tanh\left(\frac{t_s}{2}\sqrt{C_1^2 - \frac{1}{12}C_2^2}\right) = 0 \quad (23)$$

Conclusion

As it was shown in the analysis above, homogeneous field configuration in the 5D Kaluza-Klein model represents charged black hole with the scalar field inside, or the cosmological model, if event horizon is absent. It follows from the time dependencies of the conformal factor $e^{-\psi(t)}$ (which are shown on fig.1) that such model describes gravitational collapse of a homogeneous universe when $C_2 \geq 0$ and sequential inflation and collapse when $C_2 < 0$.

Solution (12)-(16) contains integration constants C_1 and C_2 , which have the following physical sense. If our field configuration has event horizon, these constants are functions of the central mass, electric and scalar charges of the black hole. Exact view of these functions is a subject for further research.

References

- Bronnikov K.A., Rubin S.G.: 2008, Lectures on Gravity and Cosmology, Moscow, Moscow Engineering Physics Institute, 2008, 460 pp. (in Russian).
 Gladush V.D., Al-Shawaf Nadim: 2015, *Odessa Astron. Publ.*, **2**, 28.
 Hongya Liu et al.: 1993, *J. Math. Phys.*, **34**, 9.
 Gladush V.D.: 1979, *Sov. Phys. J.*, **22**, **11**, 1172.

DOI:<http://dx.doi.org/10.18524/1810-4215.2019.32.181751>

CLASSICAL DESCRIPTIONS OF THE GEOMETRODYNAMICS OF CHARGED BLACK HOLES

V.D. Gladush

Oles Honchar Dnipro National University, Dnipro, Ukraine,
vgladush@gmail.com

ABSTRACT. Analytical aspects of the classical geometrodynamics of charged black holes are considered. The classical model of the charged BHs is the spherically symmetric configuration of the electromagnetic and gravitational fields in GR. The feature of such dynamic systems is that, in addition to the Killing vector, they admit two motion integrals: the total mass M and the charge Q of the configuration. Using these conservation laws, as well as the Hamiltonian constraint, the momenta as functions of configuration variables are found. In addition, the integrability conditions for the momenta as functional derivatives of the action are satisfied. This allows us to calculate the functional of action, which is a solution of the Einstein-Hamilton-Jacobi equation. Variations of action functional with respect to the mass M and charge Q lead to the solution of the Einstein equations in the configuration space.

Keywords: electromagnetic and gravitational fields, geometrodynamics, constraints, configuration space, Einstein-Hamilton-Jacobi equation.

АНОТАЦІЯ. Розглянуто аналітичні аспекти класичної геометродинаміки для сферично-симетричної (СС) конфігурації електромагнітного і гравітаційного полів ЗТВ. Особливістю цих конфігурацій є те, що вони допускають два інтеграла руху – загальну масу і заряд. Дія Ейнштейна-Гільберта для конфігурації після вимірної редукції за допомогою перетворення Лежандра зводиться до гамільтонової дії. Використовуючи закони збереження маси і заряду, а також гамільтонову в'яз, знайдені імпульси як функції змінних конфігурації. Крім того, виконуються умови інтегрованості імпульсів як функціональних похідних дії. Це дозволяє нам отримати функціонал дії як розв'язок рівняння Ейнштейна-Гамільтона-Якобі в функціональних похідних. Варіації функціоналу дії щодо маси M і заряду Q конфігурації призводять до траєкторіях руху в конфігураційному просторі.

Ключові слова: електромагнітне і гравітаційне поля, геометродинаміка, в'язи, конфігураційний простір, рівняння Ейнштейна-Гамільтона-Якобі.

1. Introduction

As is known, the space-time metric M^4 for a spherically symmetric (SS) configuration of the electromagnetic and gravitational fields in GR (as well as with the cosmological constant) admits the Killing vector. Therefore, in the R-region, when choosing Killing time, the fields do not have dynamic degrees of freedom. Therefore, to study the questions of quantization, in [Gladush 2016, 2018], we limited ourselves to considering the T-region, where these fields have a dynamic meaning. The limited nature of this direction dictates us to consider a more general, geometrodynamics approach to the SS configuration of electromagnetic and gravitational fields [Kuchar 1994, Louko 1996, Makela 1998]. In this approach, a $3 + 1$ -splitting of M^4 into a one-parameter family of space-like hypersurfaces is constructed. The corresponding parameter labeling the hypersurfaces determines the time coordinate of a normal reference frame and describes the evolution of geometric quantities defined on these hypersurfaces. This introduces the dynamics of objects defined on these hypersurfaces in M^4 .

2. The basic dynamic values of the configuration

We start from the general Arnowitt-Deser-Misner SS line element.

$$ds^2 = N^2 (dx^0)^2 - L^2 (dr + N^r dx^0)^2 - R^2 d\sigma^2, \quad (1)$$

where $x^0 = ct$ and $d\sigma^2 = d\theta^2 + \sin^2\theta d\alpha^2$. In this formula the lapse N and the shift N^r , as well as the quantities L and R , which are considered as the dynamical variables of the spacetime geometry, are assumed to be functions of the time coordinate $x^0 = ct$ and the radial coordinate r only. The electromagnetic potential is taken to be described by the SS one-form

$$A = A_0 dx^0 + A_r dr = \varphi dx^0 + \phi dr, \quad (2)$$

where $A_0 = \varphi(x^0, r)$ and $A_r = \phi(x^0, r)$. For the

Einstein-Maxwell theory the action is

$$S = -\frac{1}{16\pi c} \int_{M^{(4)}} \left(\frac{c^4}{\kappa} {}^{(4)}R + F^{\mu\nu} F_{\mu\nu} \right) \sqrt{-g} d^4x \quad (3)$$

+(boundary terms),

where $g = -N^2 L^2 R^4 \sin^2 \theta$ is the determinant of the metric (1), ${}^{(4)}R$ is the Ricci scalar, and $F_{\mu\nu} = A_{\nu,\mu} - A_{\mu,\nu}$ is the electromagnetic field tensor. Inserting the SS fields (1) and (2) and integrating over the angles α and θ we obtain, up to boundary terms, the action

$$S = \int \mathcal{L} d^2x, \quad (4)$$

$$\mathcal{L} = \frac{1}{N} \mathcal{T} + \frac{c^3}{2\kappa} NU. \quad (5)$$

Here \mathcal{L} the Lagrangian of system, \mathcal{T} and U are the kinetic and potential parts of system:

$$\begin{aligned} \mathcal{T} = & -\frac{c^3}{2\kappa} [2R(L_{,0} - (LN^r)_{,r}) \\ & + L(R_{,0} - N^r R_{,r})] (R_{,0} - N^r R_{,r}) \\ & + \frac{1}{2c} \frac{R^2}{L} E^2, \end{aligned} \quad (6)$$

$$U = L - \frac{1}{L} R_r^2 + 2 \frac{R}{L^2} R_r L_r - 2 \frac{R}{L} R_{rr}, \quad (7)$$

where

$$E = F_{0r} = -F_{r0} = \phi_{,0} - \varphi_{,r}.$$

We give the constraints that arise from the Lagrangian (5). First we write down the primary constraints

$$P_N = \frac{\partial \mathcal{L}}{\partial N_0} = 0, \quad P_{N^r} = \frac{\partial \mathcal{L}}{\partial N^r_{,0}} = 0,$$

$$P_\varphi = \frac{\partial \mathcal{L}}{\partial \varphi_0} = 0.$$

Next, we write down the secondary constraints, are the Hamiltonian, momentum (diffeomorphism) and Gaussian ones, respectively

$$\begin{aligned} \frac{\partial \mathcal{L}}{\partial N} = & -\frac{1}{N^2} T + \frac{c^3}{2\kappa} U = \\ -\frac{1}{N^2} \left\{ & -\frac{c^3}{2\kappa} 2R(L_{,0} - (LN^r)_{,r}) (R_{,0} - N^r R_{,r}) \right. \\ & \left. - \frac{c^3}{2\kappa} L (R_{,0} - N^r R_{,r})^2 + \frac{1}{2c} \frac{R^2}{L} E^2 \right\} \\ & + \frac{c^3}{2\kappa} \left[L - \frac{1}{L} R_r^2 + 2 \frac{R}{L^2} R_r L_r - 2 \frac{R}{L} R_{rr} \right] = 0, \end{aligned} \quad (8)$$

$$\begin{aligned} \frac{\delta \mathcal{L}}{\delta N^r} = & \frac{c^3}{\kappa} \frac{R}{N} \left\{ \left(L_{,0} - \frac{V}{N} (N^r L)_{,r} \right) R_{,r} \right. \\ & \left. - L \left(R_{,0r} - N^r R_{,rr} - \frac{N_{,r}}{N} R_{,0} \right) \right\} = 0, \end{aligned} \quad (9)$$

$$\frac{\delta \mathcal{L}}{\delta \varphi} = \frac{1}{c} \frac{\partial}{\partial r} \left(\frac{R^2}{NL} E \right) = 0. \quad (10)$$

The last constraint has the solution

$$\frac{R^2}{NL} E = Q. \quad (11)$$

It follows from here that

$$E = \phi_{,0} - \varphi_{,r} = NL \frac{Q}{R^2}. \quad (12)$$

This determines the electric field strength E of the charge Q .

The canonical momenta, which are conjugate to the variables L, R and α are

$$\begin{aligned} P_R = \frac{\partial \mathcal{L}}{\partial R_{,0}} = & -\frac{c^3}{\kappa N} [L(R_0 - N^r R_r) \\ & + R(L_{,0} - (LN^r)_{,r})], \end{aligned} \quad (13)$$

$$P_L = \frac{\partial \mathcal{L}}{\partial L_{,0}} = -\frac{c^3}{\kappa} \frac{R}{N} (R_0 - N^r R_r), \quad (14)$$

$$P_\phi = \frac{\partial \mathcal{L}}{\partial \phi_{,0}} = \frac{R^2}{cNL} E = \frac{Q}{c}. \quad (15)$$

A Legendre transformation, up to surface terms, leads to the Hamiltonian action

$$\begin{aligned} S_\Sigma[L, R, \phi, P_L, P_R, P_\phi; N, N^r, \varphi] \\ = \int dx^0 \int dr (P_R R_{,0} + P_L L_{,0} + P_\phi \phi_{,0} \\ - NH - N^r H_r - \varphi H_\varphi). \end{aligned} \quad (16)$$

where

$$\begin{aligned} H = -\frac{\partial \mathcal{L}}{\partial N} = & \frac{\kappa}{c^3} \left(\frac{L}{2R^2} P_L^2 - \frac{1}{R} P_R P_L \right) + \frac{cL}{2R^2} P_\phi^2 \\ -\frac{c^3}{\kappa} \left(\frac{L}{2} - \frac{1}{2L} R_r^2 + \frac{R}{L^2} R_{,r} L_{,r} - \frac{R}{L} R_{,rr} \right) = 0, \end{aligned} \quad (17)$$

$$H_r = -\frac{\delta \mathcal{L}}{\delta N^r} = L (P_L)_{,r} - P_R R_r = 0, \quad (18)$$

$$H_\varphi = -\frac{\delta \mathcal{L}}{\delta \varphi} = -\frac{\partial}{\partial r} P_\phi = 0. \quad (19)$$

Here the Hamiltonian, diffeomorphism and Gauss law constraints, which are expressed through momenta

3. The mass function and momenta of field configuration

The Einstein equations for the configuration under consideration lead to the conservation laws of charge Q (11) and the total mass function M (Gladush 2012).

$$M_{tot} = \frac{c^2}{2\kappa} R (1 + (\nabla R)^2) + \frac{Q^2}{2c^2 R}. \quad (20)$$

For metric (1), the mass function is defined as follows

$$\begin{aligned} M_{tot} = & \frac{c^2}{2\kappa} R \left[1 + \frac{1}{N^2} (R_{,0} - N^r R_{,r})^2 - \frac{1}{L^2} R_{,r}^2 \right] \\ & + \frac{R^3}{2c^2 N^2} \frac{E^2}{L^2} = m = const, \end{aligned} \quad (21)$$

or, by the formulae (13,14,15) one gets M in terms of momenta

$$M_{tot} = \frac{c^2}{2\kappa} \left[R + \left(\frac{\kappa}{c^3} \right)^2 \frac{(P_L)^2}{R} - \frac{R}{L^2} R_{,r}^2 \right] \quad (22)$$

$$+ \frac{P_\phi^2}{2R} = m.$$

Using the mass function and the Hamiltonian constraint (17), one can find the momenta P_L and P_R on the CS, which allows one to construct the action of the system as a solution of the Einstein-Hamilton-Jacobi equation (EHJ). Indeed, taking into account (15), from (22) we find P_L as a function of mass m , charge Q , and configuration variables of the system

$$P_L = \frac{c^3}{\kappa} R \sqrt{F_{tot}}, \quad (23)$$

where

$$F_{tot} = \frac{R_{,r}^2}{L^2} + F, \quad (24)$$

$$F = -1 + \frac{2\kappa m}{c^2 R} - \frac{\kappa Q^2}{c^4 R^2}. \quad (25)$$

If one substitutes this expression for P_L into Eq. (17), we get the momentum P_R

$$P_R = \frac{c^3}{\kappa \sqrt{F_{tot}}} \left[\left(\frac{R}{L} R_{,r} \right)_{,r} + \left(\frac{\kappa m}{c^2 R} - 1 \right) L \right]. \quad (26)$$

It is easy to check on that the momentum constraint (18) for the momenta (23), (26), i.e., the condition for the invariance of the action functional, is satisfied identically.

4. The action and the system trajectories in the configuration space

The EHJ equation for the action $S[L, R, \phi; Q, m; r]$ can be obtained by substituting the functional derivatives

$$P_L = \frac{\delta S}{\delta L}, \quad P_R = \frac{\delta S}{\delta R}, \quad P_\phi = \frac{\delta S}{\delta \phi} = \frac{Q}{c} \quad (27)$$

into constraint (17).

However, we will find the action in a simpler way. The last equation in (27) gives

$$S[L, R, \phi; Q, m; r] = S_0[L, R; Q, m; r] + \int \frac{Q}{c} \phi dr, \quad (28)$$

where $S_0[L, R; Q, m; r]$ is a functional independent of ϕ , and moreover,

$$P_L = \frac{\delta S_0}{\delta L}, \quad P_R = \frac{\delta S_0}{\delta R}. \quad (29)$$

The expression for P_L does not contain the derivatives of L , therefore, following (Louis-Martinez 1994), the first equation in (29) is directly integrated:

$$S_0[L, R; Q, m; r] \quad (30)$$

$$= \frac{c^3}{\kappa} \int LR dr \left\{ \sqrt{F_{tot}} - \frac{R_{,r}}{2L} \ln \frac{L\sqrt{F_{tot}} + R_{,r}}{L\sqrt{F_{tot}} - R_{,r}} \right\}$$

$$+ G(R; M, Q; r)$$

or

$$S_0[L, R; Q, m; r] S \quad (31)$$

$$= \frac{c^3}{\kappa} \int LR dr \left\{ \sqrt{F_{tot}} - \frac{R_{,r}}{L} \operatorname{arctch} \frac{R_{,r}}{L\sqrt{F_{tot}}} \right\}$$

$$+ G(R; M, Q; r),$$

where $G(R; M, Q; r)$ is a functional independent of L . Using the second equation in (29), from (30) we obtain

$$P_R = \frac{\delta S_0}{\delta R} = P_R + \frac{\delta S}{\delta R} G(R; m, Q; r). \quad (32)$$

This implies that $G(R; m, Q; r) = G(m, Q; r)$ is a functional independent of R . Here we indirectly checked the integrability conditions of functional equations (29)

As a result, we come to the action functional in the CS

$$S[L, R, \phi; Q, m; r] \quad (33)$$

$$= \frac{c^3}{\kappa} \int LR dr \left\{ \sqrt{F_{tot}} - \frac{R_{,r}}{2L} \ln \frac{L\sqrt{F_{tot}} + R_{,r}}{L\sqrt{F_{tot}} - R_{,r}} \right\}$$

$$+ \int \frac{Q}{c} \phi dr + \int dr g(m, Q; r),$$

as a solution of the EHJ equation. Here $g(M, Q; r)$ is an arbitrary function of M, Q and r .

The system trajectories in the CS or the solution of Einstein equations follow from the relations

$$\frac{\delta S}{\delta m} = c \frac{L}{F} \sqrt{F_{tot}} - cf(r) = 0, \quad (34)$$

$$\frac{\delta S}{\delta Q} = -L \frac{Q\sqrt{F_{tot}}}{cRF} + \frac{1}{c} \phi - \frac{1}{c} \phi_{(0)} = 0, \quad (35)$$

where the following notation is introduced

$$f(r) = -\frac{\partial g(m, Q; r)}{c \partial m}, \quad (36)$$

$$\phi_{(0)} = -c \frac{\partial g(m, Q; r)}{\partial Q}. \quad (37)$$

Hence it can be seen, that

$$L = \sqrt{F f^2(r) - \frac{R_{,r}^2}{F}}, \quad (38)$$

$$\phi = \phi_{(0)} + f(r) \frac{Q}{R}. \quad (39)$$

The obtained relations determine the dependence of the dynamic variables L and ϕ on the coordinate r , the variable $R(r)$ and its derivative with respect to r .

From here we find the space-time metric \mathbf{M}^4 and the potential of the electromagnetic field

$$ds^2 = N^2 (dx^0)^2 - (Ff^2(r) - F^{-1}R_{,r}^2) (dr + N^r dx^0)^2 - R^2 d\sigma^2, \quad (40)$$

$$A = \varphi dx^0 + \left(\phi_{(0)} + f(r) \frac{Q}{R} \right) dr. \quad (41)$$

The lapse N and the shift N^r can be found by passing to the Reissner-Nordstrom solution in the T -region or by using the corresponding time recovery procedure.

5. Minisuperspace metric

From relation (8) we have $N = \sqrt{2\kappa\mathcal{T}/c^3U}$. Therefore, the action (4) can be rewritten as follows

$$S = \int dx^0 \int dr \left(\frac{1}{N} \mathcal{T} + \frac{c^3}{2\kappa} NU \right) = 2 \int dx^0 \int dr \sqrt{\frac{c^3}{2\kappa} \mathcal{T}U} \quad (42)$$

or, taking into account (6), in the form

$$S = \sqrt{\frac{2c^3}{\kappa}} \int dr \int D\Omega \quad (43)$$

Here we introduce the Lie differentials by the formulas

$$DL = (L_{,0} - (LN^r)_{,r}) dx^0 \quad (44)$$

$$DR = (R_{,0} - N^r R_{,r}) dx^0 = dR - N^r R_{,r} dx^0, \quad (45)$$

$$D\phi = (\phi_{,0} - \varphi_{,r}) dx^0 = d\phi - \varphi_{,r} dx^0. \quad (46)$$

Then, the action S can be rewritten as

$$S = \sqrt{\frac{2c^3}{\kappa}} \int dr \int D\Omega, \quad (47)$$

where $D\Omega^2$ is the supermetric CS

$$D\Omega^2 = Ud\Omega_0^2 = \frac{1}{2c} U \left[-\frac{c^4}{\kappa} (2RD LDR + LDR^2) + \frac{R^2}{L} D\phi^2 \right]. \quad (48)$$

In the simplest case of curvature coordinates in the T -region, when $R = cT(x^0)$, and all spatial derivatives disappear, we have $U = L$ and the action takes the form

$$S_\Sigma = \frac{c^3}{\kappa} \int dr \int \sqrt{-(2RdR + LdR)LdL + \frac{\kappa}{c^4} R^2 d\phi^2}. \quad (49)$$

Using the field transformation

$$L^2 = \frac{1}{c\tau + x} \left(c\tau - x - \frac{y^2}{c\tau + x} \right), \quad (50)$$

$$\phi = \frac{c^2}{\sqrt{\kappa}} \frac{y}{c\tau + x}, \quad (51)$$

$$R = \frac{\sqrt{\kappa}}{c^2} (c\tau + x), \quad (52)$$

supermetric of $D\Omega^2$ is reduced to the Lorentz form, i.e. CS is flat

$$d\Omega^2 = L\Omega_0^2 = -c^2 d\tilde{\tau}^2 + d\tilde{x}^2 + dy^2, \quad (53)$$

It follows that minisupermetrics admits the motions group $O(1, 2)$. Note that the supermetric kinetic part

$$d\Omega_0^2 = \mathcal{T} (dx^0)^2 = \frac{1}{2c} \left[-\frac{c^4}{\kappa} 2RD LDR + LDR^2 + \frac{R^2}{L} D\phi^2 \right], \quad (54)$$

is conformally flat.

6. Conclusions

It is to be noted that the inequality $F_{tot} = R_{,r}^2/L^2 + F > F > 0$ in equation (23) determines the classically admissible region. Its boundary is given by the equation roots $F_{tot} = 0$. On the other hand, the T -region of Reissner-Nordstrom space-time is specified by the condition $F > 0$, while the horizon is determined by the equation $F = 0$. It is easy to see that the T -region is contained in a classically admissible region.

It is also interesting to note that the complete integrability of the considered system is preserved when the cosmological constant is added. The complete integrability of the system is due to the fact that the considered field configuration in the SS case does not have local degrees of freedom. However, the inclusion of a scalar field in the configuration completely destroys the picture. In this case, the mass function is not conserved, and the corresponding equations in the general case cannot be analytically solved. Physically, this is due to the fact that spherical symmetry allows scalar field waves. In this case, the configuration turns out to be a dynamic system with an infinite number of freedom degrees.

References

- Gladush V. D.: 2016, *Visnik DNU, Ser. Fizika, radioelectr.*, **24**, 31.
- Gladush V. D.: 2018, *Odessa Astron. Publ.*, **31**, 15.
- Kuchar K. V.: 1994, *Phys. Rev. D*, **50**, 3961.
- Louko J., Winters-Hilt S.: 1996, *Phys. Rev. D.*, **54**, 2647.
- Makela J., Repo P.: 1998, *Phys. Rev. D*, **54**, 4899.
- Gladush, V. D., Petrusenko A. I.: 2012, *Space, time and fund. interact.* **1**, 48 (in Russian).
- Louis-Martinez, D., Gegenberg J., Kunstatter G.: 1994, *Phys. Let. B* **321**, 193.

DOI:<http://dx.doi.org/10.18524/1810-4215.2019.32.181752>

GLUEBALLS

L. Jenkovszky¹, A. Shpenik² and V. Svintozelskyi³

¹ Bogolyubov Institute for Theoretical Physics (BITP), Ukrainian National Academy of Sciences, 14-b, Metrologicheskaya str., Kiev, 03680, Ukraine, jenk@bitp.kiev.ua

² Ukrainian Hungarian educational scientific institute, 88000 Uzhgorod, Universitetskaya str. 14/A, magyarkar.une@gmail.com

³ T.H. Shevchenko Kyiv National University, Kyiv, Ukraine, 1vladimirsw@gmail.com

ABSTRACT. Glueball and oddball resonances lying on the pomeron/odderon trajectories (Chew-Frautchi plot) with threshold and asymptotic behaviour required by analyticity and unitarity are predicted. While the parameters of meson and baryon trajectories can be determined both from the scattering data and from the particles spectra, this is not so for the pomeron (and odderon) trajectory, known only from fits to scattering data only.

The main idea in our approach is in use of a non-linear complex Regge trajectory for the pomeron satisfying the requirements of the analytic S -matrix theory yet fitting the data. The crucial task, on which glueball (and oddball) predictions are based is the correct fit of the pomeron (and odderon) trajectory to the data.

The basic sub-process is pomeron-pomeron scattering, producing glueballs lying on the direct-channel pomeron trajectory. Glueball в “towers”, called reggeized Breit-Wigner resonances, lie on this trajectory. Crucial for the identification of these states is knowledge of the non-linear complex trajectory, interpolating between negative and positive values of its argument. Its parameters are found from the scattering data. While the real part of the trajectory is almost linear, the recovery of the imaginary part, determining the widths of predicted glueballs, is an important ingredient in our approach.

Oddballs, resonances made of three gluons have the same right of existence as glueballs made of two gluons. Oddballs are expected to lie on the odderon trajectory exactly in the same way as glueballs lie on the pomeron trajectory.

The trajectory introduced in this paper can be applied also to studies of ordinary meson and baryon spectra (Chew-Frautchi plot).

The parameters of the pomeron and odderon trajectories are fitted to the data on high-energy elastic proton-proton scattering. The fitted trajectories are extrapolated to the resonance region to predict masses and widths of glueballs and oddballs. Appended by unitary symmetry, the Chew-Frautchi plot remains a

powerful tool to classify hadrons. The proposed trajectory opens a new avenue of research in hadron spectroscopy (Chew-Frautchi plot), applicable both to ordinary mesons and baryons as well as to glueballs lying on the pomeron and odderon trajectories.

Keywords: Regge trajectories, resonances, pomeron, odderon, glueball, meson, baryon.

АНОТАЦІЯ. Передбачено резонанси глюболів та одболів, що лежать на траєкторії померона (оддерона, графік Чю-Фраучі) з порогом та асимптотичною поведінкою, що задовільняють вимогам аналітичності та унітарності. В той час, як параметри мезонних та баріонних траєкторій можна визначити як з даних про розсіяння, так і зі спектра часинок, це неможливо для траєкторій померона (та оддерона), про які ми маємо інформацію лише з даних про розсіяння.

Основною нашою ідеєю є застосування нелінійних комплексних траєкторій Редже, що задовільняють вимогам аналітичної теорії S -матриці і при цьому описують дані. Критичним є згода з експериментальними даними.

Базовим є під-процес розсіяння померонів з продукуванням глюболів, що лежать на траєкторії померона в прямому каналі. Стовпчики глюболів, які ми називаємо реджезованими резонансами Брейта-Вігнера, лежать на цій траєкторії. Критичним для ідентифікації цих станів є знання нелінійною комплексної траєкторії, яка інтерполює між негативними та позитивними значеннями аргумента. В той час, як реальна частина траєкторії майже лінійна, знаходження її уявної частини, яка дає визначає ширини глюболів, є важливою оригінальною частиною нашого підходу.

Одболи - резонанси, які складаються з трьох глюонів, мають таке саме право на існування, як і глюболи, що складаються з двох глюболів. Ми прогнозуємо, що одболи лежать на траєкторії оддерона так само, як глюболи - на траєкторії померона.

Траекторії запропоновані в даній роботі можна застосувати також до дослідження спектрів звичайних мезонів та баріонів.

Параметри траекторії померона та оддерона прив'язані до даних високоенергетичного пружного протон-протонного розсіювання. Підігнані траекторії екстрапольовані в область резонансів для передбачення мас і ширин глюболів та одболів. Разом з унітарною симетрією, графік Чю-Фраучі є потужним інструментом у класифікації адронів.

Ключові слова: Траекторії Редже, резонанси, померон, оддерон, глюбол, мезон, баріон.

1. Introduction

Regge trajectories $\alpha(t)$ connect the scattering region, $t < 0$ with particle spectroscopy, $t > 0$. In this way they realize crossing symmetry and anticipate duality: dynamics of two kinematically disconnected regions are interrelated. The behaviour of trajectories both in the scattering and particle region is close to linear. This observation, combined with the properties of dual models and hadron strings resulted in a prejudice of the linearity of Regge trajectories. Appended by unitary symmetry, the Chew-Frautchi plot remains a powerful tool to classify hadrons.

Unitarity imposes (Barut et al., 1962) a severe constraint on the threshold behavior of the trajectories:

$$\Im\alpha(t)_{t \rightarrow t_0} \sim (t - t_0)^{\alpha(t_0)+1/2}, \quad (1)$$

while asymptotically the trajectories are constrained by (Bugrij et al., 1973)

$$\left| \frac{\alpha(t)}{\sqrt{t} \ln t} \right|_{t \rightarrow \infty} \leq \text{const.} \quad (2)$$

The above asymptotic constrain can be still lowered to a logarithm by imposing (Jenkovszky, 1987 and earlier references) wide-angle power behaviour for the amplitude. While the parameters of meson and baryon trajectories can be determined both from the scattering data and from the particles spectra, this is not true for the pomeron (and odderon) trajectory, known only from fits to scattering data only (negative values of its argument). An obvious task is to extrapolate the pomeron trajectory from negative to positive values to predict glueball states at $J = 2, 4, \dots$ non has been found. Given the nearly linear form of the pomeron trajectory, known from the fits to the (exponential) diffraction cone, little room is left for variations in the region of particles ($t > 0$.)

We continue the lines of research initiated in (Fiore et al., 2016) and (Fiore et al., 2018) in which an analytic pomeron trajectory was used to calculate the pomeron-pomeron cross section in central exclusive

production measurable in proton proton scattering. The basic idea in that approach is in the use of a nonlinear complex Regge trajectory for the pomeron satisfying the requirements of the analytic S -matrix theory and fitting the data. Fits imply high-energy elastic proton-proton and/or proton-antiproton scattering (with the odderon in mind!).

The basic sub-process is pomeron-pomeron scattering, producing glueballs lying on the direct-channel pomeron trajectory, with a triple pomeron vertex. Glueball вЪџtowersвЪџ, i.e. excited glueball states, called reggeized Breit-Wigner resonances, lie on this trajectory. Crucial for the identification of these states is knowledge of the nonlinear complex trajectory, interpolating between negative and to positive values of its argument. Its parameters are fitted to the scattering data. While the real part of the trajectory is almost linear, the recovery of the imaginary part, determining the widths of predicted glueballs, is a highly non-trivial problem.

2. Simple analytic Regge trajectory

What is the simplest ansatz for a Regge trajectory satisfying the following constrains: a) threshold behavior imposed by unitarity, Eq. (1), b) asymptotic behavior constrained by Eq. (2), c) yet compatible with the nearly linear behavior in the resonance region (Chew-Frautchi plot)? Attempts and explicit examples can be found in a number of papers, see e.g. (Fiore et al., 2016 and 2018) and (Szanyi., 2017) and earlier references therein.

The trajectory:

$$\alpha(t) = \frac{1 + \delta + \alpha_1 t}{1 + \alpha_2 (\sqrt{t_0 - t} - \sqrt{t_0})}. \quad (3)$$

where $t_0 = 4m_\pi^2$ for pomeron and $t_0 = 9m_\pi^2$ for odderon and $\delta, \alpha_1, \alpha_2$ are adjustable parameters, to be fitted to scattering ($t < 0$) data with the obvious constrains: $\alpha(0) \approx 1.08$ and $\alpha'(0) \approx 0.3$ (in case of the pomeron trajectory). Trajectory Eq. (3) has square-root asymptotic behavior, in accord with the requirements of the analytic S -matrix theory.

With the parameters fitted in the scattering region, we continue trajectory Eq. (3) to positive values of t . When approaching the branch cut at $t = t_0$ one has to chose the right Riemann sheet, For $t > t_0$ trajectory Eq. (3) may be rewritten as

$$\alpha(t) = \frac{1 + \delta + \alpha_1 t}{1 - \alpha_2 (i\sqrt{t - t_0} + \sqrt{t_0})}, \quad (4)$$

with the sign "minus" in front of α_2 , according to the definition of the physical sheet.

For $t \gg t_0$, $|\alpha(t)| \rightarrow \frac{\alpha_1}{\alpha_2} \sqrt{|t|}$. For $t > t_0$ (on the upper edge of the cut), $\text{Im}\alpha > 0$.

The intercept is $\alpha(0) = 1 + \delta$ and the slope at $t = 0$ is

$$\alpha'(0) = \alpha_1 + \alpha_2 \frac{1 + \delta}{2\sqrt{t_0}}. \quad (5)$$

To anticipate subsequent fits and discussions, note that the presence of the light threshold $t_0 = 4m_\pi^2$ (required by unitarity and the observed "break" in the data) results in the increasing, compared with the "standard" value of about 0.25 GeV^{-2} , slope.

The crucial task, on which glueball (and oddball) predictions are based is the correct fit of the pomeron (and odderon) trajectory to the data. Credibility of such predictions depend on the reliability of these fits. The most direct and reliable ways to fit the pomeron (and odderon) trajectory are those to high-energy elastic nucleon scattering, of which the LHC data on proton-proton scattering, dominated by pomeron exchange are the best. The contribution of secondary trajectories here is negligible.

The situation, however is not that simple. The smooth, nearly exponential small- $|t|$ part of the cone ($|t| \leq 0.3$ before the dip) at the LHC is too short to fit the trajectory and provide its reliable interpolation to large positive values, where glueball are expected. Fits in this limited interval are under control and the small deviation from and exponential of the cone, can be parametrized by a pomeron (and odderon) exchange within the simple Donnachie-Landshoff model (Donnachie et al., 2002), see next Section, where the resulting trajectory inherits the curvature, called "break" seen both at the ISR and LHC near $t \approx -0.1 \text{ GeV}^2$.

3. Glueballs and Oddballs

3.1. Pomeron/odderon trajectories in Central Exclusive Production

Central exclusive diffractive (CED) production continues to attract the attention of both theorists and experimentalists, see *e.g.* Refs.(Fiore et al.,2018, Ewerz et al., 2019) and references therein. This interest is triggered by LHC's high energies, where even the sub-energies at equal partition are sufficient to neglect the contribution from secondary Regge trajectories and consequently CED can be considered as a gluon factory producing exotic particles such as glueballs.

In single-diffraction dissociation or single dissociation (SD) one of the incoming protons dissociates, in double-diffraction dissociation or double dissociation (DD) both protons dissociate, and in central diffraction (CD) or double-Pomeron exchange (DPE) neither

proton dissociates. These processes are listed below,

$$\begin{aligned} \text{SD} & \quad pp \rightarrow p^*p \\ & \quad \text{or} \quad pp \rightarrow pp^* \\ \text{DD} & \quad pp \rightarrow p^*p^* \\ \text{CD (DPE)} & \quad pp \rightarrow pXp, \end{aligned}$$

where p^* represents a diffractively dissociated proton and X denotes a central system, consisting of meson/glueball resonances. Schematic diagrams are shown in Fig. 1.

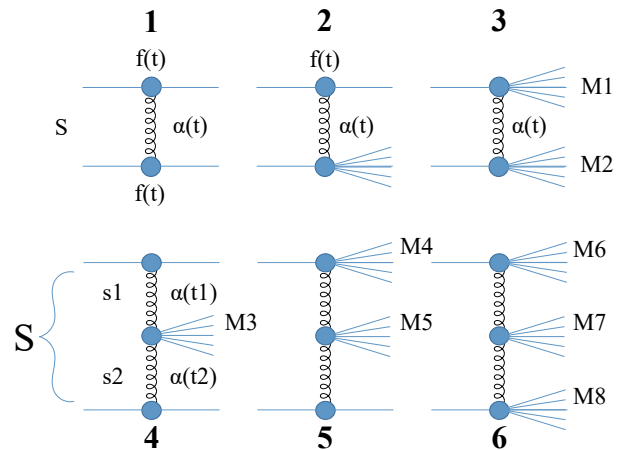


Figure 1: Regge-pole factorization.

The basic sub-process is pomeron-pomeron scattering, producing glueballs lying on the direct-channel pomeron trajectory, with a triple pomeron vertex. Glueball $\text{B}^{\text{N}}\text{towersB}^{\text{N}}\text{K}$, *i.e.* excited glueball states, called reggeized Breit-Wigner resonances, lie on this trajectory. Crucial for the identification of these states is knowledge of the non-linear complex trajectory, interpolating between negative and positive values of its argument. Its parameters are fitted to the scattering data. While the real part of the trajectory is almost linear, the recovery of the imaginary part, determining the widths of predicted glueballs, is a highly non-trivial problem.

In the present paper, by introducing a new model of the Regge trajectories, both for the pomeron and odderon, we continue studies along the lines of Ref. (Fiore et al., 2016 and 2018) . We first fit the parameters of those trajectories to high-energy elastic scattering data then extrapolate the fitted new trajectories to the particle region to predict the masses and widths of the glueballs and oddballs lying respectively on the pomeron and odderon trajectories.

3.2. Scattering amplitude, cross sections, resonances

In (Fiore et al., 2018) the resonances contribution to pomeron-pomeron (PP) cross section was calculated

from the imaginary part of the amplitude by use of the optical theorem

$$\begin{aligned} \sigma_t^{PP}(M^2) &= \Im m A(M^2, t=0) = \quad (6) \\ &= a \sum_{i=f,P} \sum_J \frac{[f_i(0)]^{J+2} \Im m \alpha_i(M^2)}{(J - \Re e \alpha_i(M^2))^2 + (\Im m \alpha_i(M^2))^2}, \quad (7) \end{aligned}$$

In this Section we concentrate on the pomeron. In this case Eq. (7) reduces to

$$\sigma_t^{PP}(M^2) = a \sum_J \frac{k^{J+2} \Im m \alpha(M^2)}{(J - \Re e \alpha(M^2))^2 + (\Im m \alpha(M^2))^2}, \quad (8)$$

where $k = f_i(0)$, and, for simplicity here we set $k = 1$.

We start by comparing the resulting glueball spectra in two ways: first we plot the real and imaginary parts of the trajectory (Chew-Frautchi plot) and calculate the resonances' widths by using the relation (see: e.g. Eq. (18) in R.Fiore et al. 0404021)

$$\Gamma(s = M^2) = \frac{2\Im m \alpha(s)}{|\alpha'(s)|}, \quad (9)$$

where $\alpha'(s) = d\Re e \alpha(\sqrt{s})/d\sqrt{s}$.

3.3. Regge-pole fits to high-energy elastic scattering data

High-energy elastic proton-proton and proton-antiproton scattering, including ISR and LHC energies was successfully fitted with non-linear pomeron trajectories in a number of paper, see (Jenkovszky et al., 2018) and references therein. Since here we are interested in the parametrization of the pomeron (and odderon) trajectories, dominating the LHC energy region, we concentrate on the LHC data, where secondary trajectories can be completely ignored in the near forward direction.

While at lower energies, e.g. at the ISR, the diffraction cone shows almost perfect exponential behavior corresponding to a linear pomeron trajectory in a wide span of $0 < -t < 1.3 \text{ GeV}^2$, violated only by the "break" near $t \approx -0.1 \text{ GeV}^2$, at the LHC it is almost immediately followed by another structure, namely by the dip at $t \approx -0.6 \text{ GeV}^2$. The dynamic of the dip (diffraction minimum) has been treated fully and successfully (Szanyi, Bence et al, 2019), however those details are irrelevant to the behavior of the pomeron trajectory in the resonance (positive s) region and expected glueballs there, that depend largely on the imaginary part of the trajectory and basically on the threshold singularity in Eq. (3).

In Fig. 2 we show a fit to the low- $|t|$ elastic proton-proton differential cross section data (The TOTEM collaboration, 2018) at 13 TeV with a simple model:

$$A_P(s, t) = a_P e^{b_P t} e^{-i\pi\alpha_P(t)/2} (s/s_{0P})^{\alpha_P(t)}, \quad (10)$$

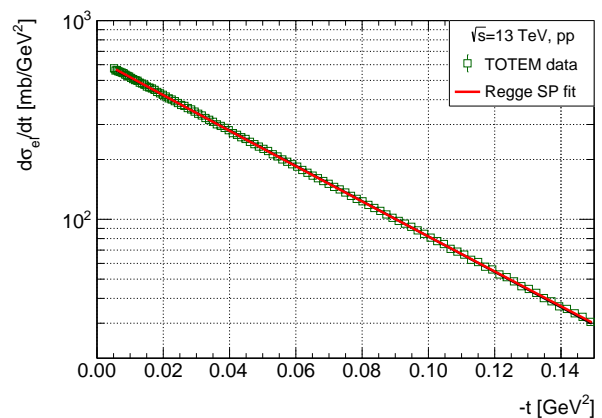


Figure 2: pp differential cross section at 13 TeV fitted to the model: Eq. (10) and trajectory Eq. (3)

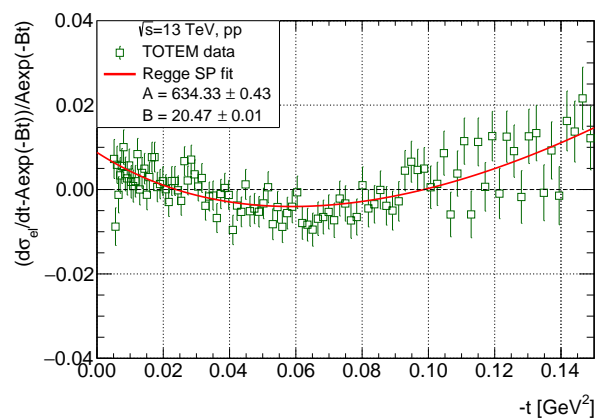


Figure 3: Normalized pp differential cross section at 13 TeV fitted to the model Eq. (10) with trajectory Eq. (3)

where $\alpha_P(t)$ is given by Eq. (3) (changing variable s to variable t). We used the norm:

$$\frac{d\sigma}{dt} = \frac{\pi}{s^2} |A_P(s, t)|^2. \quad (11)$$

Fig. 3 shows the normalized form of the differential cross section (used by TOTEM (The TOTEM collaboration, 2018)) illustrating the low- $|t|$ "break" phenomenon (Jenkovszky et al., 2018) related to the non-linear square root term in the pomeron trajectory. However, it should be also noted that the "break" may result from the two-pion threshold both in the trajectory and the non-exponential residue, as discussed in (Jenkovszky et al., 2018).

Fits with the SP model is quite simple. However, they are not sensitive to the odderon and thus are not suitable to predict oddballs. A more advanced, DP model was considered in (Szanyi et al., 2019) with the result shown in the figure below.

3.4. Glueball and Oddball spectroscopy

The non-linear trajectory can be applied to glueballs and oddballs (Szanyi et al., 2019). The real and imaginary part of the pomeron trajectory obtained by the SP (simple model of scattering amplitude) and DP (double-pole model) fits to high energy elastic scattering data are shown in Fig. 4 and Fig. 5. Fig. 4 shows also the predicted glueballs (with their widths) lying on the pomeron trajectory. The slope of trajectory is shown in Fig. 6.

The predicted pomeron component of the PP total cross section with the calculated ratios of neighboring resonances' widths both SP and DP case are shown in Fig. 7.

Table 1: Fitted parameters of the pomeron and odderon trajectories, see (Szanyi et al., 2019).

Pomeron	
a	1.08009 ± 0.00005
b [GeV^{-2}]	0.2980 ± 0.0021
c [GeV^{-1}]	0.02467 ± 0.00128

Table 2: Fitted parameters of the pomeron and odderon trajectories in the DP model, (Szanyi et al., 2019).

	Pomeron	Odderon
a	1.04592 ± 0.00005	1.6131 ± 0.0020
b [GeV^{-2}]	0.3042 ± 0.0009	0.1987 ± 0.0010
c [GeV^{-1}]	0.05880 ± 0.00046	0.08483 ± 0.00155

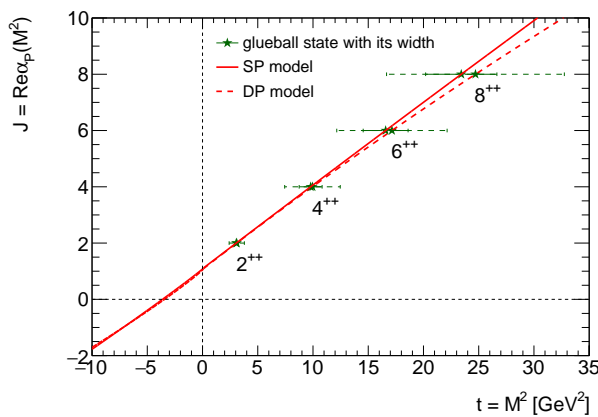


Figure 4: Real part of the pomeron trajectory Eq. (3) both for the SP and DP models as functions of t . The widths of resonances (glueballs) are shown as horizontal error bars.

Oddballs, resonances made of three gluons have the same right of existence as glueballs made of two gluons. Oddballs are expected to lie on the odderon trajectory

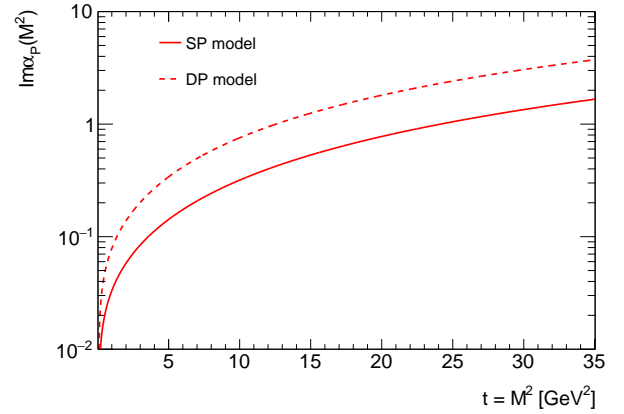


Figure 5: Imaginary part of the pomeron trajectory Eq. (3) both for SP and DP models as functions of t .

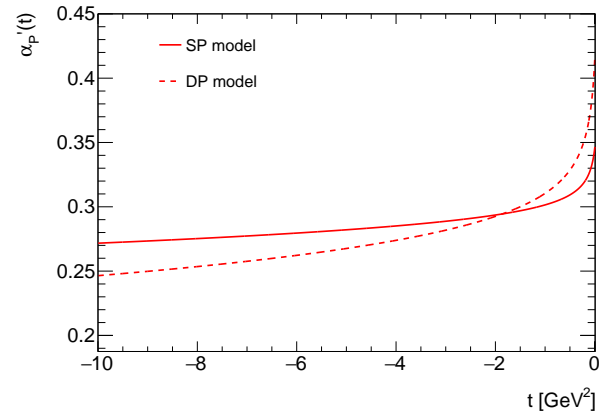


Figure 6: Slope of the pomeron trajectory Eq. (3) both for SP and DP models as functions of t .

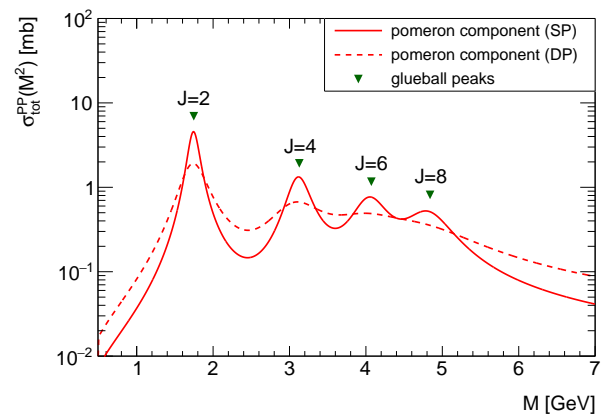


Figure 7: The pomeron component in PP total cross section for two different amplitude models.

exactly in the same way as glueballs lie on the pomeron trajectory.

The real part of the odderon trajectory are shown in Figs. 8. The predicted oddballs (with their widths)

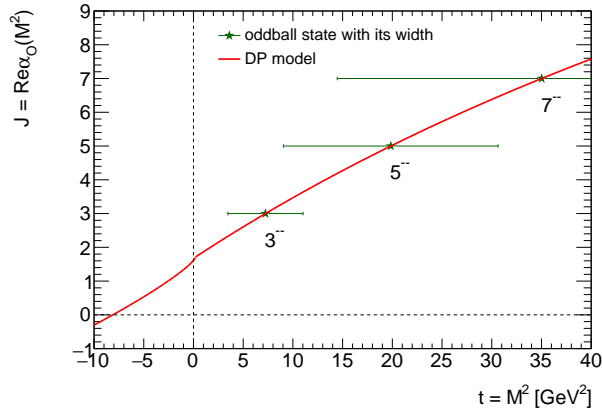


Figure 8: Real part of the odderon trajectory Eq. (3) as function of t . The widths of resonances (oddballs) are shown as horizontal error bars.

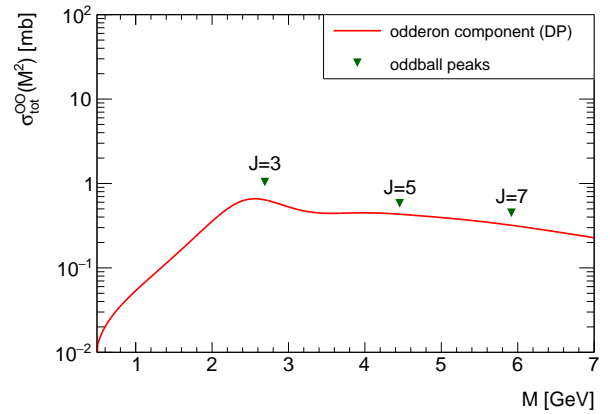


Figure 11: The odderon component in the total cross section for two different models.

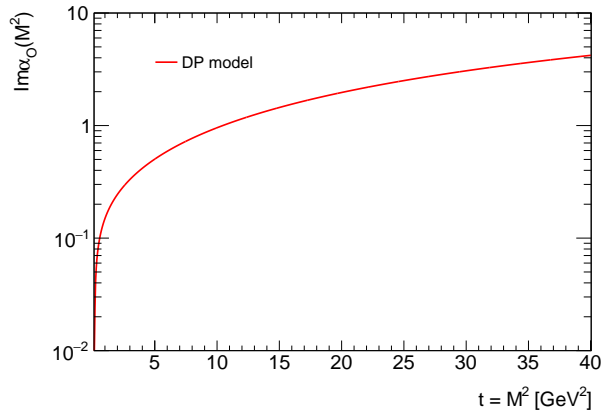


Figure 9: Imaginary part odderon of the trajectory Eq. (3) both for SP and DP models as functions of t .

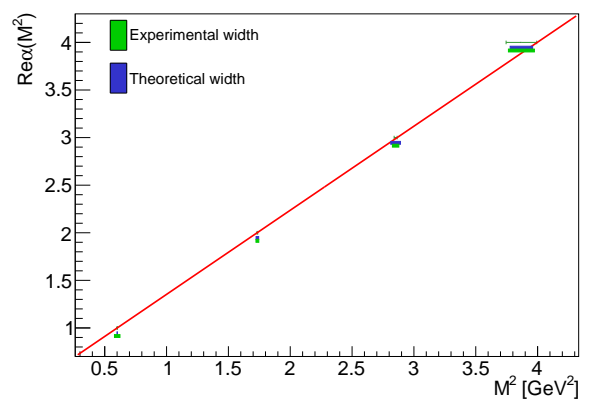


Figure 12: Fit of the non-linear ρ trajectory. Here $s_0 = 4m_\pi^2$.

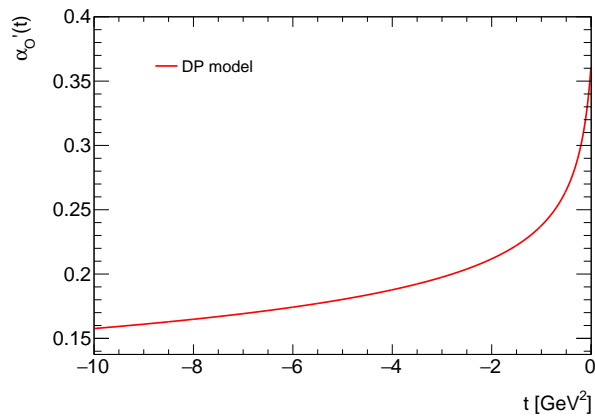


Figure 10: Slope of the odderon trajectory Eq. (3) both for SP and DP models as functions of t .

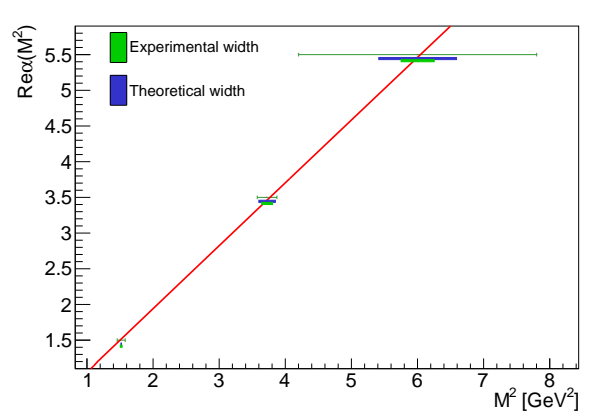


Figure 13: Fit of the Δ -trajectory trajectory, $s_0 = (m_\pi + m_p)^2$.

lying on the on the odderon trajectory are also shown.

4. Mesons and baryons

The trajectory introduced in this paper can be applied also to studies of ordinary meson and baryon spectra (Chew-Frautchi plot). Figs 12 and 13. The theoretical (calculated using non-linear trajectory) and experimental widths are shown as red and green lines, respectively. Note that the mesons and baryons' widths data is available, which is opposite to the pomeron case, which allows making more precise fits.

Data about mesons and baryons were taken from *M. Tanabashi et al. (Particle Data Group), Phys. Rev. D 98, 030001 (2018) and 2019 update.*

Table 3: Values of the parameters of the meson and baryon trajectories, calculated from corresponding fits.

	$\rho - \text{mesons}$	$\Delta - \text{baryons}$
<i>a</i>	0.466118 ± 0.001389	0.167111 ± 0.116851
<i>b</i>	0.880401 ± 0.002208	0.858974 ± 0.057756
<i>c</i>	0.017517 ± 0.000869	0.027311 ± 0.004087

5. Conclusions

Trajectory as Eq. (3) opens a new avenue in hadron spectroscopy (Chew-Frautchi plot), applicable both to ordinary mesons and baryons as well as to glueballs lying on the pomeron and odderon trajectories. Work in this direction is in progress. Appended by unitary symmetry, the Chew-Frautchi plot will remain a powerful tool in hadron spectroscopy.

Acknowledgements. L.J. thanks the Organizers of the Gamow conference for inviting him to present this paper and providing inspiring atmosphere during the Meeting. His work was supported by the Ukrainian Nat. Ac. Sc. program "Structure and dynamics of statistical and quantum-mechanical systems".

References

- Barut A.O. and Zwanziger D.E.: 1962, *Phys. Rev.*, **127**, 974.
- Bugrij A.I. et al.: 1973, *Fortsch. Phys.*, **21**, 427.
- Jenkovszky L.L.: 1987, *Riv. Nuovo Cim.*, **10 N12**, 1.
- Fiore R., Jenkovszky L., Schicker R.: 2016, *Eur. Phys. J.*, **C76**, 38.
- Fiore R., Jenkovszky L., Schicker R.: 2018, *Eur. Phys. J.*, **C78**, 468.
- Szanyi I.: 2017, *Proc. 17th conference on Elastic and Diffractive Scattering (EDS Blois 2017)*, (arXiv:1711.04743).
- Donnachie S. et al: 2002, *Camb. Monogr. Part. Phys. Nucl. Phys. Cosmol.*, **19**, 1.
- Szanyi I., Jenkovszky L. et al.: 2019, (arXiv:1910.02494).
- Ewerz C., Nachtmann O., Schicker R.: 2019, (arXiv:1908.11792).
- Jenkovszky L., Szanyi I., Tan C-I.: 2018, *Eur. Phys. J.* **A54**, 116.
- Szanyi I., Bence N., Jenkovszky L.: 2019, *J. Phys.*, **G46**, 055002.
- The TOTEM collaboration: 2018, arXiv:1812.04732.

DOI:<http://dx.doi.org/10.18524/1810-4215.2019.32.182092>

DEEP LEARNING FOR MORPHOLOGICAL CLASSIFICATION OF GALAXIES FROM SDSS

V. Khramtsov^{1*}, D. V. Dobrycheva^{2,3}, M. Yu. Vasylenko^{2,4}, V. S. Akhmetov¹¹ Institute of Astronomy, V.N. Karazin Kharkiv National University,
35 Sumska Str., Kharkiv, 61022, Ukraine² Main Astronomical Observatory of the National Academy of Sciences of Ukraine,
27 Akademika Zabolotnoho Str., 03143, Kyiv, Ukraine³ Bogolyubov Institute for Theoretical Physics of the National Academy of Sciences of Ukraine,
14-b Metrolohichna Str., 03143, Kyiv, Ukraine⁴ Institute of Physics of the National Academy of Sciences of Ukraine,
46, Nauka avenu, 03028, Kyiv, Ukraine

ABSTRACT. We present the results of applying deep convolutional neural network to the images of redshift-limited ($z < 0.1$) sample of $\sim 300\,000$ galaxies from the SDSS DR9. We aimed to classify galaxies into the two classes: Elliptical and Spiral. To create the training sample, we used a set of $\sim 6\,000$ galaxies from our previous work with visually inspected morphological types, and also added 80 000 well-confirmed galaxies from Galaxy Zoo 2 dataset, that were also classified visually. With a given sample of $\sim 86\,000$ galaxies, we used the deep neural network, namely Xception, to provide a classification of $g-r-i$ composite images (25 arcsec in each axis in size) of galaxies. Keeping in the mind a relatively small training dataset, we provided the data augmentation (horizontal and vertical flips, random shifts on ± 10 pixels, and rotations within 180 degrees), that was randomly applied to the images during learning. The data augmentation is a key technique within our algorithm to display the variative nature of the observed galaxies, and avoid overfitting problem. We compared our classification result with the Support Vector Machine (SVM) classification performed on the SDSS photometric data (absolute magnitudes, colour indices, inverse concentration index, ratios of semiaxes, etc.), and proposed a method to learn the benefits from both approaches (Deep Learning and photometric classification). We show the common mistakes of both algorithms, and propose to stack these two approaches to block these mistakes, with a main goal to increase the overall classification quality of SDSS galaxies.

Keywords: galaxies, morphological classification, machine learning.

АНОТАЦІЯ. В цій роботі ми представляємо результати застосування згорткової нейронної мережі до зображень галактик вибірки, яка обмежена по червоному зміщенню ($z < 0.1$). Вибірка містить $\sim 300\,000$ зображень галактик з цифрового огляду SDSSDR9. Ми мали на меті класифікувати галактики на два класи: Еліптичні та Спиральні. Тренувальна вибірка містить $\sim 6\,000$ зображень галактик з наших попередніх робіт, де візуально було визначено морфологічний тип кожної галактики. До тренувальної вибірки ми додали 80 000 зображень галактик з вибірки даних GalaxyZoo2, що також були класифіковані візуально. На основі даних тренувальної вибірки галактик $\sim 86\,000$ ми застосували згорткову нейронну мережу, а саме Xception, щоб зробити морфологічну класифікацію галактик використовуючи $g-r-i$ складені зображення галактик (розміром 25 на 25 кутових секунд). Для навчання моделей ми використовуємо відносно маленьку вибірку зображень, що накладає обмеження на оцінку якості моделей, та їх подальшу експлуатацію. Для покращення результатів ми використали декілька відомих прийомів (горизонтальні та вертикальні перевороти, випадкові зсуви на ± 10 пікселів та обертання в межах 180 градусів), які були випадковим чином застосовані до зображень галактик під час навчання. Збільшення кількості даних є ключовою технікою в нашому алгоритмі для відображення варіативної природи спостережуваних галактик та уникнення проблеми перенавчання моделі. Ми порівняли отримані результати класифікації з результатами нашої попередньої роботи, де використовувались фотометричні данні (абсолютні зоряні величини, показники кольору, зворотній індекс концентрації, співвідношення

*E-mail: vld.khramtsov@gmail.com

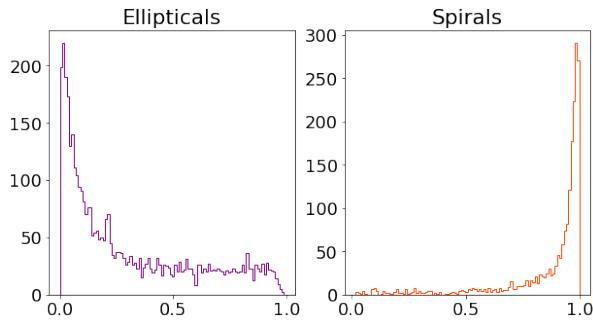


Figure 1: Probability distribution for validation sample of 6 000 galaxies, classified visually and with DL. Probabilities for Ellipticals (E) (*left*) and for Spirals (S) (*right*) of being E - and S - types, respectively.

півосей та ін.) та метод опорних векторів. В результаті, ми запропонували метод для вивчення переваг з обох підходів (глибоке навчання та фотометрична класифікація). Ми показуємо загальні помилки обох алгоритмів і пропонуємо скласти ці два підходи для уникнення помилок з метою підвищити точність морфологічної класифікації галактик SDSS.

Ключові слова: морфологічна класифікація галактик, машинне навчання.

1. Introduction

Morphological classification of galaxies can provide insights into the processes that form the evolution of Universe. The modern wide-field surveys (like the SDSS [Blanton et al. 2017]) include $\sim 10^5$ of resolved galaxies and require the machine learning application. Deep Learning (DL) methods (namely, Convolutional Neural Networks) mimics visual inspection of images by expert but with a much higher speed-performance. In this study we used Deep Convolutional Neural Network to classify 300 000 galaxies ($z < 0.1$) from the SDSS DR9 [Ahn et al. 2012, Dobrycheva et al. 2017] and compared it with photometric classification approach [Dobrycheva et al. (2018), Dobrycheva et al. (2015)]. We note that binary classification (Elliptical and Spiral galaxies) is a primary method for searching gravitational lenses [Sergeyev et al. 2018, Khramtsov et al. 2019] and locating gravitational waves' host galaxies [Dalya et al. 2018] as well as important for Zone of Avoidance identification [Vavilova et al. 2018].

2. Data and methods

We used the data from crowd-source Galaxy Zoo2 project [Willett et al. 2013] providing positional cross-matching of this catalogue with inference sample

[Dobrycheva 2013] and obtained 170 000 common sources. Then, we selected reliable classification with using flags (from Galaxy Zoo2 catalogue) for the Elliptical (`t01_smooth_or_features_a01_smooth_flag`) and Spiral (`t01_smooth_or_features_a02_features_or_disk_flag`) galaxies, that returned 15 264 Ellipticals and 64 441 Spirals. Besides this training sample we used a list of 6 163 visually inspected galaxies (4 148 Ellipticals and 2 015 Spirals) as a validation sample. We applied the Deep Convolutional Neural Network called Xception [Chollet 2016] that gives the state-of-art performance in classifying images. We trained the Xception network on 2/3 of training sample from Galaxy Zoo data and validated the results on remaining 1/3 fraction and on visually inspected galaxies. The distribution of final probabilities for visually inspected 6 000 galaxies is shown in Fig.1.

3. Results

We compare the obtained probabilities returned by our Deep Learning (DL) model with the corresponding probabilities obtained by Support Vector Machine (SVM, [Vapnik 1979]) method. One can see in Fig.1, that our DL model performed well on Spirals, when some Ellipticals from visually inspected sample flowed to the class of Spiral galaxies ($p > 0.5$). We inspected the galaxies, which have rival probabilities (i.e., were classified differently with two methods, see Fig.2, top). Galaxies classified with DL as Ellipticals and as Spirals with SVM look like smooth rounded sources, but in most of cases, they are the starforming galaxies (as we directly checked with SDSS spectra) despite the lacking of resolved spiral structure on their images. This result indicates that DL method can classify rounded sources as Ellipticals but it can not catch the spectral energy distribution properties of galaxies more clearly than SVM, trained on photometric features of galaxies. Also, the galaxies classified as Spirals with DL and as Ellipticals with SVM, are, mostly, the edge-on or face-on Spirals. This confirms that SVM method could not deal with such galaxy images and one should include the additional information (e.g., semi-axis ration) in classification [Vasylenko et al. 2019]. The total amount of differently classified galaxies is 60 000. So, an overall classification of galaxies with DL is satisfactory (Fig.2, bottom) and can be joined with SVM classification to obtain more confident result. We propose to use the Stacking algorithm, when some meta-classifier learns to select sources with using probabilities returned by some basic classifiers as input features. We expect that this method will improve the final classification adopting the best from both methods.

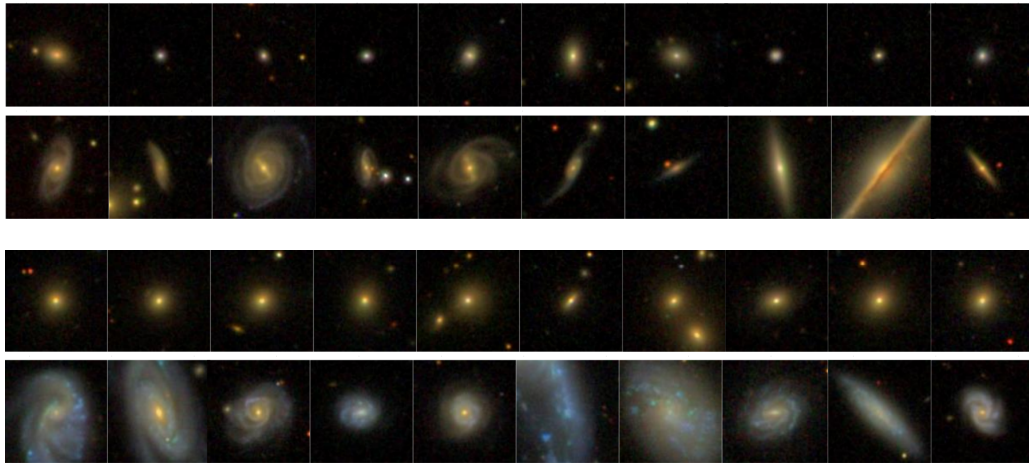


Figure 2: (Top figure) Representative galaxy sample with rival probabilities; top row: Ellipticals with DL, Spirals with SVM; bottom row: Ellipticals with SVM, Spirals with DL. (Bottom figure) Representative galaxy sample with reliable DL classification; top row: Ellipticals; bottom row: Spirals.

Acknowledgement. The work was partially supported by the grant for Young Scientists Research Laboratories (2018-2019, Dobrycheva D.V.) and the Youth Scientific Project (2019-2020, Dobrycheva D.V., Vasylenko M.Yu.) of the NAS of Ukraine.

References

- Ahn C. P., Alexandroff R., Allende P. C. et al.: 2012, *ApJS*, **203**, 21.
- Blanton M. R., Bershadsky M. A., Abolfathi B. et al.: 2017, *Astron. J.*, **154**, 35.
- Chollet F.: 2016, arXiv:1610.02357.
- Dalya G., Galgoczi G. et al.: 2018, *MNRAS*, **479**, 2374.
- Dobrycheva D. V.: 2013, *OAP*, **26**, 187.
- Dobrycheva D. V., Melnyk O. V., Vavilova I. B. et al.: 2015, *Astrophysics*, **58**, 168.
- Dobrycheva D. V. et al.: 2017, arXiv:1712.08955.
- Dobrycheva D. V., Vavilova I. B., Melnyk O. V. et al.: 2018, *Kinemat. Phys. Celest. Bodies*, **34**, 290.
- Khramtsov V., Sergeev A., Spiniello C. et al.: 2019, arXiv:1906.01638.
- Sergeev A., Spiniello C., Khramtsov V. et al.: 2018, *AAS*, **2**, 189.
- Vapnik V.: 1979, Estimation of Dependences Based on Empirical Data [in Russian].
- Vavilova I. B., Elyiv A. A., Vasylenko M. Yu.: 2018, *Radio Phys. Radio Astron.*, **23**, 244.
- Vasylenko M. Yu., Dobrycheva D. V., Vavilova I. B. et al.: 2019, *OAP*, this issue.
- Willett K. W., Lintott C. J., Bamford S. P. et al.: 2013, *MNRAS*, **435**, 2835.

DOI:<http://dx.doi.org/10.18524/1810-4215.2019.32.182511>

IMAGES DISTRIBUTION OF BINARY SYMMETRICAL GRAVITATIONAL LENS

A.T. Kotvytskiy¹, S.D. Bronza², V.Yu. Shablenko¹

¹ Dpt. of Theor. Physics, Karazin Kharkiv National University, Kharkiv, Ukraine, kotvytskiy@gmail.com, shablenkov@gmail.com

² Dpt. of Further Mathematics, Ukrainian State University of Railway Transport, Kharkiv, Ukraine, bronza.sem@gmail.com

ABSTRACT. In this paper, we study the distribution of images from a point source in N - point gravitational lenses.

It is well known that in a Schwarzschild lens ($N = 1$) from a point source, there are always two images. Moreover, one of them is always inside the Einstein ring, and the second outside it. It follows that:

- a) the image plane is divided into two areas;
- b) in each area there is always only one image;
- c) the source plane, with the exception of the caustic point (origin), is uniquely mapped onto each of the two areas of the image plane.

In our study, we describe an algorithm that allows us to determine the single-valued regions in a 2-point gravitational lens and demonstrate it using an example of a binary symmetric lens in which the distance between the point masses is 1. We have shown that in this case the full prototype of the caustic divides the image plane into eight simply connected areas that have the following properties:

- a) if the point source is inside the caustic, then it has five images in five (internal) areas;
- b) if the point source is outside the caustic, then it has three images in three (external) areas;
- c) in each area there can be no more than one image;
- d) if the image of a point source is located in one of the five internal areas, then the remaining four also have images, while none of the three external areas have images of the source;
- e) if the image of the source is located in one of the three external areas, then its images also exist in the remaining two, while none of the five internal areas contains a prototype of this source;
- f) a caustic is a continuous, piecewise smooth, closed Jordan curve that has a finite number of singular points; each smooth, open part of the caustic, the ends of which are singular points (the caustic arc) has four inverse images, of which only one belongs to the critical set, the caustic arcs are positively oriented (when going

around, the interior of the caustic remains to the left;

g) the boundaries of the regions consist of arcs (closure of the image of arcs) with a hereditary orientation; all eight regions are divided into the following two classes: four regions in which the orientation of the boundary coincides with the orientation on the caustic and four regions in which the orientation of the boundary is opposite to the orientation on the caustic.

Keywords: gravitational lensing; lens mapping, single-valued regions, image distribution.

АНОТАЦІЯ. В даній роботі ми досліджуємо розподіл зображень точкового джерела в N точкових гравітаційних лінзах.

Добре відомо, що в лінзі Шварцшильда ($N = 1$) від точкового джерела завжди існує два зображення. Причому одно з них завжди знаходиться всередині кільця Ейнштейна, а інше зовні нього. Звідси слідує що:

- a) площина зображень розбивається на дві області;
- b) в кожній області завжди знаходиться лише одне зображення;
- c) площина джерела, за виключенням точки каустики (початка координат), однозначно відображується на кожну із двох областей плоскості зображень.

В роботі описаний алгоритм, який дозволяє визначити області однозначності в 2-х точковій гравітаційній лінзі. Ми демонструємо його на прикладі бінарної симетричної лінзи в якій відстань між точковими масами дорівнює 1. Ми показали, що в такому випадку повний прообраз каустики розбиває площину зображень на вісім однозв'язних областей. Ці області володіють наступними властивостями:

- a) якщо точкове джерело знаходиться всередині каустики, то воно має п'ять зображень в п'яти (внутрішніх) областях;
- b) якщо точкове джерело знаходиться зовні

каустики, то воно має три зображення в трьох (зовнішніх) областях;

с) в кожній області може знаходитися не більше одного зображення;

д) якщо зображення точкового джерела знаходиться в одній із п'яти внутрішніх областей, то в чотирьох областях, що залишилися, також знаходяться зображення, причому в жодній із трьох зовнішніх областей немає зображень джерела;

е) якщо зображення джерела знаходиться в одній із трьох зовнішніх областей, то в двох областях, що залишилися, також існують його зображення, причому ні в одній із п'яти внутрішніх областей немає прообразу даного джерела;

ф) каустика є неперервна, кусочно-гладка, замкнута жорданова крива, що має кінцеве число особливих точок; кожна гладка відкрита частина каустики, кінці якої - особливі точки (дуга каустики) має чотири прообрази, із яких лише один належить критичній множині, дуги каустики зорієнтовані позитивно (при обході внутрішність каустики залишається зліва);

г) границі областей складаються із дуг (замикаючи зображення дуг) з спадковою орієнтацією; усі вісім областей діляться на наступні два класи: чотири області, в яких орієнтація границі співпадає з орієнтацією на каустиці, та чотири області, в яких орієнтація границі протилежна до орієнтації на каустиці.

Ключові слова: гравітаційне лінзування, лінзове відображення, області однозначності, розподіл зображень.

1. Introduction

Gravitational lensing effects (Bliokh&Minakov, 1989; Zakharov, 1997; Schneider, 1999) are becoming more and more essential, when different astrophysical objects (Gaudi et al. 2008; Han et al. 2013; Gould et al. 2014) and even the whole Universe is studied. From the one hand, it is connected with a development of technologies and engineering solutions. On the other hand, mathematical models development (Bronza & Kotvytskiy, 2017; Kotvytskiy, Bronza & Shablenko, 2017; Kotvytskiy & Bronza, 2016) allows us to do more profound conclusions based on already received observation data. In this study, we show how lens plane can be split into a several areas, where in every area there is the only one point source image. We call the areas as a single-valued region and we study their properties.

2. General approach

System of equations that describes N -point gravitational lens is:

$$\begin{cases} y_1 = x_1 - \sum_{n=1}^N m_n \frac{x_1 - a_n}{(x_1 - a_n)^2 + (x_2 - b_n)^2} \\ y_2 = x_2 - \sum_{n=1}^N m_n \frac{x_2 - a_n}{(x_1 - a_n)^2 + (x_2 - b_n)^2} \end{cases}, \quad (1)$$

where y_1, y_2 - dimensionless coordinates of point source, x_1, x_2 - dimensionless image positions, (a_n, b_n) - coordinates of point masses m_n . Dimensionless point masses are normalized:

$$\sum_{n=1}^N m_n = 1. \quad (2)$$

Equation (1) gives a single-valued mapping L

$$L : (R_X^2 \setminus A) \rightarrow R_Y^2 \quad (3)$$

of lens plane R_X^2 , where points with point masses are deleted, to source plane R_Y^2 .

We introduce new complex variables z и ζ

$$z = x_1 + x_2 i, \quad \zeta = y_1 + y_2 i. \quad (4)$$

Then system of equations (1) becomes (Kotvytskiy& Shablenko&Bronza, 2018):

$$\zeta = z - \sum_{n=1}^N m_n \frac{1}{z - A_n}, \quad (5)$$

where $A_n = a_n + ib_n$ are coordinates of point masses in complex form, Equation (5) specifies mapping

$$L : (C_z \setminus A) \rightarrow C_\zeta \quad (6)$$

of complex plane C_z (with deleted points) to complex plane C_ζ .

Mapping Jacobian (5) is given by following equation

$$J = J(L) = \frac{\partial(\zeta, \bar{\zeta})}{\partial(z, \bar{z})}. \quad (7)$$

Then equation

$$J = 0 \quad (8)$$

defines the critical set Θ of mapping (5). Set image Θ is a caustic K . The caustic is specified by mapping

$$K = L(\Theta). \quad (9)$$

Thus pre-image of the caustic is an image of critical set.

We build complete pre-image of the caustic in lens plane to define single-valued regions (Balk, Petrov & Poluchin, 1976). Inverse mapping of (6) is defined by set

$$Q = L^{-1}(K) = L^{-1}(L(\Theta)), \quad (10)$$

This is the complete pre-image of caustic. Mapping L^{-1} is not single-valued, hence sets Q and Θ do not coincide.

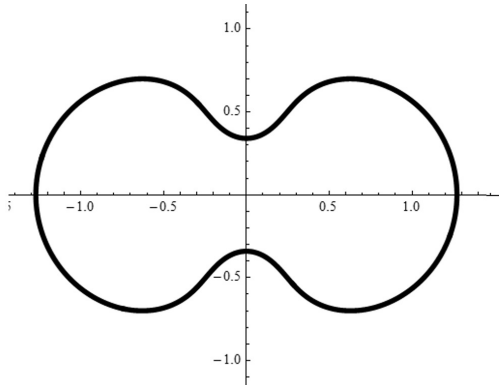


Figure 1: Critical curve of binary symmetrical lens with $a = 0.5$

3. Binary lens

We demonstrate the algorithm, described in previous paragraph, for symmetrical binary lens with equal masses. Then from (2), we have:

$$m_1 = m_2 = 1/2. \quad (11)$$

Assume without loss of generality, that point masses are located on real axis with distance a from origin, i.e.

$$A_1 = a, A_2 = -a. \quad (12)$$

In this case, equation (5) is given by:

$$\zeta = z - \frac{\bar{z}}{z^2 - a^2}, \quad (13)$$

which defines mapping (6). Then Jacobian (7) is given by

$$J = 1 - \frac{(a^2 + z^2)(a^2 + \bar{z}^2)}{(a^2 - z^2)^2(a^2 - \bar{z}^2)^2}. \quad (14)$$

It follows from (8) that critical set Θ is defined by equation:

$$1 = \frac{(a^2 + z^2)(a^2 + \bar{z}^2)}{(a^2 - z^2)^2(a^2 - \bar{z}^2)^2}. \quad (15)$$

It is known (Dank & Heyrovsky 2015), that critical set, defined by equation (15), is split on a few classes depending on parameter a . When

$$a < 1/(2\sqrt{2}), \quad (16)$$

critical curve consists of three closed Jordan curve - the two of them are inside the third. When

$$a = 1/(2\sqrt{2}) \quad (17)$$

critical set is represented as a closed curve with two self-crossing. When

$$1/(2\sqrt{2}) < a < 1, \quad (18)$$

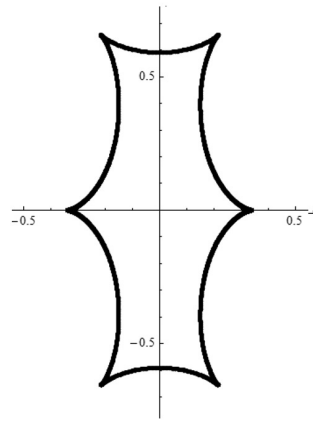


Figure 2: Caustic of symmetrical binary lens with $a = 0.5$

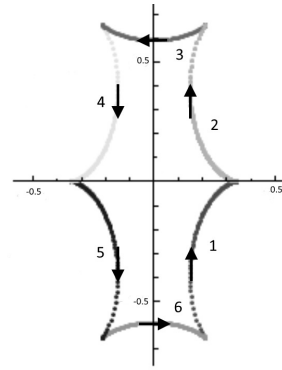


Figure 3: Caustic of symmetrical binary lens with orientation

there is a closed Jordan curve. With

$$a > 1, \quad (19)$$

there are two closed Jordan curves, the one is outside the second.

We confine the study with case (18). We chose parameter $a = 0.5$. The form of the critical curve is on Fig. 1. Caustic is the image of critical set (9). Thus, critical curve showed on Fig. 1 corresponds to caustic showed on Fig. 2.

For the following analysis we depict each arc of caustic with different style and give them number (arcs' orientation correspond to orientation that is accepted in complex analysis (see Fig. 3)).

Arc's orientation of complete caustic pre-image is induced by caustic orientation. Note, that caustic pre-image (i.e. critical curve) in complete pre-image has opposite to critical curve orientation (Fig. 4).

It is necessary to build complete caustic pre-image according to (10) to define single-valued regions, as it was noted previously. In our case, we have curve (Fig. 5).

Complete caustic pre-image split lens plane into 8 two-dimensional regions. In order to define internal

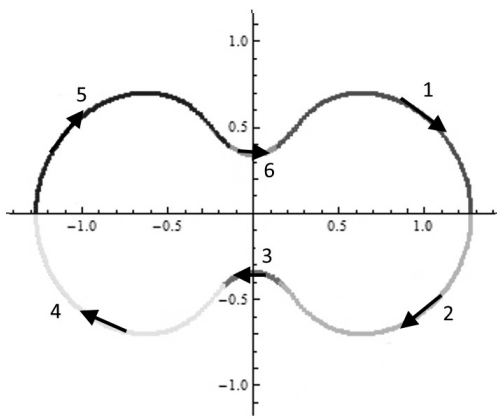


Figure 4: Critical curve of symmetrical binary lens with orientation

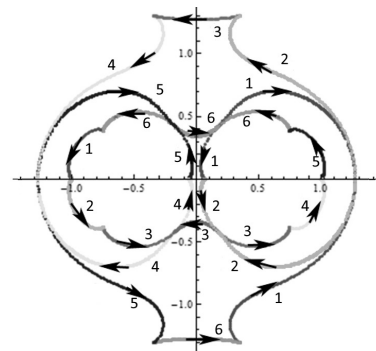


Figure 5: Complete caustic pre-image of symmetrical binary lens with orientation

and external regions on lens plane, we set three point sources on source plane, that is shown in form of triangle, square and star (Fig. 6).

Sources are located out of the caustic, on the caustic and inside the caustic respectively on Fig. 7. The caustic orientation is not shown on Fig. 7.

It is known, that source located inside the caustic has five images, on the caustic - four images, and out of the caustic - three images (Fig. 7).

It is known from the theory of functions of several complex variables, that an image of any of the five internal regions is interior of the caustic, when the mapping is L . And an image of any of the three exterior regions - caustic exterior. Moreover, restriction of mapping L on the regions is homomorphism. Thus, eight regions are single-valued regions. Consequently, if we have five images, these images are in interior regions, and then there are no images in three exterior regions. Orientation, that is defined on the caustic, induces orientation on lens plane of each of eight regions. Boundary of four regions are oriented positively, and another four - negatively (Fig 8).

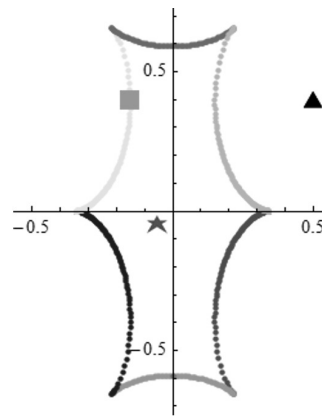


Figure 6: Caustic of symmetrical binary lens with three point sources

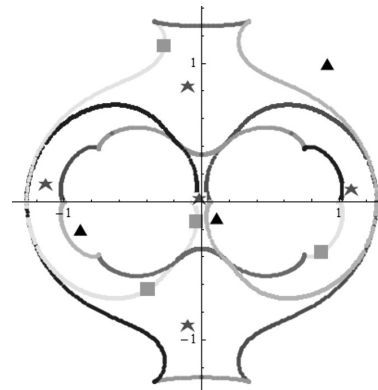


Figure 7: Distribution of caustic images and three point sources in symmetrical binary gravitational lens

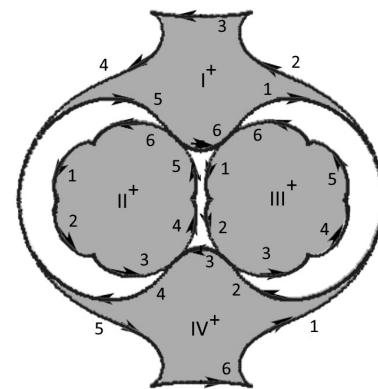


Figure 8: Division of complete caustic pre-image on positively (grey) and negatively (white) oriented regions

References

Balk M.B., Petrov V.A., Poluchin A.A.: 1976, *Zadachnik-praktikum po teorii analiticheskikh funkcij*, Prosveschenie, Moskow (in Russian), 136p.

- Bliokh P.V., Minakov A.A.: 1989, *Gravitational Lenses*, Naukova Dumka, Kiev (in Russian), 240p.
- Bronza S.D., Kotvytskiy A.T.: 2017, *Bull. Kharkiv Nat. Univ. "Physics"*, **26**, 6.
- Dank K., Heyrovsky D.: 2015, *AJ*, **806**, 99.
- Gaudi B. S., Bennett D. P., Udalski A. et al: 2008, *Sci*, **319**, 927.
- Gould A., Udalski A., Shin I.-G., et al: 2014, *Sci*, **345**, 46.
- Han C., Udalski A., Choi J.-Y., et al: 2013, *ApJL*, **762**, L28.
- Kotvytskiy A.T., Bronza S.D., Shablenko V.Yu.: 2017, *Odessa Astron. Publ.*, **30**, 35.
- Kotvytskiy A.T., Bronza S.D.: 2016, *Odessa Astron. Publ.*, **29**, 31.
- Kotvytskiy A.T., Shablenko V.Yu., Bronza E.S.: 2018, *Odessa Astron. Publ.*, **31**, 24.
- Schneider P., Ehlers J., Falco E.E.: 1999, *Gravitational Lenses*, Spr.-Verlag, Berlin, Heidelberg, 560p.
- Zakharov A.F.: 1997, *Gravitacionnye linzy i mikrolinzy*, Janus-K, Moskow (in Russian), 328p.

DOI:<http://dx.doi.org/10.18524/1810-4215.2019.32.182518>

SOME COROLLARY FACTS OF THE N-POINT GRAVITATIONAL LENS EQUATION IN A COMPLEX FORM

O.A. Osmayev¹, Yu.S. Shuvalova¹, E.S. Bronza², K.I. Matvienko³

¹ Department of Higher Mathematics, Ukrainian State University of Railway Transport, Kharkiv, Ukraine, *olosmatyev@gmail.com*, *shuvalova@kart.edu.ua*

² Faculty of Computer Science, Kharkiv National University of Radio Electronics, Kharkiv, Ukraine, *eugene.bronza@gmail.com*

³ Faculty of Mechanics and Energy, Ukrainian State University of Railway Transport, Kharkiv, Ukraine, *konstantin.matviyenko@gmail.com*

ABSTRACT. In the theory of the N-point gravitational lens equation, two groups of problems can be distinguished. These are the so-called primal and inverse problems. Primal problems include problems of image definition in a specified lens for a specified source. Inverse problems include problems of determining a lens, source, or multiple images from one or more specified images. Inverse problem have an important applications.

We studied the equation of the N-point gravitational lens in a complex form. These studies became the basis for the solution of the inverse problem in the following formulation. N-point gravitational lens has specified. It is necessary to determine all other images from one of the images of a point source in N-point gravitational lens. Determine the necessary and sufficient conditions under which this problem has solutions.

The algebraic formulation of the problem has the following form. The equation (of N-point gravitational lens) has specified. It is necessary to solve the problem of solutions unification (to express unequivocally all of the equation solutions through one parameter).

To solve the inverse problem, we used methods of algebraic geometry and function theory. Branches equations of any algebraic function admit unequivocal parameterization by Puiseux series. The solutions of the N-point gravitational lens equation are algebraic functions defined by a certain irreducible polynomial. That polynomial has unequivocally defined by the N-point gravitational lens equation. Thus, the polynomial roots also admits parameterization by Puiseux series.

In simple cases, for lenses with a small number of point masses, the solution can be obtained in a simpler form. In particular, for the Schwarzschild lens and binary lens, the inverse problem has a solution in radicals.

Keywords: gravitational lens, source image, inverse

problem, complex analysis.

АНОТАЦІЯ. Серед безлічі проблем і задач, які розглядають в теорії рівняння N-точкових гравітаційних лінз, можна виділити дві групи задач. Це, так звані, прямі і зворотні задачі. До прямих задач відносять задачі визначення зображень в заданій лінзі для заданого джерела. До зворотних – визначення лінзи, джерела або безлічі зображень по одному або декільком заданим зображенням. Зворотна задача має важливе прикладне застосування.

Ми досліджували рівняння N-точкової гравітаційної лінзи в комплексному вигляді. Ці дослідження стали основою для розв'язання оберненої задачі в наступній постановці: задана N – точкова гравітаційна лінза, необхідно, по одному із зображень в ній точкового джерела визначити всі інші зображення цього джерела. Визначити необхідні і достатні умови, при яких ця задача має розв'язок.

В алгебраїчній формулюванні задача має вигляд. Задано рівняння N-точкової гравітаційної лінзи. Необхідно розв'язати задачу уніфікації коренів (однозначно виразити усі корені рівняння через один параметр).

Для розв'язання оберненої задачі, ми використовували методи алгебраїчної геометрії і теорії функцій. Рівняння гілок будь-якої алгебраїчної функції допускають однозначну параметризацію рядами Бюрмана–Лагранжа. Корені рівняння N-точкової гравітаційної лінзи є алгебраїчними функціями визначеними незведеним многочленом. Цей многочлен однозначно визначається рівнянням N-точкової гравітаційної лінзи. Отже, корені цього многочлена, також допускають параметризацію рядами Бюрмана–Лагранжа.

У простих випадках, для лінз з малим числом

точкових мас, розв'язок може бути отриманий в більш простому вигляді. Зокрема, для лінзи Шварцшильда і бінарної лінзи зворотна задача має розв'язок в радикалах.

Ключові слова: гравітаційні лінзи, зображення джерела, обернена задача комплексний аналіз.

1. Introduction

By methods of algebraic geometry we studied the equation of N-point gravitational lens. This has led us to a special case solution of one of the inverse problems. Expressly, N-point gravitational lens is specified and the coordinates of one of the image of the point source in it are known. It is necessary to determine the coordinates of all other images. Formulate the necessary and sufficient conditions under which this problem has solutions.

The algebraic formulation of the problem has the following form. The equation (of N-point gravitational lens) has specified. It is necessary to solve the problem of solutions unification (to express unequivocally all of the equation solutions through one parameter).

In this paper, we used methods of algebraic geometry and function theory. The solutions of the equation N-point gravitational lens possible to parameterize by Puiseux series.

For lenses with a small number of point masses, the solution can be obtained in a simpler form. In particular, for the Schwarzschild lens and binary lens, the inverse problem has a solution in radicals.

2. N-point gravitational lens equation in complex form

N-point gravitational lens equation can be written in complex form:

$$\zeta = z - \overline{w(z)}, \quad (1)$$

wherein

$$w = \sum_{n=1}^N m_n \frac{1}{(z - A_n)}; \sum_{n=1}^N m_n = 1, \quad (2)$$

where m_n - normalized point masses included in the lens, A_n - their complex coordinates [Kotvytskiy, SH-ablenko, Bronza, 2018; Witt, 1990]. In [Dank, Heyrovský, 2015], it has also proved that:

$$w = \frac{1}{\deg P(z)} \frac{P'(z)}{P(z)}, \quad (3)$$

where $P(z) = \prod_{n=1}^N (z - A_n)^{m_n}$.

Using equation (1), new proofs have been obtained of previously known theorems about images of a point source in the N-point gravitational lens:

- about single extended image (Einstein ring) [Kotvytskiy et al, 2017];

- about infimum of a number of point source images in the N-point gravitational lens [Dank & Heyrovský, 2015];

- about supremum of a number of point source images in the N-point gravitational lens [Osmayev & Matvienko, 2018].

Using equation (1), a new, previously unknown, result has also been obtained. The problem of unequivocal parameterization of image coordinates has been solved. Algorithms that admit to express unequivocally the coordinate of any image through the same parameter have been designed. In particular, the coordinate of one of the images might be used as a parameter.

3. Solution of the problem of image coordinates parameterization

For the Schwarzschild lens, a theorem holds.

Theorem 1. Let z be the complex coordinate of one of the images in the Schwarzschild lens, then the coordinate of the second image is $-\frac{1}{\bar{z}}$.

Proof. Images in a Schwarzschild lens with coordinates z and $-\frac{1}{\bar{z}}$ are images of the same source as

$$\zeta(z) = \zeta\left(-\frac{1}{\bar{z}}\right) \quad (4)$$

Indeed, equation (1) for the Schwarzschild lens in complex form has the form:

$$\zeta = z - \frac{1}{\bar{z}}, \quad (5)$$

if mass of the lens is located at the origin of the coordinates.

Substitute in equation (5) $-\frac{1}{\bar{z}}$, we have:

$$\begin{aligned} \zeta\left(-\frac{1}{\bar{z}}\right) &= -\frac{1}{\bar{z}} - \frac{1}{\left(-\frac{1}{\bar{z}}\right)} = -\frac{1}{\bar{z}} - \frac{1}{\left(-\frac{1}{\bar{z}}\right)} = \\ &= -\frac{1}{\bar{z}} + z = \zeta(z) \implies \zeta(z) = \zeta\left(-\frac{1}{\bar{z}}\right). \end{aligned}$$

Therefore, relation (4) holds.

The theorem is proved.

Each point source, which located not at the origin of the coordinates, has exactly two point images in the Schwarzschild lens. Therefore, the problem of image coordinates parameterization for the Schwarzschild lens is solved.

Corollary to Theorem 1. Let g_1, g_2 the affine coordinates of one of the images in the Schwarzschild lens, then the affine coordinates of the second image

$$-g_1(g_1^2 + g_2^2), -g_2(g_1^2 + g_2^2)^{-1}.$$

Proof. Let $z = g_1 + g_2i$, then

$$\operatorname{Re}\left(-\frac{1}{\bar{z}}\right) = -g_1(g_1^2 + g_2^2), \operatorname{Im}\left(-\frac{1}{\bar{z}}\right) = -g_2(g_1^2 + g_2^2),$$

The corollary is proved.

For polynomials $P(z)$ in one variable over z the field of complex numbers, the following theorem holds.

Theorem 2. Let $P(z)$ the polynomial over the field of complex numbers and $2 \leq \deg P(z) \leq 5$, then, the problems of parameterization of roots of the polynomial $P(z)$ are solvable in radicals.

Proof. Polynomial remainder theorem implies that the difference $P(z) - P(t)$ is divided exactly by the binomial $(z - t)$. Then

$$Q(z, t) = \frac{P(z) - P(t)}{z - t}, \quad (6)$$

is a polynomial in two variables. The degree of the polynomial $Q(z, t)$ for each of the variables

$$\deg_z(Q(z, t)) = \deg_t(Q(z, t)) = n - 1, \quad (7)$$

where $n = \deg P(z)$.

If $n \leq 5$, then the polynomial $Q(z, t)$, as a polynomial from the variable z , over the field of rational functions from t , has the degree $\deg_z(Q(z, t)) \leq 4$. Therefore, each of its $n - 1$ roots can be expressed in radicals through its coefficients. Since the coefficients of the polynomial $Q(z, t)$ are rational functions of t , its roots are unequivocally expressed in terms of t . The variable t will be considered as a parameter.

Thus, the problem of parameterization of the roots of a polynomial $Q(z, t)$ is solvable in radicals.

We have an expression for $n - 1$ roots of polynomial $P(z)$ through t . We will put the remaining root of polynomial $P(z)$ equal to t .

The theorem is proved.

Remark of the theorem 2. Let the polynomial $P(z)$ meet the conditions of theorem 2, then $n - 1$ roots of polynomial $P(z)$ can be expressed in terms of the remaining root. Indeed, let have t equal to one of the roots of the polynomial.

Example to theorem 2. Let the equation be specified

$$z^3 + az^2 + bz + c = 0 \quad (8)$$

It is necessary to express two roots z_1, z_2 of equation (8) by the third z_3 .

Solution. Denote the polynomial standing in the left side of equation (8) by $P_3(z)$, i.e.

$$P_3(z) = z^3 + az^2 + bz + c. \quad (9)$$

The difference $P_3(z) - P_3(t)$ is divided exactly by the binomial $(z - t)$:

$$\begin{aligned} P_3(z) - P_3(t) &= z^3 + az^2 + bz + c - \\ &- (t^3 + at^2 + bt + c) = \\ &= z^3 - t^3 + a(z^2 - t^2) + b(z - t) = \\ &= (z - t)(z^2 + zt + t^2 + az + at + b) \end{aligned} \quad (10)$$

If z the root of a polynomial $P_3(z)$, then from (10)

$$z^2 + zt + t^2 + az + at + b = 0 \quad (11)$$

Equation (11) as regard to the variable is the quadratic equation:

$$z^2 + (t + a)z + t^2 + at + b = 0 \quad (12)$$

The roots of equation (12) are equal to:

$$z_{1,2} = \frac{t + a \pm \sqrt{(t + a)^2 - 4(t^2 + at + b)}}{2}.$$

With the $z_3 = t$ we have:

$$z_{1,2} = \frac{z_3 + a \pm \sqrt{-4z_3^2 - 2az_3 - 4b + a^2}}{2}.$$

The roots of equation (8) z_1, z_2 are expressed by the third root z_3 .

In the general case, for the N -point gravitational lens we have:

From equation (1), we have:

$$\zeta = z - \sum_{n=1}^N \frac{m_n}{\bar{z} - A_n}. \quad (13)$$

We proceed to the complex conjugation in both parts of the equation (13):

$$\bar{\zeta} = \bar{z} - \sum_{n=1}^N \frac{m_n}{z - A_n}. \quad (14)$$

Substitute the variable \bar{z} from equation (14) to (13), we have:

$$\zeta = z - \sum_{n=1}^N \frac{m_n}{\bar{z} - \sum_{n=1}^N \frac{m_n}{z - A_n} + \bar{\zeta} - \bar{A}_n}. \quad (15)$$

Equation (15) is brought into polynomial form and all summands are transferred to the left side of the equation. Denote the left side of the obtained equation by $F(z, \zeta, \bar{\zeta})$.

Compute the expression

$$Q(z, t) = \frac{F(z, \zeta, \bar{\zeta}) - F(t, \zeta, \bar{\zeta})}{z - t} = \frac{F(z) - F(t)}{z - t}. \quad (16)$$

The following theorem holds.

Theorem 3. The expression $\frac{F(z) - F(t)}{z - t}$ is a polynomial in two variables z and t .

Proof. The validity of the theorem follows from polynomial remainder theorem. The residue from dividing the polynomial $F(z)$ by the difference $(z - t)$ is equal to $F(t)$. And from the corollary of polynomial remainder theorem. The number t is the root of the polynomial $F(z)$ if and only if the expression

$F(z) - F(t)$ is divided without residue by the binomial $(z - t)$. The theorem is proved.

Polynomial $Q(z, t)$ will be termed a difference polynomial for polynomial $F(z)$. Polynomial $Q(z, t)$ as regard to the variable z has the degree [Kotvytskiy, Bronza, Shablenko, 2017]:

$$\begin{aligned} \deg_z Q(z, t) &= \deg_z F(z, \zeta, \bar{\zeta}) - 1 \leq \\ &\leq N^2 + 1 - 1 = N^2 \end{aligned} \quad (17)$$

The Z polynomial, actually, is reduced. Polynomial is presented in the form of a product of irreducible factors [Bronza & Kotvytskiy, 2017; Bronza, 2016], if it is reduced.

The problem of root parameterization of a polynomial $Q(z, t)$ may be solved by using Puiseux series. For this purpose, there is a geometric method known as "Newton's Diagram", see [Chebotarev, 1948].

4. Solution of inverse problem for binary symmetric lens

Let $S_2 = S_2(-a, a)$ is a binary symmetrical lens with masses $m_1 = m_2 = 0.5$, which located at the $-a$ and a points on the real axis. The lens equation has the form:

$$\zeta = z - \frac{\bar{z}}{\bar{z}^2 - a^2}. \quad (18)$$

Exclude from equation (18) and equation of complex-conjugate to it \bar{z} , all summands are transferred to the left side and factorized, we have:

$$\begin{aligned} (z - \zeta)[(\bar{\zeta}^2 - a^2)(z^2 - a^2)^2 + 2\bar{\zeta}(z^2 - a^2)z + \\ z^2] - (\bar{\zeta}(z^2 - a^2) + z)(z^2 - a^2) = 0. \end{aligned} \quad (19)$$

Denote the left side of equation (19) by $F(z, \zeta, \bar{\zeta})$.

Compute the polynomial by the formula (16).

$$\begin{aligned} Q &= (-a^2 + \bar{\zeta}^2)z^4 + [(-a^2 + \bar{\zeta}^2)t + \\ &+ (a^2\zeta + \bar{\zeta} - \zeta\bar{\zeta}^2)]z^3 + [(-a^2 + \bar{\zeta}^2)t^2 + \\ &+ (a^2\zeta + \bar{\zeta} - \zeta\bar{\zeta}^2)t + (2a^4 - 2\zeta\bar{\zeta} - 2a^2\bar{\zeta}^2)]z^2 + \\ &+ [(-a^2 + \bar{\zeta}^2)t^3 + (a^2\zeta + \bar{\zeta} - \zeta\bar{\zeta}^2)t^2 + \\ &+ (2a^4 - 2\zeta\bar{\zeta}^2 - 2a^2\bar{\zeta}^2)t + (-2a^4\zeta + 2a^2\zeta\bar{\zeta}^2 - \zeta)]z + \\ &+ (-a^2 + \bar{\zeta}^2)t^4 + (a^2\zeta + \bar{\zeta} - \zeta\bar{\zeta}^2)t^3 + \\ &+ (2a^4 - 2\zeta\bar{\zeta}^2 - 2a^2\bar{\zeta}^2)t^2 + \\ &+ (-2a^4\zeta + 2a^2\zeta\bar{\zeta}^2 - \zeta)t + (-a^6 + a^4\bar{\zeta}^2 + a^2 + 2a^2\zeta\bar{\zeta}) \end{aligned} \quad (20)$$

Polynomial $Q(z, t)$ as regard to the variable z has the fourth power degree. Its coefficients are polynomials in the variable t . $Q(z, t)$ roots may be expressed in radicals from its coefficients. Since, as the coefficients $Q(z, t)$, there are polynomials in the variable t , we have: $z_{1,2,3,4} = z(t)$. Among other things, since the polynomial $F(z, \zeta, \bar{\zeta})$ has another root $z_5 = t$, we have:

$$z_{1,2,3,4} = z(z_5). \quad (21)$$

The formula (21) proved the possibility to express all roots of the polynomial $Q(z, t)$ by one parameter t .

Thus, the inverse problem for a binary lens is solvable in radicals.

In particular, if a point source is located on the real axis, the lens has three images on the real axis, at the points with coordinates $z_i, i = 1, 2, 3$, the relation holds:

$$z_{2,3} = \frac{z_1 \pm z_1 \sqrt{1 + 4(z_1^2 - a^2)(z_1^2 - a^2 + 1)}}{4(z_1^2 - a^2)}. \quad (22)$$

In total, a source in the binary symmetrical lens may have either 3 or 5 images. For any real Z source is located on the real axis, it also has either 3 or 5 images. Both cases are realized.

References

- Bronza S.D.: 2016, *Scientific papers collection of UkrSURT*, **160**, 114.
 Bronza S.D., Kotvytskiy A.T.: 2017, *Bull. Kharkiv Nat. Univ. "Physics"*, **26**, 6.
 Chebotarev N. G.: 1948, *Algebraic functions theory*, (OGIZ, M.-L.), 396 p. (in Russian).
 Dank K., Heyrovský D.: 2015, *AJ*, **806**, 99.
 Kotvytskiy A.T., Bronza S.D., Shablenko V.Yu.: 2017, *Acta Polytechnica* **57(6)**, 404.
 Kotvytskiy A.T., Shablenko V.Yu., Bronza E.S.: 2018, *Odessa Astron. Publ.*, **31**, 24.
 Kotvytskiy A.T., Bronza S.D., Nerushenko K. Yu., et al: 2017, *VI Interregional Scient.-Pract. Conf. "Astronomy and Today"*, Vinnitsya, 198.
 Osmayev O.A., Matvienko K.I.: 2018, *80-th UkrSURT SSTC theses*, 216.
 Witt H.J.: 1990, *A&A*, **236**, 311.

DOI:<http://dx.doi.org/10.18524/1810-4215.2019.32.182519>

LINEAR SUBSTRUCTURES IN GALAXY CLUSTERS

E. Panko¹, V. Korshunov², S. Yemelianov³, V. Zabolotnii⁴I. I. Mechnikov Odessa National University
Odessa, Ukraine,¹panko.elena@gmail.com, ³sviatoslavem@gmail.com,
²valerij.korshunov@gmail.com, ⁴zabvitec@gmail.com

ABSTRACT. We propose detailed scheme that is describing the morphology of linear substructures in galaxy clusters. Our base morphological scheme divides galaxy clusters using numerical criteria according the parameters: concentration to the cluster center, the presence of linear substructure, orientation of images of galaxies, the role of brightest cluster members, the shape of galaxies.

Our analysis of 2D distribution of galaxies based on study more than 500 galaxy clusters. We show the linear substructures are regular peculiarity in galaxy clusters. Our approach allows to divide filamentary and edge-on wall substructures and to select galaxy clusters with possible peculiarities in hot gas and/or DM distribution.

Keywords: Galaxies: clusters: morphology.

АНОТАЦІЯ. Морфологія скупчень галактик є одним з найважливіших ключів до розуміння еволюційних процесів формування великомасштабної структури Всесвіту та вивчення її інших фізичних компонентів. Результати численних комп'ютерних симуляцій дозволяють стверджувати, що філаментарні субструктури у скупченні не є випадковими, вони відображають розподіл наймасивнішого з його компонентів - темної матерії. При цьому, розташування галактик у скупченні є найдоступнішим індикатором розподілу не тільки темної матерії, а й гарячого газу, а також воно може вказувати на взаємодію з іншим скупченням. Орієнтації галактик у субструктурах також не є випадковими: в одномірних особливостях галактики вирівнюються вдовж смуги найбільшої густини, в двомірних - дискові галактики вирівнюються до перпендикуляру неї.

Розподіл галактик у скупченні зручно описувати як його морфологічний тип. Морфологічна схема, яку у 2013 році запропоновано Панько, спирається на декілька класичних схем морфологічної класифікації різних авторів та основана на чисельних критеріях. Схему реалізовано у пакеті програм «The Cluster Cartography». Це

дозволяє проводити аналіз швидко та об'єктивно. Всі скупчення, які вивчалися, є в каталозі Панько та Фліна «The Catalogue of Galaxy Clusters and Groups» (2006); інформацію про галактики кожного скупчення взято з каталогу галактик Мюнстерського Червоного Огляду Неба (Унгруче та ін., 2003).

Ми представляємо результат аналізу особливостей лінійних субструктур в 254 багатих скупченнях без ознак концентрації до центру скупчення, 178 скупченнях з помірною концентрацією до центру, 28 скупченнях з високою концентрацією до центру та 112 скупченнях, які розташовані в областях найбільшої густини галактик. У всіх випадках доля скупчень, в яких присутні лінійні субструктури, складає приблизно 50%, що співпадає з результатами комп'ютерних симуляцій та дає можливість вважати такі субструктури регулярними.

В роботі запропоновано детальну класифікацію скупчень галактик з лінійними субструктурами. Новий підхід дає можливість виділити серед таких скупчень такі, що мають дійсно лінійні особливості або відповідають випадку розташування двомірної субструктури вдовж проміню зору.

Ключові слова: галактики, скупчення галактик, морфологія.

1. Introduction

The morphology of galaxy clusters is the accessible key to understanding the evolution of the Universe as well as to distribution of DM. Distribution of galaxies both in the space and on the celestial sphere reflected the primordial adiabatic fluctuations in beginning moments of Universe, as it shown in big number of works from Silk (1968), Peebles & Yu (1970), Sunyaew & Zeldovich (1970). The results of different numerical simulations from well quoted Millennium Simulation (Springel et al., 2005) to Illustris Project (Vogelsberger et al., 2014; Artale et al., 2017) or Cui et al. (2018) show galaxy clusters as evolved elements of large scale structure of the Universe. Galaxy fraction is small-

est part in cluster mass, nevertheless galaxies were and remain the confident optical markers of structure of clusters. The connection between distributions of main components of galaxy clusters – DM, hot gas and galaxies – was established by Dietrich et al. (2012) for A222 and A223 clusters. Their galaxies form linear substructure which duplicate the hot gas bridge and DM arch between the interacted clusters. The another case – collided galaxy clusters show different distribution of intercluster galaxies, hot gas and DM (Markevitch et al., 2004, Pearce et al., 2017).

The distribution of galaxies can be described as their morphology. Based on classical approaches, including both famous Bautz – Morgan (1970), Rood – Sastri (1971) systems and less popular López-Cruz & Gaztanaga (2001) and López-Cruz (2003) ones, Panko (2013) proposed improved and integrated scheme of morphological classification for 2D distribution of galaxies on the celestial sphere. According to the Panko scheme, galaxy clusters have types corresponding to cluster “concentration” (from *C* – compact, to *I* – intermediate, and *O* – open), “flatness signs” (*L* – line or *F* – flat, and no symbol if no indication of flatness is present) and the role of bright galaxies (*cD* or *BG*, if the bright cluster members role is significant). Other peculiarities are noted as *P*. “Flatness signs” can correspond to filamentary substructure or preferential plane in cluster. The designations can be combined, for example *CFcD* or *ILP*.

The Cluster Cartography set (hereafter CC) was created for simplification of the galaxy clusters classification (Panko & Emelyanov, 2015). As a result, it was established the linear substructures present as peculiarities in about 50% of rich galaxy clusters. We can assume the linear substructures are regular peculiarities in galaxy clusters.

The paper is organized in the standard manner. Section 2 contains the description of the observational data and the cluster mapping, section 3 presents the characters of linear substructures and its analysis, and section 4 conclusions and analysis is given at the end.

2. Observational base and the method of analysis

The main base of our research is the list of galaxies of Münster Red Sky Survey (Ungrihe et al., 2003, hereafter MRSS). It’s a result of scanning of 217 plates of Southern Sky Atlas R (ESO) by *PDS2020GM^{plus}*. The classification of objects into stars, galaxies, and perturbed objects was done by an automatic procedure with a posterior visual check of the automatic classification, which considerably diminished the number of objects erroneously classified as galaxies. External calibration of the photographic magnitudes was carried out by means of CCD sequences obtained with

three telescopes in Chile and South Africa. The catalogue of galaxies MRSS is complete to a magnitude limit of $r_F = 18^m.3$. Each form more than 5 millions of MRSS galaxies have equatorial coordinates, r_F magnitude, axes and position angle of best-fit ellipse and some another parameters. Unfortunately, MRSS is last photographic catalogue and their galaxies have not redshifts.

About 1.2 millions of galaxies are in the limit of MRSS complexness. This short list was the observational base of “The Catalogue of Galaxy Clusters and Groups” (Panko & Flin, 2006, hereafter PF catalogue) which was created for statistical study of galaxy clusters properties. PF galaxy clusters having 100 and more galaxies in cluster field we consider as rich ones.

For each PF galaxy cluster we have the list of galaxies in cluster field and each galaxy have full information from MRSS. In our research the data for each galaxy in the cluster are transformed to CC format. Real sizes of galaxies are so small for using in CC mapping. So, the symbols corresponded to galaxies are calculated from magnitudes and ellipticity as:

$$m' = 3 \cdot 2^{0.6(18.5-m)} + 6 \quad (1)$$

$$2a = \frac{m'}{\sqrt[4]{1-2E+E^2}}; \quad 2b = \frac{(m')^2}{2a} \quad (2)$$

were $2a$ and $2b$ are sizes of major and minor axes of symbol; ellipticity $E = 1 - \frac{b}{a}$. The equations (2) transform the circle to ellipse with the same area and connect symbol axes with galaxy magnitude.

The coefficients in the equation 1 were determined for MRSS galaxies and can be changed in case of using another input data. For CC standard map size – 4000×4000 arcsec – the symbol sizes calculated according to the equation 1 are optimal for visual control.

Last modification of CC set allows to exclude the central part of cluster in estimation of the degree of concentration to the main band. The degree can be noted as 5, 7, 9, 11, where numerals corresponds the band width relative to cluster diameter (1/5, 1/7, 1/9, 1/11). So we can replace marks *F* and *L* to *L5...L11* (Fig. 1).

The distribution of densities in the bands is calculates taking to account both the square of each band and full number of galaxies in the cluster.

3. The results and discussion

In our previous study we analyzed the 2D the distribution of galaxies in the galaxy clusters on the celestial sphere using CC set according to the improved scheme of morphological classification (Panko, 2013, Panko, 2015). We studied 254 rich open (Panko &

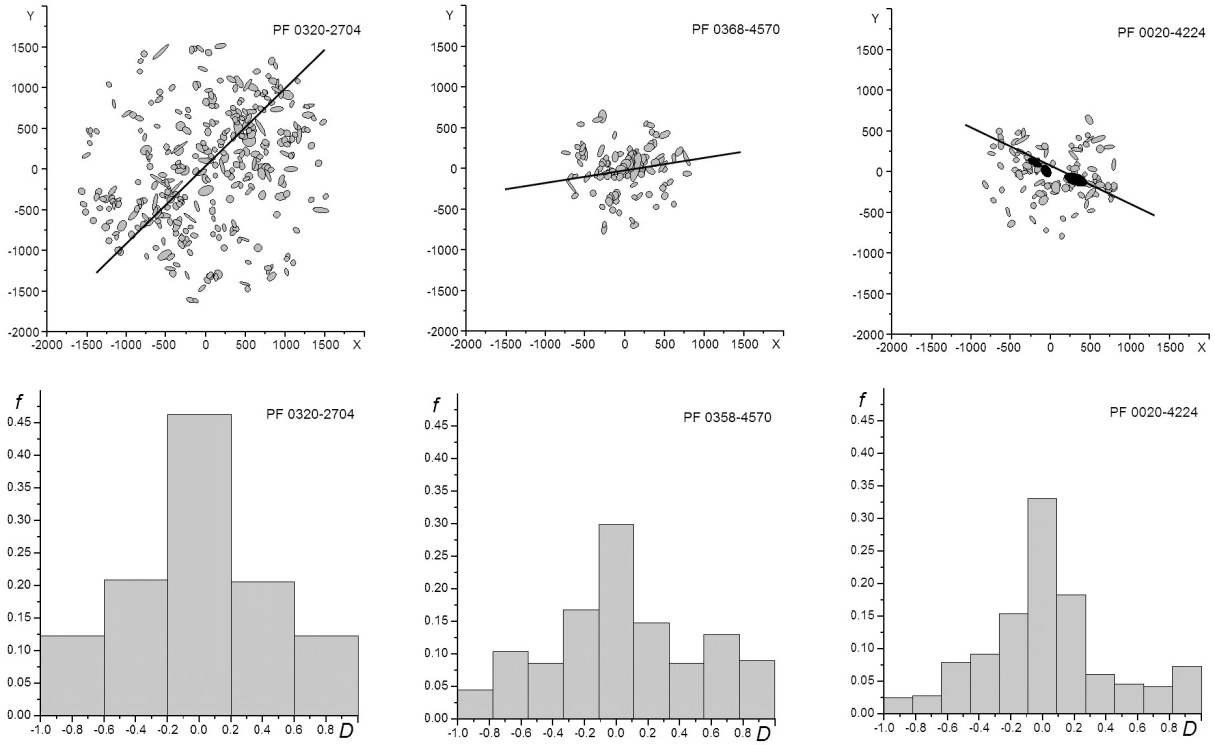


Figure 1: From left to right: maps and distribution of density of galaxies in bands for $L5$, $L9$ and $L11$ subtypes. In case PF 0368-4570, O -type, the central region was excluded.

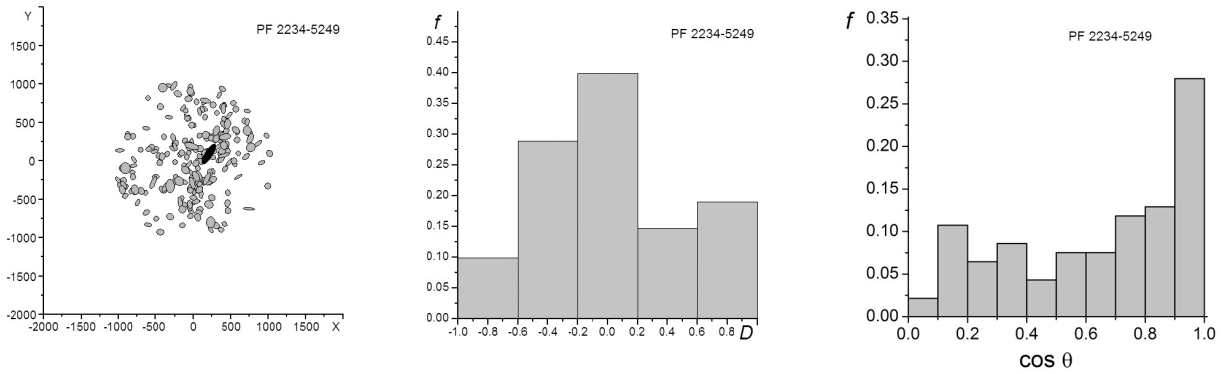


Figure 2: Orientation of galaxies in densest band in PF 2234-5249 cluster. From left to right: map, distribution of density of galaxies in the bands, corresponded to $L5$ subtype and distribution of cosines of acute angles between the direction of $L5$ -line and all galaxies inside the central (main) band.

Emelyanov, 2017, Panko et al., 2018), 178 rich intermediate (Panko et al., *in preparation*) and 28 rich concentrated galaxy clusters (Panko et al., 2018), as well as 112 ones placed in richest regions of southern sky (Panko et al., *in preparation*). Our experience allows us to simplify and to specify the detailed classification of linear substructures as $L5...L11$. Connection between hot gas distribution and linear substructure

for our input data was found by Tugay et al. (2016) for PF 2187-1958 cluster. In this case the overdense strip has the same direction as major axis of the elongated X-ray halo. The same situation was observed by Mann & Ebeling (2012) in evolved galaxy clusters MACS J0416.1-2403 A2744, A2813, MACS J0358.8-2955; L type according Panko, (2013) morphological scheme or $L9 - L11$ according to present paper.

As one can see on Fig. 1, linear substructures are statistically significant, however, the orientation of galaxies in different clusters note the possible presence in cluster filamentary substructures as well as wall-like ones. For filamentary substructures major axes of galaxies in the projection to the celestial sphere are alignment to the direction of the densest band, as it clearly seen in Fig. 2 (PF 2234-5249, *L5* subtype). In the right panel the distribution of cosines of acute angles between the direction of *L5*-line and all galaxies inside the central band points to statistically significant prevalence for small angles (values of cosine from 0.9 to 1.0). The filamentary substructure in the PF 2234-5249 cluster is curved, it is seen both in the map and in the histogram on central panel. Trend to alignment of major axes one can note for values of cosine from 0.4. Scatter of cosines in 0.1 to 0.4 bins is connected with small ellipticities of images of galaxies. In this case we have big errors for position angle values. This case corresponds to Joachimi et al.(2015) in full: in 3D simulation elliptical galaxies tend to align their major axes with the filament direction, while disc galaxies tend to align their spin perpendicular to the filament direction. For both cases we have the alignment of images of galaxies to to the filament direction.

Another case, described in Joachimi et al.(2015) paper too, is described the galaxy alignments at the surface of a void (wall). Elliptical galaxies tend to align their major axes perpendicular to the radius vector from the center of the void, while disc galaxies tend to align their spin along this direction. We found this case in our data set too. In Fig. 1, left panel, we see different orientations of galaxies in densest band in PF 0320-2704, *L5* subtype. We can assume in PF 0320-2704 we see edge-on wall.

4. Conclusion

We have constructed the scheme for detailed description of filamentary substructures in galaxy clusters. Our multifactorial analysis the morphology of clusters allows to divide galaxy clusters having the linear substructures for subtypes, described them in details. Linear substructures are regular substructures in galaxy clusters. Our approach allows to select galaxy clusters with possible peculiarities in hot gas and/or DM distribution. We have possibility to divide filamentary and edge-on wall substructures also.

Acknowledgements. This research has made use of NASA's Astrophysics Data System.

References

- Artale M.C., Pedrosa S.E., Trayford J.W. et al.: 2017, *MNRAS*, **470**, 1771.
 Bautz P., Morgan W.W.: 1970, *ApJ*, **162**, L149.
 Dietrich J.P., Werner N., Clowe D., et al.: 2012, *Nature*, **487**, 202.
 Cui W., Knebe A., Yepes G.: 2018, *MNRAS*, **473**, 68.
 Joachimi, B., Cacciato, M., Kitching, T.D. et al.: 2015, *Space Sci Rev*, **193**, 1.
 Markevitch M., Gonzalez A. H., Clowe D. et al.: 2004, *ApJ*, **606**, 819.
 López-Cruz O. & Gaztanaga E.: 2000, *ASP*, **218**, 247, *arXiv:astro-ph/0009028*.
 Lóopez-Cruz O.: 2003, in: *The Garrison Festschrift: Contribution of the Institute for Space Observations*, **No 20**, 109.
 Panko E., Flin P.: 2006, *J. Astr. Data*, **12**, 1.
 Panko E.: 2013, *Odessa Astr. Publ.*, **26**, 90.
 Panko E.: 2015, in: Proc. Polish Astr. Soc. "Introduction to Cosmology", **2**, 79.
 Panko E.A., Emelyanov S.I.: 2015, *Odessa Astron. Publ.*, **28**, 135.
 Panko E.A., Emelyanov S.I.: 2017, *Odessa Astron. Publ.*, **30**, 121.
 Panko E.A.; Andrievsky S.M.; Yemelianov S.I. et al.: 2018, *Astron. Rep.*, **62**, 911.
 Panko E., Sirginava A., Stepaniuk A.: 2018, *Odessa Astron. Publ.*, **31**, 29.
 Peebles P. J. E. & Yu J. T.: 1970, *ApJ*, **162**, 815.
 Pearce C. J. J., van Weeren R. J., Andrade-Santos F. et al.: 2017, *ApJ*, **845**, 81.
 Rood H.J., Sastry G.N.: 1971, *PASP*, **83**, 313.
 Silk J.: 1968, *ApJ*, **151**, 459.
 Springel V., White S. D., Jenkins A. et al.: 2005, *Nature*, **435**, 629.
 Sunyaev R.A. & Zeldovich Ya.B.: 1970, *Ap&SS*, **7**, 3.
 Vogelsberger M., Genel Shy, Springel V. et al.: 2014, *MNRAS*, **444**, 1518.
 Ungruue R., Seitter W.C. & Duerbeck H.W.: 2003, *J. Astr. Data*, **9**,1.

DOI:<http://dx.doi.org/10.18524/1810-4215.2019.32.182523>

INTERNATIONAL NUCLEAR DATA CENTERS NETWORK AND PROSPECTS OF ITS USE IN NUCLEAR POWER IN BELARUS

I.A. Serenkova¹, A.A. Pankov^{1,2,3}

¹ Abdus Salam ICTP Affiliated Centre at Technical University of Gomel,
Gomel 246746 Belarus *inna.serenkova@cern.ch*

² Institute for Nuclear Problems of Belarusian State University,
Minsk, 220030 Belarus

³ Joint Institute for Nuclear Research,
Dubna, 141980 Russia *apankov@jinr.ru*

ABSTRACT. We give a brief overview of the existing nuclear data base, and describe the structure of the International Nuclear Data Centres Network. Because the amount of experimental data in nuclear physics is extremely large, the note aims to show the way to modern methods of acquaintance with the characteristics of arrays of nuclei through the nuclear data banks accessible through the Web-technologies. In particular, the note describes the methods to extract information on the nuclei and nuclear reactions in nuclear data banks. The data include information on the masses and energies of the nuclei of the separation energy of nucleons and clusters, the spectra of states of nuclei, their spin, parity, isospin, charge and mass radii and densities, information about the shape of the nuclei, the cross sections of nuclear reactions, the decay of unstable nuclei. On the completeness and accuracy of the data depends on radiation and nuclear safety, and environmental acceptability of nuclear installations. Creating a nuclear databases in Belarus will monitor the quality of nuclear data supplied to consumers, and ensure that systems of constants, used in technical projects, the current international standards.

Keywords: nuclear data centre, nuclear power.

АНОТАЦІЯ. Дається короткий огляд існуючих баз ядерних даних та міжнародної мережі центрів ядерних даних. Оскільки обсяг експериментальних даних по фізиці ядра надзвичайно великий, в роботі наводяться сучасні методи ознайомлення з масивами характеристик ядер через банки ядерних даних. Зокрема, описані методи вилучення інформації про ядра і ядерні реакції через банки ядерних даних. Дані включають в себе інформацію про маси і енергії зв'язку ядер, про енергії відділення нуклонів і кластерів,

спектрах станів ядер, їх спинах, парності, ізоспінам, зарядових і масових радіусах і щільності, інформацію про форму ядер, перетинах ядерних реакцій, розпади нестабільних ядер. Від повноти і точності цих даних залежать радіаційна і ядерна безпека, а також екологічна прийнятність ядерних установок. Створення бази ядерних даних в Білорусі дозволить контролювати якість ядерних установок, що поставляються споживачам, і забезпечити відповідність систем констант, які закладаються в технічні проекти, сучасним міжнародним стандартам. На основі інформації, що містяться в базах ядерних даних, оцінюється радіаційне навантаження на корпуси реакторів АЕС і інші вузли в процесі їх експлуатації. Це дозволяє контролювати процес безпечної експлуатації корпусів атомних реакторів і оцінювати можливість продовження ресурсу експлуатації, якщо перевищує межі регламентного терміну. Результати досліджень, отримані в представленій роботі, були частково використані при визначенні та уточненні кола завдань, що вирішуються при виконанні спільних НДР в рамках Договору про науково-технічному співробітництво між Інститутом ядерних досліджень НАН України (м. Київ), ДНУ «Об'єднаний інститут енергетичних і ядерних досліджень – Сосни» НАН Білорусі (ОІЕЯД – Сосни) і УО «Гомельський державний технічний університет ім. П.О.Сухого».

Ключові слова: бази ядерних даних, міжнародна мережа центрів ядерних даних, бази ядерних даних в Білорусі.

1. Introduction. Nuclear Data Types and Data Centers

1.1. What is nuclear data?

Nuclear data are quantitative results of scientific investigations of the nuclear properties of matter. They describe properties of atomic nuclei and the fundamental physical relationships governing their interactions, thereby characterizing the physical processes underlying all nuclear technologies. Examples of nuclear data include cross sections, half-lives, decay modes and decay radiation properties, and γ -rays from radionuclides. The scope of the data collections includes all 85 natural elements with 290 stable isotopes and more than 2500 radionuclides.

The applications of nuclear data include all areas of nuclear science and technology, covering energy applications (fission reactor design; nuclear fuel cycles; nuclear safety; reactor monitoring and fluence determination; waste disposal and transmutation; accelerator driven systems; fusion device design and plasma processing technologies) as well as non-energy applications (cancer radiotherapy; production of radioisotopes for medical and industrial applications; personnel dosimetry and radiation safety; nuclear safeguards; waste disposal and transmutation; environmental monitoring and clean-up; materials analysis and process control; radiation damage studies; detection of concealed explosives and illegal drugs; exploration for oil and other minerals) and basic research (e.g. nuclear astrophysics) and education. For details of the review of nuclear data for applications and original references, see Tsytrinov A.V., Pankov A.A., Serenkova I.A.: 2015.

1.2. The role of the IAEA Nuclear Data Section

The Nuclear Data Section (NDS) of the International Atomic Energy Agency (IAEA) carries out the IAEA activities concerning development and dissemination of nuclear and atomic data for applications. In addition, the NDS is involved in technology transfer activities to assist scientists in developing countries.

The main tasks of the *data center* include compilation of new data in the databases EXFOR and CINDA (in cooperation with other participating data centers, see below), collection and maintenance of general-purpose and specialized evaluated data libraries, on-line and off-line nuclear data services with particular emphasis on the needs of developing countries, and coordination of nuclear data center networks.

Nuclear data development is conducted mainly through Co-ordinated Research Projects (CRPs). In such projects, which usually result in the production of a new (or significant upgrade of an existing) database, typically 4-10 scientific groups from different countries

work together under IAEA contracts or agreements over a period of 3-4 years.

Technology transfer to developing countries is carried out in two ways: through Technical Co-operation projects, such as the recent "Latin American Mirror Server Project" providing online nuclear data service to Latin American countries with insufficient Internet connection to the NDS, by installing a mirror server in Brazil, or the installation of a "mini data center" on a workstation in Ghana; and through nuclear data workshops such as those held at ICTP Trieste.

The *Atomic and Molecular Data Unit* of the NDS keeps databases for fusion energy and other plasma research and other applications, such as ALADDIN (numerical data) and AMBDAS (bibliographic data), and issues specialized publications (e.g. CIAMDA). The databases are kept on a separate server. The remainder of this lecture deals only with the nuclear data services of NDS.

1.3. Nuclear data types

Nuclear data are commonly categorized in two main groups: nuclear reaction data, describing the interactions of various projectiles such as neutrons, protons or photons with target nuclei, and nuclear structure and decay data, describing nuclear levels, half-lives and radioactive decay radiations. For evaluated data (both numeric) or bibliographic.

Bibliographic data: References with some description of the contents, but no numerical data. Examples are CINDA (Computer Index of Neutron Data) and NSR (Nuclear Science References).

Experimental data: Results of individual measurements as reported by the authors. The most important example is EXFOR/CSISRS, the library for experimental nuclear reaction data.

Evaluated data libraries contain recommended data based on all data available from experiments and/or theory, arrived at after critical analysis of experimental data and their uncertainties, inter- and extrapolation, and/or nuclear model calculations. They are stored in strictly defined formats such as ENDF-6 (the international format for evaluated nuclear reaction data) or ENSDF (the format of the Evaluated Nuclear Structure data File). The main cross section libraries in ENDF format usually also contain the relevant decay data needed in the main applications.

Nuclear reaction data include cross sections, angular and energy distributions of secondary particles, resonance parameters, and related quantities. For neutron-induced reactions up to 20 MeV, the libraries are very complete; the coverage for higher energies is less complete but improving. Experimental data are found in EXFOR, the related bibliography in CINDA; several evaluated data libraries exist up to 20 MeV or

higher. For charged-particle induced and photonuclear reactions, selected experimental data are compiled in EXFOR and only few evaluations exist. Heavy-ion data are partly compiled in EXFOR.

Nuclear Structure and decay data: Half-lives, decay schemes, nuclear level properties, energies and intensities of γ -rays and emitted particles, atomic masses. The major database is ENSDF, related bibliographic data are contained in NSR. There are many other nuclear structure and decay data libraries, mostly derived from or related to ENSDF; some of these are listed in Section 2 below, others - not available from NDS - include the *Table of Isotopes*, the *Isotope Explorer*, a computer program for viewing ENSDF and for interactive access to nuclear structure and decay data, and NUBASE, a library of nuclear and decay properties.

1.4. Nuclear data center networks

Both the collection and the distribution of nuclear data are organised on a world-wide scale. Two international networks are coordinated by the IAEA: the Network of Nuclear Reaction Data Centers and the Nuclear Structure and Decay Data Network. The data centers participating in these networks are involved in the various stages of data preparation between measurement and application (i.e. compilation, review and/or evaluation, processing, distribution). Specialized data centers cooperate with the major centers in the various data center functions (in particular data compilation and evaluation). The sharing of work on a world-wide basis in the various areas of work, including data distribution, is defined partly geographically and partly by data types (scope) and is coordinated by the IAEA Nuclear Data Section.

2. Overview of Data Libraries at IAEA

The IAEA Nuclear Data Section holds a total of about 100 nuclear data libraries, representing an enormous economic and scientific value. All libraries and the related documentation are available free of charge to scientists in IAEA member states. An overview is given in the document *Index of Nuclear Data Libraries available from the IAEA Nuclear Data Section*. Brief documentations of contents and/or format for most libraries are published in the IAEA-NDS- report series.

2.1. General purpose libraries

Nuclear Wallet Cards: Basic properties of ground and meta-stable states, available as a pocket booklet (from US-NNDC) and online.

NUDAT: User-friendly extract of most important

data (for applications) from ENSDF, plus thermal neutron data (cross sections and resonance integrals). Available online.

MIRD: “Medical Internal Radiation Dose”: Based on ENSDF, data processed with code “RADLST”. Tables with intensities, energies and dose of all produced radiations, including X-rays, Auger electrons, etc., and decay scheme plots, for the selected nuclide. Available online.

ENSDF: (Evaluated Nuclear Structure Data File) is the “master library” for structure and decay data, resulting from a continuous international evaluation effort coordinated by the IAEA. The master file is maintained by the US-NNDC. It contains evaluated experimental data for most known nuclides in the mass range 1 - 277. The evaluations are done for mass chains (e.g. $A=235$) and are published in the journal *Nuclear Data Sheets*. Available online.

NSR: (Nuclear Science References): Bibliographic database for low and intermediate energy nuclear physics. This is the main bibliography for structure and decay data and for non-neutron reaction data and covers the literature from 1910 to present. It is published regularly in the journal *Nuclear Data Sheets*. Available online.

CINDA: (Computer Index of Neutron Data): Bibliography of neutron data literature, covering also unofficial publications and computer files. Includes also ($\gamma,11$), (γ,f) and spontaneous fission data. References describing the same experiment are listed together. An extension of the database to include charged-particle induced and all photonuclear reactions is under preparation. Available online, as a book in several volumes, and on CD-ROM

EXFOR: Experimental nuclear reaction data, compiled continuously by the network of nuclear reaction data centers coordinated by NDS. Contains neutron, charged-particle induced and photonuclear data, including integral and all types of differential cross sections, resonance parameters, polarization data, fission product yields, and many related data types. The library contains both numerical data tables and a structured abstract with experimental and bibliographic information. The neutron data in EXFOR are linked to the CINDA bibliography. The data can be retrieved in several formats, including computational format for further processing, and graphs. The main usage of EXFOR is for evaluators (the EXFOR database is the starting point for all cross section evaluations), for applied users if no evaluation is available, and for researchers measuring or calculating cross section data. Available online and on CD-ROM.

Evaluated cross section data libraries in ENDF-6 format: the major “general purpose” evaluated libraries ENDF-B/VI (USA), BROND-2 (Russia), JEF-2 (Europe), JENDL-3 (Japan), CENDL-2 (China) are available online (“ENDF” database) and

on CD-ROM. All of these libraries cover the neutron energy range from 10^{-5} eV to 20 MeV, with some evaluations extending to higher energies (partly up to 1 GeV) and including also some charged-particle induced reactions. Output is available in several formats including plots, and software packages (Pre-Processing and Utility codes) are available for data treatment. Online comparisons of evaluated and experimental cross sections can be done using the package ZVView.

2.2. Specialized evaluated cross section libraries

FENDL-2: Comprehensive cross section library for fusion and other applications, resulting from a worldwide effort including extensive testing, coordinated by IAEA consists of several sublibraries for transport calculations, activation, fusion reactions, etc. Available online.

IAEA Photonuclear Data Library: Evaluated photonuclear cross sections for **164** isotopes for energies up to **140** MeV (most isotopes), up to about **25** MeV for the others; for shielding, medical and other applications. Available online.

Charged Particle Cross Section Database for Medical Radioisotope Production for diagnostics and monitor reactions: Production cross sections for γ -emitters and positron emitters, for incident protons through α -particles up to about 30 MeV. Available online.

RNAL (Reference Neutron Activation Library): Evaluated cross sections for 255 neutron-induced reactions leading to radioactive products, for activation analysis and various other applications. The evaluations were extracted from various regional and national projects.

NGATLAS: Atlas of neutron capture cross sections for **739** targets from 10^{-5} eV to **20** MeV. Available as a handbook (plots only) or online.

RRDF-98 Neutron cross sections for 22 dosimetry reactions. Available online.

MENDL-2 and MENDL-2P Activation cross sections for 505 stable and unstable targets between Al and Po for incident neutrons up to 100 MeV and incident protons up to 200 MeV, for transmutation and other applications. Available by FTP.

WIND and WIND-2 Cross sections for U, Np, and Pu isotopes for waste incineration, including neutron cross sections up to 100 MeV, proton cross sections for U^{238} , and neutron activation data for Pu^{239} up to 2 GeV.

Minsk Actinides Library Evaluated neutron cross sections for Th^{232} , U, Np, Pu, Am and Cm isotopes.

2.3. Other special libraries

RIPL-2 A database of input parameters for nuclear model calculations of nuclear reaction data, available online.

NMF-90 Neutron Metrology File: Integrated database for neutron spectrum adjustment (unfolding) calculations. Available online.

XG Standards(X-ray and γ -ray standards for detector calibration): This database contains for selected nuclides their half-lives and the energies and emission probabilities of γ -rays and X-rays suitable for detector and efficiency calibration. A new version will be released soon, see NDS web page.

EPDL9T (Evaluated Photon Data Library): Photon interaction data from 1 eV to 100 GeV from Lawrence Livermore National Laboratory.

SGNucDat (Nuclear Data for Safeguards): A PC database (also available as a handbook) containing nuclear data needed for the development and application of nuclear material accounting techniques.

2.4. Computer programs

The following computer code packages are available free of charge from NDS.

EMPIRE-II: system of codes for nuclear reaction calculations (Version 2.18);

ENDF Utility Codes (**Release 6.13**);

ENDF Preprocessing Codes (**PREPRO 2015**);

ENDVER: ENDF Verification support package;

ENSDF analysis and utility programs;

ZVVIEW package for interactive plotting of nuclear data.

Other computer codes for the processing of nuclear data have to be requested from the NEA Nuclear Data Bank, Issy-les-Moulineaux near Paris, France.

3. Data Access and Services

Various data distribution media are offered by NDS, including WWW, CD-ROM and hardcopies in order to serve the diverse needs of users from both developing and fully industrialized countries. A nuclear data “mirror server” has been established at IPEN in Brazil to improve on-line access for Latin America by providing WWW, FTP and Telnet access to the IAEA nuclear data services.

WWW: “Nuclear Data Services” website of the IAEA can be accessed through <http://www-nds.iaea.org> (IAEA Vienna) or <http://www-nds.ipen.br/> (Brazil mirror server). Contains links to most data libraries, electronic documents, nuclear data programs, general information,

and much more. Some data are available also by FTP and/or a Telnet-based on-line retrieval system.

Handbooks: A number of nuclear data handbooks have been produced by NDS (some of them are priced IAEA publications), including hardcopy versions of the CINDA bibliography of neutron data, and a Handbook on Nuclear Data for Safeguards; normally, the results of a Co-ordinated Research Project on nuclear data are published within the IAEA-TECDOC series.

Reports: NDS publishes informal reports in the INDC series, containing meeting summaries, unpublished nuclear data works from member states, and translations from Russian literature; most recent reports are available electronically on the NDS website.

Nuclear Data Newsletter is published biannually, and serves as the primary medium for current awareness of new nuclear data available from NDS; available in hardcopy and from the web.

Custom retrievals and other mail services can be requested by informal e-mail to services@iaeand.iaea.org.

4. Creation of a nuclear data center at Gomel State Technical University (GSTU)

The activity on the development of Scientific, Methodological and Information Basis for Nuclear and Technological Calculations had been started in 2013 in the framework of joint Project of Ukrainian Nuclear Data Center (UkrNDC) at the Institute for Nuclear Research of NAS (Ukraine) and Laboratory for Physical Studies at the GSTU (Gomel, Belarus). The name of the Project was "Accumulation, Processing, Systematization and Analyses of Information in the Nuclear Power as the basis to found the Information Nuclear Data Center".

Fourteen Webpages of the Nuclear Data Information Center (in Russian and English) at GSTU were developed and performed by Dr. O.O. Grizay. In most cases, the Russian and English versions of the pages are identical, with the exception of the "MANUAL" pages. The main Webpage is depicted in Fig. 1.

5. Concluding Remarks

The primary aims of the IAEA Nuclear Data Section are to encourage the development and organize the assembly of a wide range of atomic and nuclear databases, and ensure improvements in technical performance by providing ready access to users in Member States. To make the service more user-friendly and, at the same time, extend the retrieval possibilities, development of a combined nuclear reaction database is under way, using advanced database software, with which the EXFOR, CINDA and ENDF

Scientific, Methodological and Information Basis for Nuclear and Technology Calculations

Russian version

The activity on the foundation of Scientific, Methodological and Information Basis for Nuclear and Technological Calculations had been started in 2013 in the framework of joint Project of Ukrainian Nuclear Data Center, UkrNDC, Institute for Nuclear Research NAS Ukraine, IRE, Kyiv, Ukraine) and Physics Research Laboratory, ERL (Pavel Sukhol State Technical University of Gomel, GSTU, Gomel, Belarus). The name of the Project is "Accumulation, Processing, Systematization and Analyses of Information in the Nuclear Power sphere as the basis to found the Information Nuclear Data Center".

Goals and Objectives

- Creation of the computerized nuclear data base
- Creation of the software database for the nuclear constant preparation and carrying out the engineering calculations
- Organization of the remote access to the modern international sources of nuclear and physical information
- Creation of the teaching and educational methodological base for manpower development to carry out the production of nuclear constants and engineer calculations to ensure the regular and safe operation of nuclear installations

Data Bases	Libraries of experimental and evaluated nuclear data, some special-purpose libraries
Codes	Codes to carry out the production of nuclear constants and engineering calculations
Site Addresses	Modern international sources of nuclear and physical information
Manuals	Educational methodological and scientific literature
Contacts	Information on the personals and areas of their responsibility

Web and Database Programming: Olga Grizay, Ukrainian Nuclear Data Center
Institute for Nuclear Research NAS Ukraine, pr. Nauky, 47, Kyiv, Ukraine, 01680
Phone: +380 44 525 3987 E-mail: grizay@inn.kiev.ua

Figure 1: Main Webpage (in English) of the Nuclear Data Information Center at the GSTU.

libraries will look like one database to the user. Further improvements under way include increased distribution of databases through the Internet and the creation of additional regional copies of the "Nuclear Data Services" Websites. Creating a nuclear databases in Belarus, in particular in GSTU (Gomel) in closed collaboration with Ukrainian experts is also discussed.

Acknowledgements We would like to thank Dr. O.O. Grizay and Dr. O.I. Kalchenko for the enjoyable collaboration on the subject matter covered here.

References

- Pankov A.A., Tsytrinov A.V., Serenkova I.A.: 2015, *Nonlinear Dynamics and Applications.*, **21**, 270.

DOI:<http://dx.doi.org/10.18524/1810-4215.2019.32.182531>

INFRARED COUNTERPARTS OF X-RAY GALAXIES

A.V. Tugay¹, S.Yu. Shevchenko²

¹ Taras Shevchenko National University of Kyiv,
Kyiv, Ukraine, *e-mail: tugay.anatoliy@gmail.com*

² Schmalhausen Institute of Zoology, NASc of Ukraine,
Kyiv, Ukraine, *e-mail: astromott@gmail.com*

ABSTRACT. Population studies of the extragalactic objects are a major part of the universe large-scale structure study. Apart from radio, infrared, and visible wavelength bands, observations and further identification of extragalactic objects such as galaxies, quasars, blazars, liners, and active star burst regions are also conducted in the X-ray and gamma bands. In this paper we make identification and cross-correlate of the infrared and X-ray observational data, build a distribution of a selected sample sources by types and attempted to analyze types of the extragalactic objects at distances up to $z = 0.1$ using observational data of relevant space observatories.

Data from a leading X-ray space observatory XMM-Newton were used to compile the largest catalog of X-ray sources. Current version of XMM SSC (Serendipitous Source Catalog) contains more than half a million sources. In our previous works we selected and analyzed a sample of 5021 X-ray galaxies observed by XMM-Newton. Identification and classification of these sources is essential next step of the study. In this study we used infrared apparent magnitudes from WISE catalog of AGN candidates. In 2010 space telescope WISE performed full sky survey in four infrared bands and detected 747 million sources. WISE catalog of AGN candidates amounts 4 million of possible extragalactic sources. We built infrared color-color diagram for our sample of X-ray galaxies and assessed their types using WISE telescope data. In this study we also analyzed large scale structure of the universe (distances up to $z=0.1$). This analysis revealed Coma galaxy cluster and SDSS Sloan Great Wall. In the further studies we are planning to investigate the distribution of different types of X-ray galaxies within the large-scale structures of the Universe.

Keywords: AGN, XMM-Newton, WISE, X-ray, infrared survey.

АНОТАЦІЯ. Дослідження складу і природи позагалактичних об'єктів є важливою частиною досліджень великомасштабної структури всесвіту.

Окрім радіо-, інфрачервоного діапазону та видимого випромінення, спостереження та подальше ототожнення позагалактичних об'єктів, таких як скупчення галактик, квазари, блазари, лайнери та області з активним зореутворенням ведуться в рентгенівському та гама-діапазонах. В цій роботі ми провели ототожнення та перехресну кореляцію спостережних даних інфрачервоного та рентгенівських діапазонів та побудували розподіл в вибірці цих джерел за типом. Проаналізовано вміст позагалактичних об'єктів різних типів на відстанях до $z=0.1$ використовуючи дані відповідних космічних обсерваторій.

Для складання найбільших каталогів рентгенівських джерел використовуються дані провідної рентгенівської космічної обсерваторії XMM-Newton. Поточна версія каталогу XMM SSC (Serendipitous Source Catalog) містить понад півмільйона джерел. У наших попередніх роботах ми відібрали та проаналізували дані 5021 галактики в рентгенівському діапазоні, які спостерігались XMM-Newton. Ідентифікація та класифікація цих джерел є важливим наступним кроком дослідження. У цьому дослідженні ми використали інфрачервоні зображення інфрачервоної космічної обсерваторії WISE з каталогу кандидатів у активні ядра галактик. У 2010 році космічний телескоп WISE здійснив огляд всього повного неба у чотирьох інфрачервоних діапазонах та виявив 747 мільйонів джерел. Каталог WISE кандидатів у активні ядра галактик становить 4 мільйони можливих позагалактичних джерел. Ми побудували інфрачервону кольорову діаграму для нашої вибірки рентгенівських галактик та оцінили їх типи, використовуючи дані телескопа WISE. В цій роботі ми також дослідили великомасштабну структуру Всесвіту (на відстанях до $z=0.1$). Цей аналіз виявив скупчення галактик кластер Coma та Велику стіну Слоана (Sloan Great Wall). У подальших дослідженнях ми плануємо дослідити розподіл різних типів рентгенівських галактик у великомасштабних структурах Всесвіту.

Ключові слова: Активні ядра галактик, XMM-Newton, WISE, рентгенівське випромінювання, інфрачервоні огляди.

1. Introduction

Multiwavelength observations have a great importance for extragalactic astronomy. Many manifestations of the galactic activity could be detected in X-ray and infrared bands. In this respect the most vast database of X-ray sources is contained in XMM-Newton Serendipitous Source Catalogue (XMM-SSC). Current version of XMM-SSC, 3XMM-DR8 comprises more than 500 thousand sources (Rosen et al., 2016). We compiled a sample of extragalactic sources by previous version of XMM-SSC - 2XMM (Watson et al., 2009). Our sample, herein Xgal, contains 5021 entries (Tugay, 2014). HyperLeda database¹ (Makarov et al., 2014) was used for identification extragalactic X-ray sources and further Xgal compilation. Classification of Xgal sources is the next objective of our study. Most of X-ray emitting galaxies are more likely to have AGNs (Tugay & Vasylenko, 2011), but this statement should be verified.

For the purpose of this study we used data from the sky survey performed by Wide-field Infrared Survey Explorer (WISE). This space observatory registered more than 747 million infrared emission sources. The WISE telescope has a 40-centimeter-diameter aperture. Its' four working wavelength bands are 3.4, 4.6, 12 and 22 microns. The main astronomical sources irradiating in such bands are the following:

W1 band (3.4 micrometers) – stars and galaxies;

W2 band (4.6 micrometers) – thermal radiation from the internal heat sources of sub-stellar objects like brown dwarfs;

W3 band (12 micrometers) – thermal radiation of asteroids;

W4 band (22 micrometers) – dust in star-forming regions.

The first three band are often used to build color diagrams for classification of WISE sources. Distribution of the different cosmic objects by types and their IR colors is presented on Fig. 1² (Cutri et al., 2013). The purpose of the current work was to identify Xgal sources in WISE catalog and classify them using established infrared colors.

2. Sample Studies

One of the study objectives was to perform cross identification between WISE all sky observations

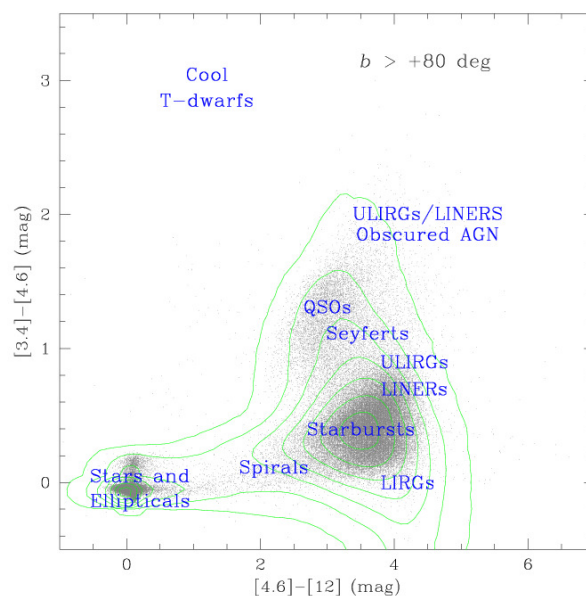


Figure 1: IR wave bands and objects types observed by Wide-field Infrared Survey Explorer (Cutri et al., 2013)

(Cutri et al., 2013; 747.634.026 sources) and X-ray sources observation using already compiled catalogues: XMM-Newton Serendipitous Source Catalogue 2XMMi-DR3 (262.902 sources); HyperLeda (2.777.804 galaxies) and Xgal (Tugay, 2012; 5.021 sources). Some previously obtained multiwavelength cross-correlation results based on data from WISE, 3XMM, and FIRST/NVSS for 2529 sources are given in paper of Mingo et al. (2016). In our study we selected the most bright X-ray galaxies with a flux $F_X > 10^{-13} mW/m^2$. Classification of these objects was performed using SIMBAD Astronomical Database.

Initially we assumed that Xgal objects should be in

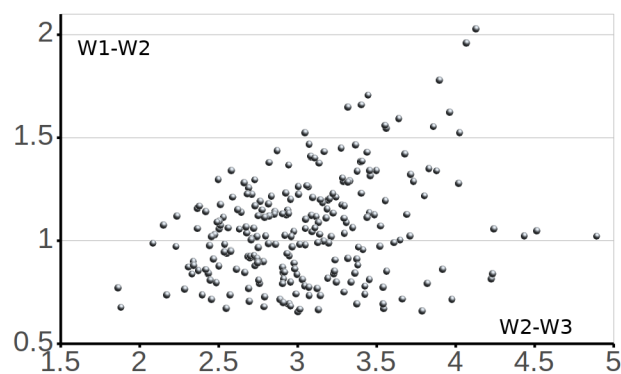


Figure 2: WISE color diagram for AGN candidates from (Assef et al., 2018) found in Xgal sample.

¹<http://leda.univ-lyon1.fr>

²<http://wise2.ipac.caltech.edu/docs/release/allsky/expsup/index.html>

WISE AGN catalog (Assef et al., 2018), since as it was mentioned above, most of X-ray galaxies are AGNs. Our results are given below on Fig. 2. We identified 267 sources with $W1-W2 > 0.5$ that corresponds to QSO region on WISE color diagram (Fig. 1). WISE AGN catalog was compiled using mentioned selection criterion and contains approximately 4 million infrared AGN candidates.

Then we performed cross correlation of Xgal with a whole AllWISE catalog (Cutri et al., 2013) and found 4 thousands matching objects that roughly corresponds to the number of X-ray WISE sources in (Mingo et al., 2016). We have split SIMBAD types into three groups: ellipticals, spirals and AGNs. Distribution of bright Xgal sources of these three types was plotted on Fig. 3. On this chart it is possible to distinguish quasars (color index $W1-W2 > 0.5$) and galaxies (color index $W1-W2 < 0.5$) which could be divided into elliptical and spiral types. Elliptical galaxies emit X-rays from cluster or group halo. Spiral galaxies may have X-ray emission from star formation regions (Tugay & Vasylenko, 2011). Such galaxies are not numerous in our sample. Moreover, the following two comments could be made here. First, in MIXR sample (Mingo et al., 2016) there is a division for spiral and star-forming galaxies. We can not make such a difference in our sample. Second, a subset of the galaxies that we mark as 'spirals' has an incorrect position on a color diagram. The explanation to this could be that some of the galaxies classified in SIMBAD as spirals are in fact Seyfert galaxies and they occupy the upper part of the plot on Fig. 3. Lower part of the 'spirals' chart indicates that there should be an X-ray halos envelope around these galaxies.

We have also analysed radial distribution of the bright X-ray galaxies in Sloan Digital Sky Survey region. In case of uniform distribution, the number of galaxies should increase as a cubic function of the distance. And vice versa, radial velocity of a galaxy V_{3K} is expected to be increased as cubic root function of galaxy order number in the list sorted by velocity value. Any major deviations from uniform spatial distribution of galaxies should lead to divergence of $V_{3K}(N)$ relation from cubic root. Such deviations becomes the most visible in our sample after replacing $V_{3K}(N)$ by $V_{3K}/1.007^N(N)$ (Fig. 4; power-law base factor equal to 1.007 was selected empirically). The main trend of such a function for the main part of the sample is a horizontal line approximation. Additional increase of this function corresponds to larger distances between galaxies, e.g. voids. The declination on the graph corresponds to dense large-scale structures (LSS) in galaxy distribution. Coma galaxy cluster and Sloan Great Wall were revealed in this distribution. Behind Sloan Great Wall the number of X-ray galaxies becomes insignificant that makes LSS detection impossible and causes rapid growth of plot on Fig. 4 for largest N.

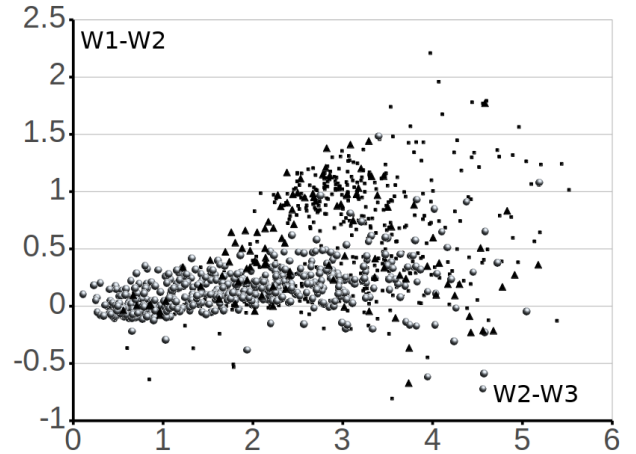


Figure 3: The MIXR sample: AGN activity versus star formation. IR color diagram for 573 X-ray galaxies with $F_X > 10^{-13} mW/s/m^2$. Balls – elliptical galaxies, galaxies in groups and clusters. Triangles – spiral and star-forming galaxies. Dots – AGN's : QSO's, Seyferts, LINERS

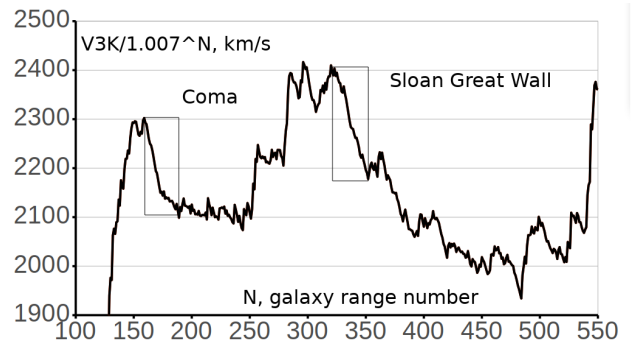


Figure 4: Large-scale structures in radial distribution of X-ray galaxies

3. Conclusion

Elliptical and clustered X-ray galaxies has a clear stand out position on the infrared color-color diagram. Main source of their X-ray emission should be explained as interstellar and intergalactic gas. Quasars also could be distinguished with WISE magnitudes. Main source of X-ray emission AGNs is accretion disc around central black hole. Star-forming galaxies has neither clear region at color diagram nor significant representation among X-bright galaxies. Some LSS elements could be resolved in radial distribution of X-ray galaxies. Such studies could be developed and combined with other methods of LSS analysis (Tugay, 2014; Tugay et al., 2016).

Acknowledgements. This study was conducted using the data from the 3XMM XMM-Newton serendipitous source catalogue compiled by the 10 institutes of the XMM-Newton Survey Science Centre selected by ESA. The authors are thankful to Dr. L.Stawarz for scientific objective targeting and consultations. We acknowledge the usage of the HyperLeda database (<http://leda.univ-lyon1.fr>); SIMBAD Astronomical Database - CDS (Strasbourg) <http://simbad.u-strasbg.fr/simbad/>

References

- Assef R.J., Stern D., Noirot G. et al.: 2018, *ApJS*, **234**, 23.
- Cutri R.M. et al: 2013, *VizieR On-line Data Catalog: II/328*.
- Makarov D., Prugniel P., Terekhova N. et al.: 2014, *A&A*, **570A**, 13.
- Mingo B., Watson M.G., Rosen S.R. et al.: 2016, *MNRAS*, **462**, 2631.
- Rosen S.R., Webb N.A., Watson M.G. et al: 2016, *A&A*, **590A**, 1.
- Tugay A.V. & Vasylenko A.A.: 2011, *Odessa Astron. Publ.*, **24**, 72.
- Tugay A.V.: 2014, *Advances in Astronomy and Space Physics*, **4**, 42.
- Tugay A.V.: 2014, *IAU Symposium*, **304**, 168.
- Tugay A.V. et al: 2016, *Odessa Astron. Publ.*, **29**, 34.
- Watson M.G., Schröder A.C., Fyfe D. et al.: 2009, *A&A*, **493**, 339.

DOI:<http://dx.doi.org/10.18524/1810-4215.2019.32.182538>

VERIFICATION OF MACHINE LEARNING METHODS FOR BINARY MORPHOLOGICAL CLASSIFICATION OF GALAXIES FROM SDSS

M. Yu. Vasylenko^{1,2}, D. V. Dobrycheva^{1,3}, I. B. Vavilova¹, O. V. Melnyk¹, A. A. Elyiv¹

¹ Main Astronomical Observatory of the National Academy of Sciences of Ukraine, 27 Akademika Zabolotnoho Str., 03143, Kyiv, Ukraine, vasmax@mao.kiev.ua

² Institute of Physics of the National Academy of Sciences of Ukraine, 46, Nauka avenu, 03028, Kyiv, Ukraine

³ Bogolyubov Institute for Theoretical Physics of the National Academy of Sciences of Ukraine, b 14-b Metrolohichna Str., 03143, Kiyv, Ukraine

ABSTRACT. We present a study on the verification of Machine Learning methods to be applied for binary morphological classification of galaxies. With this aim we used the sample of 60 561 galaxies from the SDSS DR9 survey with a redshift of $0.02 < z < 0.06$ and absolute magnitudes of $-24^m < M_r < -19.4^m$. We applied the following classification methods using own code in Python to predict correctly the morphology of Late and Early galaxies: Naive Bayes, Random Forest, Support Vector Machines, Logistic Regression, and k-Nearest Neighbor algorithm. To study the classifier, we used absolute magnitudes M_u, M_g, M_r, M_i, M_z , color indices $M_u - M_r, M_g - M_i, M_u - M_g, M_r - M_z$, and inverse concentration index to the center $R50/R90$.

We compared these new results with previous one made with the KNIME Analytics Platform 3.5.3. It turned out that Random Forest and Support Vector Machine Classifiers provide a highest accuracy, as in the previous study, but with help our code in Python we increased an accuracy from 92.9 % of correctly classified (96% - E and 84% - L) to 94,6% (96,9% - E and 89,7 % - L). The accuracy of the remaining methods also grew by 88% to 93%. So, using these classifiers and the data on color indices, absolute magnitudes, inverse concentration index of galaxies with visual morphological types, we were able to classify 60 561 galaxies from the SDSS DR9 with unknown morphological types and found 22 301 E and 38 260 L types among them.

Key words: galaxies, morphological classification, machine learning.

АНОТАЦІЯ. Подано дослідження щодо верифікації методів машинного навчання, що застосовані для автоматичної бінарної морфологічної класифікації галактик. З цієї

метою ми використали вибірку 60 561 галактик з цифрового огляду SDSS DR9 із червоними зміщеннями $0,02 < z < 0,06$ та абсолютними зоряними величинами $-24^m < M_r < -19,4^m$. Ми застосували такі методи машинного навчання, використовуючи власний код написаний на Python, щоб правильно визначити морфологію ранніх і пізніх типів галактик: наївний Байес, випадковий ліс, метод опорних векторів, логістичну регресію, k-найближч их сусідів. Для тренування класифікатора ми використовували абсолютні зоряні величини M_u, M_g, M_r, M_i, M_z , показники кольору $M_u - M_r, M_g - M_i, M_u - M_g, M_r - M_z$ та зворотній індекс концентрації кольору до центру $R50/R90$.

Ми порівняли ці результати з нашими попередніми, які були зроблені за допомогою програмного забезпечення KNIME Analytics 3.5.3. Виявилось, що метод Random Forest і Support Vector Machine також забезпечують найбільшу точність, але за допомогою нашого коду на Python ми підвищили точність з 92,9 % правильно класифікованих (96 % - E і 84 % - L) до 94,6 % (96,9 % - E і 89,7 % - L). Точність решти методів також зросла на 88 % до 93 %. Отже, тренуючи ці класифікатори на даних про показники кольору, абсолютні зоряні величини, зворотній індекс концентрації кольору до центру галактик, ми змогли визначити морфологічні типи вибірки 60 561 галактик з цифрового огляду неба SDSS DR9 і отримали 22 301 E ранніх і 38 260 L пізніх типів галактик.

Ключові слова: морфологічна класифікація галактик, машинне навчання

1. Introduction

As a result of the fast development of new technologies for the ground-based and space-born telescopes the volume of digital data about space objects (including the extragalactic ones) has grown rapidly in recent decades. The massive volume of data and more and more increasing computing power facilities change the way in how science and technology are managed. This opens up and get challenges into further research in each field, hence, instigating the search for new approaches to process this huge astroinformatics resource (see, for example, [Zaane (1999), Srivastava et al. (2012), Ivezic et al. (2014), Al-Jarrah et al. (2015), Vavilova (2016)]).

Due to the new astronomical observational surveys, their data collection is available online in the form of big science databases in all ranges of the electromagnetic spectrum: Fermi-GLAST [Acero et al. (2015)] in gamma, ROSAT [Voges et al. (2000)] and XMM-Newton [Rosen et al. (2016), Pierre et al. (2016)] in X-ray, GALEX [Lee et al. (2011)] in ultraviolet, WISE [Wright et al. (2010)] and 2MASS [Skrutskie et al. (2006)] in infrared, Extragalactic Radio Continuum Surveys [Norris et al. (2017)] or Discrete Radio Source Surveys [Braude et al. (2002)], zCOSMOS – deep sky survey [Scoville et al. (2007)], deep surveys with the Hubble Space Telescope, and SDSS – Sloan Digital Sky Survey [Gunn et al. (1998)] in optical ranges as well as other surveys.

Since 2000, the Sloan Digital Sky Survey (SDSS) collected the more data that had been amassed in the entire history of astronomy [Blanton et al. (2017)]. Now, its archive contains of about 170 terabytes of information. In this context, the astronomers, who are directly involved in the SDSS, identified the problem of the automated morphological galaxy classification as one of the extremely actual task. Machine learning methods (MLM) are able to uncover hidden relations between observed data (e.g., galaxy parameters and images) and physical properties of galaxies. First of all, we mention several works related to the morphological classification of galaxies from the SDSS such as [Andrae et al. (2010), Dobrycheva et al. (2017), Dobrycheva et al. (2018), Dominguez et al. (2018), Barchi et al. (2019)] as well as to the visual classification, ZOO project, such as [Banerji et al. (2010)], or for radio galaxies with AGNs [Zhixian et al. (2018)].

For the first time we have introduced and applied the high-order 3D Voronoi tessellation method for the identification of low-populated galaxy systems from a volume-limited SDSS DR5 to estimate environment effects [Vavilova et al. (2005), Elyiv et al. (2009)] and binary morphological content [Vavilova et al. (2009)] of 6786 galaxies with $3000 \text{ km/s} < V_{LG} < 9500 \text{ km/s}$ containing in these systems.

After enlarging the sample to 317018 galaxies with

these radial velocities from the SDSS DR9, we applied multi-parametric diagram and visual inspection to get the automated galaxy morphological classification. Namely, as for the photometry parameters diagrams we used a well-known fact that galaxy morphological type is correlated with the color indices, luminosity, de Vaucouleurs radius, inverse concentration index etc. [Karachentseva et al. (1994), Dobrycheva et al. (2012), Melnyk et al. (2012)]. We plotted the diagrams of color indices $g - i$ and one of the aforementioned parameters and discovered that these parameters may be used for galaxy classification into three classes: E – elliptical and lenticular, S – spirals Sa-Scd types, and L – late spirals Sd-Sdm and irregulars types. The accuracy is 98 % for E , 88 % for S , and 57 % for L types. The combinations of color indices $g - i$ and inverse concentration index $R50/R90$; color indices $g - i$ and absolute magnitude M_r gave the best result: 143263 E type, 112578 S type, 61177 L type [Dobrycheva et al. (2017)].

Not enough classification accuracy for L type galaxies, we undergone the different MLM for providing a binary automated morphological classification. Why is binary one, because we decided compound S and L in one class of the Late type galaxies L . We tested different MLM for the SDSS DR9 samples of 317018 galaxies at $z < 0.1$ using KNIME Analytic Platform and found that the Random Forest provides the highest accuracy, namely 91 % of galaxy types are classified correctly: 96 % Early (E) and 80 % Late (L) types [Dobrycheva et al. (2017)].

To improve accuracy of the results we developed own code for the automated morphological classification of galaxies and apply it to the sample of 60561 galaxies from the SDSS DR9 at $0.02 < z < 0.06$. Results of this study are presented in this paper.

2. Galaxy sample from SDSS DR9

We used the sample of 60561 galaxies from SDSS DR9 with the absolute magnitudes $-24^m < M_r < -19.4^m$ at $0.02 < z < 0.06$. As we said above the color indices, inverse concentration index $R50/R90$, and absolute magnitude are the good parameters for training MLM [Dobrycheva et al. (2015)][Dobrycheva et al. (2017)]. The absolute magnitude was obtained by the formula:

$$M_r = m_r - 5 \cdot \lg(D_L) - 25 - K_r(z) - ext_r,$$

where m_r - visual stellar magnitude in r band, D_L - distance luminosity, ext_r - the Galactic absorption in r , $K_r(z)$ - k-correction in r band according to [Chilingarian et al. (2010), Chilingarian et al. (2012)]. The color indices were obtained as:

$$M_g - M_i = (m_g - m_i) - (ext_g - ext_i) - (K_g(z) - K_i(z)),$$

where m_g and m_i - visual stellar magnitude in g and i band; ext_g and ext_i - the Galactic absorption

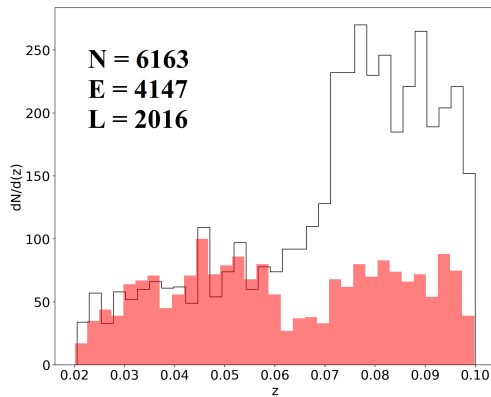


Figure 1: Distribution of galaxies by redshifts in the training sample (line - late type, pillars - early type galaxy)

in g and i band; $K_g(z)$ and $K_i(z)$ – k-correction in g and i band, respectively. Following the SDSS recommendation we involved limits $m_r < 17.7$ by visual magnitude in r -band to avoid typical statistical errors in spectroscopic flux.

3. Training galaxy sample

A training galaxy sample contains of 6 163 galaxies at $0.02 < z < 0.1$ with the absolute magnitudes $-24^m < M_r < -19.4^m$ from the SDSS DR9 (Fig. 1).

It was composed of several samples with certain morphological types of galaxies from our previous work and is based on the SDSS DR9. We split galaxies visually on two classes as E (including E, S0, S0a types) and L (from Sa to Irr types), which were selected randomly with different redshifts and luminosity. We collected 1) training sample, which contain 764 galaxies described by [Dobrycheva et al. (2018)], and 2) 5000 galaxies described by [Dobrycheva et al. (2015)]. After the beta run of machine learning for the unknown morphological types, we have done visual inspection of the randomly selecting galaxies and 3) added these galaxies to the training sample.

Additionally, we used an automatic regression method of discarding galaxies that strongly deviate from the mean value. We re-defined the mean of the magnitude in each filter and its scatter after each discard and then limited artificially this permissible deviation for the average. Thus, we got a sample of 6 163 galaxies.

4. Verification of Machine Learning methods for morphological classification

Logistic Regression is a statistical model that uses

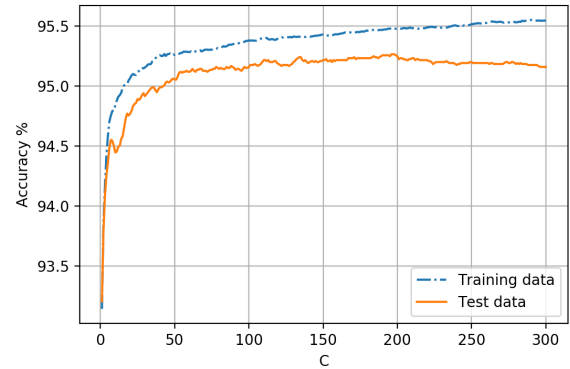


Figure 2: Training galaxy sample. Dependence of prediction accuracy for Logistic Regression Classifier on the "C" parameter

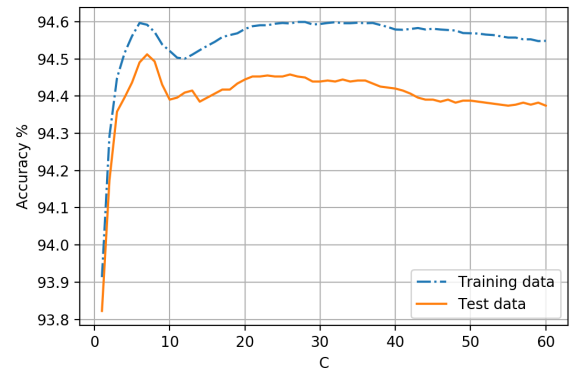


Figure 3: Training galaxy sample. Dependence of prediction accuracy for Support Vector Machine Classifier on the "C" parameter

a logistic function to model the probability of a binary dependence of an object class on its features. The corresponding probability for each class may vary from 0 to 1 depending on the features [Tolles et al. (2016)]. A function that converts a logical factor into a probability is a logistic function. This can be extended to more than two classes. The model itself simply models the likelihood of output in terms of enter data and does not perform statistical classification (it is not a classifier). It includes the quantizer function and works by selecting the cutoff value and classifying the input as more likely than the cutoff as one class, below as another.

Support-Vector Machines (SVMs) are controlled learning models that analyze data used for classification and regression analysis. Given a set of classified training cutters, the SVM learning algorithm builds a model that determines the class of objects by their parameters [Smola et al. (2004)]. The SVM model is a representation of the points of the hyperspace objects so that the samples of the individual classes are separated

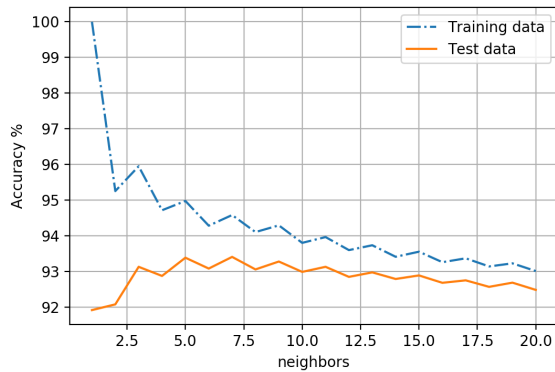


Figure 4: Training galaxy sample. Dependence of prediction accuracy for k-Nearest Neighbors Classifier on parameter "neighbors"

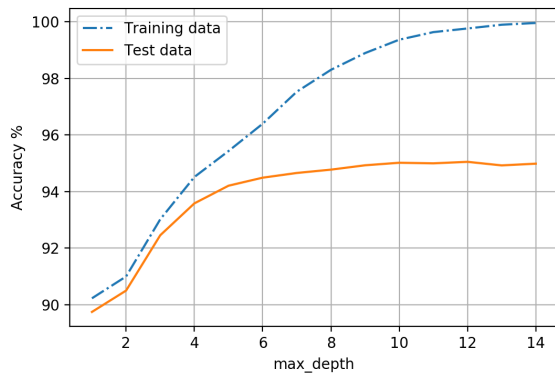


Figure 5: Training galaxy sample. Dependence of prediction accuracy for Random Forest Classifier on parameter "max_depth"

by a clear gap, which wide is maximized as possible. Then, the new objects are displayed in the same space and assumed to belong to the category based on the side of the gap to which they fall. This method has such disadvantages: it is used only for problems with two classes, it is impossible to calibrate the probability of getting to a certain class, the model parameters are difficult to interpret.

By default, Logistic Regression and SVC use L2 controller. For these methods, the "C" parameter determines the degree of regulation, where a higher degree of "C" corresponds to a lesser regulation. When "C" values height Logistic Regression and SVM trying to fit the models to the initial data as accurately as possible, then "C" is low models trying to look for a vector of coefficients closely to zero. Therefore, at low "C" values, the algorithm tries to fit the most data points, while at low "C" values it increases the contribution of each individual point. The accuracy dependencies of the "C" parameter for Logistic Regression and SVM are shown

in Figures 2 and 3, respectively.

k-Nearest Neighbors (k-NN) is a simple non-parametric method used for classification. The object is classified by multiple votes of its neighbors, and the object is assigned to the class most common among its closest neighbors, where k-number of neighbors. If $k = 1$, then the object is simply assigned to the class of one nearest neighbor in the parameter space for the selected metric. Neighbors are drawn from the training dataset [Burkov et al. (2019)]. The accuracy dependencies of the number of neighbors for k-Nearest Neighbors is shown in Figure 4. A feature of the k-NN algorithm is related to its sensitivity to the local data structure. Advantages of this method: simple implementation, adaptation to the desired task by choosing a metric, interpret-ability. The disadvantages include: poor performance in tasks with many objects in the training sample; difficulties in finding the right weight and determining what features are required for classification; dependence on the selected metric.

Naive Bayes classifiers is a family of simple probability classifiers based on the application of Bayes' theorem with strong "naive" assumptions about independence between traits. This determines a certain statistical distribution of parameters for each of the classes [Soria et al. (2011)]. The probability of falling into a class depends on the ratio of the statistical density of the distribution of classes at a point for the selected model by independent parameters. The advantages of the method are as follows: high speed of work, easy interpret-ability of the results of the algorithm. The relatively low quality of classification and the inability to take into account the dependence of the classification result on a combination of features are the main disadvantages of this method. We used this method as a reference.

Random Forest is an ensemble classification and regression method that works by constructing a large number of decision trees and averaging the result of predicting individual trees. This helps to reduce the risk of overfitting. Tree models - where the target variable can take a discrete set of class values, are called classification trees [Burkov et al. (2019)]. In these trees, the leaves represent classes, and the branches represent the set of features that lead to these classes. In branching nodes there is a logical operator. The goal is to create a model that predicts the value of the target variable with the highest precision based on multiple input variables by calibrating the tree shape. Tree construction is recursive until the subset in the node has all the characteristics of the target variable, or when splitting the accuracy of the prediction will not remain constant. The accuracy dependencies of the maximum depth of the tree for Random Forest Classifier applied to the training sample is shown in Figure 5. The main advantage of the method is the high productivity of training and forecasting; such decision trees can

be easily visualized and interpreted. The disadvantage is related to the method's propensity for retraining.

6. Results and Conclusion

Using own code in Scikit Learn Python¹ to predict correctly the galaxy morphology (Late and Early types) we verified several Machine Learning methods for binary morphological classification of galaxies. With this aim we used the sample of 60 561 galaxies from the SDSS DR9 survey with a redshift of $0.02 < z < 0.06$ and absolute magnitudes of $-24^m < M_r < -19.4^m$. Among the machine learning methods were as follows: Naive Bayes, Random Forest, Support Vector Machines, Logistic Regression, and k-Nearest Neighbor algorithm. To study the classifier, we used absolute magnitudes M_u, M_g, M_r, M_i, M_z , color indices $M_u - M_r, M_g - M_i, M_u - M_g, M_r - M_z$, and inverse concentration index to the center $R50/R90$.

Prediction accuracy was evaluated for each of these methods for training galaxy sample (see, Figures) and reaches the following values:

Naive Bayes Classifier – 0.886 ($E - 0.920, L - 0.818$) ± 0.01 ;

k-Nearest Neighbors Classifier – 0.945 ($E - 0.9389, L - 0.958$) ± 0.006 ;

Logistic Regression Classifier – 0.949 ($E - 0.968, L - 0.911$) ± 0.006 ;

Random Forest Classifier – 0.9545 ($E - 0.967, L - 0.928$) ± 0.003 ;

Support Vector Machine Classifier – 0.964 ($E - 0.961, L - 0.969$) ± 0.006 .

All the above mentioned classifiers include the K-Fold Cross Validation method.

We compared these new results with previous one, which were made using the KNIME Analytics Platform 3.5.3 ([Dobrycheva et al. (2017)]). It turned out that the method of Random Forest and Support Vector Machine provide a highest accuracy (as in the previous study for the Random Forest Method), but with help of our code in Python we increased an accuracy from 92.9 % of correctly classified (96% – E and 84% – L) to 94,6% (96,9% – E and 89,7 % – L). The accuracy of the remaining methods also grew by 88% to 93% (see, Figure 6, where the images of the correct classification are presented).

So, using the Random Forest and Support Vector Machine Classifiers, and the data on color indices, absolute magnitudes, inverse concentration index of galaxies with visual morphological types, we were able to classify 60 561 galaxies from the SDSS DR9 with unknown morphological types and found 22 301 E and 38 260 L types among them. At the same time, the results of applying the Deep convolutional neural net-

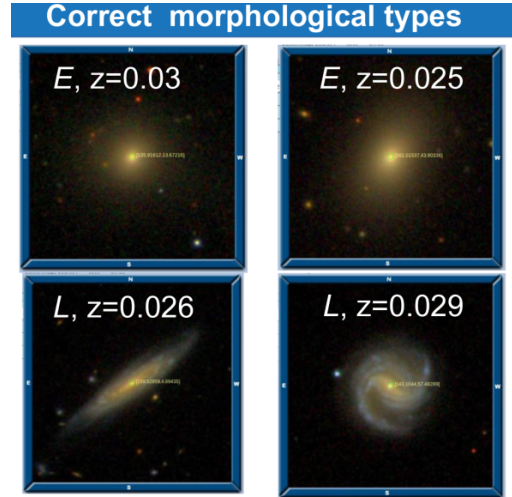


Figure 6: Images of galaxies from SDSS with the correctly classified morphology. Top: Early type (Ellipticals). Bottom: Late type (Spirals).

work (DL) to the images of redshift-limited ($z < 0.1$) sample of $\sim 300\,000$ galaxies from the SDSS DR9 by [Khrantsov et al. (2019)] with the same aim of binary morphological classification has been shown, for example, that DL method can classify rounded sources as Ellipticals but it can not catch the spectral energy distribution properties of galaxies more clearly than SVM, trained on the photometric features of galaxies.

The problem points arise when we have cases of the face-on and edge-on galaxies (Figure 7). The most of these galaxies are miss-classified as Ellipticals (early type). The good case is that methods allow us to recover gravitational lenses (point-like sources, arcs) and the most of such miss-classifications are also among Ellipticals. So, we have overestimated number of Ellipticals and underestimated number of Spirals (about of 10 %). But this problem can be decided, when we will form training samples through several steps (pre-training, fine-tuning, and classification). The step of fine-tuning should include the limitations on the axes-ratio for Ellipticals, additional photometry parameters for the face-on galaxies, as well as trainings with images and spectral features of galaxies. Results of this approach as well as a conception of the automated morphological classification of a big data sample of galaxies with a wider redshift range will be given in other papers.

The Machine learning methods are an indispensable assistant in solving morphological classification since their first application to decide this problem with the ANN-algorithm [Storrie-Lombardi et al. (1992)]. They are also effective for reconstruction of Zone of Avoidance, distance modulus for local galaxies, gravitational lenses search, where the authors have own experience ([Vavilova et al. (2018)], [Elyiv et al. (2019)], [Sergeyev et al. (2018)], respectively).

¹<https://scikit-learn.org/>

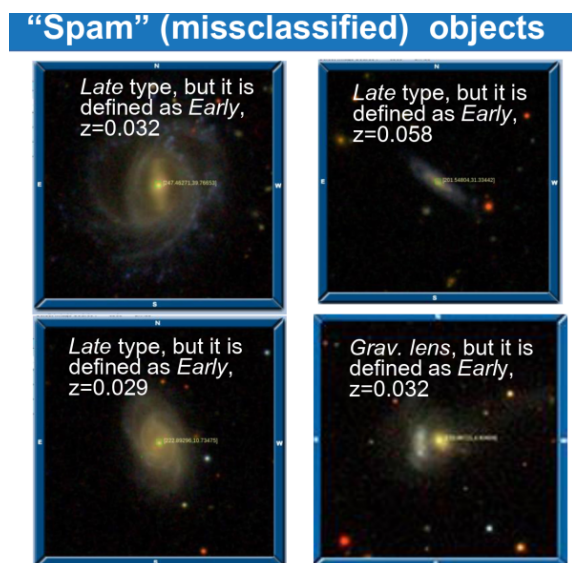


Figure 7: Images of galaxies from SDSS with the miss-classified morphology. Top and Left Bottom: Late types (Spirals), which are classified as Early type (Ellipticals). Right Bottom: gravitational lens classified as Early type galaxy (Ellipticals).

Acknowledgements. This work was partially supported by the grant for Young Scientist's Research Laboratories (2018-2019, Dobrycheva D.V.) and the Youth Scientific Project (2019-2020, Dobrycheva D.V., Vasylenko M.Yu.) of the NAS of Ukraine.

References

- Acero F., Ackermann M. et al.: 2015, *ApJS*, **218**, 41.
- Al-Jarrah O. Y., Yoo P. D., Muhaidat S. et al.: 2015, Efficient machine learning for big data: A review. *Big Data Research*, **2(3)**, 87.
- Andrae R., Melchior P. et al.: 2010, *A&A*, **522**, 19.
- Banerji M., Lahav O. et al.: 2010, *MNRAS*, **406**, 342.
- Barchi P. H., de Carvalho R. R., Rosa R. R. et al.: 2019, *arXiv:1901.07047*.
- Blanton M. R., Bershad M. A., Abolfathi B. et al.: 2017, *ApJ*, **154**, 35.
- Braude S. Ya., Rashkovsky S. L., Sidorchuk K. M. et al.: 2002, *Astrophysics and Space Science*, **280**, 235.
- Burkov A.: 2019, The Hundred-Page Machine Learning Book.
- Calderon V. F.; Berlind A. A.: 2019, *arXiv:1902.02680*.
- Chilingarian I., Melchior A. L., Zolotukhin I.: 2010, *MNRAS*, **405**, 1409.
- Chilingarian I., Zolotukhin I.: 2012, *MNRAS*, **419**, 1727.
- Dobrycheva D., Melnyk O.: 2012, *AASP*, **2**, 42.
- Dobrycheva D.V.: 2013, *OAP*, **26**, 187.
- Dobrycheva D. V., Melnyk O. V., Vavilova I. B. et al.: 2015, *Astrophysics*, **58**, 168.
- Dobrycheva D. V. et al.: 2017, *arXiv:1712.08955*.
- Dobrycheva D.V., Vavilova I. B., Melnyk O. V. et al.: 2018, *Kinemat. Phys. Celest. Bodies*, **34**, 290.
- Dominguez S.H.; Huertas-Company M., Bernardi M. et al.: 2018, *MNRAS*, **476**, 3661.
- Elyiv A., Melnyk O. et al.: 2009, *MNRAS*, **394**, 1409.
- Elyiv A.A. et al.: 2019, *arXiv:1910.07317*.
- Gunn J.E., Carr M. et al.: 1998, *ApJ*, **116**, 3040.
- Ivezic Z., Connelly A.J., VanderPlas J.T. et al.: 2014, Statistics, Data Mining, and Machine Learning in Astronomy, by Z. Ivencić et al. Princeton, NJ: Princeton University Press.
- Karachentseva V.E. et al.: 1994, *Bull. SAO*, **37**, 98.
- Khramtsov V., Sergeyev A., Spiniello, C. et al.: 2019, *arXiv:1906.01638*.
- Khramtsov V. et al.: 2019, *OAP this issue*.
- Lee J.C., Gil de Paz A. et al.: 2011, *ApJS*, **192**, 33.
- Melnyk O.V., Dobrycheva D.V., Vavilova I.B.: 2012, *Astrophysics*, **55**, 293.
- Norris R.P.: 2017, *Nature Astronomy*, **1**, 671.
- Pierre M., Picaud F. et al.: 2016, *A&A*, **592**, 16.
- Rosen S.R., Webb N.A. et al.: 2016, *A&A*, **590**, 22.
- Scoville N., Abraham R.G. et al.: 2007, *ApJS*, **172**, 38.
- Sergeyev A., Spiniello C. et al.: 2018, *AAS*, **2**, 189.
- Skrutskie M.F., Cutri R.M., Stiening R. et al.: 2006, *Astron. J.*, **131**, 1163.
- Soria D., Garibaldi J.M., Ambrogi F, et al.: 2011, *Knowledge Based Systems*, **24**, 775.
- Smola A. J., Scholkopf B.: 2004, *Statistics and Computing*, **14**, 199.
- Srivastava A.N. (Ed.): 2012, Advances in machine learning and data mining for astronomy. Chapman and Hall/CRC.
- Storrie-Lombardi M.C., Lahav O., Sodre L.Jr. et al.: 1992, *MNRAS*, **259**, 8.
- Tolles J., Meurer W. J.: 2016, Logistic Regression Relating Patient Characteristics to Outcomes, ISSN 0098-7484
- Vavilova I.B., Karachentseva V.E., Makarov D.I. et al.: 2005, *Kinemat. Physics Celest. Bodies*, **21**, 3.
- Vavilova I.B., Melnyk O.V., Elyiv A.A.: 2009, *Astron. Nachr.*, **330**, 1004.
- Vavilova I.B.: 2016, *OAP*, **29**, 109.
- Vavilova I.B., Elyiv A.A., Vasylenko M.Yu.: 2018, *Radio Phys. Radio Astron.*, **23**, 244.
- Voges W., Aschenbach B., Boller Th. et al.: 2000, *VizieR On-line Data Catalog*, **IX/29**.
- Wright E. L., Eisenhardt P. R. M., Mainzer A. K.: 2010, *ApJ*, **140**, 1868.
- Zaane O. R.: 1999. Introduction to data mining.
- Zhixian Ma et al.: 2018 *arXiv:1812.07190*.

ASTROPHYSICS

DOI: <http://dx.doi.org/10.18524/1810-4215.2019.32.182049>

DIFFUSE INTERSTELLAR BAND 6202 Å AS AN INDICATOR OF ORGANIC MATTER IN COSMOS: CEPHEID SPECTRA

S. M. Andrievsky¹, A. Shereta¹, S. V. Khrapaty², S. A. Korotin³,
V. V. Kovtyukh¹, V. I. Kashuba¹¹ Astronomical Observatory, Odesa National University,
Odesa, Ukraine, andrievskii@ukr.net,² Department of Biophysics and Medical Informatics,
National Taras Shevchenko University of Kyiv,³ Crimean Astrophysical Observatory, Nauchny 298409, Crimea

ABSTRACT. We have described the method of investigation of the diffuse interstellar band (DIB) at 6202 Å. This DIB is seen in the spectra of cepheid stars, and it is blended with two stellar lines of Ce II (6201.773 Å) and Ni I (6204.6 Å). After removal of the blending lines of ionized cerium and neutral nickel, we can determine the equivalent widths (EW) of the DIB. This procedure can be applied for the sample of cepheids (with well known distances), which enables one to construct the map of the organic matter distribution in the Galactic disc and use these values to investigate the E(B–V)–DIB EW relation. The relation found from Cepheids matches that found in B stars. This relation can help to find the reddening for newly discovered Cepheids without extensive photometric data, and thus determine their distances. The relation between E(B–V) and the DIB EW does not yield precise reddening values. It is not a substitute for better photometric or spectroscopic methods. At best, it is indicative, but it provides some information that may not be otherwise available.

Keywords: Classical cepheids; ISM lines and bands, ISM molecules, ISM structure

АНОТАЦІЯ. Відомо, що досить значна частина речовини Галактики (приблизно 20% за масою) входить до складу міжзоряного середовища (газопилова компонента). Міжзоряне середовище – основа внутрішнього взаємозв'язку систем кожної галактики. Саме в ньому відбуваються процеси зореутворення, обміну речовиною і енергією між туманностями (що є невід'ємною частиною та проявом міжзоряного середовища), системами нових зір та протозорями, чорними дірами. Тому дослідження фізики та визначення хімічного складу міжзоряного середовища протягом багатьох років

займає важливе місце в теоретичній астрофізиці та космології. Особливий інтерес представляє, зокрема в рамках сучасної космохімії, дослідження міжзоряного середовища на молекулярному рівні. Ототожнення міжзоряних молекул може відповісти на багато питань космогонії і теорії зореутворення. Одна з особливостей міжзоряного середовища полягає в значній неоднорідності речовини. Ми описуємо метод дослідження дифузної міжзоряної смуги (ДМС) на довжині хвилі 6202 Å. Ця ДМС спостерігається в спектрах класичних цефеїд, і вона блендується з двома зоряними лініями – Ce II (6201.773 Å) і Ni I (6204.6 Å). Були застосовані розрахунки синтетичного спектру зорі у межах ДМС з наступним вилученням цих зоряних ліній з профілю смуги. Ця методика дає можливість знайти істинні профілі ДМС та визначити їхні еквівалентні ширини (EW). Цю процедуру можна застосувати для цефеїд (для яких відстані добре відомі), побудувати карту розповсюдження органічної речовини в галактичному диску та використати ці значення для дослідження відношення E(B–V) EW(DIB). Це відношення може допомогти знайти почервоніння для нещодавно відкритих цефеїди, для яких ще немає достатніх фотометричних даних. Після отримання високоточних індивідуальних значень надлишків кольору для усіх програмних зір буде встановлено радіальну та довготну залежність екстинкції міжзоряного газу у площині Галактики та отримати інформацію про існування локальних неоднорідностей густини міжзоряного газу. Тут мова йде про неперервне поглинання пиловою компонентою, яка входить до складу міжзоряних газових хмар.

Ключові слова: Класичні цефеїди, міжзоряні лінії та смуги, міжзоряні молекули, структура міжзоряного середовища

1. Introduction

Diffuse interstellar bands (DIBs) are quite broad absorptions which can be found in the spectra of the different astronomical objects. In visual and near IR region there are about 500 DIBs. These bands are observed when the light of the star is absorbed when it crosses translucent clouds. The origin of the DIBs (i.e. their carriers) is still a mystery. There have been a number of theories advanced regarding the nature of interstellar absorbing material resulting in the phenomenon of DIBs in stellar spectra. No exact identification of the central wavelengths of DIBs are available at present, but there are strong belief that they are caused by complex molecular absorption. At present the widely accepted hypothesis about DIBs carriers supposes that polycyclic aromatic hydrocarbons can produce observed absorptions in the stellar spectra. Nevertheless, Cox (2011) and Salama et al. (2014) doubted this hypothesis. Another way to explain the appearance of DIBs may be to consider the absorption capacity of and/or bucky ball carbon structures.

Many works were devoted to a comprehensive observational study of DIB, their fine structure, in particular. In particular, it was found that The equivalent widths of the DIBs vary within a wide range, and in some cases correlate with the reddening along the line-of-sight. The wavelength of a DIB in the photospheric rest frame of the background source varies due to the system velocity of the background source.

As a rule, DIBs were studied in the spectra of hot O–B stars because their visual region is less crowded with spectral lines and the continuum is smooth. High resolution spectra of such stars afford an excellent possibility to study the fine structure of DIBs. Unfortunately, the distances of O–B stars can be determined with low accuracy. Therefore, if we are interested in study the spatial distribution of the DIBs absorption in our Galaxy, then we must understand that such spatial distribution can be burdened with distance inaccuracy. It would be a good opportunity to use for this purpose spectra of the stars whose distances are known with a high precision, the cepheid spectra, for instance. Cepheids are the stars of F–G spectral class, and their visual region is full of the stellar spectral lines. With a high probability any DIB profile in their spectra is spoiled with stellar lines. This is a problem that prevents the direct determination the DIB characteristics, like its equivalent width, in particular. Kashuba et al. (2015) and Kashuba et al. (2016) described a method that allows to clean 6613 Å DIB blended profile. In this paper we describe similar procedure which allows to refine 6202 Å DIB profile.

2. Method

The diffuse interstellar band at the wavelength 6202 Å was selected as an object of the study. In the cepheid spectra, in most cases this DIB is superimposed on two stellar absorption lines, namely ionised cerium (6201.773 Å) and neutral nickel (6204.6 Å) lines. In contrast to weak line of cerium, the neutral nickel line is quite strong. A correct measurement of the equivalent width of the DIB at 6202 Å is not feasible unless the blending lines of stellar origin are removed. As it was stated in Introduction Kashuba et al. (2016) developed a method that enables performing such a procedure. Similar to that method our approach concerning the DIB 6202 Å consists the following steps.

1. We checked accuracy of the oscillator strengths of two blending lines: Ce II (6201.773 Å) and Ni I (6204.6 Å). This is necessary in order to calculate synthetic spectrum of the background star in vicinity of 6202 Å DIB. Preliminary values of $\log gf$ for the lines were taken from the Vienna Atomic Line Database (VALD) (<http://vald.astro.uu.se/>). Initial values of the oscillator strengths for the considered lines were -1.949 and -1.079 respectively. Then the oscillator strengths for these two lines were updated using the solar spectrum of Kurucz et al (1984) and the cerium and nickel abundances in the Sun from Grevesse et al. (1996). The resulting values are $\log gf = -1.550$ for the cerium line and $\log gf = -1.155$ for the nickel line. The best fits for profiles of these lines in the solar spectrum are shown in Fig. 1.

2. The synthetic spectrum for a particular star is generated using its atmosphere model, which is calculated using previously known such parameters as effective temperature, surface gravity, microturbulent velocity and metallicity.

3. Then the observed spectrum is divided into synthetic spectrum, and this procedure gives us a DIB profile free of stellar spectral lines.

4. Finally, the equivalent width of the cleaned DIB profile is determined by direct integration.

3. Atmospheric parameters and synthetic spectra

The atmospheric parameters (effective temperature T_{eff} , surface gravity $\log g$, microturbulent velocity V_t and $[\text{Fe}/\text{H}]$) of the program stars were used to calculate the fragments of synthetic spectra of cepheids containing the 6202 Å DIB. We used stellar atmosphere models first applied for analysis in Kashuba et al. (2016). In synthetic spectrum calculations in the 6202 Å DIB vicinity we used cerium abundance derived from Ce II line 6043.37 Å, and nickel abundance derived from Ni I 6176.81 Å line. Both lines are situated close to the DIB region, they are not blended with

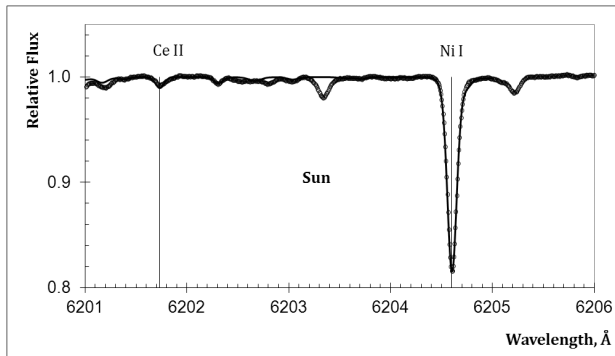


Figure 1: Observed (circles) and synthetic (thin line) spectra of the Sun in vicinity of the 6202 Å DIB.

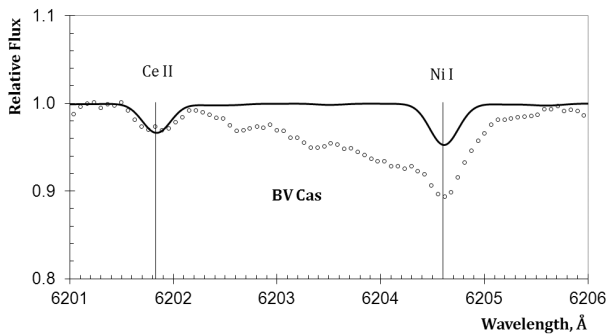


Figure 2: Observed (circles) and synthetic (thin line) spectra of BV Cas in vicinity of the 6202 Å DIB (wide absorption).

other species, and produce reliable abundances of the corresponding elements (their oscillator strengths were calibrated using the solar spectrum). In Fig. 2 we show observed and synthetic spectra in the 6202 Å DIB region for one program star: BV Cas ($T_{\text{eff}} = 5551$ K, $\log g = 1.99$, $V_t = 3.29$ km s $^{-1}$, $[\text{Fe}/\text{H}] = +0.02$).

The result of applying step 3 (see previous section) is shown for BV Cas in Fig. 3.

Measured equivalent width of the 6202 Å DIB in BV Cas is 0.1006 Å.

Conclusion

We described method which enables one to clean the 6202 Å diffuse interstellar band from the stellar blending lines of ionized cerium (6201.773 Å) and neutral nickel (6204.6 Å). This procedure gives a possibility to measure pure DIB equivalent width. In turn, this characteristic can be traced as a function of interstellar reddening caused by the absorption of light by dust particles. We plan to apply described procedure for the sample of cepheid spectra previously analyzed by Kashuba et al. (2016) with the aim of the 6613 Å DIB study.

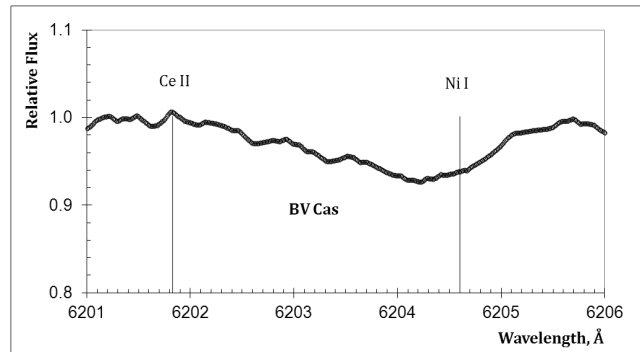


Figure 3: Normalized fragment of the spectrum of BV Cas.

References

- Cox N.L.J.: 2011, in PAHs and the Universe, C. Joblin, A.G.G.M. Tielens (eds), *EAS Publications Series* **46**, 349.
- Grevesse N., Noels A., Sauval A.J.: 1996, *ASPC* **99**, 117.
- Kashuba S.V., Andrievsky S.M., Chekhonadskikh F.A., Korotin S.A., Kovtyukh V.V., Luck R.E.: 2015, *OAP* **28**, 166.
- Kashuba S.V., Andrievsky S.M., Chekhonadskikh F.A. et al. 2016, *MNRAS* **461**, 839.
- Kurucz R.L., Furenlid I., Brault J., Testerman L.: 1984, Solar Flux Atlas from 296 to 1300 nm, *National Solar Observatory*.
- Salama F., Ehrenfreund P.: 2014, The Diffuse Interstellar Bands, J. Cami & N.L.J. Cox, eds. *Proc. IAU Symp.* **297**, 364.

DOI:<http://dx.doi.org/10.18524/1810-4215.2019.32.182083>

OPTICAL LUMINOSITY OF ACTIVE GALACTIC NUCLEI AND THE INTENSITY OF ITS HARD RADIATION IN THE FORM OF PARTICLES AND QUANTA

D. N. Doikov¹, A. V. Yushchenko²

¹ Department of mathematics, physics, and astronomy,
Odessa National Maritime University, Odessa, 65001, Ukraine doikov@mail.bg

² Astrocamp contents research institute, Goyang, 10329, Republic of Korea
avyushchenko@gmail.com

ABSTRACT. In this paper, we determine the causes of correlations between the observed logarithmic luminosity $\log L$ of galaxies with active nuclei (AGN) with particular attention to BL Lac type objects. The properties of flux variations of these galaxies in γ -rays ($\log L_\gamma$) and in optics ($\log L_O$) are associated with the combined action of cosmic rays (CR), and also with hard radiation around the entire perimeter of AGN. The necessity of using positron spectroscopy in such objects is found. The importance of high-precision measurements of 1.022 MeV line arising from the annihilation of positrons with K-electrons of multielectron atoms in the interstellar medium of disk component of the studied galaxies is emphasized. The relationship between the single-photon positron annihilation and the Doppler line broadening of the same atoms in optics is investigated in AGN. We found that indirect evidence of the presence of a sufficient number of positrons and their annihilation are the cascade channels observed in the form of Δ -resonance. According to the available data from the AGN's catalogs the calibration of their luminosity in other spectral regions is proposed.

АНОТАЦІЯ. У даній роботі визначені причини кореляцій між каталожними даними за логарифмічною світністю – $\log L$ галактик з активними ядрами (AGN). Особливу увагу приділено галактикам типу BL Lac. Особливості зміни світностей цих галактик в γ - ($\log L_\gamma$) та оптиці ($\log L_O$) були пов'язані з наявністю комбінованої дії космічних променів (КП) та жорстких випромінювань по всьому периметру AGN, їх кількісним характеристикам. Обґрунтовано можливість використання позитронної спектроскопії в таких об'єктах. Підкреслено важливість високоточних вимірювань лінії 1.022 MeV, що виникає під час анігіляції позитронів з К-електронами багатоелектронних атомів міжзоряного середовища дискової складової

досліджуваних галактик. Спираючись на попередні роботи авторів, продовжено дослідження зв'язку між однофотонною анігіляцією позитронів та доплеровским розширенням ліній цих же атомів в оптиці в AGN. Показано, що непрямим доказом наявності достатньої кількості позитронів та їх анігіляції є канали каскадів у вигляді Δ -резонансу. За наявними даними з каталогів для AGN запропоноване калібрування їх світності в інших областях спектра.

Key words: active galactic nuclei, cosmic rays, inter stellar medium.

1. Introduction

The shells of supernovae and the active nuclei of galaxies exhibit a significant field of hard radiation. The production of high-energy quanta and particles inside the young supernova shells is based on the intense radioactive decay of unstable isotopes with protons excess. Such a process is accompanied by the formation of positrons and γ -quanta. This is usual for β -processes. In the active nuclei of galaxies the charged high-energy particles are formed. Their movement along the magnetic power tubes ensures their delivery to the vast peripheral regions of AGN, providing them the sufficient energy to form their optically bright regions. The sizes of these regions can be as big as several kiloparsec in some galaxies.

Here after we are going to consider the relationship between the intensity of hard radiation and the optical luminosity produced by active nuclei of galaxies. Quite often, this luminosity noticeably exceeds the total luminosity of all stars in this galaxy. The calculations of the transport of various charged particles in the plane and halo of these galaxies (Moskalenko & Strong, 1998) and the associated processes of photo-ionization balance (Osterbrock & Ferland, 2005) allowed the qualitative estimates of the sources of excitation of optical transitions of atoms and molecules both for the plane

and for the halo of these galaxies. According to the results presented by Osterbrock & Ferland (2005) and Osterbrock (1989) the above mentioned mechanisms are not sufficient to produce the observed optical luminosities.

In this work, on the basis of taking into account the atomic photoelectric effect, previously obtained standard values of the source function of such media $S(E)$ and the electron energy distribution $f(E)$ (Doikov et al., 2018) we analyzed the reasons of excitation of the electronic structure of atoms and molecules. Basing on the results obtained by Doikov (2019) for scattering by dust particles with sizes of 10–20 nm it was concluded that the diffuse nature of interstellar dust scattering is an additional factor to increase the AGN's optical luminosity. The combined effect of ionization losses in gas-dust aggregates, over the entire AGN volume and, as a result, the formation of a radiation field with source function $S(E)$, is caused by the formation of cascade electron's transitions to the K-level. This phenomenon leads to the fact that the contribution to the excitation of optical transitions of the radiation field and of Auger electrons becomes comparable both in the absolute values of energy and also in its intensity.

After each event of a K-vacancy formation caused by an atomic photoelectric effect, several Auger electrons are thrown out by each of the atoms and each of them excites, in particular, the optical transitions. In this case, the energy transfer coefficient of hard radiation is maximal. Thus, the determination of optical luminosity requires the information on the relationship between the total kinetic energy of hard radiation and particles and the total energy emitted in the optical range. Here after we are trying to solve this problem in several main steps.

In Section 2, the selection of objects from Fermi satellite catalogs – the so-called standard AGNs – is carried out. In this paper, attention is paid to the observed properties of BL Lac type of AGN. The hard radiation fluxes from such objects are slightly distorted by the inverse Compton effect and can be used to estimate the optical luminosity.

Section 3 uses the results of previous section to find the induced radiation field $S(E)$ and the Auger electron distribution function $f(E)$.

In Section 4 we estimate the optical luminosity of AGN and the spectroscopic properties of gas-dust conglomerates associated with the presence of hard radiation, especially in their peripheral regions.

In Conclusion section the general spectroscopic criteria for observations of important spectral lines of light elements in AGN are proposed.

The Discussion section compares the proposed methods for studying the AGN optical spectra and their relationship with the γ -spectra.

2. The relationship between the AGN luminosity in hard and optical ranges

Numerous satellite and ground-based observations of galaxies with AGN have made possible the creation of catalogs where the energy fluxes in the gamma, x-ray, and optical ranges are collected. In particular, it is possible to investigate the correlations of the energy fluxes observed in B filter, with those at 1 keV and 1 GeV. It is important because the indicated energies are in the spectral ranges where the main energy is released in AGN center (1 GeV) and further transformed in the AGN's outer regions (1 keV and B-filter). The presence of synchrotron radiation energy in the indicated intervals is confirmed by the strong polarization and the additive structure of observed flux.

Synchrotron radiation polarization measurements relate exclusively to the AGN's central part. The sensitivity of these observations is limited by the near-central regions of AGN, in which the density of gas and dust is much higher than in the outer regions. Due to the randomness of the structure of gas-dust conglomerates, the depolarization of radiation proceeds rather quickly at scales of several parsec within the galactic disks. Thus, the catalog data used for integrated flows at the indicated spectral intervals can be considered to be nonpolarized without the loss of generality.

The second important parameter is the observed galaxies absolute luminosity at the indicated energies. The fact is that in order to determine the redistribution of energy between γ -quanta, protons, α -particles and the lepton component, it is necessary to solve the relativistic kinetic equation using the observed values of energy fluxes and the cross sections of reaction between the mentioned particles and quanta. The variable parameters in this case are the total energy flux and the flux of γ -quanta. Both these fluxes are determined by satellite observations.

A complete catalog of objects with the morphology of interest to us is several hundred. The homogeneous selection of BL Lac type objects is dozens of galaxies. It is sufficient for statistical sampling. To achieve the thermalization of a fully ionized hydrogen-helium plasma in the incident substance, in order to be able to fix the observed γ -quanta energies, the extremely high values of the substance density and temperature are necessary. These high values are unacceptable for the stable functioning of accretion disks around massive formations in the AGN's center.

One of the possible mechanisms to accelerate the charged particles is their acceleration due to the large difference of the electric field potentials (Blandford, 1977). An essential feature of this scenario is the possibility of the formation of a spark discharge with the emerging current of electrons and positrons parallel to the electric field. One electron (or positron) acceler-

ated by this potential difference is capable of achieving high enough energy to form γ -radiation due to the so-called photon comptonization.

These photons, initially emitted tangentially to the electric field lines, can, after passing through the gap of the central part of the accretion disk, collide with a significant perpendicular component of the magnetic field and create an electron-positron pair. The pair should be accelerated and it can be the first step of cascade.

The physical system presumably adjusts its parameters to find sufficient number of charged particles for current creation. The next step can be the transformation of this current to jet. The existence of sufficiently intense cross-sectional electric and magnetic fields and the resulting acceleration mechanisms allows us to conclude that high-energy γ -quanta are formed in jets after the acceleration of mainly protons, α -particles, and the lepton component. The use of relativistic kinetic equation at this stage allows the calculation of collision cross sections as it was proposed by Dermer (1986) and Gould (1982).

The overview of existing observations shows that AGNs flux has a significant, dense and energetically important part in γ -rays with 1 GeV energies. Given the density of particles and quanta at the base of the jets, it should be expected that the inverse Compton effect is the main mechanism to transfer the energy of accelerated particles to quanta.

It means that the energy of particles is lost mainly due to the inverse Compton effect and inhibitory losses, while the energy of γ -quanta in this case increases unlimitedly (Gould, 1975). Let us limit our consideration by the jet base only. In this case the maximum energy of charged particles accelerated flow is in the region of several GeV. At these energies, we have a discontinuity in the spectral distribution of the marked type of galaxies due to Δ -resonance. The probability of collisions of leptons with γ -quanta is significantly higher than for collisions with protons and α -particles.

Nevertheless, it is important to determine the coefficient of energy transfer from leptons to low-energy γ -quanta and protons. Assuming that upon transition from the inner, thermolysed part of the accretion disk to the jet, the protons and leptons have an upper limit of kinetic energy no more than a few MeV (with a possible scattering of the order of megavolts).

Let us consider the collision cross sections for reactions between the accelerated leptons and the γ -quanta (inverse Compton effect) as well as between the accelerated leptons and the protons (taking into account the bremsstrahlung loss). The second type of deceleration is attributed to the lepton-hadron model of the interaction of protons and α -particles with relativistic lepton.

Both types of interactions are well known in cosmic ray physics and are well studied experimentally. As-

suming that in a jet the maximum of electrons energy distribution shifts toward higher energies with the increasing distance from the center, we determine the effect of the lepton current on the energy characteristics of protons and quanta. The collision of a high-energy lepton with a photon inside the jet is given by the Klein-Nishina formula. For the kinetic energy of the electron $E = \gamma mc^2$ and the photon energy $h\nu$ according to (Lang, 1974) we have:

$$\sigma_C = \frac{3}{4}\sigma_T \left\{ \frac{1+q}{q^2} \left[\frac{2q(1+q)}{1+2q} - \ln(1+2q) \right] + \frac{1}{2q} \ln(1+2q) - \frac{1+3q}{(1+2q)^2} \right\} \quad (1)$$

In the energy range of interest to us, the frequency of the radiation ν_0 emitted as a result of the inverse Compton effect is represented by the relation $\nu_0 = \gamma mc^2/h$. The parameter q is represented by the relation: $q = \gamma h\nu/(mc^2)$. $\sigma_T = 6.65 \cdot 10^{-25} \text{ cm}^2$ is the Thomson scattering cross section.

The presence of relativistic electrons and a magnetic field at the jet's base leads to the synchrotron self-compton effect and results in a rapid energy increase of the γ -quanta of the field from 6 MeV to 1 GeV. Such an effect leads to the fact that the energies of relativistic electrons and quanta are equalized. As early as the 1950s, the rather high accuracy experiments on the scattering of fast electrons by nucleons, and the elastic character of interactions for energies less than 2-3 GeV was noticed.

Therefore, the fraction of the energy transferred from the fast electron to the proton is determined by the differential cross section $d\sigma/d\Omega_M$ of the Mott scattering, multiplied by a function that depends on the charge distribution inside the proton - $F(q)$ (called the form factor) and the spins of the interacting particles.

$$\frac{d\sigma}{d\Omega} = \frac{d\sigma}{d\Omega_M} [F(q)]^2, \quad \frac{d\sigma}{d\Omega_M} = \frac{Z^2 e^4 \cos^2(\frac{\theta}{2})}{4E^2 \sin^4(\frac{\theta}{2})} \quad (2)$$

In the interval of the energies under consideration, instead of the scattering angle θ , the Breit scattering angle - θ_B is used according to the formula:

$$ctg^2 \frac{\theta_b}{2} = ctg^2 \frac{\theta}{2} \cdot \frac{1}{1+\tau}, \quad \tau = \frac{-q^2}{4M^2} \quad (3)$$

In high-energy physics, the quantity $-q^2$ has the dimension $(\text{GeV})^2$. In the present problem $-q^2 \leq 3(\text{GeV})^2$. And the q value itself can be interpreted as the transmitted momentum. The value of the transmitted impulse, expressed in terms of the value of the incident impulse p_0 in the Rosenblatt formula, is expressed by the ratio:

$$q = \frac{2p_0 \sin(\frac{\theta}{2})}{\left[1 + \left(\frac{2E_0}{M}\right) \sin^2(\frac{\theta}{2})\right]^{1/2}} \quad (4)$$

The various mechanisms of protons and α -particles acceleration that occur in the AGN's central part provide such an acceleration of cosmic rays that their energy is sufficient to be detected by modern satellites. During the quiet phase intervals the AGN center should produce a CR luminosity of the order of $10^{44} - 10^{46}$ erg/s.

This energy is redistributed between the lepton and hadron components. For the occurrence of spallation reactions in the peripheral regions of AGN, a significant part of hadrons with energies of 3 or more GeV is necessary. The relative contents of α -particles and protons in the AGN's center are proportional to the average ratio of helium to hydrogen. If all particles start from energies of several MeV and accelerate to 2-3 GeV, then during the motion from AGN through the galactic halo due to pair collisions with relativistic electrons, the momentum represented by formula (4) is transmitted to protons and α -particles.

After the transition from accretion disk to jet, the electrons become relativistic. But it is necessary to point that the momentum transfer coefficient of the protons and α -particles acceleration by relativistic leptons is small. Each proton should experience a minimum of three thousand collisions with such electrons on the scales of the order of 1 kpc. Let us estimate the reality of such a process analyzing the properties of observed jets in AGNs of BL Lac type objects.

The scattering of electrons by protons at low energies is Coulomb, purely elastic. For the first estimates, we take into account that the characteristic interaction radius is comparable with the De-Broglie wavelength λ_D . Then the minimum impact angle at which the scattering occurs is $\theta_{min} = 2/\lambda_D v^2$. Then the differential scattering cross section takes the form:

$$\sigma^*(v) = \frac{2\pi}{v^4} \ln \frac{4}{\theta_{min}^2} = \frac{2\pi}{v^4} \ln \frac{2}{(\lambda_D)^2 v^4} \quad (5)$$

Collision frequency $\nu = Nv\sigma(v)$. Here v is the speed of the relativistic electron relative to the proton, N is the concentration of protons. The actual number of atoms in a single magnetic tube with a length L of 1 kpc is $NL = 10^{21} - 10^{26}$ particles/cm². During the movement along such tubes, the number of collisions of relativistic electrons with the proton component reaches $10^8 - 10^{13}$ events, which is enough to accelerate protons and α -particles to GeV.

Then we can say that the particle drift along the magnetic force tubes occurs in such a way that the energy distribution function of the leptons is shifted toward several MeV, and the maximum of the proton and α -particle energy distribution – towards GeV. Upon reaching the galactic disk, all protons with energies above 3-5 GeV begin to participate in inelastic scattering by hydrogen atoms, causing, among other things also the Δ -resonance, according to the scheme

with well known cross sections:

$$\begin{cases} p+H \rightarrow \pi^+ + \dots; \pi^+ \rightarrow \mu^+ + \dots; \mu^+ \rightarrow e^+ + \dots \\ p+H \rightarrow \pi^- + \dots; \pi^- \rightarrow \mu^- + \dots; \mu^- \rightarrow e^- + \dots \\ p+H \rightarrow \pi^0 + \dots; \pi^0 \rightarrow 2\gamma \end{cases} \quad (6)$$

It should be noted here that positrons are formed with a 50% probability (end of the first series of cascades), 25% end of the second series of cascades. And, finally, with 25% neutral pions - π^0 are created (Doikov et al., 2019a; Gusev et al. 2000). γ -quanta from such decays have an energy of 67.5 GeV. By varying the thickness of the galactic disk and the density of gas-dust conglomerates, we conclude that all protons, even with the cascades cross sections of 10^{-26} cm², participate in the Δ -resonance with hydrogen atoms of the interstellar medium in galactic disk with AGN.

The given observational results show one of the reasons for the correlation between luminosity in the γ - and optical spectral ranges. In other words, $\log L_\gamma / \log L_b \approx const$. The final products of such transformations, namely $-e^+$, e^- and the γ -quanta with energy of 67.5 MeV are mixed with fast electrons drifting along the magnetic tubes.

Cascade transitions to K-vacancies in atoms (including the atoms in molecules) caused by ionization losses in the atoms of the galactic disk cause the luminosity of AGN's peripheral regions. In addition to quanta formed by cascade transitions, Auger electrons are injected into the medium, carrying away half the energy stored in the K-vacancy. For media with a given chemical composition, in the previous work, the energy distribution functions of Auger electrons – $F(E)$ and the source function $S(E)$ were obtained (Doikov et al., 2018).

It follows from the calculations that half of the energy of K-vacancies is emitted by atoms in the form of soft X-ray and hard UV radiation, and the rest is carried away by Auger electrons, which excite the upper atomic and molecular shells.

These mechanisms are responsible for the luminescence of both central and peripheral regions of AGN. The conversion efficiency to high-energy radiation from high-energy protons and α -particles is 1%. The efficiency reaches 40% for secondary and primary electrons and positrons.

The correlation between the measured fluxes at 1 GeV energies and optical radiation, taken from the BL Lac type AGN catalog data (Fan et al., (2016) and given in Table 1, shows a stable, directly proportional correlation. An analysis of the spectroscopic properties of gas-dust conglomerates taking place in a medium penetrated by these cosmic rays was carried out by Doikov et al. (2018; 2019a,b). The comparability of X-ray fluxes from the AGN center and its periphery was found. It was not expected as the mentioned fluxes are the result of independent physical mechanisms.

Leptons, unlike hadrons in a jet, in the energy interval under consideration lose additional energy on synchrotron bremsstrahlung radiation (Gould, 1975). In this case, the observed results of γ -quanta flux measurements can be used to make preliminary estimate of the charged particles flux at the jet base, and also the X-ray (at 1 KeV) and optical (B-filter) fluxes. It allows estimation the spectroscopic response due to the energy transport to the AGN's peripheral regions.

Table 1 shows the observed data for AGN type BL Lac objects and our calculations for these objects. The first seven columns are taken from Fan et al. (2016). These are the designation, the redshift, the type, and the logarithms of fluxes in four spectral regions, namely in radio, optical, x-ray, and γ -ray. The last four columns are the results of our calculations and will be explained in more details in Section 4 of this paper.

The total number of BL Lac type galaxies exceeds six hundred objects. Consider, for example, the luminosity of the second galaxy in Table 1, namely J0008.0+4713. Logarithm of the total luminosity expressed in *erg/sec* is $\log L_\gamma = 44.87$. Assuming that this luminosity is caused mainly by protons, α -particles, and leptons, we can estimate the energy and fluxes of these particles (H) at the jet base using the following formula:

$$H = L_\gamma / h\nu_\gamma \approx 6.25 \cdot 10^{61.87} \text{ particles/sec.}$$

As the average size (R) of AGN is 400 parsec, the value of peripheral flux can be written as:

$$H_p = H / (4\pi R^2) \approx 1.5 \cdot 10^{20} \text{ particles/cm}^2 \cdot \text{sec.}$$

Thus, we have the upper boundary of the proton flux (not confirmed by observations). It is more realistic to use the mechanisms that occur in jets as a result of taking into account collisions of leptons (e^- and e^+) with protons and α -particles proposed by Dermer (1986).

From the point of view of the relativistic kinetic theory, only the inner part of the accretion disk can be considered to be the optically thin relativistic proton plasma. In the remaining disk parts, the medium is a two-component, proton – electron plasma. Under such conditions, only the quanta with energies of not more than several MeV can be formed. It is the contribution to 1 keV flux.

Bremsstrahlung manifests itself at the energies not exceeding tens of MeV (Gould, 1975). The formation of non-nuclear γ -quanta with several GeV energies requires the presence of strongly accelerated particles in the AGN's center, namely at the jet base, the sufficiently high probability of collision of accelerated particles with lower-energy quanta, and also the significant magnetic field gradients.

The recent AGN observations from the Pamela and Fermi satellites found the quanta and particles of superhigh (TeV) energies. It was shown that such an energy increase is possible only due to the inverse Compton effect between high-energy particles and quanta.

Note that the ratio of the concentration of photons, electrons and protons in the central region of AGN should differ from the concentration of protons and electrons by at least eight orders of magnitude.

Note that the choice of objects in Table 1 and the determination of the quantitative parameters of cosmic ray fluxes are required by the need of sufficiently strong magnetic fields and the intense fluxes in optics and γ -bands of the spectrum.

The motion of cosmic rays with relativistic energies in local magnetic fields leads to the appearance of synchrotron radio emission. Therefore, we will be limited to galaxies of the LB and IB type in the classification considered by Fan et al. (2016). For LB type of BL Lac objects we have the maximum spectral distribution for the frequencies $\log \nu_p < 14$, and for IB type – in the interval $14 < \log \nu_p < 15$.

3. Induced continuous emissions (theory)

Thus, in the the BL Lac type galaxies with AGN we have a two-component plasma at the jet base. The first component are relativistic electrons with energy reaching several GeV and the second are non-relativistic protons and α -particles with energies of the order of several MeV. Considering this physical system, we can assume that both components are in different equilibrium states. The acceleration of protons and α -particles (with energies of several MeV) by relativistic electrons (several GeV energies) is associated with momentum transfer from relativistic electrons minus losses due to synchrotron, bremsstrahlung, backward Compton scattering and ionization losses.

In the interval of logarithms of Lorentz factors $-1 \leq \log \gamma \leq 3$ related to the physical system under consideration, the cross sections for ionization losses are prevailing at the jet base where $\log \gamma = 1$. Here the electrons also achieve relativistic velocities. Then, in a halo of a BL Lac galaxy type galaxy with AGN, inside the corresponding magnetic tube, we can note the comparable values of cross sections for bremsstrahlung radiation losses due to the collision of relativistic electrons with protons and α -particles and the cross sections describing synchrotron radiation inside magnetic tubes.

Within the framework of a given physical system, protons and α -particles can be considered to be practically motionless. Then the rate of energy exchange between fast electrons and protons or α -particles is (Dermer, 1986; Gould, 1982):

$$\frac{du_e}{dt} = -\frac{du_{p,\alpha}}{dt} = -\frac{4\pi e^4}{c} \cdot \frac{n_{p,\alpha}}{M_{p,\alpha}} \left(\ln \frac{4\pi k T_e}{\omega_{p,\alpha}} + (-\gamma_e) \right) \cdot \frac{T_e - T_{p,\alpha}}{T_e} \quad (7)$$

Table 1: BL Lac type objects: observed fluxes and relative remaining part fluxes calculated for 1 kpc distance.

Object	Z	Type	Observed fluxes				Calculated fluxes for 1 kpc distance			
			L_R	L_0	L_x 1 KeV	L_γ 1 GeV	$E(\tau_H)$	$E(\tau_{He})$	$E(\tau_d)$	$E(\tau_f)$
1	2	3	4	5	6	7	8	9	10	11
J0001.2-0748		IB	42.36	45.39		45.23	0.55	0.55	0.98	0.55
J0008.0+4713	0.280	IB	41.18	45.54	43.51	44.87	0.19	0.19	0.62	0.19
J0008.6-2340	0.147	IB	40.38	44.97	43.72	43.08	0	0	0	0
J0009.1+0630		LB	42.43	45.04		45.14	0.46	0.46	0.89	0.46
J0013.2-3954		LB	42.74	44.42		45.21	0.53	0.53	0.96	0.53
J0013.9-1853	0.095	IB	39.90		43.72	42.88	0	0	0	0
J0014.0-5025		HB			45.38	44.64	0.70	0.70	1.13	0.70
J0018.4+2947	0.100	HB	40.00		43.54	42.84	0.0	0.0	0	0
J0018.9-8152		HB			45.37	45.16	0.69	0.69	1.12	0.69
J0019.4+2021		LB	43.04	44.42		44.91	0.23	0.23	0.66	0.23
J0021.6-2553		LB	41.88	45.06		45.14	0.46	0.46	0.89	0.46
J0022.1-1855		IB	41.39	45.60	44.56	45.13	0	0	0.31	0
0022.1-5141		HB			45.51	45.14	0.83	0.83	1.26	0.83
J0022.5+0608		LB	42.57	44.64		45.68	0.99	0.99	1.43	0.99

where $\omega_{p,\alpha}$ are the plasma frequencies of protons and α -particles. The corresponding relaxation time will be:

$$\tau_{e,p}(\tau_{e,\alpha}) = u_e / \frac{du_e}{dt} \quad (8)$$

The acceleration time of protons and α -particles is three orders of magnitude longer than the characteristic times of electron-electron collisions. Therefore, there are always high-energy electrons in a jet capable to transmit the momentum to protons and α -particles. Thus, having the collision frequency of relativistic electrons with slow protons and α -particles, we can obtain the value of the transferred energy:

$$\begin{cases} \frac{dE_r}{dx} \approx \frac{16}{3} N_i Z^2 \frac{e^2}{hc} \left(\frac{e^2}{mc^2} \right)^2 E \cdot \ln(\gamma) & \omega > \omega_S \\ \frac{dE_r}{dx} \approx \frac{16}{3} N_i Z^2 \frac{e^2}{hc} \left(\frac{e^2}{mc^2} \right)^2 E \cdot \ln \left(\frac{1.4}{Z^{1/2}} \frac{hc}{2\pi e^2} \right) & \omega < \omega_S \end{cases} \quad (9)$$

Substituting in the first equation of the system $Z = 1$, $N_i = 1 \text{ cm}^{-3}$ and the tabular data of the constants, we obtain the simple relation comfortable for further calculations:

$$\frac{dE_r}{dx} = 0.305 \cdot 10^{-26} E \cdot \ln(\gamma) \quad (10)$$

For small values of the Lorentz factor γ -electrons can still be considered as non-relativistic ($E \leq 6 \text{ MeV}$), and the momentum transfer can occur mainly due to collisions. Then:

$$\begin{aligned} \frac{dE_r}{dx} &= 4\pi N Z \frac{e^2}{mv^2} \cdot \ln \left[\left(\frac{4\pi\gamma^2 mv^2}{h\omega} \right) - \left(\frac{v}{c} \right)^2 \right] \\ &\approx 0.393 \cdot 10^{-27} \cdot \ln \left[\left(\frac{4\pi\gamma^2 mv^2}{h\omega} \right) - \left(\frac{v}{c} \right)^2 \right] \text{ J/cm} \end{aligned} \quad (11)$$

Formulas (10) and (11) allow us to draw the following conclusions:

1. Elastic collisions of relativistic electrons with protons and α -particles lead to the energy losses due to bremsstrahlung and to the transfer of a part of the pulse (not more than 0.01% per collision) to accelerate these particles. The cross sections for such scattering do not exceed the thomson value σ_r .

2. The collisions of nonrelativistic electrons with protons and α -particles occur in such a way that energy losses due to collisions exceed radiation losses. Formula (10) gives the correct result for the loss of electron energy up to the values of several MeV. The accelerations of protons and α -particles are the most effective in this case. As the electron energies increase, the transfer of mechanical energy to protons and α -particles becomes less efficient.

3. For acceleration of protons and α -particles to the energies of the order of 2-3 GeV at least 10^8 collisions with fast electrons are required.

4. The optical luminosity of AGN

In this section, we determine the optical luminosity of AGN from the observed data, namely using the columns with L_x and L_γ in Table 1. The study of cosmic rays formed in the centers of galaxies with various morphologies using the PAMELA satellite led to the conclusion that AGN form the particle flows with energies comparable to those generated by γ -ray fluxes. Take, for example, galaxy J0001.2-0748 of type IB with a luminosity near $L_x = 10^{45} \text{ erg/sec}$ at a quantum energy of 1 GeV. This value of luminosity and the presence of magnetic fields with intensities from hundreds gauss in the AGN's center to 10^{-4} gauss in the periphery of the magnetic tubes the particles with energies up to several GeV will be held.

Taking the average size of the AGN's luminous disk of the order of 0.4-1 kpc, we obtain an area of $1.44 \cdot 10^{42} \text{ cm}^2$. For the indicated values of L_γ , the number of particles and quanta with an energy of 1 GeV is 10^{48} charged particles and quanta. The total luminosity of the center of our Galaxy is six orders of magnitude lower, providing on average 1 particle per 1 cm^2 . Therefore, for galaxy J0001.2-0748, the upper limit of the surface flux of protons, α -particles and electrons of the order of $10^4 \text{ particles/cm}^2$ can be considered to be acceptable.

Let us try to find the energy distribution of these particles. The electrons have energies no higher than a few MeV. Protons and α -particles – no higher than 2-3 GeV. The fractional parts of electrons and protons are equal; the part of α -particles are 10 times lower than that of protons. The thickness of the galactic disk in the region of AGN is 200-300 parsecs, which gives a thickness of absorbing media for these particles equal to 10^{21} cm. The number of collisions of high-energy protons and α -particles within the specified disk thickness is: $N = N_i N_g \sigma_{\Delta} L \approx 1 - 6$ for protons and 0.1 - 0.6 for α -particles. That is, all protons and α -particles entering the disk component experienced the transformations described by equation (6) corresponding to the channels of the Δ -resonance transformation.

According to Gusev et al. (2000), the energy transfer coefficient of the initial energy in the equation (6) is 1%. It means that the final energy amount is of the order of several tens of MeV. The main mechanism of energy loss for leptons in (6) are the ionization loss, the positron annihilation, and the decay of photo-pions, as it is indicated in the third channel of (6). Ionization losses at given initial energies are caused by the formation of K-vacancies in all chemical elements or by ionization of hydrogen and helium.

The efficiency of energy transfer for the final products of equation (6) into radiation is 10-30%, depending on the chemical element in which the K-vacancy is formed. In hydrogen and helium the recombination, which depends on the concentration of ions and thermal electrons, plays a large role, but the cascades instantly appear in the remaining elements, which contribute to the excitation of optical transitions. Auger electrons are formed simultaneously with cascades and lead to the same effect.

Summing up the results of the previous work (Doikov, 2019a,b) and the calculations in this article, we can show the main results in Table 1, where the remainder of the fluxes at the distance of 1 kpc from the center of galaxy with AGN are shown in columns from 8 to 11.

The columns 8 and 9 show relative part of flux remaining after the absorption by only the hydrogen and only the helium. Column 10 takes into account the absorption by dust component, namely the carbon and silicon dust. The last column is the part of the flux remaining after the absorption by all components, tabulated in columns 8-10. The zero values in columns 8-11 indicate the full absorption of radiation at the distance 1 kpc from the center. Columns 8 and 9 are similar because the results of multiplications the concentration and the cross sections for hydrogen and helium are equal.

Let us note than hydrogen and helium absorption manifests itself only in the optical component of AGN spectrum. It produces the diffuse scattering of quanta, and also the bremsstrahlung and ionizing radiation for

individual recombination lines.

It is necessary to comment on the results of the AGN's luminosity calculations taking into account the presence of a dust component. In this case, columns eight and nine take into account the cascade transitions in elements such as Mg, Si, and O of the constituent dust. According to Doikov (2019), even in the near surface layers of dust, with a depth of 10-15 nm the above atoms form cascade transitions, with the formation of X-ray quanta. The same atoms participate in the circulation of matter of gas-dust complexes in the form of molecules and free atoms.

Of particular interest for the interpretation of radiation in x-rays are Mg and Si because their cascades $2p - 1s$, $3d - 2p$ generate x-ray quanta after filling a K-vacancy near 1 KeV. Small dust particles scatter x-ray radiation with a wavelength close to 1-10 nm. The probability of the formation of such quanta depends on the chemical composition of the medium.

The same can be said about C, N, O elements. The mentioned process of filling K-vacancies was studied by Doikov et al. (2018). It was found the diffuse filling of the peripheral regions of AGN with quanta of similar origin in the range from 100 eV to 10 KeV. In this case, the observation of x-ray flux at 1 KeV can characterize the presence of such elements as Ne, Na, Mg. But their low contents are of little use for such an analysis. The exception is Mg. Note that all elements other elements are at least six orders of magnitude less abundant.

Therefore the significant fluxes of quanta with an energy of 1 KeV are created mainly by the central part of AGN localized by the jet base, and the diffuse component is formed by the entire volume of AGN. Formed in the AGN's peripheral parts UV and soft X-rays are responsible for the formation of high-power optical luminescence caused by secondary radiation and Auger electrons. The cross sections for the excitation of optical transitions under the influence of a steady radiation field are at least five orders of magnitude larger than the photo-cross sections considered when K-vacancies are formed.

5. Discussion

The appearance of multichannel observations of AGN luminosities in various spectral regions made it possible to analyze the energy interaction of the AGN center with its periphery. At the same time, it was concluded that energy is transmitted in the form of cosmic rays and hard radiation in the form of quanta. In particular, the importance of Δ -resonance is determined.

The coefficient of transformation of the initial energy of these sources into the optical radiation is determined. It is correlated with the γ -range luminosity. One of the consequences of the interaction of high-energy protons with hydrogen atoms of the interstellar

medium is the formation of intense flux of secondary positrons.

As a result, the annihilation of secondary positrons with K-electrons gives rise to their single-photon annihilation with a γ -ray energy of 1.022 MeV and two-photon annihilation with an energy of 0.511 MeV. The intensity of the γ -lines produced by the annihilation of positrons is a unique diagnostic spectroscopic tool for AGN's studying (Doikov et al., 2019).

The most important are the determination of the fluxes of protons and α -particles with energies of 2-3 GeV and to the measurement of the Doppler broadening for optical lines of atoms involved in the annihilation of positrons with K-electrons.

6. Conclusion

The increasing amount of observations of galaxies with AGNs in various spectral ranges has expanded the range of problems to be solved and the possibility of unifying them according to measured data. In particular, the correlation between the energy fluxes in the γ -, x-ray and optical spectral regions becomes visible. Of particular interest is the correlation of the logarithms of luminosity in the γ - and optical parts of the spectrum.

As our previous calculations showed, the formation of the AGN luminescence in the form of a γ -spectrum is associated with physical processes near a compact relativistic object, often interpreted as a massive black hole. Here, a powerful flux of cosmic rays is formed simultaneously, mainly in the form of electrons, positrons, protons and α -particles.

In the present work, it was shown that the reason of the correlation between the L_γ and L_B luminosities is the transport of cosmic rays kinetic energy along the magnetic force tubes. These cosmic rays were formed together with γ -quanta and propagated to AGN's peripheral regions.

Cosmic rays are limited in energy by the upper limit of 3-5 GeV since at higher energies the cosmic rays leave AGN unhindered.

We also estimated the percentage of cosmic rays energy converted into radiation as a result of ionization losses and other types of interaction of cosmic rays fluxes with gas-dust aggregates of the AGN periphery.

It amounts to about 0.5% - 0.1% depending on the boundary conditions and the chemical composition of gas-dust conglomerates. Given the remoteness and limited information on AGN, these types of correlations allow us to estimate the expected intensity in the optical spectrum from the measured luminosity in the γ -range.

The relativistic electrons formed at the jet's base quickly lose their kinetic energy in collisions with both protons and α -particles and, when entering the periph-

eral region, are mixed with Auger electrons.

The heavy component of cosmic rays forms Δ -resonance in collisions with hydrogen in gas-dust conglomerates according to the schemes shown by the equation (6). The final products of all three channels of the indicated circuit efficiently transmit energy and participate in the formation of the optical radiation field.

Acknowledgements. This work used the data from the European Space Agency (ESA) mission Gaia (<https://www.cosmos.esa.int/gaia>), processed by the Gaia Data Processing and Analysis Consortium (DPAC, <https://www.cosmos.esa.int/web/gaia/dpac/consortium>). Funding for the DPAC has been provided by national institutions, in particular the institutions participating in the Gaia Multilateral Agreement. This work was supported by the Russian Foundation for Basic Research (grant no. 18-02-00890).

References

- Dermer C.D.: 1986, *ApJ*, **307**, 47.
 Blandford R.D.: 1977, *MNRAS*, **179**, 433.
 Crosas M., Weisheit J.: 1996, *ApJ*, **465**, 659.
 Doikov D.N., Andrievskii S.M., Yushchenko A.V.: 2018, *Journal of Physical Studies*, **22**, 2901.
 Doikov D.N., Yushchenko A.V., Jeong Y.: 2019a, *Journal of Astronomy and Space Sciences*, **36**, 21.
 Doikov D.N., Yushchenko A.V., Jeong Y.: 2019b, *Journal of Astronomy and Space Sciences*, **36**, 115.
 Doikov D.N.: 2019, *FAS*, **56**, 138.
 Fan J.H., Yang J.H., Liu Y. et al.: 2016, *ApJS*, **226**, 20.
 Gusev A.A., Jayanthi U.B., Martin I.M. et al.: 2000, *Brazilian Journal of Physics*, **50**, 590.
 Gould R.J.: 1982, *ApJ*, **254**, 755.
 Gould R.J.: 1975, *ApJ*, **196**, 689.
 Lang K.R.: 1974, *Astrophysical Formulae, Compendium for the Physicist for Physicist and Astrophysicist*. Springer (1974) (tr. Russian 1978. Mir. Moscow)
 Moskalenko I.V., Strong A.W.: 1998, *ApJ*, **493**, 694, <https://doi.org/10.1086/305889>.
 Osterbrock D.E., Ferland G.J.: 2005, *Astrophysics of gaseous nebulae and active galactic nuclei*, 2ed. by D.E. G.J.Ferland. Sausalito, CA: UniversityScienceBooks, 480 p., <http://adsabs.harvard.edu/abs/2006agna.book...Osterbrock>.
 Osterbrock D.E.: 1989, *Astrophysics of gaseous nebulae and active galactic nuclei*, Mill Valley, CA, University Science Books, 422 p., <http://adsabs.harvard.edu/abs/1989agna.book....O>

DOI:<http://dx.doi.org/10.18524/1810-4215.2019.32.182100>

SPECTROSCOPIC MONITORING OF THE B[E] OBJECTS FS CMA AND MO CAM

A.K. Kuratova¹, A.S. Miroshnichenko^{2,3,4}, S.V. Zharikov⁵, N. Manset⁶,
S.A. Khokhlov^{1,4,7}, A. Raj⁸, A.V. Kusakin⁴, I.V. Reva^{1,4}, R.I. Kokumbaeva⁴,
Usenko, I.A.^{9,10}, Knyazev, A.Y.¹¹

¹ Physical-Technical Faculty, Al-Farabi Kazakh National University,
Almaty, Kazakhstan, aizhik03@gmail.com

² Department of Physics and Astronomy, University of North Carolina at Greensboro,
Greensboro, NC, USA, a_mirosh@uncg.edu

³ Main Astronomical Observatory of the Russian Academy of Sciences, Saint-Petersburg, Russia

⁴ Fesenkov Astrophysical Institute, Almaty, Kazakhstan, raushan.raushan@mail.ru

⁵ Institute for Astronomy, Universidad Nacional Autónoma de México,
Ensenada, Mexico, zhariaunam@gmail.com

⁶ Canada-France-Hawaii Corporation, Kamuela, HI, USA, manset@cfht.hawaii.edu

⁷ NNLOT, Al-Farabi Kazakh National University, Almaty, Kazakhstan, skhokh88@gmail.com

⁸ Indian Institute of Astrophysics, Koramangala, Bangalore, India, ashishpink@gmail.com

⁹ Astronomical Observatory, Odessa National University, Odessa, Ukraine, igus99@ukr.net

¹⁰ Mykolaiv Astronomical Observatory Research Institute, Mykolaiv, Ukraine

¹¹ South African Astronomical Observatory, Cape Town, South Africa, akniazev@saa.ac.za

ABSTRACT. Objects with the B[e] phenomenon exhibit permitted and forbidden emission lines due to the presence of circumstellar ionized gas and large infrared excesses due to processing of the stellar radiation by circumstellar dust. There are five groups of stars that show this phenomenon (pre-main-sequence Herbig Ae/Be stars, symbiotic systems, proto-planetary nebulae, some supergiant, and FS CMa type objects). The latter group is the most recently discovered and the least explored. The leading hypothesis about the group nature implies that they are mostly intermediate-mass binary systems, whose circumstellar medium was created during a strong mass-transfer phase due to a Roche lobe overflow of the more massive star in the system. We have been conducting a large program of spectroscopic and photometric observations of many objects and candidates to this group. The current report is devoted to the preliminary results of our ongoing study of two objects with similar underlying early B-type stars, FS CMa (the group prototype) and MO Cam. The objects show different emission-line profiles and infrared excesses which are most likely due to different tilt angles of their non-spherical envelopes with respect to the line of sight. Variability of spectral lines is discussed here.

Key words: Stars: emission-line, Be - Stars: evolu-

tion - Stars: circumstellar matter - Stars: binaries: general.

АНОТАЦІЯ Об'єкти з феноменом B[e] демонструють дозволені та заборонені емісійні лінії завдяки присутності навколосоряого іонізованого газу та великого інфрачервоного надлишку завдяки перевипромінюванню навколосоряним пилом. Існують п'ять груп зір, які показують цей феномен (перед-ГП Ae/Be зорі типу Гербіра, симбіотичні системи, протопланетарні туманності, деякі надгіганти та об'єкти типу FS CMa). Остання група є зовсім недавно відкритою та найменш дослідженою. Головна гіпотеза щодо природи цієї групи полягає в тому, що вони у більшості є подвійними системами проміжних мас, чие навколосоряне середовище створюється на протязі фази сильного переносу маси завдяки перетіканню у порожнину Роша речовини з більш масивної зорі у системі. Ми маємо виконати велику програму спектроскопічних та фотометричних спостережень багатьох об'єктів та кандидатів до цієї групи. Це повідомлення присвячено попереднім результатам нашого інтенсивного вивчення двох об'єктів зі схожими головними ранніми зорями B-типу, – FS CMa (прототип групи) та MO Cam. Ці об'єкти показують різні профілі емісійних

ліній та інфрачервоного надлишку, але які є найбільш схожими завдяки різним кутам нахилу їх несферичних оболонок до лінії спостереження. В роботі обговорено змінність спектральних ліній цих об'єктів.

Ключові слова: B[e]-зорі, еволюція B[e]-зір, оболонки B[e]-зорь, подвійні зорі.

1. Introduction

The B[e] phenomenon is the presence of line emission (e.g., H I and Fe II) and large IR excesses due to dust in the spectra of B-type stars (Allen & Swings 1976). It is found in five stellar groups (Lamers et al. 1998): pre-main-sequence stars, symbiotic binaries, compact Proto-Planetary Nebulae, some supergiants, and FSCMa objects. Classification and determination of fundamental parameters of many objects with the B[e] phenomenon is difficult due veiling of stellar features by circumstellar material.

The group of FS CMa objects was defined with the following criteria (Miroshnichenko 2007). Observational: A hot star continuum with emission lines of H I, Fe I, O I, [Fe II], [O I], Ca II; a large IR excess peaking at $\lambda = 10 - 30\mu\text{m}$ and sharply decreasing at longer wavelengths; location outside star-forming regions; and a secondary companion (if revealed) typically either fainter and cooler or degenerate. Physical: Hot star has a spectral type between O9 and A2 and a luminosity range $\log L/L_{\odot}$ between ~ 2.0 and ~ 4.5 .

Most FS CMa objects show very strong emission-line spectra inconsistent with mass-loss from single stars. Our studies show that they are not pre-main-sequence stars or proto-planetary nebulae due to lack of cold circumstellar dust. They are thought to be binary systems after a strong mass-transfer stage, when large amounts of gas and dust were formed in the circumstellar envelope. However, only $\sim 30\%$ of the ~ 70 group members and candidates have been confirmed to be binary systems mostly due to a lack of data.

2. Observations

Optical spectroscopic observations of the group prototype FS CMa and MO Cam were obtained with échelle spectrographs (resolving power $R \sim 12000-65000$) at the following telescopes: 3.6 m Canada-France-Hawaii Telescope (CFHT, USA), 2.7 m Harlan J. Smith telescope (McDonald Observatory, USA), 2.1 m telescope of the Observatorio Astronómico Nacional San Pedro Martir (Mexico), 11.4 \times 9.8 m South African Large Telescope, 2 m Himalayan Chandra Telescope (HCT, India), and 0.81 m telescope of the Three College Observatory (USA, FS CMa only). Photometric observations were obtained with a 1 m

telescope of the Tien-Shan Astronomical Observatory (Kazakhstan) in BVR filters in 2014–2016. We have also collected V-band light curves from the ASAS SN all-sky survey (Kochanek et al. 2017) for both objects. The latter are shown in Fig. 1 (left panel).

3. The objects description

FS CMa. A peculiar spectrum of FS CMa was discovered over 120 years ago (Pickering et al. 1898) and classified as that of a Be star (Merill et al. 1925). Later a large IR excess due to radiation of circumstellar dust was found, and it became a prototype of objects with the B[e] phenomenon (Allen & Swings 1976). It was also considered a Herbig Ae/Be star (e.g., Sitko et al. 1995), but it belongs to no star forming region. Miroshnichenko (2007) included it in the B[e] subgroup of FS CMa objects, which are thought to be post mass-transfer binary systems. Its binarity has been suspected from spectro-astrometric data (Baines et al. 2006) but unconfirmed by other techniques. FS CMa shows long-term brightness variations, which are large in the visual range ($V=6.9-8.8$ mag, Miroshnichenko 1998) and much smaller in the near-IR.

MO Cam. The H α emission in the spectrum of MO Cam (also known as AS 78) was discovered by Merrill & Burwell (1933). Its large IR excess was identified in the IRAS data by Dong & Hu (1991). Initial study was done by Miroshnichenko et al. (2000), who detected brightness variations of $\Delta V \sim 0.3$ mag and P Cygni type Balmer line profiles, found the object's spectral type to be B3, and spectroscopically estimated its distance to be ~ 2.9 kpc from the Sun.

4. Results

FS CMa shows fast brightness and line profile variations on a timescale of several days. Blue peaks of double-peaked emission-line profiles vary stronger than red peaks indicating an active mass loss from the B-type star. Small emission peaks near the centers of the Balmer lines may arise in the material near the center of mass of the binary (Fig. 1, right panel). Absorption lines of He I have variable positions, which may be due to a variable contribution from the circumstellar disk.

Line profile and brightness variations of MO Cam are not as fast and not as strong as in FS CMa. Absorption components of the P Cyg type profiles in Balmer lines vary in shapes, indicating changes in the velocity of the circumstellar material in front of the B-type star (Fig. 1, right panel).

5. Conclusions

Both photometric and spectroscopic data show that FS CMa is a highly variable object, while variations of MO Cam are much smaller (Fig. 1, left panel). Brightness variations of both objects contain no periodic component. There is no clear evidence for secondary companions in the properties of both objects, but the properties are very unusual for single stars. FS CMa may undergo a strong mass transfer phase, while MO Cam might have already finished this phase. A more frequent monitoring at timescales of days to weeks may help understanding the reasons for the objects' variability. Spectroscopic distances to both objects are consistent GAIA parallaxes (0.62 ± 0.02 kpc for FS CMa and 3.0 ± 0.3 kpc for MO Cam, GAIA DR2, 2018).

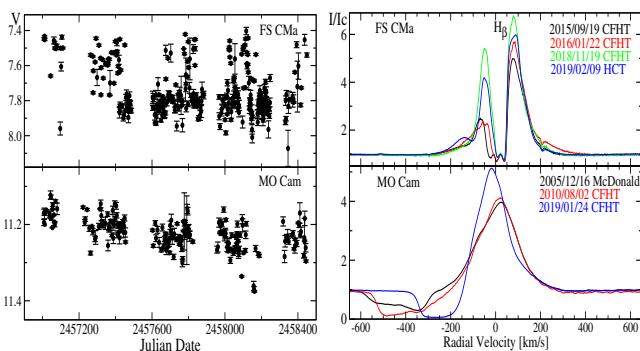


Figure 1: **Left panel.** V -band light curves of FS CMa and MO Cam from the ASAS SN survey in 2012–2018 (Kochanek et al. 2017). **Right panel.** $H\beta$ line variations in the objects' spectra. Only high-resolution data from CFHT, McDonald Observatory, and HCT are shown. Intensity normalized to the local continuum is plotted against heliocentric radial velocity.

Acknowledgements. A.M. and S.Z. acknowledge support from DGAPA/PAPIIT Project IN100614. The work was carried out within the framework of the Project No BR05236322 “Studies of physical processes in extragalactic and galactic objects and their subsystems” funded by the Ministry of Education and Science of the Republic of Kazakhstan. The results are partially based on observations obtained at the Canada-France-Hawaii Telescope (CFHT) which is operated by the National Research Council of Canada, the Institut National des Sciences de l’Univers of the Centre National de la Recherche Scientifique de France, and the University of Hawaii; South African Large Telescope, and Himalayan Chandra Telescope. We thank the staff of IAO, Hanle, and CREST, Hosakote, that made these observations possible. The facilities at IAO and CREST are operated by the Indian Institute of Astrophysics, Bangalore.

References

- Allen, D.A., & Swings, J.-P.: 1976, *A&A*, **47**, 293.
 Baines, D., et al.: 2006, *MNRAS*, **367**, 737.
 Dong, Y.S., & Hu, J.Y.: 1991, *Chinese A&A*, **15**, 275.
 GAIA Collaboration, Brown, A.G.A., Vallenari, A., et al.: 2018, *A&A*, **616**, A1.
 Kochanek, C.S., Shappee, B.J., Stanek, K.Z., et al.: 2017, *PASP*, **129**, 4502.
 Lamers, H., et al.: 1998, *A&A*, **340**, 117.
 Merrill, P.W., et al.: 1925, *ApJ*, **61**, 389.
 Merrill, P.W., & Burwell, C.G.: 1933, *ApJ*, **78**, 87.
 Miroshnichenko, A.S.: 1998, in B[e] stars, *Ap&SS Library*, **233**, 145.
 Miroshnichenko, A.S., Chentsov, E.L., Klochkova, V.G., et al.: 2000, *A&AS*, **147**, 5.
 Miroshnichenko, A.S.: 2007, *ApJ*, **667**, 497.
 Pickering, E.C., et al.: 1898, *ApJ*, **8**, 116.
 Sitko, M.L., et al.: 1995, *Ap&SS*, **223**, 186.

DOI: <http://dx.doi.org/10.18524/1810-4215.2019.32.181736>

CHEMICAL IMPRINTS IN ATMOSPHERIC ABUNDANCES IN PLANET-HOSTING STARS

T. Mishenina, N. Basak, V. Kovtyukh

Astronomical Observatory, Odessa National University, Odessa, 65014, Ukraine, tmishenina@ukr.net

ABSTRACT. We examined 12 planet-hosting stars based on homogeneous spectral data (obtained with the SOPHIE echelle spectrograph with $R = 75,000$ at the OHP, France) and using uniform techniques for determination of parameters and abundances of a series of elements (Li, C, Na, Mg, Al, S, Si, K, Ca, Sc, Ti, V, Cr, Mn, Fe, Co, Ni, Zn, Y, Zr, Ba, La, Ce, Pr, Nd, Sm and Eu).

For our set of stars with detected massive planets, we have found $[\text{Fe}/\text{H}]$ ranging from -0.3 to 0.4 dex. There is the only star for which the lithium content has been reliably shown to be lower than predicted values. Average C/O ratio (0.52 ± 0.08) is slightly lower than the solar one (0.54), and C/O ratios tend to correlate with the planetary mass. Magnesium follows the trend in Galactic chemical evolution exhibiting a dependence on the planetary mass. Manganese and barium are both slightly overabundant.

Keywords: stars: abundances – stars: atmospheres – stars: planetary systems – techniques: spectroscopic

АНОТАЦІЯ. Ми дослідили 12 зір з планетами, спираючись на однорідні спектральні дані (отримані на ешель спектрографі SOPHIE з роздільною здатністю $R = 75\,000$ в Обсерваторії От Прованс, Франція) та використовуючи єдині методики визначення параметрів й вмісту ряду елементів (Li, C, Na, Mg, Al, S, Si, K, Ca, Sc, Ti, V, Cr, Mn, Fe, Co, Ni, Zn, Y, Zr, Ba, La, Ce, Pr, Nd, Sm та Eu).

Важливу роль відіграє вивчення хімічного складу материнських зірок, які в хімічному складі атмосфери можуть нести «відбитки» присутності планетарних систем, а співвідношення елементів є важливими для вивчення утворення планет різних мас.

Наші досліджувані зірки з масивними планетами мають різну металічність $-0.3 < [\text{Fe}/\text{H}] < 0.4$. Отже, суперметалічність не може бути надійним критерієм наявності планет. Різний вміст літію в наших цільових зірках відповідає еволюційним змінам. Лише одна зірка (HD13908, вік 2.9 Гр) показує виснаження літію порівняно з прогнозом еволюції. Наші середні значення $[\text{C}/\text{O}] = -0.03 \pm 0.07$ й $\text{C}/\text{O} = 0.52 \pm 0.06$ не підтримують збагачення вуглецем в нашому зоряному зразку, але це узгоджується з результатами, отриманими Suarez-Anders *та ін.* (2018). Ми спостерігаємо невеликий тренд C/O з металічністю й масою планети. Середня величина $\langle [\text{Mg}/\text{Si}] \rangle_{\text{pl}} = -0.05 \pm 0.09$ нижче сонячної величини $[\text{Mg}/\text{Si}]_{\odot} = 0.0$, спостерігається тренд залежності $[\text{Mg}/\text{Si}]$ від маси планети. Марганець та барій виявляють деякий

надлишок вмісту. Жодна з досліджуваних зірок не продемонструвала жодних значних нахилів (залежностей) відносного вмісту вогнетривких елементів до легких від температури конденсації T_{cond} .

Ключові слова: зірки: вміст – зірки: атмосфери – зірки: планетарні системи - методи: спектроскопічні.

1. Introduction

The study of stars with planetary systems is a rapidly developing branch of astrophysics. Most exoplanets were discovered by spectrometric measurements of the radial velocity of stars and planetary transits. Studying the chemical composition of parent stars plays an important role as chemical imprints in their atmospheric abundances may be used as indicators of the presence of planetary systems while elemental ratios are essential to study formation of planets of different masses.

The first studies revealed a relationship between metallicity $[\text{Fe}/\text{H}]$ and the presence of planets (e.g. Gonzales 1997; Udry & Santos 2007 and references therein), and subsequently it was shown that such a relationship could be observed in the stars with massive planets like Jupiter (e.g. Israelian & Mayor 2001; Fischer & Valenti 2005; Sousa *et al.* 2008). Later, suggestions were made to detect exoplanets in metal-poor stars (Sousa *et al.* 2008; Adibekyan *et al.* 2012b, a; 2015). **Lithium** (Li^7) deficiency has been associated with the presence of planets (Gonzalez & Laws 2000; Gonzales *et al.* 2008, 2010; Israelian *et al.* 2004, 2009; Delgado Mena *et al.* 2014; Figueira *et al.* 2014; Mishenina *et al.* 2015, etc.) while an excess of lithium isotopes Li^6 has been deemed to indicate the presence of massive planets (e.g. Israelian *et al.* 2001 Montalban & Rebolo 2002). Delgado Mena *et al.* (2015) reported lower lithium content in the host stars of massive planets (-0.14) as compared to the stars without detected planets. However, the rotational velocities $v_{\text{ sini}}$ of stars with hot Jupiters tend to be higher on average than those of single stars suggesting that rotationally induced mixing (rather than the presence of planets) might be responsible for greater lithium depletion. A strong correlation between the lithium content and age was observed, which could be due to stellar evolution (Baumann *et al.* 2010; Carlos *et al.* 2016).

The carbon to oxygen ratios **C/O** in planet-hosting stars can provide key information about the protoplanetary discs in which the relevant planets are formed (Kuchner & Seager 2005). There are noticeable discrepancies in the estimates of C and O abundances in various studies to date.

For instance, Petigura & Marcy (2011) reported that planet-bearing systems were enriched in carbon with $C/O \geq 1.00$; however, a number of other studies (e.g. Nissen *et al.* 2013, 2014) did not support the existence of carbon-rich planets with the C/O values not exceeding 0.8. Teske *et al.* (2014) found that the mean C/O ratio for their sample of transiting exoplanet host star was 0.54 ($C/O_{\odot} = 0.54$) as compared to the previously measured C/O averages for the host stars of ~ 0.65 - 0.75 . Later, Suárez-Andrés *et al.* (2016, 2017) showed that the linear relationship between $[N/Fe]$ and $[Fe/H]$ was due to the metal-rich nature of planet-hosting stars, i.e. due to Galactic chemical evolution. They also found two different sloped trends for $[C/Fe]$ with $[Fe/H] > 0$ and $[Fe/H] < 0$, and a flat distribution of the $[C/Fe]$ ratio for all planetary masses. Recently, Pavlenko *et al.* (2019) have reported that metal-rich dwarfs with planets are richer in carbon with $\langle [C/O] \rangle = 0.05 \pm 0.05$.

The magnesium to silicon ratio $[Mg/Si]$ is higher for the stars with low-mass planets (Adibekyan *et al.* 2015); the correction for the NLTE effects (Adibekyan *et al.* 2017) has resulted in a small difference, and high $[Mg/Si]$ ratios in the stars hosting Super-Earth/Neptune-mass planets are likely to be associated with their formation. The correlation between C/O and Mg/Si is crucial to the determination of mineralogy of planetary companions (Suárez-Andrés *et al.* 2018, HARPS sample). The authors obtained $C/O < 0.8$ for their entire sample of planets. Among stars with high-mass companions, $0.8 > C/O > 0.4$ was reported for 86% of stars and $C/O < 0.4$ for 14%. Mg/Si is $1 < Mg/Si < 2$ for all the stars with low-mass planets and 85% of those with high-mass companions, and $Mg/Si < 1$ for the remaining 15% of the last ones. There were no planet-hosting stars with $Mg/Si > 2$. For planet-hosting stars with low-mass companions, C/O and Mg/Si were similar to the solar ones, whereas C/O was lower for the stars with high-mass companions.

A correlation between the abundance differences and condensation temperature T_{cond} may also be indicative of the presence of Earth-like planets. Melendez *et al.* (2009) revealed that the Sun exhibited a depletion of refractory elements relative to the volatile ones as compared to the solar twins. The finding was associated with the formation of planetary systems like our own one, in particular with the existence of terrestrial planets (Melendez *et al.* 2009). Further, it was shown that similar relationships might reflect a wide diversity of exoplanetary systems observed so far, as well as a variety of scenarios which could occur for the matter in circumstellar discs (Spina *et al.* 2016), and that the obtained dependence of the abundance differences on T_{cond} was correlated with the age and birth place in the Galaxy (González Hernández *et al.* 2013; Adibekyan *et al.* 2014, 2015; Nissen 2015) being not related to the presence of planets.

The manganese abundance differences for the stars with and without planets were determined: $[Mn/Fe]$ ratios of planet-hosting stars were higher (Kang *et al.* 2011). As regards the **neutron-capture elements**: low barium content was found in planet-hosting stars (Mishenina *et al.* 2015); and Delgado Mena *et al.* (2018) reported Ba, Sr, Ce and Zr underabundances in the stars with planets, with the only statistically significant (3σ) underabundance of 0.03 dex being observed for Ba in low-mass planet hosts.

This study is aimed at independent assessment of the relationship between the presence of massive planets and specific features of chemical composition of parent stars.

2. Observational data

We used the stellar spectra from the OHP archive (Moultaka *et al.* 2004) of the echelle-type spectrograph SOPHIE (Perrushot *et al.* 2011) obtained at $R = 75,000$ in the wavelength range 4,400 – 6,800 Å and signal-to-noise ratio (S/N) better than 80. The spectra processing was performed using the DECH20 software package developed by G.A. Galazutdinov (2007), <http://gazinur.com/DECH-software.html>.

Planet-hosting stars with detected massive planets (with the planetary masses M_{pl} greater than the mass of Jupiter M_J), as well as stellar and planetary characteristics, were adopted from the following sources: Moutou *et al.* (2014) for HD13908; Herbrar *et al.* (2016) for HD143105, HD35859, HD220842, HD12484, HD141399, HIP65407 and HD109384; Diaz *et al.* (2016) for HD191806 and HD221586; Santos *et al.* (2016) for HD219828 and Rey *et al.* (2017) for HD17674 and HD290213.

3. Determination of parameters and chemical compositions

The effective temperatures T_{eff} were derived by the calibration of the line-depth ratios for spectral-line pairs with different low-level excitation potentials (Kovtyukh *et al.* 2003), under the condition of independence of the Fe content along the Fe I lines on the low-level potential of the relevant line. The surface gravities $\log g$ were computed by the ionisation balance; the microturbulent velocity V_t was determined by factoring out the correlation between the abundances and equivalent widths of the Fe I lines. We used the Fe I lines to derive $[Fe/H]$.

The elemental abundances were determined using Castelli & Kurucz (LTE) models. The Kurucz WIDTH9 code was used for the LTE determination of Na, Mg, Al, S, Si, K, Ca, Sc, Ti, V, Cr, Mn, Fe, Co, Ni, Zn, Y, Zr, Ba, La, Ce, Pr, Nd and Sm abundances. The modified latest version of STARSP (Tsymbal, 1996) was employed for the LTE determination of Li, C, O and Eu abundances. The total uncertainty due to parameter and EW errors for the Fe I and Fe II lines are 0.06 and 0.08, respectively. The determination accuracy varies from 0.06 to 0.12 dex for different elements.

The comparison of the synthetic and observed spectra for the C I 5380 Å line for HD 17674 is presented in Fig. 1.

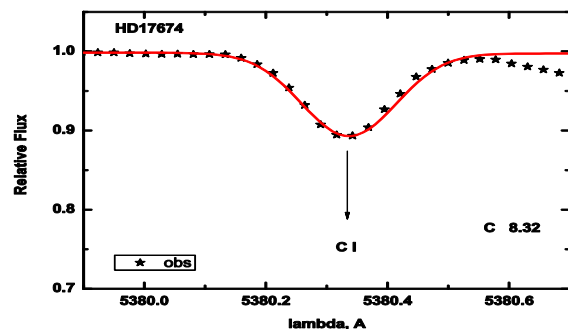


Figure 1: The observed (asterisks) and calculated (solid line) spectra in the region of the C I line for HD 17674.

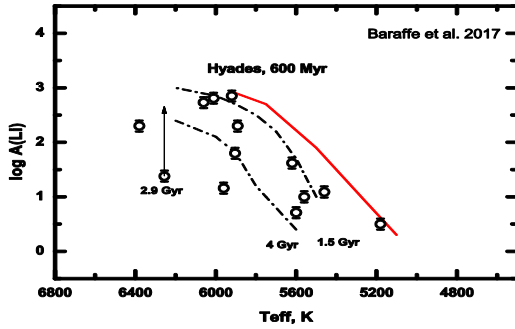


Figure 2: Li abundance vs. Teff

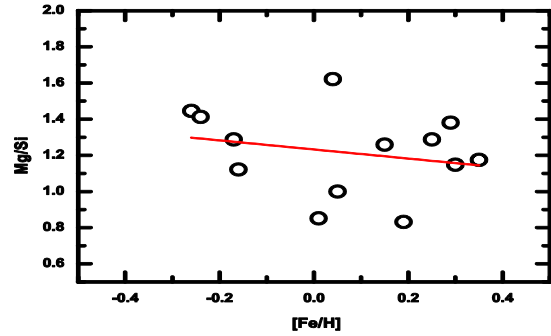


Figure 5: Mg/Si vs. [Fe/H]

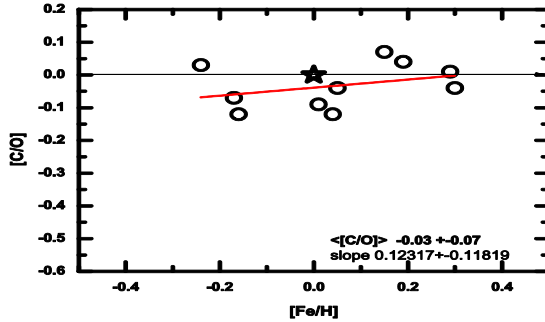
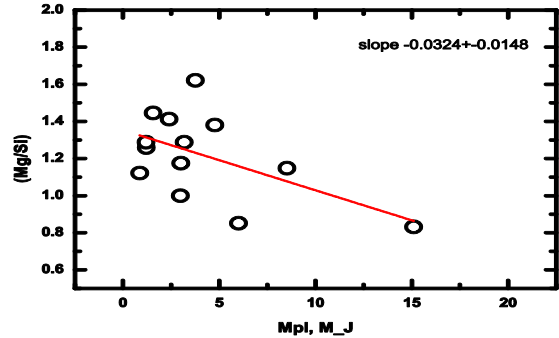
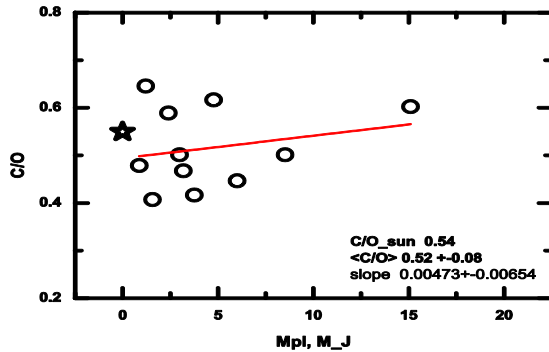
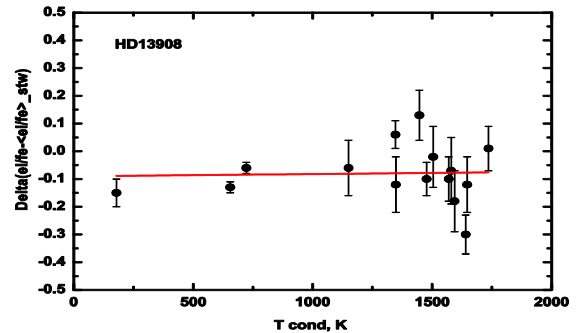


Figure 3: [C/O] vs. [Fe/H]

Figure 6: [Mg/Si] vs. planetary mass M_{pl} Figure 4: [C/O] vs. planetary mass M_{pl} Figure 7: Relationship between the relative elemental abundances and T_{cond} for the star HD13908.

4. Results and discussion

As follows from the Introduction, there are some potential chemical indicators of the presence of planets of different masses ([Fe/H], Li abundance, C/O, Mg/Si etc).

Metallicity [Fe/H]. Our target stars with massive planets differ in metallicity $-0.3 < [Fe/H] < 0.4$. Therefore, the supermetallicity cannot be the only reliable criterion of the presence of planets.

Li abundance. Fig.2 illustrates the correlation between the Li abundance $\log A(Li)$ and T_{eff} . The evolutionary tracks taken from Baraffe *et al.* (2017) are marked with dash-dotted lines for different ages.

As can be seen in Fig.2, different Li abundances in our target stars correspond to the evolutionary changes. Only one star (HD13908) with the age of 2.9 Gyr exhibits the Li depletion as compared to the evolution predictions. The star HD13105 (with $\log A(Li) = 1.16$ and rotational velocity $v_{sin i} = 8.1$ km/sec) enables to suppose that rotationally induced mixing rather than the presence of planets might be responsible for greater depletion of Li as

suggested by Delgado Mena *et al.* (2015). The separately considered low estimates of the lithium abundance with no thorough analysis of the potential causes of its depletion cannot be reckoned as a reliable criterion of the presence of massive planets either.

C/O and [C/O] ratios. Figs. 3 and 4 show [C/O] vs. [Fe/H] and C/O vs. M_{pl} . Our average values $[C/O] = -0.03 \pm 0.07$ and $C/O = 0.52 \pm 0.06$ do not support carbon enrichment in our target sample of stars, though they are consistent with the results obtained with HARPS spectrograph by Suarez-Anders *et al.* (2018): $0.8 > C/O > 0.4$ for 86% of high-mass companions and $C/O < 0.4$ for the remaining 14%. However, we observe a slight trend of C/O with metallicity and planetary mass.

[Mg/Si] ratio. The observed trend of [Mg/Si] with metallicity (Fig. 5) can be due to the Galactic evolution; the average $\langle [Mg/Si] \rangle_{pl} = -0.05 \pm 0.09$ is lower than the solar value of $[Mg/Si]_{\odot} = 0.0$. We can also see the scatter of [Mg/Si] in the region of several Jupiter masses, as well as correlation between [Mg/Si] and M_{pl} with lower values corresponding to greater masses (Fig. 6).

Relative abundance of refractory elements to volatile ones. For all our target stars, we plotted the relationship between the relative abundance of refractory elements to volatile ones and condensation temperature T_{cond} (Fig. 7).

For none of the stars did we find any significant sloped trends (correlations).

[Mn/Fe]. [Mn/Fe] ratios in planet-hosting stars are higher (Kang *et al.* 2011). Our average value is $\langle[\text{Mn/Fe}]\rangle = 0.10 \pm 0.06$.

Neutron-capture elements: with low Ba in the stars hosting low-mass planets (-0.03, Delgado Mena *et al.* 2015), we obtained $\langle[\text{Ba/Fe}]\rangle = 0.09 \pm 0.16$ for the stars with massive planets.

5. Conclusions

For the target set of stars with massive planets, we have found **metallicities** ranging from -0.3 to 0.4; there is the only star in the sample for which the **lithium** content has been reliably shown to be lower as compared to the stellar evolution predictions; the average $\langle\text{C/O}\rangle$ **ratio** = 0.52 ± 0.08 is slightly lower than the solar one (0.54) while C/O ratios tend to be dependent on the planetary mass; **magnesium** follows the trend in Galactic chemical evolution exhibiting a dependence on the planetary mass.

Our determinations of the C/O and Mg/Si ratios are in good agreement with the results of Suárez-Andrés *et al.* (2018). **Manganese** and **barium** are slightly overabundant. For none of the studied stars did we find any significant correlation (sloped trends) between the relative abundances of **refractory** elements to **volatile** ones and condensation temperatures T_{cond} . In summary, we cannot reliably single out one or another criterion. A larger sample of stars is required to ensure the determination and further application of statistically significant criteria.

References

- Adibekyan V. Z., Delgado Mena E., Sousa S. G. *et al.*: 2012a, *A&A*, **547**, 36.
- Adibekyan V. Z., Sousa S. G., Santos N. C. *et al.*: 2012b, *A&A*, **545**, 32.
- Adibekyan V., Santos N.C., Figueira P. *et al.*, 2015, *A&A*, **581**, L2.
- Adibekyan, V., Goncalves da Silva, H. M. Sousa, S. G. *et al.*: 2017, *Ap*, **60**, 325A.
- Baraffe I., Pratt J., Goffrey T. *et al.*, 2017, *ApJL*, **845**, 6B.
- Baumann P., Ramirez I., Melendez J. *et al.*: 2010, *A&A*, **519**, 87.
- Delgado Mena E., Israelian G., González Hernández J. I. *et al.*: 2014, *A&A*, **562**, 92.
- Delgado Mena E., Bertrán de Lis S., Adibekyan V.Zh. *et al.*: 2015, *A&A*, **576**, 69.
- Delgado Mena E., Adibekyan V., Figueira P. *et al.*: 2018, *PASP* 130 094202.
- Diaz e R.F., Rey J., Demangeon O. *et al.*: 2016, *A&A*, **591**, 146.
- Carlos M., Nissen P., Melendez J.: 2016, *A&A*, **587**, id. A100.
- Castelli F., Kurucz R. L.: 2004, ArXiv Astrophysics e-prints, astro-ph/0405087.
- Figueira P., Faria J. P., Delgado-Mena E. *et al.*: 2014, *A&A*, **570**, 21.
- Fischer D. A., Valenti J.: 2005, *ApJ*, **622**, 1102.
- Gaidos E.: 2015, *ApJ*, **804**, 40.
- Gonzarlez Hernarndez J. I., Delgado-Mena E., Sousa S. *et al.*: 2013, *A&A*, **552**, 6.
- Gonzalez G.: 1997, *MNRAS*, **285**, 403.
- Gonzalez G., Laws C.: 2000, *AJ*, **119**, 390.
- Gonzalez G.: 2008, *MNRAS*, **386**, 928.
- Gonzalez G., Carlson M. K., Tobin R. W.: 2010, *MNRAS*, **407**, 314.
- Herbrar G., Arnold L., Forveille T. *et al.*: 2016, *A&A*, **588**, A145.
- Israelian G., Santos N. C., Mayor M., Rebolo R.: 2001, *Nature*, **411**, 163.
- Israelian G., Santos N. C., Mayor M., Rebolo R.: 2004, *A&A*, **414**, 601.
- Israelian G., Delgado Mena E., Santos N. C. *et al.*: 2009, *Nature*, **462**, 189.
- Kovtyukh V. V., Soubiran C., Belik S. I., Gorlova N. I.: 2003, *A&A*, **411**, 559.
- Kuchner M.J. & Seager S.: 2005, arXiv:astro-ph/0504214v2.
- Melendez J., Asplund M., Gustafsson B., Yong D.: 2009, *ApJ*, **704**, L66.
- Mishenina T., Kovtyukh, V., Soubiran C., Adibekyan V. Zh.: :2015, *MNRAS*, **462**, 1563.
- Montalban J., Rebolo R.: 2002, *A&A*, **386**, 1039.
- Moultaka J., Ilovaisky S., Prugniel Ph., Soubiran C.: 2004, *PASP*, **116**, 693.
- Moutou C., Hébrard G., Bouchy F. *et al.*: 2014, *A&A*, **563**, A22.
- Nissen P.E.: 2013, *A&A*, **552** A73.
- Nissen P.E., Chen Y. Q., Carigi, L. *et al.*: 2014, *A&A*, **588**, 25.
- Onehag A., Gustafsson B., Korn A.: 2014, *A&A*, **562**, 102.
- Pavlenko Y. V., Kaminsky B.M., Jenkins J.S. *et al.*: 2019, *A&A*, **621**, id.A112.
- Perruchot, S., Bouchy, F., Chazelas, B. *et al.*: 2011, in *Proc. SPIE*, **8151**, 37.
- Petigura E., Marcy G.: 2011, *ApJ*, **735**, 41.
- Rey J., Hébrard G., Bouchy F. *et al.*: 2017, *A&A*, **601**, 9.
- Santos N. C., Israelian G., Mayor M.: 2001, *A&A*, **373**, 1019.
- Santos N.C., Santerne A., Faria J.P. *et al.*: 2016, *A&A*, **592**, 13.
- Sousa S.G., Santos N.C., Mayor M. *et al.*: 2008, *A&A*, **487**, 373.
- Spina L., Melendez J., Ramirez I.: 2016, *A&A*, **585**, 152.
- Suárez-Andrés L., Israelian G., González Hernández J.I. *et al.*: 2016, *A&A*, **591**, 69.
- Suárez-Andrés L., Israelian G., González Hernández J.I. *et al.*: 2017, *A&A*, **599**, id.A96.
- Suárez-Andrés L., Israelian G., González Hernández J.I. *et al.*: 2018, *A&A*, **614**, id.A84.
- Teske J.K., Cunha, K., Smith V.V. *et al.*: 2014, *ApJ*, **788**, 39.
- Tsybal V., 1996, *ASP Conf. Ser.*, **108**, 198.
- Udry S., Santos N. C.: 2007, *ARA&A*, **45**, 397.

DOI:<http://dx.doi.org/10.18524/1810-4215.2019.32.182111>

THE ON- AND OFF-STATE GENERATIONS IN THE CASE OF THE THICK ACCRETION DISK AND UNDEFINED PRECESSION PERIOD. 3-D NUMERICAL HYDRODYNAMICAL SIMULATIONS IN ACCRETION DISK IN MICROQUASAR CYG X-1

V.V. Nazarenko

Astronomical Observatory, Odessa National University,
Shevchenko Park, Odessa, 65014, Ukraine, nazaret@te.net.ua

ABSTRACT. In the present work we have computed the thick accretion disk (the accretion disk with radiation pressure) for the case of undefined precession over very long time (more than 14 precession periods). The calculations show that in this case the origin of the ON-states and OFF-states are strong irregular in time. The calculations also show that the jet's launches are taking place very suddenly over $7 \div 20$ minutes of the orbital time. The jet's launches over OFF-states occurs discrete as it is observed in real microquasars.

АНОТАЦІЯ. В представленій роботі ми виконали обчислення товстого акреційного диску (акреційного диску з радіативним тиском) для випадку невизначеної прецесії протягом довгого часу (більше чотирнадцяти прецесійних періодів). Обчислення показали, що в цьому випадку генерація виключених та включених станів є дуже іррегулярними з часом. Результати розрахунків також показали, що запуск джет виникає раптово протягом семи – двадцяти хвилин орбітального часу. Запуск джет протягом виключених станів в наших обчисленнях виникає дискретно, що відповідає спостереженням в реальних мікроквазарах.

Keywords: Stars: binaries - stars: jets - methods: numerical - hydrodynamics.

1. Introduction

In the present research we have continued to simulate the ON- and OFF-states generations on the base of microquasar Cyg X-1 by the methods of 3-D numerical hydrodynamics (Nazarenko & Nazarenko, 2014, 2015, 2016, 2017; Nazarenko V.V., 2018). The present work is devoted to the thick accretion rates

simulations on the base of classical microquasar Cyg X-1. The goal of the present research is to compute the donor's wind, one-point-stream formation, its motion in Roche lobe of accretor, the thick accretion disk formation and it's slaved precession for a irregular precession period. To calculate the thick accretion disk we will use in the calculations the computations of the z-direction radiation pressure in the disk volume.

2. The numerical algorithm

The description of the numerical algorithm in use in details is given in our previous works (Nazarenko & Nazarenko, 2014, 2015, 2016, 2017; Nazarenko V.V., 2018). Shortly, this algorithm is as follows: to resolve the non-stationary Euler's hydrodynamical equations we have used the astrophysical variant of "large-particles" code by Belotserkovsky and Davydov (Belotserkovskii O.M., Davydov Yu.M., 1982); to simulate one-point-stream we use the donor's atmosphere model that in turn is constructed on the base Kurucz's grid (Kurucz R.L., 1979) with the donor's parameters; we use the free-flow boundary conditions allowing to a gas to flow freely via the calculation area boundaries; to calculate mass flow real temperature we use the radiation cooling explicitly (Cox D. P., Daltabuit E., 1971). In the present calculation we use the rectangular coordinate system centred on the donor's centre. We have adopted the donor's mass to be equal to 40 solar mass and the accretor's mass to be equal to 10 solar mass. The precession period in the present simulations is about of 8 orbital periods. Hereafter all the distances will be given in units of the orbital separations; the average volume disk specific viscosity and the average volume disk specific angular momentum will be given in units of $V_0 A$, where V_0 is the orbital speed and A - the orbital separation; the time are given in the unit

such that 2π is equal to orbital period.

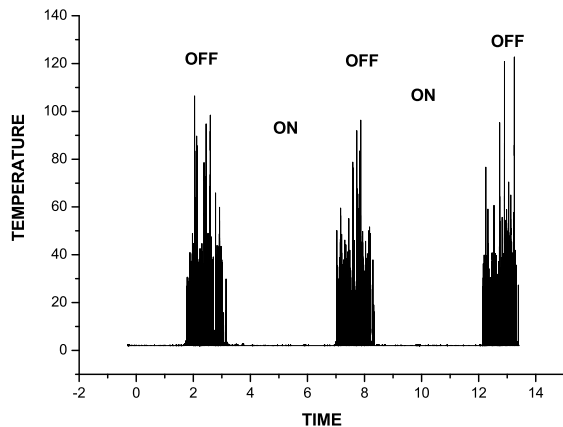


Figure 1: The central disk's temperature over the orbital plane versus time.

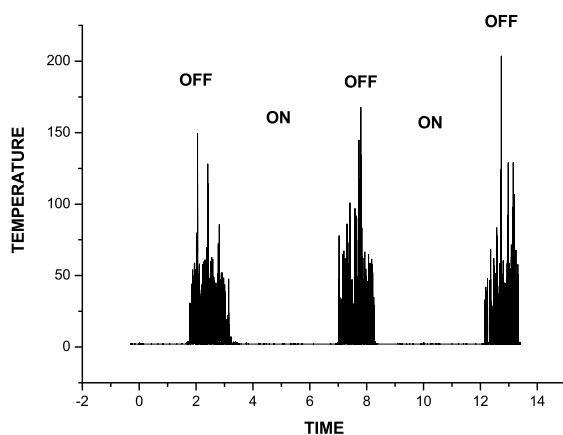


Figure 2: The central disk's temperature below the orbital plane versus time.

To calculate the radiation pressure in disk we will use the radiation model in the approach of the optically thin layers and we will use the following formula of radiation pressure: $F_{RAD} = \alpha H/C$, where α is coefficient of Thomson scattering, H is the radiation flux which is calculated in terms of thermodynamical equilibrium, C is the light speed.

We denote the X, Y and Z-coordinate of the accretor-1 as X_{ACC1} , Y_{ACC1} and Z_{ACC1} . The time evolution of these values are defined by the relations:

$$ZA19 = 0.15 \quad ZB19 = 0.15 \quad ZC19 = 0.15$$

$TET222 = TET222 + DT/8.0$ where DT is time step, given in units described above; the number 8.0 is the

quantity of the orbital periods in the one precession period. $TET222_{INIT} = -14.846$, since we start the precession motion on time 0.00 and before the precession starting we must form accretion disk and to make it in stationary state.

$$\begin{aligned} ZA199 &= ZA19 * (\cos(TET222/ZA221))^{ZAA2221}, \\ Y_{acc1} &= ZA199 * (\sin(TET222/ZA21))^{ZAA19}, \\ ZB199 &= ZB19 * (\cos(TET222/ZB221))^{ZBB2221}, \\ Z_{acc1} &= ZB199 * (\cos(TET222/ZB21))^{ZBB19}, \\ ZC199 &= ZC19 * (\cos(TET222/ZC221))^{ZCC2221}, \\ X_{acc1} &= 1.0 - ZC199 * (\cos(TET222/ZC21))^{ZCC19}, \end{aligned}$$

In the formulas written above the values $ZA19$, $ZB19$, $ZC19$, $ZA21$, $ZB21$, $ZC21$, $ZAA19$, $ZBB19$, $ZCC19$, $ZA221$, $ZB221$, $ZC221$, $ZAA2221$, $ZBB2221$, $ZCC2221$ are the parameters. These parameters are in the present calculations equal correspondingly to the following magnitudes: 0.15, 0.15, 0.15, 4.50, 2.89, 5.19, 1.0, 1.0, 1.0, 99999999.0, 99999999.0, 99999999.0, 0.0, 0.0, 0.0.

3. The results

We have begin our simulations with the start of the precession motion and have continued it over 14 precession periods to show our on-off state model on relatively long time scale. The key parameters in the present calculations are the central disk's temperature over and below orbital plane. We show the time dependencies of these parameters in Fig.1 and Fig.2. As it is led from these figures the off-states are arising every 5 precession periods and the beginning and end of these states occurs very rapidly over $7 \div 20$ minutes of orbital plane. The time intervals of off-states are about of one precession period. Thus, it means, that the jet's launches take place practically very suddenly in respect to the off-state durations. The comparison both Fig.1 and Fig.2 pictures shows that they are practically identical to a each other. It means that in the present simulations two armed jets are simulated. To show the OFF-state structure in more details we show time dependence of central disk's temperature on the vicinity of $7 \div 8$ precession period (see Fig.3). As it is led from this figure the OFF-state structure is consisting of the partial pics and this result is in good accordance with observation (Fender et al. 2003, 2004) The time dependencies of jet's velocities in the disk's centrE over and below orbital plane are showing in Fig.4 and Fig.5. As it is led from these figures the jet's launches are beginning suddenly and velocities in off-states are reaches $2000 \div 2500$ km per second. Such the relatively small jet's velocity is explained by the circumstance that jet's launches in our calculations occurs on the highness of 5000 shvarchild radius instead of real 50 ones. The details of the jet's launches on the $7 \div 8$ precession period is seen in Fig.6. From

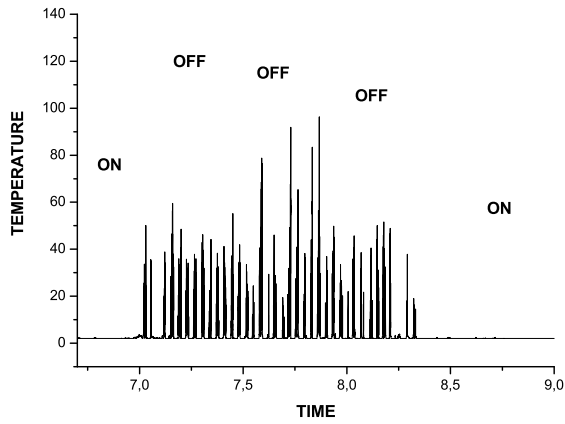


Figure 3: The central disk's temperature over the orbital plane versus time in details for the OFF-state on $7 \div 8$ precession periods.

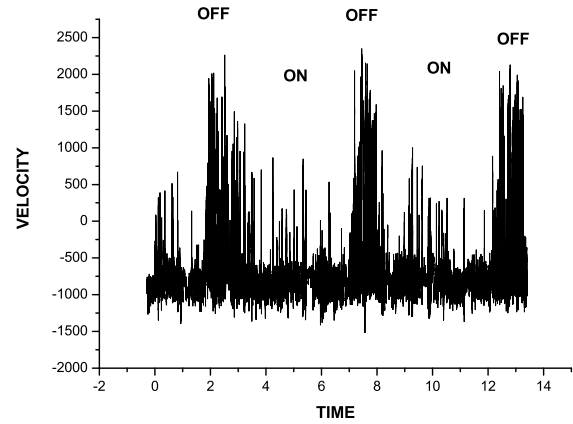


Figure 5: The central disk's velocity below the orbital plane versus time.

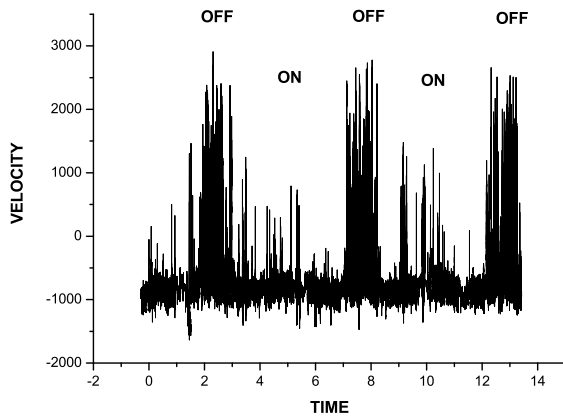


Figure 4: The central disk's temperature over the orbital plane versus time.

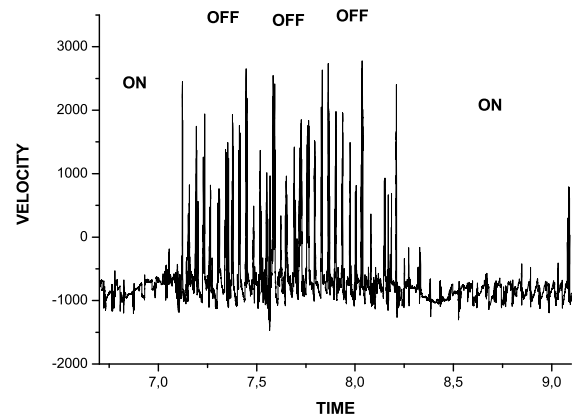


Figure 6: The central disk's velocity over the orbital plane versus time in details for the OFF-state on $7 \div 8$ precession periods.

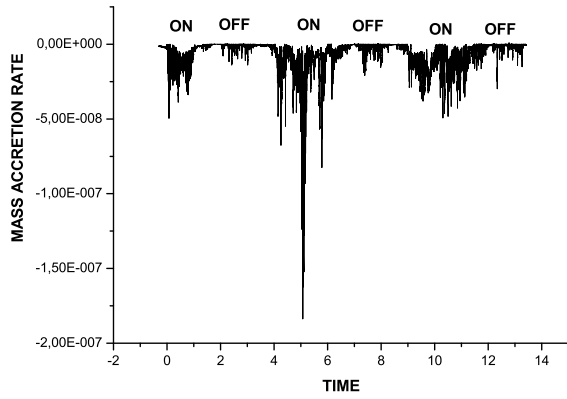


Figure 7: The mass accretion rate versus time.

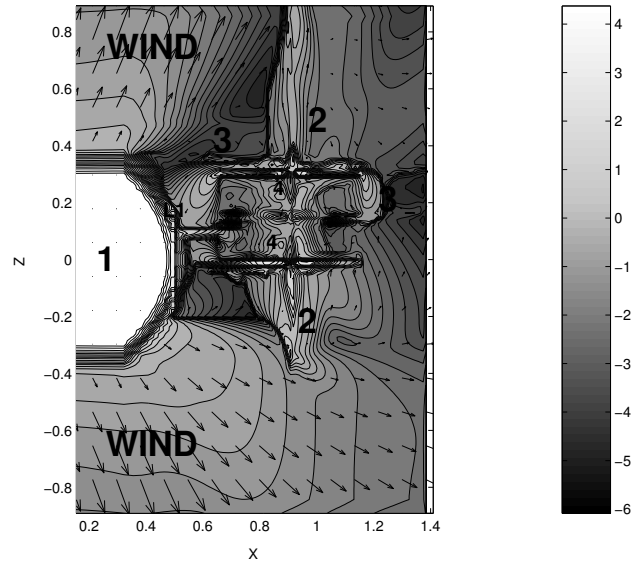


Figure 9: The cross-section of the calculation area by the Z-X plane.

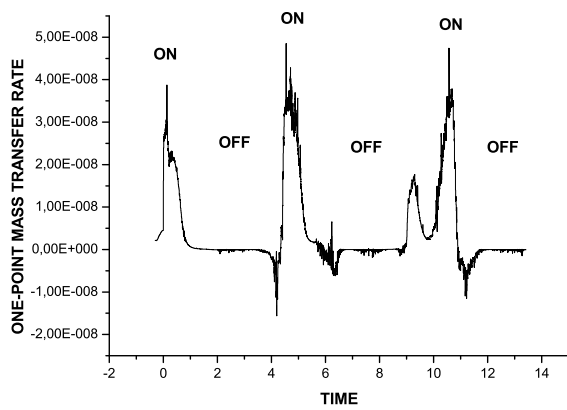


Figure 8: The mass transfer rate versus time.

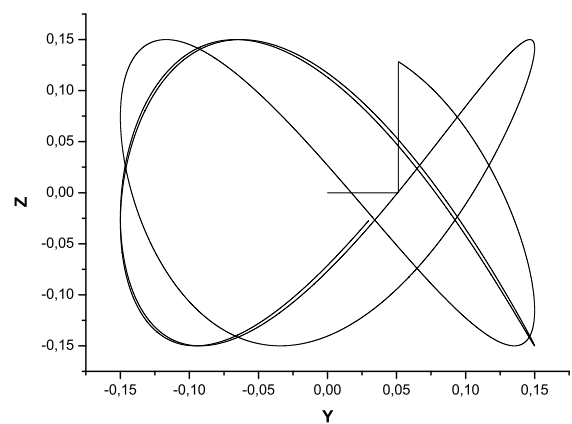


Figure 10: The accretor-1 motion in the Z-Y plane.

these figure it is good seen that the jet launches over off-state is in the view of the partial picks also as the central disk's part temperature structure. The mass accretion rate near the disk centre time dependence is shown in Fig 7. As it is led from these figure this value is anticorellated with temperature in the disk's centre. The time dependence of mass transfer rate via one-point is shown in Fig.8. These figure shows the strong variations of this value with time (here we must point out that the position of the point via which we have calculated the mass transfer rate in the present research was fixed in space and time and was corresponding to $X_{acc1} = 1.0$). Namely these variations explains the off- and on-states generation in the present research. Indeed, over high mass transfer rate value the density in the disk centre is high and the radiation cooling results in the low temperature in the disk's centre. On contrary, over low mass transfer rate the density in the disk's centre is strong decreased and radiation cooling is not affective in this case. It results in instantaneously heating the space near the disk centre and jets are launching in this moment. The one-point mass transfer rate varieties are in turn resulting from a precession motion. Such the mechanism of off- and on-states generation is working in the present research. To illustrate the vertical structure of the thick accretion disk we show this structure in Fig.9 in which the z-x plane cross-section of the calculation area is plotted. In this figure we may see the donor (the number 1), one-point stream (L_1), the jets (the number 2), the donor's wind (wind), the thick accretion disk (the number 3) and the funnel along the disk rotation axis (the number 4). To illustrate the accretor-1 motion in the present precession model we show this motion in Fig. 10.

4. Summary and conclusions

The present calculations show that in the case of undefined precession period jointly with the variable binary separation (on time scale of precession periods) the generation of off- and on-states begins to be not every precession period and off-states are arising approximately every 5 precession periods. The jet launches occur very rapidly over $7 \div 20$ minutes of orbital plane. This is very short time scale since the off-state time interval is about of 1 precession period. As it is led from the present research the off-on-states generations are explained by the precession motion of the disk. The explanation of the jet origination that is working in the present research is very convenient for the radiation-driven jets and it is in bade agreement with the magnetically-driven jets.

Finally we may conclude that our jet launch model are in very good accordance with the observations (Mirabel & Rodriquez, 1999; Stirling et al., 2001; Fender et al., 2003, 2004; Migliari & Fender, 2006) through the following points:

1. The first is that jet launch in our model is occur practically instantaneously about of $7 \div 20$ minutes of orbital plane.
2. The second is the anticorrelation between mass accretion rate and the central disk's temperature.
3. The third is the jet time structure that is in the view of the partial pics not connected with a each other.

References

- Belotserkovskii O.M., Davydov Yu.M.: 1982, "The large particles code in gas dynamics", Moscow: Nauka, 391.
- Cox D.P., Daltabuit E.: 1971, *ApJ*, **167**, 113.
- Fender R.P., Gallo E., Jonker P.: 2003, *MNRAS*, **343**, L99.
- Fender R.P., Belloni T., Gallo E.: 2004, *MNRAS*, **355**, 1105.
- Kurucz, R.L.: 1979, *ApJ.Suppl.Ser.*, **40**, 1.
- Mirabel L.F. & Rodriquez L.F.: 1999, *Ann. Rev. Astron. Astrophys.*, **37**, 409.
- Migliari S. & Fender P.: 2006, *MNRAS*, **366**, 79.
- Nazarenko V.V., Nazarenko S.V.: 2014, *Odessa Astron. Publ.*, **27**, 137.
- Nazarenko V.V., Nazarenko S.V.: 2015, *Odessa Astron. Publ.*, **28**, 171.
- Nazarenko V.V., Nazarenko S.V.: 2016, *Odessa Astron. Publ.*, **29**, 82.
- Nazarenko V.V., Nazarenko S.V.: 2017, *Odessa Astron. Publ.*, **30**, 113.
- Nazarenko V.V.: 2018, *Odessa Astron. Publ.*, **31**, 90.
- Stirling A.M. et al.: 2001, *MNRAS*, **327**, 1273.

DOI:<http://dx.doi.org/10.18524/1810-4215.2019.32.182514>

DISCOVERY OF MORE CHANGING LOOK EVENTS IN NGC 1566

V. L. Oknyansky¹, H. Winkler², S. S. Tsygankov^{3,4}, V. M. Lipunov¹,
E. S. Gorbovskoy¹, F. van Wyk², D. A. H. Buckley⁵, N. V. Tyurina¹

¹ M. V. Lomonosov Moscow State University, Sternberg Astronomical Institute,
Moscow, Russia, oknyan@mail.ru

² Dept. Physics, University of Johannesburg, South Africa

³ Department of Physics and Astronomy, University of Turku, Finland

⁴ Space Research Institute of the Russian Academy of Sciences, Moscow, Russia

⁵ The South African Astronomical Observatory, South Africa

ABSTRACT. We summarize a study of optical, UV and X-ray light curves of the nearby changing look active galactic nucleus in the galaxy NGC 1566 obtained with the *Neil Gehrels Swift Observatory* and the MASTER Global Robotic Network over the period 2007-2019. We also report on optical spectroscopy using the South African Astronomical Observatory 1.9-m telescope between Aug. 2018 and Mar. 2019. A substantial increase in X-ray flux by 1.5 orders of magnitude was observed following the brightening in the UV and optical bands during the first half of 2018 year. After a maximum was reached at the beginning of July 2018, the fluxes in all bands decreased with some fluctuations. The most remarkable re-brightenings in of the light curve following the decline from the bright phase were observed at MJD range 58440-58494 and 58603-58654. The amplitude of the flux variability is strongest in the X-ray band and decreases with increasing wavelength. Low-resolution spectra (Aug 2018) reveal a dramatic strengthening of the broad emission as well as high-ionization [FeX]6374 lines. These lines were not detected so strongly in the past published spectra. The change in the type of the optical spectrum was accompanied by a significant change in the X-ray spectrum. For the last optical spectra (31 Nov. 2018 – 28 Mar. 2019) we see dramatic changes compared to 2 Aug 2018, accompanied by the fading of broad emission lines and high-ionization [FeX]6374 line. Effectively, two changing look (CL) cases were observed for this object: changing to Sy1.2 type and then returning to the low state as Sy 1.8–Sy1.9 type. Some possible explanations of the observed dramatic changes are discussed.

АНОТАЦІЯ. Ми наводимо і обговорюємо зведені оптичні, УФ та рентгенівські криві блиску найближчого активного галактичного ядра, який змінює тип, в галактиці NGC 1566, які отримані за

допомогою Обсерваторії *Swift* і Глобальної мережі автоматизованих телескопів MASTER за період 2007-2019 рр. Ми також представляємо результати оптичної спектроскопії, отриманої на 1.9-м телескопі Південно-Африканської Астрономічної обсерваторії в період з серпня 2018 року по березень 2019 року. Було виявлено значне збільшення, на 1,5 порядку, рентгенівського потоку, а також яскравості в УФ і оптичному діапазонах в першій половині 2018 р. Після досягнення максимуму на початку липня 2018 р., потоки на всіх довжинах хвиль зменшилися з деякими коливаннями. Найбільш помітні повторні спалахи в кривій блиску після максимуму спостерігалися в інтервалах MJD 58440-58494 і 58603-58654. Амплітуда змінності потоку була найбільша в рентгенівському діапазоні і зменшувалася зі збільшенням довжини хвилі. Спектри низької роздільної здатності (серпень 2018 г.) демонструють драматичне посилення широких компонентів емісійних ліній, а також ліній високої іонізації [FeX] (наприклад, 6374 Å). Ці лінії ніколи не спостерігалися такими інтенсивними в минулому в опублікованих спектрах. Зміна типу оптичного спектру супроводжувалася значною зміною рентгенівського спектра. За останніми оптичним спектрами (31 листопада 2018 р - 28 березня 2019 р.) ми бачимо драматичні зміни в порівнянні з 2 серпня 2018 р., які супроводжуються значним ослабленням широких емісійних ліній, а також ліній високої іонізації [FeX] 6374 Å. По суті, для цього об'єкта спостерігалися два випадки зміни типу (CL): перехід в тип Sy1.2, а потім повернення в низький стан з типом Sy 1.8 - Sy1.9. Обговорюються деякі можливі пояснення спостережуваних драматичних змін.

Key words: Galaxies – active galaxies: individual: NGC 1566.

1. Introduction

The NGC 1566 was discovered at 1826 by James Dunlop and has long history of investigations (see e.g. references at da Silva et al., 2017; Oknyansky et al., 2019; Parker et al., 2019). The broad nuclear emission lines characteristic of the Seyfert phenomenon in this object were discovered in 1956 (de Vaucouleurs G. & de Vaucouleurs A., 1961; de Vaucouleurs, 1973) and confirmed in 1962 (Shobbrook, 1966). The NGC 1566 nucleus was later classified as type 1. It is one of the brightest ($V \approx 10^m.0$ but $V_{AGN} \approx 13^m.0$ in 5 arc-sec radius aperture) and nearest galaxies with AGN in the South Hemisphere. This object is also nearest Changing Look (CL) AGN (Oknyansky et al., 2019). The nucleus of NGC 1566 has a low brightness relative to the host galaxy ($V \approx 13^m.0$) and CL events there were probably discovered just because it is so close. The Changing Look active galactic nuclei (CL AGNs) are objects which undergo dramatic variability of the emission line profiles and classification type, which can change from type 1 (showing both broad and narrow lines) to type 1.9 (where the broad lines almost disappear) or vice versa within a short time interval (typically a few months). The dramatical spectral variations in NGC 1566 had been reported firstly by Pastoriza and Gerola (1970) after comparison of the spectrum obtained in 1969 with some of the earliest spectroscopic investigations, in 1956 (de Vaucouleurs G. & de Vaucouleurs A., 1961), in 1962 (Shobbrook, 1966) where broad $H\beta$ line was much more intensive. That was done soon after discovery of variability of AGNs in continuum (Fitch et al., 1967) and variability of emission lines was not too unexpected. The object had several dramatic changes of its spectrum during the past tens of years (da Silva et al., 2017) but was not identified as a CL AGN until the 2018 event (Oknyansky et al., 2018; Oknyansky et al., 2019) since this designation only came into common use in the past decade.

NGC 1566 is a galaxy with a very well-studied variable active nucleus, but most intensive multiwave photometric observations were done during past year after discovery of a new reawakening (Kuin et al., 2018; Ferrigno et al., 2018; Grupe et al., 2018a; Parker et al., 2019; Cutri et al., 2018) and new CL phase (Oknyansky et al., 2018; Oknyansky et al., 2019 and references there). A substantial increase of X-ray flux by 1.5 orders of magnitude was observed following the brightening in the UV and optical bands during the last year. After a maximum was reached at the beginning of July 2018 the fluxes in all bands decreased with some fluctuations. The amplitude of the flux variability is strongest in the X-ray band and decreases with increasing wavelength. Low resolution spectra (obtained near maximal level of state Oknyansky et al.

(2019)) reveal a dramatic strengthening of the broad emission as well as high ionisation [FeX] 6374\AA lines. These lines were not detected so strongly in the past published spectra. The change in the type of the optical spectrum was accompanied by a significant change in the X-ray spectrum. All these facts give opportunity to classify NGC 1566 as CL (Oknyansky et al., 2018; Oknyansky et al., 2019). Following monitoring with *Swift* revealed re-brightening of the object in December 2018 (Grupe et al., 2018b) and at the end of May 2019 (Grupe et al., 2019), however these outbursts were not so bright as in July 2018. Such re-brightenings after most dramatical outbursts probably are typical property of the some part of CL AGNs since were noted in several other ones of them (Oknyansky et al., 2017; Oknyansky et al., 2018; Katebi et al., 2018).

2. Observational data and results

We summarize a study of optical, UV and X-ray light curves of the nearby changing look active galactic nucleus in the galaxy NGC 1566 obtained with the Neil Gehrels Swift Observatory and the MASTER Global Robotic Network over the period 2007-2019. The light curves for 2007-2018 are presented by Oknyansky (2019) and those for the years 2018-2019 are shown in Fig. 1. It can be seen there that all variations in the optical, UV and X-ray are well correlated. We also report on optical spectroscopy using the South African Astronomical Observatory 1.9-m telescope between Aug 2018 (Oknyansky et al., 2018; Oknyansky et al., 2019) and Mar 2019. A substantial increase in X-ray flux by 1.5 orders of magnitude was observed following the brightening in the UV and optical bands during the first half of 2018 (Ducci et al., 2018; Kuin et al., 2018; Ferrigno et al., 2018; Grupe et al., 2018a; Oknyansky et al., 2018; Oknyansky et al., 2019; Parker et al., 2019). The amplitude of the flux variability is strongest in the X-ray band and decreases with increasing wavelength. After a maximum was reached at the beginning of July 2018, the fluxes in all bands decreased with some fluctuations. The most remarkable re-brightening in the light curve following the decline from the bright phase was observed at MJD range 58440-58494 (Event 1) and 58603-58654 (Event 2). Event 1 and Event 2 are indicated in Fig. 1 (see also Grupe et al., 2018b; Grupe et al., 2019). The amplitudes of the re-brightening in UV and optical bands are significantly higher for Event 1 than for Event 2. That is different from the X-ray variations for which fluxes in the maxima were about the same. This difference is well seen at Fig. 1. If we take into account the host galaxy contamination in the aperture used then the relative decreases from the maximum in July 2018 to minimum in June 2019 in the different UV/Opt bands were about the same

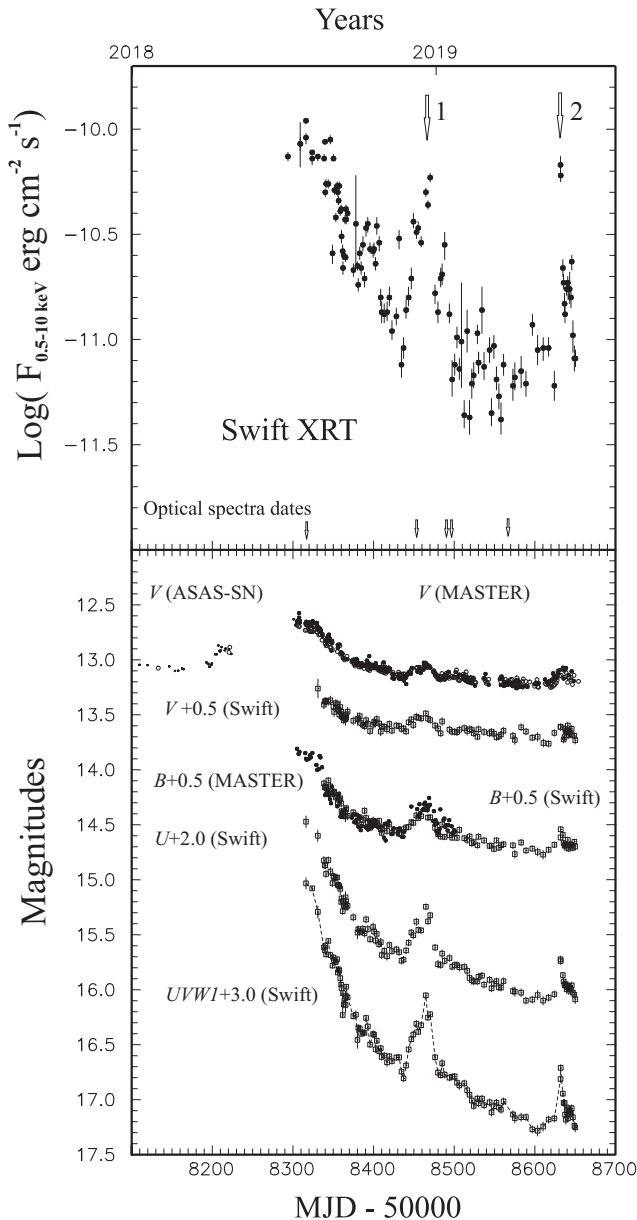


Figure 1: Multi-wavelength observations of NGC 1566 shown for 2018–2019 only. *Top Panel:* The *Swift*/XRT 0.5–10 keV X-ray flux (in $\text{erg cm}^{-2} \text{ s}^{-1}$) – (filled circles). *Bottom Panel:* The large open circles are MASTER unfiltered optical photometry of NGC 1566 reduced to the V system while the points are V ASAS-SN (nightly means) reduced to the *Swift* V system. The filled circles are MASTER BV photometry. The open boxes are $UVW1$ and UBV data obtained by *Swift*.

(9 times).

Low-resolution spectra (2 Aug 2018) (see Fig. 2) reveal a dramatic strengthening of the broad emission as well as high-ionization [FeX]6374Å lines. These lines were not detected so strongly in the past published spectra. The change in the type of the optical spectrum (Oknyansky et al., 2018; Oknyansky et al., 2019)

was accompanied by a significant change in the X-ray spectrum. For the last spectra (30 Nov 2018 – 28 Mar 2019) we see dramatic changes compared to Aug 2018, accompanied by the fading of the broad emission lines. Effectively, two changing look cases were observed by us for this object during the past year.

3. Conclusion

NGC 1566 is one of the typical examples of a CL AGN, since it demonstrates dramatical variability of broad emission lines, UV continuum, high ionisation lines like [FeVII] and [FeX], and also recurrent brightening and dimming events. NGC 1566 is one of the clearest illustrations of Seyfert spectra ranging from type 1.2 to type 1.9 AGNs at different epochs. The object is nearest the AGN and CL AGN and so it offers one of the best opportunities for studying this phenomenon. The light curves from X-ray to optical bands presented here show very good correlations over a long time interval. This result is mostly in agreement with a scenario where the variability across several wavebands (spanning X-rays–UV/Optical) is driven by variable illumination of the accretion disc by soft X-rays (see the same conclusions for another CL object, NGC2617 (Shappee et al., 2014; Oknyansky et al., 2017)). We have shown, using spectroscopy (1.9 m SAAO) and multi-wavelength photometry (MASTER, *Swift* Ultraviolet/Optical and XRT Telescopes), that NGC 1566 recently experienced a dramatic outburst in all wavelengths, including a considerable strengthening of broad permitted and high ionisation [FeX]6374Å lines, as well as substantial changes in the shape of the optical and X-ray continua (Oknyansky et al., 2019). After a maximum was reached at the beginning of July 2018, the fluxes in all bands dramatically decreased with some fluctuations. The strength of the broad permitted, high ionisation [FeX]6374Å lines and UV continuum dramatically decreased (end of March 2019) and the object can then be classified as Sy1.8–Sy1.9. So we witnessed a second CL case in NGC1566.

Despite the successes of the simple orientation-based AGN unification scheme, there are significant problems that cannot be explained solely by different orientations. A major challenge to the simple model is the existence of CL AGNs. Orientation obviously cannot change on the time-scale of the observed type changes, and hence some other explanation is needed. What must happen to make such a dramatic changes possible? An alternative explanation is that transitions from type 1 to type Sy2 AGNs or vice versa are connected with some dramatic variability of the ionizing radiation, such as temporarily switching on or switching off their engine (Lyuty et al., 1984; Penston et al., 1984; Runnøe et al., 2016; Katebi et al., 2019). More references on the possible explanations for the CL phe-

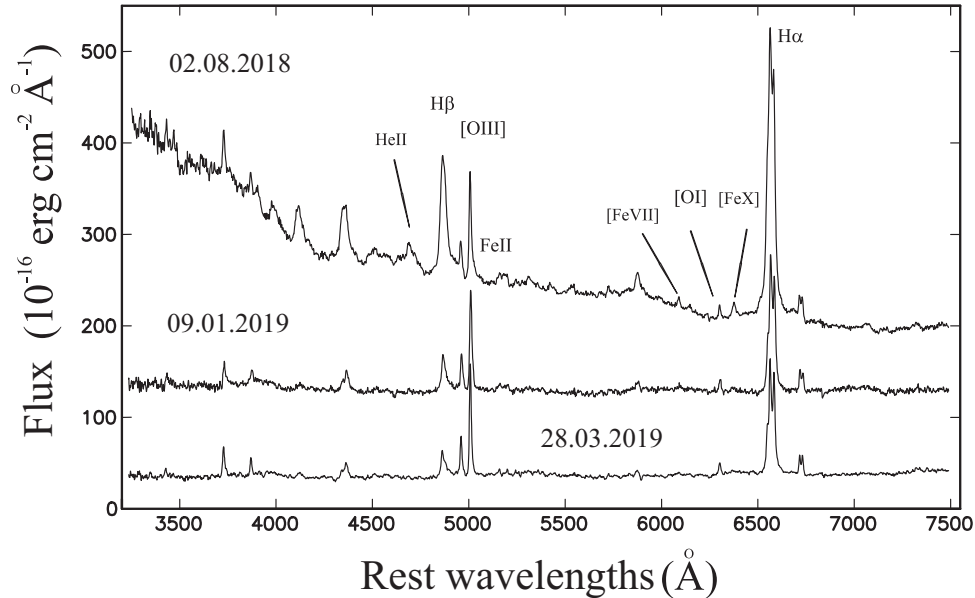


Figure 2: The isolated nuclear (low resolution) nonstellar spectra (solid line) in NGC 1566 obtained by subtraction of the host galaxy spectrum (thin line) from the original spectrum. (See details in the text). The spectra for 2 Aug 2018 and 9 Jan 2019 are shifted up $10^{-14} \text{ erg cm}^{-2} \text{ A}^{-1}$ for good seeing

nomenon can be found in discussions by MacLeod et al. (2019) and Ruan et al. (2019).

Acknowledgements. HW and FVW thank the South African Astronomical Observatory for the generous allocation of telescope time which also resulted in the spectra presented in this paper. We also express our thanks to the *Swift* ToO team for organizing and executing the observations. This work was supported in part by the Russian Foundation for Basic Research through grant 17-52-80139 BRICS-a and by the BRICS Multilateral Joint Science and Technology Research Collaboration grant 110480. MASTER work was supported by Lomonosov Moscow State University Development Programme and RSF grant 16-12-00085. DB is supported by the National Research Foundation of South Africa. We are grateful to K. Malanchev and P. Ivanov for useful discussions.

References

- Cutri R.M., Mainzer A.K., Dyk S.D.V. et al.: 2018, *The Astronomer's Telegram*, **11913**.
- da Silva P., Steiner J. E. and Menezes R.B.: 2017, *MNRAS*, **470**, 3850 [1707.02680].
- de Vaucouleurs G. and de Vaucouleurs A.: 1961, *MNRAS*, **68**, 69.
- de Vaucouleurs G.: 1973, *ApJ*, 181, 31.
- Ferrigno C., Siegert T., Sanchez-Fernandez C. et al.: 2018, *The Astronomer's Telegram*, **11783**.
- Fitch W.S., Pacholczyk A.G. and Weymann R.J.: 1967, *ApJ*, **150**, L67.
- Grupe D., Komossa S. and Schartel N.: 2018a, *The Astronomer's Telegram*, **11903**.
- Grupe D., Mikula R., Komossa S. et al.: 2018b, *The Astronomer's Telegram*, **12314**.
- Grupe D., Mikula R., Komossa S. et al.: 2019, *The Astronomer's Telegram*, **12826**, 1.
- Katebi R., Chornock R., Berger E. et al.: 2018, arXiv e-prints [1811.03694].
- Katebi R., Chornock R., Berger E. et al.: 2019, *MNRAS*, **487**, 4057.
- Kuin P., Bozzo E., Ferrigno C. et al.: 2018, *The Astronomer's Telegram*, **11786**.
- Lyutyj V.M., Oknyanskij V.L. and Chuvaev K.K.: 1984, *Sov. Astron. Lett.*, **10**, 335.
- MacLeod C.L., Green P.J., Anderson S.F. et al.: 2019, *ApJ*, **874** **8** [1810.00087].
- Oknyansky V.L., Gaskell C.M., Huseynov N.A. et al.: 2017, *MNRAS*, **467**, 1496 [1701.05042].
- Oknyansky V.L., Lipunov V.M., Gorbovskoy E.S. et al.: 2018, *The Astronomer's Telegram*, **11915**.
- Oknyansky V.L., Winkler H., Tsygankov S.S. et al.: 2019, *MNRAS*, **483**, 558 [1811.06926].
- Parker M.L., Schartel N., Grupe D. et al.: 2019, *MNRAS*, **483**, L88 [1811.10289].
- Pastoriza M. and Gerola H.: 1970, *Astrophys. Lett.*, **6**, 155.
- Penston M.V. and Perez E.: 1984, *MNRAS*, **211**, 33.
- Ruan J.J., Anderson S.F., Eracleous M. et al.: 2019, arXiv e-prints arXiv:1909.04676 [1909.04676].
- Runnoe J.C., Cales S., Ruan J.J. et al.: 2016, *MNRAS*, **455**, 1691 [1509.03640].
- Shappee B. J., Prieto J. L., Grupe D. et al.: 2014, *ApJ*, **788**, 48 [1310.2241].
- Shobbrook R.R.: 1966, *MNRAS*, **131**, 365.

DOI:<http://dx.doi.org/10.18524/1810-4215.2019.32.181741>

USING CONSUMER-GRADE DSLR CAMERA AND SMALL TELESCOPE TO FIND NEW VARIABLE STARS

M.Yu. Pyatnytsky

Private Observatory “Osokorky”, Kyiv, Ukraine, mpyat2@gmail.com
American Association of Variable Star Observers (AAVSO), observer code PMAK

ABSTRACT. Twenty-seven new variable stars were found in DSLR images captured from October 2017 to June 2019. All images were taken using unmodified Canon EOS 600D DSLR attached to a Skywatcher 150/750 Newtonian on a motorized equatorial mount. The variables were registered in The International Variable Star Index (VSX, AAVSO) as PMAK V1..PMAK V27 respectively. Most of them (twelve) were classified as semiregular variables of different subtypes, nine as eclipsing binaries (EA, EW, and EB), three rotating RS Canum Venaticorum-type stars, one rotating ellipsoidal variable (ELL), one Delta Scuti-type pulsating variable, and one as a possible nova-like (NL) star.

The setup and methodology used by the author allowed discovering of variables having a wide range of maximum brightness (from $8^m.9$ to $14^m.4$ in V band for stars described in the current work), variability range up to $\sim 0^m.1$ and less, and quite different periods of variability, from hours to hundreds of days. Although all those variables were detected using images taken by the author, detailed analysis and classification of stars required the involvement of additional data sources (automated sky surveys).

АБСТРАКТ. Двадцять сім нових змінних зір було знайдено на зображеннях, отриманих за допомогою цифрової дзеркальної камери за період з жовтня 2017 по червень 2019. Всі зображення були отримані за допомогою немодифікованої камери Canon EOS 600D, під'єднаної до телескопу-рефлектора Skywatcher 150/750. Телескоп був встановлений на моторизованому екваторіальному монтуванні. Знайдені змінні були зареєстровані у International Variable Star Index (VSX, AAVSO) як PMAK V1..PMAK V27, відповідно. Більшість з них (дванадцять) були класифіковані як напівправильні змінні різних підтипів, дев'ять як затемнювані подвійні (типів EA, EW та EB), три як зорі типу RS CVn, одна еліпсоїдальна подвійна типу ELL, одна малоамплітудна пульсуюча змінна типу DSCT та одна можлива новоподібна (NL) зоря.

Всі згадані зорі були виявлені на знімках, зроблених автором, для детального подальшого

аналізу та класифікації були залучені додаткові джерела даних (автоматизовані огляди неба).

Використана автором система з цифрової дзеркальної камери та невеликого телескопу має чутливість, яка дозволяє ефективно виявляти змінні з широким діапазоном яскравостей у максимумі (від 8.9 до 14.4 зоряної величини у фільтрі V для зірок, що описані у даній роботі) та діапазоном змін до ~ 0.1 зоряної величини та навіть меншим у випадку яскравих зір (з зоряною величиною біля 11..12 у фільтрі V або меншою).

Серед змінних зір, які були знайдені протягом даного дослідження, кілька яскравіші за 10 зоряну величину у максимумі. Це може свідчити, що існує багато невідомих яскравих змінних, які не охоплені автоматичними оглядами (такі яскраві змінні можуть становити проблему для автоматичних оглядів, які націлені на більш тьмяні об'єкти).

Довгі серії зображень, отриманих за період, більший за рік, дозволяють виявляти змінні з широким діапазоном характерної тривалості змін, від годин до сотень днів.

Keywords: variable stars, aperture photometry, DSLR.

1. Introduction

Aperture photometry with a Digital Single Lens Reflex (DSLR) camera is a popular method among amateur astronomers for the estimation of stellar brightness (Hoot, 2007; Kloppenborg et al., 2012; Pieri, 2012; Zhang et al., 2015; Blackford et al, 2016). Despite that consumer-grade DSLR cameras use Bayer matrix with non-photometric color filters, after proper calibration they can be used for the precise aperture photometry (Kloppenborg et al., 2012; Pieri, 2012; Blackford et al, 2016). In the current work, the author demonstrates that the accuracy of photometry with a modest DSLR camera and a small 150mm Newtonian makes us possible to discover new variable stars having a relatively small range of variability (from several tenths of mag-

nititude to $<0.^m1$) in a light-polluted suburban area.

Although most of the variables listed in catalogs (see, for example, probably the most comprehensive catalog of known variables: The International Variable Star Index (VSX) (Watson et al., 2006)) are discovered by automated sky surveys (such as ASAS-SN (Kochanek et al., 2017), SuperWASP (Butters et al., 2010), NSVS (Woźniak et al., 2004), ZTF (Masci et al., 2019), etc.), in many cases the stars, discovered by individual astronomers (both professional and amateur) or small groups of them are better described and properly classified. Results of a search for the new variables in sequences of DSLR images are presented in the current work.

2. Data acquisition and processing

A setup used by the author consists of 150mm f/5 Newtonian on tracking equatorial mount. Canon EOS 600D DSLR was attached to the telescope instead of an eyepiece to get images at the prime focus. The field of view of the setup was $1.7^\circ \times 1.1^\circ$. All observations have been carried out in a suburban area of Kyiv (Ukraine). Image acquisition was carried out following the procedure described by Blackford et al. (2016). Calibration frames (bias-, dark- and flat- frames) were taken at the end of each observing session with the same ISO level, the same exposure was used for dark frames as for the science images. Exposure of 30 seconds was used in most cases.

Raw images from the camera were transformed into FITS format, then were calibrated with master bias, dark and flat frames. As far as the camera uses a three-color Bayer matrix, channel separation was used to produce sets of images in green, blue and red filters in FITS format. To increase the signal-to-noise ratio (SNR), several individual images (usually 5) were averaged (stacked) to produce an image with better SNR, this also diminishes the effect of atmospheric scintillations. Before averaging, the star alignment procedure was applied to individual images. Measures for final light curves were made on those stacked images, however, for the initial search, all images taken during an observing session (night) were aligned and stacked together. So the initial search for new variables was done on a set of such nightly-averaged images.

Transforming from camera raw images to FITS, preparation of master bias, dark and flat frames, channel separation, and image stacking were done using a set of utilities created by the author (Pyatnytsky, 2018); calibration of science images and star alignments before stacking were done using IRIS software (Buil, 2010). The search for the variables was done with MuniWin/C-MuniPack software (Hroch, 2014).

A series of images (green channel only) correspond to different observing nights (one averaged image for each

night) was analyzed by the “Find Variables” module of MuniWin package. To make a search more efficient, cropped parts of the full field of view were used. MuniWin makes aperture photometry for all stars in the analyzed field of view for the series of images producing “Standard Deviation of the Magnitude vs. Magnitude” plot. “Outlying” points in that plot may correspond to variable stars.

Each “suspected” star (having a big standard deviation of magnitude across the sequence) was checked for existence in the VSX and catalogs covered by the VizieR Catalogue Service (VizieR). If the variable turned out to be a new one, aperture photometry for the suspected star was done on short stacks (5×30 s), a light curve was built and a period (if exists) was estimated. For long periodic and semiregular variables the measures were averaged by sessions (nights), for short-period stars individual measures were used. The aperture photometry was done with AstroImageJ software (Collins et al., 2017), an ensemble approach (several comparison stars) was used.

As far as DSLR uses Bayer matrix with non-standard filters, data had to be transformed (as far as it is possible) into a standard photometric system (this is especially important in case of ensemble photometry because color indices of the stars in the ensemble are different). Magnitudes of the target star measured relative to each comparison star in the ensemble were transformed from ones obtained for Bayer matrix filters to values corresponding to the Johnson V filter using a synthetic V-filter methodology (VSF) (Pieri, 2012). In this methodology a “corrected” signal of camera’s green filter is used:

$$G_c = G + aR - bB \quad (1)$$

where G_c is the corrected signal of the green filter, R , B are signals of the red and blue filters, respectively. Coefficients a and b were selected to minimize the difference between Johnson V filter output V_j and corrected signal of the green channel using the ensemble of stars with known brightness:

$$V_j = k(G_j + aR_j - bB_j) \quad (2)$$

Here k is a scaling factor. Author of VSF methodology states that it generally gives better precision for red stars than the standard transformation technique (Pieri, 2012).

Calibration of the author’s setup (finding transformation coefficients) was done using M67 standard field provided by the AAVSO (American Association of Variable Stars Observers). To make a solution of the system of equations (2) more robust, the author used a simplified approach proposed by Pieri (2019) in which a assumed to be equal to b .

The resulting magnitude for each light curve point was an average of those transformed values obtained relative to all comparison stars in the ensemble.

For better estimation of the period and other star's characteristics data from ASAS-SN (Kochanek et al., 2017), SuperWASP (Butters et al., 2010), and APASS (Henden et al., 2018) surveys were used together with data obtained by the author for further analysis. In some cases, when the author's data had poor quality (for faint stars or stars at the margin of a field of view where star's image was severely distorted by optical aberrations) only data from the mentioned surveys were used. In such cases, original images were used to detect a fact of variability itself only.

A period search for periodic and semiregular variables was performed with VStar software. If a star was proven to be a new (previously unregistered) variable, it was sent for registration to the VSX.

2. Results

Using data collected from October 2017 to June 2019, 27 new variables have been found in five starfields. They were registered in the VSX as PMAK V1..PMAK V27 respectively. The characteristics of the variables are summarised in Table 1. Most of the new variables (16) were found in a single field in Cygnus around an object 2MASS J21313973+3529220 (this is a known variable indexed as Romanov V4 in the VSX) which was the main observation target in this field. There were more than 60 observation nights for this field from October 2017 to December 2018. Such a relatively long series of images allowed us to discover periodic and semiregular variables having a wide period range, from hours to hundreds of days.

All of the new-found variables have relatively small variability range (less than one magnitude), three of them have a range less than $0.^m1$ in V band (see Table 1). This proves the good sensitivity of the setup and accuracy of the method. It is interesting to note that several of the stars are brighter than 10^m in maximum which makes them problematic targets for some automatic surveys (for example, ASAS-SN nominal saturation limit is between 10^{th} and 11^{th} magnitude in V-band (Kochanek et al., 2017)). It may indicate that there are many bright unknown variables to search for.

Additionally, photometry in Johnson V and Johnson B bands were measured for some of the new variables (as noted before, only V-band data calculated using VSF approach were used for period analysis). For two-band photometry, standard transformation (see Blackford et al., 2016; Kloppenborg et al., 2012; Henden & Kaitchuck, 1982) from Bayer green and blue channel was used based on transformation coefficients obtained from observations of M67 standard field provided by the AAVSO. Examples of light curves are shown in Fig. 1. It is seen that the author's data (PMAK) for V band are in a good agreement with ASAS-SN V band which confirms the reliability of measurements.

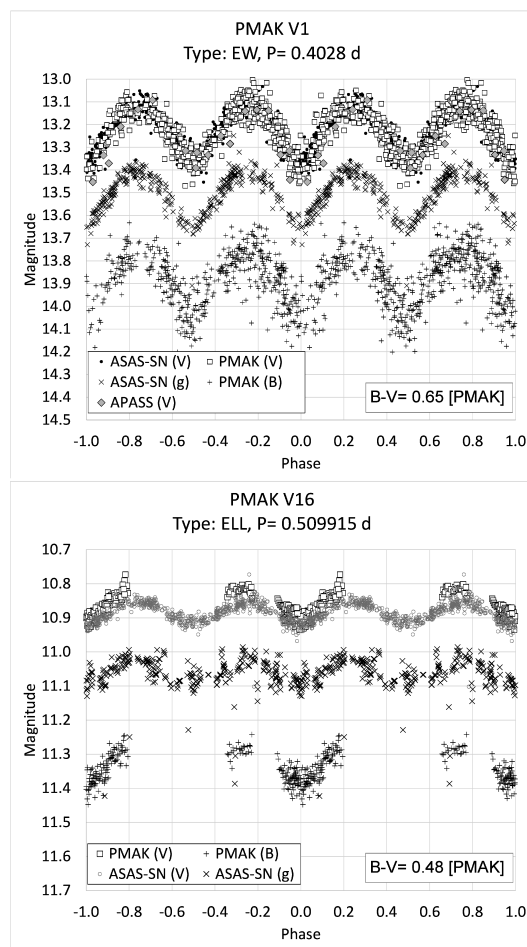


Fig. 1: Upper pane: Folded light curves of PMAK V1. Epoch (2458119.913 HJD) differs from those specified in the VSX by half of the period. Lower pane: Folded light curves of PMAK V16: a variable with the smallest range ($0.^m07$ in V band) for which light curves with author's data are available. The period has been refined.

3. Conclusion

Setup of a small (150mm f/5 in the current case) telescope equipped with DSLR camera has sufficient sensitivity which allows one to effectively detect new variables having brightness up to $\sim 14^m$ in V band and variability range up to $\sim 0.^m1$ or even less for bright stars (of about 11^m .. 12^m and brighter).

Among the stars found during the current research, several are brighter than 10^m in maximum. This is evidence that there exist many unknown bright variables which are worth searching for.

Long series of frames taken over a period of more than a year allows ones to detect variables with a wide range of characteristic duration of changes, from hours to hundreds of days.

Table 1: New variables found in DSLR images collected from October 2017 to June 2019 (data from the VSX)

VSX name	Catalog designation	Coordinates J2000	Type	Period (d)	Epoch (HJD)	Range (V)	D ²
PMAK V1	2MASS J21303361+3531290	21:30:33.62+35:31:29.0	EW	0.40280	2458119.712	13.10 - 13.38	
PMAK V2	2MASS J21300019+3537282	21:30:00.18+35:37:28.2	SRB	44.9	2458124	13.5 - 14.0	
PMAK V3	2MASS J21300722+3559550	21:30:07.23+35:59:55.1	SRS	26.3	2458159	12.8 - 13.4	
PMAK V4	2MASS J21321559+3507213	21:32:15.59+35:07:21.3	SRB	43.5	2457741	12.6 - 13.1	
PMAK V5	TYC 2712-1327-1	21:30:17.88+35:10:25.4	EA	4.7392	2458119.23	13.15 - 13.6:	10
PMAK V6	2MASS J21282963+3511375	21:28:29.63+35:11:37.5	RS	44.69	2457187.75	11.96 - 12.25	
PMAK V7	TYC 2712-183-1	21:28:43.22+35:33:39.0	SRB	49.3	2458161	10.9 - 11.4	
PMAK V8	TYC 3196-2125-1	21:41:45.58+44:05:49.4	SR	126.9	2458176	11.26 - 11.63	
PMAK V9	BD+34 4421	21:27:51.02+35:34:20.9	SRD	36.4	2455827	8.9 - 9.3	
PMAK V10	2MASS J21335644+3518525	21:33:56.44+35:18:52.5	RS	13.214	2458234	14.4 - 14.9	
PMAK V11	2MASS J21345319+3542016	21:34:53.19+35:42:01.4	EW	0.4011496	2457139.898	14.10 - 14.65	
PMAK V12	2MASS J21314096+3542209	21:31:40.97+35:42:20.9	SRB	30.27	2457755	14.1 - 14.6	
PMAK V13	2MASS J21283912+3502390	21:28:39.12+35:02:39.1	EW	0.556504	2457554.65	13.16 - 13.34	
PMAK V14 ¹	2MASS J21341089+3520285	21:34:10.89+35:20:28.5	EA	1.095355	2457139.792	14.3 - 14.9:	18
PMAK V15	BD+63 173	01:20:20.51+64:01:30.3	SRB	33.4	2457725	9.7 - 10.15	
PMAK V16	TYC 4034-1138-1	01:24 21.07+63:16:02.7	ELL	0.50991	2457204.34	10.86 - 10.93	
PMAK V17	2MASS J21400903+4410037	21:40:09.04+44:10:03.8	SRS	27.6	2457749	12.84 - 13.17	
PMAK V18	2MASS J21430699+4302568	21:43:07.00+43:02:56.8	EA	3.50965	2457729.45	12.67 - 12.9	8
PMAK V19	2MASS J13353214+7317138	13:35:32.15+73:17:13.7	RS	12.86	2457278	13.11 - 13.52	
PMAK V20	2MASS J21444177+4356214	21:44:41.79+43:56:21.4	SRS	24	2457740	12.76 - 13.12	
PMAK V21	2MASS J20335348+5956506	20:33:53.49+59:56:50.7	DSCT	0.143553	2457266.455	12.62 - 12.65	
PMAK V22	2MASS J21315159+3549238	21:31:51.59+35:49:23.8	EA	14.492	2457216.5	13.12 - 13.27	9
PMAK V23 ¹	2MASS J01153742+6328048	01:15:37.41+63:28:04.8	EB	0.693731	2457777.855	14.28 - 15.08	
PMAK V24	BD+34 4443	21:31:06.42+35:24:19.6	SRS	19.57	2455840.5	9.68 - 9.88	
PMAK V25	TYC 2712-846-1	21:34:11.36+34:56:04.1	SRD	279	2457745	11.63 - 11.76	
PMAK V26	TYC 3583-1129-1	20:56:16.68+50:15:52.2	EA	3.94548	2457105.65	11.94 - 12.03	7
PMAK V27	2MASS J13275559+7324530	13:27:55.60+73:24:52.9	NL:	-	-	12.81 - 13.05	

¹ Co-discoverers: B. Sesar et al., 2017

² Primary eclipse duration for EA-type binaries as a fraction of the width of one complete eclipse cycle in %

Acknowledgements. The author would like to thank Prof. Ivan L. Andronov for the support. Many thanks to amateur astronomer Nikolay Mishevskiy who inspired the author to start observing variable stars. This study is related to the Inter-Longitude Astronomy project (Andronov et al., 2017).

References

- AAVSO: 2019, <https://www.aavso.org>
- Andronov I.L., et al.: 2017, *ASP Conf. Ser.*, **511**, 43.
- Blackford M., et al: 2016, <https://www.aavso.org/dslr-observing-manual>
- Buil C.: 2010, <http://www.astrosurf.com/buil/iris-software.html>
- Butters O.W., et al.: 2010, *A&A*, **520**, L10.
- Collins K.A., et al.: 2017, *AJ*, **153**, 77.
- Henden A.A., et al.: 2018, *AAS Meeting #232*, id. 223.06, 2018AAS...23222306H
- Henden A.A., Kaitchuck R.H.: 1982, *Astronomical Photometry*, Van Nostrand Reinhold Co., New York, 12+392 p.
- Hoot J.E.: 2007, *26th Annual Symposium on Telescope Science, Published by the Society for Astronomical Sciences.*, p.67, 2007SASS...26...67H
- Hroch F.: 2014, *ASCL*, ascl:1402.006, <http://c-munipack.sourceforge.net>
- Kloppenborg B.K., et al.: 2012, *JAAVSO*, **40**, 815.
- Kochanek C.S., et al.: 2017, *PASP*, **129**, 104502.
- Masci F.J., et al.: 2019, *PASP*, **131**, 018003.
- Pieri R.: 2012, *JAAVSO*, **40**, 834.
- Pieri R.: 2019, *Private communication*
- Pyatnytskyy M.Yu.: 2018, <http://fits-command-line-utilities.sourceforge.net>
- Sesar B., et al.: 2017, *AJ*, **153**, 204.
- VizieR Catalogue Service, <https://vizier.u-strasbg.fr>
- VStar, <https://www.aavso.org/vstar>
- Watson C.L., Henden A.A., Price A.: 2006, *25th Annual Symposium on Telescope Science, Published by the Society for Astronomical Sciences.*, p.47, 2006SASS...25...47W
- Woźniak P.R., et al.: 2004, *AJ*, **127**, 2436.
- Zhang M., et al.: 2015, *PASP*, **128**, 961.

DOI:<http://dx.doi.org/10.18524/1810-4215.2019.32.182232>

LITHIUM-RICH CLASSICAL CEPHEID V1033 CYG: EVOLUTIONARY STATUS

S. N. Udovichenko, V. V. Kovtyukh and L. E. Keir

Astronomical Observatory, Odessa National University,
Odessa, Ukraine, udovich222@ukr.net

ABSTRACT. We investigate evolutionary status of cepheid V1033 Cyg in this work, its period of light variation consists $4^d.94$ and the star is a real candidate on first crossing of instability stripe (IS) (as well as α of UMi). At first crossing of instability stripe, that lasts all close 1000 years, cepheids demonstrate the rapid increase of period, sometimes is a presence of strong line of lithium 6707 Å. Such objects knows only four in our Galaxy, one of them - V1033 Cyg. During included in a instability stripe amplitude of pulsations headily grows from a zero to some permanent size, and on leaving from (IS) - again falls to a zero. For verification this phenomenon in the Astronomical observatory of Odesa National University (Ukraine) on the 48-cm telescope AZT-3, equipped by CCD photometer with the optical sensor Sony ICX429ALL, a 1864 measuring of light V1033 Cyg were done in the filter of V and 713 in the filter R, that are partly presented in the Table. 1 and Fig. 2, and fully accessible to address <http://cdsarc.ustrasbg.fr/viz-bin/cat>. Considerable change of amplitude it is not got by us. The position of cepheid is certain by us in the (IS) - it appeared that star is near her center. In this phase evolutionary to development and it must not be observed considerable change of amplitude (color index). The light curves, effective temperature and luminosity of V1033 Cyg are consistent with fundamental mode pulsation for a classical Cepheid on the center of the instability strip.

АНОТАЦІЯ. У даній роботі ми досліджуємо еволюційний статус цефеїди V1033 Cyg, період зміни блиску якої становить $4^d.94$, і яка є реальним кандидатом на перше перетинання смуги нестабільності (як і α UMi). При першому перетині смуги нестабільності (СН), який триває всього близько 1000 років, цефеїди демонструють швидке зростання періоду, інколи – наявність сильної лінії літія 6707 Å. Таких об'єктів відомо лише 4 у нашій Галактиці, одна з них – V1033 Cyg. Під час входу у смугу нестабільності амплітуда пульсацій стрімко зростає від нуля до якоїсь сталої величини, а при виході зі СН – знову падає до нуля. Для перевірки цього явища в Астрономічній

обсерваторії Одеського національного університету (Україна) на 48-см телескопі АЗТ-3, оснащеному фотометром з ПЗЗ-матрицею Sony ICX429ALL, були зроблені 1864 вимірювання блиску V1033 Cyg в фільтрі V, і 713 вимірювань у фільтрі R, які частково наведені в табл. 1 та на рис. 2, а повністю доступні за адресою <http://cdsarc.ustrasbg.fr/viz-bin/cat>. Значної зміни амплітуди нами не отримано. Нами визначено положення цефеїди у смугі нестабільності – виявилось що вона знаходиться біля її центру. У цій фазі еволюційного розвитку і не повинно спостерігатися значної зміни амплітуди (показників кольору). Криві блиску, ефективна температура і світність V1033 Cyg відповідають стадії фундаментальних пульсацій класичних цефеїд у центрі смуги нестабільності.

Keywords: Stars: variables: Cepheids – V1033 Cyg

1. Introduction

V1033 Cyg (GSC 2674.03107), ($\alpha_{J2000.0} = 20^h05^m20.66^s$; $\delta_{J2000.0} = +32^\circ39'32.5''$) is the classical cepheid variable star (GCVS) with amplitude $14.^m4 - 15.^m5$ (pg) and period $4.^d937512$ (Samus' et al., 2011).

The variability of the star was found by Miller (1965), using the moments of brightness on 88 photographic plates, it has defined elements of light variation and has noted, that the period of cepheid quickly changes. The star was thoroughly investigated by L. Berdnikov (1987, 1992), L. Berdnikov et al. (2019), as the cepheid that crosses the instability strip for the first time. It was reported as a Cepheid with Li over-abundance by Luck & Lambert (2011).

2. Observations

The photometric CCD observations of V1033 Cyg were obtained at the Astronomical station near Odesa during the observation seasons in 2013-15 years, in V filter, later on, in 2017 year the observations were

performed in V and R filters. We were using the 48 cm reflector AZT-3 of Astronomical observatory of Odesa National University, equipped with CCD photometer and Peltier cooler (Sony optical sensor ICX429ALL, $\sim 600 \times 800$ pixels) in the f/4.5 Newtonian focus (Udovichenko, 2012).

The datasets consists of 1864 V-band and 713 R-band data points obtained from over 60 nights of observations. Two stars were chosen as comparison and check stars as close as possible in B-V color to variable. Comparison star is USNO-A 1200-14402731, $B_{comp} = 14.^m285$, $V_{comp} = 13.^m399$ (APASS, 2010), $R_{comp} = 12.^m800$ (NOMAD, 2005); check star is USNO-A 1200-14401158).

The standard reduction of the CCD frames were carried out by using the MUNIPACK (Motl, <http://sourceforge.net/projects/c-munipack>) software. The procedures for an aperture photometry is composed of the dark-level and flat-field corrections, determination of the instrumental magnitudes and precision. The photometry was transformed to the standard VRc Johnson-Cousins system by means of the differential photometry method (Benson 1998). The transformation coefficient was determined from observations of standard stars (Udovichenko 2012). The finding chart with market-out variable, comparison and check stars is shown in Fig. 1. The errors in individual data points vary from $0^m.005$ to $0^m.02$.

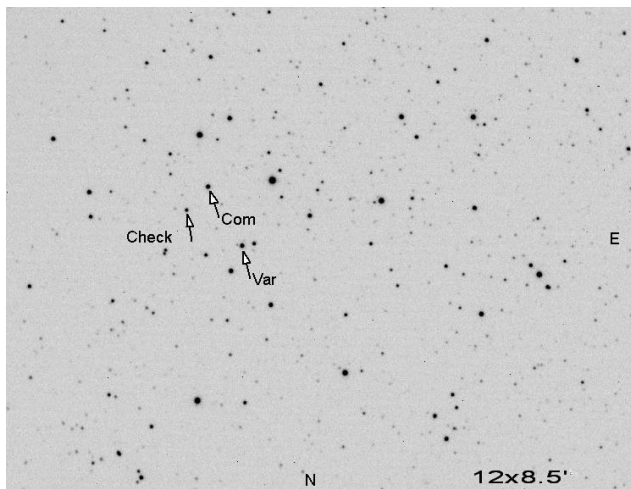


Figure 1: The finding chart V1033 Cyg with the comparison and check stars marked.

3. Results

Period. Using only the photoelectric moments of maximum from paper by Berdnikov et al (2019), current quadratic light elements of V1033 Cyg are obtained:

$$\text{MaxHJD} = 2452701.6164 + 4.9494727 E + 0.14237 \cdot 10^{-5} E^2,$$

the phases calculated for these elements are given in Table 1. The phase curve V1033 Cyg from our observations and quadratic light elements is presented in Fig. 2.

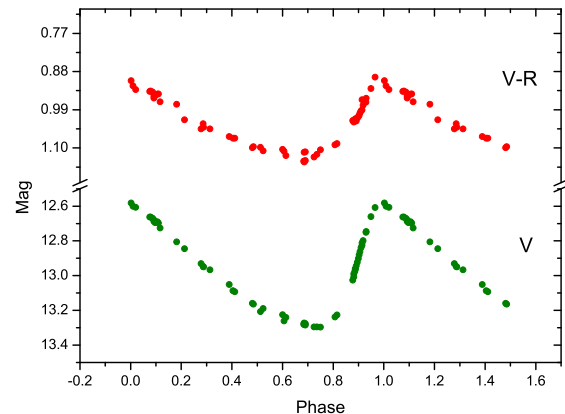


Figure 2: The phase curve in V-band and V-R color variations V1033 Cyg with quadratic light elements.

The O-C diagram covering more than 100 years indicates a rapid increase of the period of 18.2 s/yr, in agreement with a first crossing of the instability strip for this star (Berdnikov et al. 2019).

Amplitude. The Fourier decomposition was applied to Berdnikov's photoelectric and our CCD observations of V1033 Cyg. For the V-amplitude obtained values $A_V = 0.724$ mag (Berdnikov) and $A_V = 0.718$ mag (our observations). Thus, there are no rapid evolutionary changes in the amplitude of V1033 Cyg.

Temperature. Using the T_{eff} vs (B-V) calibrations from the papers by Kovtyukh (2007) and Kovtyukh et al (2008), effective temperatures (T_{eff}) for the Cepheid were obtained, its are shown in Fig. 3. The average effective temperature for V1033 Cyg is $\langle T_{\text{eff}} \rangle = 5864 \pm 45$ K (phases = 0.288 and 0.846).

Hertzsprung-Russell diagram. The absolute magnitude $M_V = -3.13$ is found using the "absolute magnitude-pulsational period" relation of Gieren et al. (1998). The loci of V1033 Cyg on the H-R diagram are shown in Fig. 4. Evolutionary tracks from Salasnich et al (2000) for $Z=0.019$ and $[\alpha/\text{Fe}]=0$ are shown for reference. These models do not develop long blue loops for stars with 2–5 M_{\odot} , and hence they do not cross the instability strip. On the other hand, stars with 5–7 M_{\odot} do show blue loops that cross the lower part of the cepheid instability strip.

In Figure 4 also shown the location of yellow

Table 1: V1033 Cyg. Observational list.

JDhel	phase	V	V - R	JDhel	phase	V	V - R	JDhel	phase	V	V - R
2450000+		mag	mag	2450000+		mag	mag	2450000+		mag	mag
8335.4033	0.887	12.960	1.019	8341.3018	0.079	12.662	0.936	8365.3242	0.929	12.751	0.968
8335.4219	0.891	12.943	1.022	8342.3057	0.281	12.962	1.054	8365.4268	0.949	12.660	0.929
8335.4395	0.895	12.923	1.014	8342.3271	0.285	12.964	1.059	8366.2520	0.116	12.726	0.967
8335.4580	0.899	12.902	1.010	8343.2939	0.481	13.159	1.099	8374.2744	0.736	13.295	1.118
8335.4766	0.902	12.880	1.006	8343.3164	0.485	13.164	1.096	8375.2354	0.930	12.746	0.957
8335.4941	0.906	12.861	0.999	8344.3057	0.685	13.273	1.112	8379.2949	0.750	13.296	1.105
8335.5137	0.910	12.839	0.993	8344.3281	0.690	13.276	1.111	8380.3623	0.965	12.608	0.896
8335.5332	0.914	12.826	0.991	8345.2754	0.881	12.990	1.020	8381.4365	0.182	12.805	0.974
8335.5527	0.918	12.798	0.977	8345.2939	0.885	12.976	1.019	8382.4619	0.389	13.051	1.067
8336.4141	0.092	12.687	0.951	8345.3115	0.888	12.963	1.016	8383.5078	0.600	13.225	1.104
8336.4287	0.095	12.685	0.947	8346.2979	0.087	12.669	0.939	8390.4492	0.002	12.581	0.906
8336.4424	0.097	12.695	0.949	8346.3193	0.092	12.679	0.956	8397.3916	0.404	13.087	1.072
8337.3340	0.278	12.930	1.045	8347.2793	0.286	12.947	1.030	8398.3965	0.606	13.260	1.109
8337.3525	0.281	12.957	1.048	8347.2930	0.288	12.950	1.040	8399.3877	0.807	13.238	1.091
8337.3701	0.285	12.953	1.035	8348.4072	0.513	13.207	1.098	8400.3916	0.009	12.601	0.921
8339.3428	0.683	13.280	1.138	8351.3438	0.106	12.690	0.945	8401.4004	0.213	12.845	1.019
8339.3604	0.686	13.282	1.140	8351.3623	0.110	12.697	0.944	8402.3809	0.411	13.092	1.072
8339.3760	0.690	13.284	1.136	8362.2725	0.313	12.966	1.045	8403.3799	0.613	13.240	1.122
8340.3037	0.877	13.026	1.021	8363.3115	0.523	13.189	1.108	8404.3818	0.815	13.226	1.087
8340.3213	0.881	13.008	1.025	8364.3105	0.724	13.295	1.126	8405.3955	0.020	12.606	0.932
8341.2842	0.075	12.662	0.937	8365.2510	0.914	12.811	0.961				

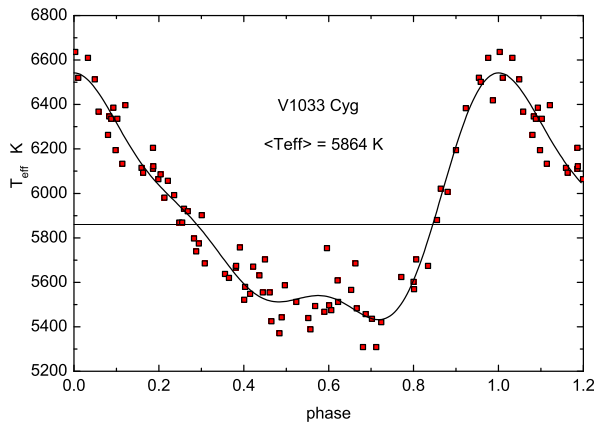


Figure 3: Variation of T_{eff} of V1033 Cyg with phase.

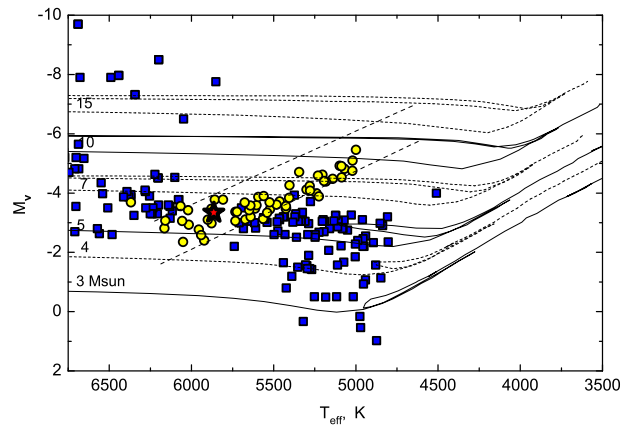


Figure 4: The H-R diagram constructed using our parameters. Classical Cepheids are plotted as open circles, supergiants as filled squares. Lines indicate evolutionary tracks by Salasnich et al (2000) for 15, 10, 7, 5, 4, and 3 M_{\odot} (top to bottom) for $z=0.019$ and $[\alpha/\text{Fe}]=0$. Dashed lines indicate IS for classical Cepheids. V1033 Cyg is shown as asteric.

supergiants and classical Cepheids in the H-R diagram (Kovtyukh et al 2010). First, we find that the $Z = 0.019$ tracks do a good job of predicting the positions of the blue loops and yellow supergiants for $M_V > -5$. The most luminous yellow supergiants in our sample have $M_V \sim -8$, consistent with the evolutionary tracks.

Conclusion

Our own analysis of V1033 Cyg, covering more than 100 years indicates a rapid increase of the period of 18.19 ± 0.08 s/yr, in agreement with a first crossing of the instability strip for this star (this paper and Berdnikov et al 2019).

It was found that the V-amplitude does not change rapidly. This is naturally explained by the position of the star in the center of the instability strip.

The results are consistent with fundamental mode pulsation in V1033 Cyg, as well as with a first crossing of the instability strip.

References

- APASS, Star catalog: 2010, <http://www.aavso.org>.
- Benson P.J.: 1998, *Intern. Amateur-Professional Photoel. Photom. Communic.*, **72**, 42.
- Berdnikov L.N.: 1987, *Perem. Zvezdy*, **22**, 530.
- Berdnikov L.N et al.: 2019, *Astronomy Letters*, **45**, 4, 227.
- Berdnikov L.N.: 1992, *Astron. Astrophys. Trans.*, **2**, 1.
- Gieren W.P., Fouqué P., Gómez M.: 1998, *ApJ*, **496**, 17.
- Henden A.A.: 1996, *Astron. J.*, **111**, 902.
- Kovtyukh V.V.: 2007, *MNRAS*, **378**, 617.
- Kovtyukh V.V., Soubiran C., Luck R.E., Turner D.G., Belik S.I., Andrievsky S.M., Chekhonadskikh F.A.: 2008, *MNRAS*, **389**, 1336.
- Kovtyukh V. V., Chekhonadskikh F. A., Luck R. E., Soubiran C., Yasinskaya M. P., Belik S. I.: 2010, *MNRAS* **408**, 1568.
- Luck R.E. & Lambert D.L.: 2011, *AJ*, **142**, 136.
- Motl D.: 2009-17 <http://sourceforge.net/projects/c-munipack>
- Salasnich B., Girardi L., Weiss A., Chiosi C.: 2000, *A&A*, **361**, 1023.
- Samus N.N., Durlevich O.V., Kazarovets E.V., Kireeva N.N., Pastukhova E.N., Zharova A.V. et al.: 2011, *General Catalogue of Variable Stars* (GCVS database, Version 2011Jan).
- Udovichenko S.N.: 2012, *Odessa Astron. Publ.*, **25**, 32.
- Zacharias N. et al.: 2005, VizieR Online Data Catalog: NOMAD Catalog (Zacharias+2005), 1297.

DOI:<http://dx.doi.org/10.18524/1810-4215.2019.32.182238>

PULSATIONAL ACTIVITY OF THE SMALL-AMPLITUDE CEPHEID POLARIS (α UMi) IN 2018-2019

I. A. Usenko^{1,2}, A. S. Miroschnichenko^{3,4,5}, S. Danford³, V. V. Kovtyukh¹

¹ Astronomical Observatory, Odessa National University, Shevchenko Park,
Odessa 65014, Ukraine, vkovtyukh@ukr.net

² Mykolaiv Astronomical Observatory, Obsevatorna 1,
Mykolaiv 54030, Ukraine, igus99@ukr.net

³ Dept. of Physics and Astronomy, University of North Carolina at Greensboro,
P.O. Box 261170, Greensboro, NC 27402, USA, a_mirosh@uncg.edu; danford@uncg.edu

⁴ Main Astronomical Observatory of the Russian Academy of Sciences,
Pulkovskoe shosse 65-1, Saint-Petersburg, 196140, Russia

⁵ Fesenkov Astrophysical Institute, Observatory 23, Almaty, 50020, Kazakhstan

ABSTRACT. We present the results of an analysis of 20 spectra of α UMi (Polaris) obtained in September 2018 – January 2019 using 0.81 m telescope of the Three College Observatory (TCO), North Carolina, USA. Frequency analysis displays an increase of the pulsational period up to 3.68 min in comparison to the August - December 2017 - January - May 2018 observational sets, and it come to 3.973216 days. The systemic velocity (γ – velocity) is equal to -11.75 km s^{-1} . The radial velocity amplitude rose to 3.50 km s^{-1} and actually returned to the previous values of 3.43 , 3.31 , and 3.81 km s^{-1} , respectively, found from the August - December 2016, January - March 2017 and August - December 2017 sets. The radial velocity's amplitude growth tendency still remains. The average $T_{\text{eff}} = 6051 \pm 22$ K shows a growth toward the value found from the 2005 – 2007 observational sets and probably has a tendency toward the T_{eff} growth. The joint TCO and *Hermes* radial velocity measurements during the last four years show the changes of Polaris' pulsational amplitude.

Key words: Stars: radial velocities; Cepheids: effective temperatures; Cepheids: pulsational periods; Cepheids: α UMi

АНОТАЦІЯ. Ми презентуємо результати аналізу 20 спектрів α UMi (Полярної), які були отримані на протязі вересня - грудня 2018 та січня 2019 років за допомогою 0.81 м телескопу Обсерваторії Трьох Колледжів (Three Colledge Observatory, TCO) штат Північна Кароліна, США. Частотний аналіз виявив зріст періода пульсації на 3.68 хв у порівнянні з спостережними сетами серпня - грудня 2017 та січня - травня 2018 років та рівний 3.973216 днів. Швидкість системи, або (γ – velocity) виявилася

рівною -11.75 km s^{-1} . Амплітуда радіальної швидкості досягла 3.50 km s^{-1} , та повернулася приблизно на рівень попередніх оцінок у 3.43 , 3.31 , and 3.81 km s^{-1} , відповідно, які були встановлені для сетів серпня - грудня 2016, січня - березня 2017 та серпня - грудня 2017 років. Тенденція зростання амплітуди радіальної швидкості все ще зберігається. Середня $T_{\text{eff}} = 6051 \pm 22$ K, та вона показує зріст до результатів сетів 2005 – 2007 років, та, вірогідно, має тенденцію до зростання. Сумісні оцінки радіальних швидкостей, отриманих на TCO та *Hermes* за останні чотири роки показують зміни пульсаційної амплітуди Полярної.

Ключові слова: Зорі: радіальні швидкості; цефеїди: ефективні температури; цефеїди: пульсаційні періоди; цефеїди: α UMi

1. Introduction

In our previous papers (Usenko et al. 2016, 2017, 2018) we found that the pulsational period and radial velocity amplitude of Polaris had increased in 2015–2018.

The former was up 8.6 minutes in comparison to the data from 2007, and the latter became 4.16 km s^{-1} (twice the one of the 2007 data). The average $T_{\text{eff}} = 6017$ K is close to the value determined from the 2001–2004 set. During August – December 2016 (37 spectra) and January – March 2017 (12 spectra) the pulsation period decreased by 17.3 min in comparison with the 2015 data. The radial velocity amplitude decreased to 3.43 km s^{-1} in 2016 and to 3.31 km s^{-1} in the beginning of 2017. The average T_{eff} was 6021

Table 1: Observational data of α UMi during September - December 2018 and January 2019

Date	HJD	T_{eff}	σ	Phase	Metals	σ	RV (km s ⁻¹)	H_{α}	H_{β}	H_{γ}
YY/MM/DD	2450000+	K	K				NL			
180906	8368.5931	6058	21	0.934	-14.49	1.70	176	-14.45	-14.84	-14.67
181019	8411.4928	6057	20	0.731	-11.50	1.77	159	-12.23	-9.93	-8.58
181021	8413.5843	6055	19	0.258	-11.68	1.68	189	-12.23	-8.92	-10.96
181024	8416.5683	6073	23	0.009	-13.01	1.61	173	-13.42	-7.80	-11.84
181029	8421.6551	5984	18	0.289	-11.19	1.78	166	-11.20	-7.53	-10.24
181030	8422.6439	5969	21	0.538	-9.95	1.86	157	-9.47	-4.03	-8.90
181116	8439.6274	6038	22	0.812	-12.35	1.69	147	-12.07	-9.87	-11.31
181117	8440.6117	6086	21	0.060	-13.20	1.91	155	-13.40	-10.75	-12.20
181119	8442.6074	6050	21	0.562	-10.69	1.86	163	-10.18	-6.94	-8.58
181120	8443.6292	6117	23	0.819	-12.37	1.60	153	-13.25	-8.88	-11.26
181205	8458.6511	6074	21	0.600	-10.72	1.48	158	-11.30	-8.21	-8.81
181216	8469.5308	6007	21	0.338	-11.29	1.47	159	-10.92	-8.52	-9.70
181217	8470.5557	6083	25	0.596	-10.63	1.59	164	-10.74	-6.97	-9.46
181222	8475.5715	6095	24	0.859	-13.30	1.20	161	-14.05	-9.15	-11.57
181224	8477.5626	5948	20	0.360	-11.40	1.34	159	-10.33	-8.56	-9.44
181226	8479.5699	6102	22	0.865	-13.09	1.45	170	-13.39	-10.70	-12.34
190105	8489.5582	6041	20	0.379	-11.07	1.51	164	-10.38	-7.44	-9.77
190115	8499.5614	6090	22	0.897	-11.85	1.37	160	-11.89	-8.81	-10.80
190125	8509.5801	6050	22	0.418	-10.21	1.46	171	-10.12	-7.02	-8.83
190130	8514.6088	6042	27	0.684	-11.03	1.63	170	-11.47	-9.57	-9.53

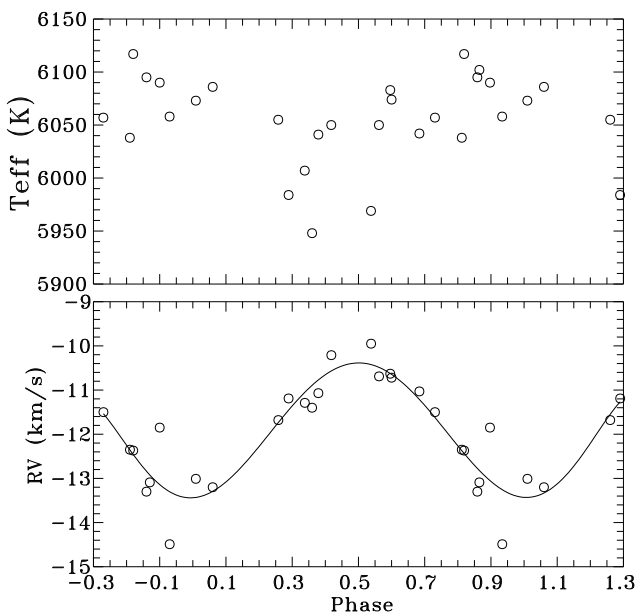


Figure 1: The effective temperature and radial velocity variations of Polaris folded with its pulsational period for the September – December 2018 and January 2019 set.

K with amplitudes of 54 K and 70 K, respectively. Instead during August–December 2017 (29 spectra) and January–May 2018 (38 spectra) the pulsational period increased to 3.^d970662 but was still less than 3.^d979872 observed in 2015. The mean radial velocity amplitudes in these sets were 3.81 km s⁻¹ and 2.80 km s⁻¹ respectively, i.e. a new amplitude decrease was obvious. The average values of T_{eff} were found to be 6017 K and 6039 K, respectively, but the T_{eff} amplitude has increased despite the decrease in the radial velocity amplitude. Therefore we have to continue our investigation to study this unusual behavior of Polaris.

2. Observations and frequency analysis

Sixteen spectra were taken in September–December 2018 and four in January 2019 with the 0.81 m telescope of the Three College Observatory (TCO), located in central North Carolina, USA. They were obtained with an échelle spectrograph manufactured by Shelyak Instruments¹ in a spectral range from 4250 to 7800 Å with a spectral resolving power of $R \sim 12000$ and no gaps between the spectral orders. The data were reduced using the *échelle* package in IRAF.

DECH30 package (Galazutdinov 2007) allows to measure the line depths and radial velocities using spectra in FITS format. Lines depths were used to determine the effective temperature (a method based on the spectroscopic criteria, Kovtyukh 2007). The derived values of T_{eff} and radial velocity for each spectrum are given in Table 1.

In the next step, we used the PERIOD04 program (Lenz & Breger 2005), which employs the Fourier and Fast Fourier Transform analysis and minimizes the residuals of sinusoidal fits to the data.

A Fourier amplitude spectrum was obtained over a frequency range of 0–1 d⁻¹ with a resolution of 0.00002 d⁻¹. The highest amplitude corresponds to a frequency of 0.251685 ± 0.000255 d⁻¹ or 3.973216 ± 0.004 days, respectively. This period is larger by 3.68 minutes compared to that of 3.970662 days determined from the August – December 2017 and January – May 2018 observational set. The systemic velocity (γ – velocity) is equal to -11.75 km s⁻¹.

The following ephemeris has been computed based on the radial velocity values:

$$RV_{\min} = HJD\ 2458440.3736 + 3.973216 \times E \quad (1)$$

Figure 1 represents phase curves of the Polaris radial velocity (lower panel) and effective temperature (upper panel) variations during our observational set.

¹<http://www.shelyak.com>

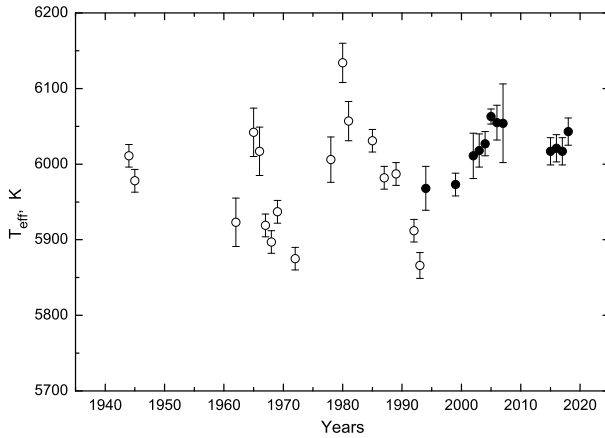


Figure 2: Variations of the mean effective temperature of Polaris during the last 75 years. Open circles show values from the $(B - V)$ vs. T_{eff} relationship by Gray (1992), filled circles show values from the line depth ratios (Kovyukh 2007).

As seen in Figure 1, in case of the data approximations by sinusoidal curves, the mean amplitudes of the radial velocity curves are 3.50 km s^{-1} , and it is somewhat larger compared to the January – May 2018 result ($A_{RV} = 2.80 \text{ km s}^{-1}$). However, it is comparable with our previous results (August - December 2016, January - March 2017 and August - December 2017 with $A_{RV} = 3.43, 3.31, \text{ and } 3.81 \text{ km s}^{-1}$, respectively).

The effective temperature variations show remarkable changes – their mean and maximum values have increased in comparison to those from previous sets with the average value of $6051 \pm 22 \text{ K}$. This value is close to the result derived from the 2005–2007 sets (Usenko et al. 2018), and probably has a tendency toward the T_{eff} growth. Figure 2 shows the variations of the mean T_{eff} of Polaris during the last 75 years, while Figure 3 demonstrates the radial velocity amplitude variations in the last ~ 125 years. As seen in Figure 3, the amplitude growth tendency still remains.

It would be interesting to compare our TCO 2015 – 2019 radial velocity measurements with those obtained by Anderson (2019) taken with the *Hermes* spectrograph. As seen in Figure 4, there is a good agreement between the TCO and *Hermes* data, therefore we can observe their positional relationship and changes of the pulsational amplitude during the last four years.

3. Summary

1. As seen from the results of our observations, the pulsational period of Polaris shows an increase by 3.68 minutes in comparison with the data obtained during the August - December 2017 and January - May 2018 observational set.

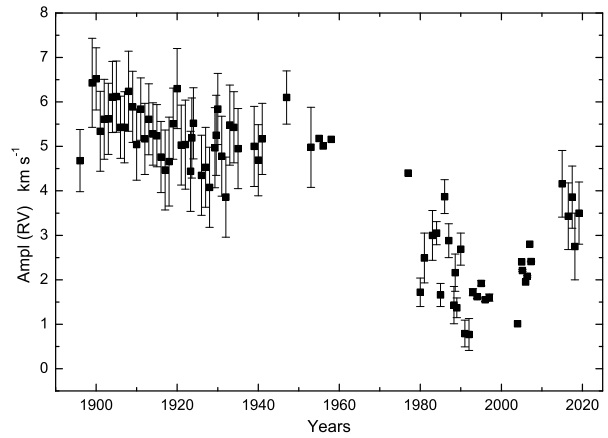


Figure 3: Radial velocity amplitude variations of Polaris over the last ~ 125 years.

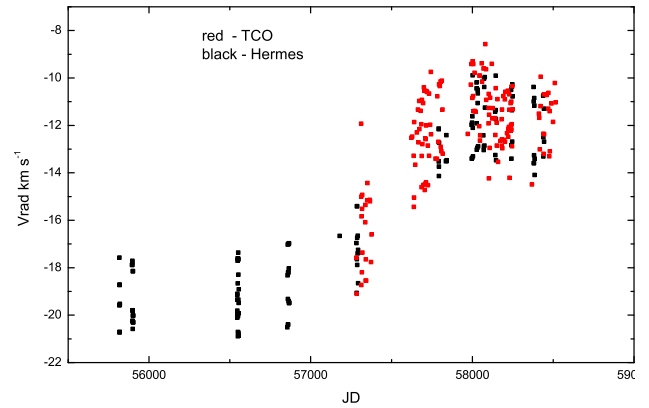


Figure 4: Radial velocity variations of Polaris over the last ten years. Red squares - TCO data, black squares - *Hermes* data.

2. The mean amplitude of the radial velocity during this observational set 3.50 km s^{-1} has returned to that of the previous sets of August - December 2016, January - March 2017 and August - December 2017. Nevertheless the pulsational amplitude growth tendency still remains.
3. The mean effective temperature of Polaris for this data set was found to be $6051 \pm 22 \text{ K}$. This value is close to those determined for the 2005–2007 sets (Usenko et al. 2018).
4. All the TCO radial velocity measurements during 2015 – 2019 have a good agreement with those measured from *Hermes* data. The joint data show the changes of Polaris' pulsational amplitude.

References

- Anderson R.I.: 2019, *A&A*, **623**, 146.
- Galazutdinov G.A.: 2007, <http://gazinur.com/DECH-software.html>.
- Gray D.: 1992, *Observation and Analysis of Stellar Atmospheres*, 2nd edn. Cambridge Univ. Press, Cambridge.
- Kovtuykh V.V.: 2007, *MNRAS*, **378**, 617.
- Lenz P. & Breger M.: 2005, *Commun. Astroseismology*, **146**, 53.
- Usenko I.A., Kovtuykh V.V., Miroshnichenko A.S., Danford S.: 2016, *Odessa Astron. Publ.*, **29**, 100.
- Usenko I.A., Kovtuykh V.V., Miroshnichenko A.S., Danford S.: 2017, *Nauka Innov.*, **13(1)**, 109.
- Usenko I.A., Kovtuykh V.V., Miroshnichenko A.S., Danford S., Prendergast P.: 2018, *MNRAS*, **481**, L115.

DOI:<http://dx.doi.org/10.18524/1810-4215.2019.32.182233>

SPECTROSCOPIC INVESTIGATIONS OF GALACTIC CLUSTERS WITH ASSOCIATED CEPHEID VARIABLES.

III. COLLINDER 394 AND BB SGR

I. A. Usenko^{1,2}, A. Yu. Kniazev^{3,4}, I. Yu. Katkov⁵, V. V. Kovtyukh¹,
T. V. Mishenina¹, A. S. Miroschnichenko^{6,7,8}, D. G. Turner⁹

¹ Astronomical Observatory, Odessa National University, Shevchenko Park, Odessa 65014, Ukraine, vkovtyukh@ukr.net

² Mykolaiv Astronomical Observatory, Obsevatorna 1, Mykolaiv 54030, Ukraine, igus99@ukr.net

³ South African Astronomical Observatory, P.O. 7925, Cape Town, South Africa, akniazev@saaao.ac.za

⁴ Southern African Large Telescope Foundation, P.O. 7925, Cape Town, South Africa

⁵ New York University, Abu Dhabi, Saadiyat Island, P.O. 129188 Abu Dhabi, UAE, ik52@nyu.edu

⁶ Dept. of Physics and Astronomy, University of North Carolina at Greensboro, P.O.Box 261170, Greensboro, NC 27402, USA, a_mirosh@uncg.edu

⁷ Main Astronomical Observatory of the Russian Academy of Sciences, Pulkovskoe shosse 65–1, Saint-Petersburg, 196140, Russia

⁸ Fesenkov Astrophysical Institute, Observatory 23, Almaty, 50020, Kazakhstan

⁹ Dept. of Astronomy and Physics, Saint Mary's University, 923 Robie Street, Halifax B3H3C3, Nova Scotia, Canada, turner@ap.smu.ca

ABSTRACT. We present the results of a spectroscopic and photometric investigation of 20 objects from the open cluster Collinder 394, which contains the Cepheid BB Sgr. Besides the Cepheid, we studied three K-giants, four B-giants, and twelve B-A-F main sequence stars. Radial velocities (RV), $v \sin i$, T_{eff} , $\log g$, were determined using spectroscopic model fitting and atmosphere models. We have derived the color-excesses, reddenings, and intrinsic colors for these stars using their T_{eff} and $\log g$ from comparison to the atmosphere models, especially for hot stars. Proper motions, RV and GAIA DR2 2018 parallax/distance values for these stars allowed us to determine their membership in the cluster and absolute magnitudes. We found that seven stars do not belong to the cluster. The parallaxes and reddenings of 13 confidently cluster members led to the distances in a range of 630–800 pc, although the majority of them (8 objects) are located at a mean distance of 657.7 ± 66.7 pc, and 5 objects with the Cepheid could probably belong to the cluster's corona. All the members have $[\text{Fe}/\text{H}]$ near 0.1 dex. The main sequence B-star No. 76 (HD 174307) has a

low rotational velocity projection, and this fact allows us to determine its chemical composition to compare with that of the Cepheid BB Sgr. Its CNO and Na abundances are close to the solar one, while the Cepheid show a deficit of carbon, an overabundance of nitrogen, nearly solar oxygen, and an overabundance of sodium. Three foreground K-giants have different C abundances (from a deficit to the solar), and Na (from the solar to an overabundance) as well as a solar-like O content. The foreground F7-8 V star No. 75 (CPD $-20^\circ 7218$) was revealed to be a Li-rich star, while the A7 V star No. 69 (BD $-20^\circ 5290$) has an anomalous deficit of CNO with overabundances of some α , r- and s-process elements.

Key words: Open clusters: radial velocities; Stars: abundance; GAIA parallaxes; Cepheids; B - giants; K-giants; individual: Collinder 394

АНОТАЦІЯ. Ми презентуємо результати спектроскопічних та фотометричних дослідів 20 об'єктів з розсіяного скупчення Collinder 394, яке вміщує цефеїду BB Sgr. Окрім цефеїди, ми

дослідили три К-гіганта, чотири В-гіганта та дванадцять В-А-Ф зір. Радіальні швидкості (RV), $v \sin i$, T_{eff} , $\log g$ отримані з використанням методів спектроскопічного фітінгу та моделей атмосфер. Ми вивели надлишки кольорів, почервоніння та справжні кольори цих зір, використовуючи їх T_{eff} та $\log g$ шляхом порівнювання з моделями атмосфер, особливо для гарячих зір. Власні рухи, RV та паралакси/відстані з GAIA DR2 2018 для цих зір дозволили встановити їх членство у скупченні та абсолютні магнітуди. Встановлено, що сім зір не належать до скупчення. Паралакси та почервоніння 13 справжніх членів скупчення дають відстані від 630 до 800 пс, хоча більшість з них (8 об'єктів) знаходяться на середній відстані у 657.7 ± 66.7 , та п'ять з цефеїдою можливо, належать до корони скупчення. Усі члени мають $[\text{Fe}/\text{H}]$ біля 0.1 dex. В-зоря ГП No. 76 (HD 174307) має мале значення проєкції швидкості оберт, та це дозволило встановити її хімічний склад для порівняння з BB Sgr. Її вміст CNO та Na близький до сонячного, тоді як цефеїда має дефіцит вуглецю, надлишок азоту, сонячний кисень та надлишок натрію. Три К-гіганти перед скупченням мають різний вміст вуглецю (від дефіциту до сонячного) та натрію (від сонячного до надлишку), та сонячний кисень. Зоря No. 75 (CPD $-20^\circ 7218$) (F7-8 V), яка теж є перед скупченням, виявилась з надлишком Li, тоді як зоря No. 69 (BD $-20^\circ 5290$) (A7 V) має аномальний дефіцит CNO з надлишком деяких елементів α , r- та s- процесів.

Ключові слова: Розсіяні скупчення, променеві швидкості, хімічний склад зір, паралакси GAIA, цефеїди, В-гіганти, К-гіганти, скупчення Collinder 394.

1. Introduction

The open cluster Collinder 394 is part of a double cluster with Collinder 393 (NGC 6716) (Turner & Prederos 1985). Being a loose grouping of B- and A-type stars, it contains a 6.^d64 Cepheid BB Sgr as a possible member of its corona. According to Turner & Prederos (1985), the earliest spectral type stars in it are B8, $E(B-V) = 0.25 \pm 0.01$, $V_0 - M_V = 9.04 \pm 0.08$, $d = 643 \pm 25$ pc, and an age near 6×10^7 yr. Collinder 394 has not been carefully studied spectroscopically except for BB Sgr. Therefore, the main goals of our investigation are as follows: 1) to measure the radial and rotational velocities of the cluster's stars, 2) to determine the atmospheric parameters, metallicities, CNO and Na abundances and compare the abundances of the objects of different spectral types, and 3) to determine the distances using GAIA DR2 parallaxes and RV data, and to check their membership in the cluster.

2. Observations

Our observations were taken at the 11 m SALT (Southern African Large Telescope) equipped with HRS (High Resolution Spectrograph). HRS is a dual-beam (3700-5500 & 5500-8900 Å) fiber-fed, white-pupil, échelle spectrograph, which uses VHP gratings as cross dispersers. We obtained one spectrum for each object using the *medium mode* with the spectral resolving power $R = 40000$, an average S/N of over 100, which is enough to reach our observational goals. These spectra will be used to derive the atmosphere parameters and chemical abundances for some elements of the open cluster members. The data were reduced using the *échelle* context in MIDAS. Also, the *feros* package developed for échelle data reduction from the Fiber-fed Extended Range Optical Spectrograph (FEROS) was used. Both FEROS and HRS provide very similar échelle data.

We used the DECH30 package (Galazutdinov 2007) designed to use the spectra in FITS format to measure the line depths and their equivalent widths. The radial and rotational velocities were measured by fitting of the observed spectra with models from Coelho (2014). The object IDs, magnitudes, spectral types, proper motions, parallaxes from the GAIA DR18 catalogue, measured radial and rotational velocities for each spectrum are given in Table 1.

3. Results and Analysis

3.1. Radial and rotational velocities, proper motions and parallaxes

As seen in Table 1, judging from proper motion, radial velocity and parallax measurements, seven objects are evident foreground or background stars. It should be noted that our results are consistent with those from other sources: $RV = 12.0 \text{ km s}^{-1}$ (Wilson & Joy 1950) for HD 124403; and $\langle RV \rangle = 11.35 \text{ km s}^{-1}$ (Lloyd-Evans 1968) for BB Sgr, respectively. According to Conrad et al. (2017), the cluster's mean radial velocity is $-1.9 \pm 6.5 \text{ km s}^{-1}$, and the majority of confident cluster members have close radial velocities.

As seen in Table 1, the Cepheid BB Sgr, three K-giants Nos. 21, 72, 74 and the F7 V star No. 75 have low $v \sin i$, while hot main-sequence (hereafter MS) stars are fast-rotating objects. It is very surprisingly to detect the MS B-star No. 76 with a low radial velocity projection.

3.2. Color-indices, color-excesses, reddenings, and atmospheric parameters

Turner & Prederos (1985) determined color-excesses, reddenings, and intrinsic colors for the cluster's ob-

jects using *UBVRI* color-indices. To improve these parameters, we have used their atmospheric parameters T_{eff} and $\log g$, determined with the model fitting method. Next, these estimates were performed for the $(U-B)_0$ and $(B-V)_0$ determinations for the hot B- and A-type stars using the Kurucz (1993) models from Bessel et al. (1998). For more evolved stars of *FGK* spectral types with a large number of narrow metallic absorption lines we have used the lines depth relation to derive T_{eff} (Kovtyukh 2007), and a Fe ionization balance to derive $\log g$. These estimates give an opportunity to determine corresponding $(U-B)_0$ and $(B-V)_0$ values for *FGK*-stars.

The described above results allowed us to determine the color-excesses, reddenings, and interstellar extinction. All these data are given in Table 2. At that we have used $(U-B)$ and $(B-V)$ color-indices from Turner & Prederos (1985). As seen from this table, the majority of hot stars have close reddening values in a range of $0.^m56 - 0.^m88$, except for the Be star No. 24 (HD 174652) and stars, which probably belong to the cluster's corona: HD 174403, Nos. 70 and 76, and BB Sgr ($0.^m97 - 1.^m19$). Our E_{B-V} values demonstrate an excellent agreement with photometrically determined ones from Turner & Prederos (1985) Table 1, except for the star No. 30. The foreground and background objects have very different parameters. Figure 1 represents a $T_{\text{eff}} - M_V$ diagram for the confident members of Collinder 394. As seen from the diagram, object No. 76 with a low rotation velocity projection is located in the middle of the cluster's MS, while the object No. 61 is located near the "turn-off" point. HD 174403, an eclipsing binary (Turner & Prederos 1983), was found at the horizontal branch. Its main component with a mass of $6 M_{\odot}$ could be a first-crossing Cepheid instability strip object.

3.3. Absolute magnitudes and distances

Table 3 contains the absolute magnitudes of the Collinder 394 objects derived from photometry by Turner & Prederos (1985) and those derived by us using the GAIA DR2 parallaxes and our T_{eff} and A_V data. As can be seen from the Table 3, the parallax-based M_V only for 8 objects determined as the confident cluster's members agree with those from Turner & Prederos (1985). Figure 2 represents a variable-extinction diagram for the cluster confident members only. We have obtained the mean distance modulus $(V_0 - M_V) = 9.09 \pm 0.21$ with the reddening law slope $R = A_V/E_{B-V} = 3.34 \pm 0.02$. Turner & Prederos (1985) estimated $R = 3.1 \pm 0.3$. Our estimate of $(V_0 - M_V)$ gives a distance of $d = 657.7 \pm 66.7$ pc, and with this value it turns out that Collinder 394 is located about 15 pc further away compared to the value from Turner & Prederos (1985). Four objects (Nos. 12, 27, 63, and 76) located at 760–824 pc could belong to the corona,

similar to BB Sgr, which has $M_V = -3.^m59 \pm 0.07$ and $d = 801 \pm 26.4$ pc, respectively.

Other objects from the list turned out to be either foreground or background stars – all three K-giants, and three MS A- and F- type stars.

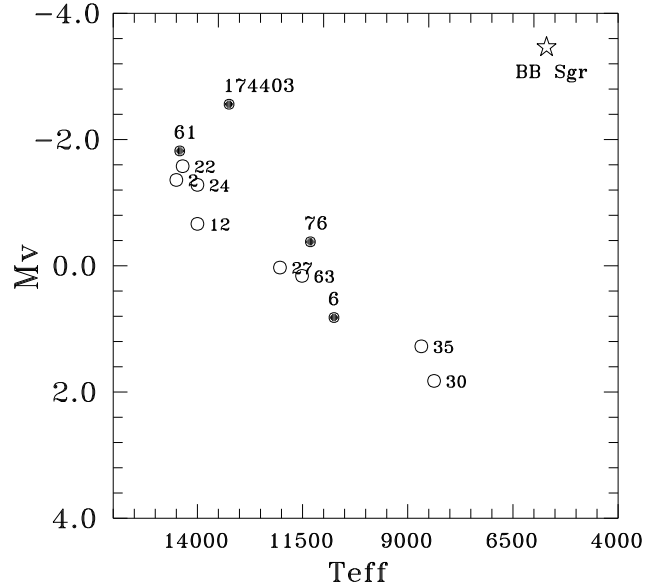


Figure 1: $T_{\text{eff}} - M_V$ diagram for the Collinder 394 confident members. Open circles show the MS stars, filled circles show the B-giants.

3.4. Chemical abundances

When the atmospheric parameters were derived, we used the VALD oscillator strengths (Kupka et al. 1999) and LTE model atmospheres from Castelli & Kurucz (2004) for determination of the element abundances. For that we have worked with stars with relatively low rotational velocity projections: BB Sgr, Nos. 21, 69, 72, 74, 75, and 76. As seen, only two of these objects are true cluster members, therefore the rest are foreground and background ones, respectively. Nevertheless the chemical abundances of each object from our list are of interest. Tables 4 and 5 present the results of our investigations. Since these objects have different evolutionary stages, we will discuss every star separately.

BB Sgr The Cepheid has a solar-like iron content, a carbon deficit, an overabundance of nitrogen and sodium, and a nearly solar oxygen abundance, i.e. typical for a yellow supergiant after the first dredge-up stage. All other elements have nearly solar abundances. Therefore, our results are close to those of Usenko et al. (2013) and Luck et al. (2006).

76 (HD 174307) This MS B-star, which is considered to be a Cepheid progenitor, demonstrates a solar CNO, Na, Fe, and other elements abundances with small overabundances of neon, argon, and sulphur,

Table 1: General data for the observed objects in Collinder 394 and derived RVs.

Object	V	Sp-type	μ_{α}	μ_{δ}	RV, km s ⁻¹	PLX (GAIA)	Membership
BB Sgr ¹	6.93	G0 Ib	+0.392	-5.078	+17.11±0.04	1.2485±0.0411	m
HD 174403	7.51	B8 II-III	-1.477	-5.987	+18.76±0.43	1.5011±0.0529	m
2 (HD 174723)	8.88	B8	-1.468	-5.838	+9.51±0.23	1.3703±0.0622	m
3 (CPD -20°7272)	11.19	B9?	-65.800	+6.600	+30.24±0.12		nm
6 (HD 174706)	10.30	B7-B8 II	-1.329	-5.268	+3.57±0.24	1.5783±0.0708	m
12 (HD 174685)	9.52	B8 V	-1.967	-6.206	+9.35±0.25	1.2743±0.0716	m
21 (CPD -20°7255)	10.45	K0 III?	+1.662	-12.445	-2.72±0.02	2.2489±0.0673	fg
22 (HD 174651)	8.47	B8 IV	-2.256	-6.227	+5.76±0.19	1.4318±0.0777	m
24 (HD 174652)	9.06	B9e	-1.417	-6.317	-0.78±1.10	1.3518±0.0612	m
27 (CPD -20°5300)	10.34	B7-B8?	-1.310	-5.728	+4.84±0.24	1.2135±0.0546	m
30 (CPD -20°7248)	11.56	AV	-2.052	-5.579	-4.40±0.09	1.5077±0.0487	m
35 (CPD -20°7240)	11.25	AV	-0.909	-5.493	+11.45±0.31	1.3115±0.0473	m
61 (HD 174594)	8.30	B5 III	-1.732	-6.284	+8.77±0.18	1.4439±0.0578	m
63 (HD 174538)	10.37	B9 III	-4.300	-6.800	+10.99±0.13	1.2839±0.0503	m
69 (BD -20°5290)	10.87	A7 V?	-0.115	-9.890	-44.24±0.04	2.4470±0.0439	fg
70 (GSC 06289-03051)	12.25	A2 V	-1.772	-4.033	+27.50±0.32	0.8821±0.0373	bg
72 (GSC 06289-03067)	11.59	K1 III?	-4.921	-11.509	-46.78±0.04	1.0858±0.0457	fg
74 (HD 174402)	9.27	K1/2 III?	-25.509	-43.853	-7.61±0.02	3.7919±0.0453	fg
75 (CPD -20°7218)	11.11	F7-8 V?	+9.694	-4.597	-22.94±0.04	4.7670±0.0357	fg
76 (HD 174307)	10.36	B8/9 II	-1.289	-6.078	+17.00±0.05	1.3155±0.0349	m

1 - Phase 0.^P624 according to Usenko et al. (2013); m - member; nm - non-member; fg - foreground object; bg - background object.

Table 2: Atmospheric parameters, rotational velocities, intrinsic colors, color-excesses, reddenings, and extinctions for the Collinder 394 objects.

Star	T_{eff}	log g	v sin i	(U-B) ₀	(B-V) ₀	E_{U-B}	E_{B-V}	A_V	R
BB Sgr ¹	5332±6	1.30±0.05	10.8±0.1	0.61	0.87	0.30	0.28	1.00	3.57
HD 174403	13245±165	3.49±0.01	198.7±1.4	-0.48	-0.13	0.22	0.29	0.97	3.33
2 (HD 174723)	14500±10	4.00±0.01	137.9±0.4	-0.54	-0.14	0.15	0.25	0.84	3.32
3 (CPD -20°7272)	10700±7	4.42±0.02	110.5±0.3	-0.16	-0.04	0.25	0.26	0.88	3.35
6 (HD 174706)	10752±10	4.32±0.02	132.8±1.3	-0.17	-0.05	0.20	0.26	0.87	3.35
12 (HD 174685)	14000±50	4.30±0.01	158.1±0.6	-0.49	-0.13	0.17	0.23	0.76	3.32
21 (CPD -20°7255)	4825±13	3.00±0.02	0.0±0.0	0.78	1.03	0.10	0.13	0.47	3.65
22 (HD 174651)	14350±77	4.00±0.01	223.3±0.6	-0.53	-0.14	0.22	0.25	0.84	3.32
24 (HD 174652)	14000±200	3.62±0.50	237.3±20.3	-0.53	-0.14	0.23	0.30	1.01	3.35
27 (CPD -20°5300)	12037±12	4.19±0.01	129.7±0.5	-0.32	-0.10	0.15	0.22	0.74	3.36
30 (CPD -20°7248)	8375±2	4.17±0.01	59.1±0.3	0.08	0.13	0.12	0.19	0.63	3.36
35 (CPD -20°7240)	8676±7	3.63±0.01	314.9±1.0	0.10	0.05	0.07	0.17	0.56	3.37
61 (HD 174594)	14418±19	3.78±0.01	155.7±0.6	-0.55	-0.15	0.17	0.26	0.84	3.29
63 (HD 174538)	11511±6	4.17±0.01	229.2±0.6	-0.26	-0.08	0.18	0.26	0.88	3.35
69 (BD -20°5290)	7705±5	3.50±0.01	1.9±0.2	0.19	0.16	0.31	0.34	1.17	3.40
70 (GSC 06289-03051)	9698±15	3.81±0.02	272.4±1.3	-0.40	-0.02	0.65	0.35	1.19	3.36
72 (GSC 06289-03067)	4683±12	2.70±0.02	0.1±0.0	0.93	1.10	0.38	0.27	0.99	3.68
74 (HD 174402)	4575±19	3.10±0.02	7.9±0.1	0.98	1.12	0.11	0.13	0.48	3.68
75 (CPD -20°7218)	6250±15	4.50±0.05	24.7±0.1	0.01	0.54	0.04	0.05	0.19	3.42
76 (HD 174307)	11313±13	3.87±0.01	0.5±0.1	-0.25	-0.09	0.19	0.35	1.17	3.35

1 - T_{eff} , log g, (U-B)₀ and (B-V)₀ for the phase 0.624 according to Usenko et al. (2013)

Table 3: Comparison between absolute magnitudes and distances, determined using GAIA DR2 parallaxes and photometric data.

Object	M_V (T&P85)	M_V (GAIA)	d (pc) (GAIA)
BB Sgr	-3.08±0.12	-3.59±0.07	800.96±26.37
HD 174403	-2.44±0.08	-2.56±0.00	666.18±23.48
2 (HD 174723)	-1.03±0.05	-1.36±0.10	729.77±33.13
3 (CPD -20°7272)	+1.36±0.08	+2.07±0.06	444.66±13.31
6 (HD 174706)	+0.44±0.08	+0.42±0.10	633.59±28.42
12 (HD 174685)	-0.27±0.07	-0.67±0.12	784.75±44.09
21 (CPD -20°7255)	-	+1.74±0.06	444.66±13.31
22 (HD 174651)	-1.35±0.08	-1.58±0.11	698.42±37.90
24 (HD 174652)	-0.95±0.08	-1.28±0.10	739.75±33.49
27 (CPD -20°5300)	+0.62±0.08	+0.02±0.10	824.06±37.08
30 (CPD -20°7248)	+1.48±0.08	+1.82±0.07	663.26±21.42
35 (CPD -20°7240)	+1.58±0.08	+1.58±0.08	762.49±27.50
61 (HD 174594)	-1.68±0.08	-1.82±0.09	692.57±27.72
63 (HD 174538)	+0.51±0.08	+0.16±0.08	778.88±30.51
69 (BD -20 5290)	+0.83±0.08	+1.64±0.04	408.66±7.33
70 (GSC 06289-03051)	+2.23±0.08	+0.79±0.09	1133.66±47.94
72 (GSC 06289-03067)	-	+0.78±0.09	920.98±38.76
74 (HD 174402)	-	+1.68±0.02	263.72±3.15
75 (CPD -20°7218)	-	+4.31±0.01	209.78±1.57
76 (HD 174307)	+0.22±0.08	-0.38±0.05	760.17±20.17

and a deficit of titanium.

69 (BD -20°5290) A MS A-star with a unique substantial CNO deficit, a deficit of Mg, Al, Si, Ca, Sc, Ti, a solar-like Fe, and an overabundance of r- and s-process elements.

21 (CPD -20°7255) An early K-giant, with an upper estimate of lithium content log A(Li)<0.4 dex. It has

a deficit of carbon, a small deficit of nitrogen and a close to solar abundance of oxygen and sodium. The rest of the elements show close to solar abundances except for a small overabundance of some s-process elements, an evident overabundance of K and Mn, and a small deficit of Rb.

72 (GSC 06289-03067) A colder K-giant has close to solar C and O abundances, a small overabundance of sodium and aluminum, the rest of the elements have a close to solar abundances, except for small overabundances of Si, S, Mn, and Eu.

74 (HD 174402) K-giant, that has solar abundances of C, O, and Na. The rest of the elements have abundances close to solar one, except for small overabundances of S, Sc, Sm, and Eu.

75 (CPD -20°7218) This F-type MS star is a lithium-rich object (see Fig. 3) with log A(Li) = 2.95. CNO and Na abundances are close to solar, but some elements, such as K, V, Zr, Pr, Sm, Eu and Gd, demonstrate evident overabundances.

Table 4: Chemical abundances for Collinder 394 objects. Part 1.

Element	BB Sgr			76 (HD 174307)			69 (BD -20°5290)				
	[E/H]	σ	NL	UAL13	LKA06	[E/H]	σ	NL	[E/H]	σ	NL
C I	-0.22	0.21	13	-0.21	-0.06				-1.18	0.13	9
C II						0.07	0.13	4			
N I	0.46	0.24	4	-	-	0.05	0.14	9	-1.45	0.18	6
O I	0.03	0.02	2	0.02	-0.13	-0.07	0.08	7	-0.92	0.12	3
Ne I						0.23	0.12	5			
Na I	0.26	0.10	2			-0.04	0.04	2	-0.02	0.19	3
Mg I	0.01	0.00	1	0.26	-	-0.02	0.12	3	-0.51	0.04	2
Mg II						-0.05	0.15	7			
Al I	0.25	0.12	5	0.45	0.15				-0.24	0.15	5
Al II						0.07	0.14	5			
Si I	0.17	0.11	16	0.25	0.14				-0.24	0.18	14
Si II	0.18	0.33	2	0.21		-0.02	0.15	15	0.18	0.21	2
S I	0.12	0.21	2	-0.05	-0.17				-0.13	0.21	3
S II						0.25	0.17	15			
K I									-0.04	0.00	1
Ar I						0.33	0.03	3			
Ca I	-0.02	0.11	3	-0.06	0.12	0.16	-	1	-0.67	0.08	5
Ca II						0.02	0.33	2			
Sc II	-0.07	0.18	2	-0.16	0.08	-0.17	0.21	3	-0.62	0.29	3
Ti I	-0.02	0.12	26	0.03	0.22				0.76	0.56	9
Ti II	-0.05	0.15	4	0.14		-0.54	0.13	10	-0.52	0.12	3
V I	-0.28	0.03	6	0.14	-0.10				0.91	0.05	2
V II	-0.26	0.02	2	-0.09		0.13	0.00	1	-0.10	0.00	1
Cr I	-0.12	0.14	16	0.12	0.09				-0.21	0.19	7
Cr II	0.23	0.14	6	0.08		-0.11	0.06	13	-0.04	0.16	5
Mn I	-0.00	0.06	5	0.06	-				-0.24	0.17	4
Mn II						0.24	0.03	4			
Fe I	0.06	0.09	185	0.07	0.08	-0.02	0.11	10	-0.02	0.08	117
Fe II	0.05	0.07	10	0.07	0.08	0.02	0.12	120	0.00	0.10	26
Co I	-0.10	0.10	7	-0.06	0.15				0.87	0.08	2
Ni I	-0.08	0.10	43	0.11	0.00				0.17	0.09	25
Ni II						-0.01	0.15	3			
Cu I	0.08	0.37	5	0.15	0.21				0.30	0.26	4
Zn I									0.72	0.11	3
Rb I	-0.13	0.00	1	-	-				1.21	0.00	1
Sr II						-0.10	0.37	2			
Y II	0.09	0.08	5	-0.04	-				0.53	0.10	4
Zr II	-0.04	0.14	2	0.20	-				0.47	0.18	2
La II	-0.05	0.14	4	0.06	0.22				0.55	0.04	2
Ce II	-0.11	0.09	7	-0.09	-0.09				0.66	0.12	6
Pr II	-0.22	0.20	5	-0.37	-				0.72	0.28	2
Nd II	-0.05	0.10	6	0.15	-0.03				0.66	0.19	6
Sm II	-0.12	0.09	4	0.12	-				0.62	0.03	3
Eu II	-0.09	0.08	3	0.18	0.04				1.44	0.93	3
Gd II	-0.30	0.00	1	-	-				-	-	-

4. Summary

1. According to the derived RV, color-indices, and parallaxes/distances only 13 of the 20 objects, which we have investigated, are confidently members of Collinder 394.
2. An overwhelming majority of the confident cluster members have high rotational velocity projections, except for star No. 76 (HD 174307) and the Cepheid BB Sgr. Five foreground objects, three K-giants and two MS stars, have low $v \sin i$ values.
3. We have revised color-excesses and reddenings for the objects that allowed us to refine their intrinsic colors, especially for the hot stars.
4. Atmospheric parameters of the hot stars were determined by fitting method, while parameters of the Cepheid, giants, and MS stars were determined exclusively by the method of atmosphere models.
5. The distances of the most cluster stars determined from the GAIA DR2 2018 parallaxes lie in a range of 633–740 pc that roughly corresponds to the mean cluster distance determined earlier by Turner & Prederos (1985) using photometry. Four MS stars and the Cepheid lie in a range of 760–824 pc, and they could belong to the cluster's corona.

6. Star No. 76 located in the middle of clusters' MS, star No. 61 is located near the "turn-off" point, and HD 174403 is located at the horizontal branch.
7. The abundances of carbon, nitrogen, oxygen, and sodium in the hot star No. 76 turned out to be close to the solar ones, while there is a deficit of C and an overabundance of N and Na with a solar-like O abundance for the cool variable supergiant BB Sgr. This fact indicates that the Cepheid have already passed through the "first dredge-up" stage.
8. The foreground A-type MS star No. 69 has an anomalous substantial deficit of CNO elements with a deficit of some α - and an overabundance of r- and s-process elements.
9. The foreground object an F7-8 MS star No. 75 is a lithium-rich object.

References

- Bessell M.S., Castelli F. & Plez B.: 1998, *A&A*, **333**, 231.
- Castelli F. & Kurucz R.L.: 2004, *arXiv: astro-ph/0405087*.
- Coelho P.R.T.: 2014, *MNRAS*, **440**, 1027.
- Conrad C. et al.: 2017, *A&A*, **600**, 106.
- GAIA DR2 2018, *CDS/ADS Collection of Electronic Catalogues*, **1345**, 0.

Table 5: Chemical abundances for Collinder 394 objects. Part 2.

Element	21 (CPD -20° 7255)			72 (GSC 06289-03067)			74 (HD 174402)			75 (CPD -20° 7218)		
	[E]/[H]	σ	NL	[E]/[H]	σ	NL	[E]/[H]	σ	NL	[E]/[H]	σ	NL
C I	-0.28	0.01	3	-0.10	0.18	4	0.02	0.05	2	-0.15	0.10	3
N I	-0.13	0.00	1	-	-	-	-	-	-	-0.02	0.12	2
O I	-0.07	0.20	3	-0.07	0.13	3	0.03	0.00	2	-0.02	0.01	2
Na I	-0.05	0.13	2	0.23	0.03	2	-0.12	0.15	3	-0.09	0.08	2
Mg I	0.09	0.15	2	-0.05	0.00	1	0.14	0.09	2	-0.05	0.00	1
Al I	0.06	0.08	5	0.31	0.12	6	0.16	0.11	6	0.01	0.08	5
Si I	0.13	0.10	15	0.28	0.10	14	0.24	0.09	10	0.02	0.13	12
Si II	0.41	0.09	2	-	-	-	-	-	-	0.25	0.06	2
S I	0.09	0.06	2	0.26	0.00	1	0.46	0.00	1	0.16	0.10	2
K I	0.21	0.00	1	0.11	0.00	1	0.10	0.09	2	0.47	0.00	1
Ca I	-0.01	0.14	8	-0.13	0.14	6	-0.09	0.07	7	-0.01	0.18	5
Sc II	0.10	0.08	5	0.12	0.08	5	0.47	0.08	5	0.89	0.00	1
Ti I	0.04	0.21	23	0.21	0.24	25	0.07	0.33	23	-0.01	0.11	4
Ti II	0.19	0.17	5	0.18	0.30	5	0.22	0.21	2	-0.25	0.06	3
V I	0.04	0.15	6	0.07	0.17	5	0.16	0.05	3	0.52	0.00	1
V II	0.07	0.11	3	0.27	0.13	4	0.31	0.10	3	0.47	0.00	1
Cr I	-0.15	0.08	17	-0.11	0.09	16	-0.20	0.09	18	-0.12	0.21	8
Cr II	0.05	0.05	6	-	-	-	-	-	-	0.18	0.19	5
Mn I	0.49	0.10	5	0.66	0.23	3	0.24	0.12	2	-0.10	0.13	6
Fe I	0.12	0.12	232	0.16	0.14	212	0.12	0.12	190	0.06	0.15	172
Fe II	0.10	0.10	25	0.17	0.12	15	0.11	0.09	2	0.07	0.14	13
Co I	0.02	0.06	6	0.35	0.15	8	0.24	0.19	5	0.20	0.06	2
Ni I	0.03	0.06	43	0.18	0.12	47	0.13	0.10	43	-0.05	0.17	31
Cu I	-	-	-	-	-	-	-	-	-	0.04	0.37	5
Zn I	-	-	-	-	-	-	-	-	-	0.01	0.07	3
Rb I	-0.30	0.00	1	-0.10	0.00	-	-0.01	0.00	1	-	-	-
Y II	-0.00	0.20	3	0.03	0.21	3	0.02	0.21	3	0.10	0.12	3
Zr II	-0.05	0.07	2	0.01	0.02	2	0.26	0.20	3	0.51	0.00	1
La II	0.10	0.05	4	0.22	0.19	6	0.20	0.14	4	0.05	0.00	1
Ce II	-0.09	0.09	3	-0.01	0.07	3	0.09	0.11	7	-0.20	0.35	2
Pr II	-0.01	0.19	4	0.04	0.20	4	0.10	0.24	4	1.03	0.00	1
Nd II	0.29	0.07	6	0.09	0.14	5	0.30	0.18	5	0.24	0.00	1
Sm II	0.16	0.06	3	0.19	0.13	3	0.44	0.11	4	1.67	0.00	1
Eu II	0.32	0.09	3	0.41	0.04	2	0.58	0.10	3	0.70	0.00	1
Gd II	0.13	0.00	1	-	-	-	0.26	0.00	1	2.44	0.00	1

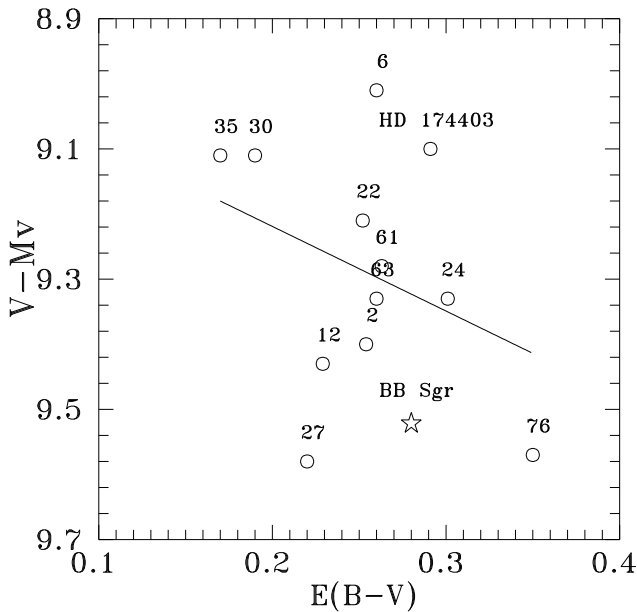
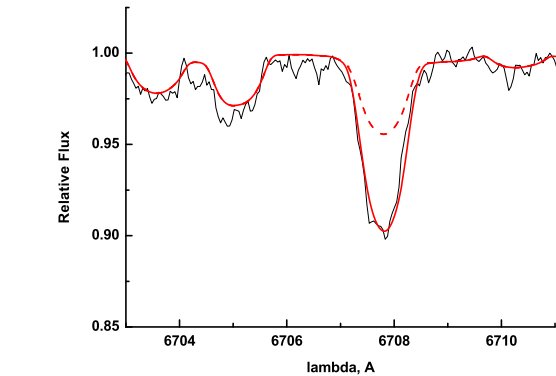


Figure 2: Variable-extinction diagram for confident Collinder 394 members.

Galazutdinov G.A.: 2007, <http://gazinur.com/DECH-software.html>.Kovtuykh V.V.: 2007, *MNRAS*, **378**, 617.Kupka F., Piskunov N.E., Ryabchikova T.A., Stempels H.S., Weiss W.W.: 1999, *A&A*, **138**, 119.Kurucz R.L.: 1993, *CD-ROM No. 23*.Figure 3: Li I 6707 Å absorption line in star 75 (CPD -20° 7218) atmosphere and its approximation by synth ($R = 40000$, $v \sin i = 25 \text{ km s}^{-1}$); $\log A(\text{Li}) = 2.5$ (dashed line) and 2.95 (solid line).Lloyd-Evans, T.: 1968, *MNRAS*, **141**, 109.Turner D.G. & Prederos M.: 1983, *IBVS*, **2263**, 1.Turner D.G. & Prederos M.: 1985, *AJ*, **90**, 1231.Usenko I.A., Kniazev A.Yu., Berdnikov L.N., Kravtsov V.V. & Fokin A.B.: 2013, *Astr. Lett.*, **39**, 432.Wilson R.E. & Joy A.: 1950, *ApJ*, **111**, 221.

RADIOASTRONOMY

DOI:<http://dx.doi.org/10.18524/1810-4215.2019.32.181773>FADING OF THE CONTINUUM OF NOISE STORMS IN THE
DECAMETER RANGE RELATED TO CME

E.A. Isaeva

Institute of Radio astronomy of NAS of Ukraine, isaevaode@gmail.com

ABSTRACT. In this paper, we studied the incomprehensible fading of a continuum of noise storms and type IV continual bursts in the decameter range, coinciding in time with coronal mass ejections (CMEs) for solar proton events (SPE). A comparative analysis showed that about 60% of the CMEs are accompanied by the fading of the continuum of noise storms and type IV continual bursts in the range of 25-30 MHz. It is shown that the fading of the continuum of a noise storm associated with a CME is distinguished by the intensity and duration of fading, as well as the width of the fading band and the frequency at which the maximum fading depth is observed. Moreover, detailed studies have shown that, against the background of a general decline in the radiation flux, a fine temporal structure at adjacent frequencies remains. This may indicate that the radiation is shielded by an external region in the path of radiation propagation. It can be a cold and dense cloud of the CME itself or absorption in the ionosphere. Absorption at low frequencies in the Earth's ionosphere is quite possible, since the x-ray and ultraviolet radiation of the flare can cause additional short-term ionization. In this regard, studies have been conducted on the relationship of the fading of the continuum of noise storms with x-ray flares. A comparative analysis showed that there is a fairly strong relationship between the integral flux and the effective duration of x-ray flares with the integral flux and the effective duration of the decrease in the continuum of noise storms, respectively. Moreover, the relationship between the effective durations is slightly higher, where the correlation coefficient between the studied values is ≈ 0.71 . It was also shown that short-term impulse fading is associated with impulse x-ray flares, and long-term with gradual long-term x-ray flares. It was noted above that absorption can also occur in the body of the CME itself, therefore, the relationship between the parameters for lowering the continuum of noise storms at a given frequency and the speed of the CME was investigated. A comparative analysis showed that there is a fairly strong relationship between the maximum fading depth and the CME speed, where the correlation coefficient between the studied values is ≈ 0.65 .

АНОТАЦІЯ. У даній роботі досліджені незрозумілі завмирання континууму шумових бур і континуальних сплесків IV типу в декаметровому діапазоні, які збігаються у часі з корональними викидами маси (КВМ) для сонячних протонних подій (СПП). Порівняльний аналіз показав, що близько 60% КВМ супровод-

жуються завмиранням континууму шумових бур і континуальних сплесків IV типу в діапазоні 25-30 МГц. Показано, що завмирання континууму шумових бур, пов'язані з КВМ, відрізняються інтенсивністю і тривалістю завмирання, а також шириною смуги завмирання і частотою на якій спостерігається максимальна глибина завмирання. Більш того, детальні дослідження показали, що на тлі загального спаду потоку радіовипромінювання зберігається тонка тимчасова структура на сусідніх частотах. Це може вказувати на те, що випромінювання екранується зовнішньої областю на шляху поширення випромінювання. Це може бути холодна і щільна хмара самого КВМ або ж поглинання в іоносфері. Поглинання на низьких частотах в іоносфері Землі цілком можливо, так як рентгенівське і ультрафіолетове випромінювання спалаху може викликати додаткову короточасну іонізацію. У зв'язку з цим були проведені дослідження зв'язку завмирання континууму шумових бур з рентгенівськими спалахами. Порівняльний аналіз показав, що існує досить сильний зв'язок інтегрального потоку і ефективної тривалості рентгенівських спалахів з інтегральним потоком і ефективною тривалістю зниження континууму шумових бур, відповідно. Причому, зв'язок між ефективними тривалостями трохи вище, де коефіцієнт кореляції між досліджуваними величинами ≈ 0.71 . Також було показано, що короточасні імпульсні завмирання пов'язані з імпульсними рентгенівськими спалахами, а тривалі з поступовими тривалими рентгенівськими спалахами. Вище зазначалося, що поглинання може відбуватися і в тілі самого КВМ, тому бул досліджен зв'язок між параметрами зниження континууму шумових бур на даній частоті і швидкістю КВМ. Порівняльний аналіз показав, що існує досить сильний зв'язок між максимальною глибиною завмирання і швидкістю КВМ, де коефіцієнт кореляції між досліджуваними величинами ≈ 0.65 .

Keywords: speed of the CME, fading continuum of noise storms, integral flux.

1. Introduction

The interest in coronal mass ejections is due to their high geoeffectiveness.

Broadband studies in the radio range showed that most of the CME formation events are accompanied by sporadic phenomena in the radio range (about 80% of the total number of cases). In 50% of cases, the phenomena in the radio band

preceding the registration of the CME are broadband. At the same time, it was shown that CMEs that are not accompanied by broadband phenomena in the radio range are ejections with a small angular width $<40^\circ$ and an average ejections velocity of not more than 700 km/s.

A generalization of the observational data in the radio range indicates that at the stage of CME formation in the meter-decameter bands, an increase in the continuum of noise storms with characteristic quasiperiodic oscillations is observed until the noise storms completely fade before the CME exit (Durasova et al., 1999, 2002). In the centimeter-decimeter ranges, at the stage of the CME formation, an increase in the microwave radiation intensity is observed, as well as powerful bursts of the GRF type with characteristic temporal fluctuations in the flux intensity with periods > 20 minutes, and short-period fluctuations in the flux intensity are observed immediately before the CME output, for 10-15 minutes with periods ranging from 6-22 seconds (Grechnev, 2003; Fridman & Sheiner, 2008).

It should also be noted that there is a strong connection between CMEs and broadband continual type IV bursts. It was shown in (Isaeva & Tsap, 2017) that there is a strong relationship between the CME velocity and the integral flux of microwave bursts (μ -bursts) for proton events. Moreover, the relationship between the speed of the CME and the integral flux of type IV continual bursts largely depends on the frequency of the continual radio burst. With a decrease in the frequency of radio emission of continual bursts, the relationship between the CME velocity and the integral flux of continual bursts sharply decreases and is practically absent already in the meter-decameter wavelength ranges.

2. Initial data and research results

The studied sample contains 112 solar proton events (SPE) for the period from 24-11-2000 to 23-07-2016 years, accompanied by CME. Of 112 CME events, 67 ($\approx 60\%$) were accompanied by the fading of a continuum of noise storms and type IV continual bursts in the decameter range at frequencies of 25-30 MHz.

For analysis, we used original recordings of the dynamic spectrums in the range of 25-180 MHz with Solar Radio Spectrograph (SRS) (<http://www.ngdc.noaa.gov/stp/space-weather/solar-data/solar-features/solar-radio/rstn-spectral/>), CME data (SOHO/LASCO CME CATALOG), list of proton events (<ftp://ftp.swpc.noaa.gov/pub/indices/SPE.txt>), original recordings of the x-ray radiation of the Sun in the range of 1-8 Å and the intensity of the proton flux I_p with an energy of $E_p > 1-100$ MeV according to GOES (https://satdat.ngdc.noaa.gov/sem/goes/data/new_avg/).

A comparative analysis showed that fading of noise storms is characterized by the frequency band width Δf , maximum intensity (depth) F_{max} , duration d and frequency f_{max} at which the maximum fading depth is observed. For most events, fading noise storms are observed in a narrow frequency band Δf from 125 kHz to 2 MHz. For most events, the maximum intensity (depth) of fading F_{max} is observed in the frequency region $f_{max} \approx 27$ MHz. In Figures 1 a) and b) show examples of the attenuation of the continuum of noise storms and type IV continual bursts at fixed frequencies taken from the original recordings of the dynamic

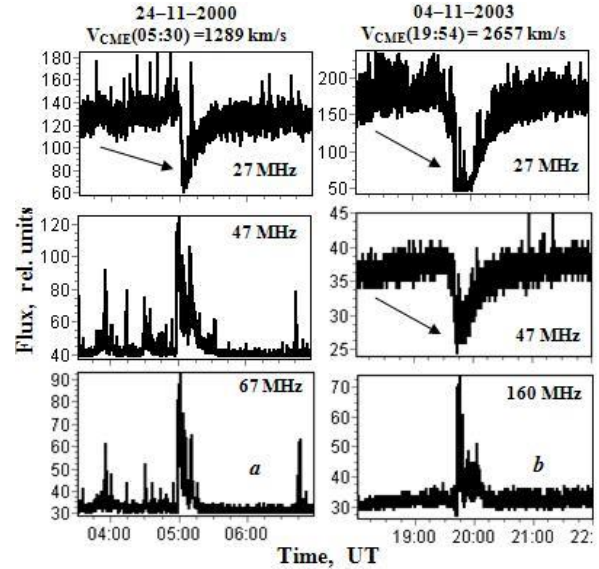


Figure 1: Examples of fading of a continuum of noise storms and continual bursts associated with a CME.

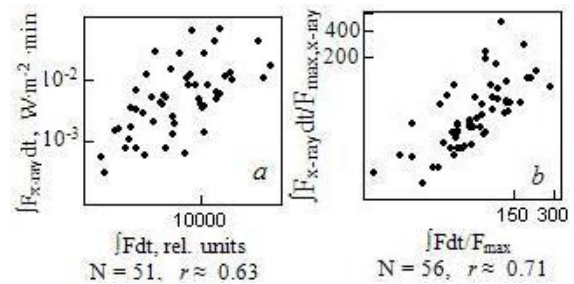


Figure 2: The relationship between the parameters of the fading continuum of noise storms and the parameters of x-ray bursts.

spectrum from Solar Radio Spectrograph. The effect of fading noise storms is shown by black arrows. Above the figures, the date, time of registration and speed of the CME are indicated. It was noted above that for most events, the effect of fading noise storms is observed in a narrow frequency band Δf from 125 kHz to 2 MHz. However, for some events, fading can be observed in the band 40-60 MHz, for example, as for the event 04-11-2003 (see Figure 1 b).

It is interesting that, against the background of a general decrease in the flux, the fine temporal structure is preserved (it can be seen from a comparison with the fine temporal structure at neighboring frequencies in Figure 1). This may indicate that the radiation is shielded by an external region in the path of radiation propagation. It can be a cold and dense cloud of the CME itself or absorption in the ionosphere. Absorption at low frequencies in the Earth's ionosphere is quite possible, since the x-ray and ultraviolet radiation of flares can cause additional short-term ionization. In connection with these, studies were conducted of the relationship between the parameters of fading noise storms at a frequency of 26.875 MHz and the parameters of x-ray bursts in the range of 1-8 Å.

A comparative analysis that there is a fairly strong relationship between the integral flux of lowering the continuum of noise storms $[F dt]$ and the integral flux of x-ray bursts $[F_x]$.

$_{ray}dt$ (see Figure 2 a), as well as between the effective duration of the decrease in the continuum of noise storms $\int Fdt/F_{max}$ and the effective duration of x-ray bursts $\int F_{x-ray}dt/F_{max,x-ray}$ (see Figure 2 b). Moreover, the relationship between $\int Fdt/F_{max}$ and $F_{x-ray}dt/F_{max,x-ray}$ is much higher, where the correlation coefficient r between the studied values is ≈ 0.71 . Additional studies have shown that there is a definite relationship between the duration of fading noise storms d and the duration of x-ray bursts and continual microwave bursts. It was also shown that short-term impulse fading is associated with impulse x-ray flares, and long-term with gradual long-term x-ray flares.

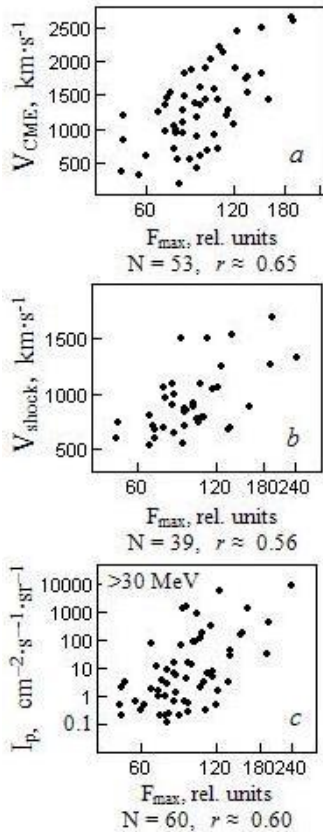


Figure 3: Relation of the intensity of the fading of the continuum of noise storms to the CME speed V_{CME} , the shock wave velocity V_{shock} , and the proton flux intensity I_p .

It was noted above that absorption at low frequencies can also occur in the body of the CME itself. In this regard, studies have been conducted on the relationship between the parameters of fading noise storms and the speed of the CME V_{CME} . A comparative analysis showed that the strongest relationship is observed between the CME speed V_{CME} and the maximum fading intensity (depth) F_{max} , where the correlation coefficient r between the studied values is ≈ 0.65 (see Figure 3 a). In this paper, we are talking about solar proton events, which, as you know, are often accompanied not only by proton fluxes, but also by coronal shock waves (CSW). A comparative analysis showed that there is a definite relationship between the fading intensity of noise storms F_{max} and the velocity of coronal shock waves V_{shock} (see Figure 3 b), where the correlation coefficient r between the studied values is ≈ 0.56 . It should also be noted that

there is a fairly strong relationship between the fading depth of noise storms and the proton flux intensity I_p with an energy of $E_p > 30$ MeV (see Figure 3 c).

3. Discussion of the results

It is known that for thermal braking radiation in the CME body or in the ionosphere, the decrease in intensity should be broadband toward low frequencies. And in this case, for most events, the decline in intensity occurs in a narrow band, decreasing not only at higher frequencies, but also at lower frequencies. In this regard, this effect cannot be associated with absorption in the CME body or in the ionosphere.

A possible alternative explanation, according to V.F. Melnikov, there may be the following effect. Usually, short-term decreases in the intensity of meter radio emission in type IV bursts are associated with a breakdown of the cone instability, which is the cause of the continual coherent radiation. The failure is caused by the injection of a new portion of energetic electrons that fill the loss cone, i.e., lead to a sharp decrease in the transverse anisotropy of the electrons trapped in the magnetic trap. Perhaps this effect works in this case. But here, too, there is a certain problem associated with narrowband. Why is the fading band so narrow? Indeed, despite the fact that radio emission in type IV bursts is coherent, i.e., locally narrow-band, a broadband of meter-decameter radiation is generally observed. This is due to the large extent and longitudinal heterogeneity of the trap (magnetic loop). The way out of the contradiction can be this: the instability breaks down only in a relatively small quasihomogeneous part of the trap, while radiation continues to be generated in other parts of the trap.

Acknowledgments. The author thanks V.F. Melnikov for discussion and assistance in interpreting the results.

References

Durasova M., Fridman V., Sheiner O.: 1999, in *Proc. 9th European Meeting on Solar Physics* (ESA,SP-448, December 1999), 972.
 Durasova M., Fridman V., Sheiner O.: 2002, in *Proc. SOLSPA* (ESA SP-477, February 2002), 373.
 Fridman V., Sheiner O.: 2008, *Solnechno-zemnyaya fizika*, № 12, 1, 79.
 Grechnev V.: 2003, *Astrophys. J.*, **588**, 1163.
 Isaeva E., Tsap Yu.: 2017, *Odessa Astron. Publ.*, **30**, 222.
 Sheiner O., Fridman V.: 2005, *Cambridge University Press*, 233.
 Sheiner O., Fridman V.: 2005, *Cambridge University Press*, 235.

DOI:<http://dx.doi.org/10.18524/1810-4215.2019.32.181776>

MULTI-FREQUENCY RADIO INTERFEROMETRY ALGORITHM

Orlov V. V., Lytvynenko O. A., Galanin V. V.

URAN-4 Observatory of IRA NASU, Odessa, Ukraine, uran4@te.net.ua

ABSTRACT. This article is a continuation of the work published in (Orlov, 2018). A method of multi-frequency beamforming of a radio interferometer is proposed. The model diagram is presented, which consists of two antenna arrays, filters, receivers and a signal summing circuit. The model works as follows. The signals received by the antennas pass through the narrow-band filters of the receiving devices, which are tuned to certain frequencies, after which they are subjected to multiplicative processing and weighted summation with their coefficients.

In this work, model the system of a radio interferometer based on multi-frequency signal processing, and study the possibilities of minimizing the level of side lobes of the antenna pattern (AP). It is shown that a decrease in the level of side lobes is possible due to the expansion of the frequency range or the application of signal processing from several clusters (antenna arrays), due to their summation in the interferometer circuit. For the case of three bases of the interferometer, consisting of the same antenna arrays, the total AP is calculated. In this case, a significant reduction of the side lobes to the level of the side lobes of a single antenna array is achieved. Further optimization of the radiation pattern can be carried out by choosing the frequency ranges of the interferometers and weights when summing the signals.

The proposed method makes it possible to adapt the interferometer AP due to time processing in frequency channels. The choice of the frequency grid and weighted multi-frequency signal processing provide a decrease in the level of side lobes and increase the resolution of the instruments. The application of the proposed algorithms will reduce the confusion effect from closely spaced radio sources. The computational possibilities of weighted processing are realized in real time, taking into account the rotation of the Earth, scanning the AP and angular arrangement of radio sources.

Keywords: antenna array, multiplicative processing, optimization, antenna pattern.

АНОТАЦІЯ. Ця стаття є продовженням опублікованої роботи (Орлов та ін., 2018). Запропоновано метод многочастотного формування діаграми спрямованості (ДС) радіоінтерферометра. Представлена схема моделі, яка складається з двох антенних решіток, фільтрів, приймальних пристроїв і схеми підсумовування сигналів. Працює модель наступним чином. Прийняті антенами сигнали проходять через вузькосмугові фільтри приймальних пристроїв, які налаштовані на певні частоти, після

чого піддаються мультипликативній обробці і вагового підсумовування зі своїми коефіцієнтами.

У роботі проводиться моделювання системи радіоінтерферометра на основі многочастотної обробки сигналів, досліджуються можливості мінімізації рівня бічних пелюстків ДС. Показано, що зменшення рівня бічних пелюсток можливо за рахунок розширення діапазону частот або застосування обробки сигналів від декількох кластерів (антенних решіток), за рахунок їх підсумовування в схемі інтерферометра. Для випадку трьох баз інтерферометра, що складається з однакових антенних решіток, розрахована сумарна ДС. В цьому випадку, досягається значне зниження бічних пелюсток до рівня бічних пелюсток одиночної антеною решітки. Подальша оптимізація ДС може здійснюватися вибором діапазонів частот інтерферометрів і вагових коефіцієнтів при підсумовуванні сигналів.

Запропонований метод дозволяє адаптувати ДС інтерферометрів за рахунок тимчасової обробки в частотних каналах. Вибір сітки частот і вагова многочастотна обробка сигналів забезпечують зниження рівня бічних пелюсток, підвищення роздільної здатності інструментів. Застосування запропонованих алгоритмів дозволить зменшити ефект сплутування від близько розташованих радіоджерел. Обчислювальні можливості ваговій обробки можуть бути реалізовані в реальному часі з урахуванням обертання Землі, сканування ДС і кутового розташування радіоджерел.

Ключові слова: антена решітка, радіоінтерферометр, оптимізація, діаграма спрямованості.

1. Introduction

The development of the low-frequency range in radio astronomy is currently accompanied by a sharp increase in the number of new radio telescopes with large antenna arrays (LOFAR, LWA, GURT, NenuFAR, etc.). The purpose of these changes is to improving the quality of resolution when evaluating the parameters of space radio sources.

The desire for the effective use of decimeter and low-frequency meter wavelength ranges in radio astronomy leads to the need to improve hardware and algorithmic means. These improvements are necessary for: increasing the sample size of the signal when evaluating the parameters of celestial bodies, increasing noise immunity,

as well as improving the quality of the antenna pattern (AP) with limited aperture sizes (Megn, 1997; Konovalenko, 2016). An effective way to increase the sample size of a signal is the property of the broadband signal, due to which, the accumulation of samples can be carried out at several frequencies (Megn, 2000; Shaw, 1965; Shepelev et al., 2017; Shepelev et al., 2019). In this case, it is necessary to take into account the dependence of the shape of the AP on the carrier frequency, especially the width of the main and side lobes. The development of digital technology for multi-frequency signal reception in the range of 10-200 MHz also creates the prerequisites for the application of optimal algorithms for the formation of AP in real time without changing the apertures of the antennas of the radio interferometer.

This article proposes algorithms for optimizing AP by processing signals at several frequencies. The system of a radio interferometer is simulated on the basis of multi-frequency signal processing, explores the possibility of minimizing the level of the side lobes of the AP.

2. The model of the studied system

The system under study based on multiplicative signal processing (fig. 1) consists of 2 antenna arrays AP_1, AP_2 , the signals from whose outputs pass through Φ_{1l}, Φ_{2l} narrow-band filters $l = 1, \dots, L$ of receivers tuned to ω_l frequencies, then subjected to MP and weighted summation with coefficients g_l .

The model of a monochromatic point source of a signal from the outputs of a pair of filters of the l frequency channel of two omnidirectional antennas can be represented as

$$\begin{aligned} U_{1l}(t) &= U \exp\{j(\omega_l(t+t_0) + \varphi_{0l})\} = \\ &= U \exp\{j(\omega_l t + \varphi_{0l} + \psi_l)\} \\ U_{2l}(t) &= U \exp\{j(\omega_l(t-t_0) + \varphi_{0l})\} = \\ &= U \exp\{j(\omega_l t + \varphi_{0l} - \psi_l)\} \end{aligned} \quad (1)$$

where t_0 – the delay time of arrival of the wave front along the aperture of MP, the size of which $d = \lambda/2 = \pi v/\omega$ is

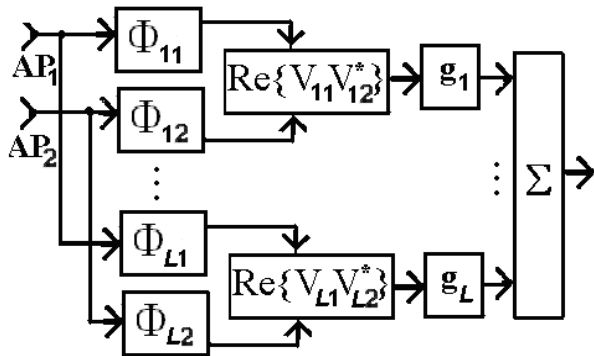


Figure 1: Radiometry system with multi-frequency processing

matched with the wavelength λ , main (first) carrier frequency $\omega = \omega_1$, speed of wave propagation v , $\psi_l = \omega_l t_0 = \pi(\omega_l/\omega)\cos\varphi$ – the phase of spatial delay of the wave front arrival at the frequency ω_l , φ – the angle of the wave front arrival relative to the normal of AP base, φ_0 – the initial phase. It is assumed that in filters Φ_{1l}, Φ_{2l} , $l = 1, \dots, L$, the amplitude, phase and mutual frequency distortions are eliminated to the accuracy of power leveling in frequency channels $P = P_l = \langle U_{1l} * U_{2l} \rangle$, $l = 1, \dots, L$, where $\langle \rangle$ are the averaging symbols of the process over time.

In (Orlov, 2018), a method for optimizing the weight processing of this model for radiometry is considered and it is shown that the level of side lobes can be reduced by more than 15 dB with a slight expansion of the main lobe of the antenna pattern.

3. Antenna pattern optimization of the multi-frequency radio interferometer

The possibilities of lowering the level of the side lobes of the AP are investigated. The frequency response is formed by summing the signals from the outputs of the frequency channels of the interferometer in the frequency separation range (narrow, compared with the previous algorithm), with a deviation from the reference frequency. The frequency response is formed by summing the signals from the outputs of the frequency channels of the interferometer in the frequency separation range (narrow, compared with the previous algorithm), with a deviation from the reference frequency $\omega = \omega_1$ within $(1 \dots 1.5) \omega$. The output signals of adjacent equidistant N – element antenna arrays 1 and 2 at an arbitrary carrier frequency, taking into account (1), have the form

$$\begin{aligned} U_{1l}(t) &= \sum_{i=1}^N U \exp\{j[\omega_l(t+t_0(i-1)) + \varphi_{0l}]\} = \\ &= \sum_{i=1}^N U \exp\{j(\omega_l t + \varphi_{0l} + (i-1)\psi_l)\} = \\ &= \frac{U \sin(N\psi_l/2)}{\sin(\psi_l/2)} \exp\{j(\omega_l t + \varphi_{0l} + (N-1)\psi_l/2)\} \\ U_{2l}(t) &= \frac{U \sin(N\psi_l/2)}{\sin(\psi_l/2)} \exp\{j(\omega_l t + \varphi_{0l} - (N-1)\psi_l/2)\}, \end{aligned} \quad (2)$$

where is $\psi_l = \omega_l t_0 = \pi(\omega_l/\omega)\sin\varphi$ – the phase of the spatial delay of the arrival of the wave front at a frequency ω_l , φ – is the angle of arrival of the wave front relative to the normal to the AP, taking values in the interval $[-\pi/2, \pi/2]$. Then the output signal after summing the responses of the frequency channels is determined

$$\begin{aligned} U_{out} &= \text{Re}\{U_{1,l} U_{2,l}^*\} = \\ &= U^2 \sum_{l=1}^L g_l \left(\frac{\sin(N\psi_l/2)}{\sin(\psi_l/2)} \right)^2 \cos\{\psi_l(N-1)\} \end{aligned} \quad (3)$$

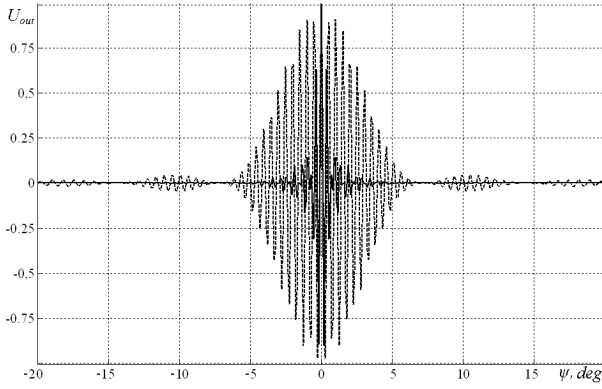


Figure 2: AP of the interferometer at one frequency and with averaging in the frequency range.

The output signal of equidistant N -element antenna arrays 1 and 2 (spaced a distance which is M times more than the size of each antenna array) at an arbitrary carrier frequency, taking into account (1) - (3), has the form

$$U_{out} = \text{Re}\{U_{1,l}U_{2,l}^*\} = U^2 \sum_{l=1}^L g_l \left(\frac{\sin(N\psi_l/2)}{\sin(\psi_l/2)} \right)^2 \cos\{\psi_l M(N-1)\} \quad (4)$$

The formation of broadband AP is carried out by summing the signals from the outputs of the frequency channels (4), i.e. averaging over a frequency range from ω_1 to ω_2 with weighted constants $G^T = [1,1,...1]/L$. Averaging is applied in the uniform grid of the frequency range $\omega_L/\omega_1=1,1$, $L=100$.

In Fig. 2 shows the radiation pattern of a radio interferometer consisting of two $N=16$ elementary antenna arrays. The base between them is $M=100$ times larger than the size of one antenna array. The dashed curve represent narrow-band AP at the same frequency, the full curve represent broadband AP. From the analysis of Fig. 2 it follows that a decrease in the level of side lobes (compared with narrow-band AP) is observed as they move away from the main lobe. At the same time, within 0.1 of the width of the main lobe of the antenna array (Fig. 3, expanded scale), the side lobes practically do not decrease - the first positive side lobe is -0.6 from the main. A decrease in their level is possible due to the expansion of the frequency range or the use of processing signals from several clusters (antenna arrays), for example, by summing these signals in an interferometer.

For the case of three bases of interferometers with sizes $M_1=100$; $M_2=125$; $M_3=150$ calculated the total DN. The calculation was carried out in accordance with (4) and taking into account the same antenna arrays.

$$U_{out} = \sum_{k=1}^3 \sum_{l=1}^L g_l \left(\frac{\sin(N\psi_l/2)}{\sin(\psi_l/2)} \right)^2 \cos\{\psi_l M_k(N-1)\}. \quad (5)$$

Fig. 4 shows a fragment of the total AP. It shows a decrease in the side lobes to the level of the side lobes of a single antenna array used in the interferometer. Further optimization of the radiation pattern is carried out by choosing the frequency ranges of interferometers and weighting factors when summing the signals.

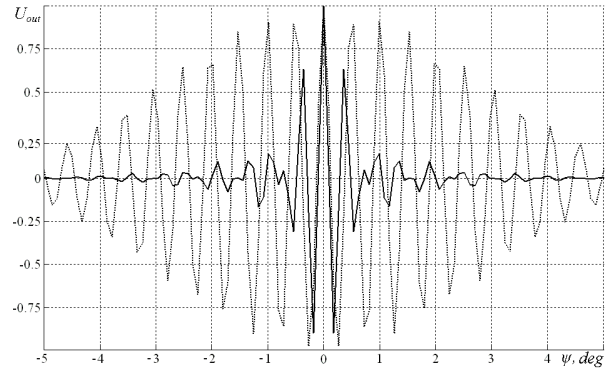


Figure 3: AP of the interferometer at the same frequency and when averaging in the frequency range (expanded scale).

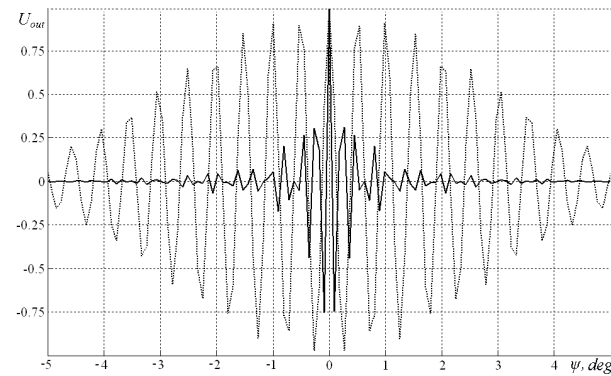


Figure 4: The total AP when summing the signals from the outputs of 3 interferometers (expanded scale).

4. Conclusion

The proposed approach extends the capabilities of radio interferometry in the formation of AP due to temporary processing in frequency channels. Due to weighted processing, the resolution of interferometers is increased, the confusion effect is reduced when receiving signals from closely located radio sources. In general, the choice of the frequency grid and weighted multi-frequency signal processing provide a decrease in the level of side lobes, increase the resolution, and also reduce the influence of interference.

The computational capabilities of weighted processing are real-time, taking into account the rotation of the Earth, scanning the beam and the angular arrangement of radio sources...The computational capabilities of weighted processing may be carry out at real-time, taking into account the rotation of the Earth, beam scanning and the angular arrangement of radio sources.

References

- Konovalenko A. et al.: 2016, *Radio phys. Radio astron.*, **21**, 2, 83.
- Megn A., Braude S., et al.: 1997, *Radio phys. radio astron.*, **2**, 4, 385.
- Megn A, Braude S.: 2000, *Radio phys. radio astron.*, **5**, 1, 5.
- Orlov V.V. et al.: 2018, *Odessa Astron. Publ.*, **31**, 137.
- Shepelev V.A. et al.: 2017, *Radio phys. radio astron.*, **22**, 4, 247.
- Shepelev V.A., et al.: 2019, 6th Gamow International Conference in Odessa: "New Trends in Cosmology, Astrophysics and HEP after Gamow" and 19th Gamow Summer School: "Astronomy and beyond: Astrophysics, Cosmology, Radioastronomy and Astrobiology", August 2019, Odessa, Program and Abstracts, 33.
- Shaw E., Davis D.: 1965, *Foreign Radio Electronics*, **11**, 103.

DOI: <http://dx.doi.org/10.18524/1810-4215.2019.32.181778>

FREQUENCY DEPENDENCE OF THE IONOSPHERE SCINTILLATION PARAMETERS ON THE OBSERVATIONS OF COSMIC RADIO SOURCES AT THE DECAMETER WAVE RANGE

S. K. Panishko, O. A. Lytvynenko

Observatory URAN-4, Institute of Radio Astronomy NASU
Pushkinskaya str., 37, Odessa, 65125, Ukraine, spanishko@ukr.net

ABSTRACT. When signal from radio source propagates through irregularity layer in the ionosphere it has fluctuations of the amplitude (scintillations) which time spectrum has power form with index $\alpha = 3$. It was shown that such form of the time spectrum of amplitude fluctuations caused by power form of the spatial spectrum of electron concentration ionosphere irregularity with index $p = \alpha + 1$, i.e. $p = 4$. Based on theoretical preconditions for such form of the spatial spectrum the frequency dependence of scintillation index m (scintillation intensity characteristic) was obtained in form power function: $m \propto f^{-n}$, $n = (p + 2)/4$, thus $n = 1.5$. Similar frequency dependence of the scintillation index was observed experimentally for case of weak scintillations ($m < 0.5$). In this work the frequency dependence of scintillation parameters was analyzed on long-term observations of power cosmic radio sources on radio telescope URAN-4 at 20 and 25 MHz. The results were compared with results of earlier carried out investigations.

Key words: radio sources: ionosphere scintillations, decameter range, frequency dependence.

АНОТАЦІЯ. При проходженні сигналу від радіоджерела через неоднорідний шар в іоносфері виникають амплітудні флуктуації радіосигналу (мерехтіння), часовий спектр яких має степеневу форму з індексом $\alpha = 3$. Було показано, що така форма часового спектру амплітудних флуктуацій впливає із форми просторового спектру іоносферних неоднорідностей електронної концентрації з індексом $p = \alpha + 1$, тобто $p = 4$. Виходячи із теоретичних припущень для такої форми просторового спектру була отримана частотна залежність індексу мерехтіння m (характеристика інтенсивності мерехтіння) в формі степеневі функції: $m \propto f^{-n}$, $n = (p + 2)/4$, тобто $n = 1.5$. Подібна частотна залежність індексу мерехтіння експериментально спостерігалась у випадку слабких мерехтіння ($m < 0.5$). В цій праці проаналізована частотна залежність параметрів мерехтіння по довготривалим спостереженням потужних космічних радіоджерел (3С144, 3С274, 3С405, 3С461) на радіотелескопі УРАН-4 на частотах 20 і 25 МГц з 1998 по 2007 рік. Індекс частотної залежності був вичислений із індексів мерехтіння, отриманих на двох частотах. Для всіх радіоджерел індекс n не є постійним, а залежить від величини індексу мерехтіння. Проаналізовані середні значення індексів частотної залежності, а також

отриманих із них спектральних індексів p для 4-х радіоджерел. Спектральні індекси p були також вичислені із індексів α , отриманих із спектрів іоносферних флуктуацій по записам спостережень радіоджерел. Порівняння цих величин між собою показало, що тільки для радіоджерела 3С405 результат співпадає з передбаченим теорією, яка допускає однократне розсіювання радіохвиль в іоносфері. Подібні результати були отримані в раніше проведених дослідженнях інших авторів і потребують щонайменше приймати до уваги такі фактори впливу як геометрія ефекту мерехтіння і багаторазове розсіювання радіохвиль.

Ключові слова: радіоджерело: іоносферні мерехтіння, декаметровий діапазон радіохвиль, частотна залежність

1. Introduction

When signal from cosmic radio source propagates in the inhomogeneous ionosphere it has fluctuations of intensity or scintillations. Scintillation effect can be characterized by scintillation index and time spectrum of fluctuations. Scintillation index defines as (Liu et al., 1986): $m = \sqrt{(\overline{I(t)} - \langle I \rangle)^2 / \langle I \rangle^2}$, where I – intensity of the received radio signal, angle brackets are the time averaging. Time spectrum of the intensity fluctuations has power shape with exponent $\alpha = 3$ and caused by the power form of the spatial spectrum of the ionosphere plasma irregularities $\Phi_{\Delta N_e}(k) \propto k^{-p}$ (k – wave number) with index (Yeh, 1982):

$$p = \alpha + 1. \quad (1)$$

Scintillations on the medium irregularities can originate under the conditions of strong and weak wave scattering (Franke, 1987). If $m \approx 1$, then scintillations are strong, saturated and if $m \ll 1$, (usually $m < 0.5$) then scintillations are weak. The single scattering of the radio signal occurs at weak scintillations and radio signal suffers multiple scattering in a case of the saturated scintillations. Data interpretation complicates by absence of the analytic decisions for strong scintillations, the approximate methods are use in this case.

Ionosphere scintillations were observed in the range from 10 MHz up to 6 GHz (Wu, 1983). For weak scintillations the frequency dependence was obtained as (Liu et al., 1986): $m \propto f^{-n}$. Thus scintillation effect is more significant as wave length of radio signal is larger.

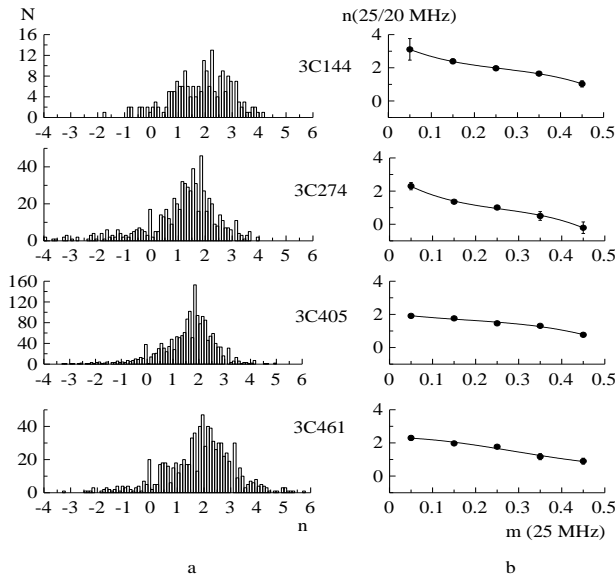


Figure 1: Behavior of the spectral index: a – histograms; b – dependences of the scintillation index (25 MHz), solid line – approximation by polynomial of the third order

Frequency dependence cannot be determinate in the case of saturated scintillations. Theoretical calculations associate spectral index n with the spatial spectrum exponent p as (Liu et al., 1986):

$$n = (p + 2)/4. \quad (2)$$

In such case for power form of the spatial spectrum $n \approx 1,5$. In the present work the analysis of the ionosphere scintillation spectral indices calculated from scintillation indices obtained from observations of power radio sources at frequencies 20 and 25 MHz was carried out.

2. Observation data

Ionosphere scintillation parameters were obtained from observations of power cosmic radio sources – 3C144, 3C274, 3C405, 3C461 which were carried out on the radio telescope URAN-4 during 1998-2007 at 20 and 25 MHz. Observation method and processing technique were considered in the works (Derevyagin et al., 2005; Panishko et al., 2019).

Index α can be determined on the slant part of the time power spectrum received from observation. Index n can be derived on the index α from equation (1) and also index n can be obtained from the scintillation index measured at two frequencies (equation (2)) as (Yeh et al., 1982):

$$n(f_1/f_2) = -\log[m_1(f_1)/m_2(f_2)]/\log(f_1/f_2), \quad (3)$$

where $f_1 = 25$ MHz, $f_2 = 20$ MHz, m_1 and m_2 – scintillation indices on the corresponding frequencies.

Thus number of 3529 values of the spectral index was obtained with using observation records of good quality (without radio interferences) and analysis of this data will be considered in the next section.

3. Results and their discussion

Histograms of the spectral indices calculated from equation (3) are presented on the Fig. 1a for 4-th radio

sources. The negative part is remarkable in all pictures that mean the larger values of scintillation index at the higher frequency. Similar result was obtained in the work (Rashkovsky, 2004) on the observations of the ionosphere scintillations of radio source 3C405 at the decameter radio wave range and this do not agree with theoretical concepts.

The dependence of spectral index n from scintillation index m at frequency 25 MHz is shown on the Fig. 1b. Data for plots was obtained by meaning of index n on scintillation index intervals with step 0.1 in limits from 0.01 up to 0.50 (weak scintillations). The dependence trend is emphasized by polynomial of the third order. From graphs you can see that the values of the spectral index do not stay constant and depend from scintillation index that coincide the case of the multiple radio wave scattering (Yeh et al, 1982). Also you can note that dependence for radio sources 3C405 and 3C461 is more sloping than for 3C144 and 3C274. Most likely that connected with the high on which radio source observed because the first sources located higher than the second and respectively the conditions of the scintillation occurrence are different (Panishko et al., 2019).

The mean values of the scintillation index and spectral index are presented in the Table 1. You can note that values of the index n and also p are consistant with theoretical values for case of the single radio wave scattering only for 3C405 that was showed by results of the work (Rashkovsky, 2004). These values are remarkably larger for 3C144 and 3C461 and smaller for 3C274 than predicted by the theory. Estimations of the indices p_1 and p_2 obtained from the radio source records have less discrepancy with theoretical data however 3C274 also have the smaller values of the spectral index.

Table 1. Mean values of the scintillation parameters

Source	m_1	m_2	n	p_1	p_2	p
3C144	0.29	0.42	1.8	3.7	3.4	5.4
3C274	0.19	0.25	1.2	3.1	3.4	2.8
3C405	0.20	0.28	1.6	4.6	4.6	4.3
3C461	0.18	0.28	1.9	4.0	4.1	5.4

4. Conclusions

From the observations of 4-th power radio sources on RT URAN-4 at 20 and 25 MHz the values of the spectral index were obtained during 1998-2007. Frequency dependence differs for each source that means different conditions of scintillation occurrence. Interpretation of this data requires the attraction of many factors which influence on the results including multiple radio wave scattering and geometry of the scintillation effect.

References

- Derevyagin V. G. et al.: 2005, *Astron. & Astrophys. Trans.*, **91**, 421.
 Franke F. J.: 1987, *Radio Sci.*, **22**, 643.
 Liu C. H. et al.: 1986, *Radio Sci.*, **24**, 363.
 Panishko S. K. et al.: 2019, *Radiofizika i Radioastronomiya*, **24**, 44 (in Russian).
 Rashkovsky S. L.: 2004, *Izv. VUZov. Radiofizika*, **47**, 705 (in Russian).
 Wu D. M.: 1983, *Radio Sci.*, **18**, 589.
 Yeh K. C. et al.: 1982, *Proc. IEEE*, **70**, 324.

DOI:<http://dx.doi.org/10.18524/1810-4215.2019.32.182527>

JOVIAN DECAMETER RADIO EMISSION: TO THE QUESTION ON THE SIZE OF SOURCES

N.O. Tsvyk

Institute of Radio Astronomy of NASU,
Kharkiv, Ukraine, natalitsv69@gmail.com

ABSTRACT. There are debated the questions on size and properties of sources of Jupiter DAM radio emission (JRE). The evolution and the parameters of the sources in the DAM Io-B-storm of October 30, 2008, consisting of a large number of S-bursts, and interspersed with L-bursts and N-bursts, are analyzed in detail. It is shown that S-bursts in this storm are most likely to occur in the northern hemisphere of Jupiter at heights $(0-0.2)R_j$ and at longitudes $\lambda_{III_s} = (195-220)^\circ$ (when Jupiter is deployed to the observer $CML = \lambda_{III} = 130-160^\circ$). The onset of the Io-B-storm is associated with sources at high altitudes, and over time the sources drop down to Jupiter (as the observed S-burst frequencies increase with time). The possibility of the appearance of L- and N-bursts on the background of S-bursts is discussed. L-bursts can arise from the southern hemisphere of Jupiter, at a height of $0.2R_j$. And N-bursts can most likely be located in the northern hemisphere at $\lambda_{III_s} = 66^\circ$ at a height of $0.2R_j$. Using the spectral data on the JRE from 30.10.08, the sizes (thickness and length) of filament-like sources of JRE - electron beams were determined, and the parameters of the MHD (Alfven) waves that activating the JRE bursts. It is shown that the L-radiation sources most likely appear to be thin filaments elongated to magnetic field lines, with a thickness of more than 10 km, and up to 2000 km in length. And the sources of S-radiation look like links with filament-like emissions less than 1 km thick (10-100 strands in a bundle) and up to 300 km in length flying at a speed of $(0.05-0.1)$ c away from Jupiter. The observed A-wave velocities are 2-3 times slower than the A-wave velocity predicted theoretically (about 0.001 c, in light velocity units). Frequency (0.2-1 MHz) and temporal (up to 1 min) diffraction modulation of "lanes" confirms the size of the S-sources less than 200 km. Conclusions are made about the theoretical prerequisites for the appearance of S-bursts with observed parameters. Estimates of the radiation intensity of S-sources indicate an additional increase in the radiation of the source near the generation region; this indicates a non-homogeneous structure of the environment in the active regions

of the Jupiter magnetosphere. The thin transverse structure of the S-sources can be explained by the mechanism of plasmas fluctuations with periods of $\tau = \tau_{ea} = 10$ ms, and with the peculiarities of the bunches of plasma clots that lead to electron leakage and to the emission of plasma plaits. The observed deceleration of the MHD wave velocities can be explained by the influence of the Io - Jupiter flow tube.

Keywords: Jupiter, DAM radio emission, MHD waves, source sizes.

АНОТАЦІЯ. Розглянуто питання про розміри і властивості джерел декаметрового радіовипромінювання Юпітера (ДРЮ). Детально проаналізовано еволюцію і визначено параметри джерел в Іо-В-бурі від 30 жовтня 2008 р., що складається з великого числа S-сплесків, і перемежається з L-сплесками і N-сплесками. Показано, що S-сплески в цій бурі, швидше за все, виникають в північній півкулі Юпітера на висотах $(0-0.2)R_j$ і на довготах $\lambda_{III_s} = (195-220)^\circ$ (коли Юпітер повернутий до спостерігача $CML = \lambda_{III} = 130-160^\circ$). Початок Іо-В-бурі пов'язаний з джерелами на великих висотах, і з часом джерела опускаються вниз до Юпітера (притому, що спостережувані частоти S-сплесків з часом підвищуються). Обговорюється можливість появи L- і N-сплесків на фоні S-сплесків. Так, L-сплески можуть бути пов'язані з джерелами з південної півкулі Юпітера, на висоті $(0-0.2)R_j$. При цьому, N-сплески, швидше за все, можуть виникати в північній півкулі на $\lambda_{III_s} = 66^\circ$ і на висоті $0.2R_j$. Використовуючи спектральні дані по ДРЮ від 30.10.08, визначено розміри (товщина і довжина) нитко-подібних джерел ДРЮ-пучків електронів, і параметри МГД (альфвенівських) хвиль, тих, що активують сплески ДРЮ. Показано, що джерела L-випромінювання, швидше за все, виглядають як тонкі нитки, витягнуті уздовж магнітного поля, товщиною більше ніж 10 км, і довжиною до 2000 км. А джерела S-випромінювання виглядають як зв'язки з нитко-подібних викидів товщиною менше

1 км (по 10–100 ниток в зв'язці) і довжиною до 300 км, що летять зі швидкістю (0.05–0.1)c в сторону від Юпітера. Спостережувані швидкості А-хвиль в 2–3 рази повільніші від значення швидкості А-хвилі, передбаченої теоретично (близько 0.001 c, в одиницях швидкостей світла). Частотна (0.2–1 МГц) і часова (до 1 хв.) дифракційна модуляція ДРЮ "доріжками" підтверджує розміри S-джерела менше 200 км. Зроблено висновки про теоретичні передумови появи S-сплесків ДРЮ зі спостережуваними параметрами. Оцінки інтенсивності випромінювання S-джерел вказує на додаткове посилення випромінювання джерела поблизу області генерації; це говорить про неоднорідну структуру середовища в активних областях магнітосфери Юпітера. Тонка поперечна структура S-джерел може бути пояснена механізмом флуктуацій плазми з періодами $\tau = \tau_{ea} = 10$ мс, і з особливостями бунчировки плазмових згустків, що приводять до витікання електронів і до викидів плазмових джгутів. Спостережуване уповільнення швидкостей МГД-хвиль можна пояснити впливом потокової трубки Іо – Юпітер.

Ключові слова: Юпітер, декаметрове радіо-випромінювання, МГД хвилі, розміри джерел.

1. Introduction

Jupiter as one of the most powerful source of radio emission in the solar system was discovered in 1955 (Burke and Franklin; see more: Ryabov and Gerasimova, 1990). The Jupiter's radio emission (JRE) has a maximum at DAM frequency range, and it consists of the bright (up to 10^7 Jy) short S-bursts of millisecond duration and the slight less brightly (up to 10^6 Jy) long L-bursts of second duration. At the frequency range of higher than 100 MHz, the continuous synchrotron radiation is observed in the equatorial region of Jupiter at heights of $2R_j$. At the same height ($2R_j$), in the kHz frequency range there is observed the relatively bright (up to 10^5 Jy) quasi-periodic 10-minute bursts, the nature and shape of which are similar to III-type solar bursts. And the same 10-minute frequency modulation is exhibit in all sources of DAM radiation that connected with the Alfvén wave modulation features.

We are interested here the main and fine size-structure of DAM Jupiter's radio emission sources on the example of one of observed storms (the storm at 30.10.2008). It give us to find out on the mechanisms of DAM JRE generation, the form of the radiation source, and the specific features of the development of the storm.

2. Properties and mechanisms of the DAM Jovian radio emission

There was established that the radiation pattern (RP) of JRE has the form of a hollow cone with a solution of $(60-90)^\circ$. In this regard, the observed sources are usually located near the limb of Jupiter, and the longitude of the source is shifted relative to the central meridian of Jupiter by approximately the magnitude of the RP (which introduces us ambiguity). In addition, Jupiter's DAM sources correlate with the phase-position of the Io satellite (Φ_{Io}), and prefer to appear at certain active longitudes (A, B, C, D sources). Therefore, for Io-correlated storms, the position of the source in longitude is uniquely determined as:

$$\lambda_{III_s} = \lambda_{III} - \Phi_{Io} + 180^\circ - \Delta\lambda,$$

where $\Delta\lambda \simeq 20^\circ$ is the source shift-advancing angle (Ryabov & Gerasimova, 1990).

The sources of L-type exhibit predominantly longitudinal correlation; and S-sources predominantly correlate with the Io phase. The latitude of the sources of DAM radiation can be determined only on the assumption that the sources in the Io-dependent storms are attached to the Io-Jupiter flux tube and are located near the northern or southern foot of the tube. In this case, it is usually considered that DAM radiation is generated in the form of fast extraordinary X-waves, and then in the Leblanc model (Leblanc, et al., 1993) the right-polarized radio wave sources (A, B) are tied to the northern Jupiter's hemisphere, and left-polarized sources (C, D) are tied to the southern hemisphere.

The mechanism of Jupiter's DAM radiation can be associated with one of the instabilities of electromagnetic or plasma waves near the cyclotron frequency, that developing (running) under the condition of resonance between waves and particles in a low-density non-equilibrium plasma ($\omega_{pe} \ll \omega_{be}$):

$$\omega - s\omega_{be} - k_{\parallel}v_{\parallel} = 0,$$

where $s = 0, -1, \dots$. There is most often it is believed that instability arises at the $s = -1$ resonance for fast extraordinary X-modes, that give us the Maser cyclotron radiation (MCR) which observed as L-bursts of JRE (Wu, 1985, Melrose, 1986, others). And the generation of S-bursts can occur due to both MCR instability ($s = -1$) and the Cherenkov plasma instability (CR) at resonance of $s = 0$ from bunched fast electron beams (see Zaitsev, et al., 1986; Boev, et al., 1991).

Moreover, there is necessary the generation of MCR into an efficient pumping of electrons with a cone velocity distribution ($T_{\perp} > T_{\parallel}$) and beam elongated. Then the energy of nonequilibrium weakly relativistic ($\gamma - 1 > 0.001$) electrons is pumped maserly into fast extraordinary wave and into plasma waves with a radiation pattern $RP = (60-90)^\circ$ to the magnetic field line in the source.

The Cherenkov radiation (CR) mechanism may be even more efficiently than the maser mechanism, and it converts the energy of electron accelerated in electron beams into plasma Z-waves near the upper hybrid frequency. However, these Z-waves not go away the source; and there is required an additional conversion of Z-waves into fast electromagnetic (X- or O-) modes, which significantly reduces the efficiency of Cherenkov source. The CR pattern is also directed almost perpendicular to the source magnetic line ($RP \simeq 80^\circ$); and under different conditions of wave transformation, a large variation of S-burst shapes can occur (see Zaitsev, et al., 1986; Boev, et al., 1993).

Jupiter and Io are binding by a flux tube along a magnetic field line. Io's electromotive force accelerates and ionizes the electrons along the Io – Jupiter flux tube (IFT) and they elongated to magnetic field line in a weakly ionized plasma. The MHD Alfvén (A) waves activate the processes of electron acceleration and the formation of bunched ejection that are the sources of S-bursts emissions.

The mechanism of acceleration of electrons may turn to runaway effects in electric fields in the region of the Io–Jupiter flux tube (see Boev et al., 2001). It was shown that the electric fields which induced by the Io tube movement increase the value of runaway Dreiser threshold. The maximum electric fields corresponding to A and B sources in the northern hemisphere are reached at longitudes $\lambda_{III_s} = (100\text{--}150)^\circ$ and $(170\text{--}250)^\circ$. Moreover, these electric field values almost exceed the Dreiser threshold in the northern hemisphere, and the electron beams can be generated at all longitudes, which responded to the S-bursts generation on this hemisphere. So, the southern hemisphere of Jupiter it is able to accelerate electron beams only in narrow selected areas; and the southern hemisphere is more variability to L-bursts generation.

3. Sizes of the sources from spectral data

The source sizes were simple estimated by spectra data of L- and S-bursts as size by burst duration (the transverse source size by longitudes) and size by height (by frequency data). The evolution of bursts in the DAM Io-B-storm of 30.10.2008 (the observations of Ryabov, et al., 2014) is analyzed in detail. It is consisting with a large number of S-bursts, as well as them alternating with L-bursts and N-bursts. The results of the analysis are given in the Tables 1, 2.

The Table 1 show the data of burst set: UT is the universal time of observed spectrum (the fragments of 2 MHz frequency width and by 1 s duration); λ_{III} is Jupiter's central meridian longitude (CML) at this UT-time moment; λ_{III_s} is the longitude of source location (when Io phase is $\Phi_{Io} = 93\text{--}98^\circ$); F is the frequency (in MHz) where bursts observed. ΔT_i is instantaneous

Table 1: Spectral data of storm at 30.10.2008 and transverse sources size (ΔL_i) by time data

UT, hr:min	λ_{III}	λ_{III_s}			
15:46	197	131			
15:52	200	133			
15:52(N)		66?			
16:00	205	140			
16:26	216	154			
16:26(L)		154			
UT, hr:min	F, MHz	Burst type	ΔF_i , MHz	ΔT_i , ms	ΔL_i , km
15:46	23	S, Io B	0.1..0.5	0.2..2	0.008
15:52	22	S, rain	0.2	2	-
	16.8	S, Io B	0.3	1	0.007
15:52	16.4	N, not Io?	0.1	0.5	0.005
16:00	27.5	S, Io B	0.3	5	0.03
	22.5	S	0.4	6	0.035
	19	S	0.6	7	0.04
16:26	31	S, Io B	0.2	10	0.06
	27	S	0.2	12	0.08
	24	S	0.3	17	0.1
16:26	18	L	0.6	>1000	>6

burst duration, and ΔL_i is transverse source size, corresponded to ΔT_i .

The Table 2 continues the Table 1, and it show the characteristics of the JRE sources obtained by frequency spectral data. B_{MCR} corresponds to the magnetic field of burst source by MCR model (when observed frequency $F = 1.1 \omega_{be}(B_{MCR})/(2\pi)$, considering the disperse wave condition). B_{CR} corresponds to the magnetic field in Cherenkov source model (when $(2\pi F)^2 = \omega_{be}(B_{CR})^2 + \omega_{pe}^2$). The burst drift (see Drift in Table 2, in MHz/s) corresponds the source velocity of u_s , which is slightly relativistic (near $0.1c$, $c = 3 \cdot 10^{10}$ cm/s). The terms of h_{sN} and h_{sS} are the height of source location (by MCR model) for northern and southern hemisphere, respectively; Δh_i is length of the source (in km, along magnetic line or to height direction). If we assume that S-bursts occur the most likely in the northern hemisphere of Jupiter, there is S-source locate in this storm of the height $(0\text{--}0.2)R_j$ (by the frame of MCR model) and at longitudes $\lambda_{III_s} = (195\text{--}220)^\circ$, when Jupiter is turned to the observer at longitude $CML = \lambda_{III} = (130\text{--}160)^\circ$.

The train of S-bursts are induced and modulated by the Alfvén (A) wave. This fact show the wide-lanes modulation on spectrum data by 0.5–1 MHz width and slow drifting, corresponding to A-wave lengths (see λ_{AS} and λ_{AN} columns in table 2) and wave velocity (c_A). According to the storm, S-bursts are induced by A-waves that go both away from Jupiter and to the Jupiter, that propagating with velocity about c_A

Table 2: The characteristics of JRE-sources in the Io B storm at 30.10.2008 and heights–length (h_s , Δh_i) of these sources by frequency spectral data, according to northern (h_{sN}) and southern (h_{sS}) hemisphere (see the text more). Source or Alfvén wave velocities (u_s , c_A) are in units of light velocity c ; heights of source are in units of R_j

Time, hr:min	Freq., MHz	B_{MCR}	B_{CR}	Drift, MHz/s	u_s/c	c_A/c	$h_{sN},$ R_j	$h_{sS},$ R_j	λ_{AN} km	λ_{AS} km	$\Delta h_i,$ km
15:46	23	7.2	5.6	-22	0.08	-0.001	0.13	0.24	2100	4300	140
15:52	22	7.1	5.4	-21	0.08	0.0001	0.14	0.25	800	3570	140
	16.8	5.4	4.3	-13.5	0.07	0.0006	0.21	0.34	2800	5700	280
15:52(N)	16.4	4.7	3.64	-5.1	0.03	0.0003	0.22	0.22	300		150
16:00	27.5	8.7	6.8	-30	0.09	0.0004	-0.02	0.16	710	1400	110
	22.5	7.1	5.5		0.1	0.0005	0.12	0.24	1100	2100	180
	19	6.1	4.8	-27	0.11	0.0007	0.16	0.3	1800	3500	320
16:26	31	10	7.8	-30	0.09	-0.0001	-0.02	0.15	710	1400	61
	27	8.7	6.8	-30	0.09		-0.02	0.15	1100	2100	71
	24	7.7	6	-30	0.1	-0.0001	0.04	0.22	1800	3500	180
16:26(L)	18	5.9	4.5	0.1?	-	0.0002	0.1	0.35	1100	2100	50

$=0.0005c$, which is in 2–3 times slower than the A-wave velocity predicted by plasma parameters "theoretically" ($0.001c$). These Alfvén waves have $\lambda_A \sim 1000$ km, and the A-waves may change the direction by reflection on Jupiter by $T_A \sim 10$ min (the table 2 indicate the change of A-wave direction, but we do not obtained T_A because of spectra fragmenting). The start of Io-B-storm is associated with sources at higher altitudes, and when time over, the sources drop down to Jupiter as O_4 (Acuna, 1975) magnetic field model predicted, despite of observed S-bursts frequencies increase with time.

There are observed L- and N-bursts simultaneously with S-bursts in this storm. Thus, L-bursts can be associated with source from the other (southern) hemisphere of Jupiter, against of S-bursts associate with northern hemisphere. The other way, N-bursts may likely arise outside the Io–Jupiter tube, and can be located in the northern hemisphere at $\lambda_{III} = 65^\circ$ and at heights of $0.2 R_j$ (at this longitudes).

On using the spectral data, there were determined the sizes (thickness and length) of the filamentous sources of the JRE-electron-beams and the parameters of the burst-activate MHD (Alfvén) waves. It is shown that the source of L-radiation the most likely looks like as thin filaments elongated along a magnetic field with a thickness of $\Delta L_i \simeq 50$ km and a length of higher 1000 km. The other way, S-radiation sources look like as bunches of elementary outbursts (plasma clots) with a thickness of $\Delta L_i = (10\text{--}100)\text{m}$ (of 10–100 threads per bunch), and a length of $\Delta h_i = (100\text{--}300)$ km, flying away from Jupiter with speed $(0.05\text{--}0.1)c$.

The fine structure of the DAM bursts in this storm detects the diffraction modulation of the JRE within the "lanes" by the frequency of $(0.2\text{--}1)$ MHz and by time (up to $T_{rep} = 1$ min). On using the Arkhipov model (2003, 2007), it is possible to estimate the size

of the sources by the diameter of the first Fresnel zone ($d_1 = \sqrt{8\pi cD/\omega_{b0}}$), and by the repetition periods (T_{rep}) of scattering inhomogeneities ($d_2 = 2\pi DT_{rep}/T_j$), assuming that the scattering inhomogeneities are located of distance (D) in close Jupiter's magnetosphere bounded by the Io torus (T_j is orbital period of Jupiter). These estimates confirm the size of the S-source is less than 200 km.

4. Discussion and theoretical interpretations

There are made conclusions about the theoretical prerequisites for the appearance of DAM JRE bursts with observed parameters. We may estimate the power intensity I_{est} of the source of Jupiter's DAM radiation by S-source volume ($V_{js} = \Delta L_i \Delta h_i^2$):

$$I_{est} = \gamma_\omega E_{is}/(\omega_{b0} S_{js}) = (\gamma/\omega_{b0})(\gamma m_e c^2 V_{js})(0.1 n_{e0})$$

Here $\gamma_\omega = 10^{-4} \omega_{b0}$ is radiation increment, $\gamma = 1.004$, $\omega_{b0} = 2\pi \cdot 20$ MHz, $n_{e0} = 10^6 \text{ cm}^{-3}$ is electron density, E_{js} is source energy, $S_{js} = 4\pi (4\text{a.u.})^2 \Delta RP$, we find for S-source: $I_{est} = 2 \cdot 10^5$ Jy. This intensity is some lower than observed ones, 10^6 Jy (see Ryabov, Gerasimova, 1990), and this fact pointed us about the additional amplification of the source radiation near the generation region. This suggests an inhomogeneous structure of the medium in active S-bursts zone. The power of L-radiation is easily to match with they sizes.

The sources of Jupiter's radio emission in all ranges of radio waves are easily explained with runaway mechanism. The fine transverse structure of the S-sources may be explained by the mechanism of electron fluctuations, with periods are considered with time scattering of electron and atoms, $\tau = \tau_{ea} = 10$ ms, and source transverse size is compared to the length of emitted waves (10 m). It is connected with the features of the bunching of electron-plasma blobs that lead to electron

runaway and to the emission of plasma bunches. Alternatively, for the L- sources we are: $\tau = \tau_i = 1$ s (time scattering of ion and atoms), and this is compared to the time of forming of plasma blobs and thick current treads. The observed reducing the A-wave velocities in comparison with the "theoretical" ones can be explained by the influence of the Io – Jupiter flow tube and the reflection events on the propagation of MHD waves.

We use mainly in spectrum interpretation the MCR model. There are need to study additionally the fine structure of all DAM sources with the UTR-2 and GURT observation, as well as to study theoretically, with attracting a possible Cherenkov mechanism for the S- and N-bursts interpretations.

References

- Acuna M.H.: 1975, *Nature*, **253**, 327.
Arhipov O.V.: 2003, *Kinemat. Phys. Celest. Bod.*, **19**, 267.
Arhipov O.V., Ruker H.O.: 2007, *Astron. Astroph.*, **467**, 353.
Boev A.G., Lukyanov M.Yu.: 1991, *Sov. Astron.*, **35**, 422.
Boev A.G., Lukyanov M.Yu., Tsvyk N.: 1993, *Kinemat. Phys. Celest.Bod.*, **9**, 27.
Boev A.G., Lukyanov M.Yu., Tsvyk N.: 1993, *Kinemat. Phys. Celest.Bod.*, **9**, 37.
Boev A.G., Udaltsova N.M., Yantsevich A.A.: 2001, *Radioph. Radioastron.*, **6**, 252.
Leblanc Y., Bagenal F., Dulk G.A.: 1993, *Astron. Astroph.*, **276**, 603.
Melrose, D.B.: 1986, *J. Geophys. Res.*, **91**, A7, 7970.
Ryabov B.P., Gerasimova N.N.: 1990, *Decameter sporadic radioemission of Jupiter (in Russian)*, Kyiv: Naukova dumka, 240 p.
Ryabov V.B., et al.: 2014, *Astron. Astroph.*, **268**, A53.
Wu C.S.: 1985, *Space Sci. Rev.*, **41**, 215.
Zaitsev V.V., et al.: 1986, *Astron.Astroph.*, **169**, 345.

DOI:<http://dx.doi.org/10.18524/1810-4215.2019.32.182536>

UTR-2 LOW FREQUENCY CONTINUUM SURVEY OF THE NORTHERN SKY. PART II

N. M. Vasilenko, M. A. Sidorchuk

Institute of Radio Astronomy, Kharkiv, Ukraine
vasnat@rian.kharkov.ua, sidor@rian.kharkov.ua

ABSTRACT. The Ukrainian T-shape radio telescope (UTR-2) has been used to carry out a multifrequency radio survey of a part of the northern sky with coordinates of the declinations $+10^\circ < Dec. < +29^\circ$, and right ascensions $0^h < R.A. < 24^h$. The observations were performed at very low radio frequencies, 12.6, 14.7, 16.7, 20 and 25 MHz. They were fulfilled by scanning the sky due the Earth's rotation with the five-beam pattern antenna at 11 fixed declinations. The observations for six five-beam strips, that covered the declinations ranges from $+10^\circ$ to $+19^\circ$, the so-called "a fast scanning mode" was used. In this mode, the antenna positions were switched in the cycle between the three selected strips at fixed declinations every 40 seconds in the observational process. For the remaining strips, both the fast scanning mode and the usual observation mode at one fixed declination were used. Each pattern pencil-beams are spaced apart by $23'$ in the meridian. The angular size of the beam is about 1° at 12.6 MHz and 0.5° at 25 MHz at the zenith. The receivers' bandwidths are 10 kHz at frequencies from 12.6 to 16.7 MHz and 40 kHz at the two highest frequencies. A calibration of the output power was performed with the aid of the etalon noise generator for the each observation. These data surveyed were obtained during the period from 1997 to 2013 only at nighttime. The total number of observation amounted to more than 700 nights. The statistics for each point of the survey varied from 5 to 40 realizations. The results of these observations are the brightness temperature maps presented here at each mentioned above frequencies of the decameter band. However, it should be noted that there are shown "raw" maps without the zero level and striping effect corrections. These maps comprise emission from discrete and extended radio sources, the Galaxy and extragalactic background. The most intense radio emission on the maps is observed from the Galactic Plane and the North Polar Spur (NPS).

АНОТАЦІЯ. Проведено багаточастотний радіо огляд частини Північної небесної півкулі з схиленнь: $+10^\circ < Dec. < +29^\circ$, і прямих

піднесень: $0^h < R.A. < 24^h$, з використанням Українського Т-подібного радіотелескопу (УТР-2). Це друга частина огляду на УТР-2, перша частина стосувалася області північного неба з координатами: $+29^\circ < Dec. < +55^\circ$, $0^h < R.A. < 21^h$. Спостереження здійснені на дуже низьких радіочастотах, 12.6, 14.7, 16.7, 20 і 25 МГц. Пропускна здатність приймачів становить 10 кГц на частотах від 12,6 до 16,7 МГц і 40 кГц на двох найвищих частотах. Спостереження були реалізовані шляхом сканування неба за рахунок обертання Землі п'ятипроменевою діаграмою спрямованості (ДС) антени на 11 фіксованих схиленнях. Кожен голкоподібний промінь ДС відстоїть один від другого на $23'$ в меридіані. Кутівий розмір променя становить приблизно 1° на 12.6 МГц і 0.5° на 25 МГц в зеніті. Для шести смуг, які охоплювали схилення від $+10^\circ$ до $+19^\circ$, спостереження виконувалися, в так званому, „режимі швидкого сканування”. У цьому режимі в процесі спостереження положення антени перемикалося в циклі, кожні 40 секунд між трьома вибраними смугами з фіксованими схиленнями. Для решти смуг використовувались як режим швидкого сканування, так і звичайний режим - спостереження на одному фіксованому схиленні. Калібрування вихідної потужності виконували для кожного спостереження за допомогою еталонного генератора шуму. Дані були отримані за період з 1997 по 2013 рік. Загальна кількість спостережень становила понад 700 ночей. Статистика для кожної точки огляду коливалася від 5 до 40 реалізацій. Результатом цих спостережень є представлені тут карти температур яскравості радіовипромінювання на кожній з вищезгаданих частот декаметрового діапазону. Однак слід зазначити, що це «сирі» карти, без редукції нульового рівня і коригування ефекту смугастості. Дані карти вміщують випромінювання як від точкових, так і протяжних радіоджерел, а також фону Галактики і Метагалактики. Найбільш інтенсивне радіовипромінювання спостерігається

від Галактичного диску і Північної Полярної Шпори.

Key words: Key words. Radio continuum: ISM, surveys, Galaxy: Structure, decameter range.

1. Introduction

Surveys of the sky radio emission at different frequencies have been carried out for more than 70 years, the first map of the Galactic radio emission at 160 MHz was made by G.Reber (1944). There are well-known maps of the all sky at frequencies 408 MHz (Haslam et al., 1982), 1420 MHz (Reich and Reich, 1982). Also a number of low-frequency surveys have been carried out, including those at 10 MHz (Antonov, 1973; Caswell, 1976), at 22 MHz (Roger et al., 1999), at 34.5 MHz (Dwarakanath and Udayashankar, 1990), at 38 MHz (Milogradov-Turin and Smith, 1973), at 45 MHz (Alvarez et al., 1997; Maeda et al., 1999). In the last years the LWA1 survey at nine frequencies from 35 to 80 MHz was presented by Dowell et al. (2017). Despitethis, obtaining maps in a wide frequency range with high resolution and sensitivity, especially at low frequencies, remains an important task in modern radio astronomy. The such maps are necessary to study spectral properties of the thermal and non-thermal components of the continuous radio emission of the Galaxy, to build a global model of sky radiation at the entire radio frequency range, for example as in (De Oliveira-Costa et al., 2008; Dowell et al., 2017). In the work, we represent the maps of the decameter waveband survey of the part of the Northern sky with declinations $+10^\circ < Dec. < +29^\circ$, and right ascensions $0^h < R.A. < 24^h$, which were carried out with the UTR-2 radio telescope. Earlier we introduced the maps of the sky in the declination range from $+29^\circ$ to $+55^\circ$ and right ascensions $0^h < R.A. < 20^h$ (Vasilenko et al., 2006).

2. Observations and data processing

The UTR-2 radio telescope has been used to carry out a multifrequency radio survey of the northern sky. This is T-shaped telescope, it consists of two NS and EW antenna arms, one of which, with dimensions $1880 \times 54 \text{ m}^2$, is located along the meridian and the other, with dimensions $900 \times 54 \text{ m}^2$, along the parallel. The effective area is approximately equal to $150\,000 \text{ m}^2$ at 25 MHz at the zenith. The directional pattern represents a fan of five pencil beams at each frequency. The beams separation ($\Delta Dec.$) is about $23'$ at the zenith. The first side-lobe level in the meridian plane is 13 dB. A detailed description of the UTR-2 can be found in Braude et al. (1978).

Under the program of the survey, the observations

were carried out at frequencies of 12.6, 14.7, 16.7 20 and 25 MHz. These observations were performed with a five-beam directional pattern, scanning the sky due the Earth's rotation, at 11 fixed declinations in the ranges from $+10^\circ$ to $+29^\circ$. Each sky strips, covered with five beams, was observed at four different hour angles ($\pm 1^h, \pm 2^h$). Since the sidelobes differ at different hour angles, this helps us to reduce the confusion errors. For six five-beam strips, in the declination ranges from $+10^\circ$ to $+19^\circ$, the so-called "fast scanning mode" was used. In this mode, the antenna positions were switched in the cycle between the three selected strips at fixed declinations every 40 seconds in the observational process. This switching speed allows, due to the Earth rotation, to move to the starting point of the cycle spaced to half of the beam-width at 25 MHz. For the remaining strips, both the fast scanning mode and the usual observation mode at one fixed declination were used. The angular resolution, receivers' bandwidths of the corresponding frequency channels are shown in Table 1.

Table 1: UTR-2 observational parameters for the Northern sky survey

Frequency (MHz)	Bandwidth (kHz)	HPBW (arcmin)
12.6	10	55×67
14.7	10	47×53
16.7	10	41×46
20.0	40	34×39
25.0	40	27×31

At the beginning and end of each observation day, a calibration of the output power was performed with the aid of the etalon noise generator connected with distributed amplifiers placed in the field of the telescope array. The method of observations and calibrations of the continuum radio emission using the UTR-2 is described in detail by Krymkin (1978).

The presented data were obtained with observations at the UTR-2 during from 1997 to 2013 only at night time. The total number of observation amounted to more than 700 nights. The statistics for each point of the survey varied from 5 to 40 realizations.

For each frequency, the survey data processing consisted of several stages.

1) Initial analysis of records and calibrations, where data subject to the influence of narrow-band interference were excluded, and if the calibrations before and after the observation session differed by more than 15%, then such a session was completely excluded from processing.

2) Statistical processing of the data was carried out separately to each observational strip, each hour angle, and each series of observations; and included the determination of the rms brightness temperatures and

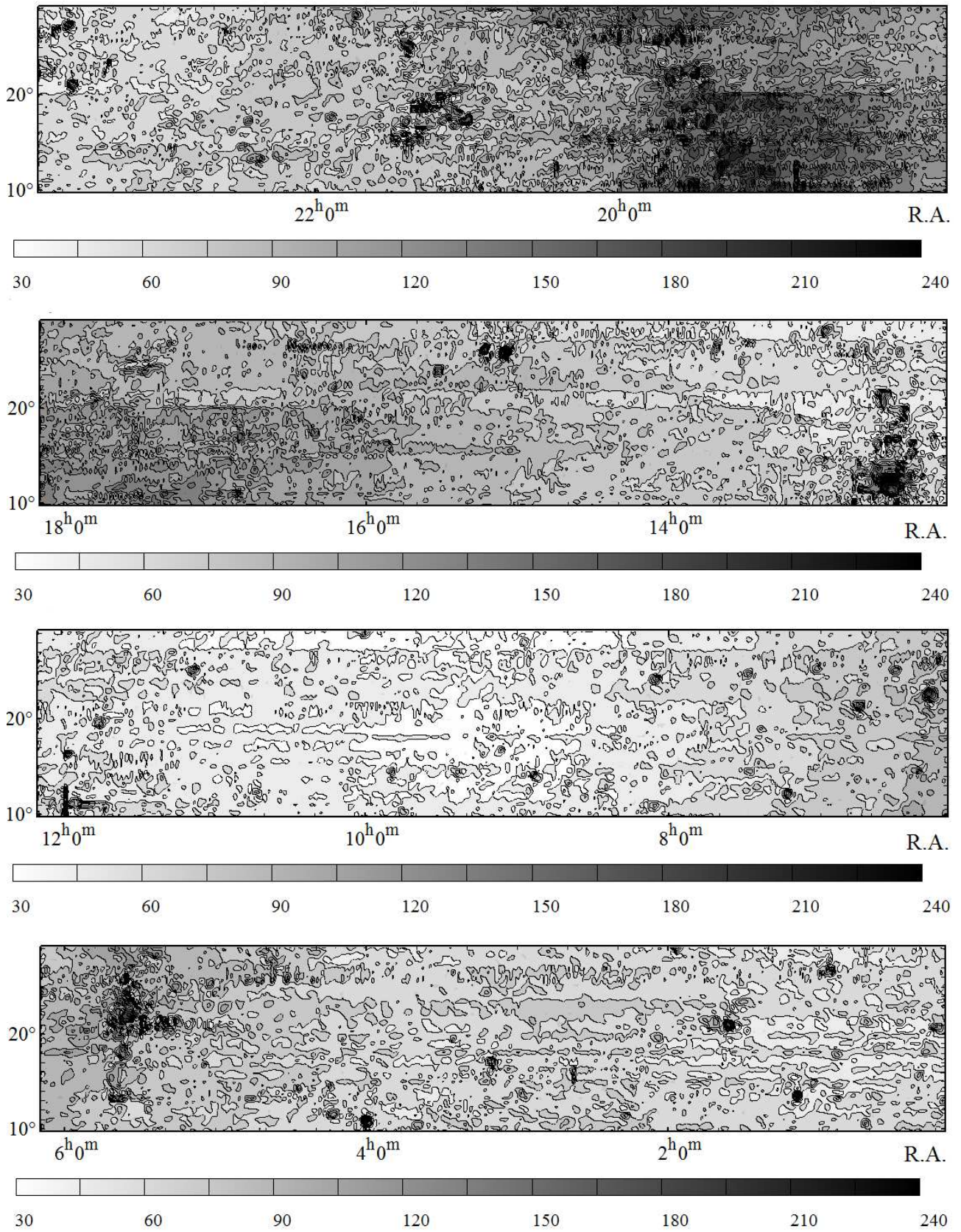


Figure 1: UTR-2 total brightness temperature map of the part of the Northern sky survey at 20 MHz. The region covered: $+10^\circ < Dec. < +29^\circ$, and $0^h < R.A. < 24^h$. The map is divided into parts at a six hours at R.A..

the filtration of the temperature values by dispersions.

3) Separation of the background component from total the radio emission using an FIR filter and its subsequent analysis.

4) Correlation analysis of the brightness temperature data arrays obtained for different hour angles and series of observations for every declination.

5) Comparison of the data for adjacent strips and obtaining the final brightness temperature scans for the observed region of the sky.

6) Mapping of the observed sky at the corresponding frequencies using the software package Sky Continuum Survey (Vasilenko et al., 2005).

3. Results

In this study, the maps of the radio emission of the part northern sky survey at the decameter wavelength are obtained. The region covered $+10^\circ < Dec. < +29^\circ$ and $0^h < R.A. < 24^h$. The survey was carried out at very low radio frequencies, 12.6, 14.7, 16.7 20 and 25 MHz, with the best angular resolution and sensitivity ever achieved at these frequencies. Note for comparison that the angular resolution in the nearest low-frequency survey carried out at 22 MHz with the DRAO radio telescope $1.1^\circ \times 1.7^\circ$ at the zenith (Roger et al., 1999). However, it should be noted that shown here is the "raw" maps without reducing of the zero level and striping effect corrections. To compare in detail ours' maps with another we need to do it. But this is the task for the next paper. The maps of brightness temperatures comprise the Galactic and extragalactic background, a part of the Galactic plane and the North Polar Spur, discrete and extended sources. Figures 1 represent the map of the total emission at 20 MHz in the equatorial coordinates for the 2000 epoch. The superim brightness temperatures are gray shaded and include isophotes. Contours of brightness temperature are indicated with a bar scale. The brightness temperatures are given in thousands of Kelvins.

4. Conclusions

The maps of the Northern sky surveys at the decameter wavelengths carried out in the lowest frequency part of the spectrum open to the ground-based observations are presented. They have the best angular resolution ever achieved for these frequencies. The presented maps are also of great importance for the analysis of the distribution of galactic synchrotron emission and morphology of the magnetic field in our Galaxy. They can be combined with high frequency data to study morphological changes of the background structures. In addition, these maps are

useful for the estimation of the required effective areas of radio telescopes to perform the various research programs for very low frequencies in the north celestial hemisphere.

References

- Alvarez H., Aparici J., May J. et al.: 1997 *Astron. Astrophys. Sup. Ser.*, **124**, 315.
 Antonov A.V.: 1973, *Izv. Vyss. Uchebn. Zaved. Radiofiz.*, **16**, 759.
 Braude S.Ya., Megn A.V., Ryabov B.P.: 1978, *Astron. Astrophys. Space Sci.*, **54**, 3.
 Caswell J.L.: 1976, *Mon. Not. R. Astron. Soc.*, **177**, 601.
 De Oliveira-Costa A., Tegmark M., Gaensler B.M. et al.: 2008, *Mon. Not. R. Astron. Soc.*, **388**, 247.
 Dowell J., Taylor G.B., Schinzel F.K. et al.: 2017, *Mon. Not. R. Astron. Soc.*, **469**, 4537.
 Dwarakanath K.S., Udayashankar N.: 1990, *J. Astrophys. Astr.*, **11**, 323.
 Haslam C.G.T., Salter C.J., Stoffel H., Wilson W.E.: 1982, *Astron. Astrophys. Suppl. Ser.*, **47**, 1.
 Maeda K., Alvarez H., Aparici J. et al.: 1999, *Astron. Astrophys. Sup. Ser.*, **140**, 145.
 Milogradov-Turin J. and Smith F.G.: 1973, *Mon. Not. R. Astron. Soc.*, **61**, 269.
 Krymkin V.V.: 1978, *Astron. Astrophys. Space Sci.*, **54**, 187.
 Reber G.: 1944, *Astrophys. J.*, **100**, 279.
 Reich P. and Reich W.: 1986, *Astron. Astrophys. Suppl. Ser.*, **63**, 205.
 Roger R S., Costain C.H., Landecker T.L. et al.: 1999, *Astron. Astrophys. Sup.*, **137**, 7.
 Vasilenko N.M., Sidorchuk, M.A., Muha, D.V. et al.: 2006, *In: IAU Joint Discussion*, **12**, 45.
 Vasilenko N.M., Mukha D.V., Sidorchuk M.A. et al.: 2005, *Radio Phys. and Radio Astron.*, **10**, 244.

SUN, SOLAR ACTIVITY AND ASTROBIOLOGY

DOI:<http://dx.doi.org/10.18524/1810-4215.2019.32.182447>MULTI-WAVELENGTH OBSERVATIONS OF
A LARGE SOLAR FLARE

S.N. Chornogor, N.N. Kondrashova

Main Astronomical Observatory, National Academy of Sciences of Ukraine,
Kyiv, Ukraine, chornog@mao.kiev.ua

ABSTRACT. We present the results of the multi-wavelength study of the two-ribbon solar flare on July 19, 2000 in the active region NOAA 9087. The evolution and morphological properties of the flare productive active region have been analyzed. The active region was growing rapidly and showed a complex multipolar magnetic field configuration. It was large, producing many events, including the flare under consideration. The 3N/M6.4 two-ribbon flare was a prominent, long duration event in the active region evolution. According to Solar Geophysical Data (SGD) the flare lasted 2.5 hours. The flare energy release took place in many sites of the active region.

We used combination of data from space and ground based observatories for study. The hard X-ray (HXR) and soft X-ray (SXR) data were obtained at the Yohkoh Telescopes (HXT and SXT) and Geostationary Operational Environmental Satellite (GOES). The full-disk magnetograms and EUV-images were provided by the Solar and Heliospheric Observatory (SOHO) Michelson Doppler Imager (MDI) and Extreme ultraviolet Imaging Telescope (EIT). We used the H_{α} filtergrams from the Meudon spectroheliograph and white light images of Big Bear Solar Observatory (BBSO).

All the data show continuously evolving SXR, EUV and H_{α} features during the flare. The HXR and the type III radio bursts were observed at the flare onset. The first H_{α} flare kernels and the surge, connected with the filament eruption, were initiated near a large positive-polarity sunspot. The main bright kernels of the flare occurred at the centre of the active region near magnetic neutral line, after that the flare ribbons appeared along it. It was found that HXR coronal source was located along a magnetic polarity inversion line of the active region. EUV loop structures indicate the observational evidence of a magnetic reconnection during the main phase of the flare.

АНОТАЦІЯ. В роботі представлено результати багатохвильового дослідження двострічкового сонячного спалаху 19 липня 2000 року в активній області NOAA 9087. Проаналізовано еволюцію та морфологічні властивості спалахово

активної області. Активна область швидко зростала і демонструвала складну багатополярну конфігурацію магнітного поля. Вона була великою, спричиняла багато подій, включно зі спалахом, що вивчається. Двострічковий спалах 3N/M6.4 був визначною, тривалою подією в еволюції активної області. За даними Solar Geophysical Data (SGD), спалах тривав 2,5 години. Викид енергії спалаху відбувався у багатьох місцях активної області.

Для дослідження використано поєднання даних космічних та наземних обсерваторій. Дані для жорсткого (HXR) та м'якого (SXR) рентгенівського випромінювання були отримані на телескопах Yohkoh (HXT та SXT) та Geostationary Operational Environmental Satellite (GOES). Магнітограми та EUV-зображення були отримані Solar and Heliospheric Observatory (SOHO) Michelson Doppler Imager (MDI) та Extreme Ultraviolet Telescope (EIT). Були використані H_{α} -фільтрограми з Meudon spectroheliograph та зображення в білому світлі з Big Bear Solar Observatory (BBSO).

Усі дані показують, що під час спалаху відбувалися постійні зміни в різних діапазонах: SXR, EUV та H_{α} . На початку спалаху спостерігалися сплески HXR та радіосплески III типу. Перші H_{α} -ядра спалаху та хромосферний викид з'явилися біля великої сонячної плями з позитивною полярністю. Основні яскраві ядра спалаху виникли в центрі активної області поблизу магнітної нейтральної лінії, після чого вздовж неї з'явилися стрічки спалаху. Було встановлено, що корональне джерело HXR розташоване уздовж лінії інверсії магнітної полярності активної області. Структури EUV-петель вказують на спостережні докази магнітного перез'єднання під час головної фази спалаху.

Keywords: active regions, solar flares, magnetic reconnections, multi-wavelength observations.

1. Introduction

Solar two-ribbon flares are extremely powerful eruptions caused by magnetic reconnections. The magnetic energy is converted into radiation, heat, particle acceleration, fluxes and waves. The development of two-ribbon flares has been studied on the base of multi-wavelength observations in many works (eg, Ding et al., 2003, Rovira et al., 2007, Kumar et al., 2010). They are often accompanied by eruption of the filament lying along the neutral magnetic line (eg, Ding et al., 2003). Surges are observed often simultaneously with two-ribbon flares. Kumar et al. (2010) reported that the trigger of the M8.9/3B flare was the activation of spiral-twisted structures. The emergence of a new magnetic flux, the movement of photospheric matter, the shear and the vortex movements at the footpoints of the loops can lead to magnetic reconnection, resulting in flares (eg, Heyvaerts et al., 1977, Gorbachev et al., 1988, Somov et al., 2002, Su et al., 2007).

We study an evolution and morphological properties of the two-ribbon solar flare on July 19, 2000 in the flare-productive active region NOAA 9087. We used multi-wavelength data and analyzed the sequence of flare images on filtergrams in the H_α line, magnetograms and extreme ultraviolet images.

2. Observational data

Space-born and ground based observations are used. The hard X-ray (HXR) and soft X-ray (SXR) data were obtained at the Yohkoh Telescopes (HXT and SXT) and Geostationary Operational Environmental Satellite (GOES). The full-disk magnetograms and EUV-images were provided by the Solar and Heliospheric Observatory (SOHO) Michelson Doppler Imager (MDI) and Extreme ultraviolet Imaging Telescope (EIT). H_α -filtergrams were obtained with the Meudon spectroheliograph, radio data with Learmonth Solar Radio Spectrograph, white light images in Big Bear Solar Observatory (BBSO).

3. Active region NOAA 9087

Morphological properties of the active region (AR) NOAA 9087 have been analyzed. The active region emerged from the edge of the solar disk on July 15 and was visible on the disk until July 27, 2000. AR developed rapidly, its structure changed. The number of spots increased from day to day, new spots appeared, while others disappeared. The shape of the spots was complex and changed over time. The active region showed a complex multipolar magnetic field configuration, which became more complicated as it developed. Parasitic polarity regions were observed,

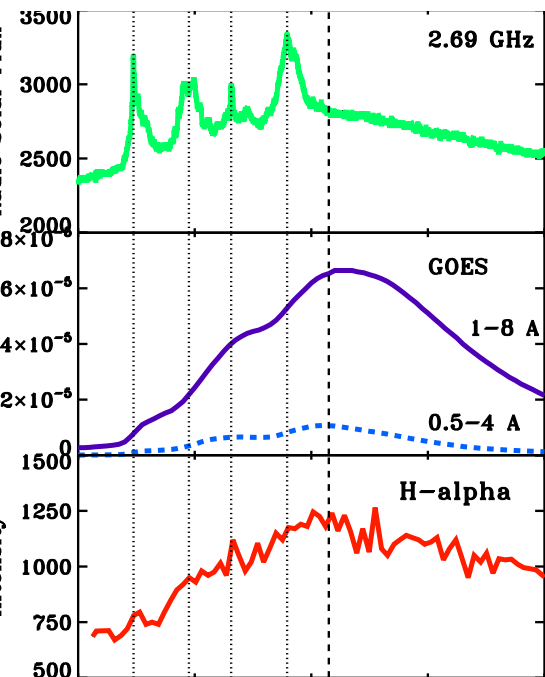


Figure 1: Different wavelength light curves (H_α intensity, soft X-ray flux, radio solar flux) for flare on July 19, 2000.

which indicates the emergence of new magnetic fluxes. The neutral magnetic line had a curved shape, its length and shape changed in time. The region produced many events, including the flares. Flare activity peaked on July 19, when the magnetic field configuration was β - γ - δ . The most powerful 3N/M6.4 two-ribbon flare in the active region occurred on that day. We analyzed the development of this flare in present work.

4. Flare evolution

According to Solar Geophysical Data (SGD) the 3N/M6.4 two-ribbon flare occurred in the active region NOAA 9087 at 06:37 UT on 2000 July 19, peaked at 07:23 UT and lasted 2.5 hours. Flare coordinates are S18E10. The flare is a long duration event. SXR, EUV and H_α data show continuously evolving features during the flare.

Hard X-ray and the type III radio bursts were observed at the flare onset. Two bursts of the HXR intensity and four radio bursts at 2.69 GHz were in the initial phase (Table 1, Figure 1). Figure 1 shows different wavelength light curves. The flux of soft X-ray radiation slowly decreased in the main phase of the flare. Flare peaks at the H_α line are later than peaks in radio emission and HXR. It indicates that magnetic reconnections took place in corona at onset of the flare.

We used the observational data in the H_α line ob-

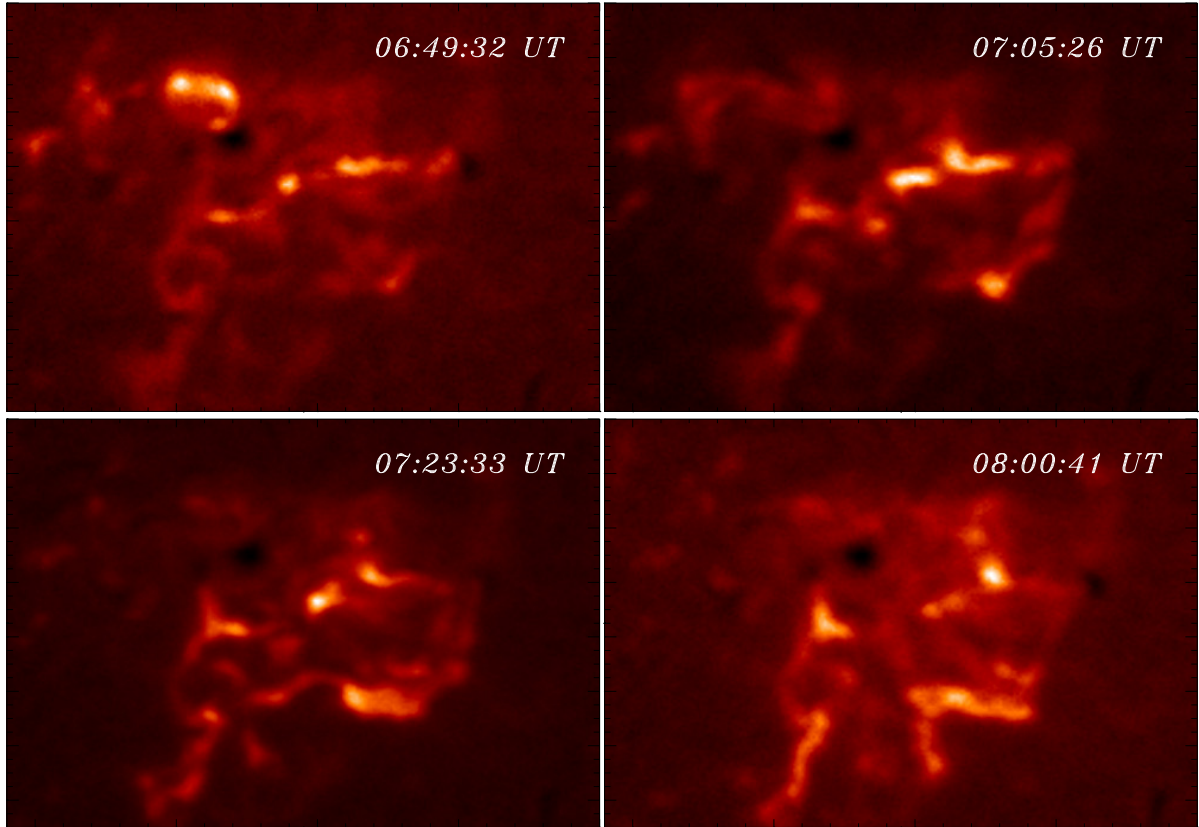


Figure 2: H_{α} -images (Meudon) for different phases of flare July 19, 2000 evolution

Table 1: Times (UT) of burst peaks in different wavelength ranges.

	Max1	Max2	Max3	Max4
HXR	06:49:27	06:57:01		
Radio	06:49	06:59	07:06	07:16
H_{α}	06:50:33	07:01:11	07:07:34	07:18:12

tained using the spectroheliograph of the observatory in Meudon for study. Filtergrams were obtained in time steps from 30 seconds to 1 minute. We have analyzed in detail the development of the flare in H_{α} -filtergrams. Figure 2 shows the evolution of the flare in the H_{α} line. At the beginning of the flare two bright kernels appeared in the region of a large spot, several plages and flare kernels brightened at first peaks of HXR and radio emission at 06:49 UT. New flare kernels appeared at the middle part of the active region. The first flare kernels near the large spot disappeared, large post-flare loops appeared and chromospheric surge occurred at this place (Fig. 2).

The position of the hard X-rays source at 06:57 UT

was obtained by Yohkoh HXT. The HXR contour image was overlaid on the MDI magnetogram, H_{α} , SOHO 195 Å and SXT images (Fig. 3). Comparison between the spatial distribution of the H_{α} kernels and that of the HXR source shows that HXR source was located in the central part of active region above the magnetic neutral line in the brightest kernel area. In most of the area, the position of the source of hard X-rays coincides with the place of the soft X-ray emission.

A new H_{α} kernel appeared at the bottom of the active region shortly before the flare maximum. Flare kernels in the other part of the active region brightened. Cold post-flare loops near large spot are visible in 304 Å. The maximum brightness of all kernels was at the main H_{α} peak of the flare at 07:23 UT (Fig. 2).

A set of consecutive images of loops in the extreme ultraviolet wavelength passband 195 Å was analyzed. EUV loop structures show the observational evidence of a new magnetic reconnection closer to the spot during the main phase of the flare (Fig. 4). New flare H_{α} kernels appeared in the magnetic reconnection area (Fig. 2).

5. Conclusions

The evolution of the two-ribbon 3N/M6.4 flare on 19 July 2000 in the flare-productive solar active region NOAA 9087 analyzed on the base of the multi-wavelength observations, combination of data from space and ground-based observatories. All the data show continuously evolving SXR, EUV and H_α features during the flare.

The active region was growing rapidly and showed a complex multipolar magnetic field configuration. It was large and produced many eruptive events. The 3N/M6.4 flare was a prominent, long duration event in the active region evolution. The flare energy release took place in many sites of the active region.

HXR and type III radio bursts were observed at the flare onset. The first H_α flare kernels and the surge were initiated near a large positive-polarity sunspot. The main bright kernels of the flare occurred at the centre of the active region near magnetic neutral line, after that the flare ribbons appeared along it.

HXR coronal source was located above magnetic neutral line of the active region in the brightest H_α kernels area. EUV loop structures show the observational evidence of the magnetic reconnections during the flare main phase.

Acknowledgements. We are grateful to the observer teams of Meudon, Yohkoh and Learmonth Observatories, GOES, BBSO and SOHO who have provided free access to their results.

References

- Ding M. D., Chen Q. R., Li J. P., Chen, P. F.: 2003, *ApJ*, **598**, 683.
 Gorbachev V. S., Somov B. V.: 1988, *Sol. Phys.*, **117**, 77.
 Heyvaerts J., Priest E. R., Rust D. M.: 1977, *ApJ*, **216**, 123.
 Kumar P., Srivastava A. K., Filippov B., Uddin W.: 2010, *Sol. Phys.*, **266**, 39.
 Rovira M. G., Simberova S., Karlicky M., et al.: 2007, *ASPC*, **368**, 461.
 Somov B. V., Kosugi T., Hudson H. S., et al.: 2002, *ApJ*, **579**, 863.
 Su Y., Golub L., Van Ballegoijen A.A.: 2007, *ApJ*, **665**, 606.

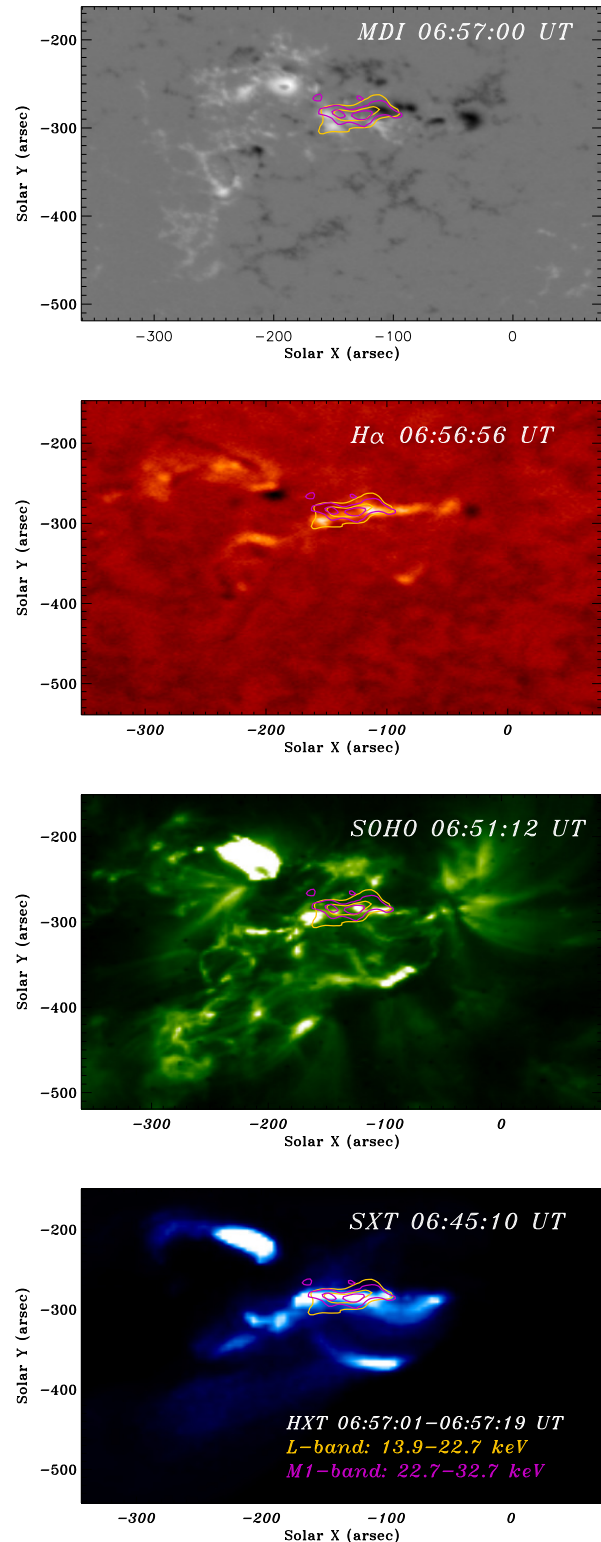


Figure 3: The Yohkoh HXR contour image is overlaid on the MDI magnetogram, H_α , SOHO 195 Å and SXT images.

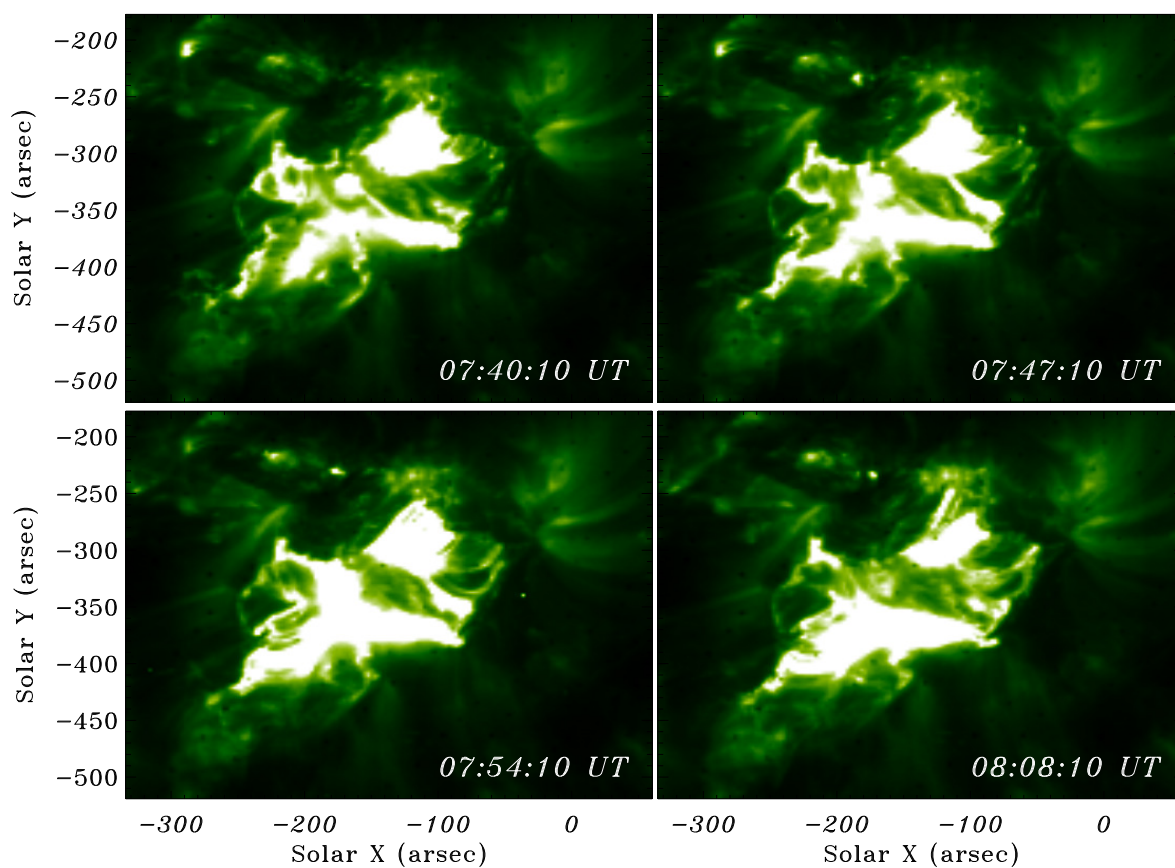


Figure 4: EUV (195 Å) images at different moments of the flare evolution show magnetic reconnections in corona at main flare phase.

DOI:<http://dx.doi.org/10.18524/1810-4215.2019.32.181797>

APPROXIMATION OF THE INTEGRAL ENERGY SPECTRUM OF PROTONS OF SCR IN THE RANGE OF $> 1-850$ MEV

E.A. Isaeva

Institute of Radio astronomy of NAS of Ukraine, isaevaode@gmail.com

ABSTRACT. This work is a continuation of the work (Isaeva E., 2018) in which a new approximation of the integral energy spectrum of solar cosmic ray (SCR) protons was presented in the range $> 1-100$ MeV. In this work, the comments and wishes of colleagues working in this field were taken into account. First, the comments were taken into account on the form of the functional for approximating the energy spectrum of protons, which must correspond in form to the functionals predicted by particle acceleration theories. Secondly, the previously obtained functional should be checked for high-energy protons with energies > 1000 MeV.

For the analysis, we used original records of the intensity of the flux of SCR protons according to the data from GOES. The studied sample contains 349 solar proton events (SPE) for the period from 03-02-1986 to 12-02-2018 years, accompanied by protons with energies in the range $> 1-850$ MeV. Of 349 SPE, 53 were accompanied by high-energy protons with energies > 850 MeV.

In this paper, we present the results of approximation of the integral energy spectrum of SCR protons with energies $> 1-850$ MeV using a functional containing power and exponential functions. A comparative analysis showed that this functional gives a very good approximation for SCR protons with energies in the range $> 1-850$ MeV.

Keywords: Proton events, energy spectrum of protons, intensity of the proton flux.

АНОТАЦІЯ. Дана робота є продовженням роботи (Isaeva E., 2018) в якій була представлена нова апроксимація інтегрального енергетичного спектра протонів сонячних космічних променів (СКП) в діапазоні $> 1-100$ MeV. У даній роботі були враховані зауваження та побажання колег, які працюють в цій галузі. По-перше, були враховані зауваження щодо форми функціоналу для апроксимації енергетичного спектра протонів, який за формою повинен відповідати функціоналам, які пророкують теорії прискорення частинок. По-друге, раніше отриманий функціонал треба перевірити для високоенергетичних протонів з енергією > 1000 MeV.

Для аналізу були використані оригінальні записи інтенсивності потоку протонів СКП за даними з GOES. Досліджувана вибірка містить 349 сонячних протонних подій (СПП) за період з 03-02-1986 по 12-02-2018 роки, що супроводжувалися протонами з

енергією в діапазоні $> 1-850$ MeV. З 349 СПП 53 супроводжувалися високоенергетичними протонами з енергією > 850 MeV.

У даній роботі наводяться результати апроксимації інтегрального енергетичного спектра протонів СКП з енергією $> 1-850$ MeV за допомогою функціоналу, що містить ступеневу і експонентну функції.

Порівняльний аналіз показав, що даний функціонал дає дуже гарне наближення для протонів СКП з енергією в діапазоні $> 1-850$ MeV.

Ключові слова: протонні події, енергетичний спектр протонів, інтенсивність протонного потоку.

1. Introduction

Currently, it is believed that SCR can be accelerated either in the region of flare energy release in the current sheets (Melnikov V. et al., 1986; 1991; Nidson A. et al., 2008; Chertok I. et al., 2009) or at the fronts shock waves that can be generated by both flares and coronal mass ejections (CMEs) (Reams D., 1999; Cliver E. et al., 2004). However, the paper (Tsap Yu. And Isaeva E., 2012) provides strong arguments in favor of the model of a two-stage acceleration mechanism proposed half a century ago (Wild J. et al., 1963).

It is known that the shape of the energy spectrum of SCR protons is directly related to particle acceleration mechanisms. In this regard, attempts are made to empirically represent the SCR spectrum based on observational data or on general physical considerations. In fact, obtaining the true spectrum of accelerated particles in the source is a very difficult task (Miroshnichenko L., 2014; 2018). Shock waves in the corona, and then the effects of the transfer of accelerated particles in an interplanetary magnetic field (IMF), associated with the dispersion of particles in velocity, strongly modify the observed spectrum. As a result, the spectrums of SPEs in the Earth's orbit are distinguished by a wide variety of shapes and intensities. Only the spectrum of particles with an energy of $E_p \geq 500$ MeV approximately corresponds to the spectrum of the source.

Figure 1 shows examples of typical integral energy spectrums of SCR protons with energies in the range $E_p > 1-850$ MeV for six SPEs.

Figure 1 clearly shows the significant differences between the events, both in the form of their spectrum and in intensity. The spectrum have a clearly pronounced variable slope, and with increasing energy, the spectrum becomes steeper. An explanation for this behavior has not yet been

found. It can only be stated that the spectrum can be described above the kink energy by a power-law function with exponential cutoff (Akin'ian et al., 1983; Ellison et al., 1985). According to (Band et al., 1993; Mewaldt et al., 2005; 2006; 2012), such spectrums are better described by a double power function.

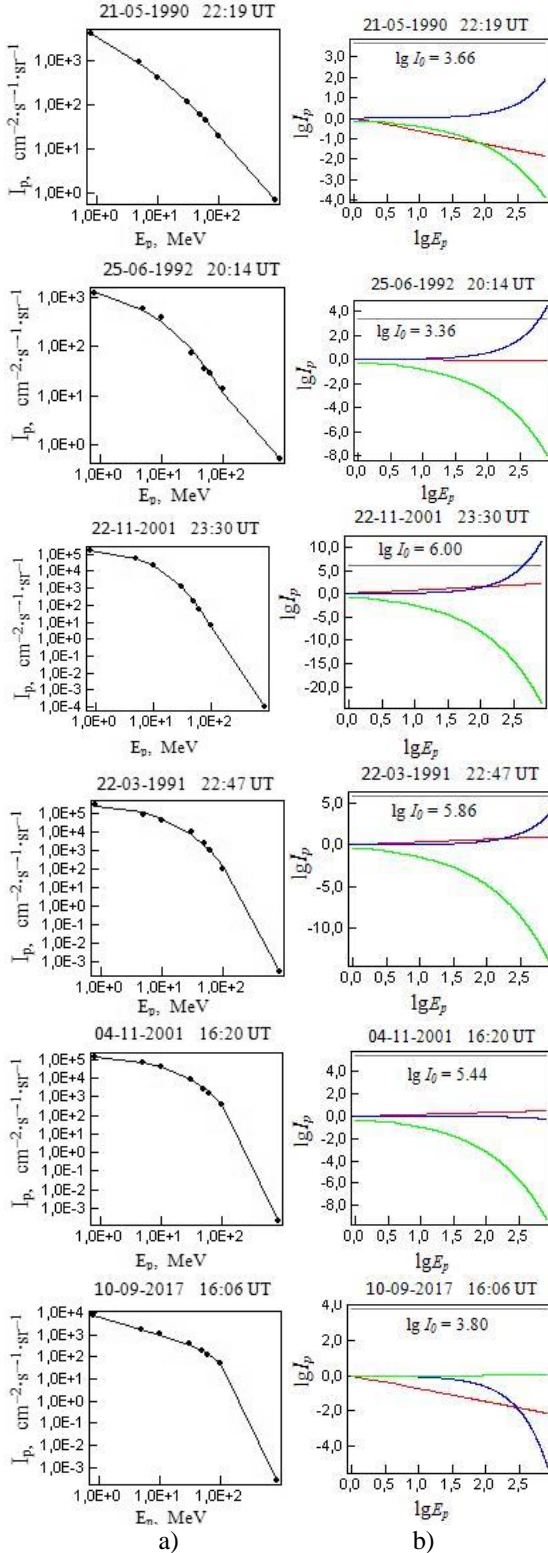


Figure 1: a) Integral energy spectrum of SCR protons. b) The contribution of each parameter in functional (1) in the formation of the integral energy spectrum of protons.

For the analysis, we used the original records of the intensity of the proton flux I_p with the energy E_p in the range $E_p > 1-850$ MeV from data from apparatuses of the GOES series (https://satdat.ngdc.noaa.gov/sem/goes/data/new_avg/), and also a list of solar proton events (SPE). The sample studied contains 349 proton events for the period from 03-02-1986 to 12-02-2018 years. This sample is complete, since it contains almost all events registered for the specified period, including very weak events and superimposed events, which were separated and identified by the author independently. In this connection, errors associated with the separation and identification of proton events are possible. In this sample of 349 SPE 168 events were identified by the author, and the remaining events are present in the SPE directory (<ftp://ftp.swpc.noaa.gov/pub/indices/SPE.txt>). For all these events, an attempt was made to find a single empirical dependence of the proton flux intensity I_p on the proton energy $E_p > 1-850$ MeV. To this end, original records of the intensity of the proton flux I_p with the energy E_p in the range $E_p > 1-850$ MeV for all 349 proton events were processed. As a parameter characterizing the proton flux, the maximum intensity of the proton flux I_p of a given energy was chosen during the proton event. The value of the I_p parameter was calculated from the preflare level. In the case of superposition of proton events, the value of I_p was calculated from the level of the previous proton event. Emissions associated with interference and with the imposition of shock waves were also eliminated.

3. Approximation of the integral energy spectrum of SCR protons in the range $E_p > 1-850$ MeV

In figure 1a) shows the characteristic types of energy spectrum for the SPEs accompanied by high-energy protons with an energy of $E_p > 850$ MeV. There are 53 such events in the studied sample. In figure 1a) the energy spectrum of protons are shown, the shape of which gradually changes from an almost rectilinear spectrum to a spectrum with a kink.

In this work, the approximation of the energy spectrum of SCR protons in the range $E_p > 1-850$ MeV was performed using functional (1), which contains power and exponential functions,

$$I_p = 10^d \cdot E_p^{-a} \cdot e^{(-bE_p + cE_p^{1/2})} \quad (1)$$

where a , b , c and d are the linear regression coefficients that were found using the least squares method. In figure 1a) the black circles indicate the observed values of the proton flux intensity, and the thin solid black line shows the values calculated using the functional (1).

It can be seen that the approximation of the spectrum using the functional (1) gives a very good approximation.

$$I_0 = 10^d \quad (2)$$

$$I_p = E_p^{-a} \quad (3)$$

$$I_p = e^{-bE_p} \quad (4)$$

$$I_p = e^{cE_p^{1/2}} \quad (5)$$

In figure 1 b) the contribution of each parameter (2-5) in the functional (1) to the formation of the spectrum is shown. The X axis represents the decimal logarithms of the proton energy E_p , and the Y axis shows the logarithms of the proton flux intensity I_p . In figure 1 b) the gray horizontal line indicates the initial values of the proton flux intensity I_0 (2), as well as the numerical values of the decimal logarithm I_0 . The red color indicates the contribution of the power function (3) to the formation of the spectrum, and the blue (4) and green (5) colors indicate the contribution from the exponential functions.

In Figure 2 shows the scattering diagrams between the observed and calculated values of the proton flux intensity SCR I_p in the range $E_p > 1-850$ MeV. Of the 349 proton events, 249 were accompanied by protons with energies $E_p > 100$ MeV and 53 events were accompanied by protons with $E_p > 850$ MeV.

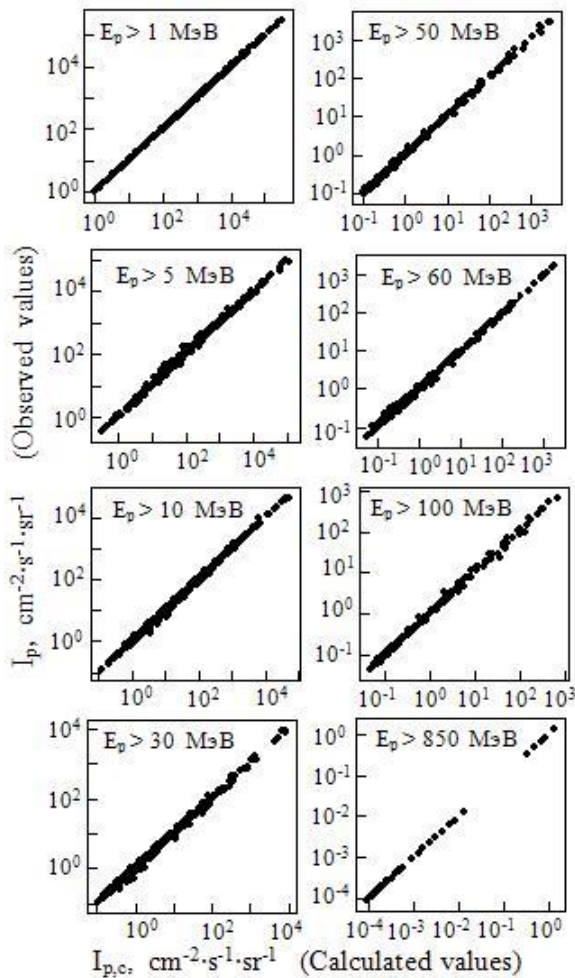


Figure 2: Diagrams of scattering between observed and calculated values of the proton flux intensity SCR.

4. Conclusion

A new approximation of the observed energy spectrum of SCR protons in the range $E_p > 1-850$ MeV gives a fairly good approximation. Therefore, a comparison of the observed proton spectrum with the spectrum predicted by SCR acceleration models can be more accurately estimated by the conditions in the acceleration source, as well as the contribution of transport effects in the interplanetary magnetic field, and the additional particle acceleration by coronal and interplanetary shock waves.

References

Akin`ian S., Logachev Iu.: 1983, Catalogue of Solar Proton Events 1970-1979, IZMIRAN.
 Band D., Matteson J., Ford L. et al.:1993, *Astrophys. J.*, **413**, 281.
 Chertok I., Grechnev V., Meshalkina N.: 2009, *Astron. Zh.*, **86**, 1133.
 Cliver E., Kahler S., Reames D.: 2004, *Astrophys. J.*, **605**, 902.
 Ellison D., Ramaty R.: 1985, *Astrophys. J.*, **298**, 400.
 Isaeva E.: 2018, *Odessa Astron. Publ.*, **31**, 147.
 Melnikov V., Podstrigach T., Kurt V. et al.: 1986, *Kosm. Issled.*, **24**, 610.
 Melnikov V., Podstrigach T., Daibog E. et al.: 1991, *Kosm. Issled.*, **29**, 95.
 Mewaldt R., Cohen C., Labrador A. et al.: 2005, *Geophys. Res.*, **110**, A09S18.
 Mewaldt R.: 2006, *Space Sci. Rev.*, **124**, 303.
 Mewaldt R., Looper C., Cohen D. et al.: 2012, *Space Science Reviews*, **171**, Issue 1-4, 97.
 Miroshnichenko L.: 2014, *Solar Cosmic Rays: Fundamentals and Applications* 2nd ed., (NewYork: Springer).
 Mirishnichenko L.: 2018, *Phys. Usp.*, **61**, 323.
 Reams D.: 1999, *Space Sci. Rev.*, **90**, 413.
 Tsap Yu. and Isaeva E.: 2012, *Bulletin of the Crimean Astrophysical Observatory*, **108**, 52.
 Tsap Yu. and Isaeva E.: 2012, *Geomagnetism and Aeronomy*, **52**, 921.
 Wild J., Smerd S., Weiss A.: 1963, *Ann. Rev. Astron. & Astrophys.*, **1**, 291.

DOI: <http://dx.doi.org/10.18524/1810-4215.2019.32.181798>

RELATIONSHIP OF THE PROTON FLUX INTENSITY WITH RELATIVE DISTANCE BETWEEN HARMONICS OF TYPE II RADIO BURSTS IN THE RANGE 25-180 MHz

E.A. Isaeva

Institute of Radio astronomy of NAS of Ukraine, isaevaode@gmail.com

ABSTRACT. In this work, the relative distance between the harmonics of type II radio bursts and its relationship with the intensity of the proton flux with an energy > 30 MeV are studied.

The studied sample contains 112 solar proton events (SPE) for the period from 24-11-2000 to 20-12-2014 years, accompanied by type II radio bursts in the range of 25-180 MHz.

For analysis, we used the original recordings of the dynamic spectrum in the range of 25-180 MHz from the Solar Radio spectrograph (SRS), as well as the original recordings of the proton flux intensity with an energy $> 1-100$ MeV according to GOES data.

A comparative analysis showed that for the vast majority of solar proton events, the relative distance between the harmonics of a type II burst varies over time over a wide range. Moreover, each event is characterized by a gradual decrease in the relative distance to the minimum value with subsequent increase.

In this work, we also studied the relationship between the proton flux intensity of solar cosmic rays (SCR) and the relative distance between the harmonics of type II radio bursts at a given time. A comparative analysis showed that there is a fairly strong relationship between the proton flux intensity with an energy > 30 MeV and the frequency f_1 at the fundamental harmonic, at which the minimum value of the relative distance between the harmonics of the type II burst is observed. It was shown that the lower the frequency f_1 at the fundamental harmonic, the higher the intensity of the proton flux.

Keywords: Solar proton events, proton flux intensity, type II radio bursts, relative distance between harmonics.

АНОТАЦІЯ. В роботі досліджено відносну відстань між гармоніками радіосплесків II типу і її зв'язок з інтенсивністю потоку протонів з енергією > 30 MeV.

Досліджувана вибірка містить 112 сонячних протонних подій (СПП) за період з 24-11-2000 по 20-12-2014 роки, що супроводжуються радіо сплесками II типу в діапазоні 25-180 МГц.

Для аналізу були використані оригінальні записи динамічних спектрів в діапазоні 25-180 МГц з сонячного радіо спектрографа (СРС), а також оригінальні записи інтенсивності потоку протонів з енергією $> 1-100$ MeV за даними з GOES.

Порівняльний аналіз показав, що для переважної більшості сонячних протонних подій відносна відстань між гармоніками сплеску II типу змінюється з плином часу в широких межах. Причому, для кожної події ха-

рактерно поступове зменшення відносної відстані до мінімального значення з подальшим зростанням.

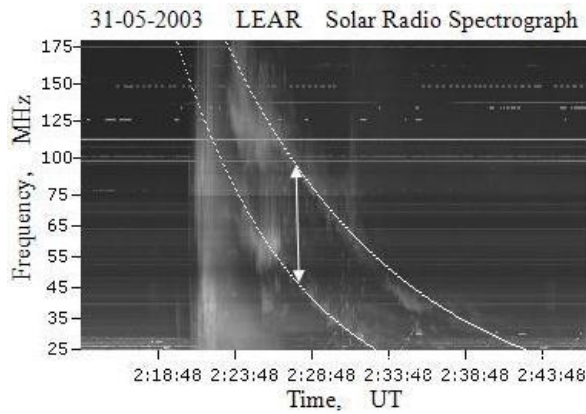
У даній роботі також був досліджений зв'язок інтенсивності потоку протонів сонячних космічних променів (СКП) з відсною відстанню між гармоніками радіо сплесків II типу в даний момент часу. Порівняльний аналіз показав, що існує досить сильний зв'язок між інтенсивністю потоку протонів з енергією > 30 MeV і частотою f_1 на основній гармоніці, на якій спостерігається мінімальне значення відносної відстані між гармоніками сплеску II типу. Показано, що чим нижче частота f_1 на основній гармоніці, тим вище інтенсивність потоку протонів.

Ключові слова: сонячні протонні події, інтенсивність потоку протонів, радіо сплески типу II, відносна відстань між гармоніками.

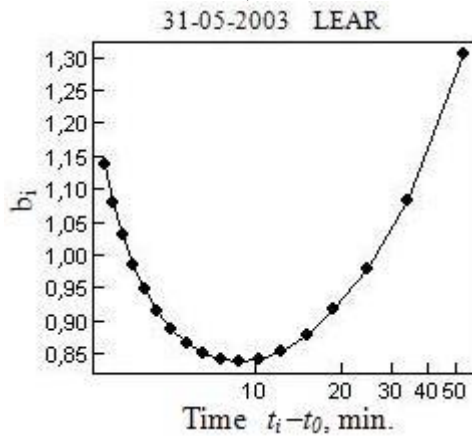
1. Introduction

To date, many indications have been received that type II radio bursts are generated at shock wave fronts (Zheleznyakov, 1970; Wild and Smerd, 1972; Nelson and Melrose, 1985). In this case, quite often, on the dynamic spectrum, one can observe splitting of the burst band into two parallel strips, which behave similarly in both intensity and drift velocity (Wild and Smerd, 1972; Nelson and Melrose, 1985; Mann, 1995, 1996; Zimovets et al., 2012; Vasanth et al., 2014). Some authors believe that the strips can merge (Mann, 1995, 1996), thereby believing it quite appropriate to characterize the distance between them at a given time t_i by the relative band width $\Delta f/f_{i,1} = (f_{i,2} - f_{i,1})/f_{i,1}$, where $f_{i,1}$ is the radiation frequency.

The observed band splitting is usually associated with the plasma mechanism of radio emission. If the ratio of the characteristic frequencies of the bands $f_{i,2}/f_{i,1}$ approximately equal to 2, then they speak of two harmonics (first and second) radiation generated by a source located either in front of or behind the front of the shock wave. If the value $f_{i,2}/f_{i,1}$ differs significantly from the integer value and is noticeably less than 2, then this splitting is also associated with the plasma mechanism of radio emission. However, in this case, the generation occurs at one harmonic in front and behind the shock front (Smerd et al., 1974, 1975; Vrsnak et al., 2001, 2002; Zimovets, 2012; Vasanth et al., 2014), where the plasma density and the generated frequency of electromagnetic waves have significantly different meanings.



a)



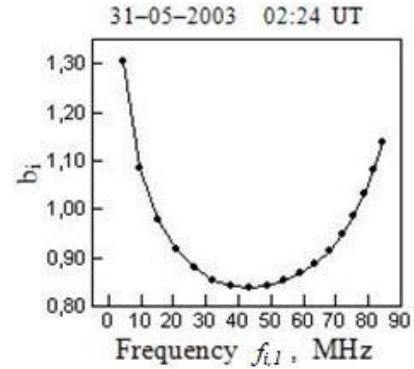
b)

Figure 1: a) Dynamic spectrum of a type II burst associated with a proton event on 31-05-2003 year. b) Change of the splitting b_i over time t_i .

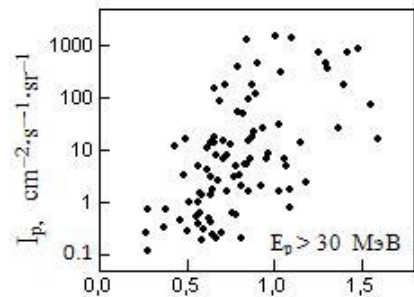
2. Initial data and research results

The studied sample contains 112 solar proton events (SPE) for the period from 24-11-2000 to 20-12-2014 years, accompanied by bursts II in the range 25-180 MHz. For the analysis, we used original records of the proton flux with an energy of $E_p > 1-100$ MeV according to the data from GOES (https://satdat.ngdc.noaa.gov/sem/goes/data/new_avg/), original recordings of the dynamic spectrum in the range of 25-180 MHz with Solar Radio Spectrograph (SRS) (<http://www.ngdc.noaa.gov/stp/space-weather/solar-data/solar-features/solar-radio/rstn-spectral/>), as well as a list of proton events (<ftp://ftp.swpc.noaa.gov/pub/indices/SPE.txt>).

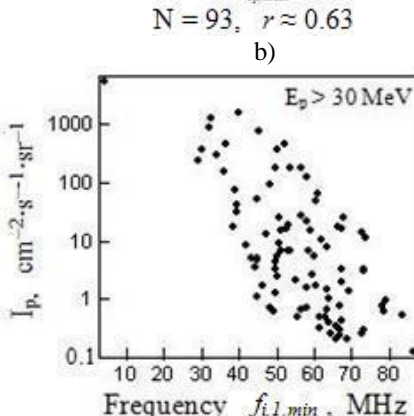
In figure 1a) shows an example of the dynamic spectrum of a type II radio burst associated with a proton burst on 31-05-2003 year. As can be seen, two bands can be distinguished corresponding to the main and second harmonics. In this work, we used a new regression model (Isaeva and Tsap, 2017) to approximate the type II burst harmonics (1), where $f_{i,j}$ is the frequency of the maximum of type II burst at a given harmonic at a given time t_i , i - reference number, j - harmonic number, a_j and d_j - linear regression coefficients.



a)



b)



c)

Figure 2: a) Dependence of the relative distance b_i on the frequency value $f_{i,1}$ at the 1st harmonic. b) The relationship between the proton flux intensity I_p and the relative distance $b_{i,min}$. c) The relationship between the proton flux intensity I_p and the frequency $f_{i,1,min}$, at which the minimum value of the relative distance $b_{i,min}$ between the harmonics of the type II burst is observed.

$$\log_{10} f_{i,j} = a_j \cdot \sqrt{t_i} + d_j \quad (1)$$

$$b_i = \frac{(f_{i,2} - f_{i,1})}{f_{i,1}} \quad (2)$$

This model makes it possible to fairly accurately estimate the frequency drift velocity for 95% of type II bursts in the range 25-180 MHz, for which the correlation coefficient r between the observed and calculated frequency values $r \geq 0.98$. For all events, the zero time moment t_0

corresponded to the beginning of a type II burst at the first harmonic at a frequency of 180 MHz.

In Figure 1a) an approximation of the harmonics of a type II burst is shown by thin white lines along the harmonics. The vertical arrow indicates the distance between harmonics in frequency $\Delta f = f_{i,2} - f_{i,1}$ at a given time t_i . For 112 type II bursts, the harmonic splitting width was studied, which was characterized by the relative distance b_i between harmonics (2), where $f_{i,1}$ and $f_{i,2}$ are frequency values at 1 and 2 harmonics at a given time t_i .

In Figure 1 b) shows a typical example of a change in the relative distance b_i over time t_i for a type II radio burst of 31-05-2003. A comparative analysis showed that over time, the width of the cleavage can vary over a wide range. It is shown that each event is characterized by a gradual decrease in the splitting width to the minimum value of $b_{i,min}$ with a subsequent increase. Moreover, for different events, the minimum value of the splitting $b_{i,min}$ is observed in different frequency ranges. In Figure 2 a) the dependence of the relative distance b_i on the frequency $f_{i,1}$ at the 1-st harmonic is shown. In figure 2 a) it can be seen that for the event of 31-05-2003 year, the minimum splitting $b_{i,min}$ corresponds to a certain frequency $f_{i,1,min}$ at 1 harmonic.

Earlier in (Tsap Yu., Isaeva E., 2013), it was shown that there is a fairly strong relationship between the relative distance b_i averaged over the entire time interval of a type II burst and the proton flux intensity I_p . Moreover, the relationship between b_i and I_p is much higher for protons with energies $> 30-100$ MeV, where the correlation coefficient r between the studied quantities is $\approx 0.65-0.70$.

In the present work, we also investigated the relationship between the relative distance b_i and the intensity of the proton flux I_p with an energy $E_p > 30$ MeV.

A comparative analysis showed that there is a fairly strong relationship between the proton flux intensity I_p and the minimum relative distance between the harmonics of the type II radio burst $b_{i,min}$ (see Figure 2b), where the correlation coefficient r between I_p and $b_{i,min}$ is approximately 0.63, which is in full agreement with the previously obtained results in the work (Tsap Yu., Isaeva E., 2013).

Also in this work, we studied the relationship between the proton flux intensity I_p and the frequency $f_{i,1,min}$ at which the minimum splitting $b_{i,min}$ is observed.

A comparative analysis showed that the relationship between I_p and $f_{i,1,min}$ is much higher than between I_p and $b_{i,min}$, where the correlation coefficient r between the studied quantities is ≈ 0.63 and ≈ 0.70 , respectively (see Figure 2 b and 2 c).

It was shown that the lower the frequency $f_{i,1,min}$ at the fundamental harmonic, the higher the proton flux intensity I_p (see Figure 2 c), where the correlation coefficient r between the studied quantities is ≈ 0.70 .

3. Conclusion

As follows from the obtained results, the often observed evolution of the splitting of bands of type II radio bursts can be associated with a change in the density jump in front and behind the shock front, which is determined by the characteristics of both the shock wave and the environment.

The inhomogeneity of the source can also make a certain contribution, which leads to a stronger absorption of electromagnetic waves in the low-frequency or high-frequency emission band at the first harmonic.

A sufficiently strong relationship between the intensity of the SCR proton flux and the frequency f_i at the first harmonic, at which the minimum value of the relative distance is observed, may be an additional parameter for diagnosing the flux of SCR protons.

References

- Isaeva E., Tsap Yu.: 2017, *Odessa Astron. Publ.*, **30**, 222.
 Mann G., Classen T., Aurass H.: 1995, *Astron. and Astrophys.*, **295**, 775.
 Mann G., Klassen A., Classen H. et al: 1996, *Astron. and Astrophys., Suppl. Ser.*, **119**, 489.
 Nelson G. & Melrose D.: 1985, eds. D.J.McLean & N.R.Labrum, 333.
 Smerd S., Sheridan K., Stewart R.: 1974, eds. G.A.Newkirk, IAU Symp., **57**, 389.
 Tsap Yu., Isaeva E.: 2013, *Cosmic Research*, **51**, №2, 108.
 Smerd S., Sheridan K., Stewart R.: 1975, *ApL*, **16**, 23.
 Wild J. & Smerd S.: 1972, *ARA&A*, **10**, 159.
 Vasanth V., Umopathy S., Vrsnak B. et al.: 2014, *Solar Physics*, **289**, 251.
 Vrsnak B., Aurass H., Magdalenic J. et al.: 2001, *Astron. and Astrophys.*, **377**, 321.
 Vrsnak B., Magdalenic J., Aurass H. et al.: 2002, *A&A*, **396**, 673.
 Zheleznyakov V.: 1970, *Radio-Emission of Sun and Planets*, Oxford: Pergamon Press.
 Zimovets I., Vilmer N., Chian A. et al.: 2012, *Astron. and Astrophys.*, **547**, id.A6, 13.

DOI:<http://dx.doi.org/10.18524/1810-4215.2019.32.181822>

EVIDENCES FOR STRONG MIXED-POLARITY MAGNETIC FIELDS IN AREA OF A SEISMIC SOURCE ASSOCIATED WITH LARGE PROTON SOLAR FLARE

V.G. Lozitsky¹, E.A. Baranovsky², N.I. Lozitska¹ and V.P. Tarashchuk²¹ Astronomical Observatory of the Taras Shevchenko National University of Kyiv, Kyiv, Ukraine, lozitsky_v@ukr.net, nloz@observ.univ.kiev.ua² Crimea Astrophysical Observatory, Nauchny 98409, Crimea
edvard@craocrimea.ru, veratar4@gmail.com

ABSTRACT. We present in a concise statement the new results based on spectral-polarization measurements of magnetic fields in an extremely powerful proton solar flare on October 28, 2003 of X17.2 / 4B class. The observation material was obtained with Echelle spectrograph of HST AO KNU, which makes it possible to analyze the spectral manifestations of the Zeeman effect in very many lines of the visible region of the spectrum, including the photospheric and chromospheric lines. The $I \pm V$ and V profiles of about ten FeI and FeII lines, as well as the $H\alpha$, $H\beta$, $H\gamma$, and $H\delta$ lines were studied in a area of the seismic source of the flare, which was localized in the sunspot penumbra of S magnetic polarity. In this flare, we found an unprecedented Balmer decrement of intensities of $H\alpha$ and $H\beta$ lines which corresponds to ratio $I(H\beta) / I(H\alpha) = 1.68$. In the FeI 5434.5 line with very low Lande factor ($g_{\text{eff}} = -0.014$), a reliable splitting of emission peaks was found, which could indicate superstrong magnetic fields (about 50 kG) of N polarity. Indications for magnetic fields with intensity ≈ 12 kG of S polarity were found too. These indications are based on the study of the Stokes V profile of FeII 5234.6 line. In this line, there were two positive and two negative peaks of profile V , indicating a two-component structure of the magnetic field. According to the simulation data, the small-scale component with the above-mentioned superstrong magnetic field had a filling factor about 0.1 and had narrow (about twice) the half-widths of the line profiles. The close contact of subtelescopic magnetic fields of different magnetic polarity, but of lower intensity ($B \approx 1$ kG) was also indicated by the comparison of the half-widths of the FeI 5247.1 and 5250.2 lines. In general, it can be concluded that the necessary conditions for the reconnection of magnetic lines were fulfilled even at the photospheric level, rather than in the corona or chromosphere, as suggested by theoretical models of solar flares.

Keywords: Sun, solar activity, solar flares, magnetic fields, spectral lines, the Zeeman effect, superstrong magnetic fields, mixed-polarity magnetic fields, sunquakes.

АНОТАЦІЯ. Ми представляємо у стислому викладі нові результати, які базуються на спектрально-поляризаційних вимірюваннях магнітних полів у винятково потужному протонному сонячному спалаху 28 жовтня 2003 р. балу X17.2/4B. Спостережений матеріал був отриманий на ешеліному спектрографі ГСТ АО КНУ, завдяки чому є можливість аналізувати спектральні прояви ефекту Зеемана у дуже багатьох лініях видимої області спектру, в тому числі у фотосферних і хромосферних лініях. Було вивчено профілі $I \pm V$ і V близько десяти ліній FeI і FeII, а також ліній $H\alpha$, $H\beta$, $H\gamma$ і $H\delta$ в області сейсмічного джерела спалаху, яке локалізувалось в області північної сонячної плями S полярності. У цьому спалаху ми виявили безпрецедентний бальмерівський декремент, при якому для інтенсивностей в лініях $H\alpha$ і $H\beta$ спостерігалось відношення $I(H\beta) / I(H\alpha) = 1.68$. У лінії FeI 5434.5 з дуже низьким фактором Ланде ($g_{\text{eff}} = -0.014$) виявлено достовірне розщеплення емісійних піків, яке може вказувати на магнітні поля ~ 50 кГс, що мали N полярність. Були також виявлені вказівки на магнітні поля з напруженістю ≈ 12 кГс, що мали S полярність. Ці вказівки ґрунтуються на вивченні Стоксового профіля V лінії FeII 5234.6. У цій лінії спостерігались два позитивних і два негативних піки профіля V , що вказує на двохкомпонентну структуру магнітного поля. Згідно з даними моделювання, маломасштабна компонента з вказаним вище надсильним магнітним полем має фактор заповнення 0.1 і звужені у 2 рази профілі спектральних ліній. На тісний контакт субтелескопічних магнітних полів різної магнітної полярності, але меншої напруженості ($B \sim 1$ кГс) вказує також порівняння півширин ліній FeI 5247.1 і 5250.2 у стоксовому параметрі I . В цілому, можна зробити висновок, що в області сейсмічного джерела спалаху виконувались необхідні умови для магнітного пересполучення силових ліній навіть на фотосферному рівні, а не в короні або хромосфері, як це припускається у теоретичних моделях сонячних спалахів.

Ключові слова: Сонце, сонячна активність, сонячні спалахи, магнітні поля, спектральні лінії, ефект Зеемана, надсильні магнітні поля, магнітні поля змішаної полярності, сонцетрясіння.

1. Introduction

Helioseismic waves (sunquakes) are the least studied phenomenon that accompanies the energy release of solar flares. They are observed in the form of perturbations on the photospheric Dopplergrams of the Sun, which extend concentrically from some source of perturbation. Such waves were observed in $\approx 50\%$ of solar flares, and some such flares had several such sources (Kosovichev, 2015).

Physically, these are acoustic waves that move not on the surface but in the bowels of the Sun (hence the name – seismic). They reflected because of the temperature gradient and reach the surface at higher speeds. The velocity of seismic waves, visible on the surface, increases with the distance from the energy source.

Some their parameters are: typical lifetime is 1-3 min, impulse $\sim 10^{24}$ g cm / s, source localization is photosphere, ($h \approx 30$ -100 km). Possible energy sources of sunquakes are electron or/and proton beams or electromagnetic forces.

To elucidate the nature of the sunquakes, detailed observational data on the deep layers of the solar photosphere are needed, including, first of all, magnetic fields as one of the probable sources of energy of sunquakes. It is such data that can be obtained from the Echelle Zeeman spectrograms of solar flares. In this paper, we present preliminary results of an analysis of such spectrograms related to the location of a seismic source in a very powerful proton solar flare.

2. Observations

The extremely powerful proton solar flare on October 28, 2003 of X17.2 / 4B class was observed with Echelle spectrograph of the horizontal solar telescope of the Astronomical Observatory of Taras Shevchenko National University of Kyiv (HST AO KNU). This instrument, the observational conditions and some other characteristics of the flare were described in detail by Lozitsky et al. (2018). Here we briefly recall that the main advantage of the instrument is that a very wide range of spectrum, from 4000 to 6600 Å, can be observed simultaneously. Also simultaneously the spectra in orthogonal circular polarizations, i.e. combinations of Stokes parameters $I + V$ and $I - V$, are recorded.

According to CORONAS, GOES, INTEGRAL, RHESSI, SOHO and TRACE data, the impulsive phase of the flare was from 11:06 to 11:16 UT and had a line-broadening temperature of a few hundred thousand degrees (Schrijver et al, 2006). From the data of High Energy Neutron Detector (HEND) onboard of the Mars Odyssey Mission it follows that the total energy of non-thermal electrons in the flash phase was from 2×10^{32} to 6×10^{33} erg (Nizamov et al, 2018). It is useful to recall that this flare was studied earlier by many authors, e.g. Kiener et al (2006), Mandrini et al (2006), Kosovichev (2006) and Zharkova & Zharkov (2007), Lozitsky (2009), etc.

Between 9:33 UT and 11:22 UT, eighteen Zeeman spectrograms of this flare were obtained. The spectrogram for 11:06:30 UT corresponds to the peak phase of the flare, while the spectrogram for 11:14:10 UT corresponds

to the post-peak phase. Below, we briefly analyze the observational data for both above-named moments. It should be noted that at the time of maximum (11:06:30 UT), the entrance slit of the Echelle spectrograph was in the immediate vicinity (≈ 0.2 degrees) from the seismic source, which was located in the region of the sunspot penumbra of S polar polarity and had coordinates $L = 291.00$ and $\varphi = -16.64$ (Kosovichev (2006) and Zharkova and Zharkov (2007)). At 11:14:10 UT, the entrance slit of the spectrograph was projected exactly on the location of the seismic source.

3. Profiles of lines and magnetic fields

According to our observations, the flare under study had an unprecedented Balmer decrement of intensities in $H\alpha$ and $H\beta$ lines, namely $I(H\beta) / I(H\alpha) = 1.68$ (Lozitsky et al., 2018). Typically, this ratio is less than unity; only four solar flares were observed, when this ratio was greater than unity. At the maximum of the flare, the emission in the $H\beta$ line exceeded the level of the nearest spectral continuum by about 3.2 times. Strong flare emissions were observed also in D3, D1, D2, MgI 5183.6, 5172.7 and 5167.3 Å lines.

Such well known lines as FeI 5250.2, 6302.5, 5247.1 and 6301.5 had in the flare pure Fraunhofer profiles, without emission peaks at their cores. More strong lines FeI 5233 and 5324.2 Å had weak and splitted emission peaks. Strong emission peaks were observed in FeI lines of 15th multiplet (Fig. 1).

From Fig. 1 it follows that all three lines have similar character of splitting of emissive peaks in line cores. However, it should be noted that for the lines Fe I 5269.5 and Fe I 5397.1, the Landé factors are positive and equal to 1.208 and 1.426, respectively (Zemanek and Stefanov, 1976).

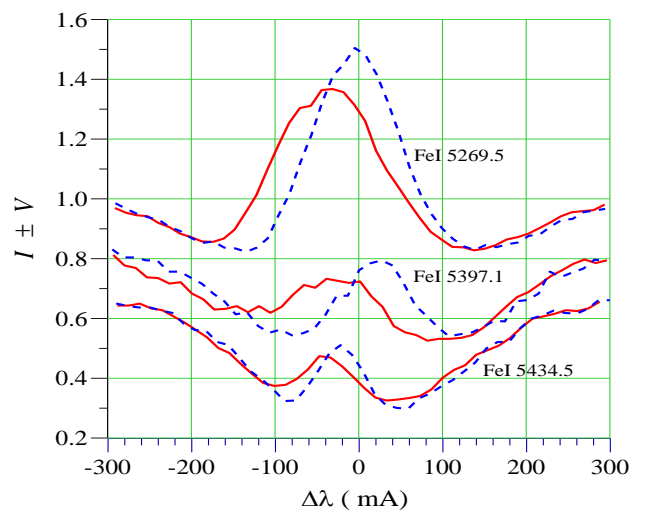


Figure 1: Observed $I \pm V$ profiles of the three FeI lines of 15th multiplet in solar flare of 2003 October 28 for time 11:14 UT (post-peak phase). Position of FeI 5397.1 line is original, whereas other lines are artificially displaced on +0.4 and – 0.2 along vertical direction for better comparison.

Line 5434.5 has a very small and negative Landé factor, namely -0.014 (Landi Degl'Innocenti, 1982). If we take this into account, as well as the actual value of the spectral splitting of the emission peaks in Fig. 1, then we obtain by these lines such magnetic fields: -1.1 , -1.3 and approximately $+50$ kG, respectively (the “+” sign corresponds to the N magnetic polarity). Thus, if the splitting of the emission peaks in the core of the 5434.5 line reflects really the Zeeman effect, we have an indication that in the region of the seismic source the magnetic fields differed by more than an order of magnitude and had different magnetic polarity. Such features of the magnetic field are noted inside an area on the Sun having an area of about 3 square mega-meters (Mm), i.e. corresponding to the spatial resolution of our observations.

4. New data to problem of superstrong fields

The question of the reality of magnetic fields of a level of ~ 50 kG is doubtful in connection with the fact that such fields must have a huge magnetic pressure that is 4-9 orders of magnitude higher than the external plasma pressure outside the corresponding structures (Lozitsky, 2015). We can expect that the magnetic field topology in areas of such superstrong fields is extremely peculiar for suppressing such huge difference of pressures even in a short time.

It would seem that to verify the reality of such giant magnetic fields, it is enough to find the corresponding manifestations of the Zeeman effect in lines with large Landé factors. However, the following methodological problems arise here.

(1) Very large Zeeman splittings must correspond to very high magnetic field strengths. For example, for a Fe I 5250.0 line with a Landé factor $g_{\text{eff}} = 3$, the Zeeman splitting should be 1.9 \AA if the magnetic field is close to 50 kG. But this line has the closest intense spectral blends at distances of 0.4 \AA and beyond. It is clear that the corresponding spectral features (i.e. Zeeman's σ components) will overlap in the spectrum on blend lines where they are difficult to detect.

(2) There are very few lines of metal in the solar spectrum with simple triplet splitting, which sometimes have emission peaks in solar flares. Namely on such peaks we can measure the magnetic field directly in the region of significant energy release, that is, in the actual solar flare, not under the flare. In the flare studied, such clear emission peaks are observed in the lines of the 15th multiplet of FeI, to which line 5434.5 also belongs. In this multiplet No. 15, the total number of spectral lines is 12, but only Fe I 5434.5 line is the Zeeman triplet. Its cleavage pattern is very simple: only two single σ components with a relative intensity of 0.5, if we consider the magnetic field to be purely longitudinal (i.e., when the central π component is absent). All other lines split anomalously, that is, the intensities of each Zeeman's σ component are distributed over some numbers of sub components with intensities of less than 0.5, which are, in addition, substantially spaced over long distances. As a result, the contrast of the observed pattern of anomalous splitting is significantly reduced for very strong fields and

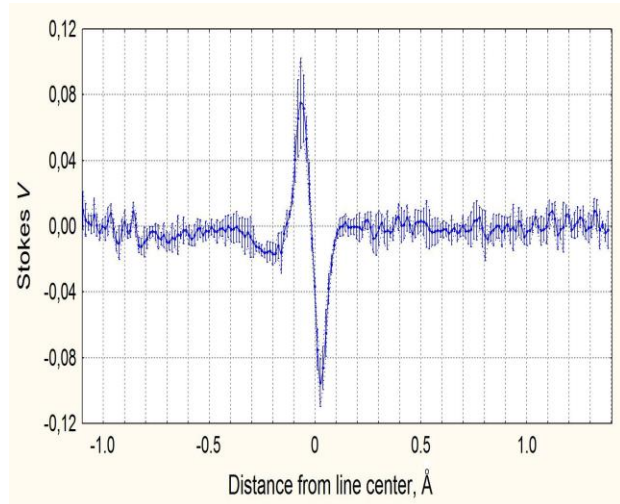


Figure 2: Stokes V profile of Fe I 5371.5 line averaged by five positions in the flare which correspond to about 5 Mm on the Sun.

in the case of photographic observations (as in our case) it could be critically small compared to instrumental noise.

(3) Therefore, the advantage of using lines with very small Landé factors is that they concentrate the spectral contributions from very strong magnetic fields in two narrow intervals of the spectrum placed symmetrically relative to the center of the spectral magnetosensitive line if the relative Doppler velocities are close to zero. Obviously, this is also true for lines with anomalous splitting, because then all sub-components of the Zeeman splitting are concentrated also in virtually the same place in the spectrum.

(4) Spectral lines with very small Landé factors are advantageous for the diagnosis of superstrong magnetic fields also because they give contrasting spectral manifestations even with a large magnetic field dispersion in spatially unresolved structures. Indeed, it would be unrealistic to assume that in such structures the magnetic field is always the same everywhere, that is, the lateral magnetic field profile is rectangular. It is known, for example, that in sunspots this profile is not rectangular but rather smooth, of a Gaussian type. But in a case of insufficient spatial resolution, sections with significantly different magnetic strengths fall simultaneously into the input aperture. Such different strengths correspond to different Zeeman splittings in the spectrum. As a result, the observed sigma components will be very blurred, with weak contrast. This factor, as well as the above factors (1) – (3), make the diagnosis of superstrong fields by lines with large Landé factors very inefficient, with low chances of success.

Considering the remark of an unknown reviewer of our paper for an another journal, we still tried to find signs of the Zeeman effect in line Fe I 5371.493 in the studied flare (Fig. 2).

This line has empirically determined and relatively large Landé factor ($g_{\text{eff}} = 0.993$) which allows to determine the magnetic field more exactly. Due to anomalous Zeeman splitting, each sigma components of this line

consist by five sub-components which have following splittings in units of normal splitting: 0.738, 0.993, 1.248, 1.503 and 1.758 (Zemanek and Stefanov, 1976). Intensity of this components equal 0.214, 0.143, 0.086, 0.043 i 0.014, respectively. In case of Zeeman triplet and longitudinal magnetic field, intensity of single sigma component should be 0.5. This means that the most intensive Zeeman sub-component (0.738/0.214) is weaker in comparison with single sigma component of a Zeeman triplet in 2.34 times, in accordance with ratio 0.5/0.214. Obviously, this circumstance makes worse the conditions of observations of the characteristic features in the spectra.

A detailed examination of the observed profiles of $I \pm V$ and V of Fe I 5371.493 line shows that one cannot really conclude that the above features exist. Regarding the Stokes profile V (Fig. 2), we can see something similar at distances of about -800 m\AA and $+750 \text{ m\AA}$, but we cannot trace the presence of weaker sub-components. These data relate to the same place in the flare where a clear splitting of emission peaks was observed by FeI 5434.5 line (Fig. 1). Possible reasons for the absence of characteristic spectral manifestations in Fe I 5371.493 line are significant magnetic field dispersion, small filling factor and thermodynamic effects in volumes with very strong magnetic fields.

It can be expected that the influence of the anomalous splitting and magnetic field dispersion will be less for weaker fields. Based on this assumption, profiles of the FeII 5234.6 line were studied in detail. This line has the effective Lande factor 0.869, its Lande factor for the lower level is 0.980, and for the upper one is 1.069, i.e. this line is not a Zeeman triplet (Zemanek and Stefanov, 1985). However, this line has a strong emission in the flare, which completely fills its Fraunhofer profile and reaches a level of 1.3 in units of the continuum level.

It was found for the flare maximum (11:06 UT) that the Stokes parameter V of this line has two positive and two negative peaks (Fig. 3). This can be interpreted as a manifestation of the two-component structure of the magnetic field, in which the weaker secondary peaks belong to the small-scale component with strong fields having a small filling factor. As the simulation showed, in this case, the magnetic field strength in the small-scale component should be about 12 kG, and the filling factor of this component is about 0.1. Magnetic polarities in both components is S , i.e. opposite regarding above-named field of $\sim 50 \text{ kG}$. The spectral width of flare emission in strong small-scale component is about 2 times smaller than in a component with a large filling factor. As to magnetic field of 12 kG in the flare, earlier Lozitsky (2015) obtained a similar result using observations in FeI 5233 line.

5. Semi-empirical model

For building of a semi-empirical model of photospheric layers of the flare, we used observations of ‘non-split’ FeI 5123.7, 5434.5 and 5576.1 Å lines and a computer program which is an independent implementation of the algorithms in the *PANDORA* code published by Avrett & Loeser (1969). This program was created by E.A. Baranovsky (with the help by E. Malanushenko) and it allows to determine the magnetic field and thermodynamical

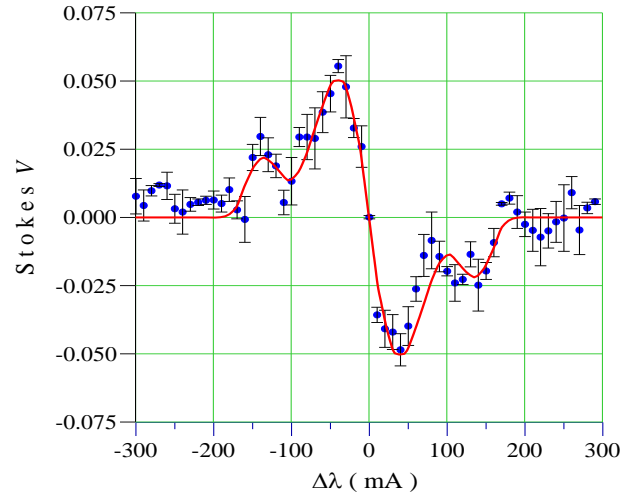


Figure 3: Observed Stokes V profile of FeII 5234.6 line in the flare. Filled circles present observations, solid line – data of simulation in frame of two-component model.

conditions on both photospheric and chromospheric levels using non-*LTE* approximation. In principle, any other program could be used for this purpose, in particular *SIR*, which allows make the optimal accordance of observations and theory in automatic regime, on a base of special algorithm. However, it is necessary take into account that *SIR* has two essential simplifies. Firstly, filling factor in this program is assumed as unchanged with high in atmosphere. Secondly, simulations for chromospheric layers carry out in *LTE* approximation. Our experience with programs *PANDORA* and *SIR* shown that for photospheric layers both programs give identical results (Andriets et al., 2012).

The semi-empirical model was built by trial and error. A large number of theoretical line profiles were calculated for various distributions with the height of the magnetic field and thermodynamic parameters and such altitude distributions were selected as the most likely that gave the best agreement of the simulations and observations.

In the semi-empirical model, the magnetic field has a remarkable feature, namely, a very narrow and high peak of the magnetic field in the range of $-3.3 \leq \log \tau_5 \leq -2.5$ (Fig. 4) where τ_5 is the optical thickness in the continuum at a wavelength of $\lambda = 5000 \text{ \AA}$. The geometrical thickness of this layer corresponds to 40-50 km. Here, the magnetic field reaches 9 T = 90 kG, which is about 2 times more than according to direct measurements of splitting of emissive peaks in FeI 5434.5 line (see Fig. 1 above).

For $\log \tau_5 \geq -2.5$, magnetic field is close to zero, which reflects the fact that there is no observed splitting in lines FeI 5123.7 and FeI 5576.1, which are formed, in general, lower than the line FeI 5434.5. As for the temperature in the flare, T_{flare} , it is increased essentially (by about 500-1500 K) for all values of $\log \tau_5 \leq -0.5$, although the maximum difference between T_{flare} and T_{quiet} is observed precisely in the range of the maximum magnetic field.

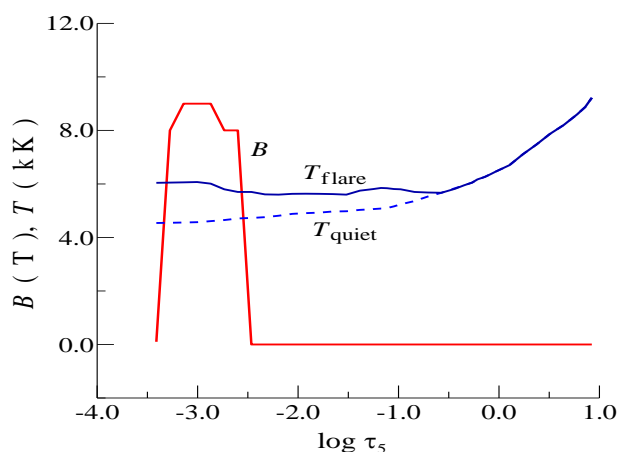


Figure 4: The distribution of the magnetic field B and the temperature T with an optical thickness of τ_5 in the flare. For a better comparison of these data, the magnetic field is presented in tesla (T), and the temperature – in kilokelvins (kK). T_{flare} and T_{quiet} are temperatures in the flare and quiet atmosphere.

6. Conclusion and short discussion

We found indications for very strong mixed-polarity magnetic fields in an exceptionally powerful solar flare of 2003 October 28 of X17.2 / 4B class. These indications relate to area of the seismic source S2 / S3 according to Kosovichev (2006) and Zharkova and Zharkov (2007) in active region NOAA 0486. In this place, Fe I 5434.5 line with very low and empirically determined Lande factor ($g_{\text{eff}} = -0.014$) has reliable splitting of emissive peaks in $I \pm V$ profiles which can reflect existence of superstrong magnetic field ($\sim 10^4$ G) of opposite (N) polarity. However, we found no evidence of such very strong fields in another line of the same multiplet of iron, Fe I 5371.5, which has $g_{\text{eff}} = 0.993$. Perhaps, this discrepancy is caused by the anomalous picture of the Zeeman splitting in second line and magnetic field dispersion in the corresponding spatially unresolved structures. A semi-empirical flare model built using the algorithm *PANDORA* code shows that the extremely strong magnetic fields could be localized in a fairly narrow altitude range (40-50 km) of the upper photosphere. Data on other photospheric lines indicate a close proximity of strong magnetic fields of opposite magnetic polarities which could create the necessary conditions for intensive reconnection of lines of force with a powerful energy release in the area of the seismic source.

The present study reveals a significant new feature of the phenomenon of superstrong magnetic fields in flares, namely, their possible concentration in a very narrow altitude range (Fig. 4). That is, the corresponding structures can hardly be imagined as very thin and long magnetic tubes or ropes that stretch from under the photosphere to the temperature minimum zone. Most likely, these are small-scale magnetic balls, whirlwinds, or at least thin magnetic sheets that rise during the flare at speeds of 1-2 km s⁻¹. The latter, apparently, indicates their

origin, i.e. they occur somewhere deep below the photosphere, where the gas and / or dynamic pressure is large enough to concentrate such a strong magnetic field. A theoretical MHD model of a magnetic vortex, in which very strong magnetic fields are possible, was proposed by Solov'ev (2013).

Acknowledgements. The authors are grateful to Prof. Alexander Kosovichev for presentation of scientific materials and useful discussions. Many thanks also to Oleg Lozitsky and Ivan Yakovkin for creating useful computer programs for processing the observational data. This study was funded by the Taras Shevchenko National University of Kyiv, projects Nos. 16БФ023-01 and 16БФ023-03, and by the Crimea Astrophysical Observatory, the project "Physical relationships of solar formations", grant РФФИ № 16-42-910467 p-аэ.

References

- Andriets E.S., Kondrashova N.N., Kurochka E.V., Lozitsky V.G.: 2012, *Bull. Crimean Astrophys. Obs.*, **108**, 1.
- Avrett E.H., Loeser R.: 1969, SAO, *Special Report* 303.
- Kiener J., Gros, M., Tatischeff, V., Weidenspointner, G.: 2006, *A&A*, **445**, 725.
- Kosovichev A. G.: 2006, *Solar Phys.*, **238**, 1.
- Kosovichev A.: 2015, *Sunquakes: Helioseismic response to solar flares*, in: V. Tong & R. García (Eds.), *Extraterrestrial Seismology* (pp. 306-322), Cambridge: Cambridge University Press, doi:10.1017/CBO9781107300668.025.
- Landi Degl'Innocenti E.L.: 1982, *Solar Phys.*, **77**, 285.
- Lozitsky V.G.: 2009, *Astron. Letter*, **35**, 136.
- Lozitsky V.G.: 2015, *Adv. Space Res.*, **55**, 958.
- Lozitsky V.G., Baranovsky E.A., Lozitska N.I. et al.: 2018, *MNRAS*, **477**, 2796.
- Mandrini C. H., Demoulin P., Schmieder B., Deluca E. E., Pariat E., Uddin, W.: 2006, *Solar Phys.*, **238**, 293.
- Nizamov, B. A.; Zimovets, I. V.; Golovin, D. V. et al.: 2018; *Journal of Atmospheric and Solar-Terrestrial Physics*, **179**, 484.
- Schrijver, C. J., Hudson, H. S., Murphy, R. J. et al.: 2006, *Ap J*, **650**:1184Y1192
- Solov'ev, A.A.: 2013, *Solar Phys.*, **286**, 441.
- Zemanek E.N., Stefanov A.P., 1976, *Vestnik Kiev Univ., Ser. Astronomii*, **18**, 20.
- Zemanek E.N., Stefanov A.P.: 1985, *Vestnik Kiev Univ., Astronomiya*, **27**, 32.
- Zharkova V.V., Zharkov S.I., 2007, *Ap J*, **664**, 573.

DOI:<http://dx.doi.org/10.18524/1810-4215.2019.32.182520>

SOLAR PLASMA DYNAMICS DURING THE FORMATION AND DEVELOPMENT OF ELLERMAN BOMBS PAIR

M. N. Pasechnik

Main Astronomical Observatory, National Academy of Sciences of Ukraine,
Kyiv, Ukraine, rita@mao.kiev.ua

ABSTRACT. The results of the specific features study of solar plasma dynamics in different layers of the active region (AR) of NOAA 11024 under the influence arisen and evolving two Ellerman bombs (EB-1 and EB-2) are presented. Spectral data with high spatial and temporal resolution were obtained with the French-Italian THEMIS solar telescope. We used spectra were obtained in the H_α -line and in the lines forming within a wide range of photospheric heights: FeI λ 630.15, 630.25, and 630.35 nm and TiI λ 630.38 nm. EBs evolved in the region magnetic flux that were emerging at the time. Changes in the velocity and direction of chromospheric and photospheric matter motion in the region of Ellerman bombs and in their immediate vicinity at different stages of EBs evolution were determined and analyzed.

Temporal variations in the line-of-sight velocities (Vlos) of the chromospheric matter at a level of the H_α core formation showed two periods in the velocity enhancement, containing several individual peaks. The maximum Vlos was -9 and 8 km/s toward and from the observer, respectively. Rapid upward and downward plasma streams (where Vlos reaches -80 and 50 km/s, respectively) were sometimes observed.

It was found that upflows were predominant at all levels of the AR photosphere. At the same time, Vlos decreased considerably in the region of EBs. Apparently, the small-scale downward flows induced by magnetic reconnections were superimposed onto the large-scale upward motion of the new magnetic flux plasma. The line-of-sight velocity in the central part of EB-1 and EB-2 varied from -1 to 0 km/s and from -1 to 0.2 km/s in the upper photospheric layer and from -1.6 to -0.2 km/s and from -1.1 to 0.25 km/s in the lower layer of the photosphere, respectively.

The studied features of temporary changes in the line-of-sight velocities of the chromospheric and photospheric matter during the formation and development of Ellerman bombs indicate that they affect both the photosphere and the lower chromosphere.

Keywords: Ellerman bombs, chromosphere, photosphere, line-of-sight velocities.

АНОТАЦІЯ. Представлено результати дослідження особливостей динаміки сонячної плазми в різних парах активної області NOAA 11024 під впливом двох бомб Еллермана (BE-1 та BE-2), які виникли і розвивалися. Спектральні дані з високою просторовою та часовою роздільною здатністю було отримано за допомогою франко-італійського сонячного телескопа THEMIS. Ми використали спектри, які було отримано в лінії H_α та в лініях, що формуються в широкому діапазоні фотосферних висот: FeI λ 630.15, 630.25 і 630.35 нм та TiI λ 630.38 нм. Бомби Еллермана розвивалися в області магнітного потоку, що виходив в той час. Визначено та проаналізовано зміни швидкості та напрямку руху хромосферної та фотосферної речовини в області бомб Еллермана та їх найближчих околиць на різних стадіях розвитку BE.

Часові зміни променевої швидкості (Vlos) хромосферної речовини на рівні формування ядра лінії H_α мали два періоди збільшення швидкості, які склалися з декількох окремих піків. Максимальна Vlos становила -9 та 8 км/с у напрямку спостерігача та від нього, відповідно. В деякі моменти спостережень існували потоки плазми вгору та вниз, де Vlos сягала -80 та 50 км/с, відповідно.

Було встановлено, що на всіх рівнях фотосфери в активної області відбувався переважно підйом речовини. У той же час спостерігалось помітне зменшення Vlos в місцях розташування BE. Ймовірно, дрібномасштабні низхідні потоки, викликані магнітними перез'єднаннями, накладалися на великомасштабний висхідний рух плазми нового магнітного потоку. Променева швидкість в центральній частині BE-1 та BE-2 змінювалася від -1 до 0 км/с і від -1 до 0.2 км/с у верхньому шарі фотосфери та від -1.6 до -0.2 км/с і від -1.1 до 0.25 км/с у нижньому шарі фотосфери, відповідно. Досліджені особливості часових змін променевих швидкостей хромосферної та фотосферної речовини під час формування та розвитку бомб Еллермана свідчать, що вони

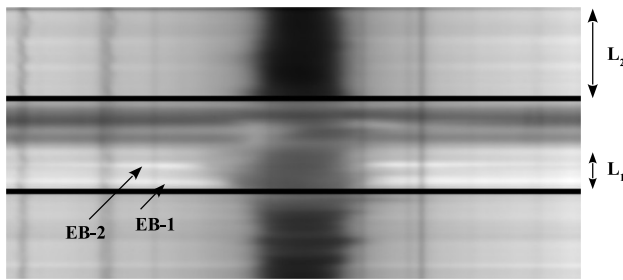


Figure 1: H_{α} spectrum of the AR obtained at 9:42:45 UT. EB-1 and EB-2 are Ellerman bombs, L1 is the analyzed area, and L2 is the AR section lies outside the region of emerging magnetic flux and without active structures.

впливають як на фотосферу, так і на нижню хромосферу.

Ключові слова: бомби Еллермана, хромосфера, фотосфера, променеві швидкості.

1. Introduction

Ellerman bombs (EBs), or moustaches, are a part of solar activity. They are short-lived, small-scale bright structures in the solar atmosphere. EBs connected with a rapid local release of energy, magnetic fields, and specific plasma motions (Nelson et al. 2013). Ellerman bombs can affect the complex dynamics of the upper solar atmosphere. They mostly appear in the young developing active regions (ARs) with a complex magnetic structure, in the regions of emerging magnetic fluxes, and in the vicinity of sunspots. Although this interesting phenomenon has been in the focus of many studies, but in which layer of the solar atmosphere magnetic reconnections triggering the formation of EBs occur still remains unclear. Some authors have suggested that Ellerman's bombs are a purely photospheric phenomena (Vissers G. J. M. et al. 2013). It is assumed that the magnetic-field energy in the process of EBs development is spent largely on acceleration of plasma flows. Jets of matter originating at the reconnection site form, differently directed motion is observed. The study of matter motion specific features at different levels of the solar atmosphere during EBs development should help determine the height of their formation.

2. Observational data

The studied Ellerman bombs (EB-1 and EB-2) emerged and evolved in active region NOAA 11024 (AR). Spectral data with high spatial (below 1 arcsec) and temporal (about 3 seconds) resolution were conducted by E.V. Khomenko with the French-Italian

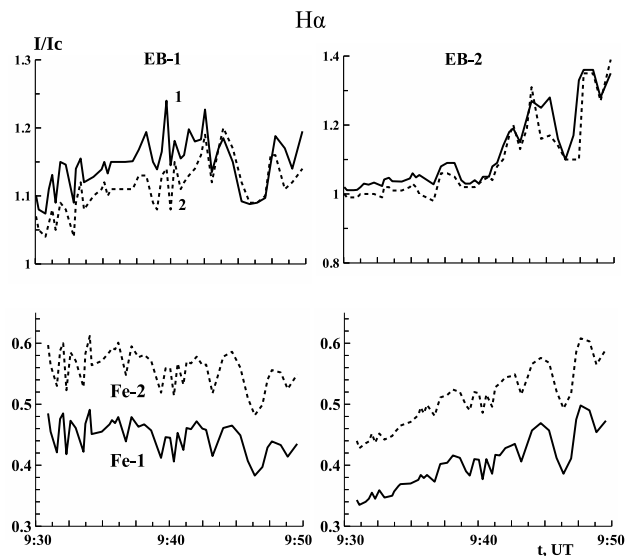


Figure 2: Temporal variations of the emission intensity (I/I_c) in the wings of the H_{α} line at the distances of 0.1 nm from its center in the long-wavelength (curves 1), short-wavelength (curves 2) wings and also Fe-1, Fe-2 line-center intensity in the spectra of EBs central part.

THEMIS 90-cm vacuum solar telescope on July 4, 2009 (Kondrashova et al., 2013). During 20 minutes, from 09:30 UT to 09:50 UT, 400 spectra of the active region NOAA 11024 were obtained. On the day of our observations AR was at an early stage of evolution, and its activity was quickly growing. In our work we used two spectral regions containing the chromospheric line H_{α} and four Fraunhofer lines forming within a wide range of photospheric heights: two strong neutral iron lines FeI $\lambda\lambda$ 630.15, 630.25 nm and two weak lines FeI λ 630.35 nm and TiI λ 630.38 nm. In the paper these lines are denoted as Fe-1, Fe-2, Fe-3 and Ti. It should be noted that two strong and two weak lines forming in upper and lower photospheric layers, respectively.

Figure 1 shows one of the H_{α} -spectra AR obtained during our observations. The width of the spectrum range containing the H_{α} line was approximately 0.6 nm. The studied AR site is marked by an arrow L1 and L2 is the AR area without active structures, which was also studied for comparison. Two extended bright narrow emission bands are seen in the wings of the H_{α} line, while a central part of the line is occupied by absorption. These bands are two Ellerman bombs (EB-1 and EB-2) having developed for that time. It is worth noting that the spectra of Ellerman bombs are opposite to the spectra of flares by appearance: in the flares, on the contrary, a strong emission in the center of the H_{α} line and not very extensive and rather weak wings are observed.

EBs evolved in the region of the emerging magnetic

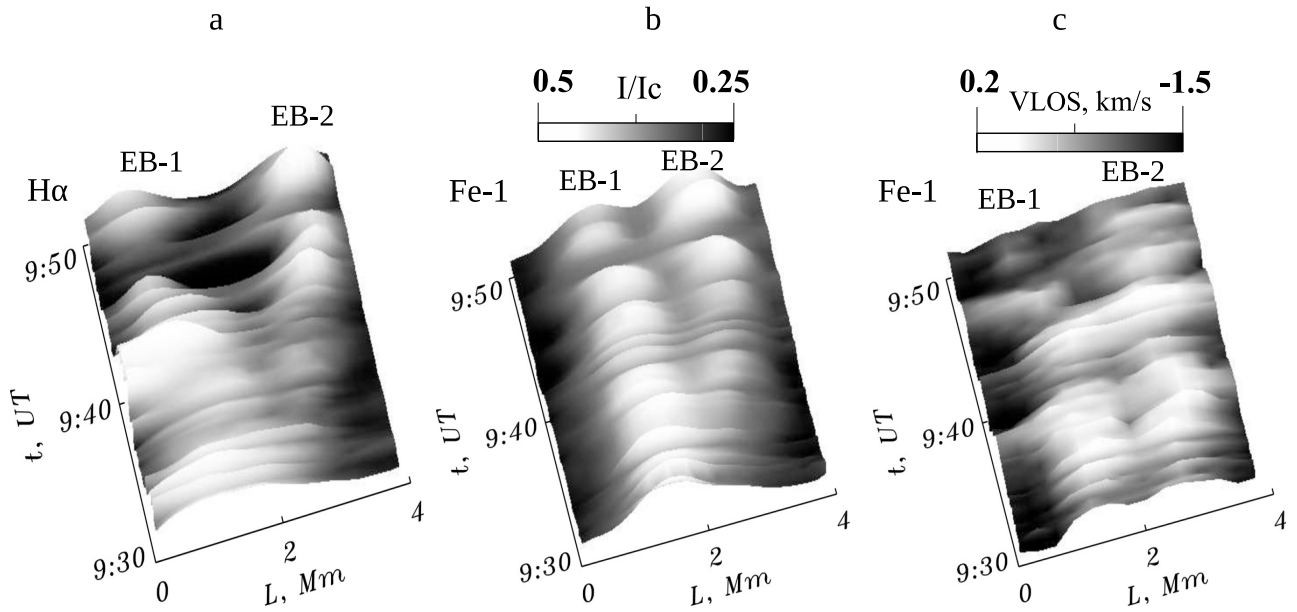


Figure 3: Intensity variations along the spectrograph slit during our observations in the blue wing of the H_{α} line at distance 0.1 nm from its center (a), in the center of photospheric line FeI-1 (b) and line-of-sight velocity determined from the shifts of the FeI-1 line core (c).

flux (Valori et al., 2012). Interestingly, the beginning of our observations coincided with the initial stage of EB-2 evolution (Pasechnik, 2016).

3. Temporal EBs evolution

In our work, we used the Stokes I profiles obtained from the spectra with an interval corresponding to the distance of 160 km on the solar surface (Pasechnik, 2016). It was found that the profiles of researched lines determined at different stages of EBs evolution were asymmetric with the emission excess in the long-wavelength wing (Fig. 2). Figures 2 and 3 a, b show changes in the intensity of the studied lines in the spectra of Ellerman bombs during our observations. It is seen that the brightness of EB-1 gradually decreased while the brightness of EB-2 increased quite sharply.

All the time curves of brightness variation are shaped like a series of peaks (Fig. 2). This indicates a pulsed release of energy.

At all photospheric levels brightness variations were of an oscillatory nature with an interval of 1–5 min (Fig. 2 and Fig 3 b).

An increase in the core intensity of all the studied photospheric lines was correlated spatially with an increase in the wing intensity of the H_{α} line (Fig. 3 a, b).

Within the first 3 min of observations three peaks (with 1-min intervals between them) are seen in all EB-1 brightness curves (Fig. 2). Figure 3 a, b

illustrates that the excitation induced by consecutive magnetic reconnections in the EB-1 region propagated along a magnetic loop and initiated the formation of EB-2, and then the two EBs evolved as a physically connected pair. It should be noted that observations showed that 50% of Ellerman bombs appear and disappear in pairs and are likely the bases of compact magnetic loops (Zachariadis et al., 1987).

4. Variations of Chromospheric and Photospheric Vlos in the studied AR site with evolving EBs

Changes in the velocity and direction of chromospheric and photospheric matter motion in the region of Ellerman bombs and in their immediate vicinity at different stages of EBs evolution were determined and analyzed (Pasechnik, 2019).

Temporal variations in the line-of-sight velocities of the chromospheric material at a level of the H_{α} core formation showed two periods in the velocity enhancement, containing several individual peaks. The maximum Vlos was -9 and 8 km/s toward and from the observer, respectively. Figure 5 a shows that the periods of the velocity growth contained three individual peaks.

It was found that upflows were predominant at all levels of the AR photosphere. While noticeable decrease of the line-of-sight velocity magnitudes was observed at the EBs location (Fig. 4). Apparently, the

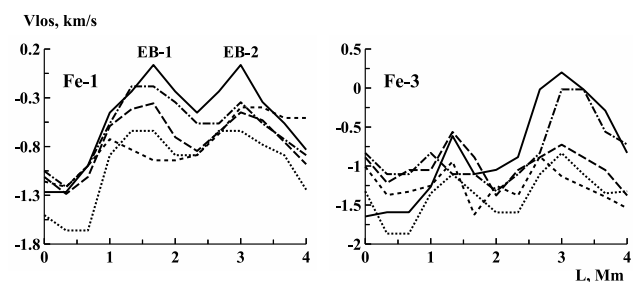


Figure 4: Line-of-sight velocity variations along the spectrograph slit at different moments of observation (Curves 1–5).

small-scale downward flows induced by magnetic reconnections were superimposed onto the large-scale upward motion of plasma of the new magnetic flux. The shape of photospheric lines profiles reinforces this conclusion. The profiles of strong lines that formed in the upper photosphere had a red asymmetry. The profiles of weak lines forming in the lower photosphere had several components in the red wing.

All the Vlos time curves are similar to the brightness variation curves in that they are shaped like a series of peaks (Fig. 2 and Fig. 5 b). This suggests that the energy release in Ellerman bombs was associated with successive intermittent magnetic reconnections. Two time periods (6 and 4 min) comprising several peaks manifested themselves. The velocity of upward motion of photospheric matter decreased considerably within these intervals. The line-of sight velocity in the central part of EB-1 and EB-2 varied from -1 to 0 km/s and from -1 to 0.2 km/s in the upper photospheric layer and from -1.6 to -0.2 km/s and from -1.1 to 0.25 km/s in the lower layer of the photosphere, respectively (Pasechnik, 2019).

The Ellerman bombs were accompanied by small chromospheric ejections (surges) with upward velocities of about 60 km/s and lasting for 0.5 – 1.5 min (Pasechnik, 2016).

5. Conclusions

Based on the research, it can be concluded that as a result of a new magnetic flux emergence, an EB-1 was formed in the studied of the active region site. In the EB-1 region pulsed energy was released due to successive magnetic reconnections. Excitation propagated from the EB-1 region along the magnetic loop and initiated the formation of EB-2, then they developed as a physically coupled pair (Pasechnik, 2016, 2018).

The studied features of the temporal changes in the line-of-sight velocity of chromospheric and photospheric matter indicate that during the development of EBs, multidirectional movement was observed - in

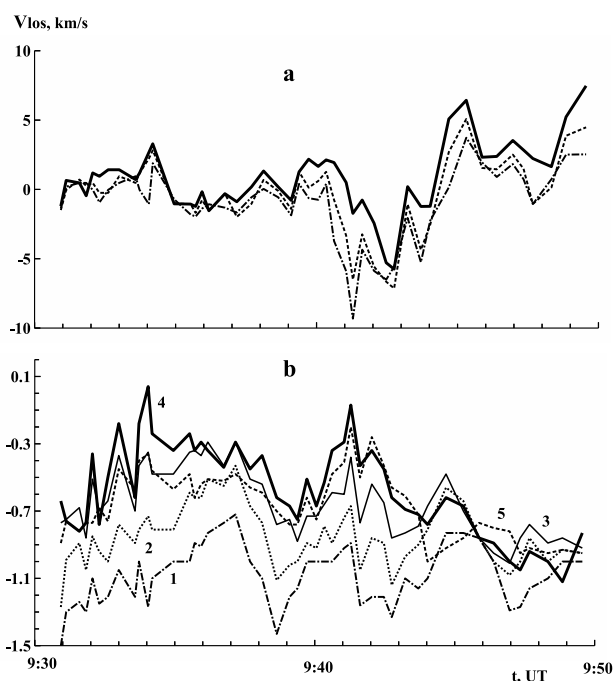


Figure 5: Temporal variations in the chromospheric and photospheric line-of-sight velocity determined from the core line shifts.

the lower chromosphere layer, where the core of the H_{α} line was formed, the matter moved upward, and in the same time downward flows reduced the velocity of ascending plasma at the photosphere level. Such a distribution of velocities could cause magnetic reconnections that occurred in the layer between the upper photosphere and the lower chromosphere. (Pasechnik, 2019). It can be concluded that Ellerman bombs affect both the photosphere and the lower chromosphere.

References

- Kondrashova N. N., Pasechnik M.N., Chornogor S.N. et al.: 2013, *Solar. Phys.*, **284**, 499.
 Nelson C. J., Doyle J. G., Erdelyi R. et al.: 2013, *Solar. Phys.*, **283**, 307.
 Pasechnik M.N.: 2016, *Kinem. Phys. Cel. Bod.*, **32**, 55.
 Pasechnik M.N.: 2016, *Kinem. Phys. Cel. Bod.*, **34**, 68.
 Pasechnik M.N.: 2016, *Kinem. Phys. Cel. Bod.*, **35**, 55.
 Valori G., Green L. M., Demouli P. et al.: 2012, *Solar. Phys.*, **278**, 73.
 Vissers G.J.M., Rouppe van der Voort L.H.M., Rutten R.J.: 2013, *ApJ*, **774**, 32.
 Zachariadis Th.G., Alissandrakis C.E., Banos G.: 1987, *Solar. Phys.*, **108**, 227.

DOI:<http://dx.doi.org/10.18524/1810-4215.2019.32.182539>

STUDY OF EFFECTS OF LUNAR TIDAL WAVE PASSAGE IN UPPER ATMOSPHERE OF EARTH ACCORDING TO MONITORING DATA AT RADIO TELESCOPE «URAN-4» RI NANU

M.I. Ryabov, L.I. Sobitnyak

URAN-4 Observatory, Radio-astronomical institute of NAS of Ukraine
ryabov-uran@ukr.net

ABSTRACT. The paper examines data on the effects of the lunar tidal wave in the Earth's upper atmosphere on the observed flux of radio sources. Monitoring of the fluxes of powerful galactic and extragalactic radio sources is carried out at the URAN-4 radio telescope of the Odessa Observatory of the Institute of Radio Astronomy of the NAS of Ukraine since 1987 till now. The monitoring program includes radio galaxies 3C274, 3C405 and supernova remnants 3C144, 3C461. Changes of fluxes of radiation sources at decimeter waves are determined by the condition of an ionosphere resulted due to space weather variation and tidal events. When radio sources are observed through a tidal wave, a "plasma lens" effect is realized in the ionosphere. Depending on the position of the radio source relative to the tidal wave, the radiation wave front is sought. As a result, various effects are realized: strong focusing, intense flickering or "blurred" recording of the radio source. According to the data of radiation monitoring of powerful radio sources, the dimensions and structure of the tidal wave zone in the upper atmosphere producing the effect of "plasma lensing" have been determined. The total size of this zone according to observations on frequent 20 and 25 MHz is on the order of 30-60 angular degrees in right ascension and declination.

АНОТАЦІЯ. У роботі розглядаються дані з дослідження впливу місячної приливної хвилі у верхній атмосфері Землі на спостережуваний потік радіоджерел. Моніторинг потоків випромінювання потужних галактичних та позагалактичних радіоджерел проводиться на радіотелескопі "УРАН-4" Одеської обсерваторії Радіоастрономічного інституту НАН України з 1987 року і по теперішній час. В програму моніторингу включені радіогалактики 3C274, 3C405 і залишки наднових 3C144, 3C461. Спостереження радіоджерел проводилися окремими сеансами в різних часових кутах, в періодах 2 години до і після часу кульмінації джерел. Спостереження проводили в аналоговому режимі реєстрації, з 1997 року в цифровому. У роботі розглядаються випадки прояву приливної хвилі, за даними моніторингу радіоджерел у цифровому режимі реєстрації, за період 1998-2004 рр. Зміни потоків випромінювання радіоджерел, на декаметрових хвилях, визначаються станом іоносфери під впливом змін космічної погоди та приливних явищ. При спостереженні радіоджерел через приливну хвилю в іоносфері реалізується ефект

"плазмової лінзи", коли в залежності від стану радіоджерела щодо приливної хвилі відбувається спотворення фронту хвилі випромінювання. В результаті реалізуються різні ефекти від сильного фокусування до інтенсивних мерехтінь або "розмивання" запису радіоджерела. За даними моніторингу випромінювання потужних радіоджерел: Кассіопея А, Лебідь А, тілець А, Діва А визначені розміри і структура зони приливної хвилі у верхній атмосфері, що виробляє ефект "плазмового лінзування". Загальні розміри цієї зони, за спостереженнями на частотах 20 і 25 Мгц, становить порядку 30-60 кутових градусів за прямим піднесенням та схиленням. У зв'язку з великим обсягом даних спостережень зближення радіоджерел з місяцем на РТ "УРАН-4" можливе подальше детальне вивчення проявів ефектів «плазмової лінзи» в іоносфері в залежності від величини приливного обурення. Важливим фактором є облік положення радіоджерел щодо максимуму приливної хвилі, що буде здійснено в наступних роботах.

Keywords: atmospheric lunar tides, upper atmosphere, radio sources.

1. Introduction

Tidal phenomena in the Earth's atmosphere arise from the gravitational forces of the Moon and the Sun (gravitational tides) and from thermal heating by the Sun (thermal tides). Apart from the difference between the physical nature of gravitational and thermal tides, they have different periodicity. Gravitational tides have a half-day period and form two tidal waves - direct and reverse. Thermal tides have a daily period and are realized in the area of the terminator.

Data from radio astronomy observations on the «Uran-4» radio telescope are the most effective method of investigating tidal waves occurring in the ionosphere.

Since 1987 at the URAN-4 radio telescope the program of monitoring powerful galactic and out of galactic sources is carried out. The monitoring program includes radio galaxies 3C274, 3C405 and supernova remnants 3C144, 3C461. Observations of these radio sources provide uniform 24-hour coverage over time and allow recording of the state of the ionosphere and the processes taking place in it by the given changes in the fluxes of radio sources and their flickering. Observations were conducted in analog recording mode, since 1997 in digital.

2. Abnormal types of radio source records

The work deals with the occurrence of a wave based on the monitoring of radio sources in the digital recording mode, for the period 1998-2004. Radio source records were chosen as the data under study when they passed near the Moon. These data were characterized by three types of records: presence of strong flickering of radio sources, strong compression or complete breakdown of recording of diagrams of direction of radio telescope. All these effects can be caused by the different race position of space radio sources relative to the maximum tidal wave in the ionosphere, which acts like a "plasma" lens, distorting the front of the wave coming from the radio source. For an example of this type of record, refer to Fig. 1-2.

The recorded abnormal records coincided with time of the close arrangement of the Moon and sources on right ascension (Fig. 3-5). During periods when observations were conducted 24 hours a day, the effects of a direct and reverse tidal wave were noted.

Detection of similar effects at on radio telescope "YPAH-4" in decameter range is related to value of angular resolution of radio telescope able to register distortion of wave front of radio source radiation under influence of tidal wave in ionosphere. Abnormal records in the presence of focusing, defocusing, and strong flickering phenomena can be interpreted as the effect of developing a "plasma lens" in the Earth's ionosphere by the formed lunar tidal wave. Applying this interpretation and taking into account the spatial realization of abnormal types of records, it is possible to estimate the dimensions of the lunar tidal wave in the ionosphere, which was in the range of 30-60 angular degrees at right ascension.

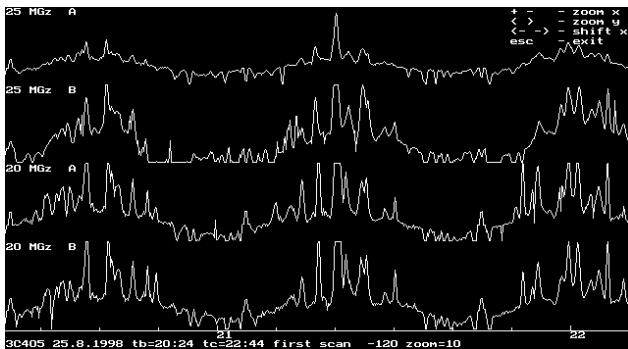


Figure 1: Sample 3C405 source record – August 25, 1998 (20-25 MHz)



Figure 2: Sample 3C144 source record - April 22, 1988 (25MHz A -80m)

The use of the radio telescope "URAN-4" having a knife pattern, a decameter range of working frequencies and the possibility of long-term tracking of the space radio source demonstrated the possibility to implement a radio astronomy method of observing tidal phenomena in the upper atmosphere of the Earth by the method of transmitting the region of tidal disturbances in the ionosphere.

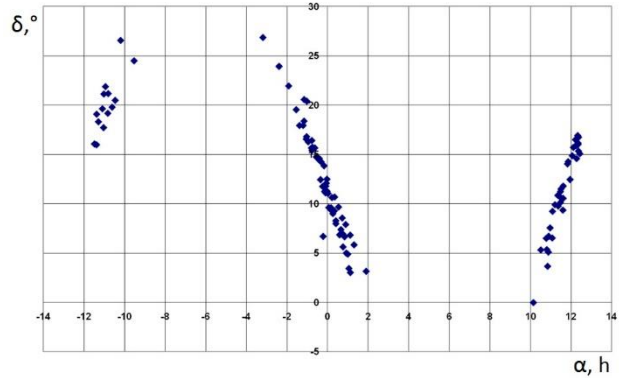


Figure 3: The position of abnormal radio 3C274 records varies depending on the distance between the Moon and the radio source by right ascension (1998-2004)

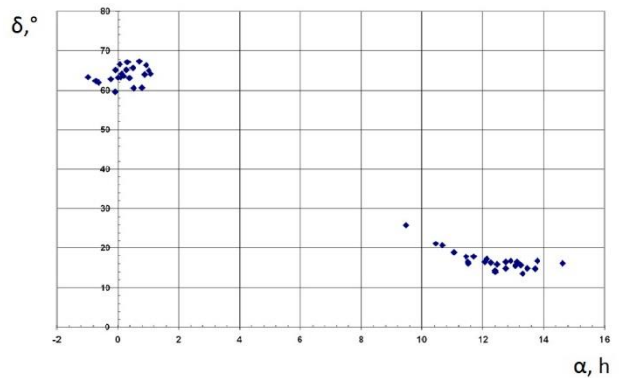


Figure 4: The position of abnormal radio 3C405 records varies depending on the distance between the Moon and the radio source by right ascension (1998-2004)

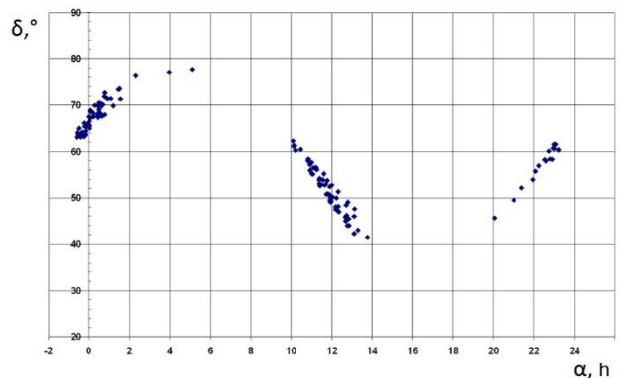


Figure 5: The position of abnormal radio 3C461 records varies depending on the distance between the Moon and the radio source by right ascension (1998-2004)

Due to the large number of observations of the approach of radio sources to the Moon, further detailed study of the effects of the "plasma lens" in the ionosphere as a result of the magnitude of tidal disturbance is possible. An important factor is the consideration of the position of the radio source relative to the maximum of the tidal wave, which will be carried out in next works.

3. Conclusion

- The possibility of investigating the passage of tidal wave in the Earth's ionosphere using the method of "transmission" by its space radio sources in the decameter wave range using the method of digital registration has been experimentally confirmed.
- The observed effects of severe flickering are associated with the passage of lunar tidal disturbance in the Earth's ionosphere, containing direct and reverse tidal waves that act like a plasma lens, distorting the shape of the radio source record.
- Observational data show that the size of the tidal perturbation is approximately 30-60 degrees in right ascension and declination from different sources.

References

- Brunelli B.E., Namgaladze A.A.: Ionosphere Physics, Moscow: Nauka, 1988, Chapter 5. Neutral atmosphere and processes in it. Tides. p. 281-288.
- Akasofu S.I., Chapman S.: Solar terrestrial physics. Oxford, 1972, Chapter 4. Dynamics of the upper atmosphere and dynamo effect, Tidal vibrations of the atmosphere p. 343-368.
- Sidorenkov N.S. Atmospheric processes and the Earth's rotation. St. Petersburg: Hydrometeoizdat, 2002. Chapter 4 Tides and Earth's rotation. p. 75-121.
- Duncan R.A.: Lunar variations in the Ionosphere. *Australian Journal of Physics*, **9**, 112.

DOI:<http://dx.doi.org/10.18524/1810-4215.2019.32.181910>

PEREGEE-SYZYGY TIDES IN ATMOSPHERE

N. S. Sidorenkov¹ and Ian Wilson²¹Hydrometcenter of the Russia, Moscow, sidorenkov@mecom.ru²The Liverpool Plains Daytime Astronomy Centre, Curlewis, NSW, Australia, irgeo8@iinet.net.au

ABSTRACT. It is shown that in 2016/17 the smoothed anomalies of air temperature in The European Territory of Russia repeated the course of the perigee distance, which varies along the sinusoid with a period of 206 days. Discovered the basic pattern perigee-syzygy tides: 206 daily beating pressure anomalies for the new moons and full moons. Pressure anomalies in the full moon and new moon can be approximated by sinusoids with periods of envelope beating about 412 days and opposite phases. The range of oscillations in the antinodes reaches 40 MB, which in order of magnitude is quite comparable to the real SYNOPTIC fluctuations in atmospheric pressure.

Keywords: lunisolar tides, lunar cycles, weather forecast, climate changes.

АНОТАЦІЯ. Стаття присвячена перігейно-сізігійний приливам в атмосфері Землі, які яскраво проявилися в незвичайному розвитку погодних процесів на Європейській території Росії (ЄТР) в останні три роки. У 2017 році ми вперше помітили, що згладжені аномалії температури повітря на ЄТР повторювали хід перігейної відстані Місяця. Показано, що додавання частот місячних аномалістичних і синодичних півмісяців породжують биття припливної сили з періодом 206 діб. Цей приливний цикл впливає на розвиток синоптичних процесів, на коливання атмосферного тиску, температури і погоди на ЄТР. 206-добовий цикл порушує правильний сезонний хід погоди, приводячи до значних аномалій метеорологічних характеристик. Встановлено співпадіння випадків з рекордною максимальною температурою з максимумом перігейної відстані Місяця, а випадків мінімальної температури – з його мінімумом. Знайдена основна закономірність перігейно-сізігійних припливів: биття аномалій тиску для молодого та повного Місяця. Аномалії тиску в молодого і повного Місяця можна апроксимувати синусоїдами, які огинають биття, з періодами близько 412 діб і протилежними фазами. Розмах коливань в пучностях досягає 40 мб, що величину цілком можна порівняти з реальними синоптичними коливаннями атмосферного тиску. Показано, що кореляція перігейної відстані Місяця з аномаліями температури порушується внаслідок того, що Місяць буває в перигелії частіше, ніж відбуваються зміни її однойменних фаз. 15 аномалістичних місяців (413,31 доби) тривають

стільки ж, скільки 14 синодичних місяців (413,42 доби). За 15 аномалістичних місяців спостерігаються дві зміни перігейної відстані – від 356 500 до 370000 км. Одна зміна здійснюється за 7 аномалістичних місяців (192,8 діб), а друга – за 8 місяців (220,4 діб). Така частотна модуляція зміни перігейної відстані сильно ускладнює синхронізацію атмосферних процесів з місячно-сонячними приливами.

Ключові слова: місячно-сонячні припливи, місячні цикли, прогноз погоди, зміни клімату.

1. Introduction

It is widely believed that global scale periodic oscillations of the Earth's atmosphere are dominated by thermal tides, which are caused, first, by heating the atmosphere from the land and water surfaces directly absorbing solar radiation and, second, by absorbing solar radiation in the stratospheric ozone layer. Naturally, thermal tides have the solar daily frequency and its subharmonics (12, 8 hours, etc.). Gravitational tides caused by the attraction of the Moon and the Sun are generally thought of as negligible and having no effect on synoptic processes in the atmosphere (Chapman, Lindzen, 1972; Volland, 1988). However, a monitoring of lunisolar tidal oscillations of the Earth's rotation rate has revealed that atmospheric processes tend to vary simultaneously with extrema of tidal oscillations of the Earth's rotation rate (Sidorenkov, 2015). Additionally, Sidorenkov (2009) has found that the spectrum of the angular momentum of the global atmosphere has lunar components with periods of a lunar year (355 days), half a lunar month (13.6 days), and a quarter of a lunar month (7 days). This is confirmed by a spectral analysis of long-term series of air temperature anomalies in Moscow that reveal lunar components with periods of 355, 206, 87, and 27 days (Sidorenkov, 2009).

The 206-day lunar cycle in the evolution of weather processes over European Russia was first noted by the author in 2017. The spring of 2017 demonstrated an unusual dynamic for the weather processes over European Russia. More specifically, from the second week of February, the daytime air temperatures rose to thawing and, in the third week of February, the daily mean temperature became positive. On March 1, the absolute temperature maxima were broken in many cities of

European Russia. The temperature reached values typical for the middle of April and the existing snow cover thawed quickly. The ice on the Don, Oka, Dnieper, Western Dvina, and Volga rivers was broken extremely early. In the second week of April, the increase in temperature ceased and negative temperature anomalies persisted until the last days of April. Then a four-day summer-like heat wave was observed, which was followed (starting from May 4) by a temperature decrease to April values. In the third week of May, the temperature began to return to normal values. However, a cold wave of Arctic air swept the region on the first days of June. As a result, the temperature reduced to extremely low values. Night frosts were still observed in many areas of European Russia in June (i.e., extremely late in the season).

2. Observations and their analysis

The Hydrometeorological Center of the Russian Federation supports the MIDL database which stores the anomalies of daily mean temperature of about 2700 Northern Hemisphere weather stations. These anomalies are computed according to Bagrov's technique (Bagrov, Loktionova, 1994). The daily mean temperature anomalies for each station were determined by applying a piecewise parabolic approximation (Gordin, 1994), that used the monthly means. Data from MIDL for several stations in European Russia were used in the present study.

Figure 1 displays the anomalies of daily mean temperature in Moscow for 2016/2017. It shows that they exhibit large day-to-day fluctuations. Sidorenkov (2015) and Sidorenkov (2009 and 2016) show that intra-monthly (i.e. semi-monthly and quasi-weekly) temperature variations can be linked to the lunisolar tides. Accordingly, daily temperature anomalies are smoothed by computing their 27-day moving averages. The smoothed data is displayed in Fig. 1 using a thick curve which mimics a sinusoidal wave with minima in November 2016, and May–June 2017, and maxima in March and September 2017.

The observed range in the temperature anomaly oscillations reaches 10°C , while the period (time interval between similar extrema) is about 204 days. This period is very close to the 206-day period obtained by Sidorenkov (2015) and Sidorenkov (2009 and 2016) from a computed periodogram of a 43-year time-series of temperature anomalies for Moscow.

Experience shows that the correlation length of the temperature anomalies for European Russia is more than 1000 km. Therefore, the plotted temperature anomalies for Moscow, well characterize the smoothed variations in temperature anomalies over the entirety of European Russia. In addition, plots like Fig. 1 were constructed for Krasnodar, Rostov-on-Don, Kazan, and Samara weather stations. These plots showed similar variations in their 27-day moving average temperature anomalies, differing only in the values and times of their daily fluctuations (Fig. 2). Finally, the temperature anomalies for all the stations cited follow the variations in the lunar perigee distance.

2.1. Origin of the 206-day lunar cycle

New and full moons are also known as syzygies. At times of syzygy, the Sun, Earth, and Moon are in a straight line. Accordingly, their tidal forces act to reinforce one another, so that the spring tides peak in strength. At times

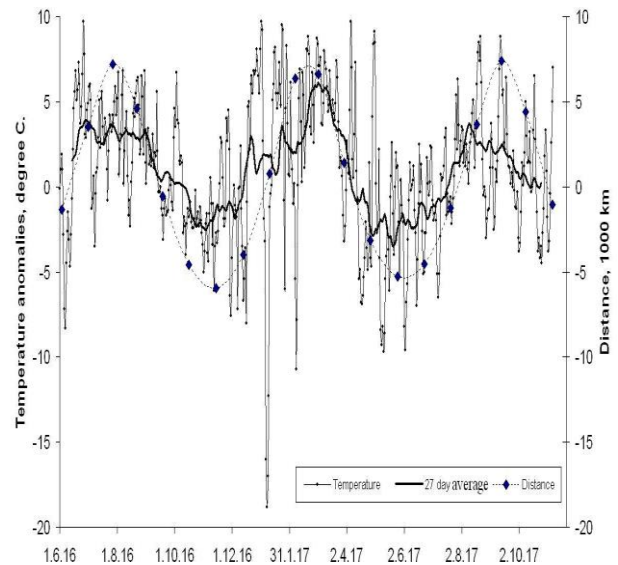


Figure 1: Deviation of the lunar perigee distance from 362464 km (diamonds) and the anomalies of daily mean air temperature in Moscow over 2016/2017 (the thin curve depicts daily mean values, and the thick curve depicts 27-day moving averages).

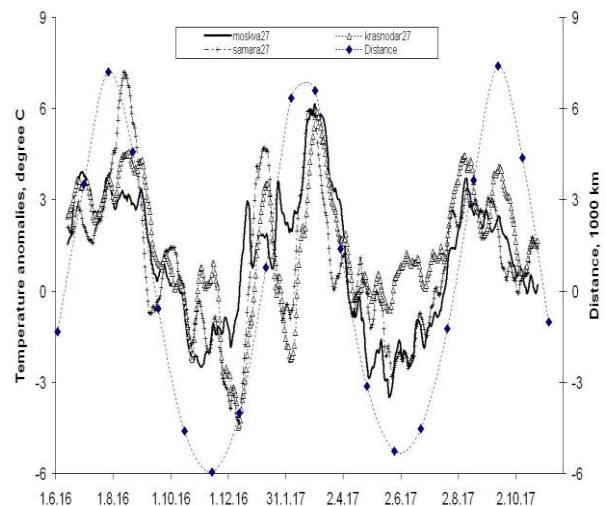


Figure 2: The 27-day moving averages of temperature anomalies in Moscow (solid), Krasnodar (triangles), and Samara (crosses) in comparison with the lunar perigee distance (diamonds connected by the dashed curve).

of quadrature (the first or third quarter phases), when the angle between the Moon and the Sun is 90° , the tides are at minimum strength (i.e. neap tides). If the lunar orbit were a circle, the strength of the spring and neap tides would not change over time. However, the lunar orbit is elliptical. The point of the Moon's orbit closest to the Earth is the perigee, while the farthest point is the apogee. A line drawn through the perigee and apogee is called the line of apsides (line-of-apse). Naturally, the tidal force of the Moon experienced by the Earth is a maximum at perigee and a minimum at apogee.

The perigee end of the line-of-apse of the lunar orbit continuously moves from west to east over the celestial sphere, returning to nearly the same position relative to the

stars every 8.85 years. The Sun makes a revolution relative to the stars in the same direction in 1 year. Therefore, if the perigee end of the line-of-apse starts at a time when it points directly at the Sun, then another 411.78 days or 1.127 years are required for it to return to the original configuration (i.e. the Sun catches up with the perigee). This is true because the frequencies of two considered revolutions are subtracted: $\frac{1}{1} - \frac{1}{8.85} = \frac{1}{1.127}$.

The 411.78-day period is called the Full Moon Cycle (FMC). Clearly, it takes roughly 206 days before the perigee end of the lunar orbit makes half a revolution. The 206-day cycle is known in astronomy as half of the FMC. From a physics point of view, the 412-day cycle is the period of beats produced by interfering the close frequencies of anomalistic (27.55 days) and synodic (29.53 days) months (Sidorenkov, 2015; Sidorenkov, 2009; 2016, Wilson, 2012) or the synodic month and the evection period in the lunar longitude (31.81 days). The important point to note is that the 206-day cycle is equal to the half-difference between the frequencies of the interfering oscillations as well as being a whole multiple of the synodic month (since $7 \times 29.53 \text{ days} = 206.7 \text{ days}$).

2.2. Manifestation in terrestrial processes

The re-alignment of the anomalistic and synodic orbital periods cited above influences lunar tidal and terrestrial atmospheric processes. For example, the distance between the Earth and the Moon at the perigee ranges from 370000 to 356000 km, with a long-term average period of about 206 days. This effect of lunar distance is illustrated in Figs. 1 and 2, where the deviation of perigean distance from its average value of 362464 km, is depicted by diamonds connected by a dashed curve. The length of the lunar anomalistic month (i.e., the time interval between two consecutive passages of the Moon through the perigee) ranges from 28.5 to 24.8 days, while its long-term average is equal to 27.554545 days.

It is important to note that the Earth's motion around the barycenter of the Earth–Moon system reflects all motions of the Moon at a scale of 1:81. Therefore, the Earth has similar variations in its pericentric distance and in its angular velocity of monthly rotation around the barycenter with a period of 206 days (Sidorenkov, 2015; Sidorenkov, 2009; 2016). However, since we are on the Earth, we cannot see or experience its motion and must use the Moon to study the motions of the Earth.

2.3. Spring tides

The 206-day cyclicity of the Earth's pericentric distance and, hence, its angular velocity of monthly rotation about the Earth-Moon barycenter, must influence processes in the Earth's spheres, primarily, in those of the atmosphere and hydrosphere. For example, Fig. 3 presents the maximum sea level heights at full and new moons in various ports around the globe (see Avsuk, Maslov, 2011).

Inspection of Fig. 3 shows that all tidal curves, for a given lunar phase (i.e. new or full), are well approximated by an enveloping sine function with a period of about 412 days and an amplitude of about 60 cm. For perigean spring curves, the period of the beats (the time interval between neighboring nodes or antinodes) is equal to 206 days.

Figure 3 provides key information for understanding the formation mechanism of 206-day oscillations of temperature anomalies in the atmosphere. It suggests that the atmosphere must exhibit pressure oscillations like the perigean spring tides in the ocean, which can lead to the formation of 206-day oscillations of air temperature. Specifically, Fig. 3 shows that the spring tides at full and new moons have opposite heights at antinodes and are nearly identical at nodes. With regards to atmospheric pressure, such behavior means that alternating semimonthly cyclonic and anticyclonic processes prevail at antinodes, but they die out at nodes. Such dynamics of atmospheric processes can lead to considerable differences between the air temperature conditions at antinodes and nodes. The period of these differences is 206 days.

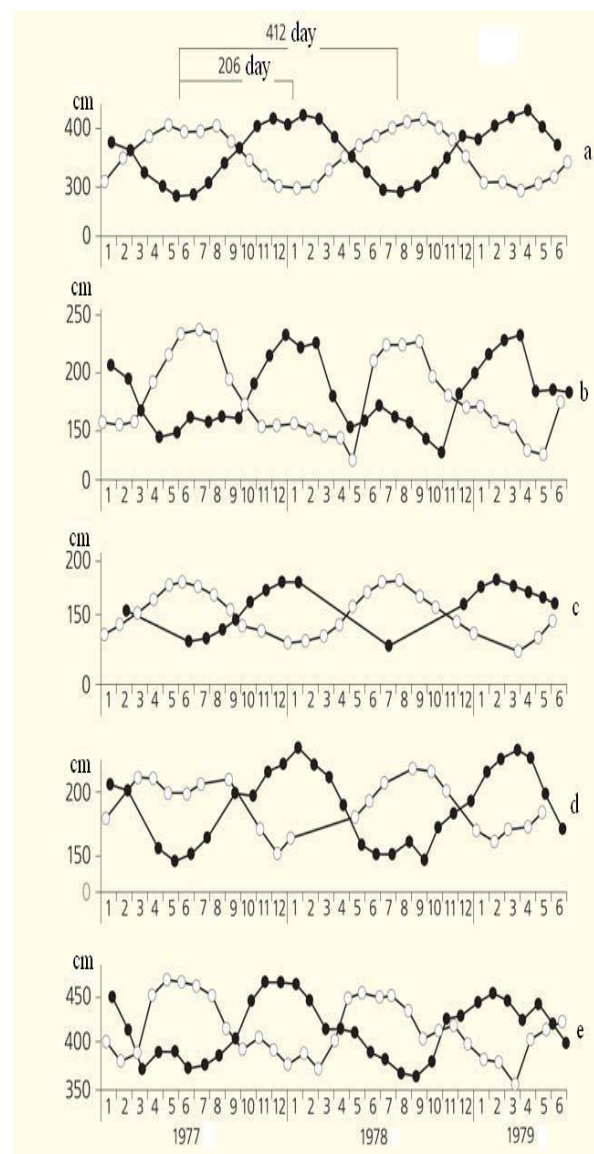


Figure 3: Highest spring tide at full moons (○) and new moons (●) in (a) Murmansk, (b) Puerto Williams (Chile), (c) Suva (Fiji), (d) Lerwick (Scotland), and (e) Magadan (Avsuk, Maslov, 2011).

The main feature of perigean spring tides is that the curve for each syzygy (i.e. new or full moon) is well approximated by a sine function (beat envelope) with a period of 412 days and a phase difference of 180° (Fig. 3). Therefore, for any tidal characteristic, each positive anomaly in one syzygy is associated with a negative anomaly in the nearest other-type syzygy. The root cause is that the lunar orbit is elliptical. If the Moon passes through perigee at full moon, then the distance to the Earth reduces to a minimum and the tidal force is maximum (positive anomalies). Roughly half a month later, at new moon, the Moon is in the opposite part of the orbit at the maximum distance (near apogee) and the tidal force becomes minimum (negative anomalies).

In 27.55 days, the Moon returns to the perigee, but this time two days ahead of full moon ($29.53 - 27.55 \approx 2$); next time, it returns four days ahead of full moon, and so on. With each revolution, the tidal force decreases at full moon and increases at new moon. About 3.5 synodic months later, the spring tides become of equal strength (at a beat node) and, then, the tidal force at new moon begins to prevail over that at full moon, reaching a maximum range (at an antinode) after about 7 syzygies. Next, the tidal range decreases over 3.5 months until the next node is reached and so on. Changes in the sign of anomalies from full to new moons and back always occur at beat nodes at intervals of about 206 days.

2.4. Spring tides in the atmosphere

The appearance of a 206-day cycle in the 2017 weather prompted our study of atmospheric spring tides, which are expected to manifest themselves in atmospheric pressure oscillations in a similar manner to the sea-level spring tides in Fig. 3 (Avsuk, Maslov, 2011). Specifically, a series of three-hour ground-surface pressure measured at the VDNKh weather station in Moscow over the last two years was used to calculate daily mean pressure values and their anomalies. The daily pressures at the Moscow State University meteorological observatory averaged over 1966–2010 were used as normals reference (Sidorenkov et al., 2008).

Next, for each full moon day, we chose the daily mean pressure anomaly over for this day. A series of atmospheric pressure anomalies for all new moons was separately generated in a similar manner. With the help of Excel, the atmospheric pressure anomalies at the VDNKh weather station were plotted for full moons (open circles on the broken curve) and for new moons (solid circles on the solid curve) over 2016–2017 (Fig. 4).

The spring tides in Kazan were additionally analyzed. With the help of Excel, the anomaly atmospheric pressure at the Kazan University weather station were plotted for full moons (open circles on the broken curve) and for new moons (solid circles on the solid curve) over 2016–2017 (Fig. 5).

Figures 4 and 5 show that the spring oscillations of atmospheric pressure are very noisy. Nevertheless, the basic features of spring tides, namely, nodes (in the summer of 2016 and May of 2017) and antinodes (in February–March and September–October of 2017) can be observed. It can clearly be seen that the pressure anomalies at new and full moons are of different signs. The pressure anomalies at full and new moons can be approximated by sinusoids with beat envelope periods

of about 412 days and opposite phases. The range of oscillations at antinodes reaches 40 mb, which is comparable in order of magnitude with actual synoptic oscillations of atmospheric pressure and close to spring tides in the ocean (Avsuk, Maslov, 2011) since a 1-cm sea level elevation is equivalent to atmospheric pressure of 1 hPa (mb).

Thus, Figs. 4 and 5 suggest that the geodynamical forces in 2016/2017 were able to overcome the stochastic thermodynamics of the atmosphere and imposed their celestial-mechanical tidal cyclicity on the weather evolution over European Russia. It is these cases of forced synchronization of atmospheric dynamics and tides that give rise to lunar components in the spectra of anomalies of meteorological characteristics (Sidorenkov, 2009; 2015; 2016) connected with atmospheric spring tides. The 206-day cycle of spring tides violated the correct seasonal variations in meteorological characteristics. Many local record extremes of daily meteorological characteristics observed across European Russia in 2016/2017 were associated with this cycle.

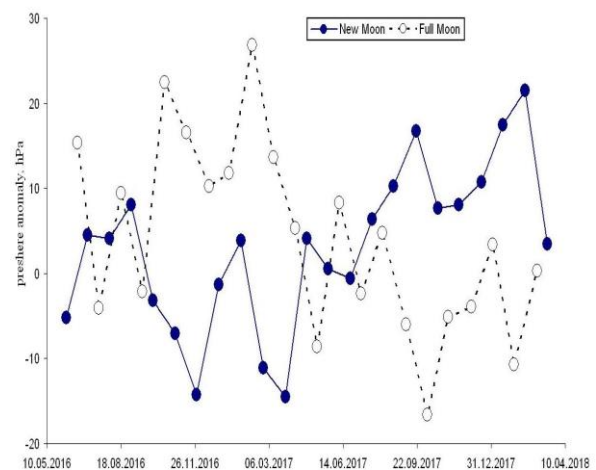


Figure 4: Spring oscillations of atmospheric pressure at the VDNKh (Moscow) weather station over 2016/2017.

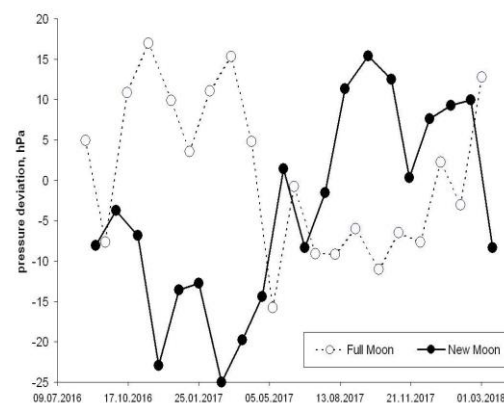


Figure 5: Spring oscillations of atmospheric pressure at Kazan weather station over 2016/2017

The 206-day cycle of temperature anomalies leads to violations of seasonal temperature variations. For example, due to its contribution, the 2016 winter over European Russia began nearly one month earlier, while the 2017 summer set in one month later than its usual time. These phenomena were followed by a shift in summer to August and a delay in fall. In January of 2018, the phases of 206-day lunar and annual solar cycles coincided, and winter came, though mild with little snow at the beginning, but frosty with much snow at the end.

Over the time interval considered, two extrema (maxima or minima) of the perigee distance and the temperature over European Russia were observed at the same time. This suggests an interesting dependence: record maximum temperatures tend to occur simultaneously with perigee distance maxima, while the cases of minimum temperature, with perigee distance minima.

For example, according to daily data from the Hydrometeorological Bulletin of the Hydrometeorological Center of Russia, near the maximum of the perigee distance on March 1, 2017, the absolute temperature maximum was exceeded in Moscow, St. Petersburg, Bryansk, Rostov-on-Don, Kirov, and some other cities. Near the next maximum of the perigee distance (on September 13), the temperature maximum for September 12 was exceeded in Velikiye Luki, Smolensk, Tver, Rybinsk, Simferopol, Anapa, Krasnodar, etc. However, absolute temperature minima are observed much less frequently, possibly due to the global warming of the climate. Near the distance minimum of May 26 to June 20, 2017, frosts were observed over European Russia and the minimum temperature extremes were exceeded in Arkhangelsk, Lipetsk, Pskov, Tambov, Ufa, etc.

The correlation presented in Figs. 1 and 2, however, between the lunar perigee distance R and the anomalies of temperature T cannot persist permanently. This is true since it is that the Moon passes through the perigee more frequently than it passes through the same phase i.e. there is a slow drift between the Synodic and Anomalistic month so that 15 anomalistic months (413.3182 days) is roughly equivalent to 14 synodic months (413.4282 days). Thus, over 15 anomalistic months, the perigee distance varies twice from 356500 to 370000 km, with one variation lasts for seven anomalistic months (192.8 days), and the other, for eight months (220.4 days). This leads to a kind of frequency modulation being imposed on the perigee distance variations that complicate the synchronization of atmospheric processes with lunisolar tides.

An analysis of long-term temperature anomalies has shown that the situation described above is a rather rare event, where there is a synchronization of oscillations in the atmospheric circulation with oscillations of geodynamic forces in the Earth–Moon–Sun system. An analysis of atmospheric pressure in Moscow starting from 1966 reveals that cases like the above-considered synchronization of pressure oscillations with perigean spring tides were observed in 1978, 1980, 1982, and 1983. Some examples of synchronization of atmospheric processes with geodynamic forces can be found in (Sidorenkov, 2016; Sidorenkov, 2009; 2016, 2017).

All meteorological features discussed previously appear because of the effects produced by perigean spring

tides on the atmosphere. Clearly, the possibility of synchronization depends on the season of the year. The 206-day cycle and four years are in the ratio of 1:7. So after four years, the phase of the 206-day cycle re-synchronizes with the seasons of the year. Hence, you would expect that the maximum correlation of the temperature anomalies T with R should have a four-year period. However, this study shows that it tends to have an eight-year period, since, in four years, the lunar phases reverse (i.e. full moons are observed instead of new moons). (Recall that the Moon is between the Sun and the Earth at new moon, while the Earth is between the Sun and the Moon at full moon, so the configuration of the gravitational forces is entirely different in these cases). Thus, the same lunar phase occurs at the same time in the seasonal cycle once every eight years, i.e., the 206-day cycle in temperature anomalies and weather features is manifested primarily when certain mutual configurations of the Earth, Moon, and Sun are repeated.

A good example of eight-year cyclicity is the still widely remembered unusually dry and warm fall observed over European Russia in 2018. Earlier similar weather anomalies in fall occurred in 2010, 2002, and 1994. Even earlier similar dry anomalies in fall were observed in 1954, 1946, and 1938.

References

- Avsuk Yu.N., Maslov L.A.: 2011, *Earth, Moon, and Planets*, **108**, Issue 1, 77, DOI 10.1007/s11038-011-9381-8.
- Bagrov A.N., Loktionova E.A.: 1994, *Meteorology and Hydrology*, **11**, 100 [in Russian].
- Gordin V.A.: 1994, *Meteorology and Hydrology*, **11**, 110 [in Russian].
- Sidorenkov N.S., Isaev A.A., Orlov I.A., Sherstyukov B.G.: 2008, in *Proc. of Hydrometeorological Center of Russia*, Issue **342**, 177 [in Russian].
- Sidorenkov N.S., Sumerova K.A.: 2012, *Russian Meteorology and Hydrology*, **37**, No. 6, 411.
- Sidorenkov N.S.: 2015, *Geophysical processes and biosphere*, **14**, No. 3, 5 [in Russian].
- Sidorenkov N.S.: 2016, in *Proc. of Hydrometeorological Center of Russia*, Issue **359**, 33 [in Russian].
- Chapman S., Lindzen R.S. *Atmospheric Tides: Thermal and Gravitational* (Springer, Netherlands, 1970).
- Sidorenkov N.S.: 2009, *The interaction between Earth's rotation and geophysical processes*. Weinheim. WILEY-VCH Verlag GmbH & Co. KGaA, 317 pp.
- Sidorenkov N.S.: 2016, *Izvestiya, Atmospheric and Oceanic Physics*, **52**, No. 7, 667, DOI: 10.1134/S0001433816070094.
- Sidorenkov N.S.: 2017, *AApTr*, **30**, Issue 2, 249, ISSN 1055-6796.
- Volland H.: 1988, *Atmospheric Tidal and Planetary Waves*. Kluwer Academic Publishers, Dordrecht, The Netherlands, 348 pp.
- Wilson I.R.G., Lunar Tides and the Long-Term Variation of the Peak Latitude Anomaly of the Summer Sub-Tropical High-Pressure Ridge over Eastern Australia, *The Open Atmospheric Science Journal*, 2012, **6**, 49.

SOLAR SYSTEM

DOI:<http://dx.doi.org/10.18524/1810-4215.2019.32.181825>

BALDONE OBSERVATORY IN THE CIRCLES OF TIME

I. Eglitis

Institute of Astronomy, University of Latvia, Raina blvd. 19, Riga, LV 1586, Latvia,
ilgmars.eglitis@lu.lv

ABSTRACT. 1957 – The first laboratory building, known as the White House, was built near Baldone on the Riekstu hill, in the territory of the next Observatory. 01.01.1958 – The Astronomy Sector was separated from the Institute of Physics and commenced independent activity as the Laboratory of Astrophysics at the Latvian Academy of Sciences (LAS). In 1967, with the decision of the Presidium of the Latvian SSR LAS the Laboratory of Astrophysics was transformed into the Radioastrophysic Observatory at LAS. Under the leadership of the first director, Janis Ikaunieks, an instrumental observation base develops – a 1.2m Schmidt telescope was installed in 1966 for optical observations. The project of the variable base radio interferometer after the death of J. Ikaunieks was unrealized. To continue astronomical observations in radio range, in 1972 10m radio telescope RT-10 was purchased.

Non-stationary processes and spectral research of carbon stars are associated with the study in optic range develops following the plan of J. Ikaunieks. After the establishment of the UL Institute of Astronomy in 1997, the field of research in the optical range is supplemented by the research direction of small objects of the solar system. However, the area of radio astronomy has stopped due to lack of funding.

The scientific potential of the Baldone Observatory remains significant. It should be mentioned that the 22,000 Schmidt telescope astroplate archive obtained in 1967-2005, will be digitized entirely this year. After digital image processing, coordinates and brightness for about of 330,000,000 objects will be obtained. The database will contain details of star movement, brightness variability (both long-term and short-term) and details of known, unknown asteroids and comets.

In 2008, monitoring of asteroids in the Solar System is started in Observatory. Up till now 77 new asteroids have been discovered in the Solar System and 11 of them have been named.

Research on carbon stars is still continuing successfully. The number of carbon stars currently discovered has reached 400. A methodology has been created for estimating the temperature and distance to the carbon stars. Work is currently underway to improve this method.

Observatory is continuing its work on popularizing astronomy. Number of visitors per year has risen from 1000 in 90s to almost four thousand in 2018.

Keywords: Baldone Observatory-history-carbon stars-photographic archive – asteroids

АНОТАЦІЯ. 1957 – перша лабораторна будівля, відома як Білий дім, була побудована поблизу Балдона на пагорбі Ріксту, на території майбутньої обсерваторії. 01.01.1958 – Астрономічний сектор відокремився від Інституту фізики і розпочав незалежну діяльність як Лабораторія астрофізики Латвійської академії наук (ЛАН). У 1967 р. Рішенням Президії Латвійської РСР ЛАН Лабораторію астрофізики було перетворено на Радиоастрофізичну обсерваторію при ЛАН. Під керівництвом першого проректора Яніса Ікаунієкса розвивається інструментальна база спостереження – в 1966 році для оптичних спостережень був встановлений 1.2-метровий телескоп Шмідта. Проект радіоінтерферометра змінної бази після смерті Я. Ікаунієкса не був реалізований. Для продовження астрономічних спостережень у радіодіапазоні, у 1972 р. було встановлено 10-метровий радіотелескоп РТ-10.

Нестационарні процеси та спектральні дослідження вуглецевих зірок, пов'язані з вивченням в області оптичного діапазону, продовжили розвиток за планом Дж. Ікаунієкса. Після створення UL Інституту астрономії у 1997 році сфера досліджень в оптичному діапазоні доповнюється напрямком досліджень малих об'єктів Сонячної системи. Однак напрямком радіоастрономії зупинилася через брак фінансування.

Науковий потенціал обсерваторії Балдона значно відновлюється. Слід зазначити, що 22 000 архівів астропластин Шмідта, отримані в 1967-2005 роках, цього року будуть повністю оцифровані. Після цифрової обробки зображень будуть отримані координати та блиск приблизно для 330 000 000 об'єктів. База даних буде містити деталі руху зірки, зміни блиску (як довгострокової, так і короткострокової) та деталі відомих і невідомих астероїдів та комет.

У 2008 році в обсерваторії розпочато моніторинг астероїдів у Сонячній системі. Дотепер у Сонячній системі було виявлено 77 нових астероїдів, 11 з них отримали назву.

Дослідження вуглецевих зірок досі успішно тривають. В даний час кількість виявлених вуглецевих зірок досягла 400. Створена методологія для оцінки температури та відстані до вуглецевих зірок. Зараз ведуться роботи з удосконалення цього методу.

Обсерваторія продовжує роботу над популяризацією астрономії. Кількість відвідувачів за рік зростає з 1000 у 90-х майже до чотирьох тисяч у 2018 році.

Ключові слова: Балдонська обсерваторія – історія, вуглецеві зорі – фотографічний архів – астероїди

1. Historical review

The Astrophysics Observatory of the Institute of Astronomy of the University of Latvia in Baldone Riekstu hill began its activities in 1958. The Astronomy Sector was separated from the Institute of Physics and commences independent activity as the Laboratory of Astrophysics at the Latvian Academy of Sciences (LAS). A year ago, the first laboratory building was built in the territory of the next observatory, 5 km from Baldone town near Riekstu hill, the so-called "White House". The founder and first director of the Observatory was Janis Ikaunieks (1912-1969). He planned to develop two directions of research: to create a large base radio interferometer and research late-type stars in the optic. In 1959, an agreement was signed with Carl Zeiss factory of East Germany (GDR) on the construction of a Schmidt telescope to ensure the performance of optical observations.

In 1962, by coordinating the astronomical plans of the Baltic republics, it is planned that the Astrophysics Laboratory of LAS would become a radio astronomy center in the Baltics region. The name of the Astrophysics Laboratory was changed in 1967 with the LAS decision to Radioastrophysical Observatory at the LAS. At this moment in time, the project of a two-kilometre long rig for multi-antenna for variable base radio interferometer has been completed. This project does not succeed because of the premature death of Janis Ikaunieks. The further development of the area of radio interferometry, 30 m rotating radio antennas were built in Roņū Island and the cities of Engure and Salacgrīva also was also discontinued. An interesting deviation – similar plan was realized many years after in Mullard radio observatory in England. Thanks to the efforts of Arturs Balklavs (1933-2005), the next long-term director of the Observatory, the direction of radio astronomy studies remains with the 10 m radio antenna purchased in 1972, at 755, 610 and 326 MHz.

The development of optical astronomy went in line with Janis Ikaunieks's idea. On the first days of January 1965, the 1.2 m large field (19 square meters field of view) Schmidt system telescope with an input aperture of 0.8 m has arrived to the Observatory. It is the twelfth largest Schmidt telescope in the world to date (Figure 2).

The construction of pavilion for telescope was carried out with the help of Latvian specialists only and was completed in June 1966. The pavilion and the dome of the telescope were designed by the Latvian Design and Construction Bureau of the Latvian SSR LAS. Construction work was led by the repair and construction department of LAS. The dome was made by the Riga Ship Repair Plant and assembled by a specialized assembly plant. These organizations met for the first time with such a special object, therefore there were many difficulties in their work (Figure 3). The first observations with Baldone Schmidt telescope were made in December 1966. The test results have shown, that it is a very high-quality instrument.

After gaining political independence in 1991, the process of reorganization in all sectors of the economy and science began in Latvia. As a result of science reform, the institutes of LAS were integrated into universities. The LAS Radioastrophysical Observatory together with Astrophysical Observatory of the University of Latvia (UL) formed independent Institute of Astronomy at the UL in

1997. Previously the sharp decline of finance amount for science leads to the abandonment of the radio astronomical research at the Baldone Observatory. Research of carbon stars and nova continues in the newly established UL Institute. Following the recommendation of the Red Giant Working Group of the International Astronomical Union, an updated version of the Galactic Carbon Star Catalogue was prepared and published by the institute astronomers, in 2001. The average amount of visits to the catalogue home page is close to 100,000 per year.



Figure 1: 10 m Baldone Observatory radio telescope RT-10.



Figure 2: Baldone Schmidt telescope



Figure 3: Baldone Schmidt telescope pavilion

2. Research in Baldone Observatory

The properties of carbon (C) stars are still successfully studied in the optical range. Over 300 new carbon stars have been discovered on the objective prism photographs taken with the Baldone Schmidt telescope. A green-yellow survey was made with the resolution about 500 or 1000 at H-gamma. The region of the sky covered by the survey: 4.5 degrees wide zones centered on the galactic latitudes +7 and -7 degrees between longitudes 68 and 200 degrees on the equatorial zone at longitudes 84-96 degrees and 172-180 degrees on several other separate fields with five degrees diameter. Some infrared plates were made on the Kodak plates 1N with resolution 500 near the A band of Earth atmosphere. The region of the sky covered: 4.5 degrees wide zone centered on the galactic latitude +7 degrees between longitudes 128 and 140 degrees, region between latitudes +9.5 and -9.5 degrees and longitudes between 80 and 96 degrees. In the last ten years occasional prism observations were made with CCDs: CCD ST – 10XME and STX-16803. More than 50 new carbon stars were discovered in Cygnus, Perseus and Cassiopeia regions (Eglitis & Sokolova, 2018). Non-stationary processes are being studied not only in the newly discovered C stars, but also in 70 flaming stars which were discovered in Andromeda Galaxy. Spectrophotometric studies of C stars reveal that gradients [757 -- 685] shows the correlation with Teff taken from Bergeat et al. (2001). It reveals a possibility to classify carbon stars by temperature indices and to detect effective temperatures of stars with accuracy ± 350 K. Investigations of C stars in LMC by Mauron (2008) give possibilities to create a method to evaluate absolute magnitude of late carbon stars using (J – K)_o color indices. The calculation of distances was made by the equation:

$$M_k - m_k + 5 \lg r + A_k + 10 = 0, \text{ where } r \text{ is in kpc.}$$

Now our methodology is testing using GAIA parallax measurements.

On the subject of carbon stars General Catalogue of Cool Carbon Stars (CGCS) (Alksnis et al., 2001) and four monographs were prepared, two of which were reissued in the US.

In 2005/2006 years, the Baldone Astrophysics Observatory has exhausted the astroplates reserves, as manufacturers have already abandoned astronomical photo plate production. The transition period to new light receivers is successfully used for the recoating with aluminium of the main mirror of Baldone Schmidt's telescope in Germany, and from 2007 the telescope continues to observe with a small 3.2 megapixel CCD camera that uses only 0.4% of the telescope's field of view. As the telescope opportunities change, research topics are also changing. Although the theme of traditional carbon star research has been retained, in 2008 monitoring of the asteroids in the solar system had started. Despite the very small sky coverage, the new direction of research brings positive results thanks to the uniquely high telescope light sensitivity. The 21mag threshold is reached by the telescope in the red part of the spectrum with an 8-minute exposure which allows the recording of 50m bodies in the Main Asteroid Belt (i.e., at distances 330 to 480 million km). In the next 7 years, 49 new asteroids are being discovered. 11 of them were named.

Table 1. Asteroids discovered at the Baldone Astrophysical Observatory.

Number	Name	Year of designation	Discovering year	Diam (km)
274084	Baldone	2011	2008	1.5
284984	Ikaunieks	2012	2010	1.5
294664	Trakai	2012	2008	3.5
321324	Vytautas	2012	2009	3
330836	Orius	2013	2009	35
343157	Mindaugas	2013	2009	3.5
392142	Solheim	2014	2009	3
332530	Canders	2015	2008	2
353646	Blumbahs	2015	2008	1.5
428694	Saule	2016	2008	0.6
457743	Balklavs	2016	2009	1

In 2010, three UL institutes – Atomic Physics and Spectroscopy, Astronomy, Geodesy and Geoinformatics – establish the Association FOTONIKA-LV. A year later, the Association in the fierce competition earns FP7 3.7 million EUR REGPOT project FOTONIKA-LV, which has a positive push for research growth in all three institutes. In 2012–2013, several master theses and three doctoral theses have been taught in astrophysics. Using FOTONIKA-LV project funds, high-precision scanners are being purchased, which lay the foundations for the Baldone Schmidt telescope's more than 22,000 (direct) and 2,300 (spectral) astronomical plates archive digitization. The scanning process of direct plates in this year is in the final stages. After completing the next step – digital image processing with special programs developed by the National Academy of Sciences of Ukraine at the Main Astronomical Observatory (Andruk et al., 2014, Andruk et al., 2016a, b), a large astronomical database will be obtained. The evaluation shows that around 330,000,000 stars will have accurate equatorial coordinates and brightness. It will be an exclusive database for refining the visible movement of stars, for variability of brightness studies, for asteroids and comets, both known and new research. As shown by the processing of digital images of some of the astroplates obtained in the ecliptic region, they contain dozens of asteroid images up to 17 B (blue spectrum range) many of which were discovered decades later than the photographic observations in Baldone observatory. This result points to a real opportunity to discover new unknown asteroids and comets near Earth. Publication of data of U – ultraviolet observation is also important, as the number of publications in the Astronomical Data System of Strasbourg with U magnitudes are close to hundred, while articles with the visual and near infrared measurements are tens of times more.

2016 – 2017 years were filled with intensive work on optimizing the optical system of Schmidt telescope. As a result of the optical system calculations, the Institute of Astronomy managed to develop an additional lens to be placed in the optical system of the Schmidt telescope to make the convex compatible Schmidt telescope focal plane with the flat bed plane of CCD. There are now two 16.8 megapixel cameras STX-16803 in the focus of the telescope. Each CCD



Figure 4: Two CCD cameras are located in the focal plane of the Schmidt telescope.

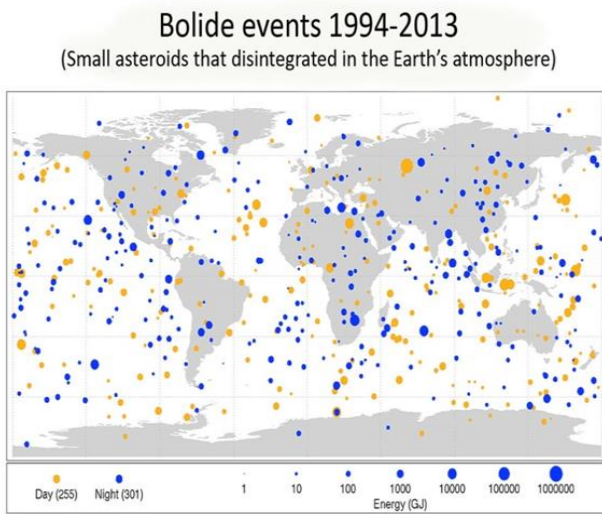


Figure 5: Largest blue (night) and yellow (day) circles match the energy of the Chelyabinsk event. (<https://www.nasa.gov/jpl/bolide-events-1994-2013/>).

is covering one degree of sky (see Figure 4). As a result, the effectiveness of Baldone Schmidt telescope increased 25 times. This benefit was confirmed by the first observations with an improved optical system in the August-September

2017, when 21 new asteroids were discovered in a short period of time. Up to now 77 new asteroids were discovered in Observatory. The direction of research is important to protect the Earth from the fall of asteroids and to mine the minerals on them in future. Events such as the fall of Chelyabinsk's meteorite seem rare. However, as shown by NASA's published radar map of bolides fall, similar events on Earth are on average every five years (Figure 5) and only because of the uneven population distribution on Earth it is not as often observed.

The new capabilities of telescope allow for intensification not only of classical carbon star research, but also expand research field: to study the physical properties of comets and asteroids, and to start investigations in the field of relativistic particle. The co-operation with radio astronomers allowed winning the Latvian Science Council's basic and applied research project "Complex Solar System Small Body Research".

The popularity of the Baldone Astrophysical Observatory is growing in the world, thanks to work on digitizing the archives of astronomical photographic plates, preparing many scientific publications, participating in international conferences and creating a Planetarium in the dome of the Schmidt Telescope. The number of popular science lecture visitors has increased from 1000 in 2012 to almost 4000 in 2018. Baldone Astrophysical Observatory has been invited as a member in three international projects related to the popularization of natural sciences (Scientist Night, Night 2018-2019," Youth attraction to astronomy (projects Est-Lat Interreg SpaceTem and Online Observatory)).

References

Alksnis A., Balklavs A., Dzervitis U. et al.: 2001, *Baltic Astronomy*, **10**, 1.
 Andruk V.M. et al.: 2014, *Odessa Astron. Publ.*, **27**, 53.
 Andruk V.M. et al.: 2016a, *Kinematics Phys. Celestial Bodies*, **32**, 38.
 Andruk V.M. et al.: 2016b, *Kinematics Phys. Celestial Bodies*, **32**, 260.
 Bergeat J., Knapik A., Rutily B.: 2001, *A&A*, **369**, 178.
 Eglitis I., Sokolova A.: 2018, *Odessa Astron. Publ.*, **31**, 70.
 Mauron N.: 2008, *A&A*, **482**, 151.

DOI:<http://dx.doi.org/10.18524/1810-4215.2019.32.181826>

INVESTIGATION OF NEO ASTEROIDS 2006 VB14 AND 1986 DA

I. Eglitis

Institute of Astronomy, University of Latvia, Raina blvd. 19, Riga, LV 1586, Latvia,
ilgmars.eglitis@lu.lv

ABSTRACT. 566 positions and photometric observations of NEO objects 2006 VB14 = Y5705 = 345705 and 1986 DA were obtained with Baldone Schmidt telescope in 2018 and 2019, to detecting rotation period and other physical characteristics. A Fourier transform was applied to determine the rotation period for asteroid 1986 DA=6178. Value 3.12 ± 0.02 h was obtained. Observations confirm the previously obtained rotation period $P = 3.25$ h for 2006 VB14.

Keywords: NEO – asteroids – rotation periods

АНОТАЦІЯ. 566 позиційних та фотометричних спостережень об'єктів NEO – 2006 VB14 = Y5705 = 345705 та 1986 DA – отримано за допомогою телескопа Балдона Шміда у 2018 та 2019 роках для виявлення періоду обертання та інших фізичних характеристик. Для визначення періоду обертання астероїда 1986 DA=6178 було застосовано перетворення Фур'є. Отримали значення 3.12 ± 0.02 год. Спостереження підтверджують раніше отриманий період обертання $P = 3.25$ год. для 2006 VB14.

Ключові слова: NEO – астероїди – періоди обертання

1. Introduction

The surfaces of smallest planets and moons of the Solar system are covered with large number of craters created by asteroids. Every day, Earth is bombarded with more than 100 tons of dust and millimeter-sized particles from space. About once a year, a two meter sized asteroid hits Earth's atmosphere, often creating a bolide event as the friction of the Earth's atmosphere causes them to disintegrate – sometimes explosively. About every five year Chelyabinsk type event take part. The largest impact during this 20-year interval was the recent daytime Chelyabinsk event (440,000 – 500,000 tons of TNT) recorded over central Russia on February 15, 2013. This small asteroid that exploded in the atmosphere near Chelyabinsk, Russia was about 16 meters in size before it hit the Earth. While that impact focused public attention on the potential hazards of NEO impacts with Earth, space scientists have long known that such events are just a part of Earth's geologic history. Scientific assessments of the risk of, as well as the hazards posed by, future asteroid impacts with Earth vary. In an article published in Nature (2013) by Peter Brown and his colleagues reported that "telescopic surveys have only discovered about 500 near-Earth asteroids that are 10-20 meters in diameter (comparable to the

Chelyabinsk asteroid) of an estimated near-Earth asteroid population of around 20 million, implying that a significant impactor population at these sizes could be present but not yet cataloged in the discovered near-Earth asteroid population (Brown et al., 2013). The importance of the small body studies in the Solar system can be properly evaluated if we recall the volcanic eruption effects in Iceland, comparable to the effect caused by the fall of a small asteroid. The fall of an asteroid larger than 50 m will be a disaster that can stop the progress in the world for several years, but the fall of a 300 m and larger body can terminate the development of civilization on the Earth for several decades, or even destroy the humanity at all. At the 5th meeting of the PECS Committee in on 27 of May 2009 in Esrin (Italy), the total number of NEO and hazard asteroids, is assessed as 66 000 (Bobrinsky, 2009). NASA congress on 5 of March 2007 provided the assessment of the problem in Near-Earth Object Survey and Deflection Analysis of Alternatives. It concluded that only the wide ground base plus space sensor observations of Venus, like the orbit, can allow a more prompt solution of the problem, i.e. to discover the NEO asteroids (up to 90%) in the nearest future (Milani et al., 2012). Finally, the research of asteroids manages to draw vast attention of mass media, thus promoting the awareness of the importance of science, including astronomy, among public at large, young people in particular. From the other point of view the investigation of asteroids properties are important for development of evolution theory of the Solar system and classification of small objects in the Solar system. Photometric study of light curves can obtain additional information about size, rotation period, structure of objects, existence of craters and ice fields on the surface, which is very important data for space missions and for fantastic ideas about mining of minerals on asteroids. The Earth was not formed in a radial location where water can directly condense. Water must have been delivered to the Earth from "elsewhere": exogenically, i.e., from asteroids and comets, or else endogenically, i.e., from accreting water-absorbed bodies. It is another motive to perform the research of the small bodies in the Solar system.

2. Observation

Observations of NEO asteroids were made in 2018–2019 with 16.8 Mb camera STX-16803 installed on Baldone Schmidt telescope. Baldone. Schmidt has 1.2m main mirror, correction lens 80 cm, focal length 2.4m.

In 2018, 1028 CCD images were obtained covering 200 square degrees of sky and 7 new asteroids were discov-

ered. Common number of observed asteroids was 826. Baldone observatory work at high declinations ($\delta > 50$ degrees), because the sky covering in this region is very weak (see Sky coverage map at <https://www.minorplanetcenter.net/iau/SkyCoverage.html>). Without monitoring of asteroids the purpose of this research were obtaining the light curves of 2006 VB14 and 1986 DA in order to determine their rotational period. 566 positions and photometric observations of NEO objects 2006 VB14 = Y5705 = 345705 and 1986 DA were obtained, to detecting rotation period and other physical characteristics. Description of obtained images is given in Table 1.

Table 1. NEO asteroids observed at the Baldone Astrophysical Observatory.

Object/Date	Number of CCD images
2006 VB 14 = 345705	
14.10.2018	3
17.10.2018	3
17/18.10.2018	53
04/05.11.2018	40
28/29.11.2018	125
29/30.11.2018	108
30.11/01.12.2018	90
1986 DA = 6178	
16/17.04.2019	27
17/18/04.2019	25
22/23/04.2019	23
28/29.04.2019	34
05/06.05.2019	21

3. Processing of CCD images

In order to reduce the images, flats, bias, and dark calibration images were taken each night. The program Maxim DL was used to reduce and align the images. The flat-field images were taken against the twilight sky. The darks were exposed for the same time as the respective light images, two or three minutes for both asteroids. The red filter was used for observation.

Afterward, the program MPO Canopus v10.2.1.0 (Warner, 2011) was used to perform differential photometry on the reduced data. For each data set, five stars were used for brightness comparison to the asteroid. Aperture photometry using a differential photometry technique was done to determine the brightness of comparison stars and the asteroid. The errors in magnitude for stars and asteroids were found and plotted in a phase diagram. Relative magnitude (the difference between brightness and average day brightness of asteroid) versus rotation phase form light curve. 339 brightness measurements of 2006 VB14 and 130 for 1986 DA were obtained using "g" GAIA magnitudes of more than 30 reference stars.

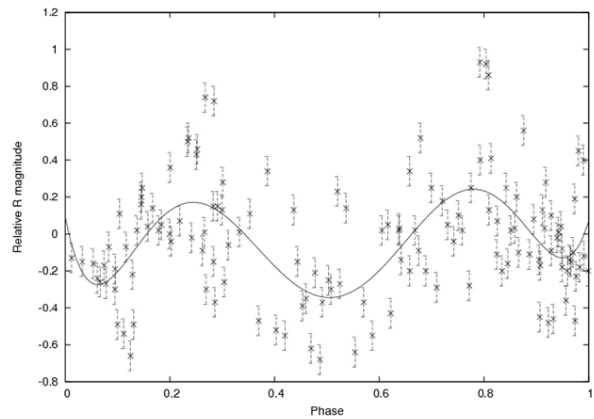


Figure 1: Light curve for NEO 2006 VB14.

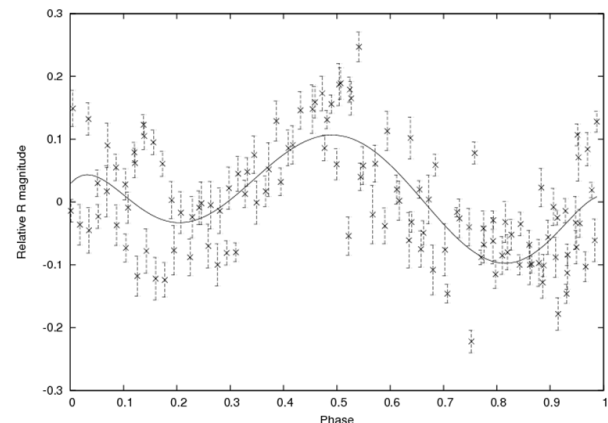


Figure 2: Light curve for NEO 1986 DA.

4. Results

A Fourier transform was applied to determine the rotation period for both asteroids. Light curves were created also using MPO Canopus software.

The rotation period 3.25 ± 0.02 h better fitted to our measurements for 2006 VB14. The period is in agreement with the earlier work of Skiff et al. 2012. The sharp fall of brightness in phases 0.3 and 0.8 and the brightness peak in phase 0.1, indicate on possible presence of a crater and the bright surface area (frozen gas field or water) on the asteroid surface, respectively.

The rotation period 3.25 ± 0.02 h better fitted to our measurements for 1986 DA. The similar reduction and processing procedure was used for 130 CCD images of asteroid 1986 DA. A Fourier transform was then applied to determine the rotation period. A Fourier transform was then applied to determine the rotation period. Value 3.12 ± 0.02 h was obtained.

This research is funded by the Latvian Council of Science, project "Complex investigations of Solar System small bodies", project No. lzp-2018/1-0401.

References

- Brown P.G. et al.: 2013, Nature, <http://dx.doi.org/10.1038/nature12741>.
- Brian D.W.: 2016, *Minor Planet Bull.*, **43**, 240.
- Milani A. et al.: 2012, *Minor Planet Bull.*, http://belissima.aob.rs/Conf2012/Milani_2012.pdf
- Skiff B.A. et al.: 2012, *Minor Planet Bull.*, **39**, 111.
- Warner, B.D.: 2011, MPO Canopus software v10.2.1.0, <http://www.minorplanetobserver.com/>.

ONGOING OPERATION AND PERSPECTIVES OF SIMPLE VLBI NETWORKS OF GEOSTATIONARY SATELLITES MONITORING

M.Kaliuzhnyi ¹, Z.Zhang ², F.Bushuev ¹, O.Shulga ¹, V.Bezrukovs ³,

O.Reznichenko ⁴, S.Melnychuk ⁵, Y.Malynovskyi ⁶

¹ Research Institute “Mykolaiv Astronomical Observatory” (RI “MAO”), Mykolaiv, Ukraine, *dir@mao.nikolaev.ua*

² Shanghai Astronomical Observatory, Shanghai, People’s Republic of China, *zbzhang@shao.ac.cn*

³ Ventspils University College, Ventspils, Latvia, *virac@venta.lv*

⁴ Institute of Radio Astronomy of the NASU, Kharkiv, Ukraine, *rai@ri.kharkov.ua*

⁵ Western Center of Radio Engineering Surveillance, Mukacheve, Ukraine, *ckako@i.ua*

⁶ Rivne Minor Academy of Science of School Age Youth, Rivne, Ukraine, *man.rivne@ukr.net*

ABSTRACT. The report is dedicated to introducing the operation and prospects of further development of simple VLBI networks which were created in Ukraine, Latvia, and China for monitoring the orbital information of geostationary satellites. The Ukrainian-Latvian network consists of five stations located in Mykolaiv, Kharkiv, Mukacheve, Ventspils, and Rivne, and it operates since 2015. The Chinese network consists of three stations located in Shanghai, Duyun, and Urumqi, and it formally carried out a network observation from June 2019.

The networks have identical hardware and software. The main principle of the operation of the networks learned from the VLBI is correlation analysis of broadband noise-like signals of satellite television DVB-S, which are emitted by satellites and synchronously received by the stations of the networks. Single-frequency GPS receivers are used for the synchronizing of network stations. Time difference of arrival (TDOA) between the signals paths from the identical TV satellite to different stations is obtained via using correlation analysis. These values of TDOA are used to determine orbital elements of the tracked satellites which are given in the report. Notably, the cost of one set of station equipment does not exceed \$2000, and the current operating costs are about \$50 per day.

The prospects of further development of the simple VLBI networks include a) the possibility of continuous independent non-invasive high-precision determination of the position of arbitrary active satellites (especially important in the case of their co-location), b) the possibility to fully automate targeting and operation, c) the possibility of using accumulated observational data to solve scientific geophysical and astronomical tasks, d) relatively few funds necessary for the modernization and operation of the networks.

АНОТАЦІЯ. Доповідь присвячена ознайомленню з роботою та перспективам подальшого розвитку мереж простих РНДБ, створених в Україні, Латвії і в Китаї для моніторингу орбітального положення геостационарних супутників. До складу українсько-латвійської мережі, яка функціонує з 2015 року, входять п’ять станцій, розташованих в містах Миколаїв, Харків, Мукачеве, Вентспілс і Рівне. Китайська мережа складається із 3-х станцій, розташованих в Shanghai, Duyan і в Urumqi і офіційно проводить спостереження з червня 2019.

Мережі мають ідентичне апаратне і програмне забезпечення. Основним принципом функціонування мереж, запозиченим з РНДБ, є кореляційний аналіз широкосмугових шумоподібних сигналів супутникового телебачення DVB-S, які випромінюються супутниками і синхронно приймаються станціями мережі. Для синхронізації станцій мережі використовуються одночастотні GPS-приймачі. В результаті кореляційного аналізу визначаються значення TDOA (Time Difference Of Arrival) сигналів супутникового телебачення. Виміряні значення TDOA використовуються для визначення елементів орбіти контрольованих супутників та створення каталогів, фрагменти яких наводяться в доповіді. Зазначимо, також, що вартість одного комплексу обладнання станції не перевищує \$2000, а поточні експлуатаційні витрати – \$50/доба.

Перспективність подальшого розвитку мереж простих РНДБ обумовлена а) можливістю безперервного незалежного неінвазивного високоточного визначення положення довільних активних супутників (особливо важливо у випадку co-location), б) можливістю повної автоматизації націлювання та функціонування, в) можливістю використання накопичених даних спостережень для вирішення наукових геофізичних та астро-

номічних задач, г) порівняно незначні кошти, необхідні для модернізації і експлуатації мереж.

Keywords: geostationary satellite, TDOA, orbital elements, DVB-S.

1. Introduction

Simple VLBI network uses correlation analysis of digital satellite television signals, synchronously received by geographically spaced network stations, to calculate the time difference of arrival (TDOA) of these signals to the network stations (Bushuev et al., 2016). The obtained values of the TDOA and the known station coordinates are used to determine the orbital elements of a tracked satellite. It is shown in (Bushuev et al., 2017) that the error of calculating satellite coordinates by a network of three or more stations is 223 m. The error of calculating coordinates by a network of two stations exceeds 7000 m.

Herewith the network is a prototype of passive correlation ranging (PaCoRa) system developed by Fraunhofer IIS and SES in 2010-2013 (ESA, 2019). It is reported that PaCoRa systems are created in the US and Europe and that the systems enable SES to track 80% of its geostationary satellites (SatMagazine, 2019).

2. Operation of the Ukrainian-Latvian and Chinese networks

The Ukrainian-Latvian network operates since December 2015 (Kaliuzhnyi et al., 2017) and initially tracked the single satellite Eutelsat-13B located in the geostationary cell 13°E together with two other satellites Eutelsat-13C and Eutelsat-13E. An additional sixth station was put into operation in Mykolaiv in September 2018. This allowed two triplets of stations to track two satellites Eutelsat-13B and 13C. The results of these observations are used to determine the orbit elements of the satellites using two models of motion: the analytical model SGP4 / SDP4 and the numerical model of integrating the equations of motion of the satellites (Kaliuzhnyi et al., 2016). Today, the Eutelsat-13B and Eutelsat-13C catalogs contain orbit elements obtained for 1175 and 106 days, respectively.

Works on modernization the network continues. Today, two additional stations, located in Mykolayiv and Rivne, are constantly operating and the ninth station in Ventspils is being set up. Upon commissioning the ninth station, three triplets of stations will be able to simultaneously tracking all three satellites located in the geostationary cell 13°E. This would track the relative position of the satellites in the geostationary cell and determine the moments of the approach of the satellites to each other.

The Chinese network of three stations located in Shanghai, Deyun, and Urumqi has begun tracking the Apstar-6C satellite (134°E) in June 2019. Only one satellite is located in the geostationary cell 134°E. The network observations have been used as to determine the error of the TDOA measurement, and the orbit elements of the satellite. The standard deviation of the TDOA at an averaging interval of 60 s for all pairs of stations is ± 8.6 ns and coincides with the TDOA error obtained by the Ukrainian-Latvian network (Bushuev et al., 2016). The fact that the SGP4/SDP4 model is significantly less accurate than the numerical model was also confirmed. So the stan-

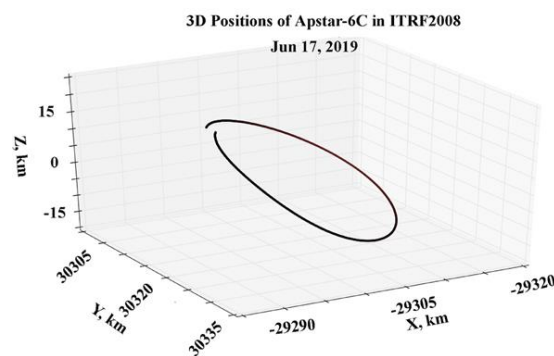


Figure 1: The 3D position of Apstar-6C in ITRF2008 on June 17, 2019.

dard deviation of the residuals of measured and model values of the TDOA about 20 times less for the numerical model than for the SGP4/SDP4 model.

The obtained daily orbit elements (numerical model) are used to calculate the 3D position of Apstar-6C in ITRF2008 that is shown in Fig. 1.

3. Prospects: a network of global monitoring of geostationary satellites

A detail list of the benefits of a simple VLBI network or passive correlation ranging system over traditional satellite positioning systems is given on the website (ESA, 2019). The prospects of using such systems, first of all, in our opinion, depend on their cost and the value of the error of determining the orbital position of the satellite. The price of one station of the simple VLBI networks is about \$2000. This is three orders of magnitude less than the cost of a single VGOS (VLBI Global Observing System) station. Herewith operating costs are at a level of about \$50 per day for the existing network stations.

The error of satellite orbit determination is proportional to the TDOA error. The physical limit of the TDOA error is inversely proportional to the width of the signal spectrum and is estimated at 0.1 ns for digital satellite television signals. It is proposed to reach the limit by using a quantum reference oscillator for synchronizing and as an ADC reference oscillator. Then the error of coordinate determination will be at the level of about 1 m. Despite the significant increase in the cost of the upgraded station, the cost of a simple VLBI network of five such stations is estimated at the cost of one VGOS station. The operating costs of the upgraded simple VLBI network would remain low because of the fully automate targeting and operation. Herewith the network of such stations could track almost all geostationary satellites that radiate TV signals, for example, on Europe. Therefore, it is possible to create a simple VLBI network for global monitoring of geostationary satellites, which will consist of separate regional networks or clusters.

4. Conclusion

Two simple VLBI networks separately operate now in Europe and China. They could be considered as two clusters of the network of global monitoring of geostationary satellites. Relatively few funds are necessary for the mod-

ernization and operation of the networks to provide coordinate accuracy of about 1 m. The modernized networks could be used also for accumulated observational data to solve scientific geophysical and astronomical tasks.

In the short term, it is proposed to carry out joint observations of satellites that have DVB-S transponders with a footprint as in Europe and China.

References

- Bushuev F., Kaliuzhnyi M., Sybiryakova Ye. et al.: 2016, *Latvian Journal of Physics and Technical Sciences*, **53**, No. 5, 5.
- Bushuev F., Kaliuzhnyi V., Shulga O. et al.: 2017, in *Proc. of the 9th IAASS Conference Session 11: Space Traffic Control – I*, Toulouse (France), 18-20 October 2017, 213.
- ESA. TELECOM ARTES.PROGRAM. Passive Correlation Ranging (PaCoRa), [online]. Available at: <https://artes.esa.int/projects/passive-correlation-ranging-pacora> [Accessed 15 October 2019].
- Kaliuzhnyi M., Bushuev F., Shulga O. et al.: 2016, *Odessa Astron. Publ.*, **29**, 203.
- Kaliuzhnyi M., Bushuev F., Sibiriakova Y. et al.: 2017, *Science & Innovation*, **13(1)**, 41.
- SatMagazine. Year in Review 2016: Part VII [online]. Available at: <http://satmagazine.com/story.php?number=2062213544> [Accessed 15 October 2019].

DOI:<http://dx.doi.org/10.18524/1810-4215.2019.32.182510>

EVOLUTION OF COMET-LIKE ORBITS OF METEORITE-PRODUCING GROUPS AND THEIR PARENT BODIES

N. A. Konovalova¹, Yu. M. Gorbanev², N.H. Davruqov³¹ Institute of Astrophysics of the Academy of Sciences of the Republic of Tajikistan, nakonovalova@mail.ru² Astronomical Observatory of Odessa National University, Ukraine, skydust@ukr.net³ Institute of Astrophysics of the Academy of Sciences of the Republic of Tajikistan, Naqqosh89@mail.ru

ABSTRACT. This paper presents the results of the study of evolution of Jupiter-family comet-like orbits of six meteorite-producing groups, including sporadic fireballs from the IAU MDC database 2007 [1], sporadic meteors from the SonataCo database [2], instrumentally observed H5 and L3.5 ordinary chondrites, as well as near-Earth asteroids which are potential parents of the examined groups. In order to verify the relationship between meteorite-producing groups and their potential parents, we performed backward numerical integration of the orbital motion of these groups' members over several millennia. The numerical integration was carried out using the Halley software [3]. The equations of motion factored in gravitational perturbations due to the major planets, radiation pressure effects and the Poynting-Robertson drag. The equations of motion were numerically integrated using the 11th-order Everhart method applicable to studying the motion of Jupiter-approaching short-period comets. The numerical integration of the mean orbital elements of a group, as well as those of the relevant meteorite and potential parent asteroid, over 5,000 years has shown that the respective perihelia, eccentricities and arguments of perihelion evolved in a similar manner over the specified period. The D_{SH} -criterion of Southworth and Hawkins [4], which is a quantitative measure of orbital similarity, has remained below 0.3 [5] for about 5,000 years in the groups of Neuschwanstein and Mason Gully meteorites and for about 3,500 to 4,500 years in the groups of Benešov and Park Forest meteorites. In the groups of the Košice and Příbram meteorites, the mean orbits and those of their potential parents remained similar as defined in terms of the D_{SH} -criterion over a relatively short period of about 2,000 to 3,000 years. We can infer from our findings that meteorite-producing sporadic fireballs and sporadic meteors are related to the H5 and L3.5 ordinary chondrites and their potential parents, i.e. near-Earth asteroids, in the investigated groups. The estimated time intervals, over which the evolving orbits of the groups' members have shown good similarity, are indicative of relatively recent formation of meteorite-producing groups as a result of fragmentation of their parent bodies.

АНОТАЦІЯ. У статті представлені результати аналізу еволюції кометоподібних орбіт сімейства Юпітера шести метеоритоутворюючих груп, що включають спорадичні боліди з метеорної бази даних

IAU MDC-2007 [1], спорадичні метеори з SonataCo бази даних [2], звичайні хондрити типу H5, L3.5, що спостерігалися інструментально, і навколоземні астероїди - потенційні батьківські тіла досліджених груп. Щоб перевірити зв'язок між метеоритоутворюючими групами і їх потенційними батьківськими тілами, ми виконали чисельне інтегрування орбітального руху членів метеоритоутворюючих груп протягом кількох тисячоліть. Інтегрування проводилося кількісно з використанням програмного забезпечення Halley [3]. Гравітаційні обурення великих планет, вплив радіаційного тиску і опір Пойнтінга-Робертсона враховувалися в рівняннях руху. Чисельне інтегрування рівнянь руху виконувалося методом Еверхарт 11-го степеня, які можуть застосовуватися для дослідження руху короткоперіодичних комет, які зазнають зближення з Юпітером. Чисельне інтегрування орбітальних елементів середньої орбіти групи, метеорита і потенційного батьківського астероїда за 5000 років показує, що перигелії, ексцентриситети і аргументи перигелію еволюціонують аналогічним чином за цей період часу. D_{SH} -критерій Саутворта і Хокінса [4], який є кількісною мірою подібності між орбітами, залишається нижче 0.3 [5] протягом близько 5000 років в групах метеоритів Neuschwanstein і Mason Gully і близько 3500-4500 років – в групах метеоритів Benešov і Park Forest. У групах метеоритів Košice і Příbram середня орбіта груп і орбіти їх потенційних батьківських тел залишаються близькими згідно D_{SH} -критерію на невеликому проміжку часу близько 2000-3000 років. Отримані результати дозволяють зробити висновки про зв'язок метеоритоутворюючих спорадичних болідів і спорадичних метеорів зі звичайними хондритами типу H5, L3.5 і їх потенційними батьківськими тілами – навколоземними астероїдами в досліджених групах. Отримані інтервали часу, протягом яких еволюціонуючі орбіти членів груп демонструють гарний збіг, вказують на відносно недавнє утворення метеоритоутворюючих груп в результаті фрагментації їх батьківських тел.

Keywords: evolution – orbit – group – fireball – meteorite – ordinary chondrite – comet-like – Jupiter-family.

1. Introduction

According to the classical model for cometary nuclei being envisioned as conglomerates of volatile ices and dust grains, meteoroid streams form through the ejection of dust grains up to a few centimetres in size from comets [6]. After being ejected, these meteoroids travel in a heliocentric orbit just as their parent comet's nucleus does. The time required for the ejected dust grains to spread about the whole orbit of their parent forming a closed meteoroid swarm is estimated to be several hundreds of years [7]. Therefore, the time required to form a closed curve is short as compared to the age of meteoroid stream members which are several-thousand-year old. When cometary dust grains, whose orbits are Earth-crossing, reach Earth, they enter its atmosphere creating a meteor event. Meteor showers have been observed for millennia, with material being regularly fed into the stream throughout this period from the parent and material lost through the external effects, mainly under the action of gravitational perturbations by the planets and due to radiation pressure effects. The bulk of the scattered material forms the sporadic meteoroid background. Catastrophic break-up of cometary nuclei is another mechanism for producing meteoroid streams. Big boulders can be produced through such a mechanism as observed during the C/1999 S4 (LINEAR) comet break-up.

The idea of meteoroid streams and meteors asteroidal origin has been considered previously [8-11]. Halliday *et al.* [12] analysed orbits of 89 fireballs – namely, 56 from the MORP (Meteorite Observation and Recovery Project network in western Canada) data and 33 from the PN (Prairie Network in central USA) list - which could survive the passage through the atmosphere with a non-zero terminal mass. The authors suggested existing of four possible meteorite-producing groups, among which group 1 included instrumentally observed Innisfree meteorite, and inferred the asteroidal origin of some fireball streams. Greenberg & Chapman [8] reported that stony-iron mesosiderites formed at the core-mantle interfaces of small asteroidal parents of 100-200 km in diameter while pallasites formed in smaller parent bodies of 50-100 km in diameter. The authors assumed that meteorites might be pieces of large main-belt asteroids derived primarily by cratering collisions rather than disruptive fragmentation. Shestaka [13] examined a swarm of meteorite-producing bodies containing the Innisfree and Ridgedale fireballs. The author found out that the investigated swarm also included nine small meteoric swarms, several asteroids and 12 fireballs photographed by the PN and MORP cameras. The orbit of this swarm approaches Earth's orbit annually in early February. With the aim of investigating the annual fireball activity profile, Beech [14] analysed the occurrence time data for 2,373 fireball events predominantly observed across Canada and documented in the Millman Fireball Archive. The author reported that all known cometary meteor showers producing prominent meteors and fireballs are represented as distinct peaks in the annual fireball

activity profile. Several other peaks in the activity profile, which did not correspond to any recognised cometary meteor showers, were also identified; some of those could be related to asteroidal meteorite streams.

Unlike comets which regularly feed meteoroid streams when passing around the perihelion of their orbits, asteroids rarely experience disruptive events; hence, swarms of asteroidal meteoroids are likely to result from once-off events, which could be, for instance, asteroids smashing into each other or colliding with large meteoroids. Therefore, the spatial density of asteroidal meteoroid swarms should be lower while their meteor activity should differ from that of the meteoroid streams of cometary origin. No doubt that collisions (as impact events) result in disruption of the parent body with the debris in the form of small particles and bigger fragments, such as cobbles and pebbles, partially surviving in its orbit. In such a scenario, meteoroid swarms can only be produced from the collision of relatively large bodies with the asteroid-impactor of several tens of metres in diameter. Asteroid (4) Vesta with its fragments expelled through striking with the impactor can be an example of asteroidal origin of meteorites. Some of these fragments upon crossing Earth's orbit fall to the earth's surface as meteorites. Gravitational perturbations caused by Jupiter and other planets in the solar system, as well as rotational instability, can also cause disruption of near-Earth objects (NEOs). The situation when an asteroid-like object in the comet-like orbit may turn out to be a dormant comet in disguise, which is covered by a crust up to 10 m thick built up on its surface with time and has ceased to show any cometary activity, has been investigated in many studies.

2. Distribution of sporadic meteor and meteorite-producing fireball events throughout a year

Based on several sources of data, we performed the analysis of the annual activity of large and small sporadic meteors and meteorites, including 737 bright sporadic fireballs (brighter than -6 mag) from the International Astronomical Union Meteor Data Centre (IAU MDC) database [1], 1,416 small meteors (from -2.5 to -5.0 mag) from the SonataCo database [2] and 338 meteorites with known fall dates. The fireballs were selected if the following conditions were met: the fireball terminal height $H_e \leq 35$ km; pre-atmospheric velocity $V_\infty \leq 25$ km sec⁻¹; terminal velocity $V_e \leq 10$ km sec⁻¹ and a non-zero terminal mass. The resulting data set was grouped into bins by an increment of 10 degrees in the solar longitude L_\odot . The distribution of the number of investigated events as a function of the solar longitude L_\odot was plotted and analysed to identify the periods of activity of sporadic fireballs, meteors and meteorites with known fall dates throughout a year. The resultant distribution of sporadic meteor and fireball activity throughout a year is shown in Figs. 1 and 2. Several prominent peaks of activity lasting for 20-30 days can be observed at the solar longitude $L_\odot \approx 30^\circ, 60^\circ, 140^\circ, 220^\circ, 270^\circ, 300^\circ$ and 350° .

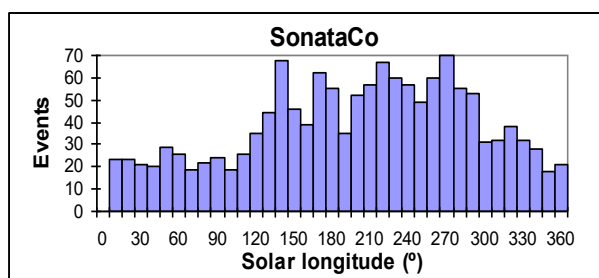


Figure 1: The number of sporadic meteor events versus the solar longitude L_{\odot} .

3. The selected groups of meteorite-producing meteoroids in Jupiter-family comet-like orbits and their plausible parent bodies

The constructed histograms of the annual activity of sporadic fireballs and meteors (Figs. 1 and 2) gave us an impetus to further study the issue of the existence of groups of meteorite-producing sporadic meteoroids in the near-Earth space. In the previous paper [15], the authors reported the detection of six groups of meteorite-producing meteoroids and L3.5 – H5 type ordinary chondrite meteorites observed over certain periods of the increased fireball activity. Those groups were named after the known member meteorites. The similarity between the orbits of members of each group established with application of the Southworth-Hawkins D_{SH} criterion as a quantitative measure of orbital similarity was the group-membership condition to be met. The value of $D_{SH} \leq 0.3$ was adopted for the investigated groups. Nowadays, it is generally assumed that the method for associating groups of meteorite-producing sporadic meteoroids with their potential parents, i.e. comets or asteroids, based only on the D_{SH} orbital similarity function, is not sufficient.

Similarly to meteoroid swarms and their connection with their parents, the arrangement of meteorites into groups and their lifetime in the near-Earth space are governed by evolutionary processes. The relationship between meteorite-producing groups and their potential parents, i.e. NEOs, should be verified by the backwards analysis of their orbital evolution over a time span of several millennia. The possibility to associate a plausible parent body with a certain group and estimate the formation age of the group of genetically related meteorite-producing meteoroids is crucial for the establishment of the relationship between the meteorite-producing group and comets or asteroids, as well as for the study of the mechanism for yielding meteorite-producing meteoroid swarms.

4. Evolution of meteorite-producing groups and associated NEOs

In the studies of the orbital evolution of meteoroids and near-Earth objects carried out in recent years, a common approach to the research on this issue has been developed:

- Meteoroids within a swarm or group, as well as their probable parent body (NEOS), should have orbits similar by the D_{SH} -criterion of Southworth and Hawkins. It makes it possible to associate a plausible parent body with a group

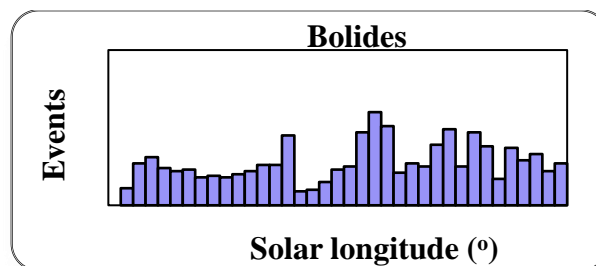


Figure 2: The number of meteorite-producing fireball and meteorite events versus the solar longitude L_{\odot} .

and determine the meteoroid group age. The determination of the age of meteorite-producing groups is essential for the establishment of relationship between meteorite groups and their parents, which could be either asteroids or extinct comets, as well as for the study of the mechanism of formation of the investigated meteorite groups.

- With a large number of the near-Earth asteroids discovered so far, there is a high probability of coincidental similarity between any two orbits at the current time. Therefore, the orbital evolution should be further studied to adopt as real couples of asteroids and groups only those ones whose orbits remained similar for a long period of time of about 5,000 years [9].

- In addition to dynamic properties, common taxonomic features can also be indicative of the common origin of meteoroid groups and their parents – near-Earth objects – in the solar system.

To analyse the orbital evolution of the meteorite-producing groups investigated in this study, the equations of motion were numerically integrated using the 11th-order Everhart method, which is one of the most precise methods for examining the orbital evolution of the solar system bodies and is applicable to studying the motion of Jupiter-approaching short-period near-Earth objects. The backward numerical integration of the orbital motion equations of the group members was carried out over a period of 5,000 years using the Halley software [3]. The equations of motion factored in gravitational perturbations due to the major planets, radiation pressure effects and the Poynting-Robertson drag.

4.1. Orbital evolution of the Benešov group, meteorite (L3.5, H5 type) and near-Earth asteroid 2000 JF5

The Benešov fireballs and meteorite were observed over a period of 1 Min ($L_{\odot} \approx 60^{\circ}$) increase in the fireball activity. The backward numerical integration of the mean orbital elements of the group (Mean) and near-Earth asteroid 2000 JF5 was carried out over a period of 5,000 years. The relevant perihelia q , eccentricities e and arguments of perihelion ω evolved in a similar manner throughout the whole specified period. The D_{SH} -criterion of similarity between the mean orbit of the group and that of NEA 2000 JF5 remained below 0.25 for about four and a half thousand years which may indicate that the meteoroids broke off from the parent asteroid in the beginning of the specified period.

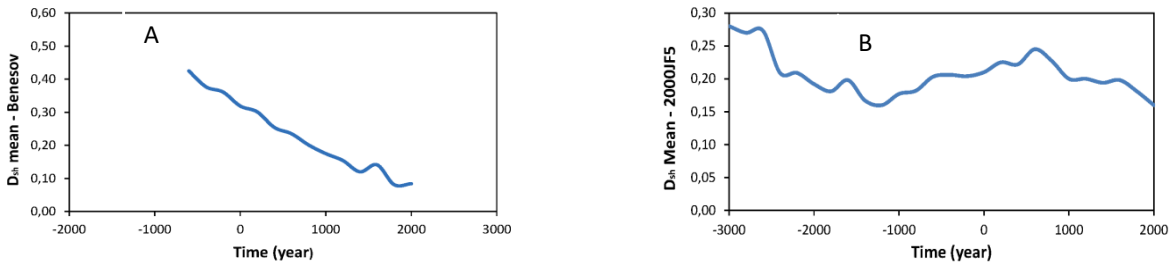


Figure 3: Evolution of the D_{SH} -criterion of similarity between the mean and Benešov meteorite orbits (A) and the mean and NEA 2000 JF5 orbits (B) over 5,000 years.

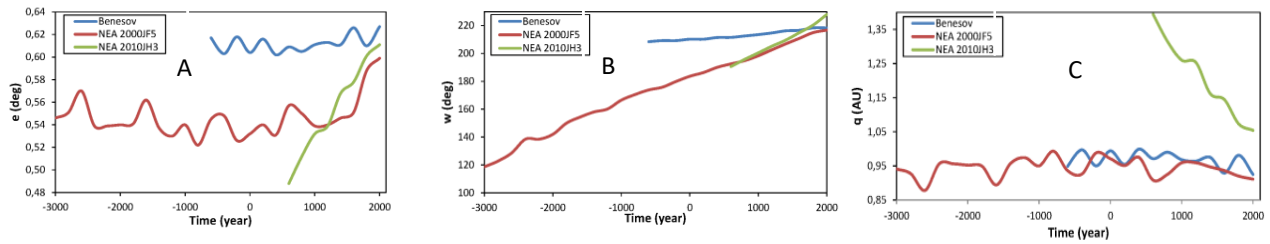


Figure 4: Evolution of the orbital elements (A – the eccentricity e ; B – the argument of perihelion ω and C – the perihelion q) of the Benešov meteorite, NEA 2000 JF5 and NEA 2010 JH3 over 5,000 years.

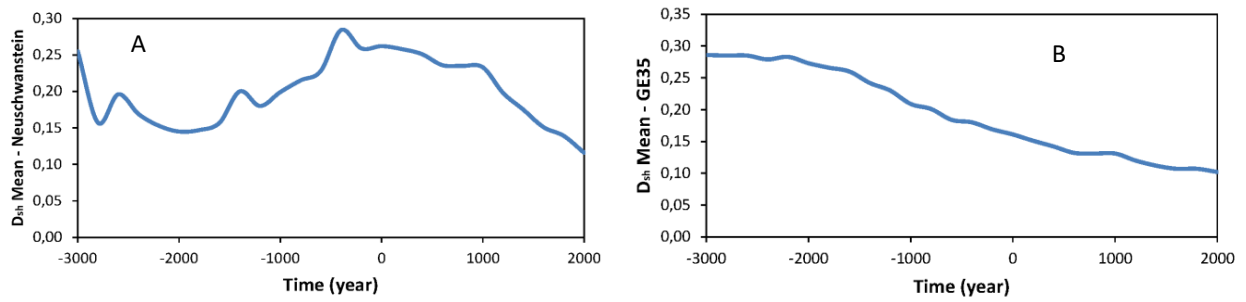


Figure 5: Evolution of the D_{SH} -criterion of similarity between the mean and Neuschwanstein meteorite orbits (A) and the mean and NEA 2010 GE35 orbits (B) over 5,000 years.

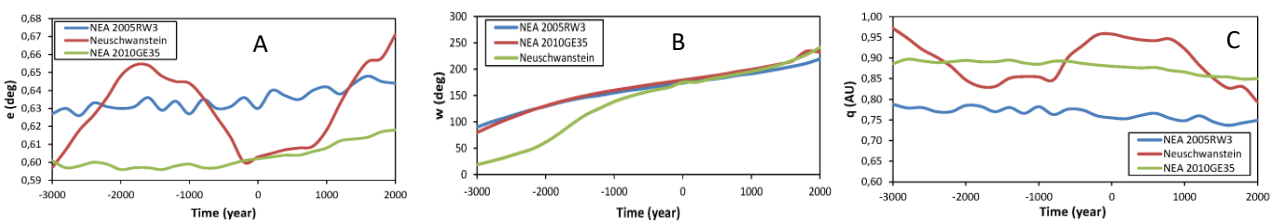


Figure 6: Evolution of the orbital elements (A – the eccentricity e ; B – the argument of perihelion ω and C – the perihelion q) of the Neuschwanstein meteorite, NEA 2010 GE35 and NEA 2005 RW3 over 5,000 years.

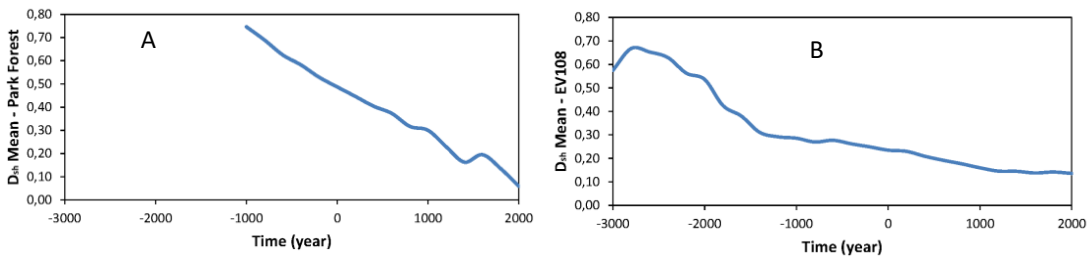


Figure 7: Evolution of the D_{SH} -criterion of similarity between the mean and Park Forest meteorite orbits (A) and the mean and NEA 2013 EV108 orbits (B) over 5,000 years.

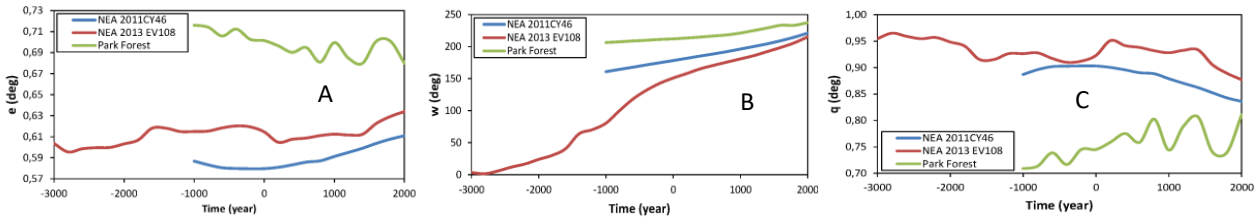


Figure 8: Evolution of the orbital elements (A – the eccentricity e ; B – the argument of perihelion ω and C – the perihelion q) of the Park Forest meteorite, NEA 2013 EV108 and NEA 2011 CY46 over 5,000 years.

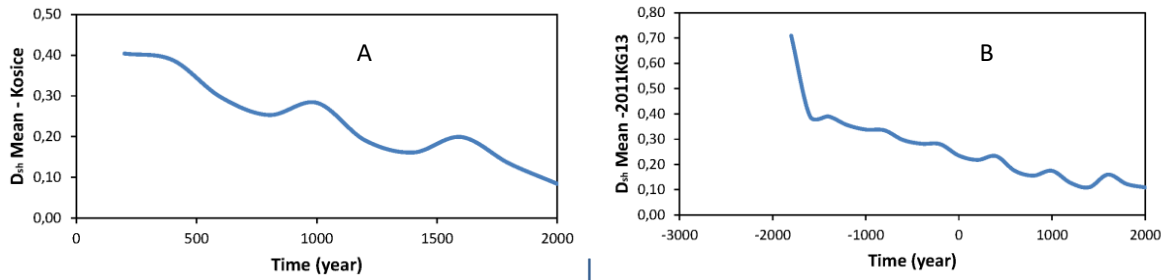


Figure 9: Evolution of the D_{SH} -criterion of similarity between the mean and Košice meteorite orbits (A) and the mean and NEA 2011 KG13 orbits (B) over 5,000 years.

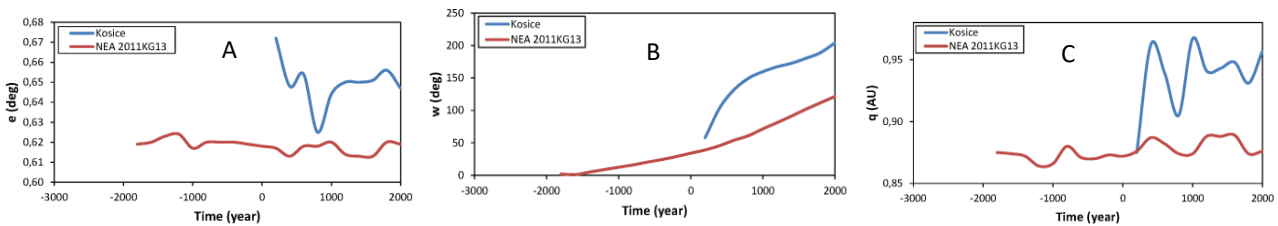


Figure 10: Evolution of the orbital elements (A – the eccentricity e ; B – the argument of perihelion ω and C – the perihelion q) of the Košice meteorite and NEA 2011 KG13 over 5,000 years.

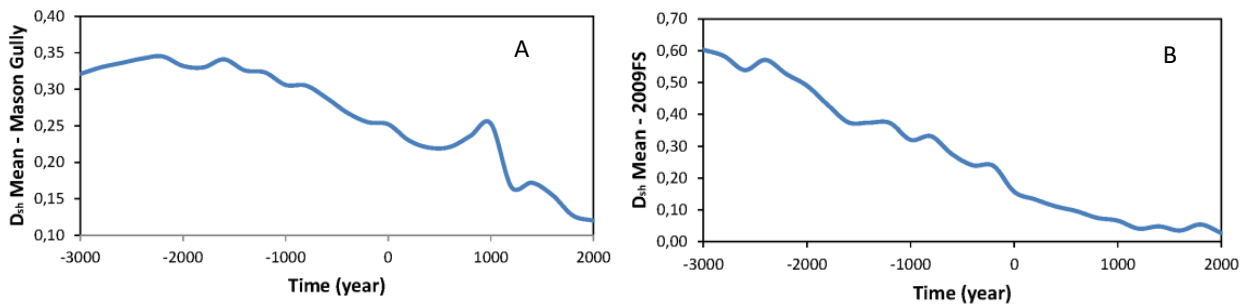


Figure 11: Evolution of the D_{SH} -criterion of similarity between the mean and Mason Gully meteorite orbits (A) and the mean and NEA 2009 FS orbits (B) over 5,000 years.

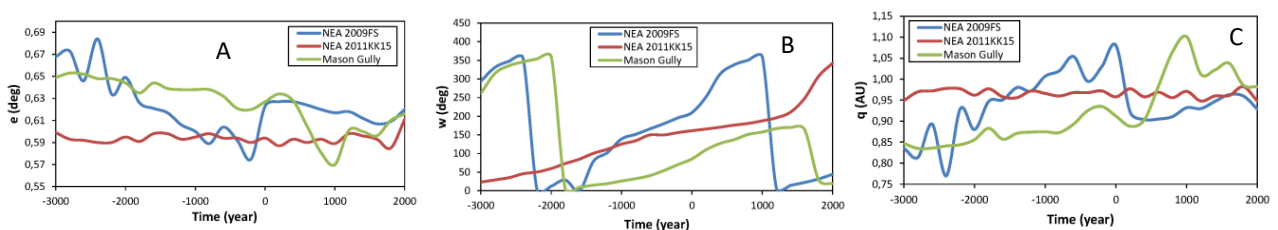


Figure 12: Evolution of the orbital elements (A – the eccentricity e ; B – the argument of perihelion ω and C – the perihelion q) of the Mason Gully meteorite, NEA 2009 FS and NEA 2011 KK15 over 5,000 years.

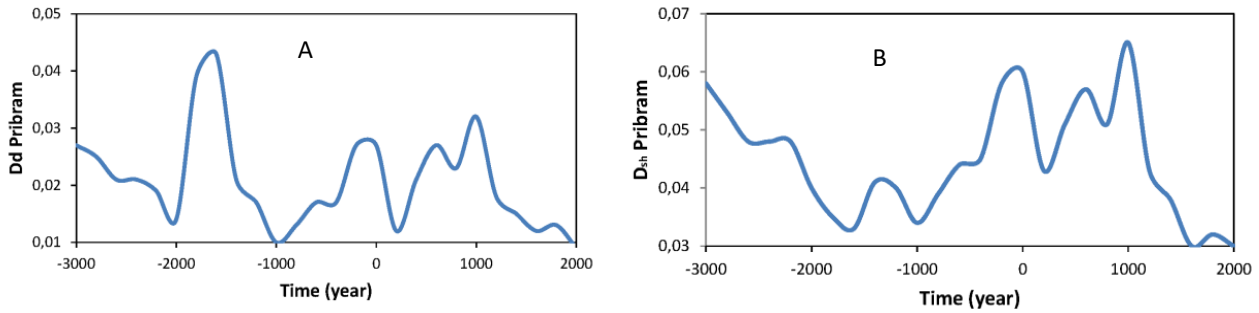


Figure 13: Evolution of the D_D -criterion (Fig. 13A) and D_{SH} -criterion (Fig. 13B) of similarity between the orbits of the Pribram and Neuschwanstein meteorites over 5,000 years.

4.2. Orbital evolution of the Neuschwanstein meteoroid group, meteorite (EL6 type) and near-Earth asteroid 2010 GE35.

The Neuschwanstein fireballs and meteorite were observed over a period of 1 Maj ($L_\odot \approx 30^\circ$) increase in the fireball activity. The results of the backward numerical integration of the mean orbital elements of the group (Mean) and near-Earth asteroid 2010 GE35 over a period of 5,000 years are illustrated in Figs. 5 and 6. The relevant perihelia q , eccentricities e and arguments of perihelion ω evolved in a similar manner throughout the whole specified period. The D_{SH} -criterion of similarity between the mean orbit of the group and that of NEA 2001 GE35 remained below 0.2 for about five thousand years which may indicate that the meteoroids broke off from the parent asteroid in the very beginning of the specified period.

4.3. Orbital evolution of the Park Forest meteoroid group, meteorite (L5 type) and near-Earth asteroid 2013 EV108.

The Park Forest meteorite was observed on 27 March 2003. The Park Forest fireballs and meteorite were observed over a period of 1 Maj ($L_\odot \approx 30^\circ$) increase in the fireball activity. The results of the backward numerical integration of the mean orbital elements of the group (Mean) and near-Earth asteroid 2013 EV108 over a period of 5,000 years are depicted in Figs. 7 and 8. The relevant perihelia q , eccentricities e and arguments of perihelion ω evolved in a similar manner throughout the whole specified period. The D_{SH} -criterion of similarity between the mean orbit of the group and that of NEA 2013 EV108 remained below 0.3 for about three and a half thousand years which may indicate that the meteoroids broke off from the parent asteroid in the beginning of the specified period.

4.4. Orbital evolution of the Košice meteoroid group, meteorite (H5 type) and near-Earth asteroid 2011 KG13

The Košice meteorite was observed on 28 February 2010. The Košice group and meteorite were observed over a period of 6 Maj ($L_\odot \approx 300^\circ$) increase in the fireball activity. The results of the backward numerical integration of the mean orbital elements of the group (Mean) and near-Earth asteroid 2011 KG13 over a period of 5,000 years are presented in Figs. 9 and 10. As can be inferred from the figures, the D_{SH} -criterion of similarity between the mean

orbit of the group and that of the Košice meteorite remained below 0.4 for about two thousand years while the mean orbit and that of the plausible parent, i.e. NEA 2011 KG13, were similar for about three and a half thousand years. The relevant perihelia q , eccentricities e and arguments of perihelion ω evolved in a similar manner throughout the whole specified period which may be indicative of the age of the Košice meteoroid group.

4.5. Orbital evolution of the Mason Gully meteoroid group, meteorite (H5 type) and near-Earth asteroid 2009 FS

The Mason Gully meteorite (observed on 13 April 2010) and the relevant group of fireballs were observed over a period of 1 Maj ($L_\odot \approx 30^\circ$) increase in the fireball activity. The results of the backward numerical integration of the mean orbital elements of the group (Mean) and near-Earth asteroid 2009 FS over a period of 5,000 years are plotted in Figs. 11 and 12. As can be seen from the figures, the D_{SH} -criterion of similarity between the mean orbit of the group and that of the Mason Gully meteorite remained below 0.35 for about five thousand years while the mean orbit and that of the plausible parent, i.e. NEA 2009 FS, were similar ($D_{SH} < 0.35$) for about three and a half thousand years which may be indicative of the time of the group formation. The relevant perihelia q , eccentricities e and arguments of perihelion ω evolved in a similar manner throughout the whole specified period.

In Figs. 4, 6, 8 and 12 which illustrate the orbital evolution of meteorites and their probable parent asteroids (NEAs), for the sake of comparison, the evolution of orbital elements of two near-Earth asteroids is shown; in particular, one of these NEAs has been chosen as a parent asteroid (red line) while another NEA (green line) depicts the evolution of an orbit different from those of the group, meteorite and chosen parent asteroid.

4.6. Orbital evolution of the Pribram (H5 type) u Neuschwanstein (EL6 type) meteorites

The Pribram meteorite was observed on 27 March 2003. The Pribram group was observed over a period of 1 Maj ($L_\odot \approx 30^\circ$) increase in the fireball activity. The results of the backward numerical integration of the mean orbital elements of the Pribram and Neuschwanstein meteorites over a period of 5,000 years are shown in Fig. 13. Based on the results of the numerical integration, the D_D -criterion

and D_{SH} -criterion of similarity between the meteorite orbits were calculated with an increment of 200 years. At the present time (epoch 2000.0) both criteria are extremely small ($D_D = 0.009$ and $D_{SH} = 0.025$) which enables to deduce that the Pribram and Neuschwanstein meteorite orbits evolved in a similar manner over the specified period and preserved the similarity of their orbits.

In the study [13], a near-Earth asteroid with the structure similar to that of asteroid Itokawa was considered as a potential parent of the Pribram and Neuschwanstein meteorites. The disruption of the asteroid with such a pattern might result in ejecting both large fragments (cobbles and pebbles) and smaller debris (meteoroids) which could form a group of meteorite-producing meteoroids in the near-Earth orbit.

5. Conclusions

– The evolutionary analysis using the method of backwards numerical integration of the mean orbital elements of a group, as well as those of the relevant meteorite and potential parent near-Earth asteroid over a period of 5,000 years has shown that the respective perihelia, eccentricities and arguments of perihelion evolved in a similar manner throughout the specified period.

– The D_{SH} -criterion, which is a quantitative measure of orbital similarity, has remained below 0.3 for about 5,000 years in the groups of Neuschwanstein and Mason Gully meteorites and for about 3,500 to 4,500 years in the groups of Benešov and Park Forest meteorites. In the groups of Košice and Pribram meteorites, the mean orbits and those of their potential parents remained similar as defined in terms of the D_{SH} -criterion over a relatively short period of about 2,000 to 3,000 years.

– Our findings enable us to infer that meteorite-producing sporadic fireballs and sporadic meteors are related to the H5 and L3.5 ordinary chondrites and their potential parents, i.e. near-Earth asteroids, in the groups of Neuschwanstein and Mason Gully meteorites and also those of Benešov and Park Forest meteorites. The estimated time intervals, during which the evolving orbits of the groups' members exhibit good similarity, are indicative of relatively recent formation of the examined meteorite-producing groups as a result of fragmentation of their parent bodies.

– The data on the mean orbit of a group of meteorite-producing meteoroids enable to relate the group to its probable origin which is either asteroidal or cometary. The results indicating the existence of groups of meteorite-producing meteoroids in Jupiter-family comet-like Earth-crossing orbits suggest that relatively large and solid meteoroids, which are members of these groups, can survive the passage through the atmosphere and fall to the surface as meteorites. In such a case, these meteorites are potentially samples of cometary material which can be examined using laboratory techniques.

– The investigated groups can still contain objects which are potentially hazardous for the Earths' biosphere and nowadays may fall to Earth as meteorites. This can provide a strong incentive to carry out targeted monitoring of the fireballs and meteors in these groups at their radiant points over specified periods of the group activity.

References

1. IAU MDC database: <http://www.astro.sk/~ne/IAUMDC/Ph2007/database.html>
2. SonotaCo database: <http://sonotaco.jp/doc/SNM/index.html>
3. Bondarenko Yu. Halley software, 2010.
4. Southworth R.B., Hawkins G.S.: 1963, *Smiths. Contrib. Astrophys.*, **7**, 261.
5. Kramer E.N., Musii V.I., Shestaka I.S.: 1980, *Komety i Meteory*, **29-31**, 83.
6. Whipple F.L.: 1940, *The Scientific Monthly*, **51**, 579.
7. Jones J., Hawkes R.: 1986, *Mon. Not. R. Astr. Soc.*, **223**, 479.
8. Greenberg R., Chapman C.R.: 1984, *Icarus*, **57**, Is. 2, 267.
9. Porubcan V., Williams I.P., Kornos L.: 2004, *Earth, Moon, Planets*, **95**, 697.
10. Trigo-Rodríguez M.J., Lyytinen E.: 2007, *Mon. Not. R. Astron. Soc.*, **382**, Is.13, 1933.
11. Torth, P., Veres, Kornos L.: 2011, *Mon. Not. R. Astron. Soc.*, **415**, 1527.
12. Halliday I., Blackwell A.T., Griffin A.A.: 1990, *Meteoritics*, **25**, 93.
13. Shestaka I. S.: 1994, *Astronomicheskii Vestnik*, **28**, No. 6, 94.
14. Beech M.: 2006, *WGN, the Journal of the IMO*, **34:4**, 104.
15. Konovalova N.A., Gorbanev Ju.M.: 2018, *Odessa Astron. Publ.*, **32**, in press.

DOI:<http://dx.doi.org/10.18524/1810-4215.2019.32.183899>

SIMULATION OF THE ORBITING SPACECRAFT TO ANALYSIS AND UNDERSTAND THEIR ROTATION BASED ON PHOTOMETRY

Koshkin N.¹, Melikyants S.¹, Korobeinikova E.¹, Shakun L.¹, Strakhova S.¹,
Kashuba V.¹, Romanyuk Ya.², Terpan S.¹

¹ Astronomical Observatory, Odessa National University, Odessa, Ukraine,
nikkoshkin@yahoo.com

² MAO NASU, Kyiv, Ukraine

ABSTRACT. Analysis of the photometric information allows to determine the parameters of spacecraft rotation. We will consider the light curves of a rotating satellite. Smooth changes in brightness, which are caused by diffuse scattering of sunlight, are characterized by the amplitude, quantity, shape and asymmetry of brightness variation during the rotation period of the body. In addition, the so-called “specular” flashes of light of very large amplitude are present on light curves. By analyzing the observed light curves of the inactive satellites Topex/Poseidon and Sich-2, the determination of pole orientation these objects in space is demonstrated. To interpret the light curve's contained information, we are planning to create optical-geometrical models of this satellite and simulated geometrical conditions by its orbit passages. Further comparison of the model and observed light curves should allow us to confirm the correctness of the satellite attitude determination. For the simulation, we used the MaxScript programming language, which allows to create a satellite model, and simulate the optical-geometric conditions of its passage, including the complex rotation of the spacecraft.

Keywords: Earth's artificial satellite, space object, photometry, light curve, rotation period.

АНОТАЦІЯ. Для контролю навколосемного космічного простору використовуються оптичні засоби спостереження. Аналіз фотометричної інформації дозволяє визначити параметри обертання космічного апарату. Ми розглянули криві блиску супутника, що обертається. Плавні зміни блиску, які обумовлені дифузним розсіюванням сонячного світла, характеризуються амплітудою, кількістю, формою і асиметрією коливань блиску протягом періоду обертання тіла. Крім того, на реєстрованих кривих блиску присутні так звані “дзеркальні” спалахи блиску, тобто короточасні підвищення блиску дуже великої амплітуди. Такі спалахи блиску обумовлені дзеркальним відбиттям сонячного світла від гладких поверхонь на корпусі КО. На основі аналізу спостережуваних кривих блиску неактивних супутників Topex/Poseidon та Sich-2 викладено методику визначення орієнтації цих об'єктів у просторі. Щоб інтерпретувати інформацію, що міститься в кривій блиску, ми плануємо створити детальні оптико-геометричні моделі цього супутника і

симулювати геометричні умови в його проходах по орбіті. Подальше порівняння моделі і спостережуваних кривих блиску має дозволити нам підтвердити правильність визначення орієнтації супутника. Для моделювання ми використовували мову програмування MaxScript, який дозволяє створювати модель супутника і моделювати оптико-геометричні умови його проходження, в тому числі складне обертання космічного корабля.

Ключові слова: Штучний супутник Землі, космічний об'єкт, фотометрія, крива блиску, період обертання.

Optical surveillance tools are used to of near-Earth space situations awareness. A satellite moving in orbit around the Earth is visible to the observer when it is illuminated by the Sun. Registration of the satellite's position against the background of stars allows us to solve the problem of the subsequent determination of its orbital parameters. In the case of inactive SO, the problem of determining its own rotation around the center of mass is solved by two types of measurements – high-frequency laser ranging (in the case when the target object is equipped with corner cube reflectors, CCR) and high-quality high-speed photometry (in all other cases) (Kucharski D. et al., 2018; Schildknecht Th. et al., 2015). The motion of the satellite relative to the center of mass is of great importance for many applications – from actively removing an inactive satellite (space debris) from orbit to accurately determine the real orbit to conjunction predict with other resident space objects.

If telescope track the space object along visible flight trajectory above the surveillance point, then it is possible to register a change in its brightness over a long time interval. This process is called photometry and the result is the so-called “light curve” of SO. Obviously, the density of the radiation flux reflected by the SO surface in direction of the observer (photometer) depends on the body shape and the optical characteristics of its surface, and its variation is determined by the changing geometric conditions of lighting and the aspect of the SO visibility, as well as its own rotation around the center of mass. In many cases, we do not have information about the real optical characteristics of the SO surface (indicatrixes of light scattering of different parts of the body) and even a specific configuration of the SO body shape not always is known (for example, location of solar panel relative to the body, or the composition of all parts of the SO after fragmentation).

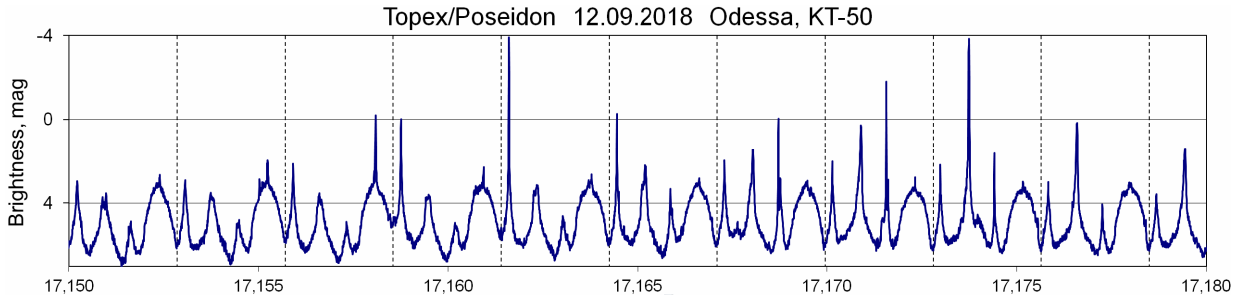


Figure 1: A fragment of the light curve of the rotating Topex satellite obtained September 12, 2018 using KT-50 telescope in Odessa

Consider the light curves of a rotating SO. Smooth changes of the brightness, which are caused by diffuse scattering of sunlight, are characterized by the amplitude, quantity, shape and asymmetry of the maximums and minimums of brightness during the rotation period of the body. In addition, so-called “specular” flashes of the brightness are often present on recorded light curves, that is, short-term increases in brightness, often of very large amplitude (from 1 to 5-6 magnitudes). Such flashes of brightness are caused by specular reflection of sunlight by smooth surfaces on the SO body. It can be flat surfaces or so-called “developable surfaces” (for example, cylindrical or conical), which are a smooth surface with zero Gaussian curvature. When the normal to a flat surface or to one of the developing surfaces coincides with the phase angle bisector (PAB), then there is a specular reflection of sunlight in the direction of the observer.

Since the diffuse component in the light curve is rather difficult to analyze, if there is no exact information on the indicatrices and reflection coefficients of the SO surface elements, then we can focus on the analysis of specular flashes. If the direction of “SO-observer” did not change in space, the interval between successive short-term flashes of brightness would accurately characterize the rotation period of the satellite in the fixed (inertial) coordinate system. In fact, this is not so, and the interval between flashes is called the “visible” (or synodic) period of the SO rotation. The visible period is determined by the vector sum of two rotations - the SO's own rotation and its orbital motion relative to the observer. In this paper, we consider some of the observed features of the alternation of specular flashes and changes in the visible rotation period using the example of the light curves of the inoperative Topex/Posseidon satellite (Koshkin N. et al., 2017; Atlas of light curves of space objects, 2014-2015; Atlas of light curves of space objects, 2016-2018).

Figure 1 shows a fragment of the representative light curve of a freely rotating former Topex satellite. This light curve was obtained on September 12, 2018 using the KT-50 telescope in Odessa. A characteristic feature is the presence of periodic bright flashes of light. Sharp specular maxima, characterized by rapid increase and decrease in brightness, are especially noticeable. The apparent period of the satellite rotation is marked by vertical dashed lines on the graph. In this fragment of the light curve during one revolution of the satellite, we see one broad “diffuse” maximum, with which a specular flash also sometimes coincides, and three sharp maxima are approximately equally spaced. The amplitudes of all specular brightness

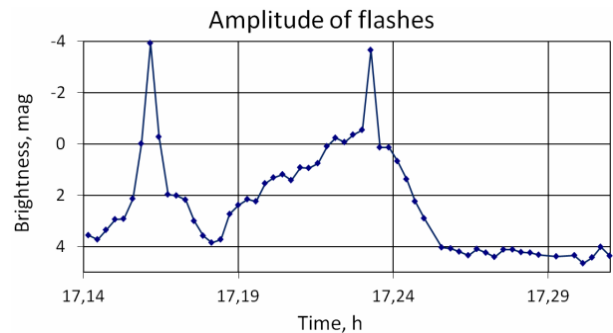


Figure 2: The change of amplitude of specular flashes during the satellite passage above the observation point in Odessa.

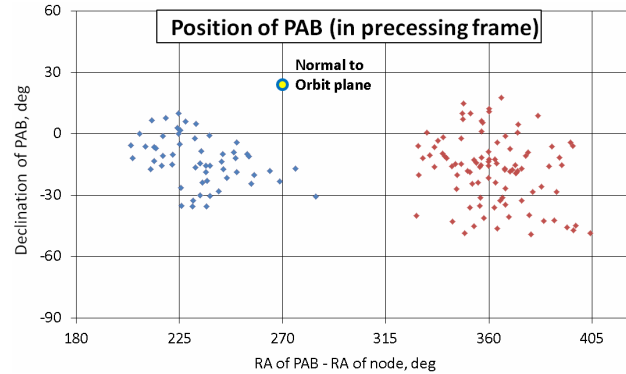


Figure 3: The position of the PAB vectors for 152 light curves of Topex obtained from September 1, 2009 to October 18, 2018.

fluctuations are not constant. Four maximums per period may indicate that the light-reflecting planes are located on the sides of the satellite body, which has the shape of a rectangular prism (a box).

Let us first consider one sequence of specular flashes of brightness following after a broad maximum in each cycle. This outburst is observed with different intensities throughout the curve. Figure 2 shows the change in its amplitude during the passage of the satellite above the observation point. We see that its amplitude experienced both slow and fast changes and rapidly increase twice, when specular reflection of light was occur, and the reduced to the standard distance brightness reached -4m at this time. This should indicate a variation in the angular distance between the normal to the light-reflecting surface and the phase angle bisector. The trajectory of the PAB is an arc in the celestial sphere, and it can be assumed that during the

satellite passage the same normal to a flat smooth face move closer on a certain small angle in relation the PAB twice, when the observer could see a specular reflection at the corresponding phase of the body rotation.

For all 152 light curves of Topex obtained by us from September 1, 2009 to October 18, 2018, we calculated the positions of the PAB vector at the moments when the flashes has specular character and amplitude of the light fluctuations are noticeable increase. Figure 3 shows the all positions of the PAB in a slowly rotating coordinate system, which the Z axis coincides with rotation pole of the Earth, and the X axis lies at the equator plane and is directed to ascending node of the Topex orbit.

We see that the positions of the PABs at the moments of bright specular flashes are concentrated in a limited region. This indicates that the rotation pole is “fixed” (and are fixed with it the orientation of Topex body itself) in the orbital coordinate system for a very long monitoring time. However, the separation of the positions of PAB vectors into two separate limited regions was unexpected. This should indicate that the considered sequence of specular flashes is produced by surfaces with different direction of the normal. The scattering of points in each region can also be caused by nutation oscillations of the satellite rotation axis.

Let the moments of successive flashes of brightness of any one face of a satellite rotating with a certain constant period be calculated for a stationary observer as

$$T_{N,calc} = T_0 + P_{Inert} * N,$$

where T_0 is the first moment of the sequence, P_{Inert} is the inertial period of rotation, N is the cycle number. The real moments of observed flashes twill be shifted relative to such the linear ephemeris due to a change of the phase angle and aspect of observation caused by orbital motion. In fig. 4 filled dots show the phase shift of the considered repeated outbursts relative to the linear ephemeris with inertial period of 10.2665941 seconds. We see that, despite a twofold increase in the amplitude, the phase shift of this flashes occurs smoothly and does not imply two different reflecting surfaces on the satellite’s body.

Moreover, it is possible to find the position of the assumed rotation axis of the satellite at which the longitude displacement of the PAB vector is of the same range. In fig. 4 the dashed line shows the shift of the longitude (phase) of the PAB vector in this Topex’ passage dated 09/12/2018 for the rotation axis with coordinates: right ascension $\alpha_\Omega = 100^\circ$ and declination $\delta_\Omega = 26^\circ$. However, this solution for the Topex’ rotation pole is significantly different from the value that follows from the pole motion model found in Kucharski (Kucharski et al., 2017). If light reflection, at the moments of these flashes of brightness, was produced by a flat face, then the phase shift of the flashes would be well described by just such model, and the found position of the rotation axis in this passage would correspond to the real one. However, in the case of Topex, we are apparently dealing with a different phenomenon.

Firstly, the Topex’ light flashes that follow after a broad maximum on the light curves are observed in many passes almost throughout the entire observation time with variable light intensity and degree of specularity. Secondly, as mentioned above, the phase displacement of flashes produced different planar faces should be similar and described by the model of PAB phase displacement. Figure 5 shows the phase shift of two series of flashes – the flash

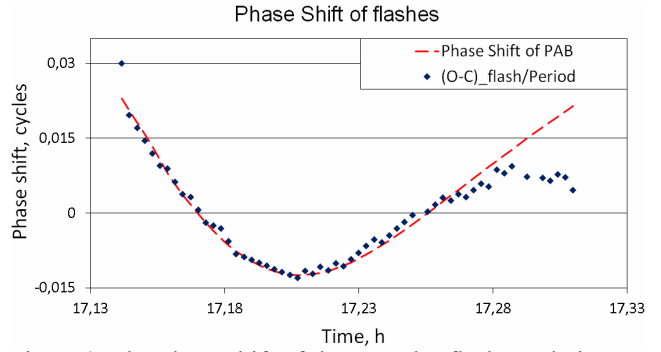


Figure 4: The phase shift of the specular flashes relative to the linear ephemeris with inertial period of 10.2665941 seconds (dots). Dashed line shows the shift of the longitude of the PAB vector in this Topex passage dated 09/12/2018 for the rotation axis with coordinates: right ascension $\alpha_\Omega = 100^\circ$ and declination $\delta_\Omega = 26^\circ$.

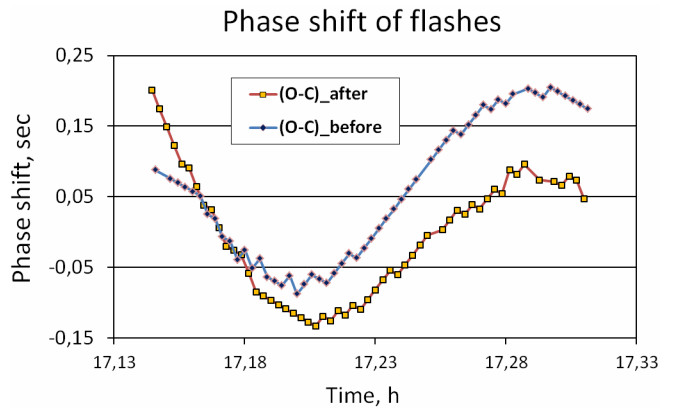


Figure 5: The phase shift of two series of flashes — the flash series after a wide maximum (as in fig. 4), and another flash series appearing before wide maximum.

series after a wide maximum (discussed above), and another flash series appearing before this maximum. We note the non-synchronous phase shift of these two different flashes. The phase difference between them reaches 0.1 sec or 1% of the rotation period. This may mean that at least one of the flashes is due to reflection from a non-planar surface.

We calculated the positions of the PAB vectors for another inactive satellite Sich-2 at those moments when the specular character of flashes is observed with a noticeable increase in the amplitude of the brightness oscillations. This space object is a rectangular prism with four solar panels and its light curves also occasionally present of the specular light reflection by the body surface (Koshkin et al., 2018). Figure 6 shows all the positions of the PAB in a slowly rotating coordinate system (the Z axis of which coincides with the Earth’s rotation pole, and the X axis lies at the equator plane and is directed to the ascending node of the Sich-2 orbit) for those passes when specular flashes of light appeared. The moments of the appearance of specular flashes of light are marked on each PAB trajectory with a red dot. We see that for the case when sunlight is reflected from flat faces, all the PAB vectors lie near one straight line on the celestial sphere. In the case of Sich-2, when the body shape is well known, it can be argued that the rotation axis of the satellite is the pole of this large circle on the sphere, and has the coordinates: right ascension $\alpha_\Omega = 91.5^\circ + \alpha_{node}$ and declination $\delta_\Omega = +34.7^\circ$.

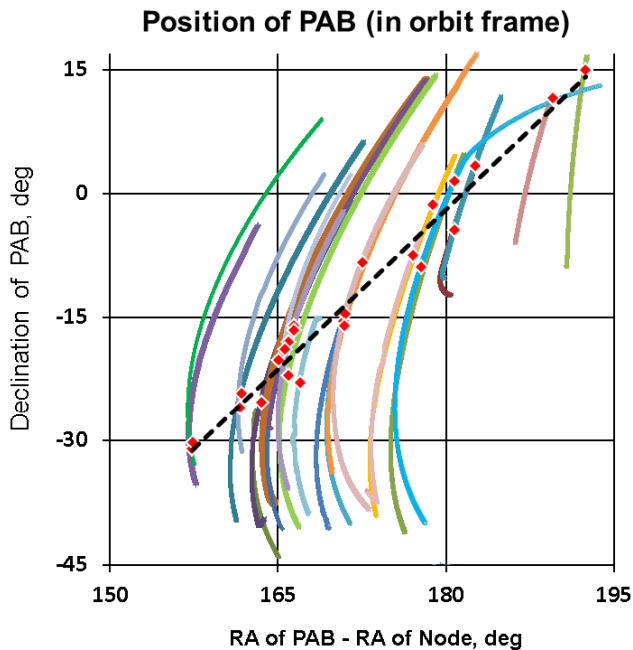


Figure 6: The positions of the PAB in a slowly rotating coordinate system (the Z axis of which coincides with the Earth's rotation pole, and the X axis lies at the equator plane and is directed to the ascending node of the Sich-2 orbit) for the passes when specular flashes appeared (red dots).

Summarizing the above analysis of the light curves of the inactive Topex satellite, it can be stated that the observed features of its brightness variations require consideration of the detailed shape of the body surface and the optical properties of even small structural elements. It can be assumed that long sequences of flashes (episodically very bright and specular) are due to

reflection from a conical smooth surface, different parts of one have different normals direction. The separation of the PAB position areas in the orbital coordinate system during such bright specular flashes is expressed this. Topex computer simulation should confirm this assumption (Melikyants et al., 2007).

References

- Atlas of light curves of space objects. Part 4: (2014-2015) /ed. N.I.Koshkin; Odessa, 2016, 183 p. (<http://dspace.onu.edu.ua:8080/handle/123456789/8480>).
- Atlas of light curves of space objects Part 5: (2016-2018) / ed. N.I.Koshkin; Odessa, 2018, 295 p. (<http://dspace.onu.edu.ua:8080/handle/123456789/23814>).
- Koshkin N., Savanevich V. et al.: 2017, *Odessa Astron. Publ.*, **30**, 226 (DOI: <http://dx.doi.org/10.18524/1810-4215.2017.30.117655>).
- Koshkin N., Shakun L. et al.: 2018, *Odessa Astron. Publ.*, **31**, 179 (<http://oap.onu.edu.ua/article/view/147807>).
- Melikyants, S., Shakun, L. et al.: 2007, *Odessa Astron. Publ.*, **20**, p. 72, (2007OAP...20...72M).
- Kucharski D. et al.: 2017, *AGU Earth and Space Science*, **4**, 661 (<https://doi.org/10.1002/2017EA000329>).
- Kucharski D. et al.: 2018, in: *Proc. 21st IWLR2018, Canberra, Australia, 5-9 Nov. 2018*, https://cdis.nasa.gov/iw21/docs/2018/papers/SessionSD4_Kucharski_paper.pdf.
- Schildknecht Th. et al.: 2015, in: *Proc. of the Adv. Maui Optical and Space Surveillance Technologies Conf., held in Wailea, Maui, Hawaii, September 15-18, id.25 (2015amos.confE.25S)*, <http://www.amostech.com/TechnicalPapers/2015/NROC/Schildknecht.pdf>.

DOI:<http://dx.doi.org/10.18524/1810-4215.2019.32.181906>

FIRST RESULTS OF CLARIFYING OF ORBITAL ELEMENTS OF LOW-ORBIT SPACECRAFT USING OBSERVATIONS OF THE RI "MAO" DOPPLER STATION

V.Kriuchkovskiy, F.Bushuev, M.Kaliuzhnyi, M.Khalaley, M.Kulichenko, O.Shulga

Research Institute "Mykolaiv Astronomical Observatory" (RI "MAO")
Mykolaiv, Ukraine, dir@mao.nikolaev.ua

ABSTRACT. 18 artificial satellites of the Earth, which emit radio signal at a frequency of 430-440 MHz during their flight in the Mykolaiv visibility zone, were found as a result of the searching carried out in the RI "MAO". 10 of 18 satellites during not less than 7 days each were automatically tracked by the Doppler station created in the RI "MAO". The frequency of received radio signal was automatically determined as a result of spectral processing of radio signal amplitudes registered by the station during satellite tracking. Herewith 5 of 10 satellites emitted non-harmonic broadband signals. The radial velocity of satellites is calculated using the frequency of received radio signals.

The obtained values of radial velocity changing in time were used to clarify TLE (Two-Line Element) orbital elements of satellites. Initial orbital elements were downloaded from the space-track.org site. It would be noted that model values of Doppler shift of frequency, obtained using the initial orbital elements, also use for searching radio signals emitted by tracked satellites and received by the station. The regular (mean) and random (standard deviation) components of the difference (O-C) of measured and model values of radial velocity were calculated. A comparison of the regular and random components of O-C was made, which showed their slight decreasing after clarifying orbital elements.

In order to improve the accuracy of the orbit determination, it is proposed to upgrade the station's hardware and software in order to reduce synchronizing and frequency determination errors. It is also proposed to use more accurate models as Doppler measurements, and the motion of satellites.

АНОТАЦІЯ. В результаті проведеного в НДІ «MAO» пошуку виявлено 18 штучних супутників Землі, які при прольоті в зоні видимості Миколаєва випромінюють радіосигнал на частоті 430-440 МГц. Доплерівською станцією, створеною в НДІ «MAO», в автоматичному режимі проведено супроводження 10 із 18 супутників протягом не менше, ніж 7 діб кожен. Частота прийнятого радіосигналу визначалася в автоматичному режимі в результаті спектральної обробки амплітуди сигналів, зареєстрованих станцією під час супроводження супутників. При цьому із 10 супутників 5 випромінювали негармонічний ширококутовий сигнал. За частотою прийнятого радіосигналу обчислювалася радіальна швидкість супутника.

Отримані значення радіальної швидкості, що змінюються у часі, використовувалися для уточнення

елементів орбіти супутника в форматі TLE (Two-Line Element). Початкові значення елементів орбіти завантажуються з сайту space-track.org. Зауважимо, що модельні значення доплерівського зсуву частоти, отримані з використанням початкових елементів орбіти, використовувалися також для пошуку радіосигналів, випромінюваних супутником і прийнятих станцією. Обчислювалися регулярна (середнє) та випадкова (СКП) складові різниці (O-C) виміряних і модельних значень радіальної швидкості. Проведено порівняння регулярної і випадкової складових O-C, яке показало незначне зменшення регулярної і випадкової складових O-C після уточнення елементів орбіти.

Для підвищення точності визначення орбіти пропонується провести модернізацію апаратури та програмного забезпечення станції з метою зменшення похибки синхронізації та похибки визначення частоти радіосигналів. Також пропонується використовувати більш точні моделі як доплерівських вимірювань, так і руху супутників.

Keywords: Doppler's effect, radio beacon, low-orbit satellite.

1. Introduction

Over the last few years, ambitious projects have emerged to create global high-speed Internet satellite systems, such as (OneWeb Satellites, 2019; STARLINK, 2019; Telsat, 2019). According to our estimates, about 16000 of these satellites will be put into service by 2030. Herewith 4500 of these satellites will have an orbit altitude of 350 km and 11500 satellites will have an orbit altitude of 850-1450 km. It is estimated that there will be 20 or more satellites in the plane of one orbit. For comparison, the constellation of 27 GPS satellites is placed in 6 orbits of 4-5 satellites (slots) in each plane (Global Positioning System, 2019). Given the height of the orbits, the density of placing satellites in orbits of the Internet systems will be at least 50 times higher than in the GPS. However, in our opinion, slight deviations from the uniform distribution of the density of satellites in the orbit plane could significantly affect the quality of the Internet for end-users due to the corresponding significant displacement (given the orbit height) of the Earth's surface coverage. Therefore, a problem of constant independent high-precision determination of the position of low-orbit satellites will become even more urgent. A solution to the

problem may be the creation networks of passive Doppler radars (stations) that determine the orbital position of satellites using the Doppler shift of frequency of radio signals emitted by the satellites. These could be either special monochromatic radio beacon signals (continuous wave) or non-harmonic broadband payload signals.

The Doppler station was developed and tested in the RI “MAO” to investigate the possibility of using such stations to clarify the orbit of low-orbit satellites (Bushuev, 2018). The station uses a compact high-tech receiver of up to 1766 GHz frequency range that greatly simplifies and reduces the cost of its hardware (GNSS-SDR, 2019). Initial orbits of tracked satellites are taken from (SPACE-TRACK.ORG, 2018). Model values of Doppler shift of frequency, obtained using the initial orbits, are used for searching radio signals emitted by tracked satellites and received by the station. It would be noted that 58 satellites were checked to search radio beacon signals. Radio beacons were detected for 18 satellites and 8 of them emit continuous waves.

2. Upgrading the post-processing of observation data obtained by the Doppler station

There are two stages to clarify orbit elements of the given satellite: real time and post processing (Bushuev, 2018). In real time the radio signals are recorded in wav-files using software defined radio and freeware program HDSDR (High Definition Software Defined Radio). Post-processing includes analyzing the wav-files to determine the radial component of the satellite velocity (v_{obs}) and clarifying of the satellite orbital elements using v_{obs} . The program SatDoppler is used to determine $v_{obs}(t)$ as the function of time t , and program WinMNK takes into account $v_{obs}(t)$ to clarify of the satellite orbit elements.

The program SatDoppler has been significantly upgraded compare with (Bushuev, 2018). The upgraded program uses model values of Doppler shift of frequency (f_{dop}) and correlation analyses for searching radio signals emitted by tracked satellites and received by the station. The model values of f_{dop} are calculated using the initial orbit elements of tracked satellite downloaded from (SPACE-TRACK.ORG, 2018). Let $A_{obs}(t,f)$ denote the amplitude of the received signal as a function of time (t) and frequency (f). Let also $A_{mod}(t,f)$ denote the pattern equal 0 anywhere except some points where $A_{mod}=1$. The points where $A_{mod}=1$

correspond a function $f(t)$ that equal model values of radio beacon frequency at a moment t . Correlation function of A_{obs} and A_{mod} is calculate at first to find the radio signal emitted by the tracked satellite and received by the station. Herewith intervals of t and f for which function A_{obs} is determined must be greater than for function A_{mod} . The position Δt and Δf of the maximum of the correlation function is found next. The coordinates Δt and Δf give an offset of A_{mod} relative to the beginning of A_{obs} . The desired signal is searched in the frequency range of ± 70 Hz near the points where $A_{mod} = 1$ after the shift. So, the errors of synchronizing (Δt) and determination of frequency (Δf) of the received radio signal are also obtained as a result of the correlation analysis. The value of Δf is due to the difference in the nominal frequency of the receiver reference generator from the valid one (Bushuev, 2018).

3. Results of satellite orbit clarifying

The results of the clarifying of the orbit of 10 satellites are shown in Table 1. Each satellite was tracked automatically by the Doppler station for at least 7 days. The obtained records of signals of satellite radio beacons were analyzed by SatDoppler and the measured values of the radial component of the satellite velocity v_{obs} were determined. The WinMNK program used measured values of v_{obs} to clarify orbit elements of the satellites. The model values of the radial velocity were calculated before (v_{Bmod}) and after (v_{Amod}) clarifying of the satellite orbit. Herewith the orbit elements downloaded from space-track.org were used to calculate v_{Bmod} . Means (Mean) and standard deviations (SD) of the difference $\Delta_B=(v_{obs} - v_{Bmod})$ are shown in the columns “Before” of Table 1. The values of Mean and SD of the difference $\Delta_A=(v_{obs} - v_{Amod})$ are shown in the columns “After”. The differences of absolute values of the mean and standard deviation of Δ_A and Δ_B are shown in columns “Diff [Mean]” and “Diff SD” of Table 1. The row “Total average” contains the average values of the data above it.

It follows from the data in Table 1 that the clarifying of the orbit elements of the satellites results in a slight decrease (by an average of 1.6 m/s) of both means and standard deviations of the difference of the measured and model values of the radial velocity of the tracked satellites.

It would be noted that the radio beacons of five satellites from Table 1 emitted non-harmonic broadband signals.

Table 1: Results of satellite orbit clarifying.

Name	Before		After		After-Before	
	Mean, m/s	SD, m/s	Mean, m/s	SD, m/s	Diff [Mean], m/s	Diff SD, m/s
OSCAR-19	-0.2	5.4	-0.3	4.8	0.1	-0.6
CUTE-1	0.2	2.2	0.0	1.8	-0.2	-0.4
CUTE-1.7	-1.2	10.4	-0.3	10.2	-0.9	-0.2
SEEDS	-0.1	3.4	-0.2	3.0	0.1	-0.4
KESEKI	0.0	8.9	0.1	8.4	0.1	-0.5
ITUPSAT-1	18.8	120.5	5.0	114.4	-13.8	-6.0
XIWANG-1	-0.2	3.8	-0.4	3.6	0.2	-0.1
GOMX-1	-0.5	28.7	-1.6	22.9	1.1	-5.8
AIST-2D	-0.6	8.4	-0.6	7.6	0.0	-0.8
TECHNOSAT	-5.4	24.7	-2.7	23.3	-2.7	-1.3
Total average	1.1	21.6	-0.1	20.0	-1.6	-1.6

4. Conclusion

The ground Doppler station of the RI “MAO” automatically tracked 10 low-orbit satellites for at least 7 days each. Herewith the radio beacons of five satellites emitted non-harmonic broadband signals. The orbit elements of these satellites have been clarified using measurements of the Doppler shift of frequency of their radio beacons. The regular (mean) and random (standard deviation) components of the difference (O-C) of measured and model values of radial velocity were calculated. A comparison of the regular and random components of O-C was made, which showed their slight decreasing (in average at 1.6 m/s) after clarifying orbital elements.

The following is proposed to improve the accuracy of orbit determination:

- upgrading station’s hardware and software to decrease synchronizing and frequency determination errors;
- using more accurate models as Doppler measurements, and the motion of satellites to clarify their orbit.

References

- Bushuev F., Kaliuzhnyi M., Khalaley M. et al.: 2018, *Odessa astronomical publications*, **31**, 167.
- Global Positioning System [online] Available at: <https://encyclopedia.thefreedictionary.com/Global+Positioning+System> [Accessed 15 October 2019].
- GNSS-SDR operation with a Realtek RTL2832U USB dongle DVB-T receiver, [online] Available at: <http://gnss-sdr.org/node/50> [Accessed 15 October 2019].
- OneWeb Satellites [online] Available at: <https://onewebsatellites.com/> [Accessed 15 October 2019].
- SPACE-TRACK.ORG, [online] Available at: <https://www.space-track.org/auth/login> [Accessed 10 October 2018].
- STARLINK [online] Available at: <https://www.starlink.com/> [Accessed 15 October 2019].
- Telsat [online] Available at: <https://www.telesat.com/services/leo/why-leo> [Accessed 15 October 2019].

DOI:<http://dx.doi.org/10.18524/1810-4215.2019.32.181908>

RESULTS OF POSITIONAL AND PHOTOMETRIC MEASUREMENTS OF METEOR TRAJECTORIES OBSERVED IN MYKOLAIV 2017-2018

M.O. Kulichenko¹, O.V. Shulga¹, Yu.M. Gorbanev²

¹ Research Institute “Mykolaiv Astronomical Observatory”,
Mykolaiv, Ukraine, <niiko4kulichenko@gmail.com>

² Astronomical Observatory of the I.I. Mechnikov Odessa National University,
Odessa, Ukraine, <skydust@ukr.net>

ABSTRACT. Regular meteor observation using TV CCD unintensified techniques was started in 2011 in RI «Mykolaiv astronomical observatory» (RI MAO). The method of meteor registration is based on using “track-and-stack” technique for obtaining frames with reference stars and online meteor detection software developed at RI NAO. The main accent of the research is made on precise astrometry and meteoroid orbits calculation. New observational campaign with baselines 11.7 and 100 km was started in 2017-2018 in collaboration with Astronomical Observatory of the I.I. Mechnikov Odessa National University. Eight telescopes with narrow field lens ($f=50$ mm, $f/1.2$) were installed in Mykolaiv and Odessa. More than 3000 single station meteors and 221 double station meteors were detected during 2017-2018. Uncertainties of meteor trajectory and orbital parameters are calculated using Monte Carlo method. Catalog of meteor trajectory positions and photometric parameters has created. Standard deviation of approximation of a meteoric trajectory in a large circle is (15-20)". Kinematic parameters of atmospheric meteoric trajectories and elements of heliocentric orbits for 3 meteors were calculated based on the results of television observations with cameras with a field of view $<10^\circ$ at a baseline distance 100 km. The average uncertainty of visible radiant estimation is in $(0.3-0.7)^\circ$ with baseline 100 km. The geocentric velocity estimation uncertainty is 0.5 km/s, elevation uncertainty is 50-150 m.

Keywords: meteors, meteoroid orbits, video observation.

АНОТАЦІЯ. Регулярні спостереження метеорів з використанням невідсиленої телевізійної ПЗЗ техніки було розпочато в 2011 р. в НДІ «Миколаївська астрономічна обсерваторія» (НДІ MAO). Метод спостережень заснований на використанні способу накопичення зі зміщенням для отримання кадрів з опорними зорями і програмному забезпеченні, що реєструє метеори в режимі реального часу, розробленого в НДІ MAO. Головний акцент дослідження робиться на отримання високоточних положень точок метеорної траєкторії та визначенні орбіт метеороїдів. Новий етап спостережень почався в 2017 р. на станціях з базисними відстанями 11.7 та 100 км в співробітництві з астрономічною обсерваторією Одеського національного університету ім. І.І. Мечникова. Вісім телескопів з малими полями зору ($f=50$ mm, $f/1.2$) були встановлені в Миколаєві та Одесі.

Протягом 2017-2018 зафіксовано більше 3000 однопунктних метеорних реєстрацій та 221 базисний метеор. Невизначеності параметрів атмосферної траєкторії та елементів геліоцентричної орбіти метеороїда були обчислені з використанням методу Монте-Карло. Був створений каталог позиційних та фотометричних параметрів спостережених метеорних траєкторій. Середнє квадратичне відхилення апроксимації метеорної траєкторії великим колом складає $(15-20)''$. За результатами спостережень камерами з полями зору $<10^\circ$ на базисній відстані 100 км були обчислені параметри атмосферної траєкторії та елементи геліоцентричної орбіти для 3 метеороїдів. Невизначеність в обчисленні видимих екваторіальних координат радіанта на базисній відстані 100 км складає в середньому $(0.3-0.7)^\circ$. Невизначеність в обчисленні геоцентричної швидкості складає 0.5 км/с, в обчисленні висот – 50-150 м.

Ключові слова: метеори, орбіти метеороїдів, телевізійні спостереження.

1. Introduction

Meteor observation using video techniques was started at Research Institute «Mykolaiv astronomical observatory» (RI MAO) in 2011. This is the third big meteor research campaign in Ukraine after Odessa (Gorbanev, et al., 2006; Gorbanev, 2009) and Kiev (Hajdukova, et al., 1995; Kozak, 2001). The research is based on a system of fixed telescopes equipped with TV CCD cameras for both single and double station observation. The main goals were setting completely automatic observation of meteors, and obtaining astrometric and atmosphere trajectory parameters of meteors (radiant point coordinates, velocities, orbit elements) using original software developed in RI MAO. Results of double station observations in Mykolaiv are in (Kulichenko, et al., 2014; Kulichenko & Shulga, 2018).

2. Meteor observation methods and facilities

2.1. Meteor telescopes

In 2017-2018 Video observations of meteors at the RI MAO are conducted using meteor patrol, which includes 8 optical telescopes ($f = 50$ mm, $f/1.2$) equipped with a TV CCD cameras WAT-902H2 (768×576 , $8.6 \times 8.3 \mu$). The field

of view of each telescope is $5.6^\circ \times 7.4^\circ$. Comparing with previous work (Kulichenko, et al 2015) such optical systems allow to increase amount of detected meteors and average angular length of observed meteor trajectory. System doesn't have any intensifier. Each video system is contained in a hermetic capsule to prevent it from rain and other aggressive meteorological conditions (Figure 1). Cameras work in the interlace mode with rate 50 half-frames per second. Three stations with baselines 11.7 and 100 km were set: 1) Mykolaiv, RI MAO, consists of 4 telescopes ($\varphi=46.972667$, $\lambda=31.972055$); Mykolaiv, Vitovka, consists of 2 telescopes ($\varphi=46.871598$, $\lambda=32.018309$); Kryzhanovka, Astronomical Observatory of the I.I. Mechnikov Odessa National University (AO ONU), consists of 2 telescopes ($\varphi=46.560722$, $\lambda=30.806500$).

2.2. Observation method

The original observation method was developed at RI MAO for observation of objects having high apparent rates on stare telescopes (Shulga, et al., 2009, 2011). Firstly it was used for observation of artificial satellites. The main idea of the method is obtaining frames with stars and moving object separately for more accurate coordinate measurement. The automated meteor detection software was designed in 2010, based on the experience with real-time video stream processing.

Parallel to the real-time detection process the star images are accumulated with a 30 s exposure using the «track-and-stack» technique. Accuracy of the reference system is less than 6 arc sec. Limiting magnitude for stars (12-13)^m.

The method of double station synchronization is based on using PPS-impulse from GPS receiver Resolution-T as reference impulse. Accuracy of time synchronization is 10^{-4} s.

2.3. Software

The modified software is used for the calculation of the equatorial coordinates of the meteor trajectories. There are four main steps of calculation:

- 1) stars processing (software – TraEx (written in Python, developed in RI MAO), reference star catalogue – Tycho2;
- 2) extracting and measuring the meteor trajectory points in frame coordinate system (software – TraEx);
- 3) calculation of the equatorial coordinates of the meteor trajectories using results of the previous steps (software – TraEx);
- 4) searching for meteors observed simultaneously from two stations and calculation of parameters of atmosphere trajectories and elements of heliocentric orbits (software developed in RI MAO).

Uncertainties of meteor trajectory and orbital parameters are calculated using Monte Carlo method (Albin, et al. 2016). The Monte Carlo method is based on the generation of random numbers in accordance with the statistical distributions of the measured equatorial coordinates of the meteor and, as a consequence, the corresponding distributions for all the kinematic and orbital parameters of the meteor body. This approach allows us to estimate the standard deviation of the desired quantities, as well as to specify their mathematical expectation.

3. Results

3.1. Single station observation

During 2017-2018 more than 3000 single station meteors were observed. The mean duration of observed meteor trajectories is in 0.04-1.2 s. Mean amount of frames is about 8-10. The distribution of meteors over meteor magnitude has two maxima at 0^m and 2^m. Arc length of meteor trajectories is in (0.08-7.5)^o.

The main parameter of single station meteor trajectory is the position of meteor's path big circle pole (Gorbanev & Golubaev, 2009). This parameter is used for further calculating of radiant point coordinates and heights (Astapovich, 1958). The mean accuracy of pole coordinates estimation is about (0.05-0.1)^o.

3.2. Meteoroid orbits

Due to large amount of detected phenomena only short period of observation for two stations with baseline 100 km (4 telescopes) is completely processed. Total number of observed meteors was 220, number of simultaneous observed meteor trajectories – 130. In the period from April 2018 to July 2018 213 single station meteors were detected, but only 3 meteors (Table 1) were observed simultaneously because of difficulty with correct pointing of narrow field telescopes on distance 100 km. After pointing correction in August 2018 preliminary searching for double station meteors in the period of next 4 months gave result of 218 meteors. The velocity estimation uncertainty is 0.5 km/s, elevation uncertainty is 50-150 m. Uncertainties of heliocentric orbital elements calculation are shown in the table 1.

Table 1: Results of meteoroid orbit determination for 3 meteoroids observed in April-May 2018 with baseline 100 km

Parameter	20180413_2 739090_A3 K1	20180413_2 804334_A3 K1	20180502_2 746108_A3 K1
Radiant equatorial coordinates, °	276.4±0.03 -32.3±0.08	322.1±0.9 0.5±1.7	333.8±0.3 5.3±0.8
Geocentric velocity Vg, km/s	66.4±0.06	41.8±0.2	65.7±0.6
Height H1, km	117.2±0.06	118.8±0.09	115±0.6
1/a, au ⁻¹	0.22±0.006	1.32±0.02	-0.07±0.06
a, au	4.43	0.75	--
Perihelion distance q, au	0.72±0.001	0.08±0.02	0.59±0.02
Eccentricity e	0.83±0.004	0.89±0.02	1.04±0.04
Inclination i, °	156±0.1	152±3	175±1
Argument of perihelion om, °	247±0.3	18±2	100±3
Longitude of ascending node Om, °	23.77	23.79	42.30

4. Conclusion

Since 2011 regular automatic monitoring of meteors with the use of “track and stack” technique is conducted. In 2017-2018 eight meteor telescopes worked, located at tree stations at a distances of 11.7 km and 100 km. An array of data containing more than 3000 single station meteor trajectories has been obtained. Catalog of meteor trajectory positions and photometric parameters has created. Standard deviation of approximation of a meteoric trajectory in a large circle – (15-20)". Kinematic parameters of atmospheric meteoric trajectories and elements of heliocentric orbits for 3 meteors were calculated based on the results of television observations with cameras with a field of view $<10^\circ$ at a baseline distance 100 km. The velocity estimation uncertainty is 0.5 km/s, elevation uncertainty is 50-150 m.

Acknowledgements. Our acknowledgements to Alexander Grinchenko and Gennadiy Vorsin from UALeks Scientific Industrial Concern without whom double station observation with short baseline would be impossible.

References

- Albin T., D. Koschny, R. Soja, et al.: 2016, in *Proc. of the International Meteor Conference, Egmond, the Netherlands, 2-5 June 2016*, Eds.: Roggemans, A., Roggemans, 20.
- Astapovich I.S.: 1958, *Meteor phenomena in Earth atmosphere*. (Fizmatgiz, Moscow).
- Gorbanev Y. M., Golubaev A. V., Zhukov V. V., et al.: 2006, *Solar System Research*, **40**, 5, 412.
- Gorbanev Y. M.: 2009, *Odessa Astron. Publ.*, **22**, 60.
- Gorbanev Y. M., Golubaev A. V.: 2009, *Odessa Astron. Publ.*, **22**, 4.
- Hajdukova M., Kruchinenko V. G., Kazantsev A. M., et al.: 1995, *Earth, Moon, and Planets*, **68**, 1-3, 297.
- Kozak P. M., Rozhilo A. A., & Taranukha Y. G.: 2001, in *Proc. of the Meteoroids 2001 Conference, 6 - 10 August 2001, Kiruna, Sweden*. Ed.: Barbara Warmbein. ESA SP-495, Noordwijk: ESA Publications Division, ISBN 92-9092-805-0, 337.
- Kulichenko N., Shulga O., Kozyryev Y., et al.: 2014, in *Proc. of the International Meteor Conference, Poznan, Poland, 22-25 August 2013*. Eds.: Gyssens, M.; Roggemans, P.; Zoladek, P. International Meteor Organization, 2014, ISBN 978-2-87355-025-7, 50.
- Kulichenko N., Shulga O., Kozyryev Y., et al.: 2015, *WGN*, **43**, 3, 81.
- Kulichenko M.O., Shulga A.V.: 2018, *Odessa Astron. Publ.*, **31**, 186.
- Shulga O., Kozyryev Y., and Sybiryakova Y.: 2009, in *Proc. of IAU Symposium № 248 “A Giant Step: From Milli- to Micro-arcsecond Astrometry”*, Shanghai, 2007, 128.
- Shulga O., Kozyryev Y., and Sybiryakova Y.: 2011, in *Proc. Of Gaia follow up network for solar system objects workshop held at IMCCE, Paris observatory, France*, 2011, 97.

DOI:<http://dx.doi.org/10.18524/1810-4215.2019.32.182512>

MODEL OF GRAVITATIONAL EFFECTS IN SATURN'S RINGS

L.D. Manchenko

Department of Theoretical Physics named by academician I. M. Lifshits,
V. N. Karazin Kharkiv National University Kharkiv, Ukraine, lil.dmitrievna@gmail.com

ABSTRACT. In this work, we consider one possible gravitational interaction in a system consisting of Saturn, its satellites and rings. The structure of rings can be changed because of such interactions leading to some sculpting of rings. In consequence of not trivial gravitational effects, various perturbations are observed on the edges of rings. We use methods of celestial mechanics to describe a system containing the planet, two satellites and the ring placed between them. In such a system, gravitational forces lead to running waves that deform the ring. These effects are peculiar to Saturn's F ring. The description of these perturbations needs more difficult physical model. In particular, to find the change in the ring's edge it's necessary to go to the non-inertial reference frame. To describe some effects we expect to employ methods of nonlinear physics to build the model.

АНОТАЦІЯ. Завдяки місії Кассіні за останні роки було отримано багато даних про планету Сатурн та її кільця. Було виявлено, що система кілець Сатурна та його супутників має безліч прикладів прояву гравітаційних взаємодій. У даній роботі ми розглядаємо одну з можливих взаємодій в гравітаційному полі системи. Структура кілець може змінюватись залежно від прояву сил гравітації, що призводить до нерівномірного розподілу речовини в кільцях. Відомо, що частинки на границях кілець можуть відчувати збурення внаслідок проходження поряд супутників. Ми розглядаємо систему, що складається з планети, її кільця, що розташоване між двох супутників. Траєкторії частинок у такій системі описуються методами небесної механіки. Гравітаційні сили в системі можуть призводити до збурень у вигляді біжучих хвиль. Ця картина притаманна кільцю F планети Сатурн. Для опису цих збурень, треба перейти до неінерціальної системи відліку, пов'язаної з частинкою у кільці, щоб побачити зміну траєкторії. У подальшому ми збираємось описувати деякі ефекти, що можуть виникнути у системі, за допомогою методів нелінійної фізики.

Keywords: Saturn's rings, gravitation, rotating reference frame.

1. Introduction

After the end of the Cassini Mission in 2017 scientists are still processing and analyzing obtained images of Saturn's and its rings. One of the main conclusions based on obtained data is that a structure of Saturn's rings is fairly difficult. Scientists assume complex models of gravitational interactions in order to explain the heterogeneity in the distribution of rings matter. For example, the gap between rings A and B is explained by gravitational resonance 2:1 of A ring with the Mimas and named Cassini Division. Other interesting interactions due to orbital resonance are considered in work (Araujo et al., 2015). The satellites Janus and Epimetheus are influenced by orbital resonance 7:6 (Proco et al., 1987) and impact on the edge of the A ring. Thereby, there are perturbations in the form of waves on the ring's edge. Such waves have a three-dimensional structure and fade out with extending deep into the ring. Janus and Epimetheus are located on the close orbits, and when the one overtakes another, their orbits switch (every 4.2 years). In (Fig. 1) the change of orbits is demonstrated in dependence on a period of time. Appeared gravitational

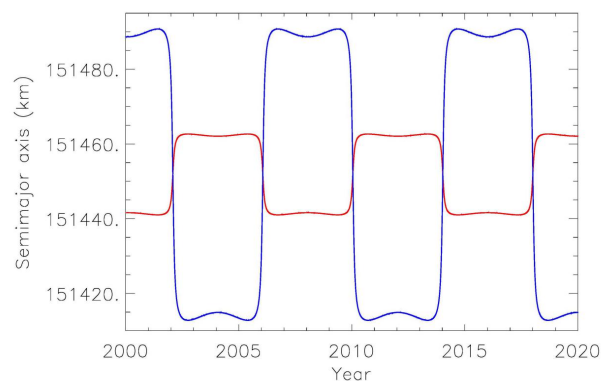


Figure 1: Semi-major axis for Janis (red) and Epimetheus (blue) as a function of time between 2000 and 2020 years, from a numerical integration, fitted to Cassini data (Cooper et al., 2015)

force due to such a switching causes perturbations on the edge. These perturbations are small in comparing with the size of the ring and do not change its overall structure. It is assumed that waves fade out enough quickly then we can speak about particles bonds in the ring.

In this work, we concern with another problem. Consider the thin ring between two moons in orbital resonance. This situation is realized for an F ring of Saturn surrounded by Prometheus and Pandora. The F ring is far from the main rings system, therefore is not influenced by them. The F ring can have dynamical changing in structure (Fig. 2) due to a satellites impact.



Figure 2: In the left corner is Pandora, and in the right is Prometheus, acquired by the Cassini spacecraft [solarsystem.nasa.gov]

2. Physical model

Each ring surrounding Saturn consists of dust and ice particles that move on stable orbits. If the outer gravitational field of Saturn is supplemented by a small perturb additive (it can be caused by distant satellite or tidal forces of the planet) then the search of orbital parameters will be more difficult. One of the ways to describe such a motion is presented in (Burns, 1976). If the ring is located between orbits of two satellites moving in gravitational resonance, the variable in time and localized in space gravitational field, that could be not assumed as small, acts on the particles. In result, the strong perturbations, distorting the ring, are observed. To describe the motion of the particle in

the ring in such a case, we suggest using the Newtonian approach: the gravitational force, acting on the particle, consists of force sourced by the planet, and perturbation forces sourced by satellites. To describe the latter, we introduce disturbing potential. The technique of introducing such potential is presented in (Shu et al., 1984; Renner et al., 2006) Obtained equations, generally speaking, describe perturbed motion and is a case of N-body problem.

For numerical simulation of the motion of such a gravitational system one should use the following equations:

$$m_i \frac{d^2 \vec{r}_i}{dt^2} = G \sum_{i \neq j}^N \frac{m_i m_j (\vec{r}_i - \vec{r}_j)}{|\vec{r}_i - \vec{r}_j|^3} \quad (1)$$

The system of equations (1) with initial conditions describe the N-body problem completely. Unfortunately, this system is not applicable for the analytical study and can be time-consuming for the numerical simulation. Here we propose an alternative approach that is lack of the mentioned disadvantages. We will study an orbit of a separate particle in the non-inertial frame that rotates around the central mass with the angular velocity of the ring. In such a frame non-perturbed particle should rest, while perturbed particles oscillate about their rest points. Moreover while the amplitude of such oscillation evidently much smaller the ring radius, it can be comparable with the distance between satellites and ring, producing non-trivial and non-linear dynamics. For two particles an equation has a form:

$$\frac{d^2 \vec{r}}{dt^2} = -\frac{GM}{|\vec{r}|^3} \vec{r} + 2 \left[\frac{d\vec{r}}{dt}, \vec{\Omega} \right] + \left[\vec{\Omega}, \left[\vec{r}, \vec{\Omega} \right] \right] \quad (2)$$

where \vec{r} – is a radius vector directed from the particle with mass m , M – is a mass of moving particle in the new reference frame, $\vec{\Omega}$ – is an angular frequency vector of rotating reference frame.

3. Discussion

Besides, we propose to consider the classical task of celestial mechanics from the point of view nonlinear physics and to describe perturbation as non-small additive in the equation of motion in the rotating reference frame. In result, we aim to find an analogue with soliton solutions (Kosevich et al., 1978), that is a case in propagation nonlinear waves in a medium. This analogue could describe some dynamical effects, that can have a place in Saturn's rings.

4. Conclusions

We have proposed a physical model of gravitational interactions for the Saturn's F ring to describe the change of its structure. This approach should simplify the numerical simulation for the N-body problem and enables analytical studies. In the future using this physical model, we might describe the dynamical structure and the change of the separate particle orbit.

Acknowledgements. The author wishes to thank Stanislav S. Apostolov for the interesting discussion and the very constructive comments that helped in improving the final manuscript, Irina B. Vavilova for the contribution to this work and the organizing committee for a given opportunity to participate in the conference.

References

- Araujo N. et al.: 2019, *MNRAS*, **486**, 4, 5037.
Burns J. A.: 1976, *American Journal of Physics*, **44**, 944.
Cooper N.J. et al.: 2015, *AJ*, **149**, 27.
Kosevich A.M. & Kovalev A.S.: 1978, Kiev: Naukova Dumka, 304 p. [in Russian]
Proco C.C., Nicholson P.D.: 1987, *Icarus*, **72**, 437.
Renner S. & Sicardy B.: 2006, *Celestial Mechanics and Dynamical Astronomy*, **94**, 237.
Shu F.H.: 1984, in: *IAU Colloq. 75: Planetary Rings* /eds. Greenberg R., Brahic A., 513.

DOI:<http://dx.doi.org/10.18524/1810-4215.2019.32.182231>

MATHEMATICAL MODEL AND METHOD OF OPTIMAL PLACEMENT OF OPTICAL-ELECTRONIC SYSTEMS FOR TRAJECTORY MEASUREMENTS OF AIR OBJECTS AT TEST

A.D. Tevjashev¹, I.S. Shostko¹, M.V. Neofitnyi¹, S.V. Kolomiyets¹,
I.Yu. Kyrychenko¹, Yu.D. Pryimachov²

¹ Kharkiv National University of Radio Electronics,
Kharkiv, Ukraine, *iryua.kyrychenko2@nure.ua*

² V.N. Karazin Kharkiv National University,
Kharkiv, Ukraine

ABSTRACT. To study the dynamic properties of the new generation of airplanes, helicopters, unmanned aerial vehicles, rocket and artillery weapons and ammunition at test sites (polygons) use mobile laser optical-electronic stations of the trajectory of measurement (LOETMS). Each LOETMS provides the detection of test air objects in the visible and infrared spectral ranges, their high-precision tracking, measurement and delivery of the parameters of the coordinates of the movement of air objects in real time. In order to eliminate systematic and suppress random errors of trajectory measurements, LOETMSs are integrated into a unified polygon information-measuring system (UPIMS). Since the cost of each LOETMS is high enough, when constructing the UPIMS, the problem arises of choosing the minimum number of LOETMSs and their location along the test tracks of the polygon so that the dispersion of estimates of the parameters of the coordinates of the movement of air objects is minimal or at least less than or equal to a given threshold. The report provides a mathematical formulation and solution of the two-criterion problem of optimal placement of LOETMS on the territory of the polygon. The main attention is paid to the mathematical formulation and the method of solving the problem of metrological certification of the UPIMS for a fixed number and location of LOETMSs along the test tracks of the polygon. It is shown that the solution of the UPIMS metrological certification problem is reduced to linearizing the non-linear function of random arguments (model of the trajectory of air objects) and calculating the dispersions of dependent variables (parameters of motion coordinates) from known dispersions of independent variables. The results of solving the problems of optimal placement of LOETMSs on the territory of the polygon and metrological certification

of UPIMS are given. The studies are relevant not only for field testing of aircraft, but also of scientific and practical interest in the construction of monitoring systems for airspace in the visible and infrared spectral ranges and the study of the trajectories of objects of artificial and natural origin in the Earth's atmosphere.

АНОТАЦІЯ. Для дослідження динамічних властивостей нового покоління літаків, вертольотів, безпілотних літальних апаратів, ракетного та артилерійського озброєння і боєприпасів на полігонах використовують мобільні лазерні оптико-електронні станції траєкторії вимірювання (ЛОЕСТВ). Кожна ЛОЕСТВ забезпечує виявлення випробовуваних повітряних об'єктів у видимому і інфрачервоному діапазонах спектру, їх високоточне супровід, вимір і видачу параметрів координат руху повітряних об'єктів в режимі реального часу. Для усунення систематичних і придушення випадкових помилок траєкторних вимірювань ЛОЕСТВ інтегруються в єдину інформаційно-вимірювальну систему полігону (ЕІВСП). Так як вартість кожної ЛОЕСТВ досить висока, то при побудові ЕІВСП виникає проблема вибору мінімальної кількості ЛОЕСТВ і їх розташування уздовж випробувальних трас полігону таким чином, щоб дисперсія оцінок параметрів координат руху повітряних об'єктів була мінімальною або, принаймні, менше або рівною заданому порогу. У доповіді наводиться математична постановка і рішення двукритеріальної задачі оптимального розміщення ЛОЕСТВ на території полігону. Основна увага приділена математичній постановці і методу рішення задачі метрологічної атестації ЕІВСП для фіксованої кількості та розташування ЛОЕСТВ уздовж випробувальних трас полігону. Показано, що рішення задачі метрологічної

атестації ЕІВСП зводиться до лінеаризації нелінійної функції випадкових аргументів (моделі траєкторії руху повітряних об'єктів) і розрахунку дисперсій залежних змінних (параметрів координат руху) від відомих дисперсій незалежних змінних. Наводяться результати вирішення завдань оптимального розміщення ЛОЕСТВ на території полігону та метрологічної атестації ЕІВСП. Проведені дослідження актуальні не тільки для полігонних випробувань літальних апаратів, а й представляють науковий і практичний інтерес, при побудові систем моніторингу повітряного простору в видимому і інфрачервоному діапазонах спектру і дослідження траєкторій руху об'єктів штучного і природного походження в атмосфері Землі.

Key words: trajectory measurements, information-measuring system, laser optoelectronic stations, optimal placement, mathematical model of coverage.

1. Introduction

Increasing the efficiency of use of modern weapons leads to the need to expand the dynamic and functional characteristics of aircraft (aircraft), cruise and anti-aircraft guided missiles, models of artillery equipment. Under these conditions, the problem of the study of the dynamic characteristics of LA, testing and evaluation of their extreme (maximum permissible) characteristics becomes extremely relevant (Dodonov & Putiatin, 2017).

The mobile laser optical-electronic stations of the trajectory of measurement (LOETMS) developed at KHNURE (Semenets et al., 2018) can be used for various flight experiments, certification of aircraft and rocket-artillery systems, providing trajectory information and video information to control the characteristics of various aircraft with coordinate measurement, observation and recording of video information and subsequent detailed analysis of the dynamic and functional characteristics of the investigated aircraft.

Each LOETMS in its area of responsibility is programmed to track a target in a predicted path segment. The programming process is automated and runs simultaneously for all LOESTI. To synchronize and adjust the delivery of goals for each LOETMS, the technology of wireless sensor information and communication network is used in the process of aircraft maintenance. Each LOETMS in the process of tracking an aircraft transmits its current coordinates via a communication channel to LOETMS, which is in the waiting queue. Based on these data, the coordinates of the expected capture point and the flight path of the aircraft are adjusted relative to the predicted.

The article presents a mathematical formulation and a method for solving the problem of optimal placement of LOETMS along the most probable flight paths of an

aircraft over the territory of the the test site. Before conducting flight tests, this problem must be solved, and the relative position of LOETMS on the territory of the test site is known. To determine the coordinates of each LOETMS, we use dual-frequency GPS receivers mounted on the vertical axis of the LOETMS supporting and turning arrangement. The results of measuring the coordinates of each LOETMS and their errors are entered into the LOETMS database and are periodically updated in accordance with the regulations. Thus, UPIMS is a set of spatially distributed, interconnected wireless sensor information and communication networks LOETMS and other auxiliary technical means for receiving video and measuring information, its transformation, processing in order to present data on the trajectory parameters of the observed aircraft in the required form.

Significant spatial distribution of LOETMS on the test site, the need to take into account the errors of binding coordinates of each LOETMS to the topbase using the global navigation satellite positioning system (GPS), the errors of leveling the LOETMS platforms, alignment errors (linking each local spherical coordinate system of LOESTI to the global geocentric coordinate system), individual metrological characteristics of each LOETMS, identifying and eliminating systematic errors and suppressing random errors of general measurements by several LOETMS, led to the fact that the problem of metrological certification UPIMS aircraft is extremely complex and relevant.

2. The structure and purpose of the complex

Supporting and turning arrangement on which are installed:

- visible range camera;
- thermal camera with teleobjective lens;
- laser ranging equipment;
- GPS receiver for geodetic reference;
- Horizon laser level for positioning supporting and turning arrangement;

Fig. 1 and Fig. 2 show views of the turning arrangement (Semenets et al., 2018).

The purpose of the system. Designed to solve a wide range of tasks of monitoring airspace in the optical and infrared ranges:

- detect all moving objects;
- automatic recognition of the type of aircraft;
- selection (automatic / manual) of a specific object;

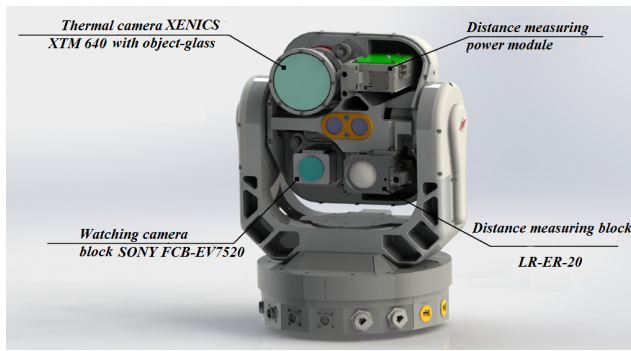


Figure 1: Front view of the turning arrangement

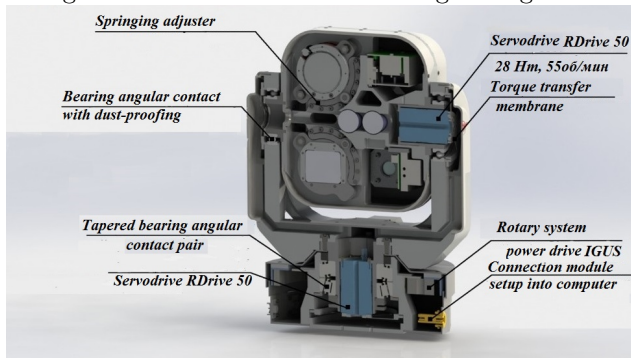


Figure 2: Back view of the turning arrangement

- its precision tracking;
- automatic calculation of coordinate parameters (coordinates, velocity projections) of each moving object in the local (spherical) and global (Greenwich) coordinate systems.

3. Task and goals of work

The problem can be formulated as follows: it is necessary to completely cover a certain rectangular area, called the coverage area, with some objects, called nodes of the wireless sensor network, so that the observed point of the object is detected by three nodes at the same time, while technological restrictions are observed.

One of the technological limitations may be restrictions on the minimum and maximum allowable distances between the centers of the nodes of the wireless sensor network and the border of the coverage area, as well as between the centers of the "neighboring" nodes of the wireless sensor network (Antoshkin et al., 2001).

The aim of the work is to develop a mathematical model and optimize the placement of nodes of the wireless sensor network in the rectangular region of a unified polygon information-measuring system.

The object of study is the process of mathematical modeling and optimization of the placement of

nodes of a wireless sensor network in a unified polygon information-measuring system.

The subject of the study is optimization methods for covering a rectangular area with LOETMS control zones.

4. Domain description

There is a need to create control and management systems in which the objective function is defined not only as a direct assessment of the characteristics and conditions of the object, but also with the help of some additional (for example, signal) information. A physical model linking the characteristics of the object and additional information should be constructed in such a way that it is possible to track and diagnose the parameters of the object.

In this case, each controlled point in the region should be in the coverage area of at least one receiver (sensor). The area that the sensor controls is shown as a circle. Then, the qualities of an adequate model of control and monitoring systems can be considered the circular coverage (circles) of the region R^2 with additional restrictions arising from the physical characteristics of the equipment used (Antoshkin & Pankratov, 2016).

5. Solving the problem of regular coverage of a rectangular area

In (Fejes Toth, 1972), the coverage criterion is defined as follows: for the Ω set, which should be a circular cover for the Υ set, it is necessary and sufficient that any intersection point of the circles belong to at least three circles, and each intersection point of the circle and the boundary of the region belong to at least two circles, as shown in Fig. 3.

As part of this task, we assume that the area of a unified polygon information-measuring system is a rectangle.

It is known (Fejes Toth, 1972) that the optimal coverage of a plane with circles is achieved using the so-called regular or lattice coverage. Therefore, we use regular coverage to cover the rectangle with circles.

The set-theoretic model of the problem of covering a rectangle P with the number n of circles is as follows:

$$P \subset \bigcup_{i=1}^n C_i \tag{1}$$

That is, each point of the region T_0 belongs to at least one of the circles C_1, C_2, \dots, C_n . The mathematical model of the task in the absence of additional restrictions can be represented as:

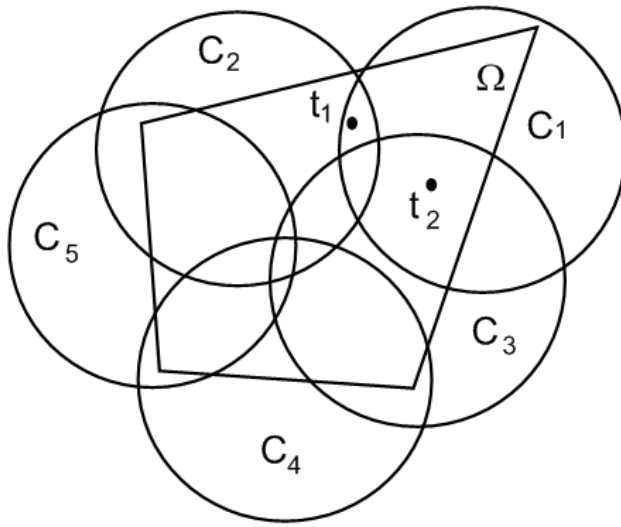


Figure 3: Coverage criteria

$$\max_{t \in T_0} \min_{i \in I_m} \rho(t_i, t) \leq R, \tag{2}$$

where $\rho(t_i, t)$ - distance between points; t_i and $t = (t_x, t_y) \in \Omega$; $t = (x_i, y_i)$ - center of i -th circle; $I_m = \{1, 2, \dots, m\}$, R -radius of circles.

The set of vectors:

$$r = na_1 + ma_2, n, m \in Z, \tag{3}$$

where $a_1 = (a_{1x}, a_{1y}), a_2 = (a_{2x}, a_{2y})$ - linearly independent, is called a lattice with basis a_1, a_2 and is denoted $L = \text{Lambda}(a_1, a_2)$; Z - the set of integers, Lambda - the operator that maps the set of pairs of vectors to the set of families of the form (3).

Covering $\{\tau_y\}, i, j \in Z$ with planes in circles $\tau_u = \tau(ia_1 + ja_2) = \tau(0, 0) + ia_1 + ja_2, i, j \in Z$ is called a single (lattice-frequent) covering of the circle $\tau(0, 0)$ which is performed along the basis (a_1, a_2) of the lattice $L = (a_1, a_2)$ where $\tau(0, 0)$ circle τ centered at $(0, 0)$.

The solution method is to generate (with a given step) a set of basis vectors that guarantee the existence of a accomplished covering by the constructed bases, and choose the best of the constructed lattice coverings.

Now we turn to the problem of the correct sectional-regular coating of the rectangle using circles. The solution to this problem is reduced to the solution of two problems of covering a rectangle with vertically and horizontally located sections of a rectangular shape. Since the tasks in the statement coincide, in what follows we restrict ourselves to considering the first of them.

The objective function of this problem has the same properties as the objective function of the problem of regular covering of a rectangle, with the exception of periodicity. In addition, the dependence of the result

on the parameters is complex and difficult to formalize. This leads to the need to use approximate methods for solving the problem. For example, the application of the method of applying a grid to the region of possible solutions allows us to solve the problem of sectional-regular coating in two stages (Pankratov et al., 2002):

- solving a number of problems of uniform regular cutting of sections $A \times h_k$ by the method described above;
- item selects the optimal combination of sections.

First, it is worth solving a number of inverse problems of regular coverage. Namely, for a given number of detection zones, it is necessary to determine the maximum possible section size, it is covered by a given number of detection zones. It should be noted that when solving the problem of regularly covering the entire rectangle with this method, all these solutions can be obtained as intermediate results.

We now turn to solving the problem of choosing the optimal set of sections. In its statement, this problem is similar to the well-known one-dimensional knapsack problem (Korbut & Filkenshtein, 1969) if we interpret the number of circles k located in the section as the weight of the element, and the value h_k as the length of the element. However, the function of the goal in this case is unconventional, namely: it is necessary to find a set of elements of minimum weight, providing overflows or at least full filling of the knapsack.

An interesting feature of the proposed method for constructing section-regular coatings is that it can be naturally generalized to the case of dividing a rectangular region into sections that are regularly covered with circles of different radii.

In Fig. 4 and 5 show the results of separation of sections of regular and regular coverage of section A using circles of radius 5700, respectively. Although both coatings are formed by 31 circles, regular sectional coating is preferable as it is more technologically advanced.

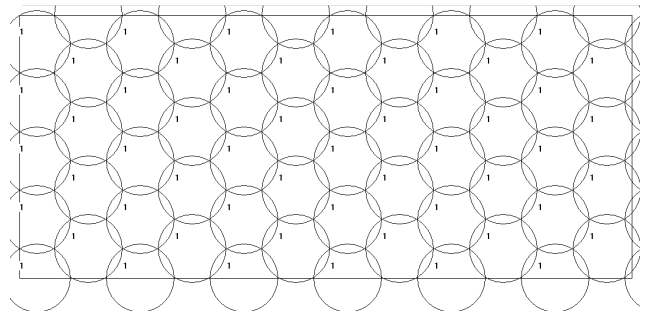


Figure 4: Regular coverage

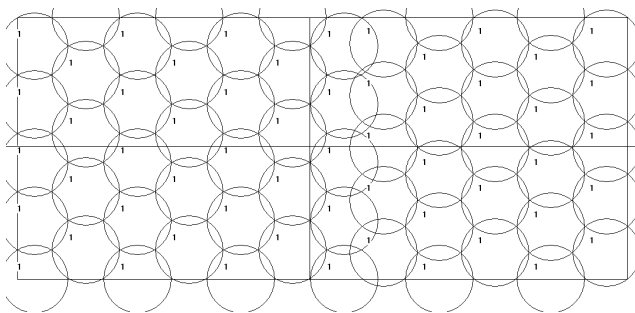


Figure 5: Sectional-regular coverage

In accordance with theoretical considerations, as the number of circles increases, a method of sectional-regular coverage gives less and less advantage than a method of regular coverage. For the entire plane, the use of sectional-regular coverage will lose its meaning. However, for the vast majority of practical tasks, the use of sectional-regular coverage gives a significant effect. The coverage criterion is considered equal to the total area of the covering circles.

Conclusions

Since the study solves the problem of the optimal placement of LOETMS along the most probable flight paths of an aircraft over the training ground, an important class of problems is created for creating circular coatings covering a rectangular area.

A mathematical model and optimization of the location of the nodes of the wireless sensor network in the rectangular region of a unified polygon information-measuring system is proposed.

Using methods of regular and sectional-regular coverage, the stated problem of the need for a certain rectangular area, called the coverage area, can be completely covered by some objects, which are called nodes of the wireless sensor network, so that the observed point of the object is detected simultaneously by three nodes, each time subject to technological limitations.

Coverage criteria highlighted: in order for one multitude to be a circular cover of another multitude, it is necessary and sufficient that any intersection point of the circles belong to at least three circles, and each intersection point of the circle and the boundary of the region belong to at least two circles.

Thus, using these methods and meeting the criteria, the task is completed - the observed point of the object is detected simultaneously by three points.

For the vast majority of practical applications, the method of sectional-regular coatings has an advantage over the method of regular coatings.

References

- Antoshkyn A.A., Pankratov A.V., Patsuk V.N., Romanova T.E., Shekhovtsov S.B.: 2001, *Radioelektronika i informatika*, Khar'kov: KHNURE, **N 3**, 31 (in Russian).
- Antoshkin O., Pankratov O.: 2016, *Eastern-European Journal of Enterprise Technologies*, **6**, N 4(84), 45. DOI: 10.15587/1729-4061.2016.86171.
- Dodonov A.G., Putiatin V.G.: 2017, *Matematychni mashyny i systemy*, **4**, 30 (in Ukrainian).
- Fejes Toth L.: 1972, *Acta Math. Acad. Sci. Hungar.*, **24**, 417.
- Korbut A.A., Finkel'shteyn Yu.Yu. Diskretnoye programmirovaniye. M.: Nauka, 1969. 368 s. (in Russian).
- Pankratov A.V., Patsuk V.N., Romanova T.Ye., Antoshkin A.A.: 2002, *Radioelektronika i informatika*, **1(18)**, 50.
- Semenets' V.V., Tevyashev A.D., Shostko I.S., Neofitnyy M.V., Kolyadin A.V.: 2018, *Tezy dopovidy VI Mizhnarodnoyi naukovo-praktychnoyi konferentsiyi "Problemy koordynatsiyi voyenno-tekhnichnoyi ta oboronno-promyslovoyi polityky v Ukrayini. Perspektyvy rozvytku ozbroynennya ta viys'kovoyi tekhniky" (Kyiv, 11-12 zhovtnya 2018)*, p. 234 (in Ukrainian).

DOI:<http://dx.doi.org/10.18524/1810-4215.2019.32.181911>

MATERIAL OF COMETARY NUCLEI AND ASTEROIDS CAN BE STUDIED IN THE EARTH'S ORBIT

A. P. Vidmachenko, A. F. Steklov

Main astronomical observatory of the NAS of Ukraine
Kyiv, Ukraine, vida@mao.kiev.ua, stec36@i.ua

ABSTRACT. The Solar system is formed from a primary gas-dust cloud. Asteroids and cometary nuclei are made of the same substance. Therefore, the study of their debris will help determine their properties. It is best to investigate the substance of meteoroids in the laboratory. The presence of radioactive chemical elements in meteorites provides important information about their age. The study of the isotopic composition and content of uranium and thorium gives an age of a meteorite substance of ≈ 4.6 billion years. Measurement of cosmogenic isotopes in meteorites and analysis of their content allows us to determine the size, mass and age of meteoritic bodies before falling to Earth. By measuring the content of tritium and helium in a meteorite, the average intensity of the cosmic rays bombarding the sample is estimated. Every day, 100-1000 tons of meteorite material falls on the Earth's surface. A large mass falls to the surface under the action of meteor showers. Meteor showers are formed from the remnants of the nuclei of known comets and asteroid bodies. To study the substance of the nucleus of comet Churyumov-Gerasimenko, a spacecraft was sent to it worth about 1 billion euros. We offer, that to study the material of some nuclei of comets and asteroids, it is possible to take meteoroid samples directly in outer space in the Earth's orbit. There, meteoroid particles must be captured, preserved and delivered to Earth for a thorough study. To capture matter from a specific parent cometary nucleus or asteroid in outer space, traps made of silicon dioxide, which are filled with airgel, can be used. The material of the traps allows you to capture particles flying at high speed without overheating them. This allows you to save organic and other molecules in such particles. Such traps should be activated at the moments of maximums of the selected meteor showers.

Keywords: meteor, meteor shower, gas-dust cloud, isotope composition, capture of matter.

АНОТАЦІЯ. Сонячна система сформована з первинної газопилової хмари. З такої ж речовини складаються астероїди і кометні ядра. Тому вивчення їх уламків допоможе визначити їх внутрішні властивості. Найкраще речовину метеороїдів досліджувати в лабораторних умовах. Наявність радіоактивних хімічних елементів в метеоритній речовині дає важливу інформацію про їх вік. Вивчення ізотопного складу і вмісту урану і торію дає вік метеоритної речовини $\approx 4,6$ млрд. років. Вимірювання космогенних ізотопів в метеоритах та аналіз їх вмісту дозволяє визначити розміри, масу та вік метеоритних тіл до падіння на Землю. За зміною вмісту тритію та гелію в метеориті оцінюють середню інтенсивність бомбардуючих зразок кос-

мічних променів. Щодня на поверхню Землі падає 100-1000 тонн метеоритної речовини. Більша маса потрапляє на поверхню у час дії метеорних потоків. Метеорні потоки утворюються із залишків ядер відомих комет і астероїдних тіл. Для дослідження речовини ядра комети Чурюмова-Герасименко, до неї був направлений космічний апарат вартістю близько 1 млрд. євро. Ми пропонуємо, що для вивчення матеріалу деяких ядер комет та астероїдів, можна відбирати зразки метеороїдів прямо в космічному просторі на орбіті Землі. Там метеороїдні частинки необхідно піймати, законсервувати і доставити на Землю для ретельного дослідження. Для захоплення речовини з конкретного батьківського кометного ядра або астероїда, в космічному просторі можна використовувати виготовлені з діоксиду кремнію пастки, які заповнені аерогелем. Матеріал пасток дозволяє захопити частинки, що летять з великою швидкістю, не перегріваючи їх. Це дозволяє зберігати в таких частинках органічні та інші молекули. Подібні пастки повинні бути задіяні в моменти близькі до максимумів обраних метеорних потоків.

Ключові слова: метеороїд, метеорні потоки, газопилова хмара, ізотопний склад, захоплення речовини

The Solar system was formed from a primary gas-dust cloud. Asteroids and cometary nuclei consist of the same primary substance. In this regard, we can assume that the secret of the origin of our system can remain inside asteroids and cometary nuclei.

Therefore, the study of their fragments will help answer many of the questions posed. The invasion of these meteoroids into the Earth's atmosphere leads to their interaction with air molecules.

The degree of this interaction and its consequences depend on the value of the extra-atmospheric speed of the meteoroid. Its boundary value is determined by the magnitude of the second cosmic velocity for our planet and for the solar system. The speed of the Earth in its orbit around the Sun is ≈ 30 km/s. And the maximum possible speed of meteoroids in the Earth's orbit is ≈ 42 km/s. Therefore, the speed of the oncoming meteoroid relative to the Earth will be equal to ≈ 72 km/s; and meteoroids that catch up with the Earth – a little more than 11 km/s. Under such conditions, the rate of meteoroid invasion of the atmosphere is in the range of 11.2-72 km/s. At such high speeds, the energy of a meteoroid with a mass of ≈ 7 g and a speed of 72 km/s exceeds 20 MJ.

With such energy values, a body entering the Earth's atmosphere transfers a huge impulse to air molecules. Each collision heats a portion of the front of its surface and slows down its movement. With a deeper penetration

of the body into the atmosphere, air density increases; the number of its interactions with atmospheric molecules is also growing. This leads to mechanical fragmentation of the meteorite into parts. Moreover, more fragile bodies begin to fragment at a high height, and more durable ones at a much lower level.

It is best to determine the structure, mass, density and chemical composition of a meteoroid in a laboratory study of its substance. But for now, we can only remotely observe meteors, or obtain information when registering the interaction of meteoroid dust particles with special sensors installed on spacecraft.

The presence of radioactive chemical elements in meteorites provides important information about their age. It is determined using the decay laws of natural radioactive isotopes. For example, some isotopes of uranium and thorium, having half-lives from 700 million to 14 billion years, decay, forming lead isotopes. Therefore, the study of the modern isotopic composition of lead and the relative contents of uranium and thorium gives the age of a meteorite substance equal to 4.6 billion years. Cosmogenic isotopes also play an important role in determining the time intervals from the moment of fall, i.e., the age of terrestrial meteorites.

Measurements of some cosmogenic isotopes have also shown that meteorites are tens and hundreds of thousands of years old. An analysis of their content allows us to determine the initial size and mass of meteorite bodies before falling to Earth.

So, under the influence of cosmic rays in meteorites, a radioactive helium isotope is formed - tritium. Therefore, according to changes of the tritium and helium content in the meteorite with depth, the average intensity of the cosmic rays, which bombarded the sample, is estimated. And the initial "pre-atmospheric" form, volume and mass of the meteorite body are also may estimated by the content of the helium isotope. In terms of chemical composition, meteorites practically do not differ from terrestrial rocks. But in meteorites, which have been found on Earth surface, rare or generally unknown minerals. Sometimes tiny grains of diamond come across, apparently, arising as a result of some kind of impact.

Until now, it was possible to study the composition of those cometary nuclei and asteroids whose meteorite materials fell to the Earth's surface (Churyumov et al. 2016). Every day, 100-1000 tons of meteorites falls here (Churyumov et al. 2014; 2015; Vid'Machenko 1995; Vidmachenko 2009; Vidmachenko et al. 1979; Vidmachenko & Morozhenko 2014; Vidmachenko & Steklov 2013).

And most of their mass appeared on the surface during the action of meteor showers. They arise when the Earth, during its orbital motion, passes through long clusters of meteoric matter in orbit around the Sun. This is repeated annually, and their active action lasts from several days to months (Dashkiev et al., 2018).

Most of these flows are formed from the remnants of the nuclei of known comets, and for several – from asteroid bodies (Dashkiev et al. 2017, Vidmachenko & Vidmachenko 2007). For example, the parent body of meteor shower Quadrantides – is asteroid 2003 EH; Virginides – 2003 BD44, 2002 FC and 1998 SJ70; Geminides – 3200 Phaeton; Arietides – 1566 Icarus. For the meteor shower Lirides is considered as source Comet C / 1861, for eta-Aquarids and Orionides – are Halley's comet; alpha-Capricornids – 169P / NEAT, Delta-Aquarids – 96 / Machgolts, Perseides – Swift-Tuttle 1862III, Draconides – 1900III Jacobini-Zinner, Taurids – Enke, Leonids – Tempel-Tuttle, Ursids – 8P / Tuttle.

Therefore, samples of the nuclei of the above comets and some asteroids can be taken in near space.

Recall that to study the substance of the nucleus of comet Churyumov-Gerasimenko, an apparatus was sent to it, worth about 1 billion euros. NASA after 2021 is planned to catch a small asteroid using an unmanned probe; then it will be delivered to the orbit of the Moon, and, after the selection of the necessary samples, they will be sent to Earth for a detailed study. But we offer that in order to study the material of some cometary nuclei or asteroids, it is not necessary to "catch" an entire object at great distances. To do this, we can take meteoroid samples of some selected comets or asteroids from the above list, right in outer space in Earth's orbit. It is here that meteoroid particles can be captured, mothballed and delivered to Earth for research using high-quality equipment (Vidmachenko & Steklov 2018).

Devices for capturing matter in outer space can be traps filled with an airgel made of silicon dioxide. These were used in the study of the substance of the comet 81P / Wild by the probe "Stardust" (Rietmeijer, 2016). The material of the traps allows you to capture particles flying at high speed without overheating them.

This allows you to save both organic and other molecules in such particles (Gorlenko et al., 2000; Kozyrovska&Vidmachenko, 2018; Vidmachenko&Steklov, 2017). We propose equipping orbital cometic systems with such cells, which should be used at the moments of the maximums of the selected meteor showers. Micrometeorites captured by such cells in space and delivered to Earth will not be affected by high temperature. Therefore, they can be delivered here for thorough research. Ensuring the sterility of the meteoroid substance will provide valuable information that may relate to possible extraterrestrial life during astrobiological studies.

And wherein, to study samples of the nuclei of comets and asteroids, it is not necessary to send special probes for millions of kilometers. To implement such a program, it is necessary to capture matter from the parent cometary nucleus or asteroid during the action of a particular meteor shower.

References

- Churyumov K.I., Steklov A.F., Vidmachenko A.P. et al: 2015, *ASR*, **11**(2), 99.
- Churyumov K.I., Steklov A.F., Vidmachenko A.P. et al.: 2016, *Meteoroids 2016*, ESTEC, Noordwijk, 63.
- Churyumov K.I., Steklov A.F., Vidmachenko A.P. et al.: 2014, Some results of regular observations of the twilight bolides (FOP "Kostiyk N.P." Vinnytsia.) 98.
- Dashkiev G.N., Steklov A.F., Vidmachenko A.P.: 2017, *48LPSC*, Texas LPI Co. 1964, id.1135.
- Dashkiev G.N., Vidmachenko A.P., Steklov A.F. et al.: 2018, *49LPSC*, Texas LPI Co. 2083, id.1107.
- Gorlenko V.M., Zhmur S.I., Duda V.I. et al.: 2000, *OLEB*, **30**, 6, 567.
- Kozyrovska N.O., Vidmachenko A.P.: 2018, *20 ISC AS YS*, Uman, 86.
- Rietmeijer F.J.M.: 2016, *Meteoritics & PS*, **51**(3), 574.
- Vid'Machenko A.P.: 1995, *KPCB*, **1**(4), 14.
- Vidmachenko A.P.: 2009, *ASR*, **6**(1), 56.
- Vidmachenko A.P., Klimenko V.M., Morozhenko A.V.: 1979, *AAfiz.*, **39**, 84.
- Vidmachenko A.P., Morozhenko O.V.: 2014, The phys. Char. of surface Earth-like planets. (MAO, NULESU, Kyiv), 388.
- Vidmachenko A.P., Steklov A.F.: 2013, *ASR*, **9**(2), 146.
- Vidmachenko A.P., Steklov A.F.: 2017, *19 ISC AS YS*, Ukraine, 21.
- Vidmachenko A.P. Steklov A.F.: 2018, *ASR*, **14**(1), 15.
- Vidmachenko A.P., Vidmachenko H.A.: 2007, *AstAlm*, **53**, 195.

ASTROINFORMATICS

DOI:<http://dx.doi.org/10.18524/1810-4215.2019.32.181557>NEW ASTROMETRIC REDUCTION OF THE SUPERCOSMOS
PLATE ARCHIVE: FIRST RESULTSV.S. Akhmetov¹, V.M. Andruk², Yu.I. Protsyuk³, H. Relke⁴, I. Eglitis⁵¹ Institute of Astronomy, V. N. Karazin Kharkiv National University, Kharkiv, Ukraine, akhmetovvs@gmail.com² Main Astronomical Observatory of the National Academy of Sciences of Ukraine, Kyiv, Ukraine, andruk@mao.kiev.ua³ Research Institute Mykolaiv Astronomical Observatory, 1 Observatorna Str., 54000 Mykolaiv, Ukraine, yuri@nao.nikolaev.ua⁴ Walter Hohmann Observatory, Essen, Germany, helena_relke@yahoo.com⁵ Institute of Astronomy, University of Latvia, Riga, Latvia, ilgmars.eglitis@lu.lv

ABSTRACT. The arrivals of the new more accuracy reference catalogs and development of new methods and approaches for reduction astrometric data give the new life for photographic plates archives. Gaia DR2 is not only a giant step in the astrometric accuracy allowing to measure new objects it also provides plates archives observed in the past with modern accuracy. In this work we present the first results of astrometric reduction in the system of Gaia DR2 for some photographic plates that were obtained by UK Schmidt telescope (UKST) and digitized by the SuperCOSMOS scanning machine. To date the UKST has taken over 17,000 plates, the plates are stored in the Plate Library at the Royal Observatory, Edinburgh. The photographic plates are digitized to 15 bits (32768 grey levels) with a resolution of 10 microns (0.67 arcsec/pixel). Each digitized Schmidt plate has size 32256x32256 pixels and produces about 2 Gbyte pixel data. We are making new reduction of photographic plates that allowing to provide valuable data for future researches in astrometry as well as in astrophysics. The results of our research showed some problems for further successful implement of works started to process the digitized scans with such large size in the frame of the SuperCOSMOS program. However, the internal estimation of the accuracy position of objects are better the same results of the SuperCOSMOC reduction and will be improved after the solving these problems.

Keywords: stellar catalogs, digitized plate processing, photometry, UBV system.

АНОТАЦІЯ. Поява нових високоточних опорних каталогів, а також розробка нових методів та підходів для астрометричної редукції даних дають нове життя архіву фотографічних платівок. Gaia DR2 – це не лише гігантський крок у астрометричній точності, що дозволяє вимірювати нові об'єкти, а також дозволяє отримати та порівнювати архівні спостереження в минулому із су-

часною точністю. У цій роботі ми представляємо перші результати астрометричної редукції деяких фотографічних платівок в систему опорного каталогу Gaia DR2, які були отримані Шмідт телескопом Англо-Австралійській обсерваторії та були оцифровані за програмою сканування SuperCOSMOS. Фотографічні платівки оцифровані 15 біт (32768 рівнів сірого кольору) з роздільною здатністю 10 мкм на піксель, створюючи близько 2 Гбіт піксельних даних. На сьогоднішній день існує понад 17 000 платівок отриманих такими Шмідт телескопами, які зберігаються в бібліотеці фотографічних платівок у Королівській обсерваторії, місто Единбург. Ми робимо нову обробку фотографічних платівок, що дозволить отримати цінні дані для майбутніх досліджень як у галузі астрометрії, так і астрофізики. Результати наших досліджень виявили деякі складності для подальшого виконання роботи по обробці таких великих за розміром платівок програми SuperCOSMOS. Але, внутрішня оцінка точності положень об'єктів краща ніж аналогічні результати отримані SuperCOSMOS та будуть покращені після вирішення представлених проблем.

Ключові слова: зоряні каталоги, обробка оцифрованих зображень, фотометрія, система UBV.

1. Introduction

This work has been done to explore the possibility of extending the FON project into "deep" - from $B = 17^m$ to $B = 22^m$ (Pakuliak, 2016; Andruk, 2017a). In the FON project digitized scans of photographic plates with the size of 13000x13000 pixels were processed to create a catalog of positions and B-magnitude stars of the Northern Sky (Andruk, 2017b). In this paper, we examined the possibility of using our software tools (Hambly N.C. et al., 2001a) to digitized photographic plates from the Schmidt telescope at

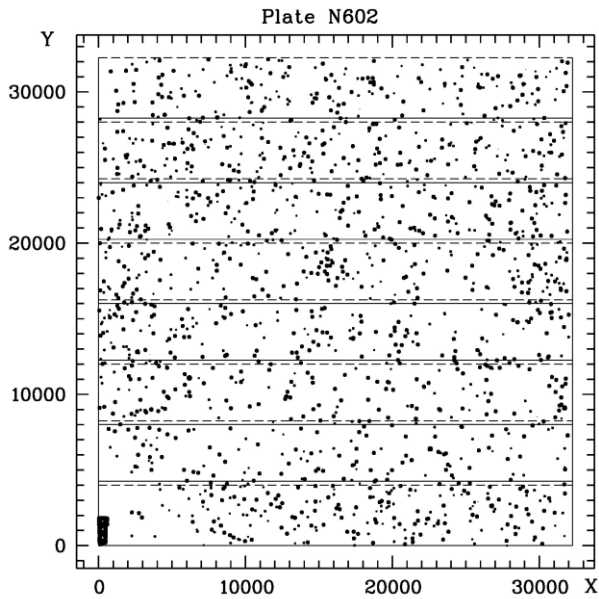


Figure 1: The 8-parts splitting scheme for the plate number 602. Only images of bright stars after the processing of the scan in the MIDAS/ROMAFOT environment are mapped.

the Anglo-Australian Observatory. This is a classic Schmidt with the following parameters: the diameter of the mirror is 1.83 m; focal distance – 3.07 m; a square photographic plate with the size of 356x356 mm covers 6.4x6.4 degrees of sky; scale – 67.12 arcsec/mm; spatial resolution – 670 mas/pixel. To date, there are more than 17,000 photographic plates obtained by this Schmidt telescope which are stored in the Plate Library at the Royal Observatory, Edinburgh. Several plates from this Plate Library were digitized by the SuperCOSMOS scanning machine. The astronegatives were digitized to 15 bits (32768 gray levels) with a spatial resolution of 10 microns per pixel. They have dimensions of 32256x32256 pixels and a volume of 2 Gbytes of pixel data (Hambly N.C. et al., 2001b). For the extracting of the star images we used the MIDAS software environment. But it has a size limit: the size of scan to be processed is no more than 20,000 x 20,000 pixels. The authors found an opportunity to use the Midas software environment by splitting each scan into 8 overlapped parts (bands) by the coordinates of Y. The width of the overlapped zones is 256 pixels. As our small experience of the data processing shown, instrumental photometric values in the overlapping bands are needed for photometric alignment of all eight bands. The splitting scheme of the scan for the plate No.602 is shown on the figure 1.

2. The first results of the processing of plates with the size of 32256x32256 pixels

Processing of digitized scans in the MIDAS/ROMAFOT environment allows to obtain data for all registered objects: rectangular coordinates X,Y; photometric values m and FWHM. The reduction of the rectangular coordinates of X,Y into the system of equatorial coordinates was carried out in the system of Tycho-2 catalog (Hog E. et al., 2000) for stars in the range of $B = 9^m - 14^m$ (Andruk, 2015; Andruk, 2016). Brighter stars were not used because of the generation of se-

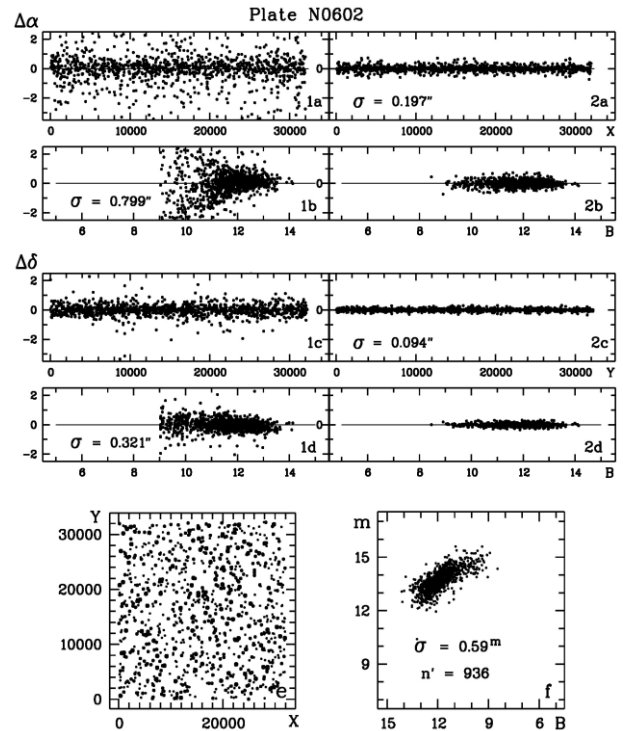


Figure 2: The distribution of errors definition of equatorial coordinates σ (represented as differences of $\Delta\alpha$, $\Delta\delta$) in the system of Tycho-2 catalog for the plate 602 at the initial (left panel 1a, 1b, 1c, 1d) and the final (right panel 2a, 2b, 2c, 2d) stages of reduction. Panel e is a map of the sky of bright stars. Panel f shows the plot of instrumental photometric values m again stellar B-values of the Tycho-2 catalog for 936 stars.

veral doubles objects instead of real one. The figure 2 shows the distribution of errors definition of equatorial coordinates σ (represented as differences of $\Delta\alpha$, $\Delta\delta$) in the system of Tycho-2 catalog for the plate 602 at the initial (left panel 1a, 1b, 1c, 1d) and the final (right panel 2a, 2b, 2c, 2d) stages of reduction relatively rectangle coordinates X,Y and stellar B-values. On the bottom of the left panel (e) is a map of the sky of bright stars, on panel (f) – the plot of instrumental photometric values m against stellar B-values of the Tycho-2 catalog for 936 stars.

At this stage of the study the authors could not implement the photometric reduction of the instrumental values m into the B-magnitude of Johnson's system by using a characteristic curve. Due to the generation of an arbitrary number of false objects instead of real one for bright stars it was not possible to build the part of the real characteristic curve for stars brighter than $B < 10^m$ in order to somehow adequately calibrate characteristic curve across the entire range of stellar values of registered objects in the system of photoelectric measurements of stars or at least in the B-system of Tycho-2 catalog (Relke, 2015). Therefore the authors made a photometric assessment to determine the b_{lim} values of the extremely weak registered objects for several processed plates with one exposure in the B-magnitude system of the Gaia DR2 (Gaia Collaboration, 2018). Results of the photometry of the scan number 602 in the B-system of the Gaia DR2 are presented on the Figure 3. On the a-panel is the plot of instrumental photometric measures m

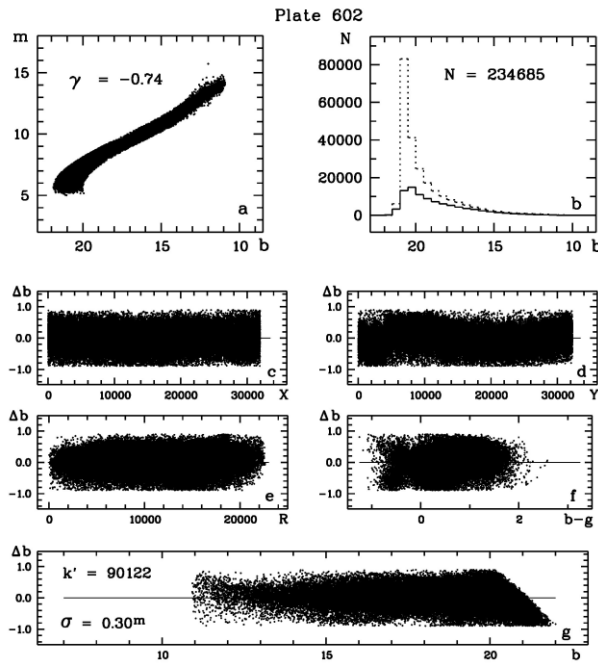


Figure 3: The results of the photometry of the scan number 602 in the B-system b of the Gaia DR2 catalog. On the a-panel is the plot of instrumental photometric measures m against the B-magnitudes of the Gaia DR2 catalog ($\gamma = -0.74$ is the contrast coefficient of photo emulsion). On the b-panel – distribution of all 234685 recorded objects (points) and 90122 identified stars from the Gaia DR2 catalog (continuous line) by star intervals. On the c, d, t, f and g panels – the differences between the calculated b' and the catalogue b values $\Delta b = b' - b$ ($\sigma = 0.30^m$) relative to the rectangular coordinates X , Y , the distance from the center of the plate R , the $b-g$ color and B-magnitudes of the Gaia DR2 catalog respectively.

Table 1. Results of the processing of scans for seven plates

Np/RA/DEC	Epoch	$\sigma_{RA}/\sigma_{DE}/\sigma_B$	Nobj/blim
190 22 ^h 34 ^m 54 ^s -54°47'20"	16.09.79	0.22" 0.09" 0.28 ^m	267 000 21.3 ^m
289 22 ^h 25 ^m 40 ^s -44°51'51"	17.06.75	0.13" 0.07" 0.28 ^m	303 000 21.6 ^m
345 22 ^h 33 ^m 29 ^s -39°51'16"	16.09.77	0.17" 0.08" 0.29 ^m	296 000 21.5 ^m
405 22 ^h 25 ^m 53 ^s -34°49'25"	11.08.80	0.82" 0.18" 0.26 ^m	264 000 21.4 ^m
468 22 ^h 38 ^m 50 ^s -29°50'49"	02.10.80	0.66" 0.17" 0.22 ^m	204 000 20.1 ^m
533 22 ^h 23 ^m 50 ^s -24°48'07"	25.06.80	0.25" 0.11" 0.30 ^m	232 000 21.1 ^m
602 22 ^h 27 ^m 00 ^s -19°47'00"	26.09.87	0.20" 0.09" 0.30 ^m	235 000 21.2 ^m

against the stellar B-values of the Gaia DR2 catalog ($\gamma = -0.74$ is the contrast coefficient of photo emulsion). On the b-panel – distribution of all 234685 recorded objects (points) and 90122 identified stars from the Gaia DR2 catalog (continuous line) by star intervals. On the c, d, t, f and g panels – the differences between the calculated b' and the catalogue b values $\Delta b = b' - b$ ($\sigma = 0.30^m$) relative to the rectangular coordinates X , Y , the distance from the center of the plate R , the $b-g$ color and stellar B values the of the Gaia DR2 catalog respectively.

The results summary of the processing of scans for seven selected astronegatives obtained by the Schmidt Telescope of the Anglo-Australian Observatory is presented in the table 1. The first column shows the number of plate N_p and centers coordinates RA, DEC; the second one – observation epoch'. The reduction errors for the coordinates RA, DEC in the system of Tycho-2 catalog σ_{RA} , σ_{DE} and the error of B-magnitudes in the B-system of Gaia DR2 catalog σ_B are entered in the third column. The fourth column shows the total number of registered objects N_{obj} and the magnitude value for extremely weak objects in the B-system of the Gaia DR2 catalog b_{lim} .

3. Conclusions

The use of the automatic splitting of scans into several (eight) parts in the MIDAS/ROMAFOT environment allows the processing of the plates with the size of 32256x32256 pixels. However the results of our researches showed some problems that need to be solve for further successfully implement of works started to process of the digitized scans with such size in the frame of the SuperCOSMOS program.

1. In the photometric sense eight zones 4,256 pixels wide with overlapping 256 pixels at the Y coordinate combine not quite correctly (figure 3, d-panel). In the astrometric sense there is no such problem (figure 2, 2c-panel).

2. At the MIDAS/ROMAFOT processing stage, you need to split up the registered objects into two sequences, weaker than $B > 11^m$ (FWHM < 30 pixels) and a brighter $B < 11^m$. Bright objects need additional filtration (smoothing) procedures to prevent the generation of false objects. Dividing objects into two sequences will need about 50% more processing time.

References

- Andruk V.M., Pakuliak L.K., Golovnia V.V. et al.: 2015, *Odessa Astron. Publ.*, **28**, 192.
 Andruk V.M., Golovnia V.V., Ivanov G.A. et al.: 2016, *Kinem. Phys. Cel. Bodies*, **32**, N1, 32.
 Andruk V., Yuldoshev Q., Eglitis I. et al.: 2017, *Odessa Astron. Publ.*, **30**, 159.
 Andruk V.M., Pakuliak L.K., Golovnia V.V. et al.: 2017, *Science and Innovation*, **13**, N1, 17.
 Andruk V., Eglitis I., Protsyuk Yu. et al.: 2019, *Odessa Astron. Publ.*, **32**, in press.
 Gaia Collaboration 2018, *A&A*, **616**, A1.
 Hambly N.C. et al.: 2001a, *MNRAS*, **326**, 1279.
 Hambly N.C., Irwin M.J., MacGillivray H.T.: 2001b, *MNRAS*, **326**, 1295.
 Hog E. et al.: 2000, *A&A*, **355**, L27.
 Pakuliak L.K., Andruk V.M., Golovnia V.V. et al.: 2016, *Odessa Astron. Publ.*, **29**, 132.
 Protsyuk Yu.I., Kovylianska O.E., Protsyuk S.V. et al.: 2014, *Odessa Astron. Publ.*, **27**, 63.
 Relke E., Protsyuk Yu.I., Andruk V.M.: 2015, *Odessa Astron. Publ.*, **28**, 211.

DOI:<http://dx.doi.org/10.18524/1810-4215.2019.32.181596>

PHOTOMETRY OF STARS FOR ASTRONEGATIVES WITH A SINGLE EXPOSURE

V. Andruk¹, I. Eglitis², Yu. Protsyuk³, V. Akhmetov⁴, L. Pakuliak¹,
S. Shatokhina¹, O. Yizhakevych¹

¹ Main Astronomical Observatory of National Academy of Sciences,
27 Akad. Zabolotnogo St., 03143 Kyiv, Ukraine, andruk@mao.kiev.ua

² Institute of Astronomy, University of Latvia,
Boulev. Rainis 19. LV-1586 Riga Latvia, ilgmars.eglitis@lu.lv

³ Research Institute Mykolaiv Astronomical Observatory,
1 Observatorna Str., 54000 Mykolaiv, Ukraine, yuri@nao.nikolaev.ua

⁴ Institute of Astronomy of V. N. Karazin KNU,
4 Svobody Sq., 61022 Ukraine Kharkiv, Ukraine, akhmetovvs@gmail.com

ABSTRACT. The paper discusses the construction of characteristic curves for various astronegatives with a single exposure. Particular attention is paid to the question of extrapolation of the characteristic curve for the region of the weakest stars in the absence of standards. A new method for constructing an individual characteristic curve for digitized films and plates in the UBVR system has been proposed and implemented. The processing of frames of digitized plates and films with sky areas is carried out using LINUX/MIDAS/ROMAFOT software tools. ROMAFOT application allows us to extract astrometric rectangular coordinates X, Y and photometric characteristics such as instrumental photometric magnitudes m , FWHM, and the intensity in the center of the star image I_c for all fixed objects on each astronegative. For all frames, the connection between instrumental photometric values m with stellar magnitudes in any system (Johnson UBVR, Tycho-2 or GAIA catalogs, etc.) is not linear and multipurpose. It is presented as the characteristic curve for each astronegative. In general, the characteristic curve is approximated by a 5-degree polynomial and should take into account the color equation and the photometric field error. In practice, the most and the sometimes unsolvable problem is the lack of photometric standards for the flat part of the characteristic curve (the region of faint and extremely faint stars). As a rule, the photometric standards for characteristic curve restoration from astronegatives, exposed in Johnson U, B, V or R bands (hereafter U, B, V, R), are photoelectric data of stars in the same system. The present work concentrates on the issue of a correct definition of stellar U, B, V, R magnitudes from astronegatives obtained with a single exposition in the case when photometric standards are absent for the flat part of the characteristic curve. Currently, the determination of U, B, V, R magnitudes of stars and other space objects is in progress for astronegatives with the single exposure obtained in the frameworks of selected observational projects.

Keywords: stellar catalogs, digitized plate processing, photometry, UBVR system.

АНОТАЦІЯ. В статті обговорюються питання побудови характеристичних кривих для астронегативів з однією експозицією. Особливу увагу приділено питанню екстраполяції характеристичної кривої на ділянку найслабкіших зір за відсутності фотометричних стандартів. Запропонований новий метод побудови індивідуальної характеристичної кривої для оцифрованих плівок і пластинок, отриманих в UBVR системі. Метод використаний в низці спостережних проєктів. Обробка кадрів для оцифрованих платівок і плівок з зображеннями ділянок зоряного неба робиться в програмному середовищі LINUX/MIDAS/ROMAFOT. Використання пакета програм ROMAFOT дозволяє отримувати астрометричні (прямокутні координати X, Y) та фотометричні характеристики (інструментальні фотометричні величини m , FWHM, інтенсивність в центрі зображення I_c) для всіх зареєстрованих на конкретному астронегативі об'єктів. Для астронегативів (платівки, плівки) зв'язок інструментальних фотометричних величин m з зоряними величинами в якійсь системі (наприклад UBVR Джонсона, каталогів Tycho-2, Gaia DR2 тощо) не є лінійною та універсальною і задається в вигляді характеристичної кривої для конкретного астронегатива. В загальному випадку характеристична крива апроксимується поліномом п'ятої степені і повинна враховувати рівняння кольору та фотометричну похибку поля. На практиці великою і інколи не варішуваною проблемою є відсутність фотометричних стандартів для пологої частини характеристичної кривої (область слабких і гранично слабких зір). Як правило, фотометричними стандартами для побудови характеристичних кривих для астронегативів, експонованих в U, B, V чи R смугах системи Джонсона є фотоелектричні виміри зір в цій же ж системі. Питанню коректного визначення зоряних U, B, V, R величин для астронегативів з однією експозицією за відсутності фотометричних стандартів для пологої частини характеристичної кривої і присвячена дана робота. На даний час виконуються роботи по визначенню U, B, V, R величин зір та інших об'єктів для астронегативів, експонованих з

однією експозицією за вибраними спостережними програмами з різних обсерваторій.

Ключові слова: зоряні каталоги, обробка оцифрованих зображень, фотометрія, система UBVR.

1. Introduction

The processing of frames for digitized plates and films with sky areas in the software package LINUX/MIDAS/ROMAFOT. The application of ROMAFOT allows obtaining the astrometric (rectangular coordinates X , Y) and photometric characteristics (instrumental photometric magnitudes m , FWHM, intensities in the center of the image I_c) for all registered objects on the individual astronegative. As a rule, for faint objects, the limit of their formation and registration is set by the relation $\text{signal}/\text{noise } s > 3$. The related problems and their solutions have been considered in (Andruk, 2010; Andruk, 2017). For astronegatives (plates, films), the relation between instrumental photometric magnitudes m and stellar magnitudes in some photometric system (for example, Johnson UBVR, Tycho-2, Gaia DR2 catalogs, etc) is not linear. It is set as a characteristic curve for every negative.

In general, the characteristic curve is approximated by a 5-degree polynomial and should take into account the color equation and the photometric field error. In practice, the most and the sometimes unsolvable problem is the lack of photometric standards for the flat part of the characteristic curve (the region of faint and extremely faint stars). As a rule, the photometric standards for characteristic curve restoration from astronegatives, exposed in Johnson U, B, V or R bands (hereafter U, B, V, R), are photoelectric data of stars in the same system (Relke, 2015). If the negative was obtained with two exposures – long and short ones (Andruk, 2012), the problem of the whole characteristic curve restoration is simplified and successfully solved in practice as it was done when FON project had been realizing (Akhmetov, 2018; Andruk, 2015; Andruk, 2016a; Andruk, 2016b; Andruk, 2017; Pakuliak, 2016; Yuldoshev, 2016; Yuldoshev, 2017a; Yuldoshev, 2017b) or for other programs as it presented in (Protsyuk, 2017; Yizhakevych, 2015; Yizhakevych, 2017; Shatokhina, 2018).

The present work concentrates on the issue of a correct definition of stellar U, B, V, R magnitudes from astronegatives obtained with a single exposition in the case when photometric standards are absent for the flat part of the characteristic curve.

2. Plotting of the empirical characteristic curve from astronegatives with a single exposure

For creating an empirical characteristic curve, we used two plates №1834 and №1809 from the glass collection of the 1.2-m Schmidt telescope of the Baldone Observatory, Latvia. Plates have the exposures 40 and 60 minutes in U color band (ORWO ZU2 emulsion with UG1 filter) (Eglite, 2016). The digitizing of astronegatives was carried out using the Epson Expression 10000XL commercial scanner (Eglitis, 2017). Plates cover the sky area with NGC 7419 cluster ($RA=23^h01^m30^s$, $DEC=60^\circ32'$).

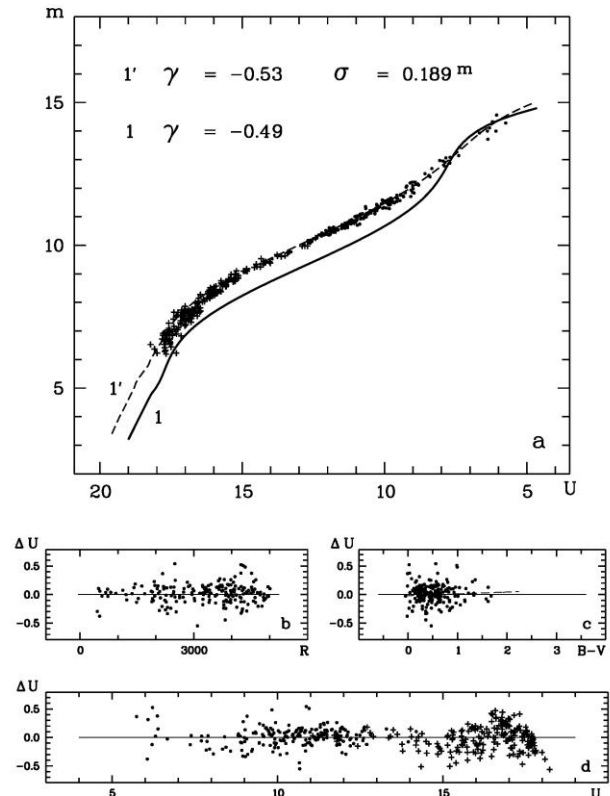


Figure 1: Characteristic curves for plates №1834 (**1'**) и №1809 (**1**), exposed in U color on 1.2-m Schmidt telescope at Baldone (**a**-panel). Panels **b**, **c** and **d** contain sections of characteristic curve **1'** vs a distance to the center of the plate, relative to a color index B-V, and vs U magnitudes respectively. Points and crosses on the plot correspond to photoelectric and CCD measurements of star images.

The upper panel **a** of Fig. 1 presents next data: U scale is along the X-axis, the instrumental scale is along the Y-axis, points and crosses are the stars with photoelectric and CCD measurements respectively. The linear part of the characteristic curve **1'** from the astronegative №1834 covers the interval $U = 10-15^m$ and characterizes the image contrast of $\gamma = -0.53$, the dispersion of points is $\sigma_U = 0.189^m$.

On the flat part of the characteristic curve (from $U > 15^m$ to $U < 18^m$), all the faint and extremely faint stars down to $U=18^m$ are fixed, which were used as a standard for the restoration of the curve. Dashed line (below $m < 6^m$) is the region of the extrapolation. Panels **b**, **c**, **d** in Fig. 1 show the section of the characteristic curve ΔU in relation to the distance from the center of the plate R, color index B-V, and U magnitude itself. On the right and below the first curve **1'** there is the characteristic curve **1** of the astronegative №1809 ($\gamma = -0.49$). Further, we use the tabular representation of this curve for the restoration of individual curves from other negatives.

3. An example of the individual characteristic curve restoration

The characteristic curve of the shape **1** in Fig.1 was restored from the astronegative exposed in U-band. It is characterized by a contrast ratio of $\gamma = -0.49$. In general, if

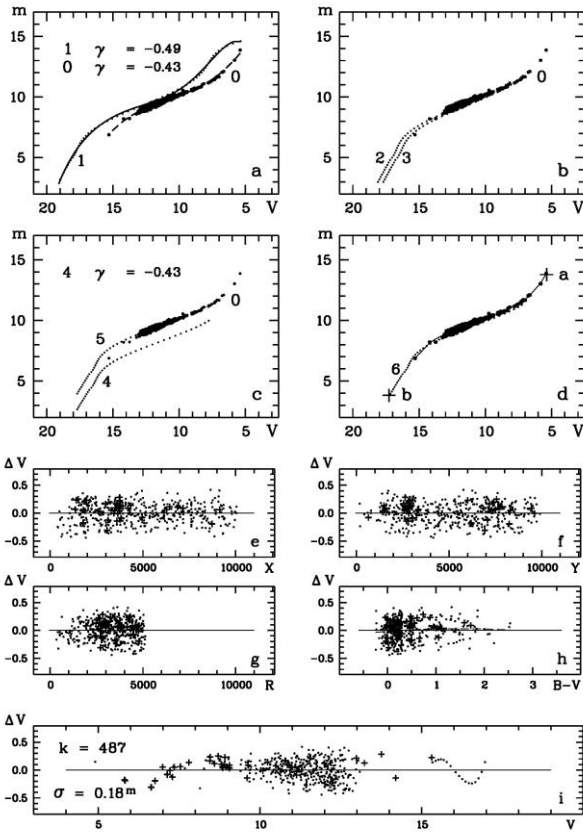


Figure 2: Steps of the extraction of a characteristic curve from the film №624 exposed in the V-color on the 1.2-m Schmidt telescope at Baldone.

the astronegative is not spoiled by a flare and other deteriorating factors, the value of the ratio depends on the exposition duration and the sensitivity of the photo emulsion. That is, the shape of the curve **1** will vary for other emulsions and/or exposures of other duration, and in the procedure of curve restoration from other negatives, the important task is the possibility and necessity of changing the contrast from the original value of $\gamma = -0.49$ to the real one for a particular image.

Consider the extraction of the characteristic curve for the film exposed in the V-band (Fig. 2). Here, V magnitudes are along the X-axis, photometric magnitudes *m* in the instrumental system are along the Y-axis. Panel **a** in Fig. 2 demonstrates next: a solid line **1** represents the empirical curve for U-plate №1809, the sequence of points **0** is a part of the real characteristic curve for the film (A600 film, ZS17 filter) with the flat part absent in the region of underexposure. The film was obtained on 1.2-m Schmidt telescope with 5-minute exposure and the cluster NGC 7063 (RA=21^h27^m, DEC=37°42') as the object of interest. The real characteristic curve **0** has a contrast ratio of $\gamma = -0.43$.

To extract the characteristic curve throughout its length from bright to extremely faint stars registered on the film, first, we cut the empirical curve **1** (b-panel, Fig. 2) in the region of bright stars and shift it by two steps (curves **2** and **3**, Fig. 2) to the right. Then, the contrast of the empirical curve ($\gamma = -0.49$) is reduced to the contrast of the film ($\gamma = -0.43$). In the figure, it is represented by the curve **4**. Then

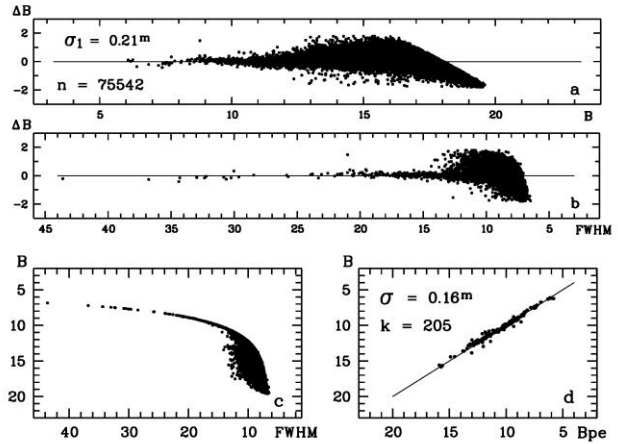


Figure 3: The assessment of the accuracy of determined stellar magnitudes for two plates with 20-minutes exposures in B-color on 1.2-m Schmidt telescope.

this line is shifted vertically to the curve **5** shown in c-panel of the figure. The shift of the curve **5** to the right is the last step for the restoration of the complete characteristic curve, which is the sum of curves **0** and **6**. The complete curve, restored from the film №624 obtained in V band is shown in d-panel of Fig. 2. In this panel, crosses **a** and **b** indicates the limiting values of instrumental photometric data for bright and faint objects fixed on this film.

When restoring the curve from the film, we used both photoelectric measurements from the catalog (Relke, 2015) (panels **e**, **f**, **g**, **h**, **i**, crosses) and values *V_j* from the catalog Tycho-2 (points in the same panels). The standard error of curve restoration $\sigma = 0.18^m$ is shown in the panel **i** of Fig. 2. It should be noted that all the shifts of the empirical curve **1** and the changes in its contrast relative to the real characteristic curve of the film were made based on the comparative analysis of linear parts of both curves using data on lower left points of the real characteristic curve. The algorithm for constructing the individual characteristic curve and determining U, B, V or R stellar magnitudes on its basis for all objects registered on the astronegative allows these processes to be started in automatic mode using the specially developed software.

4. About the errors of stellar magnitude determination.

We evaluated the accuracy of determined stellar magnitudes in a case of using the empirical characteristic curve on the example of two plates obtained with exposure 20 minutes in B color band on 1.2-m Schmidt telescope. Plates were obtained on two different nights with different observing conditions. Both plates are covered with the emulsion ORWO ZU2, the filter used was GG13. The sky area covered with plates is the region of NGC 1664 cluster (RA=04^h50^m, DEC=42°27').

After the determination of stellar magnitudes for all registered objects on two plates, the number of identified stars on both plates was $n = 75\ 542$. For all of them, the differences of stellar magnitudes ΔB were calculated, and the standard error of one difference was obtained $\sigma_1 = 0.21^m$. The trends of differences ΔB relative to stellar

magnitude **B** and values of **FWHM** are represented in panels **a** and **b** of Fig. 3. The **c**-panel of the figure shows the connection of values **B** and **FWHM** averaged over two plates. The **d**-panel demonstrates the linear connection between calculated mean values of **B** with a standard errors of one measure $\sigma = 0.16^m$ and their photoelectric counterparts **B_{pe}** for $k=205$ stars.

5. Conclusions

The method outlined in this paper on the determination of U, B, V stellar magnitudes from astronegatives with a single exposure is already widely applied in practice. In particular, it was used for the determination of B magnitudes for 387 plates obtained on the fourth tube of 7-camera telescope of Odessa observatory at Mayaki observational site during 1966-1998 (Kashuba, 2019). It was also applied for the determination of U and V magnitudes of stars from 300 plates and 2200 films exposed on 1.2m Schmidt telescope at Baldone observatory (Eglitis, 2019). Analogous works on the determination of U, B, V, R stellar magnitudes in frameworks of some current observational projects at different observatories are in their progress.

The work was carried out as a part of the Ukrainian Virtual Observatory (UkrVO) project. (Vavilova, 2012a; Vavilova, 2012b; Vavilova, 2016; Vavilova, 2017).

References

- Akhmetov V.S., Khlamov S.V., Andruk V.M., Protsyuk Yu.I.: 2018, *Odessa Astron. Publ.*, **31**, 199.
- Andruk V.M., Butenko G.Z., Yatsenko A.I.: 2010, *Kinem. Phys. Cel. Bodies*, **26**, **N3**, 146.
- Andruk V.M., Ivanov G.A., Yatsenko A.I. et al.: 2012, *BTSNU*, **N48**, 11.
- Andruk V.M., Pakuliak L.K., Golovnia V.V. et al.: 2015, *Odessa Astron. Publ.*, **28**, 192.
- Andruk V.M., Golovnia V.V., Ivanov G.A. et al.: 2016, *Kinem. Phys. Cel. Bodies*, **32**, **N1**, 32.
- Andruk V.M., Pakuliak L.K., Golovnia V.V. et al.: 2016, *Kinem. Phys. Cel. Bodies*, **32**, **N5**, 260.
- Andruk V., Yuldoshev Q., Eglitis I. et al.: 2017, *Odessa Astron. Publ.*, **30**, 159.
- Andruk V.M., Pakuliak L.K., Golovnia V.V. et al.: 2017, *Science and Innovation*, **13**, **N1**, 17.
- Eglite M., Eglitis I.: 2016, *Odessa Astron. Publ.*, **29**, 120.
- Eglitis I., Andruk V.: 2017, *Open Astronomy*, **26**, **N1**, 7.
- Eglitis I., Shatokhina S., Yizhakevych O. et al.: 2019, *Odessa Astron. Publ.*, **32**, In press.
- Kashuba S., Kashuba V., Andruk V.: 2019, *Odessa Astron. Publ.*, **32**, In press.
- Pakuliak L.K., Andruk V.M., Golovnia V.V. et al.: 2016, *Odessa Astron. Publ.*, **29**, 132.
- Protsyuk Yu.I., Kovylianska O.E., Protsyuk S.V., Yizhakevych O.M. et al.: 2017, *Science&Innovation*, **13**, **N1**, 89.
- Relke E., Protsyuk Yu.I., Andruk V.M.: 2015, *Odessa Astron. Publ.*, **28**, 211.
- Shatokhina S.V., Kazantseva L.V., Yizhakevych O.M., Andruk V.M.: 2018, *Kinem. Phys. Cel. Bodies*, **34**, **N5**, 270.
- Vavilova I.B., Pakulyak L.K., Shlyapnikov A.A. et al.: 2012, *Kinem. Phys. Cel. Bodies*, **28**, **N4**, 85.
- Vavilova I.B., Pakuliak L.K., Protsyuk Yu.I. et al.: 2012, *Baltic Ast.*, **21**, **N3**, 356.
- Vavilova I.B.: 2016, *Odessa Astron. Publ.*, **29**, 109.
- Vavilova I.B., Yatskiv Ya.S., Pakuliak L.K.: 2017, *IAUS*, **325**, 361.
- Yizhakevych O.M., Andruk V.M., Pakuliak L.K.: 2015, *Odessa Astron. Publ.*, **28**, 213.
- Yizhakevych O.M., Andruk V.M., Pakuliak L.K.: 2017, *Kinem. Phys. Cel. Bodies*, **33**, **N3**, 142.
- Yuldoshev Q.X., Muminov M.M., Ehgamberdiev Sh.A. et al.: 2016, *Odessa Astron. Publ.*, **29**, 160.
- Yuldoshev Q.X., Muminov M.M., Ehgamberdiev Sh.A. et al.: 2017, *Odessa Astron. Publ.*, **30**, 205.

DOI:<http://dx.doi.org/10.18524/1810-4215.2019.32.181558>

ON THE FON ASTROPLATE PROJECT ACCOMPLISHMENT

V.M. Andruk¹, L.K. Pakuliak¹, I. Eglitis², Q. Yuldoshev³, A. Mullo-Abdolv⁴,
S.V. Shatokhina¹, O.M. Yizhakevych¹, Yu.I. Protsyuk⁵, H. Relke⁶, V.S. Akhmetov⁷,
M.M. Muminov⁸, Sh.A. Ehgamberdiev³, G. Kokhirova⁴

¹Main Astronomical Observatory of National Academy of Sciences,
27 Akad. Zabolotnoho St., 03143, Kyiv, Ukraine, *andruk@mao.kiev.ua*

²Institute of Astronomy, University of Latvia,
Boulevard Rainis 19. LV-1586 Riga, Latvia, *ilgmars.eglitis@lu.lv*

³Ulugh Beg Astronomical Institute of the Uzbekistan Academy of Sciences,
33 Astronomicheskaya str., 100052 Tashkent, Uzbekistan, *q.astrin@gmail.com*

³Research Institute Mykolaiv Astronomical Observatory,
1 Observatorna Str., 54000, Mykolaiv, Ukraine, *yuri@nao.nikolaev.ua*

⁴Institute of Astrophysics of the Academy of Sciences of Republic Tajikistan,
22 Bukhoro Street, 734042 Dushanbe, Tajikistan, *aziz.sherzod@gmail.com*

⁵Research Institute Mykolaiv Astronomical Observatory,
1 Observatorna Str., 54000 Mykolaiv, Ukraine, *yuri@nao.nikolaev.ua*

⁶Walter-Hohmann-Observatory,
159 Wallneyer St., 45133 Essen, Germany, *helena_relke@yahoo.com*

⁷Institute of Astronomy of V. N. Karazin KNU,
4 Svobody Sq., 61022 Ukraine Kharkiv, Ukraine, *akhmetovvs@gmail.com*

⁸Andijan State University, 129 Universitetskaya St.,
170100 Andijan, Uzbekistan, *muminov1951@gmail.com*

ABSTRACT. The plan of the photographic survey of the northern sky (FON) was proposed in 1976 in Golosiv observatory (now MAO NAS of Ukraine) by I. Kolchinsky and A. Onegina. The final project of the Compiled FONAC catalog (FON Astrographic Catalog) is based on the digital data of photographic plates exposed at four observatories. They are MAO NAS of Ukraine (Kyiv, Ukraine), Kitab astronomical observatory (Tashkent, Uzbekistan), Hissar astronomical observatory (Dushanbe, Tajikistan), and Baldone observatory (Latvia). The total amount of plates is 5700. The result is expected to be the catalog of positions and B-magnitudes of stars covered the declination area from -20 to 90 degrees. The estimated mean epoch of the catalog is ~1987. The limiting B-magnitude is ~17.5^m. The reference system for positions is Tycho-2. B-magnitudes are being obtained in the system of photoelectric standards. The resulted data of photometric reduction are corrected for the photometric color equation in B magnitudes. The complement for the photometric content of the catalog is U and V magnitudes of stars being obtained from the processing of 5400 plates from the glass collection of 1.2 m Schmidt telescope in Baldone. Photometric data of bright stars with $V < 8.5^m$ U, B, V magnitudes cannot be obtained from photographic material, so those objects will gain photometric data from photoelectric catalogs. The catalog will be complemented with proper motions from GAIA.

Keywords: stellar catalog, digitized plate processing, photometry, UBV system

АНОТАЦІЯ. План фотозйомки північного неба (ФОН) був запропонований у 1976 році в Голосіївській обсерваторії (нині MAO НАН України) І. Колчинським та А. Онегіною. Остаточний проект каталогу складеного FONAC (FON Astrographic Catalog) ґрунтується на цифрових даних фотопластинок, експонованих у чотирьох обсерваторіях: MAO НАН України (Київ, Україна), Кітабська астрономічна обсерваторія (Ташкент, Узбекистан), Гіссарська астрономічна обсерваторія (Душанбе, Таджикистан) та Балдонська обсерваторія (Латвія). Загальна кількість пластинок – 5700. В результаті повинен бути створений каталог положень і B-величин зірок, який охоплюватиме область неба від -20 до 90 градусів DEC. Орієнтовна середня епоха каталогу – 1987 рік. Гранична B-величина становить ~ 17,5^m. Опорною системою є Tycho-2. B-величини визначаються у системі фотоелектричних стандартів. Отримані дані фотометричної редуції коригуються за фотометричне рівняння кольору у величинах B. Доповненням для фотометричного вмісту каталогу є величини U та V зірок, отримані при обробці 5400 пластинок 1,2 м телескопа Шмідта в Балдоне. Фотометричні дані яскравих зірок з величиною $V < 8,5^m$ U, B, V не можуть бути визначені з фотоматеріалу, тому ці об'єкти отримуватимуть фотометричні дані з фотоелектричних каталогів. Каталог буде доповнений власними рухами з GAIA.

Ключові слова: зоряні каталоги, обробка оцифрованих зображень, фотометрія, система UBV

1. Introduction

The plan of the photographic survey of the northern sky (FON) was proposed in 1976 in Golosiiv observatory (now Main astronomical observatory NAS of Ukraine) by I.G.Kolchinsky and A.B.Onegina (Kolchinsky & Onegina, 1977). The idea arose after the acquisition of Carl Zeiss wide-angle astrographs of the same type with aperture 40 cm and focal length 2 or 3 m by 6 observatories of the former USSR.

They are Main Astronomical (Golosiiv) observatory of Ukraine, Zvenigorod observatory of Russia, Hissar observatory of Tadjikistan, Abastumani observatory of Georgia, Zelenchuk observatory of Russia and Kitab observatory of Uzbekistan (Pakuliak et al., 2016). Systematic observations of FON project had started in 1982 and lasted until 2000. Unfortunately, the initial idea of four-fold overlapping of the whole northern sky wasn't realized completely. In the final realization of the Compiled FON catalog, we involve wide-angle plates exposed in 3 observatories of Kyiv, Kitab, and Dushanbe. Since 2016, plates of 1.2m Schmidt telescope of Baldone observatory obtained in U and V color bands were got involved into the project to enhance the photometric part of the catalog (Eglitis et al., 2017; 2018). In MAO NAS of Ukraine FON project is carried out in the framework of UkrVO project (Vavilova et al., 2012ab; 2016; 2017).

2. Components of the FON Compiled catalog

1. On the basis of data of 2260 digitized plates from the glass collection of Double Wide-angle Astrograph (DWA) MAO NAS of Ukraine the catalog of positions and B-magnitudes of objects in the zone DE from -4 to $+90$ degrees was created (Andruk et al., 2015; 2016ab). Digitizing of astronegatives was carried out using two commercial scanners Microtek ScanMaker 9800XL TMA and Epson Expression 10000XL with 1200 dpi resolution. Linear dimensions of most of the plates were 30×30 sm, and digital images are of 13000×13000 pixels (Protsyuk et al., 2014).

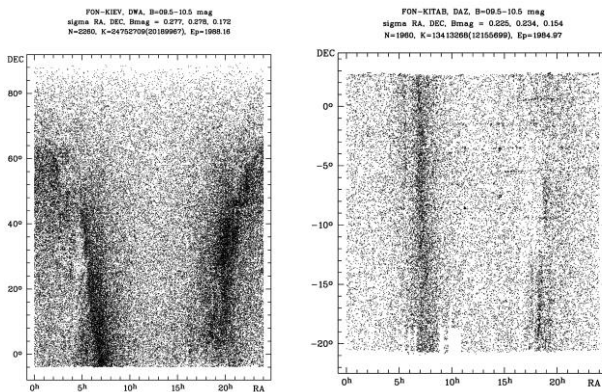


Figure 1: FON-Kyiv star map containing stars of 10^m (left) and the sky map of FON-Kitab catalog (right)

The catalog includes 24.7 million stars and galaxies brighter than $B \leq 16.5^m$ for the mean epoch 1988.2. The reference frame for positions is Tycho-2, and B-magnitudes were obtained in the system of photoelectric standards. The internal accuracy of the catalog for all objects is $\sigma_{RA,DE} = \pm 0.28''$ and $\sigma_B = \pm 0.17^m$. For stars with $B = 7^m - 14^m$ these errors are $\sigma_{RA,DE} = \pm 0.13''$ and $\sigma_B = \pm 0.08^m$. The convergence between calculated and reference positional data is $\sigma_{RA,DE} = \pm 0.06''$, the convergence of photometric data with photoelectric B-magnitudes is $\sigma_B = \pm 0.14^m$. Fig.1, the left panel, shows the FON-Kyiv star map containing stars of 10^m

$= 7^m - 14^m$ these errors are $\sigma_{RA,DE} = \pm 0.13''$ and $\sigma_B = \pm 0.08^m$. The convergence between calculated and reference positional data is $\sigma_{RA,DE} = \pm 0.06''$, the convergence of photometric data with photoelectric B-magnitudes is $\sigma_B = \pm 0.14^m$. Fig.1, the left panel, shows the FON-Kyiv star map containing stars of 10^m

2. The Kitab part of FON project has been finished in the zone of DE from -20.5 to $+2.5$ degrees. The catalog of positions and B-magnitudes of 13.4 million objects brighter than $B \leq 17.5^m$ for the mean epoch 1985.0 has been created from the digital data of 1963 plates processing (Yuldoshev, 2016, Yuldoshev, 2017a; Yuldoshev, 2017b). Digitizing of astronegatives was carried out using commercial scanner Epson Expression 10000XL. Parameters of digitization, linear dimensions of plates, positional and photometric reference systems are the same as in FON-Kyiv case. The internal accuracy for all objects of the catalog is $\sigma_{RA,DE} = \pm 0.23''$ and $\sigma_B = \pm 0.15^m$. For objects in the magnitude interval from 7^m to 14^m these errors are $\sigma_{RA,DE} = \pm 0.085''$ and $\sigma_B = \pm 0.054^m$. The convergence between calculated and reference positions is $\sigma_{RA,DE} = \pm 0.042''$, the convergence between calculated B magnitudes and photoelectric reference data is $\sigma_B = \pm 0.16^m$.

Fig.1, the right panel, shows the FON-Kitab star map built for 10^m stars.

3. Kyiv and Kitab parts of the FON catalog have the overlapping zone on the declination from -4 to $+2.5$ degrees. The compiled catalog was created after the cross-identification of common objects. This catalog contains 36.7 million stars and galaxies for the mean epoch 1987.0. For objects, encountered two or more times positional errors are $\sigma_{AC,DE} = \pm 0.26''$ and photometric ones $\sigma_B = \pm 0.17^m$. For stars in the range $B = 7^m - 14^m$ these errors are $\sigma_{AC,DE} = \pm 0.120''$ and $\sigma_B = \pm 0.072^m$ (Andruk, 2017a).

4. The FON glass collection of Institute for astrophysics of Academy of Sciences of Republic Tajikistan located in Dushanbe includes 1560 plates (Mullo-Abdolv, 2017). The digitizing of plates has been performed using the commercial scanner model Microtek ScanMaker 1000XL Plus. The preceding tests of the scanner gave the errors of star image center estimation $\sigma_{xy} = \pm 0.054$ px. Both errors are given for stars brighter than $B = 13.5^m$. The insertion errors of scanner in photometric estimations has been found $\sigma_m = \pm 0.020^m$. The first results of processing 71 plates from the collection in the zero declination zone and 58 plates from the declination zones 64, 68, 72 give the positional accuracy $\sigma_{RA,DE} = 0.33''$ for stars in the magnitude range 5^m to 17^m . The photometric accuracy has occurred to be $\sigma_B = 0.12^m$. The convergence between calculated and Tycho2 reference positions of objects is $\sigma_{AC,DE} = 0.12''$, while photometric one is $\sigma_{BT} = 0.19^m$. The convergence with photoelectric data is $\sigma_B = 0.14^m$ (Mullo-Abdolv, 2018).

5. The photometric content of the Compiled catalog can be supplemented with data in two other color bands V and U. For this purpose, photographic plates obtained with 1.2m Schmidt telescope in the observatory of Baldone are being involved (Eglitis, 2018). Baldone collection numbers 780 U and 4660 V plates. The processing procedures for them are the same as for wide-angle FON plate collection. Plates were digitized using Epson Expression 10000XL commercial scanner. The preceding tests of the

scanner were made by comparing digitized images of grey 8-bit and 16-bit color depth to assess the accuracy which could be achieved (Eglitis, 2017). The results have shown the instrumental system errors of ± 0.0026 px and $\pm 0.0024^m$ for rectangular coordinates and magnitudes respectively. For the assessment of positional and photometric errors of the scanner, six consequent images of the same plate with 1200 dpi resolution were processed and compared. The scanner errors obtained for stars brighter 13.5^m in U-band are $\sigma_{xy} = \pm 0.021 \div 0.027$ px and $\sigma_m = \pm 0.014^m \div 0.016^m$ for positions and instrumental magnitudes respectively.

3. Photometric determinations from plate images with two exposures

Wide-angle observational material of FON project was obtained with two exposures of different durations shifted by both coordinates. The aim was to restore the characteristic curve for photometric determinations as a compiled one from two exposures in order to achieve the same accuracy for stars on the entire range of magnitudes.

Fig.2 shows the characteristic curves **1** and **2** for long (20 minutes) and short (20 seconds) expositions of the plate from FON collection (DWA, Kyiv) (Andruk, 2012). On the **a**-panel, there is the connection of diameters of star images **f1** of the long exposure given in respect to the short one **f2**. The **b**-panel presents the connection of diameters of two exposures **f1**, **f2** and photoelectric magnitudes B_{pe} . The **c**-panel shows the connection of instrumental magnitudes **m1** and **m2** of both exposures. On the **d**-panel, there are characteristic curves for two expositions. The **f**-panel demonstrates the combined characteristic curve. The combined characteristic curve **1'** has been obtained by shifting the characteristic curve of short exposure **2** by ΔB in order to continue the long exposition curve **1** to the region of faint and extremely faint stars with $B > 13^m$. In practice, the curve **1'** has been used for determination of photographic B_{ph} magnitudes of objects registered on all 2260 negatives of FON collection.

4. Photometry from plate images with a single exposure

The photographic material of Baldone Schmidt telescope was obtained with a single exposition. Fig. 3 presents the example of the characteristic curve from the Baldone digitized astronegative and the errors of its restoration.

The errors are given as the differences between calculated U-magnitudes and their photoelectric counterparts U_{pe} versus rectangular coordinates X and Y, the distance from the plate center R, a color index B-V, and photoelectric magnitudes U_{pe} .

5. The photometric system of the catalog

FON observational material was exposed by telescopes-refractors. Due to this, the results of the photometric processing of digitized plates comprise a color equation. The letter means that obtained photographic magnitudes B_{ph} are burdened by systematic errors (corrections) depended on the B-V color index of the star. We used characteristic curves calibrated by reference stars with photo-

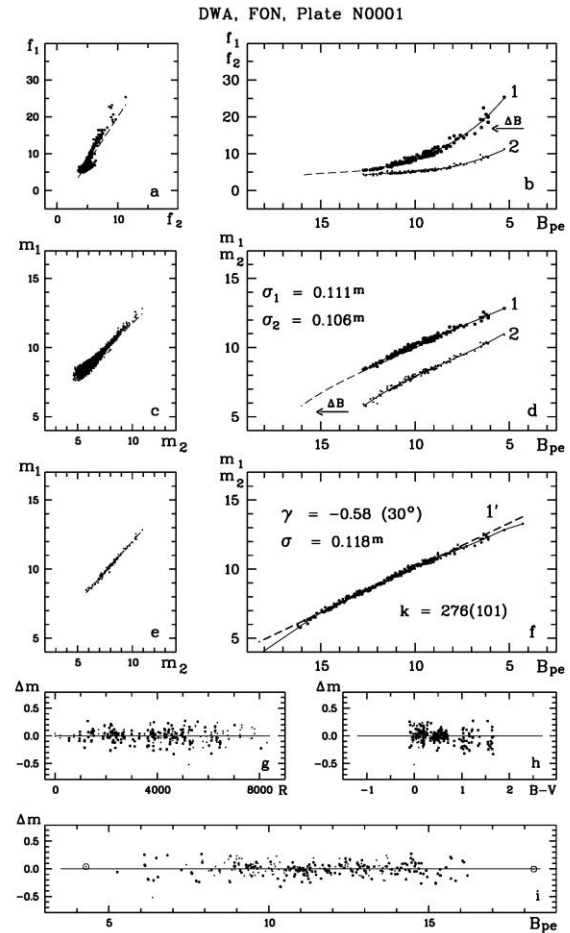


Figure 2: Photometry of stars from plates with two exposures

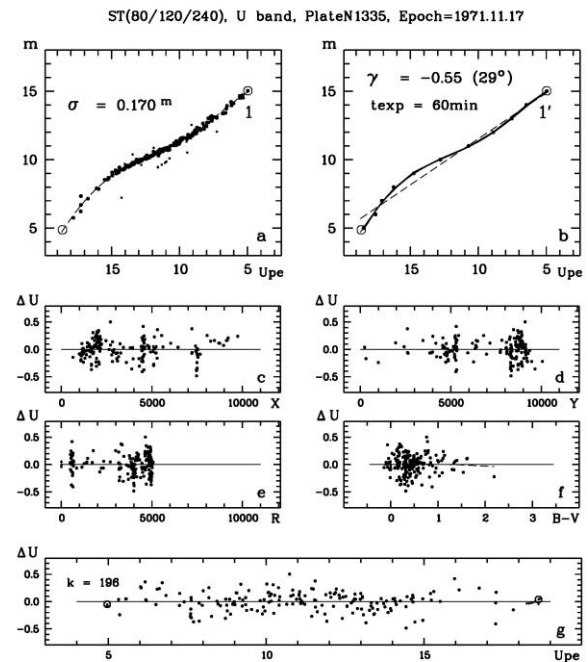


Figure 3: Photometry of stars from plates with a single exposures

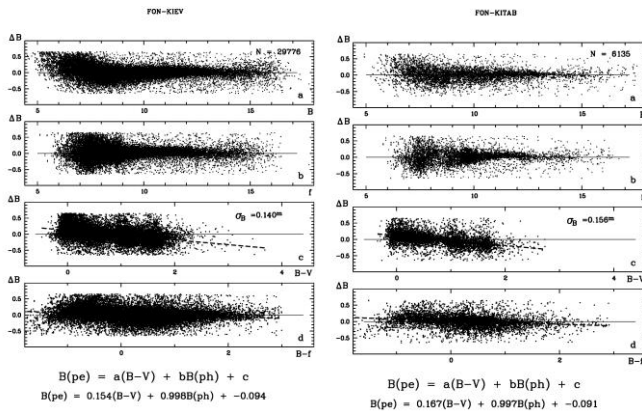


Figure 4: Photometric systems of FON-Kyiv (left) and FON-Kitab(right) catalogs

electric values in order to derive photographic magnitudes B_{ph} (Kornilov, 1991; Mermilliod, 1991; Andruk, 1995; Relke, 2015; Andruk, 2017). The results of the comparison of photometric differences $\Delta B = B_{ph} - B_{pe}$ for calculated and reference stars are given in Fig. 4.

Panels **a** and **c** show the trend of differences ΔB relative to B_{pe} for Kyiv and Kitab parts of FON catalog. Panels **b** and **d** give the dependences of ΔB on photoelectric data $B-V$. The numbers of compared stars for parts of the catalog are 29 776 and 6135. Rms errors σ_m of magnitude differences are $\pm 0.140^m$ and $\pm 0.156^m$ respectively. Panels **c** and **d** for Kitab demonstrate the conspicuous color equation with the value of $0.16(B-V)$ of star magnitude.

6. Final steps

The complete steps of catalog compilation include the completion of Dushanbe FON part digitizing and processing, the completion of the Baldone UV collection digitizing and processing, the completion of photometric content enhancement and correction.

In publications (Akhmetov, 2016; Akhmetov et al., 2018; Protsyuk et al., 2016) the results of the comparison of three obtained (FON-Kyiv, FON-Kitab) or being created (FON-Dushanbe) catalogs are given. The estimation of random accuracy of stars positions from the mentioned catalogs was performed by the Wielen method (Wielen, 1995). Final dispersions were calculated for every sub-range of magnitudes. The results of the comparison of mentioned catalogs with PMA (Akhmetov et al., 2017), XPM (Fedorov, 2009), UCAC4 (Zacharias et al., 2013), PPMXL (Roeser et al., 2010) are represented in corresponding publications. The external accuracy of stars position of catalogs of FON project is in a good agreement with their internal accuracy and equal from 50 and 300 mas for brightest and faintest stars correspondingly.

The software devised for the processing of Kyiv and Kitab FON plates was successfully tested on the plates with images of Solar system bodies resulted in catalogs of positions of major planets and their moons, asteroids, and comets (Eglitis et al., 2016ab; Protsyuk et al., 2015b, 2017; Shatokhina et al., 2018, Vavilova et al., 2014, Yizhakevych et al., 2017).

References

Akhmetov V.S.: 2016, *Odessa Astron Publ.*, **29**, 116.
 Akhmetov V.S. Fedorov P.N., Velichko A.B., Shulga V.M.: 2017, *MNRAS*, 469, 763.
 Akhmetov V.S., Khlamov S.V., Andruk V.M., Protsyuk Yu.I.: 2018, *Odessa Astron Publ.*, **31**, 199.

Andruk V., Kharchenko N., Schilbach E. et al.: 1995, *AN*, **316**, 225.
 Andruk V.M., Ivanov G.A., Yatsenko A.I. et al.: 2012, *Bull. T. Shevchenko Nat. Univ. Kyiv. Astron.* **N48**, 11.
 Andruk V.M., Pakuliak L.K., Golovnia V.V. et al.: 2015, *Odessa Astron. Publ.*, **28**, 192.
 Andruk V.M., Golovnia V.V., Ivanov G.A. et al.: 2016, *Kinem. Phys. Cel. Bodies*, **32**, N1, 32.
 Andruk V.M., Pakuliak L.K., Golovnia V.V. et al.: 2016, *Kinem. Phys. Cel. Bodies*, **32**, N5, 260.
 Andruk V., Yuldoshev Q., Eglitis I. et al.: 2017, *Odessa Astron. Publ.*, **30**, 159.
 Andruk V.M., Pakuliak L.K., Golovnia V.V. et al.: 2017, *Science and Innovation*, **13**, N1, 17.
 Eglitis I., Eglite M., Pakuliak L.K. et al.: 2016, *Odessa Astron. Publ.*, **29**, 126.
 Eglitis, I.; Eglite, M.; Shatokhina, S. V.; Andruk, V. M. 2016, *Odessa Astron. Publ.*, **29**, 123.
 Eglitis I., Andruk V.: 2017, *Open Astronomy*, **26**, N1, 7.
 Eglitis I., Eglite V., Andruk V. et al.: 2018, *Odessa Astron. Publ.*, 31, 208.
 Fedorov P.N., Akhmetov V.S., Bobylev V.V., Gontcharov G.A.: 2011, *MNRAS*, 415, 665.
 Kolchinsky I.G., Onegina A.B.: 1977, *Astrometry and Astrophysics*, **N33**, 11.
 Kornilov V.G., Volkov I.M., Zakharov A.I. et al.: 1991, *Trudy GAIS*, **63**, 1.
 Mermilliod J.C.: 1991, *Online Data Catalog: Homogeneous Means in the UBV System (Mermilliod 1991)*. URL: http://adsabs.harvard.edu/cgi-bin/nph-data_query?bibcode=2006yCat.2168...0M&link_type=DATA&db_key=AST&high=.
 Mullo-Abdolov, A.; Kokhirova, G.; Relke, H.; et al.: 2017, *Odessa Astron Publ.*, **30**, 186
 Mullo-Abdolov A., Relke H., Kokhirova A. et al.: 2018, *Odessa Astron Publ.*, **31**, 224
 Pakuliak L.K., Andruk V.M., Golovnia V.V. et al.: 2016, *Odessa Astron. Publ.*, **29**, 132.
 Protsyuk Yu.I., Andruk V.N., Muminov M.M. et al.: 2014, *Odessa Astron. Publ.*, **27**, 61.
 Protsyuk Yu., Relke E.: 2016, *Odessa Astron. Publ.*, **29**, 144.
 Protsyuk Yu.I., Kovylanska O.E., Protsyuk S.V., Yizhakevych O.M. et al.: 2017, *Science&Innovation*, **13**, N1, 89.
 Relke E., Protsyuk Yu.I., Andruk V.M.: 2015, *Odessa Astron. Publ.*, **28**, 211.
 Roeser S., Demleitner M., Schilbach E.: 2010, *AJ*, 139, 2440.
 Shatokhina S.V., Kazantseva L.V., Yizhakevych O.M., Andruk V.M.: 2018, *Kinem. Phys. Cel. Bodies*, **34**, N5, 270.
 Vavilova I.B., Pakulyak L.K., Shlyapnikov A.A. et al.: 2012, *Kinem. Phys. Cel. Bodies*, **28**, N2, 85.
 Vavilova I.B., Pakuliak L.K., Protsyuk Yu.I. et al.: 2012, *Baltic Ast.*, **21**, N3, 356.
 Vavilova I., Golovnia V., Andruk V. et al.: 2014, *Odessa Astron. Publ.*, **27**, 65.
 Vavilova I.B.: 2016, *Odessa Astron. Publ.*, **29**, 109.
 Vavilova I.B., Yatskiv Ya.S., Pakuliak L.K. et al.: 2017, *Proc. IAU Symposium*, Vol. **325**, pp. 361-366.
 Wielen R.: 1995, *A&A*, 302, 613.
 Yizhakevych O.M., Andruk V.M., Pakuliak L.K.: 2017, *Kinem. Phys. Cel. Bodies*, **33**, N3, 142.
 Yuldoshev Q.X., Muminov M.M., Ehgamberdiev Sh.A. et al.: 2016, *Odessa Astron. Publ.*, **29**, 160.
 Yuldoshev Q.X., Muminov M.M., Ehgamberdiev Sh.A. et al.: 2017, *Odessa Astron. Publ.*, **30**, 205.
 Yuldoshev Q.X., Ehgamberdiev Sh.A., Muminov M.M. et al.: 2017, *Kinem. Phys. Cel. Bodies*, **33**, No. 5, 250.
 Zacharias et al.: 2013, *AJ*, 145, 44.

DOI:<http://dx.doi.org/10.18524/1810-4215.2019.32.181599>

ASTEROID SEARCH RESULTS FOR DIGITIZED ASTROPLATES OF 1.2m TELESCOPE IN BALDONE

I. Eglitis¹, O. Yizhakevych², S. Shatokhina², Yu. Protsyuk³, V. Andruk²¹ Baldone Observatory, Institute of Astronomy, University of Latvia,
Raina blvd. 19, Riga, LV 1050, Latvia, ilgmars.eglitis@lu.lv² Main Astronomical Observatory of National Academy of Sciences,
27 Akad. Zabolotnogo St., 03680, Kyiv, Ukraine, yizh_net@ukr.net, svetash@mao.kiev.ua³ Research Institute Mykolaiv Astronomical Observatory, Mykolaiv, Ukraine

ABSTRACT. The work on the mass search for asteroids on astroplate images and the determination of their coordinates was begun in 2016. The basis for current search was the processing results of digitized photographic plates and films obtained at the observatory in Baldone in 1967-1993.

Observations with a single exposure in different spectral bands were carried out using the 1.2m Schmidt telescope in Baldone. We used all observations in the U Johnson's spectral band (on plates) and significant part of them in V band (on films). Photometric band U was realized by combining emulsion ORWO Zu1 (Zu2 or Zu21 or Kodak 103aO or ПаО) with UG1 filter. For films with A600 emulsion and filter ZS17 a photometric band V was implemented.

Based on the results of digital processing about 300 U-plates and more than 1460 V-films, a preliminary catalog of 1700 asteroid positions was compiled. Among the objects in this catalog are asteroids of particular interest. These include the distant objects (136108) Haumea and (136472) Makemake and some Main belt asteroids, the positions of which were fixed on the plates many years before their own discoveries.

All observed positions of asteroids were compared with ephemeris DE431. An analysis of the convergence of the observed positions with their theoretical data for different spectral bands showed that the observations on V-films are better consistent with theory.

However, the internal accuracy of determining coordinates from U-plates, on the contrary, is higher than from V-films. This discrepancy is especially noticeable for right ascension, when the root-mean-square errors on V-films can reach values exceeding 1.8 arc seconds. These significant errors are a consequence of the curvature unevenness of the film surface during scanning.

Keywords: catalog, asteroid positions

АНОТАЦІЯ. Робота з масового пошуку зображень астероїдів та комет на фотографічних пластинках минулих років та визначення їх координат розпочата у 2016 році. Основою для цього були результати обробки оцифрованих фотографічних пластинок та плівок, отриманих в обсерваторії в Балдоне в 1967-1993 роках.

Спостереження з однією експозицією в різних спектральних смугах системи Джонсона проведені за

допомогою 1,2-метрового телескопа Шмідта в Балдоне. Використані всі спостереження у спектральній смузі U (пластинки) та значна їх частина у V смузі (плівки). Фотометричну смугу U було реалізовано шляхом поєднання емульсії ORWO Zu1 (Zu2 або Zu21 або Kodak 103aO або ПаО) з UG1 фільтром. Для плівок з емульсією A600 та фільтром ZS17 була реалізована фотометрична смуга V.

На основі результатів цифрової обробки близько 300 U-пластинок та понад 1460 V-плівок було складено попередній каталог 1700 положень астероїдів. Серед об'єктів цього каталогу є астероїди, які представляють особливий інтерес. До них віднесені віддалені об'єкти (136108) Haumea і (136472) Makemake та деякі астероїди Головного поясу, положення яких було зафіксовано на цих пластинках за багато років до їх відкриття.

Усі спостережувані положення астероїдів порівнювали з ефемеридою DE431. Аналіз збіжності спостережуваних положень з їх теоретичними даними для різних спектральних смуг показав, що спостереження на V-плівках краще відповідають теорії.

Однак внутрішня точність визначення координат за U-пластинками, навпаки, вища, ніж за V-плівками. Ця розбіжність особливо помітна у прямому піднесенні, коли значення середньоквадратичної похибки на V-плівках можуть перевищувати 1.8 кутових секунд. Ці значні похибки обрахунку координат є наслідком нерівномірності викривлення поверхні плівки під час сканування.

Ключові слова: каталог, положення, астероїд

1. Introduction

The purpose of this work is to search for images of small bodies of the Solar System from digitized plates of clusters observations in 1967-1993 at the astronomical observatory in Baldone. Determining the coordinates and compiling a catalog of asteroid positions are the main tasks of this work.

In 1965, a Schmidt SmA camera was installed in Baldone on the territory of the Astronomical Observatory of

the Institute of Astronomy of the University of Latvia with the following parameters: diameter of the mirror - 120 cm, diameter of the correction plate - 80 cm, focal length - 240 cm, field of view 446' x 446' min. The first effective observations were obtained in December 1966.

Over 40 years of photographic observations on various programs, the Baldone's collection of astronegatives including more than 22,000 direct images in a wide range of exposures. Among them there are approximately 780 photographic plates in U spectral band exposed with a UG1 filter, 4600 films in V band exposed with a ZS17 filter (Eglitis et al., 2016a).

From 2013 the regular digitization and processing of photographic astroplates started in Baldone observatory. The plates were digitized using Epson Expression 10000XL and 11000XL commercial scanners with the resolution 1200 dpi. The further software for scan processing was developed and implemented in MAO NASU to process the digitized astronomical negative plates as well as to obtain the final product in the form of a catalogue of positions and stellar magnitudes for all registered objects on the plate. For detail the techniques of astroplate digitization and further processing and determination of coordinates and magnitudes of stars are described in the series of publications (Andruk et al., 2016a; 2016b; Protsyuk et al., 2014). The special modernized programs were developed at MAO NASU for constructing individual characteristic curves and determining stellar U, V values with a single exposure (Andruk et al., 2019).

The equatorial coordinates α , δ and stellar magnitudes of all objects on the plates were obtained in the reference system of Tycho-2 at the epoch of exposition of each plate. The magnitudes of all objects are obtained in the system of photoelectric standards.

2. Results

The processing results (Eglitis et al., 2016a; 2017; 2018) of digitized photographic observations of star clusters in UBVR bands at the Baldone observatory during 1967-1996 were used for a global search for small bodies of the Solar system. An online internet service from JPL was used for this (<https://ssd.jpl.nasa.gov/sbfind>). The first stage of this search was begun in 2016. As a result 87 images of minor planets from 9.8 to 17.1 stellar magnitude and 2 images of comets were identified on 152 plates (Eglitis et al., 2016b). Now we continued this work and carried out the search for asteroids based on the results of processing the remaining plates observed in U, V bands. A total of 272 plates were used in the U band and more than 1,400 films in the V band. Asteroids and comets were detected on 107 plates (361 positions) in U band and 223 films (1401 positions) in V band. Their positions were compiled into a preliminary catalog.

In addition, in vicinity of each position of the asteroid, stars from the Gaia DR2 catalog were selected to determine the possible coverage of the images of stars with an image of the asteroid on the plate. In these cases, the coordinates or magnitudes of the asteroid are determined ambiguously on the plate. Such asteroid positions were excluded from the compiled catalog.

The quantitative distribution of all used photographic observations over the years compared to the number of

effective observations for the search for asteroids is presented in Fig. 1 and Fig. 2.

As a result of reduction processing with the reference catalog of Tycho-2, the root-mean-square (RMS) errors σ of determining the coordinates of stars on the plates were obtained. For U-plates, the internal accuracy of determining the coordinates of stars is approximately in the range of 0.05-0.53 arc seconds. For V-films, the range of RMS errors is much wider, especially for right ascension, when these values reach 1.8 arc seconds. This may be due to the uneven curvature of the film surface during scanning (Table 1).

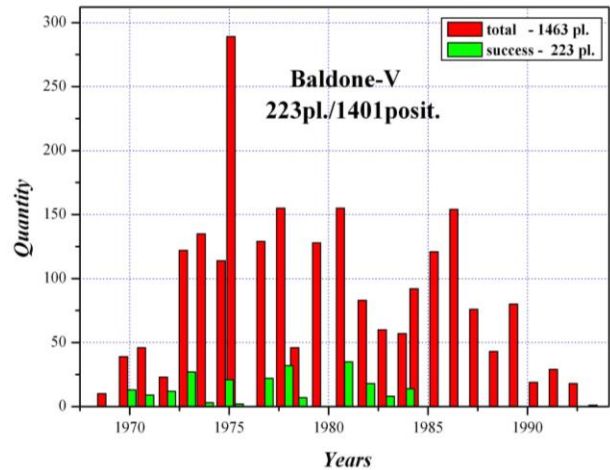


Figure 1: Distribution on time scale of all observations in V band in Baldone observatory.

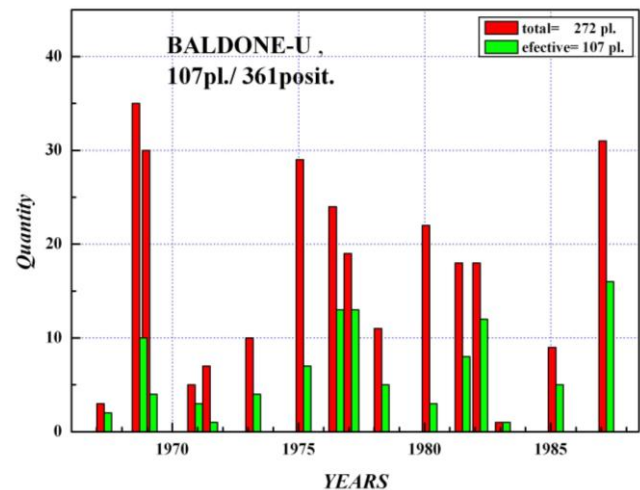


Figure 2: Distribution on time scale of all observations in U band in Baldone observatory.

Table 1: Ranges of root-mean-square errors of determining the coordinates of stars for U and V plates.

107 U-plates			223 V-films		
σ_{RA} , arcsec	σ_{Dec} , arcsec	σ_U , mag	σ_{RA} , arcsec	σ_{Dec} , arcsec	σ_V , mag
1	2	3	4	5	6
0.05-0.53	0.05-0.34	0.01-0.39	0.05-1.76	0.06-0.63	0.12-0.53

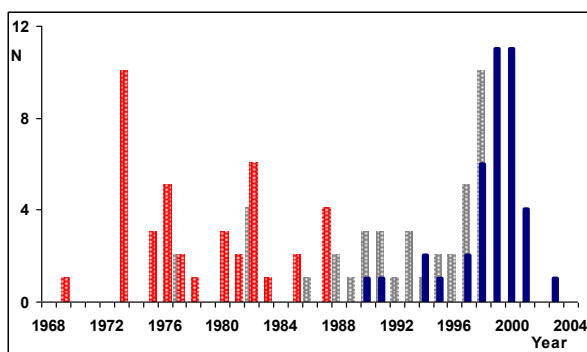


Figure 3: Observational moments for 40 asteroids in Baldone and their first observations according to the MPC database (http://www.minorplanetcenter.net/db_search)

Using JPL ephemeris, an analysis of O-C differences was performed for 361 positions of asteroids identified in U-plates. Of particular interest are the 40 positions of asteroids fixed on the U-plates in the period 1969-1987. These Main belt asteroids have been discovered by automatic telescopes during 1998-2003 in the LINEAR (<http://www.ll.mit.edu/linear>), LONEOS (<https://asteroid.lowell.edu/asteroid/loneos>) and NEAT projects (<http://neat.jpl.nasa.gov>).

The MPC database contains a small number of their positions obtained from observations no earlier than 10-20 years before the official discoveries of asteroids. There are no earlier observations of these asteroids.

Figure 3 for each of these 40 asteroids shows the observational moment of asteroid in 1969-1987 in Baldone (left side), the first productive moment of its observation in 1977-1998 in the world (in the center and according to the MPC), the moment of its official discovery (right side). For many of these asteroids, their observations in Baldone are the earliest and over the next 10-25 years, there are no observations of these asteroids. Using the digitized archives of previous photographic observations in Baldone, this interval can easily be filled with new identified and processed observations.

However, such asteroid positions should have high accuracy for further kinematic and dynamic solutions of asteroid orbits. After comparison with an ephemeris, the obtained values of the O-C differences for many interesting asteroids have a large scatter and can reach 5 arc seconds. This may be due to great random errors in determining the coordinates of the asteroids or insufficiently accurate recorded moments of observation. On the one hand, these are faint (16-18^m) objects with low signal/noise level. For example, for the faint stars (16-18^m), the random error component of the coordinate determination increases rapidly and reaches 1.5 - 2 arc seconds on plates from the FON project (Shatokhina et al., 2019).

On the other hand, great O-C values are not always the result of errors in determining the coordinates of asteroids. For example, images of asteroid 9414 were identified on plates obtained in 1982-1985 in Baldone observatory and in the FON (Kyiv part) project (Shatokhina et al., 2018). The O-C values for these two positions are approximately 4 arc seconds. However, they are in good agreement with each other and with the O-C values for the other nearest MPC positions. In addition, the Baldone archive has about 10-15 unprocessed observations of this asteroid for the same time period and in different spectral bands of UBVR. Their processing can significantly supplement the existing observations of asteroid 9414 with new data.

The work on identifying asteroids by V-films is not finished. A large range of errors in determining coordinates due

to the curvature unevenness of the film surface during scanning does not always allow this to be done quickly and unambiguously. However, the films contain unique information in previous years about the locations of TNO and other interesting objects in the Solar system. Therefore, the processing results will be carefully analyzed and, possible, re-digitized.

3. Conclusion

Long-term sets of photographic observations made in previous years can become the basis not only for creating catalogs of coordinates of stars and galaxies but also for determining precise positions of small bodies of the Solar system. Using the digitized photographic plates of the archives of the Baldone Observatory, we can identify faint moving objects up to 18^m and determine their coordinates and magnitudes with high accuracy. Among those may be objects which were discovered much later than were fixed on those astronegatives, and unique asteroids and comets including selected trans-Neptunian distant objects.

Using data about precise positions and magnitudes of asteroids, some tasks of refining ephemeris, studying changes in asteroid orbits over time, non-gravitational effects in the evolution of asteroid's orbits, constructing light curves and phase dependencies can be solved.

Cooperation with Ukrainian Virtual Observatory (UkrVO) gives the opportunity to expand this work, involving numerous additional files of digitized observations and different services and software for modern processing of observation and, ultimately, to increase the number of new original data about Universe.

Intensive work on the creation of catalogs of stars and galaxies and small bodies of the Solar system based on digitized photographic observations of star clusters of archives in Baldone was successfully carried out with the active support of UkrVO [Vavilova et al., 2016; 2017].

The main results of such studies have been previously reported at different conferences.

Acknowledgment. The work was partially supported by Ukrainian Astronomical Association.

References

- Andruk V.M., Golovnia V.V., Ivanov G.A et al.: 2016, *Kinem. Phys. Cel. Bodies*, **32**, N1, 38.
- Andruk V.M., Pakuliak L.K., Golovnia V.V. et al.: 2016, *Kinem. Phys. Cel. Bodies*, **32**, N5, 260.
- Andruk V., Eglitis I., Protsyuk Yu. et al.: 2019, *Odessa Astron. Publ.*, **32**, in press.
- Eglitis, I.; Eglite, M.; Pakuliak, L. K. et al.: 2016, *Odessa Astron. Publ.*, **29**, 126.
- Eglitis I., Eglite M., Shatokhina S.V. et al.: 2016, *Odessa Astron. Publ.*, **29**, 123.
- Eglitis I., Andruk V.: *Open Astron.*, 2017; **26**, 1, 7.
- Eglitis I., Eglite V., Andruk V. et al.: 2018, *Odessa Astron. Publ.*, **30**, 208.
- Protsyuk Yu.I., Andruk V.N., Kazantseva L.V.: 2014, *Odessa Astron. Publ.*, **27**, 59.
- Shatokhina S.V., Kazantseva L.V., Yizhakevych O.M. et al.: 2018, *Kinem. Phys. Cel. Bodies*, **34**, N5, 270.
- Shatokhina S.V., Kazantseva L.V., Andruk V.: 2019, *Odessa Astron. Publ.*, **32**, in press.
- Vavilova I.B.: 2016, *Odessa Astron. Publ.*, **29**, 109.
- Vavilova I.B., Yatskiv Ya.S., Pakuliak L.K.: 2017, *IAUS*, **325**, 361.

DOI:<http://dx.doi.org/10.18524/1810-4215.2019.32.181603>

PROBABILITIES OF PHYSICAL LINK BETWEEN THE COMPONENTS OF THE SELECTED MULTIPLE SYSTEMS FROM WDS CATALOG

N.V. Maigurova, Yu.I. Protsyuk

Research Institute "Mykolaiv Astronomical Observatory", Ukraine,
nadija@nao.nikolaev.ua, yuri@nao.nikolaev.ua

ABSTRACT. Astrometric CCD observations of visual components of double and multiple stars were performed using the RI MAO Axial Meridian Circle (AMC) with new Apogee Alta AI-F8300 CCD camera mounted at the telescope in 2018. Observations were carried out automatically in drift-scan mode using a standard R filter. Objects for observational program were selected from the Washington Double Star Catalog (WDS). During the 23 nights, 983 observations of 579 double and multiple systems from the WDS catalog were obtained. Astrometric reductions of the observations showed high accuracy, with an average error of one position about 0.1" in right ascension and declination for stars up to 16^{mag}, which were observed more than 3 times.

The purpose of our study was to measure the parameters of the mutual configuration of pairs from the original images and to draw some conclusions about the physical connection of the components in the selected systems. The measurement array that will be sent to the WDS database includes values of positional angle, angular separation, stellar magnitude difference, and epoch of the observation. A detailed analysis of the pairs of stars in the selected 5 systems to clarify their composition and the nature of the link between them was made. Positional data from the Hipparcos, Tycho2, UCAC4, Gaia DR2, and Pan-STARRS (PS1) catalogs were used as sources of additional information about the investigated stars. The search for possible invisible stars in the selected systems was performed using the statistical Wielen method, based on the analysis of the differences of instantaneous and long-term averaged proper motions of the stars. The proper motions of the space Gaia DR2 catalog were considered to be instantaneous, the long-term averaged proper motions were used from Tycho-2 and UCAC4 catalogs. Obtained values of the statistical parameter in some cases indicate a high probability of existence of invisible close components in the studied systems. Detailed comments of the results for each of the selected systems are provided.

Keywords: Double and multiple stars, binary stars, CCD observations, astrometric positions, common proper motions.

АНОТАЦІЯ. Астрометричні ПЗЗ-спостереження візуальних компонентів подвійних та кратних зірок виконувались за допомогою Аксиального меридіанного круга НДІ МАО з новою ПЗЗ-камерою Apogee Alta AI-F8300, що була встановлена на телескопі у 2018 році. Спостереження проводились у автоматичному режимі методом переносу заряду з використанням стандартного

фільтру R. Об'єкти для програми спостережень було обрано з каталогу подвійних зірок Вашингтонської обсерваторії (WDS). Протягом 23 ночей отримано 983 спостереження 579 подвійних та кратних систем з каталогу WDS. Астрометричні редуції спостережень показали досить високу точність, середня похибка одного положення складає близько 0.1" для прямого піднесення та схилення для зірок до 16 зоряної величини, що спостерігались більше 3 разів.

Метою нашого дослідження було вимірювання параметрів взаємної конфігурації пар з оригінальних зображень та отримання певних висновків щодо фізичного зв'язку компонентів у обраних системах. Массив вимірювань, що буде надіслано до бази даних WDS, включає значення позиційного кута, кутового розділення, різниці зоряних величин та епоху спостережень. Виконано детальний аналіз пар зірок, що входять до обраних 5 систем для уточнення їх складу та природи зв'язку між ними. Позиційні дані з каталогів Hipparcos, Tycho2, UCAC4, Gaia DR2 та Pan-STARRS (PS1) використовувались як джерела додаткової інформації про зірки, що досліджувались. Виконано пошук можливих невидимих зірок у обраних системах з застосуванням статистичного методу Вілена, що базується на аналізі різниць миттєвих та усереднених довгострокових власних рухів зірок. Власні рухи каталогу Gaia DR2 було розглянуто як миттєві, в якості довгострокових власних рухів залучено дані каталогів Tycho-2 та UCAC4. Отримані значення статистичного параметру в деяких випадках вказують на високу ймовірність існування невидимих близьких компонент в досліджуваних системах. Представлені детальні коментарі до результатів для кожної з розглянутих систем.

Ключові слова: подвійні та кратні зоряні системи, фізично зв'язані подвійні зорі, ПЗЗ-спостереження, астрометричні положення, власні рухи.

1. Introduction

Binary and multiple stars are unique objects for direct determining physical characteristic of stars (primarily mass), through a combined analysis of photometric, astrometric, and spectroscopic data. This paper has deal mainly with positional observations to determine the separation between components of star and the position angle at the observational epoch in order to supplement the observation

history. These parameters are also value information for clarify the nature of the link between the system components and in case of the existence of a gravitational link between stars, these data can be used to obtain elements of the orbits of the binary system. The principal database of double and multiply stars is Washington Double Star Catalog (WDS) (Mason et al., 2001) maintained by the United States Naval Observatory. The WDS lists 149730 (as the autumn, 2019) of resolved stellar systems with two and more components. But the main question for researchers is whether the pair that they see in their telescopes is gravitationally connected to each other, or this is the result of the random arrangement of stars on the celestial sphere, which are very far from each other in reality. Only a small part of the WDS records have enough observations to detect the orbital motion of stars around each other. The *Sixth Orbit Catalog* (ORB6) included only 2,662 orbits of 2,558 systems as of 25 April 2016 (<https://www.usno.navy.mil/USNO/astrometry/optical-IR-prod/wds/orb6>). Therefore ground-based observations such objects do not lose their value despite the many existing modern astrometric dense catalogs.

2. Telescope and Observational Program

The regular observations of binary and multiply stars at RI MAO have been carried out at two telescopes: Axial Meridian Circle (2013 – 2015, 2018-2019) (Bodryagin et al, 2015) and KT-50 of Mobitel complex (2014-2019), (Bodryagin et al, 2016;2017, Maigurova et al.,2018) . For several years, we did not observe double stars at AMC for technical reasons. With the installation of a new camera in 2018, observations were resumed. The all characteristics of updated instrumental system are given at Tab. 1.

The observations of visual double and multiply stars from WDS catalog were performed during 2018/05 - 2018/10 in drift scan mode. During 23 nights we obtained 983 observations for 579 WDS system in R photometric band. Mean epoch of our observations is 2018.5 and mean time difference between last observation in WDS database and our observations is 6 years, but 10% stars have the differences in range from 15 up to 100 years. So this indicates that our data can be useful for extend the arc length of the observed orbit of binary system. Distribution of observations over celestial sphere is shown in Fig. 1.

Table 1: The characteristics of AMC instrumental system

Telescope	AMC RI “MAO” (Mykolaiv, Ukraine)
λ, φ (°)	31.9701, 46.9721
Type	Refractor
D (mm)	180
F (mm)	2500
CCD	Apogee Alta AI-F8300
Size (pix)	3326 x 2504
Pixels, (μm^2)	5.4x5.4
Scale (arcsec/pix)	0.45"/px
FOV (arcmin)	25'x25'
Exposure (dec=0°, s)	100
Filter Weal	FL-CFW-2-7
Filters	AN-R-50R, AN-V-50R AN-B-50R

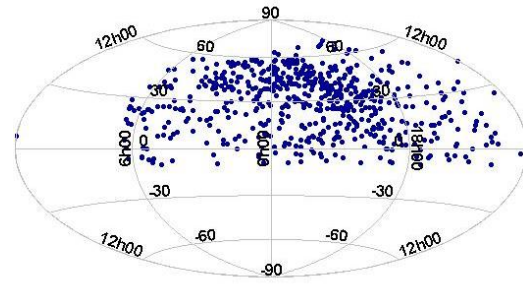


Figure 1: Distribution of the observations over celestial sphere.

3. Measurements

We carried out all astrometric reductions with the “Astrometrica” software (<http://www.astrometrica.at>). The root mean square errors of the differences (O - C), where O - obtained equatorial coordinates, C – Gaia DR2 equatorial coordinates, of the stars up to 16^{mag} in R-band (with N_{obs} >=3) were **0.12**” in right ascension and **0.11**” in declination. It should be noted that here we used astrometric reductions mainly for confident identification of program objects and obtaining exact values of the image orientation angle regarding the celestial equator for further measurements of the parameters of the mutual configuration of the investigated components. The measurements of position angles and separations were made with REDUC software (<http://www.astrosurf.com/hfosaf/reduc>), according standard processing procedure. The final array of measurements includes values of positional angle, separation, difference magnitude, magnitude difference, number of observations for all pairs of the WDS system and known notes about link. The example of table with measurement results for selected pairs presented in Tab.2. Column 3, 4, 5 with adding exact observational epoch will send to WDS database. Information from Stelle Doppie web-resource (<https://www.stelledoppie.it>) about nature of link between components based on their proper motions, is given at last column in Tab.2, where G means gravitationally bounded double, U- nature of this double is uncertain, N – optical double.

Table 2: Measurements of the selected WDS systems

WDS	Pair	PA, °	Sep, "	dMag, mag	N	Link
00318+3658	AB*	-	-	-	23	G
	AC	165.4	31.5	2.9	13	U
	AD	174.4	43.6	1.3	16	N
	BD*	-	-	-	11	N
02157+1046	CD	195.7	13.5	1.6	12	N
	AB	236.2	14.5	0.4	34	G
	AC	275.3	71.9	2.4	16	U
	AE	5.1	174.6	1.1	14	U
03325+5420	BE	8.6	184.0	0.7	13	U
	AB	1.2	20.5	2.1	7	U
	AC	319.9	26.6	2.5	7	N
05519+4844	BC	269.7	17.4	0.3	7	N
	AB	316.4	9.0	1.2	17	G
	AD	259.8	116.7	0	16	G
22105-0251	BC	307.7	32.9	1.9	9	U
	AB	4.0	51.1	1.2	8	U
	AC	94.8	51.1	0.5	9	U
	BC	139.4	72.6	0.8	8	U

*- not measured

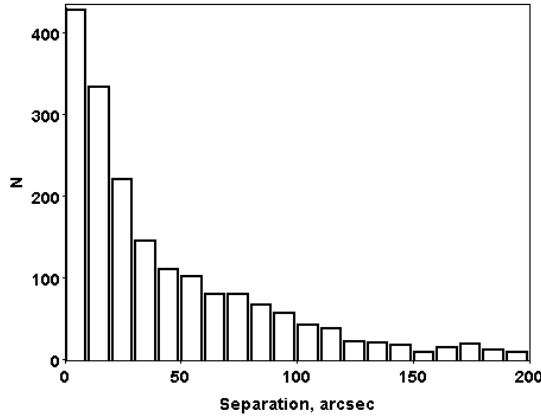


Figure 2: Distribution of the angular separation for all pairs of our observations.

There are several reasons why direct measurements of the mutual configuration parameters from astrometric CCD observations are impossible. The main star is often too bright and its image is oversaturated, some of the components in the systems under study had too weak magnitudes for the instrument. In general direct measurements were possible only for pairs with separation which at least exceeds 3 FWHM (in case of the AMC the mean FWHM is about 3"). The distribution of the angular separation for our observations is presented in the Fig.2.

As could be seen from the Fig.2, significant part of components is not available for direct measurements. In our opinion a large number of known pairs with a low angular resolution suggest that some stars from double and multiple systems may have invisible undiscovered components. Statistical method for detecting and searching of the invisible components of stars was proposed Wielen (Wielen, et al., 1999) back in the 90s. These stars are called delta- μ binaries. The method is based on the comparison of proper motions of stars obtained for various time intervals and the assumption that the movement of its photo center for a sufficiently long period of time is not linear but wavy for a binary system with an invisible companion. If the normal practice of obtaining proper motions by ground based observations is based on observations with the difference of epochs of 20–50 years or more, the proper motions obtained with the Hipparcos and Gaia DR2 space catalogs can be considered within this methodology as instantaneous. For a long time, the main limitation of this method was the insufficient accuracy of long-term averaged proper motions. For a now there are some catalogs with accuracy proper motions like Tycho2 (Hog et al., 2000) and UCAC4 (Zacharias et al., 2013) catalogs. In addition the appearance of high-precision space catalog Gaia DR2 made possible to calculate high precision long term averaged proper motions for Hipparcos stars on 24 years difference epoch. Search secondary object for nearby stars based on anomaly between the long-term proper motion vector and the Gaia DR2 (or Hipparcos) measurements was performed by Kervella (Kervella et al., 2019). These calculations are in the Strasbourg database and may be available for wide use. Perhaps this is the most accurate averaged proper motions, but unfortunately only for Hipparcos catalog stars. In this study we used proper

motions and their errors from Tycho2 catalog primarily and then UCAC4. The Gaia DR2 parallax, proper motions, averaged long term proper motions from UCAC4 and Tycho 2 catalogs and their errors are presented in Tab.3 for all stars that included in selected WDS system. The last column of Tab.3 contains value F -criteria calculated as :

$$F = \sqrt{\left(\frac{\Delta\mu_{RA}}{\varepsilon_{\Delta\mu_{RA}}}\right)^2 + \left(\frac{\Delta\mu_{DEC}}{\varepsilon_{\Delta\mu_{DEC}}}\right)^2}$$

where $\Delta\mu_{RA}, \Delta\mu_{DEC}$ are corresponding differences between long term and instantaneous proper motions, while $\varepsilon_{\Delta\mu_{RA}}, \varepsilon_{\Delta\mu_{DEC}}$ are errors of their determination.

Stars with a value criteria $F > 2.49$ were considered as $\Delta\mu$ -double candidates with a 95% probability.

3.1. WDS 00318+3658

There are 5 entries for 4 stars of the system in WDS catalog. The separation between A and B component is 6.8" and this is reason we can't measure B component from our images. The main star is 2509 Hipparcos. The Gaia DR2 parallaxes confirm that A and B stars are gravitationally bounded pair while C component doesn't bound with them. C component have significantly different parallaxes and radial velocity. F – values for stars of the WDS 00318+3658 system doesn't show possible invisible companion in them.

3.2. WDS 02157+1046

The system includes 4 entries. Common proper motions and parallaxes indicate that pair AB is a physical binary system only. Despite star C is included in Tycho Double Star Catalogue (Fabricius et al., 2002) proper motions and parallax star C significantly different, which makes it unlikely that star C belongs to the AB system. The belonging of the star E to the system remains uncertain since there are no proper motions and parallax data for the star in the Gaia DR2 catalog.

3.3. WDS 03325+5420

Apparently there are no physically connected pairs in this system; large value F for star C could indicate the presence of invisible satellite. There is a weak object at a distance of 0.2" from star C in the Gaia DR2 catalog. Unfortunately with no information about parallax and proper motions of this star and bad accuracy averaged proper motions of the star C, this this conclusion remains uncertain.

3.4. WDS 05519+4844

There are 4 stars and 3 entries for this system in WDS catalog. Stars A, B, D form triple system, star C is not included there.

3.5. WDS 22105-0251+5420

According Gaia DR2 data star B and star C could be physical pair, but they have different radial velocities. Star B also have large value F parameter that could be point on presence invisible satellite near to this star.

Table 3: Measurements of the selected WDS systems

	Gaia DR2						Long-term data					
	Plx, mas	ϵ , mas	PMRA, mas/year	ϵ , mas/year	PMDE, mas/year	ϵ , mas/year	PMRA, mas/year	ϵ , mas/year	PMDE, mas/year	ϵ , mas/year	Source	F
00318+3658												
A	5.02	0.06	-15.0	0.1	4.4	0.1	-15.8	2.2	8.0	2.1	Tycho2	1.73
B	5.00	0.05	-14.8	0.1	4.0	0.1	-14.9	2.5	4.2	2.5	UCAC4	0.08
C	1.03	0.10	-16.0	0.1	-6.9	0.2	-10.3	3.0	-3.0	3.1	UCAC4	2.27
D	2.37	0.06	19.6	0.1	-1.6	0.2	17.5	3.3	-5.2	3.2	Tycho2	1.28
02157+1046												
A	9.89	0.04	59.6	0.1	-65.6	0.1	58.9	0.9	-66.5	1.0	UCAC4	1.23
B	9.91	0.04	61.1	0.1	-70.9	0.1	60.2	1.0	-71.4	1.4	UCAC4	0.95
C	2.30	0.05	32.8	0.1	-14.8	0.1	31.3	1.7	-14.1	1.3	UCAC4	1.03
E*	5.30	0.25	53.3	3.6	-31.3	1.2	54.7	0.7	-30.0	1.7	UCAC4	0.75
03325+5420												
A	2.25	0.04	15.7	0.1	-5.0	0.1	13.1	1.9	-4.7	1.9	Tycho2	1.37
B	0.46	0.21	-0.6	0.4	-0.1	0.4	6.1	4.9	3.0	1.9	UCAC4	2.10
C	0.96	0.02	1.3	0.1	-3.1	0.1	-7.7	9.2	1.6	2.1	UCAC4	2.44
05519+4844												
A	1.45	0.06	2.0	0.1	-6.4	0.1	3.8	1.7	-7.8	1.7	Tycho2	1.34
B	1.38	0.19	3.3	0.3	-6.7	0.2	3.3	1.6	-9.6	1.5	Tycho2	1.91
C	2.06	0.04	18.2	0.1	-42.5	0.1	16.6	61.4	-39.6	2.0	UCAC4	1.45
D	1.65	0.05	6.4	0.1	-7	0.1	6.6	1.3	-7.0	1.3	Tycho2	0.15
22105-0251												
A	7.65	0.17	68.4	0.2	6.6	0.2	71.0	2.3	5.6	2.5	Tycho2	1.19
B	0.43	0.08	4.3	0.1	-5.8	0.1	15.0	1.8	-3.4	2.5	UCAC4	6.71
C	0.62	0.10	4.7	0.1	-4.5	0.1	4.4	1.2	-2.8	2.5	UCAC4	0.72

* - Hipparcos data

4. Conclusion

Star masses are the key for understanding of the stars and star systems (their birth, evolution and death), therefore regular observations of binary and multiple stars are very important for enlargement observed arc orbit and small ground-based telescopes can be used for this purpose. New positional data (separation, positional angle) were obtained from CCD observations with AMC of RI MAO. Observational data will be sent to the coordinators of the WDS catalog and include to the general database.

The question of the reliability of the existence of gravitational link between the system component is the main one in the study of binary and multiple systems. Combination of the precise astrometric data from Gaia DR2 catalog with similar data from modern astrometric catalogs (Hipparcos and Tycho, Tycho-2, UCAC2, 4) with other observational epoch allow us to clarify the composition of known systems. The search for probable nearby invisible component in multiple systems using the method checking differences between instantaneous Gaia DR2 proper motions and averaged long-term proper motions was conducted.

Acknowledgements. The authors are grateful to colleagues who have taken part in observations of WDS double and multiple systems: M. Kulichenko, M. Kaliuzhnyi, V. Kryuchkovskiy, D. Bodryagin, F. Bushuev, I. Osadchuk.

References

- Astromerica, [on-line resource]. Available at: <http://www.astromerica.at>
- Bodragin D.V., Bondarchuk, L. Ye., Maigurova N.V.: 2017, *Sci. Innov.*, **46**.
- Bodragin D. V., Bondarchuk, L. Ye.; Maigurova, N. V.: 2016, *JDSO*, **320**.
- Bodryagin D., Maigurova N.: 2015, *Odessa Astron. Publ.*, **28**, 163.
- Fabricius C., Høg E., Makarov V.V.: 2002, *A&A*, **384**, 180.
- Gaia Collaboration: 2018, *A&A*, **616**, 1.
- Hog E., Fabricius C., Makarov V.V. et.al.: 2000, *A&A*, **355**, L27.
- Kervella P., Arenou F., Mignard F. et.al: 2019, *A&A*, **623**, 72.
- Maigurova N.V., Protsyuk Yu.I., Bondarchuk L.E.: 2018, *Odessa Astron. Publ.*, **31**, 220.
- Mason B.D., Wycoff G.L., Hartkopf W.I.: 2001, *AJ*, **122**, 3466.
- REDUC software, [on-line resource]. Available at: <http://www.astrosurf.com/hfosaf/reduc>
- Sixth Catalog of Orbits of Visual Binary Stars, [on-line resource]. Available at: <https://www.usno.navy.mil/USNO/astrometry/optical-IR-prod/wds/orb6>
- Stelle Doppie [on-line resource]. Available at: (<https://www.stelledoppie.it>)
- Zacharias N., Finch C.T., Girard T.M. et al.: 2013, *AJ*, **145**, 44.
- Wielen R., Dettbarn C., Jahreiss H. et al.: 1999, *A&A*, **346**, 675.

DOI:<http://dx.doi.org/10.18524/1810-4215.2019.32.182230>

COMPARISON OF THE RESULTS OF PROCESSING OF CCD OBSERVATIONS OF SELECTED OPEN CLUSTERS

Yu.I. Protsyuk¹, O.M. Kovalchuk¹, V.M. Andruk^{1,2}

¹Research Institute “Mykolaiv Astronomical Observatory”, Mykolaiv, Ukraine,
yuri@mao.nikolaev.ua

²Main Astronomical Observatory NASU, Kyiv, Ukraine

ABSTRACT. Observations of open clusters at the Research Institute “Mykolaiv Astronomical Observatory” (RI MAO) were performed using the KT-50 telescope (D=500mm, F=3000mm) in 2011 – 2018. As the light receiver, a CCD camera Apogee Alta U9000 (3K x 3K, FOV 42.6' x 42.6') in short drift scan mode was used. In short drift scan mode each observation consisted of several CCD frames with partial overlap in right ascension. All observations were performed using R light filter. The exposure time was 20 seconds for all frames. All previous astrometric processing was carried out by the Astrometrica program and UCAC4 reference catalog. Using this data we received two catalogs of positions of 4.2 million stars (J2013.6) and 3.3 million stars (J2017.3) in the vicinity of open clusters with accuracy (0.03-0.07)". Unfortunately, current version of Astrometrica program have problem with data reduction with Gaia reference catalog in areas with big star density, like vicinity of open clusters near the plane of the Galaxy. At this article, we compared our old results with the new one for several open clusters which carried out with the author's set of programs with primary processing in the MIDAS environment. As reference stars the Tycho2, UCAC4 and Gaia DR2 catalogs were used. The reduction of 548 frames was performed using a polynomial of the third degree. The results obtained by author programs with reference catalogs UCAC4 and Gaia, showed good convergence. Several catalogs of positions of stars up to 17.5^m was obtained. The accuracy of the catalogs is $\sigma_{RA}=0.027''$ and $\sigma_{Dec}=0.033''$ for Gaia reference catalog and $\sigma_{RA}=0.032''$ and $\sigma_{Dec}=0.036''$ for UCAC4 reference catalog. At the same time, the accuracy of intraframe processing with the Gaia reference catalog turned out to be near 2 times better than the analogous one with the UCAC4 catalog. The comparison showed the possibility of receiving more good results with Gaia reference catalog.

Keywords: Astrometry – Open clusters – Data analysis – catalogs

АБСТРАКТ. Спостереження площадок з розсіяними скупченнями в Науково-дослідному інституті «Миколаївська астрономічна обсерваторія» (НДІ МАО) були виконані за допомогою телескопа КТ-50 (D = 500 мм, F = 3000 мм) у 2011 – 2019 рр. В якості приймача світла використовувалась ПЗЗ-камера Apogee Alta U9000 (3K x 3K, FOV 42,6 'x 42,6') в режимі вкороченого переносу заряду. У режимі вкороченого

переносу заряду кожне спостереження складалося з декількох ПЗЗ-кадрів з частковим перекриттям по прямому піднесенню. Всі спостереження проводилися з використанням світлового фільтра R. Час витримки складав 20 секунд для усіх кадрів. Вся попередня астрометрична обробка проводилася програмою Astrometrica в системі опорного каталогу UCAC4. Користуючись цими даними, ми отримали два каталоги положень 4,2 млн зірок (J2013,6) та 3,3 млн зірок (J2017,3) в площадках навколо розсіяних скупчень з точністю (0,03-0,07)". На жаль, поточна версія програми Astrometrica має проблеми з обробкою даних з опорним каталогом Gaia у площадках з великою зірковою щільністю, як-от поблизу розсіяних скупчень біля площини Галактики. У цій статті ми порівняли наші старі результати з новими для кількох розсіяних скупчень, які проводилися авторськими програмами з первинною обробкою в середовищі MIDAS. В якості опорних зірок використовувались каталоги Tycho2, UCAC4 та Gaia DR2. Редукцію 548 кадрів було виконано за допомогою полінома третього ступеня. Результати, отримані авторськими програмами з опорними каталогами UCAC4 та Gaia, показали хорошу збіжність. Отримано кілька каталогів положень зірок до 17,5^m. Точність каталогів становить $\sigma_{RA} = 0,027''$ і $\sigma_{Dec} = 0,033''$ для опорного каталогу Gaia і $\sigma_{RA} = 0,032''$ і $\sigma_{Dec} = 0,036''$ для опорного каталогу UCAC4. У той же час, точність внутрішньої кадрової обробки з опорним каталогом Gaia виявилася майже в 2 рази кращою, ніж аналогічна з каталогом UCAC4. Проведене порівняння показало можливість отримання більш хороших результатів з використанням опорного каталогу Gaia.

Ключові слова: Астрометрія – Розсіяні скупчення – Аналіз даних – Каталоги

1. Introduction

Observations of open clusters at the Research Institute “Mykolaiv Astronomical Observatory” (RI MAO) were performed using the KT-50 telescope (D=500mm, F=3000mm) in 2011 – 2018 and were obtained near 35000 CCD frames. As the light receiver, a CCD camera Apogee Alta U9000 (3K x 3K, FOV 42.6' x 42.6', scale 0.83"/pixel) in short drift scan mode was used (Apogee Alta CCD Camera, 2018). In short drift scan mode each observation consisted of several CCD

frames with partial overlap in right ascension. All observations were performed using R light filter. The exposure time was 20 seconds for all frames. For this work we took observations of 7 open clusters (NGC884, NGC1039, NGC1245, NGC1528, NGC1545, NGC2420 and NGC2682) obtained in 2011-2017. All open cluster observed several times in different date. Each observation have from 4 to 9 CCD frames in depend on declination. Also, all this open clusters were observed in 2018 at the Maidanak Observatory with the Zeiss-1000 telescope (Protsyuk et al., 2018). All previous astrometric processing of our data was carried out by the Astrometrica program (Raab, 2018) and UCAC4 (Zacharias et al., 2013) reference catalog. Using this data we received two catalogs of positions of 4.2 million stars (J2013.6) and 3.3 million stars (J2017.3) in the vicinity of open clusters with accuracy (0.03-0.07)". In this work we repeated data reduction of selected open clusters with the Astrometrica program and Gaia DR2 (Gaia Collaboration, 2018) reference catalogs and the author's set of programs with primary processing in the MIDAS environment (Andruk et al., 2005; 2017; Protsyuk et al., 2014a, 2014b) and different reference catalogs. This software was created to process images that are part of the Ukrainian Virtual Observatory (Vavilova et al., 2012; 2017).

2. Data reduction

The reduction of 548 CCD frames was performed using a polynomial of the third degree. As reference stars in our programs the Tycho2, UCAC4 and Gaia DR2 reference catalogs were used. With Astrometrica program we used Gaia DR2 reference catalogs. Unfortunately, current version of Astrometrica program have problem with data reduction with Gaia reference catalog in areas with big star density, like vicinity of open clusters near the plane of the Galaxy. So, for several open clusters we limited magnitude of Gaia catalog to 14.5^m or 15.5^m in Astrometrica to make reduction (Fig. 1).

The results in scale obtained by author programs with all reference catalogs, showed good convergence (Fig. 2). Integrated star catalog of positions for all plates upto 17.5^m was obtained by author's programs. The accuracy of the catalog in UCAC4 system is $\sigma_{RA}=0.040''$ and $\sigma_{DEC}=0.046''$. The accuracy of the catalog in Gaia system is $\sigma_{RA}=0.037''$ and $\sigma_{DEC}=0.042''$ (Fig. 3). The accuracy of single observation is shown in Tab. 1. Astrometrica not good yet with Gaia reference catalog in all frames.

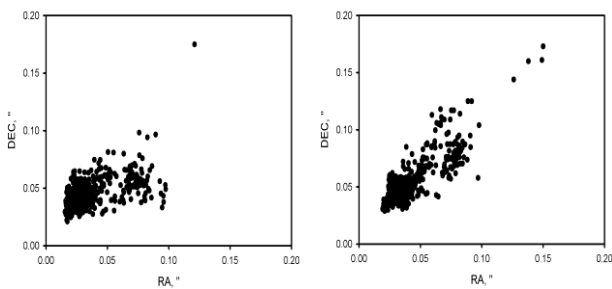


Figure 1: Root mean square (RMS) errors of intra-frame reduction with Gaia limited magnitude 14.5 (left) and 16.5 (right)

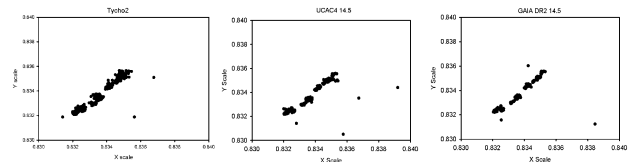


Figure 2: Scale values distribution for all CCD frames depending on the reference catalog Tycho2, UCAC4, Gaia DR2

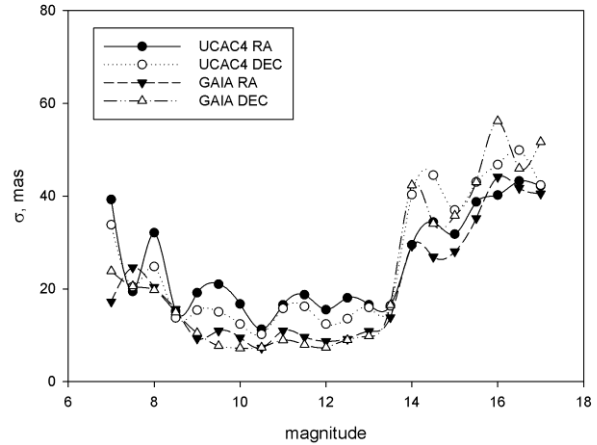


Figure 3: Distribution of our catalogs accuracy from magnitude for reference UCAC4 and Gaia

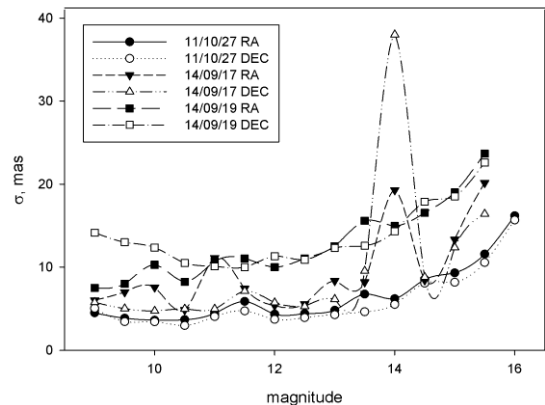


Figure 4: Distribution of inner accuracy in mas for NGC1545, observed in three dates, after processing with reference catalog Gaia DR2

Not so good accuracy near 14 magnitude is explained by some influence from bad columns in CCD matrix in several dates. Weather conditions in different nights also have influence to accuracy. Examples for three dates of NGS1545 observation which reduced with Gaia reference catalog are shown on Figure 4.

At the same time, the inner accuracy of intraframe processing with the Gaia DR2 reference catalog turned out to be 2-3 times better than the analogous one with the UCAC4 catalog. Example for NGC1545 observed at 2011/10/27 shown on Fig.5. Middle RMS for this open cluster at this date is 7 mas for reduction with Gaia and 17 mas with UCAC4. This result obtained from 2000 stars in vicinity of open cluster which were observed approximately 20 times per night.

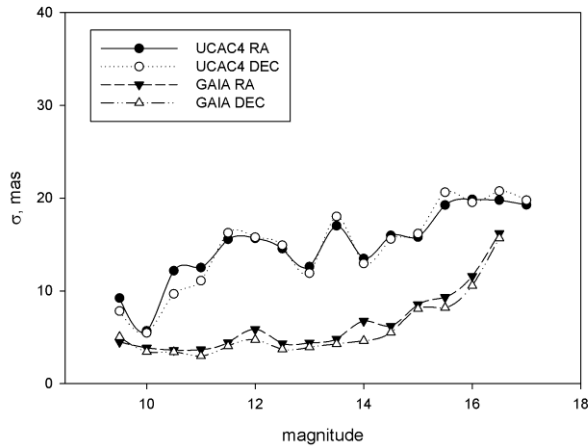


Figure 5. Distribution of RA/DEC inner accuracy in mas of processing of NGC1545 at 2011/10/27 with the reference catalogs UCAC4 and Gaia DR2

Table 1: Comparison of the accuracy of single observation with different software reductions

Software	Ref.cat	N ref. stars	N stars	RA, mas	DEC, mas
Astrometrica	UCAC4	28816	44157	90.5	93.5
Astrometrica	Gaia	11355	58202	131.8	139.2
Author's	UCAC4	-	23441	82.3	91.0
Author's	Gaia	-	23314	71.9	84.9

Table 1 show the number of reference stars, number of stars in received catalogs and accuracy of single observation for this catalogs. Astrometrica found more objects but overall accuracy with Gaia catalog worse. Despite the greater accuracy of intraframe processing with Gaia reference catalog (Fig.5) we obtained a slight improvement in the accuracy of the resulting catalogs for the Gaia reference catalog. This is due to the different quality of observations on different nights and a rather significant random error.

3. Conclusion

The processing of observations with new reference catalog GaiaDR2 gives significantly better results with our software. To further improve the result, we need to pre-filter images before processing in MIDAS software. The high accuracy of intraframe processing with the Gaia reference catalog shows great potential for further improving the accuracy of our catalogs.

References

- Andruk V.M., Pakuliak L.K., Golovnia V.V. et al.: 2017, *Science and Innovation*, **13(1)**, 17.
- Andruk V.M., Vidmachenko A.P., Ivashchenko Yu.M.: 2005, *Kinem. Phys. Cel. Bodies., Suppl.* **5**, 544.
- Apogee Alta CCD Camera, [online] Available at: (<https://optcorp.com/products/apogee-alta-f9000-d07-mono-chrome-ccd-camera>).
- Gaia Collaboration: 2018, *A&A*, **616**, A14.
- Protsyuk Yu.I., Martynov M.V., Mazhaev A.E. et al.: 2014, *Kinem. Phys. Cel. Bodies.*, **30, N6**, 296.
- Protsyuk Yu.I., Andruk V.M., Kazantseva L.V.: 2014, *Odessa Astron. Publ.*, **27**, 59.
- Protsyuk Yu. I., Shukhratov Sh. Sh., Kovalchuk O. M. et al.: 2018, *Odessa Astron. Publ.*, **31**, 231.
- Raab H., Astrometrica, [online] Available at: (<http://www.astrometrica.at/>).
- Relke E., Protsyuk Yu.I., Andruk V.M.: 2015, *Odessa Astron. Publ.*, **28**, 211.
- Vavilova I.B., Pakulyak L.K., Shlyapnikov A.A. et al.: 2012, *Kinem. Phys. Cel. Bodies.*, **28, N4**, 85.
- Vavilova I.B., Yatskiv Ya.S., Pakuliak L.K. et al: 2017, *IAUS*, **325**, 36.
- Zacharias N., Finch C.T., Girard T.M. et al.: 2013, *Astron. J.* **145**, 44.

DOI:<http://dx.doi.org/10.18524/1810-4215.2019.32.181731>

THE RE-PROCESSING RESULTS OF PHOTOGRAPHIC OBSERVATIONS OF ASTEROIDS WITH GAIA CATALOG AT THE MAO NAS OF UKRAINE

S.V. Shatokhina¹, L.V. Kazantseva², V.M. Andruk¹

¹Main Astronomical Observatory of National Academy of Sciences,
27 Akad. Zabolotnogo St., 03680, Kyiv, Ukraine, svetash@mao.kiev.ua

²Taras Shevchenko National University of Kyiv, Astronomical Observatoty,
Kyiv, Ukraine, kazl@ukr.net

ABSTRACT. In total, about 4,500 asteroid positions were determined from photographic observations conducted at the MAO NAS of Ukraine in 1952-1996. These are the early positions of the selected minor planets, mostly bright, the observations of which were initiated by the founders of the ORBITA observational program and were made in 1952-1986. The second later positions of asteroids obtained from digitized plates from photographic observations of the Northern Sky Survey project in 1981-1996.

Using digital plate processing technologies, 2292 asteroid positions were obtained, the images of which were fixed during observations and identified during processing. The new star catalog Gaia DR2 was used to study changes in determining the accuracy of equatorial coordinates for various faint objects on plates. For several 8 plates with images of Pluto comets and faint asteroids of particular interest due to the lack of observations in the past, new complete processing of scans of these plates was performed. The Gaia DR2 was used as a reference catalog.

The asteroid positions from early observations of 1952-1986 were determined in accordance with classical linear reduction algorithms. These are 1651 positions of minor planets determined in the PPM catalog system and obtained from observations with the Double Wide-Angle Astrograph. The remaining 591 positions were determined in the systems of old reference catalogs of stars Yale, SAO, AGK3, and obtained from observations with the Double Long-Focus Astrograph. It was for these positions that the calibration with the Gaia catalog was performed. The data on the positions of minor planets digitized from publications and additional data on their reference systems deposited in previous years at VINITI (now VINITI Database RAS) were used.

Comparison with JPL ephemeris was performed both for new determinations of asteroid coordinates with the Gaia catalog, and for past determinations obtained in systems of other reference catalogs.

Keywords: reference catalog, asteroids positions.

АНОТАЦІЯ. Загалом з результатів фотографічних спостережень, виконаних в ГАО НАНУ в 1952-1996 рр., визначено близько 4500 положень астероїдів. Це ранні положення вибраних малих планет, переважно

яскравих, спостереження яких були ініційовані засновниками програми ОРБИТА і виконані у 1952-1986 рр. Інші, більш пізні положення астероїдів отримані з оцифрованих платівок за спостереженнями Фотографічного огляду північного неба у 1981-1996 рр.

Із застосуванням цифрових технологій обробки платівок отримано 2292 положень астероїдів, зображення яких були зафіксовані на фотонегативах під час спостережень і ідентифіковані під час обробки. З метою вивчення змін при визначенні точності екваторіальних координат для різних слабких об'єктів на платівках був використаний новий зоряний каталог Gaia DR2. При цьому для декількох платівок із зображеннями Плутона, комет і слабких астероїдів, що представляють особливий інтерес за відсутності спостережень у попередні часи, було здійснено нову повну обробку сканів цих платівок. При цьому Gaia каталог використано в якості опорного.

Положення астероїдів ранніх часів спостережень обчислювались відповідно до класичних лінійних алгоритмів редукції. Це 1651 положень малих планет, визначених в системі каталогу PPM і отриманих за спостереженнями на телескопі ПША. Решта 591 положень визначені в системах старих опорних каталогів зірок Yale, SAO, AGK3 і отримані на телескопі ПДА. Для їх калібрування з каталогом Gaia використано оцифровані з публікацій дані про положення малих планет, а також додаткові дані щодо відповідних опорних систем, депоновані у попередні роки в ВІНІТІ (нині ВІНІТІ РАН).

Порівняння з ефемеридами JPL проведено як для нових визначень координат астероїдів з каталогом Gaia, так і для минулих визначень, отриманих в системах інших опорних каталогів.

Ключові слова: опорний каталог, положення астероїдів.

1. Introduction

Old astrometric observations are still in use in the astronomical research and collected in different databases. Observations made on a long interval of time are necessary to model the evolution of these objects and dynamical

study of Solar System objects. The recent availability of the Gaia Data Release 2 allows us to make a new reduction of old data and to get observations of the past with today's accuracy. Old observations have been reduced using reference star catalogs accurate from 100 up to 1000 mas. Besides, these catalogs were built with different reference frames. The Gaia reference star catalog can provide star positions accurate to one mas at the beginning of the XX-th century, allowing us to make a new and precise astrometric reduction of old observations. Moreover, these old observations will be reduced in the same reference frame than current ones. In the same way, photometric calibrations based on catalogs dating back by several decades, had a very low accuracy by modern standards. The Gaia photometric data will allow a new photometric reduction of old photographic plates.

To increase the accuracy of the coordinates of asteroids, comets, planets, and their satellites, we used the new star catalog Gaia DR2 for a new reduction of old photographic observations.

The influence of the various catalog reference system on the positions of asteroids obtained from photographic observations has been studied previously (Maigurova et al., 2017; Major et al., 1996; Protsyuk et al., 2016). According to these results the new processing of digitized images of some selected minor planets using modern reference catalogs of stars has led to a significant increase in positional accuracy compared to previous results.

2. Results

In total, about 4,500 asteroid positions were determined from photographic observations conducted at the MAO NAS of Ukraine in 1952-1996. These are the early positions of the selected minor planets, mostly bright, the observations of which were initiated by the founders of the ORBITA observational program and were made in 1949-1996 (Golovnya et al., 2001; Major et al., 1984; Onegina et al., 1970; Vasilenko et al., 1979). The second later positions of asteroids obtained from digitized photographic observations of the Northern Sky Survey project in 1981-1996 (Shatokhina et al., 2018).

Fig. 1 shows the time distribution for all positions of asteroids obtained from photographic observations at the MAO NASU. All early observations were made using two telescopes: the Double Long-Focus Astrograph (DLFA, 400/5500) in 1952-1986 and the Double Wide-Angle Astrograph (DWA, 400/2000) in 1976-1996. As a result of processing these observations using classical linear reduction algorithms, the positions of selected minor planets were determined. Various reference catalogs of stars were used.

591 positions of selected minor planets from observations on DLFA were determined in reference systems of catalogs Yale, SAO, AGK3. And 1651 positions of these planets from observations on DWA were determined in the PPM catalog system.

On the contrary, the later 2292 positions of asteroids obtained from the digitized observations of the FON project in 1981-1996 were determined using the modern Tycho-2 reference catalog of stars and non-linear algorithms for reduction calculations.

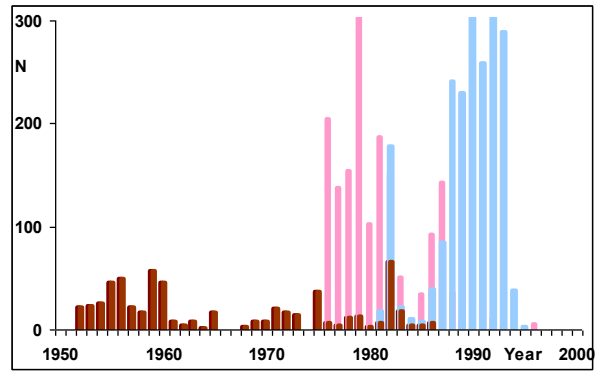


Figure 1: The distribution on time for all positions of asteroids received from photographic observations at the MAO NASU with DLFA and DWA (including FON observations).

Therefore, we examined two approaches to the re-processing of old observations using the Gaia catalog: 1) for digitized photographic plates of the FON project; 2) for non-digitized and previously processed oldest photographic observations in 1952-1986. The first results from that processing were presented.

2.1 New full processing of digitized images of plates with Gaia DR2 catalog

The first approach was a new full reprocessing of scans accumulated in the Joint Digital Archive of the Ukrainian Virtual Observatory. The Gaia catalog was used as a reference for obtaining optimal solutions in reduction algorithms. From the collection of observations of the FON project, plates with images of faint asteroids (7676) and (25467) of the particular interest for us were selected. In addition, 2 plates with images of comet 65P and 3 plates with images of Pluto were selected too. Their scans were obtained previously with the Epson commercial scanner with 1200 dpi resolution. The previous processing results of these scans with the Tycho-2 reference catalog were available too. Additionally, the scan of each plate was processed three times with the reference catalog of Gaia. Reference stars in each case were limited in magnitude to the 13^m, 14^m, and 17^m. As a model of coordinate reduction was a sixth-order polynomial.

As an example, for plate 56, the standard errors σ of determining the coordinates of stars for 4 independent processing options shown in Table 1. When the total number of reference stars on the plate was increased by faint stars up to 17 magnitudes, the mean square errors in determining the coordinates of the stars increased by more than 3 times compared to similar other processing options of this plate.

Table 1: The comparison results of scan processing with Tycho-2 and Gaia catalogs for plate GUA040C000056A

Pl=56, Reference catalog	N reference stars	σ_{RA} ,	σ_{Dec} ,	σ_B , mag
		arc sec	arc sec	
stars				
Tycho-2	1198	.13	.10	.11
Gaia 13-m	1958	.27	.25	.12
Gaia 14-m	3615	.14	.13	.11
Gaia 17-m	11301	.50	.49	.12

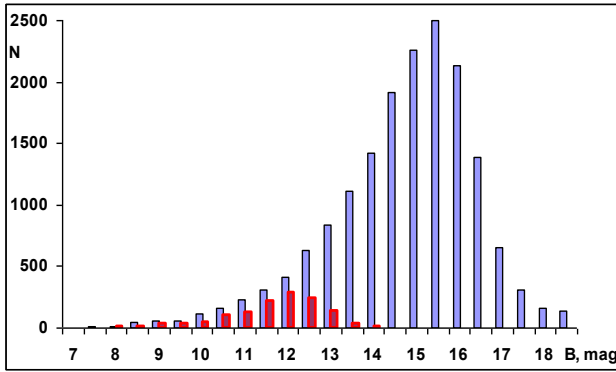


Figure 2: Distribution of 17 552 identified stars from Gaia DR2 (blue bars) and 1320 from Tycho-2 (rose bars) along B magnitudes on the plate № 56.

The coordinates of 17,552 stars from 7 to 18 magnitude obtained from plate processing were identified with the corresponding coordinates of the stars of the Gaia catalog (Fig. 2). For comparison, the same figure shows the number of stars identified with the stars of the Tycho-2 catalog.

Stars with absent proper motions and stellar magnitudes of the Gaia catalog were excluded from further analysis, as well as visually binary and triple stars. For the remaining 16,031 stars, individual differences O-C on both coordinates were formed, where the "O" values are the coordinates of the stars obtained from the plate, and the "C" values are their corresponding coordinates from the Gaia catalog at the observational moment. The mean O-C values and their root-mean-square (RMS) errors on both coordinates for B magnitudes intervals were determined and shown in Fig.3 (a,b,c,d).

In processing with Gaia 17-m the smallest mean O-C values (Fig.3a, Fig.3b) for all stars in each magnitudes interval were obtained. Besides, these values are most stable over the entire range of stellar magnitudes. In other processing options, mean O-C values differ systematically and randomly from the previous one. The trend line of the mean O-C difference values is especially pronounced in the RA coordinate.

Fig.3c, Fig.3d shows the RMS errors of the O-C values. Only processing from Gaia 17-m leads to the smallest and constant values of RMS errors of O-C on a wide range of magnitudes from 9 to 14. The results from processing from Gaia 14-m are the closest to similar results from Gaia 17-m. A large increase in RMS errors for all processing options is observed for stars fainter than 14-15 magnitudes.

Table 2: The O-C values for asteroids identified on plate 56 and processed with Tycho-2 and Gaia 17-m catalogs.

Asteroid	Mv	Tycho-2		Gaia	
		(O-C), RA, arcsec	(O-C), Dec, arcsec	(O-C), RA, arcsec	(O-C), Dec, arcsec
6	9.87	.61	.36	-.08	.31
87	12.49	-.61	.45	-.50	.76
414	14.76	-.20	-.35	.23	.00
521	13.10	.04	1.08	-.39	1.40
567	13.31	-.59	.44	.30	.31
859	14.83	.05	1.05	-.07	.77
3754	14.53	-1.19	.15	-2.27	.52
6325	15.72	-3.24	.06	-3.16	.45
7676	15.84	-3.20	2.16	-3.02	2.57

In addition to studying the accuracy of determining the coordinates of stars for different stellar magnitudes intervals, we compared the coordinates of asteroids identified on this plate for four plate processing options. To determine the O-C of asteroids, comets and Pluto we used ephemeris from JPL NASA (<https://ssd.jpl.nasa.gov/?horizons>). The results for nine asteroids identified on plate 56 and processed with Tycho-2 and Gaia 17-m catalogs presented in Table 2. The O-C values have changed but remained still large for faint asteroids with asteroid's apparent visual magnitudes M_v equal to 15^m.

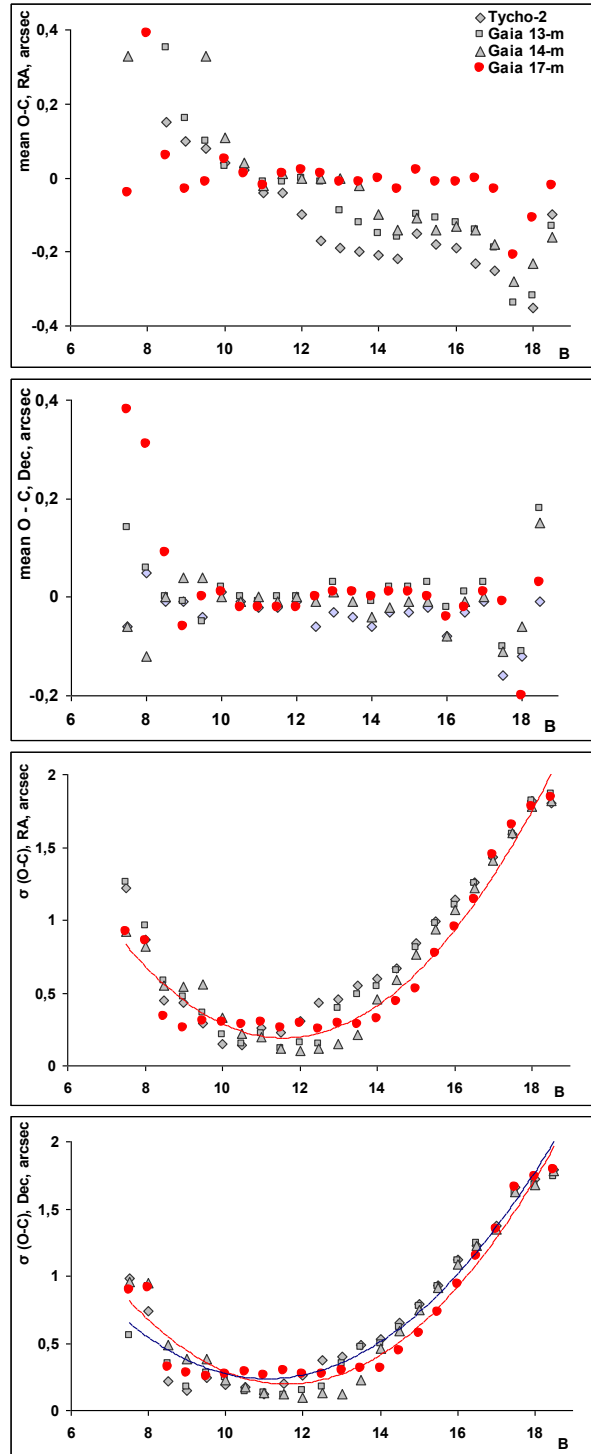


Figure 3(a,b,c,d): Mean O-C coordinate differences for 16,031 stars and their RMS errors in RA, Dec plotted against B magnitudes intervals for four processing options: Tycho-2, Gaia 13-m, Gaia 14-m, Gaia 17-m.

2.2 Processing of non-digitized oldest photographic observations in 1952-1986 with the Gaia catalog

For the earliest observations of minor planets, plate measurements and the results of their processing were not preserved. But, in addition to the positions of minor planets, detailed information about the reference catalog, reference stars for reduction calculations, their coordinates and dependences has been preserved. The publication of such additional data on the positions of selected minor planets was envisaged by the founders of the ORBITA observational program for their repeated reprocessing with other reference catalogs. But without the availability of these data in digital formats and the use of online Internet services to search for stars in catalogs in Strasbourg astronomical Data Center (<http://cdsweb.u-strasbg.fr>), this work did not seem real. Now it can be done quickly and easily.

Therefore, to re-process such observations with the Gaia catalog, we decided to use another approach. It was as follows. New positions of minor planets were obtained by adding the corresponding coordinate differences of the reference stars in two reference catalogs, weighted by the values of the dependencies. Note that earlier such observations of minor planets were processed using linear methods of reduction calculations. Therefore, our approach to calibrating the positions with the Gaia catalog data is identical to the new complete re-processing of these observations.

Comparison with JPL ephemeris was performed both for new determinations of asteroid coordinates with the Gaia catalog, and for past determinations obtained in reference systems of other catalogs.

Fig. 4 shows the comparison results for 60 positions of Ceres and 57 positions of Pallas. For each from them, the O-C calculated in reference systems of Gaia, Tycho-2 and other catalogs (Yale, SAO, AGK3). Differences of the type “original catalog minus Gaia” and “Tycho-2 catalog minus Gaia” were formed for each of the two O-C values calculated from the positions of the asteroid in two reference catalog systems.

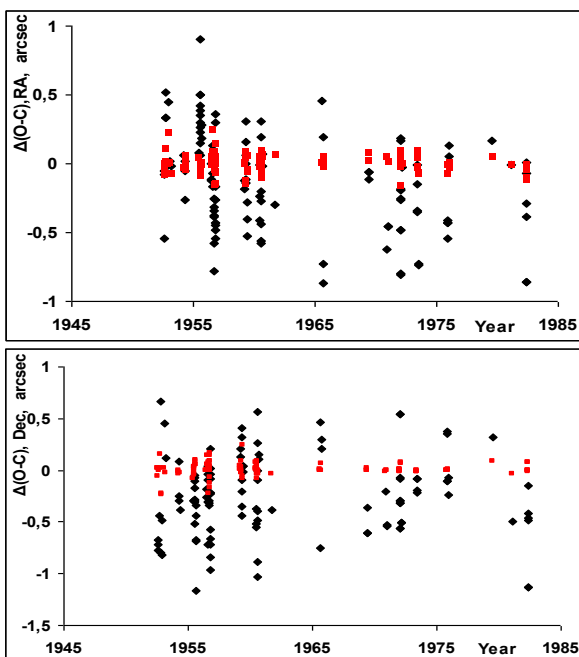


Figure 4: Individual differences between the two O-C values for each two asteroid positions that were determined in two catalog systems: Original catalog and Gaia (black markers) or Tycho-2 and Gaia (red markers) (top – on coordinate RA, below – on coordinate Dec).

The values of O-C for the asteroid positions in the Gaia catalog system are almost identical to the similar values in the Tycho-2 catalog system. But at the same time, these values differ significantly from the O-C in the systems of the previous original catalogs Yale, SAO, AGK3.

3. Conclusion

The main idea was to find ways to improve the accuracy of coordinates for faint asteroids of 14^m–16^m and for observations of small bodies of the solar system with epoch differences of more than 50 years and processed using various reference catalogs of stars. And as an additional result, a complete catalog of all the positions of asteroids from photographic observations at MAO NASU was compiled.

According to the re-processing of digitized images of several plates with the Gaia DR2 catalog, the most optimal solution was processing with the inclusion of all stars up to 17 magnitudes in the reference system. The systematic component of the error in determining the coordinates has become minimal and stable over a wide range of stellar magnitudes. For faint objects, the random component of the coordinate error is still large and amounts to about 1 arc second. A possible reason for this may be, first of all, insufficient exposure of the plates to reliably determine the coordinates of faint objects.

According to published data, a catalog of 591 positions of selected minor planets obtained from observations with the DLFA telescope in 1952-1986 was collected. It is part of a complete catalog of all asteroid positions obtained from photographic observations at the MAO NASU.

Experience in calibrating the positions of the bright selected minor planets in the Gaia and Tycho-2 catalog systems showed that no significant differences in the coordinates of the asteroids were found. But compared with the old reference catalogs Yale, SAO, AGK3, the differences in the coordinates of the asteroids are great both in the random and in the systematic component. It should be noted that the reference stars on each plate were bright stars from only 8 to 11 magnitudes, which could have an effect on the conclusion obtained.

It is necessary to conduct additional studies on different observational material about the influence of the use of the Gaia catalog as a reference on the coordinates of celestial objects.

References

- Gaia collaboration: 2016, *A&A*, **595**, A1-A7, A133.
 Golovnya V., Major S.: 2001, On-line Data Catalog: DBGPA 3/05. publ. in: gua.db.ukrvo.org/starcatalogs.php?whc=asteroids
 Maigurova N.V., Chernetenko Yu.A., Kryuchkovskiy V.F.: 2017, *Science and Innovation*, **13**, N1, 69.
 Major S.P., Moroz G.V.: 1984, *Astrometria i astrofizika*, **51**, 69.
 Major S.P., Shatkhina S.V.: 1996, *Kinematics Phys. Celest. Bodies*, **12**, N4, 64.
 Onegina A.B., Zaslavskaya S.A.: 1970, *Byull. Inst. Teor. Astron.*, **12**, 434.
 Protsyuk Yu., Maigurova N., Protsyuk S. et al.: 2016, *Odessa Astron. Publ.*, **29**, 147.
 Shatkhina S.V., Kazantseva L.V., Yizhakevych O.M. et al.: 2018, *Kinem. Phys. Cel. Bodies*, **34**, N5, 270.
 Vasilenko N.A., Demenko I.M.: 1979, *Byull. Inst. Teor. Astron.*, **14**, N8, 499.

DOI:<http://dx.doi.org/10.18524/1810-4215.2019.32.181732>

ON THE “SOLAR SYSTEM BODIES” ASTROPLATE PROJECT OF THE UKRAINIAN VIRTUAL OBSERVATORY

S.V. Shatokhina¹, O.M. Yizhakevych¹, Yu.I. Protsyuk³, L.V. Kazantseva²,
L.K. Pakuliak¹, I. Eglitis⁴, H. Relke⁵, Q.X. Yuldoshev⁶, A.Sh. Mullo-Abdolv⁷, V.M. Andruk¹

¹ Main Astronomical Observatory of the National Academy of Sciences of Ukraine, Kyiv, Ukraine, svetash@mao.kiev.ua

² Taras Shevchenko National University of Kyiv, Astronomical Observatoty, Kyiv, Ukraine

³ Research Institute Mykolaiv Astronomical Observatory, Mykolaiv, Ukraine

⁴ Institute of Astronomy, University of Latvia, Riga, Latvia

⁵ Walter Hohmann Observatory, Essen, Germany

⁶ Ulugh Beg Astronomical Institute of the Uzbekistan Academy of Sciences, Tashkent, Uzbekistan

⁷ Institute of Astrophysics of the Academy of Sciences of the Republic of Tajikistan, Dushanbe, Tajikistan

ABSTRACT. The UkrVO Joint Digital Archive of astroplates and the newest digitized data processing services allowed us to form a new approach for the creation of catalogs of astrometric and photometric characteristics of the Solar System bodies. Given this, the main goal of this approach was not only to complete the processing with the best possible accuracy of high-quality and unprocessed earlier photographic observations of the Solar System bodies but also to find new original data from these observations.

As a result, more than 6,500 new astrometric positions and stellar magnitudes of asteroids, and 3,036 positions of outer planets (Pluto, Uranus, Neptune, Saturn, Jupiter) and their satellites have been determined. Most of the positions obtained from observations of large stellar surveys of the northern sky FON (Kyiv and Kitab parts) and other surveys (MEGA, Equatorial Catalog).

The number of new obtained positions of asteroids is comparable to the total number of all positions of asteroids obtained at the Main Astronomical Observatory of the NAS of Ukraine in 1949-1996. The accuracy of new positions is higher than in traditional determinations from photographic observations, but it cannot be comparable to the accuracy of modern CCD observations.

Contrary to traditional classic definitions, digitized images of plates have produced a large number of faint asteroids down to 17.5 magnitudes, which were discovered in the early 21st century. For some of them, observations are either completely absent or not enough over the certain time interval preceding the moments of their official discoveries. These data can be obtained from photographic observations only. Based on our observations, about 300 such asteroids were found. The collection of missing data on positions over certain time intervals and their analysis can be useful not only for modern ephemeris calculations but also for studying the evolution of asteroid orbits over time.

The cooperation between UkrVO and the observatory in Baldone of the University in Latvia, astronomical and astro-

physical institutes of Uzbekistan and Tajikistan make it possible to expand this work by involving numerous additional archives of digitized observations and processing services and thus obtaining new original data about the Universe.

Keywords: archives, catalog, positions, Solar System bodies

АНОТАЦІЯ. Об'єднаний цифровий архів фотографічних платівок UkrVO та новітні цифрові сервіси обробки даних дозволили сформувати новий підхід щодо створення каталогів астрометричних та фотометричних характеристик тіл Сонячної системи. З огляду на це основною метою такого підходу є не тільки завершення опрацювання якісних і необроблених раніше фотографічних спостережень тіл Сонячної системи з максимально кращою точністю, але й знаходження нових оригінальних даних з цих спостережень.

В результаті оцифрування фотоплатівок та сучасної обробки сканів було визначено понад 6500 нових астрометричних положень та зоряних величин астероїдів, 3036 положень зовнішніх планет (Плутон, Уран, Нептун, Сатурн, Юпітер) та їх супутників. Більшість з них отримані із довготривалих програм спостережень великих зоряних оглядів північного неба ФОН (Київська та Кітабська частини) та інших оглядів (МЕГА, Екваторіальний каталог).

Кількість отриманих нових положень астероїдів може бути порівняна із загальною кількістю всіх положень астероїдів, отриманих у Головній астрономічній обсерваторії НАН України у 1949-1996 роках. Точність нових положень вища, ніж точність класичних визначень координат з фотографічних спостережень, але вона не може бути порівняна з точністю сучасних ПЗЗ спостережень.

На відміну від традиційних класичних визначень, за цифровими зображеннями платівок отримано велику кількість положень слабких астероїдів до 17.5 зоряної

величини, які були відкриті на початку 21 століття. Для деяких з них спостереження зовсім відсутні або їх замало у певний часовий інтервал, попередній до їх офіційних відкриттів. Інформацію про це можна отримати тільки з фотографічних спостережень. За даними наших спостережень було знайдено біля 300 таких астероїдів. Накопичення даних про положення астероїдів у певні часові проміжки та їх аналіз може бути корисним не тільки для сучасних розрахунків ефемерид, але і для вивчення еволюції орбіт астероїдів.

Кооперація між UkrVO і Обсерваторією в Балдоне Університету в Латвії, астрономічними та астрофізичними інститутами Узбекистану і Таджикистану дають можливість розширити цю роботу, додаючи нові архіви оцифрованих спостережень і сервіси їх обробки і отримуючи, таким чином, нові оригінальні дані про Всесвіт.

Ключові слова: архіви, каталог, положення, тіла Сонячної системи

1. Introduction

The existing world databases of positional observations of the small bodies of the Solar System have a large number of photographic, modern CCD and satellite observations for these objects. Modern observations far exceed the previous ones in the accuracy of coordinates and number of positions, where new mathematical methods for the automated CCD images processing, positional frame-to-frame guidance and discovery of Solar system small bodies have a crucial role (see, for example, Savanevych et al., 2015; Savanevych et al., 2015; Savanevych et al., 2018).

However, we hope to find from digitized photographic archives those original observations that could be used in the solutions of modern kinematic and dynamic problems. By applying the methods of digitization of astronegatives developed by us, the subsequent processing of scans using the latest reference catalogs and methods, we can achieve the maximum accuracy of coordinates and magnitudes of objects. Using online Internet services, we can search, identify the necessary objects and perform a preliminary analysis of their obtained characteristics.

2. Main results

2.1. Catalogs of asteroid positions based on observations of the FON project

The results of processing of digitized plates from the Photographic Survey of the Northern Sky (the FON project) (Andruk et al., 2016; Pakuliak et al., 2016; Yuldoshev et al., 2017) contain not only the coordinates and magnitudes of stars, but also all objects that were fixed on these plates at the time of observations. They were used for a global search for small bodies of the Solar System on these plates (Golovnia et al, 2017; Kazantseva et al, 2015; Shatokhina et al, 2017; Vavilova et al, 2014). The identification is performed according to the coordinates and stellar magnitudes of asteroids, and the diameter and maximum intensity of the central pixel of the asteroid image are also taken into account. Ephemeris support of asteroids and comets at the moments of observation was

made by used from the online Internet service <https://ssd.jpl.nasa.gov/sbfind>. After identification the corresponding equatorial coordinates and B-magnitudes of asteroids from astronegatives of Kyiv and Kitab parts of the FON project were collected in catalogs (Shatokhina et al., 2018a; Shatokhina et al., 2018b). Earlier, in cooperation with the observatory of the University of Latvia in Baldone, the catalog of 89 positions and stellar magnitudes of asteroids and comets was obtained from processing observations of clusters in the UBVR spectral bands in 1967-1996 (Eglitis et al., 2016).

We continued this work and performed the search for asteroids based on the results of processing the remaining plates observed in U, V bands. Based on the results of digital processing about 300 U-plates and more than 1460 V-films, a preliminary catalog of 1700 asteroid positions was compiled.

These catalogs contain 6958 positions of asteroids and 14 positions of comets in total (see Tabl.1). To detect ambiguous identifications, all positions of asteroids were compared with the coordinates of stars in the Gaia DR2 stellar catalog.

The quantitative and qualitative characteristics of the compiled catalogs are analyzed. Fig.1 shows the distribution of all identified asteroids by equatorial coordinates RA, Dec for all used plates from Kyiv and Kitab parts of the FON project. Most of the identified asteroids attributed to the Main Belt. Only several of them attributed to the Hilda and Mars crosser families, potentially dangerous and unnumbered ones.

Table 1: The number of identified positions of asteroids and comets in catalogs

Photographic Survey	Number of used astronegatives	Number of identified positions of asteroids \ comets	Number of asteroids that have no positions earlier 1982-1996 (or these positions are single)
FON-Kyiv (1981-1994)	2260	2282/10	4(10)
FON-Kitab (1981-1989)	1963	4589/2	~280
Baldone (1967-1996)	1760	1700/3	>40

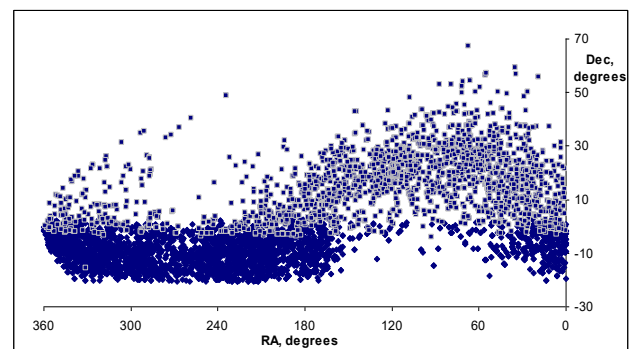


Figure 1: Distribution of coordinates RA, DEC for 4533 identified asteroids of the Kitab part (dark points) and for 2293 asteroids in the Kyiv part (light points) of the FON project.

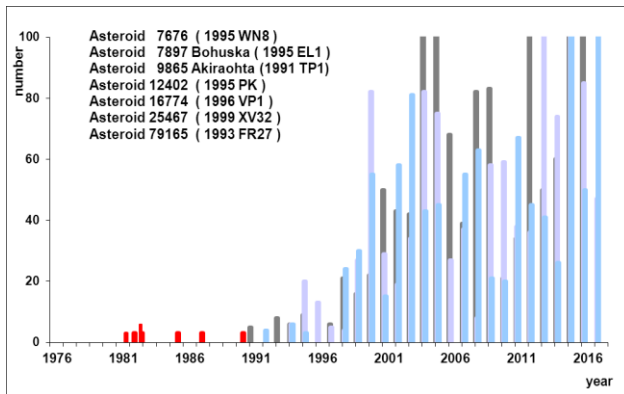


Figure 2: Time distribution of global observations of 7 asteroids according to MPC database as compared with observations of these asteroids from FON-Kyiv, FON-Kitab (red markers).

The unique fact is that we found 300 asteroids, which have the positions at that observational date only on the UkrVO astroplates. These observations of asteroids belong to those early oppositions of these asteroids which have insufficient or completely absent observational data. As an example, Fig.2 schematically shows the distribution of all known world observations of asteroids (7676), (7897), (9865), (12402), (16774), (25467) and (79165). They were discovered later and had no other observations earlier 1991. Observation of these asteroids in 1981-1991 from the FON project is shown with red markers.

Soon, we plan to continue the global search for small bodies of the Solar System based on the results of processing observations from Dushanbe part of the FON project and observations in the U, V spectral bands of the Observatory of the University of Latvia in Baldone. Using processing observations from the Dushanbe part of the FON project the first results of asteroids identification were obtained (Yizhakevych et al., 2018).

The catalog of asteroids from Kyiv part of the FON project is placed on the website of UkrVO (<http://gua.db.ukr-vo.org/starcatalogs.php>) and in Strasbourg astronomical Data Center (<http://cdsweb.u-strasbg.fr>).

2.2. Catalog of positions and B-values of Pluto

A catalog of 90 positions and magnitudes of Pluto for the period 1961-1996 was obtained from digitized photographic observations from the Joint Digital Archive of UkrVO and the Observatory of the University of Latvia. Pluto observations were made using telescopes of the Main Astronomical Observatory of the National Academy of Sciences of Ukraine (MAO NASU), Astronomical Observatory of the Taras Shevchenko National University of Kyiv, Research Institute “Mykolaiv Astronomical Observatory” (RI MAO) and Baldone Observatory of the University of Latvia.

Previously, 59 digitized astronegatives covering the period 1961-1990 were processed and obtained a catalog of astrometric positions and photometric values of the planet has been obtained (Kazantseva et al., 2015).

Both previously processed and unused astronegatives were included in the new processing. The identical type of re-scan of all astronegatives and the subsequent processing of scans were performed. Additionally, the positions of Pluto from astronegatives with multiple exposures

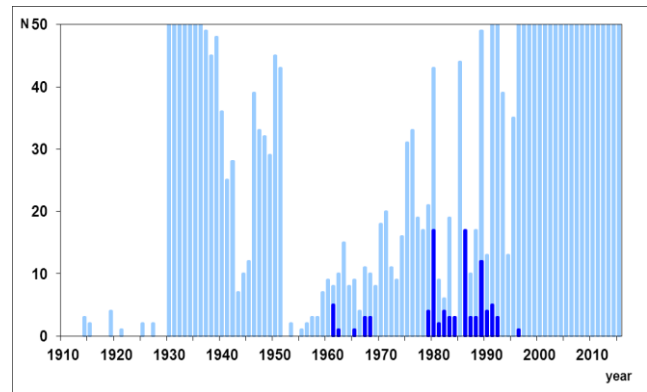


Figure 3: The number of positions of Pluto observed in the world in 1914-2015, according to the MPC data (UkrVO astroplate collection - dark blue, all - blue).

were obtained. (Previously, only one exposure from these astronegatives was processed.) The improvement of the software for digital image processing allowed us to extract all closely located Pluto images of multiple exposures. Besides, 8 images of Pluto from the archives of observations of large photographic sky surveys of the FON, MEGA, “Equatorial catalog” were found and processed. As a result we obtained additionally 31 new positions and magnitudes of Pluto and included them in our catalog.

A comparison of all resulting positions of Pluto with the JPL PLU055 / DE431 ephemeris was performed. As a result of the comparison, mean values (O-C) for all positions were obtained, which are -0.09 and -0.15 arcsec for RA and DEC, respectively. Their standard errors are 0.58 and 0.55 arcsec.

Fig. 3 shows 90 observations of Pluto, obtained by us in 1910-2015 during the most active period of Pluto’s observations in the world. Pluto’s observations in 1950-1990 years are a few in the world in comparison with the observations of the periods of planet discovery and the beginning of the 21st century. Our observations were made exactly at that time. The rotation period of Pluto around the Sun is 249 years. Since the discovery and till our time only a small part of one revolution of Pluto on its orbit around the Sun covered with observations.

This catalog is placed on the website of UkrVO (<http://gua.db.ukr-vo.org/starcatalogs.php>) and in Strasbourg astronomical Data Center (<http://cdsweb.u-strasbg.fr>).

2.3. Positional catalogs of Uranus, Neptune and satellites of Jupiter, Saturn, Uranus, and Neptune based on observations at the MAO NASU and RI MAO

The glass photographic collection of UkrVO contains plates of several observational projects with images of celestial objects of different nature including external planets and their satellites. These plates were digitized using flatbed commercial Epson scanners and processed using the software developed for image processing of digitized FON photographic plates. The software has been modified to meet the requirements of the new task and takes into account the peculiarities of the observations of planets and their satellites.

Firstly, satellites of the major planets cover the wide range of stellar magnitudes and they are the dynamic objects of the Solar System. To take the photographic images

Table 2: Some statistic characteristics as the results of the processing of archive photographic observations of major planets' satellites.

Object	B, mag	n	(o-c) _α	(o-c) _δ	σ _α	σ _δ
U1 Ariel	12.1	2	-.95	.64	.43	.64
U2 Umbriel	14.4	9	-.12	.27	.63	.46
U3 Titania	13.2	33	-.09	.44	.12	.44
U4 Oberon	13.2	33	.06	.51	.17	.35
N1 Triton	13.0	9	.65	.38	.57	.46
J6 Himalia	15.2	27	.17	-.18	.36	.50
J7 Elara	15.7	7	-.10	-.09	.27	.17
J8 Pasiphae	15.9	1	.58	.08	-	-
S2 Enceladus	11.7	12	.48	.16	.68	.48
S3 Tethys	10.3	20	-.01	.10	.62	.45
S4 Dione	10.4	40	.07	.07	.44	.43
S5 Rhea	9.7	57	.15	.07	.41	.38
S6 Titan	8.3	84	.09	-.03	.35	.37
S7 Hiperion	14.2	8	-.04	.10	.01	.46
S8 Japetus	12	78	.11	.04	.41	.38
S9 Phoebe	16.4	1	.44	-.27	-	-

of such faint objects like distant Jupiter's satellites, one should apply long expositions. During the exposure, the satellite can tangibly shift against stars. To hold the projection of the expected satellite image at the same point on the plate, it is necessary to compensate for the movement of the satellite by shifting the plate in the direction of its displacement (Medkof method).

Secondly, the constant movement of satellites along their orbits often causes the merger of satellite images with the image of the planet or the image of the other moon. To avoid it, every plate was exposed several times with various exposures. The split of the plate image into separate frames was made by the program algorithm.

The accuracy of the photographic plate reduction depends on telescope parameters, plate field dimensions, and a number of reference stars on the plate. The more reference stars on the plate the more accurate the connection of the rectangular coordinate system of the plain plate with the spherical star coordinate system can be established.

All observations of the satellites of the major planets in MAO NASU were conducted using four telescopes: two astrographs DLFA (D/F=400/5500) and DWA (D/F=400/2000) in Golosiiv (Kyiv, Ukraine), DAZ astrograph (D/F=4000/3000) in Kitab (Uzbekistan), and 60 cm Zeiss reflector Z600 (D= 600, Cassegrain-focus = 7500) installed on mt. Maidanak (Uzbekistan). Observations of the major planets in RI MAO was conducted using Zonal Astrograph (ZA, D/F=120/2040) telescope.

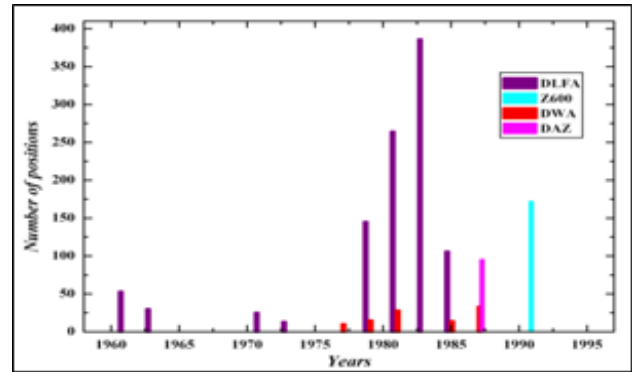


Figure 4: The distribution of observations of Saturn's satellites by year.

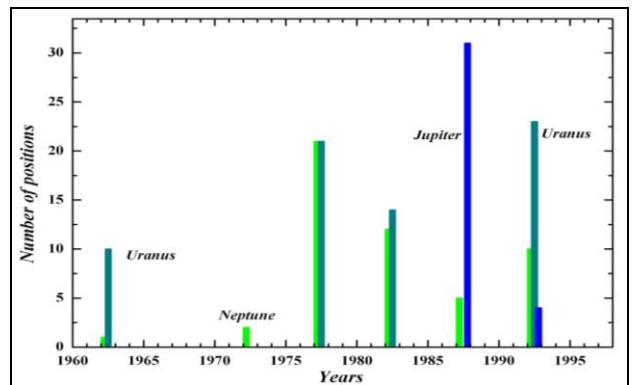


Figure 5: The distribution of observations of Uranus, Neptune, Jupiter, and their families by year.

For the reduction of observations obtained with ZA, DWA and DAZ, the sixth-order polynomial was applied. The processing of DLFA plates was made using third-order polynomial. The Z600 observations were processed with a linear model. Astronegatives were digitized on the Epson commercial scanners in 1200 dpi mode. Tycho-2 catalogue was used as reference one. The internal accuracy of observations on the four telescopes DLFA, Z600, ZA and DAZ is almost the same and lies within the limits $\pm 0.08 - \pm 0.19$ arcsec. The accuracy of the reduction for DWA telescope is lower and is approximately equal $\pm 0.17 - \pm 0.24$ arcsec along both coordinates. Differences in accuracy have accordance to focal length of telescopes and pixel scale of plate images. All observations have accuracy near 0.1 pixel (Protsyuk et al., 2014).

Tabl.2 demonstrates the coherence of determined positions of satellites and their theoretic values. Columns 4 and 5 of the Table contain the mean values (O-C) for every satellite obtained as the result of comparison of calculated positions with according ephemeris data from IMCCE (<http://nsdb.imcce.fr/multisat/nssephme.htm>). The last two columns contain RMS errors of these differences.

Fig. 4 and Fig. 5 give the quantitative distributions of obtained positions of Saturn's, and Jupiter's, Uranus's, and Neptune's satellites by year along the total period of their observations in MAO NASU.

The processing of 750 original plate images with observations of major planets and their moons conducted in 1961- 1994 resulted in the creation of 4 catalogs:

1) catalog of 1385 topocentric positions of eight Saturn's satellites S2-S9 (Yizhakevych et al., 2017a);

2) catalog of 750 positions of Uranus and 77 positions of its satellites U1-U4 (Protsyuk et al., 2015, 2017; Yizhakevych et al., 2016);

3) catalog of 690 positions of Neptune and 9 positions of its satellite N1Triton (Protsyuk et al., 2015, 2017; Yizhakevych et al., 2016);

4) catalog of 35 positions of distant moons of Jupiter J6-J8 (Yizhakevych et al., 2017b).

These catalogs of outer planets and their satellites are placed on the website of UkrVO and in Strasbourg astronomical Data Center.

3. Conclusion

The use of new digital technologies for processing observations made it possible to increase the total number of positions of small bodies of the Solar System by searching for images from various digitized archives of observations, as well as to increase their accuracy. To maximize the accuracy of astrometric positions and increase the number of original positions of individual asteroids, we plan to use the Gaia DR2 stellar catalog and digital archives of the UkrVO also. The new processing of digitized images of some selected minor planets using modern reference catalogs of stars, performed at the RI MAO, has led to a significant increase in position accuracy compared to previous results (Protsyuk et al., 2016).

The covering of certain time intervals with missing data on asteroid positions and their analysis can be useful not only for modern ephemeris calculations, but also for studying the evolution of asteroid orbits along time. These missing data can be obtained from the digital observational archives of UkrVO and other databases. A global search of observations of such asteroids in the databases of the UkrVO (Vavilova et al., 2012; 2016; 2017) with subsequent processing of the plates will substantially increase their number.

Acknowledgment. The work was partially supported by Ukrainian Astronomical Association.

The authors are sincerely grateful to Vavilova I. B. for her support and active participation in the discussion of the results of the work and the problem as a whole.

References

- Andruk V.M., Pakuliak L.K., Golovnia V.V. et al.: 2017, *Science and Innovation*, **13**, N1, 17.
- Golovnia V., Yizhakevych O., Shatokhina S. et al.: 2017, *Odessa Astron. Publ.*, **30**, 170.
- Eglitis I., Eglite M., Shatokhina S.V. et al.: 2016, *Odessa Astron. Publ.*, **29**, 123.
- Kazantseva L.V., Shatokhina S.V., Protsyuk Yu.I. et al.: 2015, *Kinem. Phys. Cel. Bodies*, **31**, N1, 37.
- Pakuliak L.K., Andruk V.M., Golovnia V.V. et al.: 2016, *Odessa Astron. Publ.*, **29**, 132.
- Protsyuk Yu.I., Kovylianska O.E., Protsyuk S.V. et al.: 2014, *Odessa Astron. Publ.*, **27**(1), 63.
- Protsyuk Yu., Yizhakevych O., Kovylianska O. et al.: 2015, *Odessa Astron. Publ.*, **28**(2), 204.
- Protsyuk Yu., Maigurova N., Protsyuk S. et al.: 2016, *Odessa Astron. Publ.*, **29**, 147.
- Protsyuk Yu.I., Kovylianska O.E., Protsyuk S.V. et al.: 2017, *Science and Innovation*, **13**, N1, 89.
- Savanevych V.E., Briukhovetskyi A.B., Ivashchenko Yu.N. et al.: 2015, *Kinem. Phys. Cel. Bodies*, **31**, N6, 302.
- Savanevych V.E., Briukhovetskyi O.B., Sokovikova N.S. et al.: 2015, *MNRAS*, **451**, Is. 3, 3287.
- Savanevych V.E., Khlamov S.V., Vavilova I.B. et al.: 2018, *Astronomy & Astrophysics*, **609**, id.A54, 11 pp.
- Shatokhina S., Golovnia V., Andruk V.: 2017, *BTSNU*, **55**, 6.
- Shatokhina S.V., Kazantseva L.V., Yizhakevych O.M. et al.: 2018, *Kinem. Phys. Cel. Bodies*, **34**, N5, 270
- Shatokhina S.V., Relke H., Yuldoshev Q.X. et al.: 2018, *Odessa Astron. Publ.*, **30**, 235.
- Vavilova I.B., Pakulyak L.K., Shlyapnikov A.A. et al.: 2012, *Kinem. Phys. Cel. Bodies*, **28**, N2, 85.
- Vavilova, I.; Golovnya, V.; Andruk, V. et al.: 2014, *Odessa Astron. Publ.*, **27**, 65.
- Vavilova I.B.: 2016, *Odessa Astron. Publ.*, **29**, 109.
- Vavilova I.B., Yatskiv Ya.S., Pakuliak L.K. et al.: 2017, *Proc. IAU Symposium*, **325**, 361.
- Yizhakevych O.M., Andruk V.M., Pakuliak L.K. et al.: 2016, *Odessa Astron. Publ.*, **29**, 155.
- Yizhakevych O.M., Andruk V.M., Pakuliak L.K.: 2017, *Kinem. Phys. Cel. Bodies*, **33**, N3, 70.
- Yizhakevych O.M., Andruk V.M., Pakuliak, L.K., 2017, *Odessa Astron. Publ.*, **30**, 201.
- Yizhakevych O.M., Mullo-Abdolv A.Sh., Relke H.V. et al.: 2018, *Odessa Astron. Publ.*, **30**, 247.
- Yuldoshev Q.X., Ehgamberdiev Sh.A., Muminov, M.M. et al.: 2017, *Kinem. Phys. Cel. Bodies*, **33**, N5, 250.

DOI:<http://dx.doi.org/10.18524/1810-4215.2019.32.181734>

THE ASTROMETRIC AND PHOTOMETRIC RESULTS OF DIGITIZED PLATES ON EPSON EXPRESSION 10000XL SCANNER WITH DIFFERENT RESOLUTIONS

Q. Yuldoshev¹, V. Andruk², M. Muminov³

¹ Ulugh Beg Astronomical Institute of the Uzbekistan Academy of Sciences,
33 Astronomy Str., 100052 Tashkent, Uzbekistan, qudratillo@astrin.uz

² Main Astronomical Observatory of National Academy of Sciences of Ukraine,
27 Akademika Zabolotnogo Str., 03143, Kyiv, Ukraine, andruk@mao.kiev.ua

³ Andijan State University, 129 University Str., 170100 Andijan, Uzbekistan,
muminov1951@gmail.com

ABSTRACT. This work was done to assess the accuracy of the plate processing method and to study in detail the Epson Expression 10000XL scanner, which is used to digitize the FON-Kitab astronomical plates from the photographic archive collection of the Ulugh Beg Astronomical Institute (UBAI) of the Uzbekistan Academy of Sciences. The glass archive of the UBAI has about 15 thousand photographic plates with images of various space objects. To process the plates the specially developed software in the LINUX/MIDAS/ROMAFOT was used. From comparing the results of processing digitized files with grayscale 8 and 16 bits, an assessment of the accuracy of the developed method for determining rectangular coordinates and photometry was made. The Epson Expression 10000XL flatbed scanner together with developed software can be used to digitize and process the astronegatives and obtain characteristics of objects (high, medium and moderate brightness) with an internal accuracy better than 0.05" and 0.015^m for equatorial coordinates and B-magnitudes, respectively. To assess the repeatability of astrometric and photometric errors of the scanner, six consecutive scans of one plate with 600, 900, 1200, 1500, 1800, 2100, 2400 and 2540 dpi spatial separations were processed. The average accuracies of measurements were $\sigma_{\alpha\delta}=0.07''$ for the equatorial coordinates and $\sigma_m=0.13^m$ for B-magnitudes. The results of the experiments showed that a scan mode with a spatial resolution of 1200 dpi is the best option for plate digitization. Higher resolution scanning modes require a significant increase of digitizing and processing times of a plate, but they do not affect on an accuracy of the obtained results.

Keywords: stellar catalogs, scanning, processing of digitized photographic plates, astrometry, photometry, UVV system, stellar B-magnitudes.

АНОТАЦІЯ. Робота виконана з метою оцінки точності методу обробки платівок та детального дослідження сканера Epson Expression 10000XL, за допомогою якого оцифровуються платівки ФОН-Кітаб із колекції склотеки Астрономічного інституту Академії наук Республіки Узбекистан. У скляному

архіві Астрономічного інституту є близько 15 тис. астроплатівок із зображеннями різних космічних об'єктів. Для обробки астроплатівок використовується програмне забезпечення, створене в програмному середовищі LINUX/MIDAS/ROMAFOT. Із порівняння результатів обробки оцифрованих файлів з градаціями сірого 8 та 16 біт зроблено оцінку точності розробленого методу визначення прямокутних координат та фотометричних величин. Планшетний сканер Epson Expression 10000XL разом з розробленим програмним забезпеченням дозволяє оцифровувати і обробляти платівки та отримувати характеристики об'єктів (високої, середньої та помірної яскравостей) з внутрішньою похибкою не гірше 0.05" і 0.015^m для екваторіальних координат та величин В відповідно. Для оцінки повторюваності астросметричних та фотометричних похибок сканера було оброблено по шість послідовних сканів однієї платівки з просторовим розділенням 600, 900, 1200, 1500, 1800, 2100, 2400 та 2540 dpi. Середня точність вимірювань становила $\sigma_{\alpha\delta}=0,07''$ для екваторіальних координат та $\sigma_m=0,13^m$ для зоряних В-величин. Результати досліджень показали, що режим сканування з просторовою роздільною здатністю 1200 dpi - найкращий варіант для оцифрування платівок. Режими з більшою роздільною здатністю сканування потребують значного збільшення як часу сканування, так і часу обробки сканів і не приводять до суттєвого покращення точності для отримуваних результатів.

Ключові слова: зоряні каталоги, сканування, обробка оцифрованих платівок, астросметрія, фотометрія, UVV система, зоряні величини В.

1. Introduction

Astronegatives which were obtained under the project Photographic Sky Survey (PSS, in Russian – FON) [Andruk, 2017b; Pakuliak, 2016] using Zeiss Dual Astrograph, are contained main part of glass archive of the Astronomical Institute of the Uzbekistan Academy of Sciences (UBAI). Fourfold overlap of sky method was used for all astronegatives

in zones from -20° to $+28^\circ$ by DEC (shifting to 2 degrees by RA). In addition, the archive contains observational images of following projects: galaxies and nebulas, open and globular star clusters, Solar system bodies (planets, comets, asteroids) [Shatkhina, 2018; Yizhakevych, 2018], close open clusters and star-formation regions, variable stars, radio-source regions, and others.

In present, the astronegatives are being digitized and cataloged in international format WFPDB (Wide-Field Plate Database). For digitization, the Epson Expression 10000XL flatbed scanner which is used in many observatories of the world is used [Andruk, 2015; Eglitis, 2017; Muminov, 2017; Protsyuk, 2014]. In this paper, it is presented method and processing results of digitized images which were scanned with different resolutions (600, 900, 1200, 1500, 1800, 2100, 2400 and 2540 dpi).

2. Estimation of processing accuracy in the MIDAS/ROMAFOT software environment

The digitized images were obtained in TIF format with 16-bit grayscale using the flatbed scanner Epson Expression 10000XL. For the processing in the MIDAS/ROMAFOT package, all digitized images were converted into a FIT format, and the number of color gradations can be arbitrary. Depending on the grayscale gradations (16-bit or 8-bit), file sizes differ up to twice and it affects the amount of disc space to store them. Since the files were converted from 16-bit (frame A) to 8-bit (frame B) the estimation of possible losses of precisions for astrometric and photometric determinations a comparison of the processing results was made. Frames A and B with spatial resolution were obtained for plate No. 399, exposed in the B-band of FON project. Objects on the astronegative were registered with two exposures: long and short exposures are 28 and 1 minute, respectively. After processing of both frames for each object in the MIDAS/ROMAFOT software environment, we have their astrometric (rectangular X , Y coordinates) and photometric characteristics (instrumental magnitudes m , diameters of the objects f (FWHM) on the plate and intensity values I_c in the center of the image). For the study the stars in long-exposure which have pair stars in short-exposure were selected, the amount of them was $n=3147$ [Andruk, 2012]. Results of comparison of differences between calculated rectangular coordinates, instrumental magnitudes and diameter of the objects are presented in Fig. 1. The upper part of Fig. 1 shows the differences between the calculated values for astrometric (1a, 1b) and photometric (1c, 1d) characteristics of stars for the A and B frames, according to their rectangular coordinates (X , Y), instrumental magnitudes (m) and objects' diameters (f). Bigger and smaller values of m and f correspond to bright and faint stars. The root-mean-square errors rms of the difference between the first and second methods of digitization are indicated. At the bottom of the figure (1a, 1b, 1c, 1d), these differences are shown as real (continuous lines) and theoretical (dashed lines) distribution functions versus the corresponding intervals of Δx , Δy , Δm , and Δf . The length of interval (0.4 values of standard deviations) and determined X^2 values are presented on the bottom of the figure. The data were obtained for the stars in the range of $B=7^m \div 14^m$. The limited

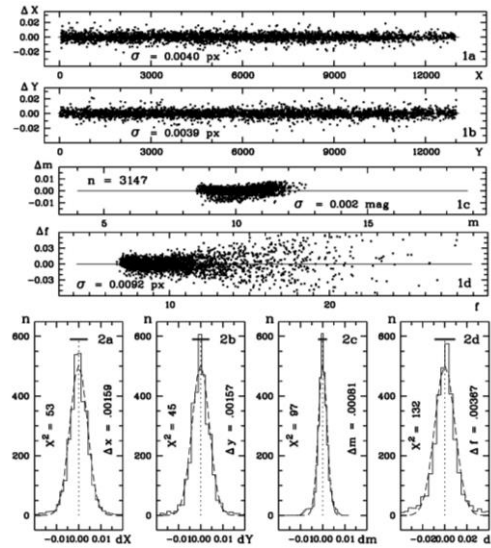


Figure 1: The differences of astrometric and photometric results between A (8-bit) and B (16-bit) frames.

magnitude was $B=17.5^m$ for long exposure stars. The errors increase twice for extremely faint stars. Since rms less than 0.004 px and 0.002^m for the rectangular coordinates and stellar magnitudes, it can be concluded that the digitization could be made with 8-bit color depth without losing the accuracy of the results.

3. Repeatability of the results of scanning and scanner errors

Six consecutive scans of the same plate were processed for assessing the astrometric and photometric errors of the scanner. Digitizing was made with different spatial resolutions: 600, 900, 1200, 1500, 1800, 2100, 2400 and 2540 dpi. Calculations for the long-exposure stars that have twins with a short exposure are explained below. The characteristics of the objects averaged over six scans were obtained for each scanning mode – rectangular coordinates X , Y and instrumental photometric magnitudes m and object diameters f (FWHM). Table.1 shows the average errors for eight resolution modes from 600 to 2540 dpi for stars brighter than $B \leq 14^m$. Here, k' is the number of stars, σ_x , σ_y , σ_m , σ_f are the mean values of the root-mean-square errors for determining rectangular coordinates and photometric parameters. The errors are $\sigma_{xy}=0.017 \div 0.021$ px and $\sigma_m=0.007^m$ for rectangular coordinates and instrumental magnitudes in 1200 dpi scan mode. Taking into account the scale factors (scale value is 1.45 for astrometry and for photometry, it is about 2 because of the contrast of the emulsion), practically, the errors will be 1.5-2 times larger. It allows for making the following conclusion. The Epson Expression 10000XL flatbed scanner and the developed software can be used digitizing and processing the plates and obtaining the characteristics of objects with internal accuracy better than 0.05^m and 0.015^m. For boundary faint objects ($B=16^m \div 17^m$), our studies yielded a result about two times worse.

Fig. 2 shows the relationship between instrumental magnitudes of long (m_1) and short (m_2) exposures for eight

Table 1. RMS errors of the rectangular coordinates and instrumental magnitudes

dpi	k'	σ_x	σ_y	σ_m	σ_f	Scale (""/px)
600	1833	0.020	0.014	0.008	0.039	2.893
900	2048	0.013	0.024	0.004	0.017	1.928
1200	2881	0.017	0.021	0.007	0.028	1.446
1500	2887	0.020	0.037	0.009	0.051	1.157
1800	2795	0.019	0.024	0.004	0.027	0.964
2100	2578	0.016	0.027	0.008	0.078	0.826
2400	2129	0.035	0.018	0.007	0.061	0.723
2540	1752	0.070	0.045	0.008	0.082	0.683

Table 2. RMS errors of the equatorial coordinates and magnitudes

dpi	N	σ_α	σ_δ	σ_m	Scale (""/px)
600	1275	0.104	0.109	0.122	2.893
900	1282	0.071	0.083	0.103	1.928
1200	1487	0.067	0.070	0.139	1.446
1500	1472	0.066	0.070	0.124	1.157
1800	1120	0.055	0.055	0.120	0.964
2100	1144	0.057	0.052	0.128	0.826
2400	868	0.060	0.066	0.129	0.723
2540	854	0.053	0.055	0.137	0.683
		0.067	0.070	0.125	1.328

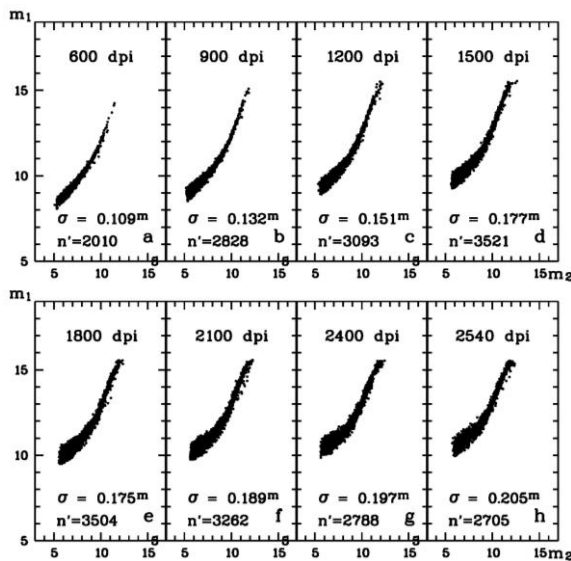


Figure 2: Relationships between instrumental magnitudes for different resolution of the scanner.

resolution modes of 600, 900, 1200, 1500, 1800, 2100, 2400 and 2540 dpi. n' is the number of studied stars for each scan mode. The relationship between the magnitudes is non-linear, and the accuracy of photometry σ increases via increasing of the scanning resolution.

4. Errors of reduction in the systems Tycho-2 and Johnson's B system

Table. 2 presents following parameters for the modes: N is the number of reference stars in Tycho-2; σ_α , σ_δ are errors of reduction of rectangular X , Y coordinates into the equatorial coordinates system - Tycho-2 [Andruk, 2015; Andruk, 2016] and σ_m is an error of the reduction of the instrumental magnitudes m into Johnson's B System [Andruk, 2017a; Relke, 2015].

5. Conclusion

The calculations and made analysis allow the authors to conclude as follows. Errors for each measurement are $\sigma_{\alpha\delta}=0.07''$ for the equatorial coordinates and $\sigma_m=0.13^m$ for B -magnitudes in different resolution modes of the scanning. In practically, we have obtained the identity results for the processing of digitized images with 8-bit and 16-bit of color gradations. The scanner Epson Expression 10000XL is suitable for astrometric and photometric researches on the limit of accu-

racy of photographic plates. Studies show that the best option for digitizing is the 1200 dpi spatial resolution mode. High-resolution modes require more processing and digitizing time, and do not give a gain in accuracy for the obtained results. For example, the digitizing time with a resolution of 2400 dpi is 20 minutes, and with 1200 dpi, it is 8 minutes for astronegatives 30x30 cm size. Processing time also increases respectively to resolution.

Until today, close to 2700 (the main part of them are astroplates of the FON project) of more than 15000 astronegatives had been digitized. Digitization was made with a resolution 1200 dpi, and 16-bit, gray color depth. A photographic catalog of equatorial coordinates and B -magnitudes of stars was created using the FON project astroplates [Yuldoshev, 2016a; Yuldoshev, 2016b; Yuldoshev, 2017a; Yuldoshev 2017b]. The catalog is available via this link <http://vizier.u-strasbg.fr/viz-bin/VizieR?-source=I/346>.

References

- Andruk V.M., Ivanov G.A., Yatsenko A.I. et al.: 2012, *BTSNU*, **N48**, 11.
 Andruk V.M., Pakuliak L.K., Golovnia V.V. et al.: 2015, *Odessa Astron. Publ.*, **28**, 192.
 Andruk V.M., Golovnia V.V., Ivanov G.A. et al.: 2016, *Kinem. Phys. Cel. Bodies*, **32**, N1, 38.
 Andruk V.M., Pakuliak L.K., Golovnia V.V. et al.: 2017, *Science and Innovation*, **13**, N1, 17.
 Andruk V., Yuldoshev Q., Eglitis I. et al.: 2017, *Odessa Astron. Publ.*, **30**, 159.
 Eglitis I., Andruk V.: 2017, *Open Astronomy*, **26**, N1, 7.
 Muminov M., Yuldoshev Q., Ehgamberdiev Sh. et al.: 2017, *Bulgarian Astronomical Journal*, **26**, 3
 Pakuliak L.K., Andruk V.M., Golovnia V.V. et al.: 2016, *Odessa Astron. Publ.*, **29**, 132.
 Protsyuk Yu.I., Andruk V.N., Muminov M.M. et al.: 2014, *Odessa Astron. Publ.*, **27**, 61.
 Relke E., Protsyuk Yu.I., Andruk V.M.: 2015, *Odessa Astron. Publ.*, **28**, 211.
 Shatkhina S.V., Relke H., Yuldoshev Q. et al.: 2018, *Odessa Astron. Publ.*, **31**, 235.
 Yizhakevych O.M., Andruk V.M., Yuldoshev Q. et al.: 2018, *Odessa Astron. Publ.*, **31**, 251.
 Yuldoshev Q.X., Usmanov O., Egamberdiev E., et al.: 2016, *BTSNU*, **N54**, 28.
 Yuldoshev Q.X., Muminov M.M., Ehgamberdiev Sh.A., et al.: 2016, *Odessa Astron. Publ.*, **29**, 160.
 Yuldoshev Q.X., Muminov M.M., Ehgamberdiev Sh.A., et al.: 2017, *Odessa Astron. Publ.*, **30**, 205.
 Yuldoshev Q.X., Ehgamberdiev Sh.A., Muminov M.M., et al.: 2017, *Kinem. Phys. Cel. Bodies*, **33**, No. 5, 250.

HISTORICAL REVIEWS

DOI:<http://dx.doi.org/10.18524/1810-4215.2019.32.181753>

**THE PROBLEM OF "ZERO ELEMENTS" IN
THE WORKS OF D. I. MENDELEEV.
NEUTRON MATTER AS A PRIMARY COSMOLOGICAL AND
MODERN DARK MATTER OF THE UNIVERSE**

G. B. Ryazantsev ¹, G.K. Lavrenchenko ², S. S. Nedovesov ³

¹ Lomonosov Moscow State University, Russia, anis-mgu@rambler.ru

² Institute Low-Temperature Energy Problems, Odessa, Ukraine,
lavrenchenko.g.k.@gmail.com

³ Taras Shevchenko National University of Kyiv, Ukraine, pc.remont.tk@gmail.com

ABSTRACT. D.I. Mendeleev assumed the existence of elements X ("Newtonium") and Y ("Coronium") in front of hydrogen in the zero group of the periodic system of chemical elements (PS). It should be recalled that Mendeleev was not mistaken in his predictions of new elements. When he applied the periodic law (PL) to analogues of boron, aluminum and silicon, he had complete confidence in success, because everything was obvious to him there. The idea of elements before hydrogen came to him immediately after the opening of the PL, but he published this only before his death. This question haunted him almost his entire creative life. D.I.Mendeleev did not have time to solve this problem, and his students and followers tried to forget it as "erroneous". It should be noted that after D.I.Mendeleev the question of "zero" elements was repeatedly raised by many authors both in the past and in the present centuries, however, for brevity, we only mention the very first and most famous of them: for example, Ernest Rutherford in 1920 and Andreas von Anthroff in 1926. Anthroff was the first to propose the term "*neutronium*" to refer to a hypothetical element with atomic number zero, which he placed at the beginning of the periodic table (PT). At present, neutron matter, like neutron stars, is a recognized reality in astro- and nuclear physics. From the standpoint of general chemistry, a neutron substance can be classified as chemically simple (that is, it cannot be decomposed into simpler ones by chemical means), then the question inevitably arises of the corresponding element and its place in the PS. Based on the logic of the PL – (ordinal number – electric charge) – the ordinal number of neutron matter will correspond to zero, which makes us remember and develop the ideas of Dmitry Ivanovich Mendeleev about the zero group and period. Based on the works of Tamm, Hund and Migdal, the possibility of the stable existence of neutron matter at the micro level, and not

only at the macro level, as is now believed in astrophysics, is stated. Neutron matter is considered as the primary cosmological substance, a candidate for dark matter and its production in laboratory conditions on Earth.

Keywords: D.I.Mendeleev, periodic law, newtonium, coronium, neutronium, neutron matter, zero group and period, dark matter.

АНОТАЦІЯ. Д.І.Менделєєв допускав існування елементів-Х ("Ньютоній") і Y ("короній") перед воднем в нульовій групі періодичної системи хімічних елементів (ПС). Слід нагадати, що Менделєєв не помилився у своїх прогнозах нових елементів. Коли він застосував періодичний закон (ПЗ) до аналогам бору, алюмінію і кремнію, у нього була повна впевненість в успіху, тому що там все було очевидно для нього. Ідея ж доводневих елементів з'явилася у нього відразу ж після відкриття ПЗ, але опублікував він це тільки перед своєю кончиною. Це питання переслідувало його практично все творче життя. Д.І.Менделєєв не встиг вирішити цю проблему, а його учні та послідовники постаралися забути її як "помилкову". Слід зазначити, що після Д.І.Менделєєва питання про "нульові" елементи неодноразово піднімалося багатьма авторами як в минулому, так і в цьому столітті, проте для стислості згадаємо лише найперших і відомих з них: наприклад, Ернеста Резерфорда в 1920 році і Андреаса фон Антропоффа в 1926 році. Антропофф першим запропонував термін "нейтроніум" для позначення гіпотетичного елемента з атомним номером нуль, який він помістив в початок періодичної таблиці (ПТ). В даний час нейтронна матерія, як і нейтронні зірки, є визнаною реальністю в астро- та ядерній фізиці. Нейтронну речовину з

позиції загальної хімії можна класифікувати як хімічно просту (тобто її не можна розкласти на простіші хімічними засобами), тоді неминуче постає питання про відповідний йому елемент і його місце в ПС. Виходячи з логіки ПЗ – (порядкове число – електричний заряд) – порядокове число нейтронної матерії буде відповідати нулю, що змушує згадати і розвинути ідеї Дмитра Івановича Менделєєва про нульову групу і період. На підставі праць Тамма, Хунди і Мигдала стверджується можливість стабільного існування нейтронної речовини на мікрорівні, а не тільки на макрорівні – як зараз вважається в астрофізиці. Розглядається нейтронна речовина в якості первинної космологічної і як кандидат на темну матерію, та її отримання в лабораторних умовах на Землі.

Ключові слова: Д. І. Менделєєв, періодичний закон, ньютоній, короній, нейтроній, нейтронна речовина, нульова група і період, темна матерія.

1. Introduction

It was previously shown (Ryazantsev et al., 2014, 2016, 2017, 2018, 2019) that neutron matter in our time is a specific physical reality that requires its rightful place in the PS and the study of not only physical, but also chemical, and, possibly, in the near future, engineering and technical properties. A neutron substance, or rather its corresponding element begins (zero period) and ends (supercritical atoms) PS. The neutron substance is given stability already at the micro level by Tamm interaction, and it is stable not only at the macro level (neutron stars) due to gravitational interaction, as is now believed in astrophysics. The possibility of neutronization is shown not only due to gravitational interaction, but also through other mechanisms (supercritical increase in atomic number of elements (Zel'dovich & Popov, 1971) and condensation of ultracold neutrons (Shapiro, 1976; Ignatovich, 1996), so there is a fundamental possibility of producing neutron matter in terrestrial conditions (Ryazantsev et al., 2017, 2018, 2019). Neutron matter is consistent with the initial concept of PL and PS proposed by Dmitry Ivanovich Mendeleev (Mendeleev, 1934, 1991; Dobrotin et al., 1984).

From the standpoint of general chemistry, a neutron substance can be classified as chemically simple (that is, it cannot be decomposed into simpler substances by chemical means or reduced to allotropic modifications of already known substances), then the question inevitably arises of the corresponding element and its place in the periodic system. Based on the logic of PL – (ordinal number – electric charge) – the ordinal number of neutron matter in the PS will correspond to zero, which makes us recall and develop the ideas of Dmitry Ivanovich Mendeleev about the zero group and period.

D. I. Mendeleev wrote about the elements before hydrogen: *“The chosen subject has long occupied my thoughts, but for various reasons I did not want to talk about it, especially because I myself was not quite satisfied with the few clarifications that I considered able to withstand*

criticism, and I expected everything from the experiments with which I intended to continue my first attempts, answers that were more encouraging in the correctness of the conclusions made. However, the years passed, the more persistent affairs were torn off, and no one touched on the issue that seemed burning to me, so I decided to say in relation to him - what and how I can, without pretending to solve it, at least approximate.” Elements in front of hydrogen inevitably fall into the zero group and are analogues of inert gases. *“This position of the argon analogs in the zero group is a strictly logical consequence of understanding the periodic law,”* - stated D. I. Mendeleev.

He admitted the existence of elements X (*“Newtonium”*) and Y (*“Coronium”*) in front of hydrogen in the zero group. It should be recalled that Mendeleev was not mistaken in his predictions of new elements. He wrote: *“When I applied the periodic law to the analogs of boron, aluminum and silicon, I was 33 years younger, I lived in the full confidence that sooner or later the foreseen must certainly be justified, because I could see everything there clearly. The excuse came sooner than I could have hoped. I didn't risk it then, now I do. It takes determination. It came when I saw the radioactive phenomena ... and when I realized that it was impossible for me to postpone and that perhaps my imperfect thoughts will lead someone to a path more correct than the possible one that seems to my failing vision.”*

D. I. Mendeleev did not have time to solve this problem, and his students and followers tried to forget this topic as “erroneous”. Modern knowledge of neutron stars and neutron matter persistently compels to recall his ideas about elements in front of hydrogen and to affirm the truth of his ingenious foresight, which is more than 100 years ahead of the natural sciences of his time.

2. Stability of neutron matter

In neutron matter, due to its size (larger than the total absorption layer), the electron emitted during decay is captured by the remaining protons, which, in turn, are converted into neutrons, due to which the dynamic equilibrium of the system is maintained. In fact, this corresponds to both the theory of Igor Evgenievich Tamm (1975), which he put forward in his time (1934) to explain the mechanism of nuclear forces for ordinary nuclei, and the ideas of Frederick Hund (1936). It should be noted that the theory of I.E.Tamm was not satisfactory for ordinary atoms (but he himself valued his “unsuccessful” theory of nuclear forces more than the Nobel work on Cherenkov radiation and considered his best theoretical achievement), but it is consistent and can be realized for neutron matter of an appropriate scale (200-300 and more femtometers), giving it additional stability.

In strongly interacting systems, there are many virtual particles and all kinds of interactions that are allowed for invariance considerations are realized. So, in our opinion, the “original” theory of Igor Tamm’s β -nuclear forces (lepton exchange between nucleons), and not just its modification by Hideki Yukawa (π -nucleon exchange), is still awaiting recognition (because besides the meson cloud around the nucleon, of course, there are other particles) and

“dominates” the neutron matter of the Universe, ensuring its stability and wide spatial distribution.

An initial study of this problem was also given by Frederick Hund (1936) in the first microscopic description of the equation of state of nuclear matter in beta equilibrium in the article “Substance at very high pressures and temperatures”, only if Tamm has virtual electrons, Hund implements beta equilibrium completely real particles, but most importantly, both mechanisms contribute to the stability of supercritical nuclear matter, and in strongly interacting systems there is no fundamental difference between virtual and real particles.

It is the additional interaction due to nuclear β -forces that gives stability to neutron matter already at the micro level, and not only at the macro level due to gravitational interaction, as is now considered in astrophysics!

The possibility of the existence of a super dense neutron nucleus was also considered in the work of A. B. Migdal (1983) “*Theory of finite Fermi systems and properties of atomic nuclei*” in the section: “*Application of Theory of finite Fermi systems in nuclear physics*”. Migdal considered: “... neutron nuclei can be stable with respect to beta decay and fission, with $Z \ll N$ and $N > 10^3 - 10^5$. Such nuclei could be observed in cosmic rays in the form of large fragments.” A. B. Migdal proposed to search for neutron nuclei in the form of exotic traces in photographic emulsions after exposure to cosmic rays.

The theories of Tamm, Hund and Migdal admit the stable existence of hyperheavy neutron nuclei at $Z \gg 175$, $N > 10^3 - 10^5$ and sizes of 200-300 and more femtometers.

Nevertheless, it was widely believed that the minimum mass for the stable existence of a neutron object is 0.1 of the mass of the Sun (Potekhin, 2010). It is believed that the equations of state used in this case are based on rich (?). Supposedly experimental material and therefore give a fairly accurate value of the minimum mass. The very fact of the existence of a minimum neutron star mass is justified by the fact that at low densities neutrons, due to susceptibility to beta decay, cannot be the predominant component of matter, and the high neutron density in them is ensured only by gravitational interaction.

Most models of the structure of neutron stars were based on the solution of the Tolman-Oppenheimer-Volkov equation (Potekhin, 2010). Currently, there are several dozen models extending from the so-called “soft” equations of state (derived from models in which, at densities of the order of the nuclear, the average interaction energy corresponds to attraction) to rigid equations of state (obtained for models in which even at densities below the nuclear there is repulsion). Since various models corresponding to different equations of state lead to a rather wide range of parameters characterizing a neutron star, one would hope that an exact determination of such parameters would make it possible to specify the very equation of state of neutron matter, the very nature of the internucleon interaction.

Unfortunately, to date, it has not been possible to obtain reliable estimates of even the basic characteristics of neutron stars. So, the accuracy in determining the radius R is on average 50-100%. To date, the equation of state has not been obtained in the framework of quantum chromodynamics. Thus, the minimum mass of a neutron

star considered equal to 0.1 of the mass of the Sun is obtained from extremely approximate equations with an error of 100% or more, as indicated in many works on this subject, nevertheless, this number is widely replicated. Based on the conclusions from the theories of Tamm, Hund and Migdal, we can expect a stable existence of microscopic neutron objects ($Z \gg 175$, $N > 10^3 - 10^5$) and neutron stars with a mass of less than 0.1 of the Sun.

The author of the very concept of neutron stars Fritz Zwicke (nuclear “goblins” Zwicke (1958) wrote about the possibility of the existence of neutron objects of much smaller sizes (3-10 m) under certain conditions. He believed that further analysis of matter nuclear density is important not only for our understanding of eruptions in stars, from ordinary flares of stars to supernovae, but it also promises to radically change some of the current ideas on the formation of elements in the theory of evolution of the Universe.

The question of the possibility of obtaining neutron matter under laboratory conditions on Earth is partly a rhetorical one. The fact is that two aspects must be distinguished: mono- (ultracold neutrons (Shapiro, 1976) and polynuclear (similar to cosmic space) matter. As for mononeutron matter, it has long been obtained under terrestrial conditions, although it is not stable (Ignatovich, 1996). The question of obtaining a poly-neutron substance remains to be solved in the near future (Ryazantsev, 2018). The situation is now similar to that in the late 30s of the last century, when a breakthrough was made in the mastery of nuclear energy, although very many doubted the possibility of this.

3. Neutrons condensation

It should be noted that Georgy Antonovich Gamov (1946) first spoke about the condensation of cold neutrons. This idea is rarely mentioned, which over time has found application in the theory of neutron stars. G.A. Gamow in the late 30s of the last century showed that when a neutron gas is compressed, a new superdense state of matter arises. Gamow’s main hypothesis: “*We can anticipate that neutrons forming this comparatively cold cloud were gradually coagulating into larger and larger neutral complexes ...*”.

In further development, the theory of the initial cold Universe was rejected and with it the idea of neutron condensation was forgotten. However, is this true? Neutron condensation is possible not only at low temperatures (ultracold neutrons), but also at ultrahigh pressure at temperatures below critical. In the theory of the Big Bang of a hot Universe, nucleon formation begins at about $t = 10^{-5}$ s, temperature $T = 10^{12}$ K, and particle energy $E = 0.1$ GeV. In this case, protons and neutrons are implied, but for some reason, mainly only protons are considered for possible thermonuclear fusion. Although, if you calculate the density of matter at this moment, then it exceeds the density of a neutron star. That is, under these conditions, the overwhelming majority of nucleons will be in the form of neutrons, not protons, since neutronization conditions are satisfied.

It is more likely to expect the possibility of collective neutron condensation (in the mass, rather than sequential

addition of individual neutrons, as suggested by Gamov and co-workers) upon reaching a critical temperature (which is an energetically more favorable process (Ryazantsev, 2017) than thermonuclear fusion from a minimum number of protons in those same conditions. Fragmented condensation of neutrons due to quantum gravitational density fluctuations occurs with the release of additional energy, which enhances the formation of hyperheavy stable neutron nuclei, which are the source of nonrelativistic dark matter (neutrality, femto, pico and nanoscale sizes, relict cooling makes it difficult for us to detection). The observable part of the Universe is formed from the residual part of protons and subsequently decaying single neutrons and unstable fragments of neutron matter (with $Z > 175$, but $N < 10^3 - 10^5$).

Usually on Earth we deal with neutron radiation of various energies, but not with neutron matter. This was until 1968, when an experiment was conducted at the Laboratory of Neutron Physics, led by Corresponding Member of the USSR Academy of Sciences Fedor Lvovich Shapiro (1976), in which the phenomenon of confinement of very slow neutrons in vessels predicted by academician Yakov Borisovich Zel'dovich (Ignatovich, 1996) was first observed. The behavior of neutrons held in evacuated vessels resembles the behavior of a very rarefied gas in a vessel. Such neutrons are called ultracold (UCN). The retention of UCNs in vessels attracts researchers with the opportunity (in comparison with a single neutron passage through the experimental volume) to observe this elementary particle longer in the experimental setup, which gives a significant increase in the sensitivity and accuracy of experiments on the interaction of neutrons with fields and matter.

For example, the use of UCNs made it possible to significantly lower the limit of existence of the electric dipole moment of the neutron necessary to verify the law of conservation of time parity; more accurately measure the lifetime of a free neutron before β -decay. The most important feature of UCNs is that they behave not as radiation, but as a substance, and it is possible to work with them as a substance similar to a discharged inert gas. Moreover, it is possible to study both physical and its chemical properties. Physical properties are already being studied, but UCN chemistry, it seems, does not even raise the question, because by default it seems somehow obvious that they should be similar to inert gases. This seems to be true, but now we already know well that inert gases, albeit with difficulty, enter into chemical reactions and form, even if not stable, but chemical compounds. Could this happen to UCN? Based on the fact that Chemistry is only the interaction of electron shells of atoms, as many believe, a categorical negative answer follows. But, if Chemistry is understood more broadly, in general, the ability of micro (nano, pico or even femto) objects to interact and form relatively stable compounds, then why not?

Yes, neutrons do not have an electric charge and free electrons, so all ideas about possible classical chemical bonds (ionic, covalent, etc.) immediately disappear unambiguously. But, neutrons have precisely the magnetic moment and possibly the electric dipole moment (the essential role of which is well known in chemistry), can this not serve as the ability to interact with other objects

and form though not stable, but still observable compounds? For example, the interaction of UCNs with molecules of substances with an odd number of electrons is quite possible, and an experiment to detect the products of this interaction is quite real (Ryazantsev, 2017).

The development of new sources of UCN is being actively carried out all over the world, some of them are based on the use of solid deuterium at a temperature of 4.5 K (LANL, USA; PSI, Switzerland), while others are based on the accumulation of UCN in superfluid helium (KEK-RCNP-TRIUMF, Japan-Canada; ILL, France) (Serebrov et al., 2011). Similar work is intensively carried out in Russia: the Neutron Laboratory at the Joint Institute for Nuclear Research (Dubna) and the St. Petersburg Institute of Nuclear Physics (PNPI). In Gatchina, work is underway to create a high-intensity source of UCN. With its help, they hope to obtain data that will give answers to the most important questions of modern physics. The designed source will make it possible to obtain a flux of ultracold neutrons (UCN) with a density of 10^4 cm^{-3} , which is many times higher than the maximum densities now achieved (Serebrov et al., 2011). This task – obtaining intense UCN flows – is today considered one of the priorities in neutron physics. A more and more increase in the density of UCNs will inevitably lead to the question of their possible condensation and the production of a condensed neutron substance under laboratory conditions, such as space.

Not so long ago, a decisive breakthrough was made into a new area: a radically new type of matter, the so-called Bose condensates of atoms of matter, was created. Are neutron condensates possible? Condensates whose density and strength will be comparable to the density and strength of atomic nuclei. In other words, how close have they come to the frontier of creating cosmic neutron matter in the laboratory today?

The 2001 Nobel Prize in Physics was awarded to researchers Eric A. Cornell, Wolfgang Ketterle and Carl E. Wieman for obtaining and investigating the properties of the fifth state of matter – the Bose-Einstein condensate, they were able to get the first Bose condensate (Cornell et al., 2003). It was possible to do this using methods developed shortly before this, in addition to cooling particles by laser beams and magnetic field. The Bose condensate of atoms was obtained in a form convenient for research and laboratory analysis. Soon reports of the receipt of Bose condensates of various atoms sprinkled from everywhere. Scientists were greatly encouraged by the fact that Bose condensate plants were relatively inexpensive – experiments were well underway in many countries. Soon, methods were also found for producing Bose condensates of half-integer spin particles, fermions, which include neutrons. In them, particles combine in pairs, then collecting in the Bose condensate. In many properties, neutrons are close to the lightest atoms.

For example, the mass of a neutron is almost equal to the mass of a hydrogen atom, the Bose condensate of which was obtained by Ketterle in 1997. But, unlike atomic Bose condensates, whose natural compression during Bose condensation is an insurmountable obstacle to their electron shells, nothing prevents the compression of the neutron Bose condensate. In such a condensate, UCN gas forms pairs with opposite spins; upon reaching critical density and

temperature, it spontaneously shrinks to almost nuclear density when nuclear forces come into play, forming a stable state – a condensed neutron substance. If in space a stable polynuclear substance is formed at ultrahigh pressures, then on Earth it will be obtained at ultra-low temperatures with a sufficient concentration of UCNs, which sooner or later researchers will come to receive.

4. Conclusion

Thus, neutron matter in our time is a very specific physical reality that urgently requires its rightful place in the PS and the study of not only physical, but also chemical, and possibly in the near future, and engineering properties. A neutron substance, or rather an element corresponding to it, begins (zero period) and ends (supercritical atoms) PS elements. The neutron substance is given stability already at the micro level due to the additional (Tamm, Hund, Migdal) interaction, and not only at the macro level due to gravitational interaction, as is now believed in astrophysics. The possibility of polyneutronization is shown not only due to gravitational interaction, but also by other mechanisms (supercritical increase in the sequence number of elements and condensation of UCNs), thus, there is a fundamental possibility of obtaining neutron matter in Earth conditions (at $Z \gg 175$, $N > 10^3 - 10^5$ and the size of 200-300 or more femtometers). Neutron matter is a necessary link (bridge) from micro to macro and mega-world, from free neutron to neutron stars and black holes. Such an extremely concentrated substance is the thermodynamically and statistically most stable state of matter as such. This substance can be represented as a set of densely packed neutrons, with scattered residual protons and electrons among them.

Now it is believed that almost all chemical elements appeared in the “thermonuclear reactors” of stars and supernovae. The Big Bang prepared only fuel for them: a few of the lightest elements. The lion's share fell on hydrogen, which so far (and by a wide margin) remains the most abundant in the Universe. However, in small amounts, helium, beryllium, and lithium formed at the same time.

Theorists explained with good accuracy why they were formed in one or another quantity. With one exception: the content of lithium in the Universe cannot be predicted by modern models. The isotope of lithium-7 is three times less than that obtained in theory, and lithium-6 is several orders of magnitude more. This non-docking remains a real headache for cosmology: it is not possible to “fit” the Big Bang model under it, and some suitable explanations call into question the Big Bang itself.

Thus, it is necessary to take into account the possibility of the formation of neutron matter fragments as dark matter (neutrality, femto-, pico- and nano-sizes, relict cooling make them difficult to detect) already at the initial moments of the birth of the Universe, which is the dominant process, and not thermonuclear fusion from initial small amount of protons. Next, the process goes according to the generally accepted scenario.

Neutron matter fits consistently into the original concept of the Periodic Law and the System put forward by Dmitry Ivanovich Mendeleev, the 150th anniversary of which we celebrate this year (Mendeleev, 1934; Ryazantsev et al., 2018).

References

- Cornell E. A., Wieman C.E., Ketterle W.: 2003, *UFN*, **173**, №12, 1319 <http://ufn.ru/ru/articles/2003/12/c/>.
- Dobrotin R.B. et al.: 1984, *Letopis' zhizni i deyatel'nosti D.I.Mendeleeva*. Ed. Storonkin A.V., L.: Nauka (in Russian).
- Gamow G.: 1946, *Phys. Rev.*, **70**, 572.
- Hund F.: 1936, *Ergebnisse der exakten Naturwissenschaften*, **15**, 189.
- Ignatovich V. K.: 1996, *UFN*, **166**, №3, 303.
- Mendeleev D. I.: 1934, Sochineniya. L.-M., T.2 /Eds. A.N.Bakha, B.N.Vyropaeva, I.A.Kablukova et al., L.: Goskhimtekhnizdat, 520 s. (in Russian).
- Mendeleev D.I.: 1991, *Granits poznaniya predvidet' nevozmozhno*. Sobranie rabot. Ed.: Yu.I. Solov'ev, M. (in Russian).
- Migdal A.B.: 1983, *Teoriya konechnykh Fermi sistem i svoystva atomnykh yader*, M.: Nauka, Glavnaya redaktsiya fiziko-matematicheskoy literatury, 54 p. (in Russian).
- Potekhin A.Yu.: 2010, *UFN*, **180**, №12, 1279.
- Ryazantsev G. B., Lavrenchenko G. K.: 2014, *Tekhnicheskije gazy*. №1, 3-10 (in Russian).
- Ryazantsev G. B.: 2014, *Nauka i zhizn'*, № 2, 76 <http://www.nkj.ru/archive/articles/23734/> (in Russian).
- Ryazantsev G. B., Lavrenchenko G. K.: 2016, *Tekhnicheskije gazy*. №4, 41 (in Russian).
- Ryazantsev G.B., Lavrenchenko G.K., Khaskov M.A., Beckman I.N.: 2017, *ISINN-24. 24th International Seminar on Interaction of Neutron with Nucle*. Dubna, JINR, Russia, 65.
- Ryazantsev G.B., Lavrenchenko G.K., Beckman I. N., Buntseva I. M., Nedovesov S. S.: 2018, *Odessa Astron. Publ.*, **31**, 33.
- Ryazantsev G.B., Lavrenchenko G.K., Beckman I.N., Buntseva I.M.: 2018, *18-th Gamow Summer School*. Odessa, Ukraine, Abstracts, 15.
- Ryazantsev G.B., Beckman I.N., Lavrenchenko G.K., Buntseva I. M., Nedovesov S.S.: 2019, *ISINN-26. 26th International Seminar on Interaction of Neutrons with Nuclei*. Dubna, JINR, Russia, 37.
- Shapiro F.L.: 1976, *Sobranie trudov*. Moskva: Nauka, **2**, 348 (in Russian).
- Serebrov A.P. et al.: 2011, *Physics Procedia*, **17**, 251.
- Tamm I.E.: 1975, *Sobranie nauchnykh trudov*, T.1, Nauka, M., 283 (in Russian).
- Zel'dovich Ya.B., Popov V.S.: 1971, *UFN*, **105**, 403.
- Zwicky F.: 1958, *Publications of the Astronomical Society of the Pacific*, **70**, № 416, 506.

Наукове видання

Одеські Астрономічні Публікації

том 32 (2019)

Англійською мовою

Технічний редактор *В. В. Ковтюх*
Комп'ютерна верстка *С. Л. Страхова*

Підписано до друку 19.12.19.
Формат 60x84/8. Папір офсетний. Друк різнограф.
Ум. друк. арк. 24,99. Обл.-вид. арк. 28.0. Тираж 300 екз. Зам. № .

Друкарня ТОВ "ПРОМАРТ"
61023, Харків, вул. Весніна, б. 12, оф. 17
Свідоцтво про внесення до Держреєстру суб'єкта видавничої справи
серія ДК №5748 від 06.11.2017 р.
тел. (057) 717-28-80

